

UNIVERSITY OF WESTERN MACEDONIA  
FACULTY OF ENGINEERING  
DEPARTMENT OF MECHANICAL ENGINEERING

PhD Thesis

Tzoulia Kraia

Mechanical Engineer

*"Remediation of Black Sea ecosystem through H<sub>2</sub>S decomposition in conventional catalytic converters and proton conducting solid oxide membrane reactors for "Green" H<sub>2</sub> production"*

Supervisor: Associate Professor George E. Marnellos

KOZANI

JUNE, 2017





ΔΙΔΑΚΤΟΡΙΚΗ ΔΙΑΤΡΙΒΗ

ΚΡΑΪΑ Γ. ΤΖΟΥΛΙΑΝΑΣ

Διπλωματούχου Μηχανολόγου Μηχανικού

*«Παραγωγή  $H_2$  μέσω της διάσπασης του  $H_2S$  της  
Μαύρης Θάλασσας σε συμβατικούς καταλυτικούς  
μετατροπείς και σε αντιδραστήρες μεμβράνης  
στερεού ηλεκτρολύτη αγωγών πρωτονίων»*

Επιβλέπων: Αναπληρωτής Καθηγητής Γεώργιος Ε. Μαρνέλλος

ΚΟΖΑΝΗ

ΙΟΥΝΙΟΣ, 2017



PhD Thesis

Tzouliana Kraia

Mechanical Engineer

*"Remediation of Black Sea ecosystem through H<sub>2</sub>S decomposition in conventional catalytic converters and proton conducting solid oxide membrane reactors for "Green" H<sub>2</sub> production"*

Submitted to the Department of Mechanical Engineering,  
University of Western Macedonia

Defended June 14, 2017

Committee Member

Associate Professor George E. Marnellos, Dissertation Committee chair

---

Dr. Spyridon Voutetakis, Three-member Advisory Committee

---

Associate Professor Vassilis Stathopoulos, Three-member Advisory Committee

---

Associate Professor Michalis Konsolakis, Seven-member Examining Committee

---

Associate Professor Dimitris Tsiplakidis, Seven-member Examining Committee

---

Assistant Professor Eleni Heracleous, Seven-member Examining Committee

---

Dr. Kyriakos Panopoulos, Seven-member Examining Committee

---

The work was performed within the frame of the joint program Black-Sea ERA.NET under the FP-7 initiative of the European Commission and funded by the Greek General Secretariat for Research and Technology GSRT (grant No. 11BS\_10\_28).



Part of this work was realized via the program “Scholarships of IKY in the Marine and Inland Management of Water Resources” (Contract Nr. 11) and was co-funded by EEA grants– Financial Mechanism 2009–2014 (85%) and the General Secretariat for Investments and Development (15%).



## ACKNOWLEDGEMENTS

I dreamed, during my bachelor studies, of doing scientific research, which came true after the completion of my master. The past 5 years were a great journey and learning period in research, education and well-being. Finally, this PhD journey is finished and it gives me the immense pleasure to acknowledge my sincere thanks to the people who have helped me directly or indirectly, by being always there, supportive to make this day possible.

First of all and foremost, my sincere and deepest gratitude to my “Scientific Father” and supervisor *Associate Professor George Marmellos* for selecting and providing me this great opportunity to work in such an interesting topic. His guidance, support, fruitful discussions and new ideas were most essential into developing me the researcher that I am today. I am extremely fortunate to have him as advisor.

I would like to thank *Dr. Spyridon Voutetakis, Researcher A*; and the whole personnel of Laboratory of Process Systems Design and Implementation (LPSDI), Chemical Process and Energy Resources Institute (CPERI), Centre for Research and Technology Hellas (CERTH), where this PhD work was completed (2012-2017). In order to have everything under control, credits for many things related to reactors, gas lines, chemicals and generally everything that constitutes an experiment go to **Panagiotis Tampareskos, Aris Moudiotis, Dimitris Fardis** and **Marios Nikiforakis**. Without their creative, fast and uncomplicated help, none of the experiments would have worked like they did.

My thanks also to *Associate Professor Vassilis Stathopoulos*, for his helpful encouragement, support and his patience through some of the most challenging times of my PhD career.

Special acknowledgements to *Associate Professor Michalis Konsolakis*, who improved my writing and analytical thinking, for his sincere support and important suggestions about the material synthesis and the results throughout this PhD. Our cooperation, which was extended in a cheerful and friendly manner, will be always memorable. His inclinations and hunger towards research have been a source of inspiration for me.

I would like also to thank the **rest of my doctoral committee members Associate Professor Eleni Heracleous** and *Dr. Kuriakos Panopoulos, Researcher B*; for their insightful comments, valuable suggestions and constructive criticism.

I especially acknowledge the contribution and astounding approachability of *Associate Professor Dimitrios Tsiplakidis* and *Researcher B*; *Dr. Stella Balomenou*. Their helpful discussions and pointed questions were integral part of this PhD work. I would like to share my sincere gratitude to *Dr. Kalliopi Papazisi*, for the valuable discussions regarding the scientific work, for the good moments and for all the things she taught me related to research and beyond, in my early steps in the “scientific world”.

This doctoral thesis was performed within the frame of the joint program *Black-Sea ERANET* under the FP-7 initiative of the European Commission and funded by the Greek General Secretariat for

Research and Technology GSRT (grant No. 11BS\_10\_28), which is gratefully acknowledged. I would like to thank *Professor Roland Dittmeyer* who invited and gave me the excellent opportunity to travel to Karlsruhe, Germany and stay in the Institute of Micro Process Engineering (IMVT), Karlsruhe Institute of Technology (KIT) for one month to perform experiments in the frame of BS-ERA.NET H<sub>2</sub>S-PROTON project.

Parts of the electrochemical studies were carried out during the exchange collaborative research visit at the group of Solid State Electrochemistry (FASE), under the *IKY-EEA 2014-2015 Scholarship Programme*, the time period from January to September 2016 (9 months). I knew only basic about the proton conducting membrane reactors until I met *Professor Truls Norby* who brought me into the wonderful world of solid state proton conductors and electrochemistry. I would like to express my gratitude to Professor Norby, who gave me the opportunity to work at his group lab Fermio, Oslo, Norway. It has been a great learning experience and I am certain it is something that will shape my future. I would like also to thank my co-supervisors *Dr. Ragnar Strandbakke* and *Dr. Einar Vøllestad*, who have been immensely helpful throughout my entire visit at their laboratory. I am thankful to the whole research group for both their help and input in scientific discussions and the pleasant office environment created by all and especially to *Dr. Sebastian Wachowski* for his sharing knowledge and patience during my stay in Oslo. We also had very funny moments and jokes in the coffee room.

I have to say thanks to my “roommates” *Dr. Zisis Ioakeimidis, Dr. Ioannis Garagounis, Angeliki, Maria, Thodoris, Alexis and Tasos* for their friendship, support and nice chats during our breaks. I would like also to name those in my personal life, who inspired me and made my life full of various positive contributions with their friendship, *Alexandra, Nikos, Theologos, Anna, Elpida, Sofia, Sany, Maria, Xaris, Xristos, Elissavet* and *Christos*. I feel really fortunate for my two big true “research” friendships, *Dr. Anna Karapatsia* and *Dr. Jovana Milencovic*. I could not imagine myself without their physical appearance, during the completion of my PhD career.

My heartfelt gratitude to *Dr. Giannis Penloglou*. He has been patient and supportive throughout the completion of this PhD and especially during the past few months. I think there are no words to describe his indispensable moral support, guidance, understanding and patience. He was instrumental at this achievement as he challenged me to grow as an individual.

My infinite love to my *parents Georgios and Sofia*, because all I have accomplished in my life is the result of their unconditional love and years of sacrifice. My dad is the hardest working person I know and I am inspired by his success, while my mom with her great heart, she taught me that kind of person I am. Thanks to *Stergios*, my brother, who was always there for me and encouraged during all endeavors.

*Tzouliana Kraia*

*...It is not just a piece of paper*

*... It's a feeling!*

*Dedicated to my beloved Family and to You...*



# Abstract

The emerging energy and environmental concerns have recently forced the society to utilize “clean” energy resources and develop efficient energy conversion technologies. Hydrogen sulfide ( $H_2S$ ) is abundantly found in Black Sea waters and hails as an important  $H_2$  source, while its efficient removal from Black Sea waters will protect the surrounding ecosystem. Various processes have been suggested to produce hydrogen from  $H_2S$  decomposition, which are currently at different stages of development. The most commonly employed method is the catalytic decomposition of  $H_2S$ , which however takes place at high temperatures in order to achieve conversions exceeding 80%. A novel approach based on stable ceramic  $H^+$  conducting electrochemical reactor is proposed here, which could also act as a method to eliminate  $H_2S$  emissions in petroleum hydro-treatment operations, natural gas and coal gasification industries. In the present PhD thesis,  $H_2S$  electrolysis is carried out in a proton-conducting ceramic electrochemical membrane reactor. In specific,  $H_2S$  diluted in excess  $H_2O$  (simulating the mixture derived from Black Sea waters) is fed at the anode, while the cathode is exposed to oxidizing conditions. When an anodic overpotential is applied,  $H_2S$  and  $H_2O$  are electrolyzed producing  $H^+$ , which are transferred to cathode where the evolution of  $H_2$  takes place. Thus, pure  $H_2$  is generated and separated in a single stage.

In such a complex process, the major issue is to identify efficient and stable catalyst composites to be applied as anode material for this reactor. In this context and prior to the electrochemical tests, a series of catalysts, namely, i) 20 wt.% Cu supported REOs (Cu/REOs), ii) 20 wt.% Cu supported  $Ce_{1-x}Sm_xO_8$  (20 wt.% Cu/ $Ce_{1-x}Sm_xO_8$ ), iii) ceria supported transition metal (Co, Ni, Fe and Cu) and iv) bimetallic ( $Cu_{20-x}Co_x/CeO_2$ ) ( $x = 0, 5, 10, 15, 20$  wt.%), were synthesized via the wet impregnation method and evaluated in terms of their activity and stability towards  $H_2S$  decomposition in the absence/presence of excess  $H_2O$ . The Co/ $CeO_2$  sample demonstrated the optimum activity and stability performance both in absence and presence of  $H_2O$ , reaching  $H_2S$  conversions close to those predicted by the reaction equilibrium (34% at 850 °C). An initial activation period was found to be necessary for the establishment of a steady-state, due to the progressive reduction/sulfation of the catalyst's counterparts under the reaction conditions. The superior behaviour of the  $Co_3O_4/CeO_2$

catalyst was attributed to the in-situ formation of highly active and stable sulfated phases (i.e.,  $\text{Co}_{1-x}\text{S}_y$  and  $\text{Ce}_{10}\text{S}_{14}\text{O}_y$ ) from its counterparts during the  $\text{H}_2\text{S}$  decomposition reaction.

In general, the optimization of suitable electrode materials is a fundamental step in the development of tolerant and efficient electrochemical membrane reactor cells. In this work,  $\text{BaZr}_{0.7}\text{Ce}_{0.2}\text{Y}_{0.1}\text{O}_3$  (BZCY72) was selected as the solid electrolyte and  $\text{Co}_3\text{O}_4\text{-CeO}_2$  mixed oxide was employed as the anodic electrode, while  $\text{BaGd}_{0.8}\text{La}_{0.2}\text{Co}_2\text{O}_{6-\delta}$  (BGLC) perovskite was used as the cathode. Various methods and thermal treatments were examined to fabricate a conductive cell, which was physicochemically characterized with XRD and SEM methods. The corresponding electrochemical characterization involved polarization, AC impedance and electrocatalytic studies under  $\text{H}_2/\text{H}_2\text{O}$  and  $\text{H}_2\text{S}/\text{H}_2\text{O}$  mixtures at 900-1200 K and atmospheric pressure. It was revealed that, in the presence of  $\text{H}_2/\text{H}_2\text{O}$ , the optimum performance was achieved at  $T = 850\text{ }^\circ\text{C}$ ,  $p_{\text{H}_2} = 10\text{ kPa}$  and  $p_{\text{H}_2\text{O}} = 2.5\text{ kPa}$  with an ohmic resistance of  $22\text{ Ohm}\cdot\text{cm}^2$  and polarization resistance equal to  $8\text{ Ohm}\cdot\text{cm}^2$ . The most crucial step affecting the electrode performance was found to be the diffusion of protons to the electrochemical active three-phase boundary (electrode/electrolyte/gas phase), which was additionally hindered at high hydrogen and steam partial pressures due to the charge space effect. In the presence of  $\text{H}_2\text{S}/\text{H}_2\text{O}$ , cobalt and cerium were in-situ converted to sulphides, which presented a beneficial effect on the performance and durability of the cell, thus leading to a strong increase of conductivity. In addition the in-situ rearrangement of conductive phases improved the in plane conductivity leading to higher proton fluxes. A high electrochemical performance is a prerequisite for the implementation of the present electrochemical-aided concept, opening new horizons for the efficient management of  $\text{H}_2\text{S}$ -containing streams in industrial (refineries) and natural (Black Sea, geothermal wells) sources.

Finally, the feasibility of an integrated scaled up process towards the remediation of the Black Sea ecosystem and  $\text{H}_2$  generation through the co-electrolysis of rich  $\text{H}_2\text{S}/\text{H}_2\text{O}$  mixtures was examined. Two different process flow diagrams were developed and assessed depending on the downstream management options of the generated  $\text{SO}_2$  by-product. Both process flow diagrams were assessed in terms of operating flexibility, electricity/heat requirements and economic criteria. It was found that the proposed technology is initially far from economically affordable for any investor. On the other hand, as it was thoroughly discussed in the present thesis, the utilization of Black Sea  $\text{H}_2\text{S}$  is stimulated more from

environmental and social motivations than from economic. Though, taking into account the great emphasis given by the European and the nearby countries on the amelioration of the Black Sea ecosystem, an additional “optimized” scenario is assessed to realistically evaluate the technical, economical and, in the same time, the environmental sustainability of the designed plants.



# Περίληψη

Οι παγκόσμιες απαιτήσεις σε ενέργεια βαίνουν διαρκώς αυξανόμενες εξαιτίας της συνεχούς αύξησης του πληθυσμού, της ανάπτυξης και του βιοτικού επιπέδου. Συνεπώς, νέες πηγές ενέργειας, καθαρές και σε αφθονία, πρέπει να υιοθετηθούν για την κάλυψη των παγκόσμιων ενεργειακών αναγκών. Το υδρογόνο ( $H_2$ ) ως καύσιμο μπορεί να αποτελέσει σημαντικό ενεργειακό φορέα στο μέλλον. Προς την κατεύθυνση αυτή το υδρόθειο ( $H_2S$ ), το οποίο βρίσκεται σε αφθονία στα ύδατα του Εύξεινου Πόντου, παρά τις επιβλαβείς επιπτώσεις στην ανθρώπινη υγεία και στο οικοσύστημα της Μαύρης Θάλασσας μπορεί να αποτελέσει μια αξιόπιστη μελλοντική πηγή ενέργειας. Η παραγωγή  $H_2$  από  $H_2S$  μπορεί να επιτευχθεί με τη χρήση διαφόρων διεργασιών, με την ηλεκτροχημική μέθοδο να θεωρείται ως η πλέον υποσχόμενη προσέγγιση προς τη ζητούμενη κατεύθυνση. Ειδικότερα, οι ηλεκτροχημικοί αντιδραστήρες μεμβράνης στερεού ηλεκτρολύτη αγωγού πρωτονίων μπορούν να αποτελέσουν μια πολύ αποτελεσματική και ταυτόχρονα οικονομική λύση για την παραγωγή  $H_2$  από  $H_2S$ . Καθοριστικής σημασίας προς την ανάπτυξη της προτεινόμενης μεθόδου αποτελεί ωστόσο η σύνθεση καινοτόμων υλικών, τα οποία θα επιδεικνύουν υψηλή ηλεκτρονιακή αγωγιμότητα, ηλεκτροκαταλυτική ενεργότητα και θα ανθίστανται στην παρουσία  $H_2S$ , προκειμένου να χρησιμοποιηθούν ως ανοδικά ηλεκτρόδια κατά την ηλεκτροχημική διάσπαση του  $H_2S$  προς  $H_2$ .

Στο πλαίσιο αυτό, και πριν από τις ηλεκτροχημικές δοκιμές, στην παρούσα διδακτορική διατριβή εξετάστηκε αρχικά η καταλυτική διάσπαση του  $H_2S$  απουσία και παρουσία περίσσειας  $H_2O$  σε μια σειρά καταλυτικών συστημάτων (20 κ.β.% Cu/REOs, 20 κ.β.% Cu/Ce<sub>1-x</sub>Sm<sub>x</sub>O<sub>δ</sub>, 20 κ.β.% M/CeO<sub>2</sub>, Cu<sub>20-x</sub>Co<sub>x</sub>/CeO<sub>2</sub>). Η αξιολόγηση τους υπέδειξε την υπεροχή των καταλυτών Co/CeO<sub>2</sub>, τόσο ως προς την ενεργότητα, όσο και ως προς την σταθερότητα τους, καθώς επέτυχαν τις υψηλότερες μετατροπές σε όλο το εύρος των θερμοκρασιών, καθώς επίσης και αξιοσημείωτη σταθερότητα. Η ανωτερότητα τους αποδίδεται στα εν γένη χαρακτηριστικά του Co και στον επί τόπου σχηματισμό θειούχων ενώσεων (Co<sub>1-x</sub>S<sub>y</sub> and Ce<sub>10</sub>S<sub>14</sub>O<sub>γ</sub>) από τα αρχικά συστατικά του καταλύτη, οι οποίες εμφανίζονται εξαιρετικά δραστικές και σταθερές κατά τη καταλυτική διάσπαση του  $H_2S$  προς παραγωγή  $H_2$ .

Σε μια τόσο πολύπλοκη διαδικασία, ένα από τα σημαντικότερα ζητήματα όπως αναφέρθηκε παραπάνω, είναι η επιλογή των βέλτιστων υλικών του ηλεκτροχημικού αντιδραστήρα. Βάσει όλων των παραπάνω τελικώς αναπτύχθηκαν μικτά οξειδία  $\text{Co}_3\text{O}_4\text{-CeO}_2$  τα οποία χρησιμοποιήθηκαν ως ανοδικά ηλεκτρόδια, ενώ ως στερεός ηλεκτρολύτης επιλέχθηκε ο  $\text{BaZr}_{0.7}\text{Ce}_{0.2}\text{Y}_{0.1}\text{O}_3$  (BZCY72) και ως κάθοδος χρησιμοποιήθηκε ο περοβοσκίτης  $\text{BaGd}_{0.8}\text{La}_{0.2}\text{Co}_2\text{O}_{6-\delta}$  (BGLC). Αρχικά, πραγματοποιήθηκε ο φυσικοχημικός χαρακτηρισμός των οξειδίων προκειμένου να αναγνωριστούν τα βασικά δομικά χαρακτηριστικά τους. Στην συνέχεια ακολούθησε ο ηλεκτροχημικός χαρακτηρισμός σε αντιδρώντα μίγματα  $\text{H}_2/\text{H}_2\text{O}$  και  $\text{H}_2\text{S}/\text{H}_2\text{O}$ , σε θερμοκρασιακό εύρος 650-850 °C και σε ατμοσφαιρική πίεση. Διαπιστώθηκε ότι παρουσία  $\text{H}_2/\text{H}_2\text{O}$  η βέλτιστη απόδοση επιτεύχθηκε στους  $T = 850$  °C,  $p_{\text{H}_2} = 10$  kPa και  $p_{\text{H}_2\text{O}} = 2,5$  kPa, με ωμική αντίσταση  $22 \text{ Ohm}\cdot\text{cm}^2$  και αντίσταση πόλωσης ίση με  $8 \text{ Ohm}\cdot\text{cm}^2$ . Βρέθηκε ότι το κύριο στάδιο που επηρεάζει την διεπιφανειακή (ηλεκτρόδιο/ηλεκτρολύτης) αντίσταση ήταν η διάχυση των πρωτονίων προς την ηλεκτροχημικά ενεργή τριεπιφάνεια. Παρουσία  $\text{H}_2\text{S}/\text{H}_2\text{O}$ , τόσο το  $\text{Co}_3\text{O}_4$  όσο και το  $\text{CeO}_2$  μετατράπηκαν σε σουλφίδια, τα οποία παρουσίασαν ευεργετική επίδραση στην ηλεκτροχημική απόδοση και ανθεκτικότητα του συστήματος. Τα ιδιαίτερα ενθαρρυντικά αποτελέσματα παρουσία  $\text{H}_2\text{S}$  αποδόθηκαν εκτός από την θείωση των συστατικών του ηλεκτροδίου και στην αναδιάταξη των αγώγιμων φάσεων του ηλεκτροδίου συμβάλλοντας στην επέκταση της ηλεκτροχημικά ενεργής ζώνης σε σχέση με το ηλεκτρόδιο  $\text{Co}_3\text{O}_4/\text{CeO}_2$  απουσία μιγμάτων  $\text{H}_2\text{S}$ . Η υψηλή αγωγιμότητα αποτελεί αναγκαία προϋπόθεση για την εφαρμογή αυτού του υλικού ως ηλεκτρόδιο, ανοίγοντας νέους ορίζοντες για την αποτελεσματική διαχείριση βιομηχανικών (διυλιστήρια) ή φυσικών (Μαύρη Θάλασσα, γεωθερμικές πηγές) μιγμάτων που περιέχουν  $\text{H}_2\text{S}$ .

Τέλος, στην παρούσα εργασία παρουσιάστηκε μία ολοκληρωμένη μελέτη σχεδιασμού ενός αυτόνομου συστήματος παραγωγής υδρογόνου μέσω διάσπασης  $\text{H}_2\text{S}$ , προερχόμενο από τη Μαύρη Θάλασσα, με σκοπό τόσο την αποκατάσταση του οικοσυστήματος της, όσο και της παραγωγής  $\text{H}_2$  μέσω της ταυτόχρονης ηλεκτρόλυσης μιγμάτων  $\text{H}_2\text{S}/\text{H}_2\text{O}$ . Δύο διαφορετικά διαγράμματα ροής αναπτύχθηκαν και αξιολογήθηκαν από άποψη λειτουργικής ευελιξίας, απαιτήσεων ηλεκτρικής ενέργειας/θερμότητας και οικονομικών κριτηρίων, ως προς τη διαχείριση του παραγόμενου παραπροϊόντος  $\text{SO}_2$ . Αρχικά, διαπιστώθηκε πως η προτεινόμενη τεχνολογία είναι μη οικονομικά προσιτή για κάθε επενδυτή. Όμως, έχοντας

ως γνώμονα, όπως αναλύεται διεξοδικά στην παρούσα διατριβή, πως η χρήση του H<sub>2</sub>S της Μαύρης Θάλασσας είναι περισσότερο υποκινούμενη από περιβαλλοντικά και κοινωνικά κίνητρα παρά από οικονομικά και λαμβάνοντας υπόψη το μεγάλο ενδιαφέρον που δίνουν οι ευρωπαϊκές και οι γειτονικές χώρες για τη βελτίωση του οικοσυστήματος της Μαύρης Θάλασσας, αξιολογείται ένα πρόσθετο «βελτιστοποιημένο» σενάριο για τη ρεαλιστική αποτίμηση της τεχνικής, οικονομικής και ταυτόχρονα περιβαλλοντικής βιωσιμότητας της προτεινόμενης μελέτης.



# Contents

Chapter	Page
Abstract	i
Περίληψη	v
Contents	ix
Chapter 1 - INTRODUCTION	1
1.1. PREFACE	3
1.2. SCOPE	5
1.3. ADDED VALUE	7
1.4. OUTLINE	7
REFERENCES	12
Chapter 2 - THE BLACK SEA H <sub>2</sub> S POTENTIAL AS AN ALTERNATIVE H <sub>2</sub> SOURCE	13
2.1. INTRODUCTION	15
2.2. PRESENT ENERGY STATUS	15
2.2.1. Conventional Energy and Fuels	16
2.2.2. The Evolution of the Energy Mix	16
2.2.3. Energy Consumption	17
2.2.4. Major Energy Policies and Directives	19
2.3. HYDROGEN: A MODERN RENEWABLE ENERGY RESOURCE	20
2.3.1. Hydrogen: Characteristics, Benefits and Drawbacks	21
2.3.2. Hydrogen as an Energy Vector	23
2.3.3. Hydrogen Production Methods	24
2.4. PRODUCTION OF HYDROGEN FROM HYDROGEN SULFIDE	30
2.4.1. H <sub>2</sub> S Properties and Characteristics	31
2.4.2. H <sub>2</sub> S Sources	33
2.4.3. Methods for Hydrogen Production from H <sub>2</sub> S	34
2.5. PRODUCTION OF HYDROGEN FROM BLACK SEA H <sub>2</sub> S	39
2.5.1. Black Sea	39
2.5.2. H <sub>2</sub> S in Black Sea Waters	41
2.5.3. H <sub>2</sub> S Production in Black Sea Waters	42
2.5.4. H <sub>2</sub> S Contribution to Environmental Degradation in Black Sea	43
2.5.5. Environmental Security Policy in Black Sea	45
2.5.6. Extraction and Utilization of Hydrogen Sulfide from Black Sea waters	45
REFERENCES	48
Chapter 3 - PROTON CONDUCTORS	53

<b>3.1. INTRODUCTION</b>	<b>55</b>
<b>3.2. SOLID ELECTROLYTES: DEFINITION AND TYPES</b>	<b>55</b>
<b>3.3. PROTON CONDUCTORS, H<sup>+</sup></b>	<b>58</b>
3.3.1. Low Temperature Proton Conductors	59
3.3.2. Proton Conductors in the Temperature Range of 100-190 °C	59
3.3.3. Proton Conductors in the Temperature Range of 190-350 °C	60
3.3.4. High Temperature Proton Conductors (T>400 °C)	61
<b>3.4. PROTON CONDUCTOR MEMBRANE REACTORS: OPERATION AND DESIGN</b>	<b>65</b>
<b>3.5. APPLICATIONS OF PROTON CONDUCTOR MEMBRANE REACTORS</b>	<b>66</b>
3.5.1. Selective Conduction of Ions	67
3.5.2. Electrochemical Promotion of Catalytic Reactions	68
3.5.3. Chemical Cogeneration	69
3.5.4. Methane Conversion to C <sub>2</sub> Hydrocarbons	71
3.5.5. Other Reactions of Methane Activation	73
3.5.6. Decomposition of Alcohols	75
3.5.7. Reactions of Alkanes and Alkenes	75
3.5.8. Forward and Reverse Water Gas Shift	77
3.5.9. Steam Electrolysis	78
3.5.10. Ammonia Synthesis and Decomposition	78
3.5.11. Decomposition and Reduction of NO <sub>x</sub>	82
3.5.12. Hydrogen Sulfide Decomposition	82
<b>3.6. CONCLUSIONS</b>	<b>86</b>
<b>REFERENCES</b>	<b>87</b>
<b>PART I - H<sub>2</sub>S CATALYTIC DECOMPOSITION IN H<sub>2</sub>O ABSENCE/PRESENCE</b>	<b>95</b>
<b>I.1. INTRODUCTION</b>	<b>97</b>
I.1.1. Thermodynamic Calculations	101
<b>REFERENCES</b>	<b>104</b>
<b>Chapter 4 - MATERIALS AND METHODS</b>	<b>107</b>
<b>4.1. INTRODUCTION</b>	<b>109</b>
<b>4.2. CATALYSTS PREPARATION</b>	<b>110</b>
4.2.1. Impregnated Catalysts	111
4.2.2. Drying	112
4.2.3. Calcination	113
4.2.4. Grinding	113
<b>4.3. MATERIALS</b>	<b>114</b>
<b>4.4. CHARACTERIZATION METHODS</b>	<b>116</b>
4.4.1. Textural Characterization (BET)	116
4.4.2. Structural Characterization (XRD)	117
4.4.3. Morphological Characterization (SEM)	117

4.4.4. Surface Characterization (XPS)	117
4.4.5. Chemical Analysis	118
<b>4.5. EXPERIMENTAL EQUIPMENT AND SAMPLE PREPARATION</b>	<b>118</b>
4.5.1. Design Considerations	118
4.5.2. Description of Individual Units	121
4.5.2.1. Feedstock Section	121
4.5.2.2. Reaction Section	122
4.5.2.3. Analysis Section	124
4.5.3. Procedure	126
4.5.3.1. Initiation of the Experiment	126
4.5.3.2. Process Operation	127
4.5.3.3. Completion of the Experiment	127
4.5.4. Testing of the Experimental Set-up	129
4.5.5. Safety Precautions	129
<b>REFERENCES</b>	<b>129</b>
<b>Chapter 5 - H<sub>2</sub>S CATALYTIC DECOMPOSITION IN THE ABSENCE OF H<sub>2</sub>O</b>	<b>131</b>
<b>5.1. INTRODUCTION</b>	<b>133</b>
<b>5.2. H<sub>2</sub>S CATALYTIC DECOMPOSITION OVER 20 wt.% Cu/REOs</b>	<b>133</b>
5.2.1. Textural and Structural Characterization (BET and XRD Analysis) of 20 wt.% Cu/REOs Catalysts	133
5.2.2. Surface Characterization (XPS Analysis) of 20 wt.% Cu/REOs Catalysts	135
5.2.3. Reducibility Studies (H <sub>2</sub> -TPR) of 20 wt.% Cu/REOs Catalysts	138
5.2.4. Surface Morphology (SEM/EDAX) of 20 wt.% Cu/CeO <sub>2</sub> Catalysts	140
5.2.5. Catalytic Activity Studies - Effect of Support Type (REOs)	140
<b>5.3. H<sub>2</sub>S CATALYTIC DECOMPOSITION OVER 20 wt.% Cu/Ce<sub>1-x</sub>Sm<sub>x</sub>O<sub>8</sub> CATALYSTS</b>	<b>142</b>
5.3.1. Textural and Structural Characterization (BET and XRD Analysis)	142
5.3.2. Catalytic Activity Studies	144
<b>5.4. H<sub>2</sub>S CATALYTIC DECOMPOSITION OVER CERIA SUPPORTED TRANSITION METAL (Co, Ni, Fe and Cu) CATALYSTS</b>	<b>145</b>
5.4.1. Textural and Structural Characterization (BET and XRD Analysis)	146
5.4.2. Surface Characterization of M/CeO <sub>2</sub> Catalysts	149
5.4.3. Surface Morphology (SEM/EDAX) of 20 wt.% Co/CeO <sub>2</sub> Catalysts	151
5.4.4. Catalytic Activity Studies – Effect of Metal Type in H <sub>2</sub> S Decomposition	151
<b>5.5. H<sub>2</sub>S CATALYTIC DECOMPOSITION OVER BIMETALLIC (Cu<sub>20-x</sub>Co<sub>x</sub>/CeO<sub>2</sub>) (x = 0, 5, 10, 15, 20 wt.%) CATALYSTS</b>	<b>155</b>
5.5.1. Textural and Structural Characterization (BET and XRD Analysis) of Bimetallic Cu <sub>20-x</sub> Co <sub>x</sub> /CeO <sub>2</sub> (x = 0, 5, 10, 15, 20 wt.%) Catalysts	155
5.5.2. Surface Characterization of Bimetallic Cu <sub>20-x</sub> Co <sub>x</sub> /CeO <sub>2</sub> (x = 0, 5, 10, 15, 20 wt.%) Catalysts	158
5.5.3. Catalytic Activity Studies - Effect of the Surface Support of Cu <sub>20-x</sub> Co <sub>x</sub> /CeO <sub>2</sub> (x = 0, 5,	

10, 15, 20 wt.%) Catalysts	161
5.6. STABILITY TESTS OVER OPTIMUM 20 wt.% Co/CeO <sub>2</sub> CATALYST	163
5.7 "AGED" OPTIMUM 20 wt.% Co/CeO <sub>2</sub> CATALYSTS CHARACTERIZATION	166
REFERENCES	171
Chapter 6 - H <sub>2</sub> S CATALYTIC DECOMPOSITION IN THE PRESENCE OF H <sub>2</sub> O	175
6.1. INTRODUCTION	177
6.2. CHARACTERIZATION STUDIES	177
6.3. CATALYTIC EVALUATION STUDIES	178
6.3.1. Effect of the Reaction Conditions	178
6.3.2. Effect of Co-Loading (0-100 wt.%)	179
6.3.3. Comparison of Optimum Catalytic Systems in the Absence/Presence of H <sub>2</sub> O	180
6.4. STABILITY TESTS OVER THE OPTIMUM CATALYTIC SYSTEM	182
6.5. 30 wt.% Co/CeO <sub>2</sub> "SULFATED" CATALYST CHARACTERIZATION	186
REFERENCES	190
PART II - DEVELOPMENT OF PROTON CONDUCTING ELECTROCHEMICAL CELLS FOR H <sub>2</sub> S ELECTROLYSIS	193
II.1. INTRODUCTION	195
REFERENCES	199
Chapter 7 - EXPERIMENTAL METHODS, EQUIPMENT AND TECHNIQUES	201
7.1. INTRODUCTION	203
7.2. CELL FABRICATION	203
7.2.1. H <sup>+</sup> Conducting Solid Electrolyte/Membrane, BaZr <sub>0.7</sub> Ce <sub>0.2</sub> Y <sub>0.1</sub> O <sub>3</sub> (BZCY72)	204
7.2.2. Anode Electrode, Co <sub>3</sub> O <sub>4</sub> Supported on CeO <sub>2</sub> Catalysts (Co <sub>3</sub> O <sub>4</sub> /CeO <sub>2</sub> )	205
7.2.3. Counter Electrode, BaGd <sub>0.8</sub> La <sub>0.2</sub> Co <sub>2</sub> O <sub>6-δ</sub> (BGLC)	206
7.3. EFFICIENT ELECTRODE DEPOSITION ON BZCY72 TECHNIQUES	206
7.3.1. Basic Principle	207
7.3.1.1. Ink Formulation	208
7.3.1.2. Drying Step	209
7.3.1.3. Sintering Step	209
7.3.2. Anode Electrode, Co <sub>3</sub> O <sub>4</sub> Supported on CeO <sub>2</sub> Catalysts (Co <sub>3</sub> O <sub>4</sub> /CeO <sub>2</sub> )	210
7.3.3. Counter Electrode, BaGd <sub>0.8</sub> La <sub>0.2</sub> Co <sub>2</sub> O <sub>6-δ</sub> (BGLC)	211
7.3.4. Final Electrodes Processing Methods	212
7.4. CHARACTERIZATION STUDIES	213
7.4.1. H <sup>+</sup> Conducting Solid Electrolyte/Membrane, BaZr <sub>0.7</sub> Ce <sub>0.2</sub> Y <sub>0.1</sub> O <sub>3</sub> (BZCY72)	213
7.4.2. Anode Electrode, Co <sub>3</sub> O <sub>4</sub> Supported on CeO <sub>2</sub> Catalysts (Co <sub>3</sub> O <sub>4</sub> /CeO <sub>2</sub> )	214
7.4.3. Counter Electrode, BaGd <sub>0.8</sub> La <sub>0.2</sub> Co <sub>2</sub> O <sub>6-δ</sub> (BGLC)	215
7.5. EXPERIMENTAL SETUP, REACTOR DESIGN AND PROCEDURE	217
7.5.1. Electrochemical Performance Employing Ideal (H <sub>2</sub> /H <sub>2</sub> O/Ar Mixtures) Reaction	

Conditions	217
7.5.1.1. Gas Flow and Temperature Control	217
7.5.1.2. The Reactor Cell System	218
7.5.1.3. Electrochemical Measurements	220
7.5.2. Electrochemical Performance of the Cell, Employing H <sub>2</sub> S/H <sub>2</sub> O/Ar Reaction Conditions, Single Chamber	221
7.5.2.1. Gas Flow and Temperature Control	221
7.5.2.2. The Reactor Cell System	222
7.5.2.3. Electrochemical Measurements	224
7.5.3. Electrochemical Performance of the Cell, Employing H <sub>2</sub> /Ar and H <sub>2</sub> S/H <sub>2</sub> O/Ar Mixtures Reaction Conditions, Double Chamber	225
7.5.3.1. Gas Flow and Temperature Control	226
7.5.3.2. The Reactor Cell System	227
7.5.3.3. Electrochemical Measurements	229
<b>7.6. THEORY</b>	<b>229</b>
7.6.1. Electrochemical Impedance Spectroscopy (EIS)	229
7.6.2. Equivalent Circuit Models	232
<b>REFERENCES</b>	<b>233</b>
<b>Chapter 8 - ELECTROCHEMICAL EXPERIMENTS</b>	<b>235</b>
<b>8.1. ELECTROCHEMICAL CHARACTERIZATION OF CO<sub>3</sub>O<sub>4</sub>/CEO<sub>2</sub> MIXED OXIDE ELECTRODE IN A PROTON CONDUCTING SOLID OXIDE SYMMETRICAL CELL</b>	<b>237</b>
8.1.1. Effect of Cell Temperature at Dry and Wet Hydrogen Containing Mixtures	237
8.1.2. Effect of Hydrogen Partial Pressure	244
<b>8.2. ELECTROCHEMICAL PERFORMANCE OF A CO<sub>3</sub>O<sub>4</sub>- CEO<sub>2</sub>/BZCY72/CO<sub>3</sub>O<sub>4</sub>- CEO<sub>2</sub> PROTON CONDUCTING SOLID OXIDE CELL FED WITH H<sub>2</sub>S/H<sub>2</sub>O MIXTURES</b>	<b>246</b>
8.2.1. Effect of H <sub>2</sub> S Feed Concentration	247
8.2.2. Effect of Cell Temperature	250
8.2.3. Physicochemical Characterization Studies	252
8.2.4. Electrochemical Performance of a Co <sub>3</sub> O <sub>4</sub> -CeO <sub>2</sub> /BZCY72/BGLC Proton Conducting Solid Oxide Cell Fed with H <sub>2</sub> S/H <sub>2</sub> O Mixtures	256
<b>REFERENCES</b>	<b>257</b>
<b>Chapter 9 - PRELIMINARY FEASIBILITY STUDY OF THE INTEGRATED APPROACH</b>	<b>259</b>
<b>9.1. INTRODUCTION</b>	<b>261</b>
<b>9.2. PROCESS FLOW DIAGRAM DEVELOPMENT AND BRIEF DESCRIPTION</b>	<b>261</b>
9.2.1. Process Flow Diagram 1 Description: Production of H <sub>2</sub> SO <sub>4</sub> through SO <sub>3</sub> Absorption/Reaction in H <sub>2</sub> O	262
9.2.2. Process Flow Diagram 2 Description: Production of H <sub>2</sub> SO <sub>4</sub> through SO <sub>2</sub> and Iodine Cycle	264
<b>9.3. MASS AND ENERGY BALANCES</b>	<b>269</b>

9.3.1. Process Flow Diagram 1 Description: Production of H <sub>2</sub> SO <sub>4</sub> through SO <sub>3</sub> Absorption/Reaction in H <sub>2</sub> O	269
9.3.2. Process Flow Diagram 2 Description: Production of H <sub>2</sub> SO <sub>4</sub> through SO <sub>2</sub> and Iodine Cycle	270
<b>9.4. ECONOMIC EVALUATION AND OVERALL ASSESSMENT</b>	<b>272</b>
9.4.1. Equipment Sizing, Dimensioning and Related Costs	272
9.4.1.1. Reactors/Distillation Columns	272
9.4.1.2. Heat Exchangers	273
9.4.1.3. Pumps	273
9.4.1.4. Flash Tanks/Storage Vessels	274
9.4.1.5. Compressors/Turbines	274
9.4.1.6. Furnace	275
9.4.1.7. Electrolyzer	275
9.4.1.8. Purchased Equipment Cost	275
9.4.2. Economic Analysis of the Overall Process	276
9.4.2.1. Material/Energy Utilities and Product Related Costs	278
9.4.2.2. Fixed Capital Cost Calculations and Operational Expenses	279
9.4.2.3. Economic Indices and Final Assessment	279
<b>REFERENCES</b>	<b>284</b>
<b>Chapter 10 - CONCLUSIONS AND SUGGESTIONS FOR FUTURE RESEARCH</b>	<b>285</b>
<b>10.1. CONCLUSIONS</b>	<b>287</b>
10.1.1. Overall Concept	287
10.1.2. H <sub>2</sub> S Catalytic Decomposition in the Absence/Presence of H <sub>2</sub> O	289
10.1.3. H <sub>2</sub> S Electrolysis in the Proton (H <sup>+</sup> ) Conducting Electrochemical Membrane Reactor	293
10.1.4. Feasibility Analysis	295
<b>10.2. SUGGESTIONS FOR FUTURE RESEARCH</b>	<b>296</b>

# CHAPTER

# 1

## INTRODUCTION

Contents	Page
1.1. Preface. . . . .	3
1.2. Scope. . . . .	5
1.3. Added value. . . . .	7
1.4. Outline. . . . .	7
References. . . . .	12



## 1.1. PREFACE

As energy is crucial for global growth and development and the energy demands constantly increase, the past and present dependence on non-Renewable Energy Sources has led to severe socio-economic and environmental implications (Armor, 1999). Therefore, a worldwide energy policy, based on clean energy sources and efficient conversion technologies, has to be adopted. In this framework, H<sub>2</sub> has the potential to become one of the major future energy “currencies”. Among others, H<sub>2</sub>S that is abundantly found in Black Sea waters can be considered as an important H<sub>2</sub> source (Reverberi et al., 2016). Generally, the Black Sea is unique, because 90% of its water is under anaerobic conditions and contains H<sub>2</sub>S, with a content that steadily increases with depth: to 0.36 mmol/l at 1,000 m, 0.38 mmol/l at 2,000 m, up to 0.60 mmol/l at the bottom (Naman and Veziroğlu, 2013; Baykara et al., 2007). Apart from the well-known harmful effects of the Black Sea H<sub>2</sub>S to human health and the surrounding ecosystem Black Sea may serve as one of the world’s largest hydrogen sulfide deposit which, in fact, could be a source of commodity sulfur, as well as, energy. If assume that annual increase of hydrogen sulfide of the Black Sea is not less than 4-9 million of tones, then the total of its reserves could be estimated by fairly impressive value of 28-63 billion of tones (Azarenkov et al., 2014). From theoretical calculations, it is estimated that it could be possible to produce 270 Mio. tons of H<sub>2</sub> ( $3.83 \cdot 10^{19}$  J thermal or  $8.97 \cdot 10^{15}$  Wh electrical energy), energetically equivalent to 808 Mio. tons of gasoline or 766 Mio. tons of natural gas (Midilli et al., 2007). As a consequence, if H<sub>2</sub> is to be produced from Black Sea H<sub>2</sub>S, the energy demands of the regional countries can be partially compensated and surplus H<sub>2</sub> fuel can be transported to Europe.

In principle, the hydrogen production process from Black Sea H<sub>2</sub>S consists of the following steps (Figure 1.1):

- Pumping sea water from approximately 1,000 m depth.
- Extraction of concentrated H<sub>2</sub>S/H<sub>2</sub>O mixtures.
- Enrichment of H<sub>2</sub>S concentration in the H<sub>2</sub>S/H<sub>2</sub>O mixtures from 12-14 to 10,000 ppm.
- Electrolysis of H<sub>2</sub>S/H<sub>2</sub>O gas mixtures at high temperatures, leading to H<sub>2</sub> production, or employment of the produced H<sub>2</sub> in a fuel cell (under regenerative mode) for the co-generation of electricity and heat.

The decomposition of  $H_2S$  to  $H_2$  can be achieved using various technologies, categorized as thermal, thermochemical, electrochemical, photochemical and plasmochemical methods (Zaman and Chakma, 1995). Both thermal and thermochemical processes require high temperatures (1,000-1,200 K). Moreover, the plasmochemical and photochemical methods are presently in an early stage of development. Therefore, the electrochemical process, which operates at intermediate temperatures (700-1,000 K), is considered as the most promising approach.

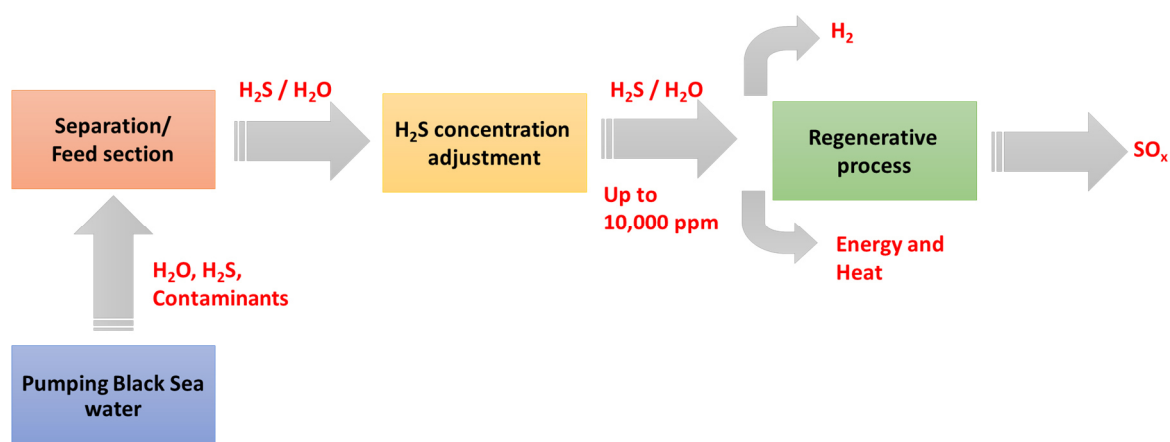


**Figure 1.1:** Schematic flowsheet of the  $H_2$  production from Black Sea  $H_2S$  process, up to the major step of  $H_2S$  electrochemical decomposition.

Thus, the central idea of the present PhD thesis is to develop and utilize an electrochemical membrane reactor for the remediation of the Black Sea ecosystem, through the decomposition of  $H_2S$  in conventional catalytic and proton conducting solid oxide membrane reactors for “green”  $H_2$  production. Great focus is given upon the construction of a  $H_2S$  tolerant, active and electrochemically conductive anode composite.

It should be highlighted that the work described in the present PhD thesis was carried out both in the Laboratory of Process Systems Design and Implementation (PSDI) of the Chemical Process and Energy Resources Institute (CPERI) of the Centre for Research and Technology Hellas (CERTH), located in Thessaloniki, Greece, and in the Department of Mechanical Engineering of the University of Western Macedonia (UOWM), located in Kozani, Greece, under the supervision of Associate Professor George Marnellos. It comprises the main contribution of the Greek partner to the International research Black Sea ERA.NET

project, which was funded by the the General Secretariat for Research and Technology (GSRT) Hellas. The international collaborating partners in this project were the Department of Chemical Engineering of the Yildiz Technical University (YTU), Turkey (Professor Baykara) and the Institute for Micro Process Engineering (IMVT) of the Karlsruhe Institute of Technology (KIT), Germany (Professor Dittmeyer).

Notice that for brevity purposes and in an attempt to minimize any confusion, both for the author and the reader, a list of references has been compiled separately for each chapter (appearing at the end), rather than a large combined list at the end of the complete thesis.

## 1.2. SCOPE

In the general concept of ameliorating the environmental threat that  $\text{H}_2\text{S}$  constitutes for the Black Sea environment, addressing in the same time the energy security problem, by producing a clean and renewable energy vector (i.e.,  $\text{H}_2$ ), the present thesis focuses on the study of the electrochemical decomposition of  $\text{H}_2\text{S}$ . The selected method is already a well-known and well-established technology, offering significant advantages over alternative methodologies, though it needs to be optimized and intensified towards the efficient and cost-effective production of  $\text{H}_2$ . The critical step of the proposed  $\text{H}_2\text{S}$  utilization method is its decomposition to  $\text{H}_2$  and S in the  $\text{H}^+$  conducting solid electrolyte membrane reactor. The significant advantages of this stable ceramic  $\text{H}^+$  conductor is that it can be applied both in electrochemical reactors and fuel cells, operate at easily achieved by the current technology temperatures (around  $800\text{ }^\circ\text{C}$ ) and promote shifting of the reaction equilibrium, due to the  $\text{H}^+$  transportation.

The major parts of these type of electrochemical reactors are the porous anode and cathode and the dense solid electrolyte membrane. In the proposed approach, the anode is exposed to  $\text{H}_2\text{S}/\text{H}_2\text{O}$  mixtures to facilitate the decomposition of  $\text{H}_2\text{S}$  to  $\text{H}^+$  and S. Thereupon, the generated protons migrate through the membrane to the air-exposed cathode, where they are either converted to  $\text{H}_2$  (hydrogen pumping mode) or to  $\text{H}_2\text{O}$  for power generation (fuel cell mode). Generally, the proton conductor solid electrolyte membrane reactor can be connected to: a) a voltmeter, b) an external resistance, or c) an external current source, as can be seen in Figure 1.2. In case a), the catalyst properties and the reaction mechanisms

can be studied by altering the voltage value. In case b), the reactor is utilized as an electrochemical hydrogen pump. Finally, in case c), the reactor operates as a fuel cell by converting chemical into electrical energy.

For the completion of this multi-disciplinary approach, there are clear objectives to be addressed, such as, the production of  $H_2$  with high purity, the efficient separation in the proton reactor and the maximization of the  $H_2$  production rate (achieved by manipulating the equilibrium of the  $H_2S$  decomposition reactions and by introducing the electrochemical promotion approach). To this end, the excess hydrogen production can be utilized for the generation of additional heat and power at the proton electrolyte membrane reactor, via the fuel cell operation. The thermally autonomous and flexible operation routes of the process are also challenges that need to be successfully overcome.

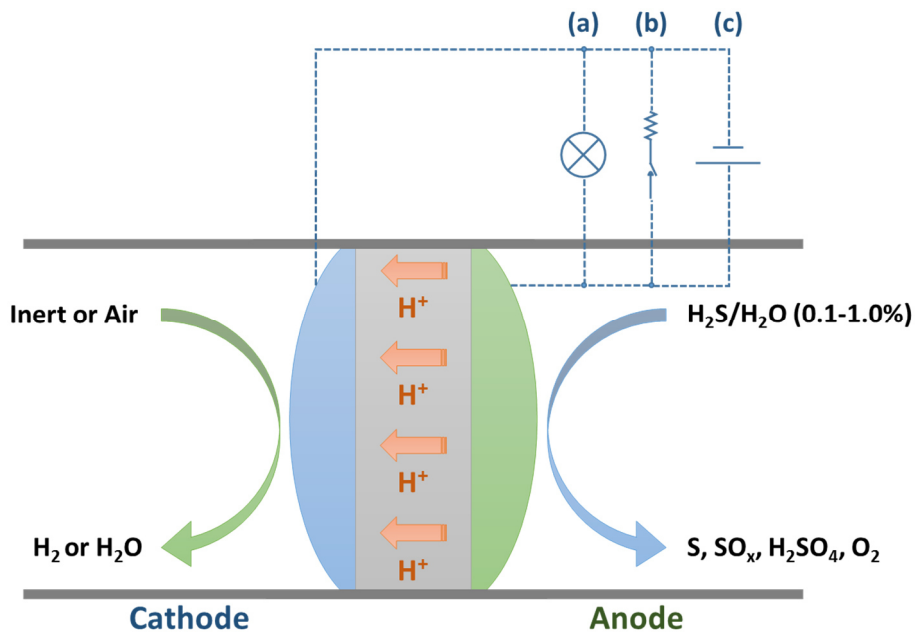


**Figure 1.2:** Schematic of the Proton Conductor Solid Electrolyte Membrane Reactor.

Other requirements that need to be taken into consideration involve the materials used for the development of the  $H^+$  solid electrolyte membrane reactor. The reactor should be constructed from materials that are tolerant to  $H_2S$  and, in the same time, present high ionic conductivity (at 700-1,000 K), mechanical tolerance and chemical stability. Moreover, the porous electrodes should be also tolerant and present efficient mechanical strength against

the corrosion potential of  $H_2S$ . Finally, both electrodes need to be constructed using materials with large electronic conductivity and catalytic activity.

### 1.3. ADDED VALUE

Nowadays, it is accepted that hydrogen is a promising solution for securing a sustainable growth and addressing the large worldwide dependence on fossil fuels. As the latter are presently the cornerstones of the world economic development, their extensive use is steadily leading to the depletion of their sources, raising the question whether they will be able to meet the increased energy demands of the future. Moreover, their environmental impact is seriously negative and does not meet the present requirements of a sustainable society and economy. The core of the proposed technology is to address the key issue of diversifying energy supply, by developing methods and processes that will exploit the great hydrogen potential of Black Sea waters. A positive side-effect is the reduction of the  $H_2S$  level in the marine ecosystem. This concept will enable the regional countries to partially fulfill their energy requirements from this source and possibly to export surplus hydrogen.

In the Black Sea region countries,  $H_2$  is a possible mean for securing their energy supply for the future. With the exception of Russia and Azerbaijan, most other countries of the region are energy importers. As a result,  $H_2$  can play a significant role for these countries in developing their independent industries for energy supply. This could provide a significant opportunity for the regional countries to secure their economic growth and increase their economic immunity to potential crises related to fuels supply. A further positive aspect of the utilization of  $H_2$  fuel from Black Sea for the surrounding countries is the promotion of cooperation among them. More specifically, collaboration in the areas of industrial development and operation of the relevant infrastructure, chemical and power plants will be necessary, when large-scale hydrogen production and utilization will become reality.

### 1.4. OUTLINE

The present PhD dissertation is structured in ten chapters that are briefly described below. Chapter 1 summarizes the incentives of the research, the scope of the work implementation,

along with the potential impact, and the structure of the dissertation itself. The primary objective of the present work is to develop an innovative electrochemical membrane reactor, which contains a solid electrolyte proton conductor, for the production of  $H_2$  via the decomposition of Black Sea  $H_2S$ . Thus, the aim is to demonstrate the transformation of an environmental threat into a potential source of “pure” hydrogen ( $H_2$ ). Particular emphasis is given to the selection, synthesis and physicochemical/electrochemical characterization of efficient and innovative reactor materials (electrodes and solid electrolyte), for their utilization in solid oxide proton conductor cells, when using concentrated  $H_2S/H_2O$  mixtures as feedstock. This combination may potentially have a significant contribution to a sustainable energy future. Therefore, the objective is dual and is related with the protection of the Black Sea ecosystem and the production of “renewable”  $H_2$ .

In Chapters 2 and 3, the theoretical background of the research is presented. More specifically, Chapter 2 highlights the energy challenge and analyzes the necessity for exploration, exploitation and adoption of new alternative and renewable forms of energy, as well as, for environmentally friendly energy conversion technologies. Thus, the current trend of primarily covering the global energy needs via the use of fossil fuels can be reversed. To this end, the reasons why  $H_2$  constitutes an excellent energy carrier are explored and its basic production technologies are described in detail. Following, there is an extensive literature review on the various  $H_2$  production methods from  $H_2S$ , with particular emphasis on the electrochemical method, while the case of  $H_2S$  presence in abundance at the Black Sea waters is also analyzed. Despite its harmful effects on human health and the Black Sea ecosystem,  $H_2S$  can deliver significant amounts of  $H_2$  through its decomposition. Finally, the general characteristics of the Black Sea, the amount of  $H_2S$  present in its waters, the general environmental concerns, as well as, the methods of extraction and separation of  $H_2S$  are also described.

In Chapter 3, an overview of the state-of-the-art, regarding the solid electrolytes and the operating principles of solid oxide cells, is initially presented. More specifically, focus is given on the general properties of solid electrolytes and their classification. Among them, the different types of  $H^+$  ion conductors and their properties are discussed in more detail. Special emphasis is placed upon the high-temperature ceramic proton conductors (HTPC), which include the proton conductors based on perovskite mixed oxides, since the BZCY72 solid

electrolytes, used in this doctoral thesis, belong to this category. Finally, the progress over the last decades on proton conductivity electrochemical solid electrolyte membrane reactors (PCMRs) is also presented.

The majority of the remaining chapters of this thesis are separated in two parts. Part I contains the experimental work on the catalytic hydrogen sulfide decomposition for hydrogen production, both in the presence and absence of water excess. Part I includes Chapters 4, 5 and 6. In more detail, Chapter 4 lists and compares the most significant methodologies for the preparation of catalysts. Among them, the wet impregnation method is selected and applied in this dissertation. Moreover, the techniques used for the physicochemical characterization of the catalysts are also described. In particular, the catalysts were characterized using a plethora of structural (BET, XRD, SEM, EDS) and surface techniques (XPS). The aforementioned techniques were used to verify the success of the synthesis methodology, as well as, to correlate the activity and performance of the catalysts with their structural and surface properties. Furthermore, a separate section is dedicated to the detailed presentation of the entire list of catalysts prepared and tested. In the next step, the experimental apparatus used to perform the catalytic experiments and measurements for the decomposition of hydrogen sulphide to hydrogen, is described. Finally, the operating principles and conditions of the experimental-analytical devices and instruments and the remaining upstream and downstream equipment are analysed.

In Chapters 5 and 6, the experimental results, obtained during the decomposition reaction of  $\text{H}_2\text{S}$ , in the absence and presence of  $\text{H}_2\text{O}$ , respectively, are presented and analysed. In order to evaluate the developed catalytic systems, both the activity and stability of all catalysts is measured and compared. In particular, in Chapter 5, the investigation of the catalytic decomposition of  $\text{H}_2\text{S}$  to  $\text{H}_2$  in the absence of  $\text{H}_2\text{O}$ , in initially conducted using Cu-based catalysts, supported on rare earth oxides (i.e.,  $\text{La}_2\text{O}_3$ ,  $\text{CeO}_2$ ,  $\text{Sm}_2\text{O}_3$ ,  $\text{Pr}_6\text{O}_{11}$ ,  $\text{Nd}_2\text{O}_3$ ,  $\text{Gd}_2\text{O}_3$ ). The objective is to identify an active catalyst with the properties and general potential to be used in direct hydrogen sulphide feed in SOFCs applications. Subsequently, the possibility of structural reinforcement of the Cu/ $\text{CeO}_2$  optimum catalyst, via the synthesis of mixed  $\text{Ce}_{1-x}\text{Sm}_x\text{O}_\delta$  (where  $x = 0, 0.25, 0.5, 0.75$  and  $1$ ) oxides as carriers, is investigated. In parallel, the effect of the pure oxides on the  $\text{H}_2\text{S}$  decomposition reaction is thoroughly studied. Additionally, the significant effect of the metal type on the catalytic activity of the employed

catalysts is investigated, with respect to the selected transition metal catalysts (i.e., Co, Ni, Fe and Cu), supported on CeO<sub>2</sub>. In an attempt to optimize the efficiency of the catalytic system, the enhancement of the catalysts active Co phase via the presence of a second transition metal (Cu) is also explored. To do so, various parameters like the operating temperature and the Cu/Co ratio of the Cu<sub>20-x</sub>Co<sub>x</sub>/CeO<sub>2</sub> (x = 0, 5, 10, 15, 20) catalysts are considered. Finally, the efficiency of the established as optimal catalyst (i.e., 20 wt.% Co/CeO<sub>2</sub>), during long-term stability experiments is also presented, along with the relevant physicochemical characterization studies.

In Chapter 6, the examination of the optimum catalytic systems (originally discovered under “dry” conditions), regarding their activity and stability is performed under conditions that simulate the Black Sea water. Thus, the catalytic study of H<sub>2</sub>S decomposition in the presence of H<sub>2</sub>O is conducted to identify, evaluate and select the optimum catalytic systems under “wet” conditions. Initially, activity tests are performed to study the effect of the operating temperature under different feedstock compositions. Moreover, the experimental investigation is extended to include the effect of the net oxide system. In all cases, the quantitative results are accompanied by the qualitative characterization of the catalysts.

The second part (Part II) of this dissertation deals with the experimental findings on the electrochemical dissociation of hydrogen sulfide to hydrogen, in the presence of excess water and consists of Chapters 7 and 8. In more detail, in Chapter 7, the methodology used for the preparation and deposition of materials (solid electrolyte and electrodes), the construction of the reactor and the interconnection of all electrochemical devices, is discussed. Moreover, all the conducted electrochemical measurements, associated with the electrochemical characterization of the electrodes, are analyzed. Finally, the geometries used for the electrochemical reactors and their impact on the process behavior are also described.

In Chapter 8, which is the last experimental section of this thesis, the electrochemical results, obtained when using mixtures of H<sub>2</sub> and H<sub>2</sub>S/H<sub>2</sub>O as the feedstock of a symmetrical ceramic cell proton conductor, based on BZCY72 solid electrolyte and Co<sub>3</sub>O<sub>4</sub>/CeO<sub>2</sub> electrode, are firstly presented. The electrochemical phenomena at the electrode-electrolyte interface are examined for different temperatures and feedstock compositions, using electrochemical

impedance spectroscopy techniques and polarization phenomena. The electrochemical experiments are conducted in a ProboStat single chamber reactor.

In Chapter 9, the objectives are extended to include a detailed techno-economic analysis and assessment of the proposed technology. The analysis focuses on the design, optimization and economic evaluation of an integrated process, which takes into account the process steps for the collection and utilization of the contained in the Black Sea water  $H_2S$  for the production of  $H_2$ . The sustainability assessment is performed at a scale high enough to theoretically support the potential industrial implementation of the proposed technology (i.e.,  $H_2$  capacity of 100 kg/hr).

Finally, the PhD dissertation is completed with the presentation of the main conclusions, as well as, with recommendations for future research (Chapter 10).

In conclusion, this thesis is characterized by scientific excellence and originality and includes the following new elements:

- Insights about the correlation of the physicochemical properties of the used materials with their catalytic and electrochemical performance. By using several physicochemical and surface characterization methods, particular emphasis was given to identify the links between the surface chemical and structural morphology of the catalysts, and their catalytic activity and stability, towards  $H_2$  production, during the decomposition of  $H_2S$ . The tailor-made structural and surface modification of the catalysts, and, consequently, the control of their physicochemical and electron qualities (reducibility, oxidation state), can be now facilitated, depending on the designated reaction and process.
- Development of resistant  $Co_3O_4/CeO_2$  electrodes for the simultaneous electrolysis of  $H_2S$  and  $H_2O$  in ceramic proton conductor cells. Specifically, the present thesis innovates in terms of the generation of active and stable catalysts/electrodes, in conditions that involve mixtures of  $H_2S/H_2O$ .
- A technical and economic feasibility study to investigate the major aspects and perspectives of the integrated process, designed to efficiently exploit the Black Sea  $H_2S$  for the production of  $H_2$ .

## REFERENCES

- Armor J.N. (1999). Striving for catalytically green processes in the 21<sup>st</sup> century. *Applied Catalysis A: General*, 189: pp. 153-162.
- Azarenkov N.A., Borts B.V., Tkachenko V.I. (2014). Hydrogen sulfide energy of the Black Sea. *East European Journal of Physics*, 1: pp. 4-21.
- Baykara S.Z., Figen E.H., Kale A., Veziroglu T.N. (2007). Hydrogen from hydrogen sulphide in the Black Sea. *International Journal Hydrogen Energy*, 32: pp. 1246-1250.
- Midili A., Ay M., Kale A., Veziroglu T.N. (2007). A parametric investigation of hydrogen energy potential based on H<sub>2</sub>S in Black Sea deep waters. *International Journal of Hydrogen Energy*, 32: pp. 117-124.
- Naman S.A., Veziroğlu A. (2013). The low cost hydrogen production from hydrogen sulfide in Black Sea. In: Veziroğlu A., Tsitskishvili M. (Eds.), *Black Sea Energy Resource Development and Hydrogen Energy Problems*. NATO Science for Peace and Security Series C: Environmental Security. Springer, Dordrecht.
- Reverberi A.P., Klemes J.J., Varbanov P.S., Fabiano B. (2016). A review on hydrogen production from hydrogen sulphide by chemical and photochemical methods. *Journal of Cleaner Production*, 136: pp. 72-80.
- Zaman J., Chakma A. (1995). Production of hydrogen and sulfur from hydrogen sulfide. *Fuel Processing Technology*, 41: pp. 159-198.

# CHAPTER

# 2

## THE BLACK SEA H<sub>2</sub>S POTENTIAL AS AN ALTERNATIVE H<sub>2</sub> SOURCE

Contents	Page
2.1. Introduction. . . . .	15
2.2. Present energy status. . . . .	15
2.3. Hydrogen: a modern renewable energy source. . . . .	20
2.4. Production of hydrogen from hydrogen sulfide. . . . .	30
2.5. Production of hydrogen from Black Sea H <sub>2</sub> S. . . . .	39
References. . . . .	48



## 2.1. INTRODUCTION

It is well known that the global energy demands constantly increase due to the worldwide urbanization and despite several on-going regulations and directives the energy resources are diminishing. For many decades now, crude oil has been and still is the most important fuel and energy source, which drives the whole world and fuels the global economy. As the Earth's population continuous to rise (by 2025 it is expected to exceed 8 billion persons) the primary problems that the human race faces today are energy security, climate change, air pollution and quality and global warming (Dorokhina and Tessema, 2011).

As a result, there is an urgent need for clean and renewable energy sources to reduce the associated environmental problems and improve energy efficiency. In this context, many governmental energy departments, research and environmental institutes and industries focus on renewable energy resources (RES) (Kaltschmitt and Streicher, 2007). To achieve near zero or at least low carbon societies, strong decisions need to be made to replace or improve the present energy technologies and to introduce innovative and efficient energy systems (Stambouli et al., 2002). More specifically, the abatement of CO<sub>2</sub> and other greenhouse gases (GHG) in stationary and transportation sources is a critical issue; an immediate plan towards full exploitation of RES is also needed to shift to more environmentally sustainable societies. Among RES (e.g., solar, wind and tidal energy, biomass, etc.) hydrogen, combined with novel conversion technologies, such as fuel cells, is one of the emerging, though presently unexploited, sources with large potential (Kleijn and Der Voet, 2010). Beyond the wide acceptance that H<sub>2</sub> has gained as an energy carrier during the last decades, there are many technologic, economic and political challenges that need to be addressed prior to a successful transition to a hydrogen, and in general, to a renewable energy economy.

## 2.2. PRESENT ENERGY STATUS

Recently, energy has become one of the major issues that attract the interest of the global society. Energy is used to provide house heat and lighting, power for mechanical equipment, transportation fuels for vehicles, and, in general, comforts and conveniences accustomed

during the industrial age. Energy is derived from many different sources, but the most utilized form until now is energy from fossil resources.

### 2.2.1. Conventional Energy and Fuels

Fossil fuels, which are presently combusted in vehicles, homes, industries and power generation plants, were naturally formed in microorganisms' tissues approximately 100-500 million years ago. Originally, the energy of fossil fuels came from the conversion of solar to chemical energy via photosynthesis, in a really slow process. In more detail, the chemical energy contained in living tissues concentrated in compressed hydrocarbon compounds, due to the decomposition of tissues. Thus, fossil fuels can be produced only when organic materials are broken down in anaerobic environments (e.g., bottoms of lakes, swamps and shallow seas). Despite that it took nature millions of years to generate these resources, within few decades fossil fuels will be depleted by their neglectfully use (Dutta et al., 2014).

As the global power and energy needs almost run ahead of supply, due to the constantly increasing demands at alarming rate, the recent severe energy crisis has forced the world to develop new and alternative methods for power generation, which though cannot be adopted so far due to several barriers (e.g., efficiency of the resources, production cost, etc.). It is also widely recognized that the fossil fuels (coal, petroleum and natural gas) may not be sufficient or suitable to keep pace with these increasing demands. Moreover, the utilization of fossil resources towards energy generation causes pollution, which is likely to be more acute in future, due to the large capacity and the greater awareness of people in this respect (Barreto et al., 2003; Dincer, 1999).

### 2.2.2. The Evolution of the Energy Mix

From immemorial times, humans have developed methods of exploiting available materials and resources, in order to produce heat and energy and cover every day vital needs. During antiquity era, wood burning was the major method used for such purposes. Later on, along with the world population growth, wood became less obtainable and a new source of fuel, coal, emerged. Especially during the Industrial Revolution, coal was massively used to fuel steam engines and produce mechanical power. The second critical point at the evolution of

the energy mix was the exploitation of petroleum. Having a significant larger calorific value than that of coal (i.e., 43,000 kJ/kg for petroleum, instead of 15,000-27,000 kJ/kg for coal), petroleum gradually substituted the older energy forms; until now it owns a dominant position. Natural gas came to the forefront in the mid-20<sup>th</sup> century as a 'modern' energy source, which can partially cover the energy demands and contribute to the environmental sustainability, due to its low GHG emissions compared to petroleum (Goltsov et al., 2006).

Lately, renewable forms of energy have gained major interest in response to the significant problems of the extensive utilization of fossil fuels (Ohta, 2006; James et al., 2011). However, despite their strong potential, RES still face significant obstacles. For instance, solar, wind and tidal energy are not continually available, thus the energy derived from those sources must be immediately used. In addition, biomass suffers from a short-term storage capacity, while geothermal energy is retained underground until needed. As a result, until today it is easier and cheaper to dig or drill for fossil fuels than to extract energy from renewable sources (Rand and Dell, 2007).

Presently, the idea of introducing hydrogen as an energy carrier in fuel cells and batteries is approved with enthusiasm. H<sub>2</sub> is considered as an alternative and clean energy source that can be obtained from any primary energy source. However, due to its ability to form strong covalent compounds with most elements, elemental hydrogen cannot be found in significant amounts on Earth, but mostly in compounds. A major advantage is that there are no CO<sub>2</sub> gas emissions through hydrogen combustion, while water can be obtained. Therefore, H<sub>2</sub> can definitely contribute to the mitigation of GHG emissions, provided that a non-polluting source of hydrogen is utilized (Midilli et al., 2005). By all means, hydrogen can provide a promising pathway to achieve sustainability in the future energy sector (Barreto et al., 2003).

### 2.2.3. Energy Consumption

The large increase in energy consumption during the last two centuries is strongly linked to several problems, since the energy economy is supported by a system that is vulnerable, socially unbalanced and detrimental to the environment (Rand and Dell, 2007). These problems are more evident today, as many of the resources are limited and the relevant reserves are worryingly reducing. For instance, it seems that the peak in oil production has

been already reached and the peak in coal production is predicted for the near future (2025). As a result, the current energy model is becoming obsolete (Muldera et al., 2007).

The global society has evolved from consuming 1 billion tons of oil equivalent (toe) in 1910 to more than 12 billion toe in 2010, as can be seen in Figure 2.1 (BP, 2016). Despite the decrease in 2009 (the first one since 1982), there was a growth of 5.6% immediately after (2010), which represents the highest recorded since 1973. In 2015, the world primary energy consumption grew by a below-average 1%, the slowest growth rate since 1998.

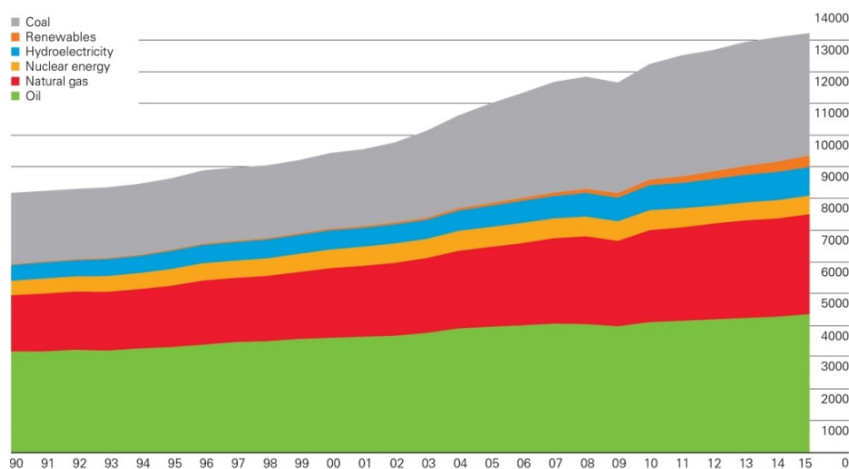


**Figure 2.1:** World primary energy consumption (1990-2015) in million tons of oil equivalent (toe) per fuel type (BP, 2016).

A similar growth rate is expected for the years to come; in 2035 the world primary energy consumption is estimated to exceed the 17 billion toe mark (Figure 2.2) (BP, 2016). It should be noted that the growth is expected to be different between regions, since the more developed countries will stabilize their consumption (in a high rate though), while the developing countries, will continue consuming resources vastly. Beyond the high level of energy demands, the urgent need for a new energy model emerges also due to additional issues, like resources exhaustion, environmental consequences and social inequities. Considering the first factor, with the current consumption rate, it is predicted that oil reserves will last less than 50 years, while the prediction for coal is also concerning (Figure 2.3) (BP, 2016).

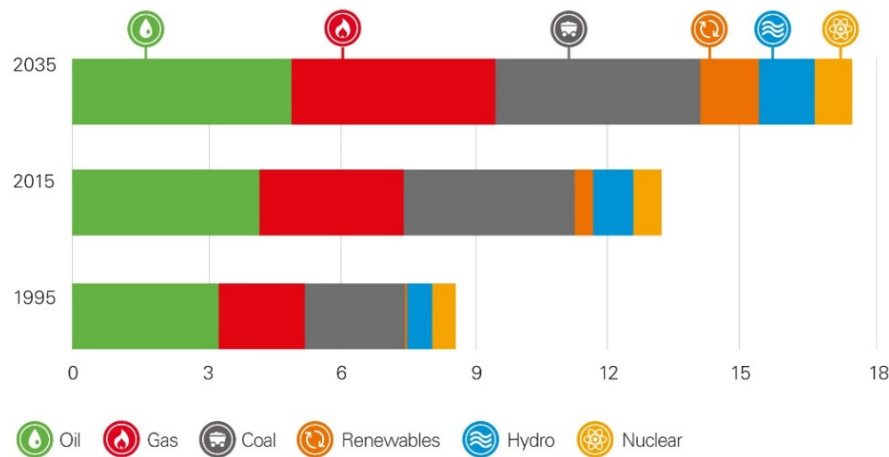


**Figure 2.2:** World primary energy consumption for 1995 and 2015 and prediction for 2035 (1990-2015) in billion tons of oil equivalent per fuel type (BP, 2016).

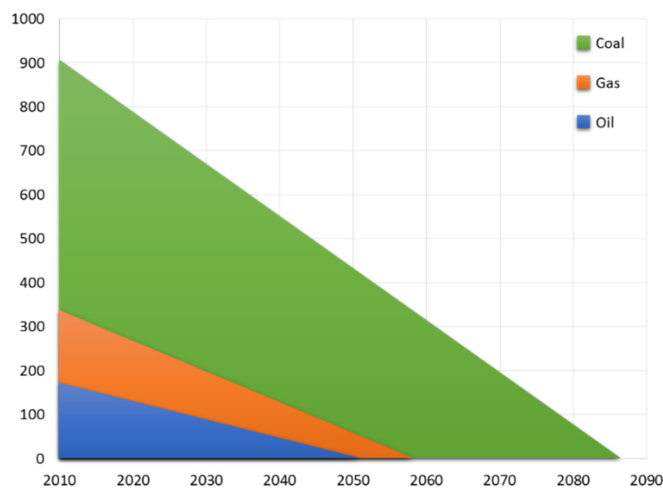


**Figure 2.3:** Prediction of fossil energy reserves consumption up to depletion (in million tons of oil equivalent) (BP, 2016).

#### 2.2.4. Major Energy Policies and Directives

As discussed previously, European and world countries face rising energy demands, volatile fuels and energy prices, and in some cases disruptions to energy supply. Coupled also with the need to reduce the environmental impact of the energy sector, a clear and modern energy strategy is needed to tackle these problems. Having defined three primary goals for the future, namely, security of supply, competitiveness and sustainability, the European Commission (EC) has launched plans to ensure secure, affordable and climate-friendly energy for citizens and businesses. Initially, with the Directive 2009/28/EC of the European Parliament, the 2020 Energy Strategy defined the energy priorities between 2010 and 2020

(European Parliament, 2009). More specifically, it aimed to: i) reduce GHG by at least 20%, compared to 1990 levels; ii) increase the share of renewable energy in the energy mix to at least 20% of consumption; and iii) improve energy efficiency by at least 20%. More recently, with a new Directive (2015/1513), the EC set the climate and energy key targets for the year 2030 (European Parliament, 2015): i) at least a 40% reduction in GHG emissions, compared to 1990; ii) at least 27% share for renewable energy; and iii) an energy efficiency increase of at least 27%, with the potential to raise the target to 30%. This energy framework was adopted by EU leaders in October 2014. Building on the 2020 and 2030 climate and energy packages, the clear target for 2050 is an 80-95% cut in GHG emissions compared to the 1990 levels.

In the global level, during the Paris climate conference (COP21) in December 2015, 195 countries adopted the first-ever universal, legally binding global climate deal (Paris Climate Change Conference, 2015). In principle, the Paris Agreement is a bridge between today's policies and climate-neutrality before the end of the century. In this framework, the participating governments agreed: i) on a long-term goal of keeping the increase in global temperature to well below 2 °C, above pre-industrial levels; ii) to aim to limit the increase to 1.5 °C, since this would significantly reduce the impact of climate change; iii) on the need for global GHG emissions to peak as soon as possible, recognizing though that it will take longer for developing countries; and iv) to undertake rapid reductions thereafter, in accordance with the best available science.

The above initiatives significantly help to progress towards a low-carbon economy and build an energy system that ensures affordable energy for all consumers, increases the security of the energy supply, reduces the dependence on fossil resources, creates new opportunities for growth and jobs and brings environmental and health benefits. However, even if all these goals are successfully accomplished, it would be necessary to adopt in the future additional, and possibly stricter, directives and policies.

### 2.3. HYDROGEN: A MODERN RENEWABLE ENERGY RESOURCE

Hydrogen is well-known and well-established as an ideal and clean energy source with the potential to reduce CO<sub>2</sub> emissions and, therefore, play a major role in decreasing the global

warming (Midilli et al., 2005). The eventual realization of a H<sub>2</sub> economy requires inexpensive and readily available hydrogen sources and relevant efficient conversion technologies (Barreto et al., 2003). Beyond water, which is an ideal source, CH<sub>4</sub> and H<sub>2</sub>S are considered as alternative and promising sources for H<sub>2</sub> production (Midilli et al., 2007). Notice that the energy required for decomposition of both these sources is significantly smaller than the respective decomposition energy of H<sub>2</sub>O ( $\Delta H_{\text{CH}_4}=74.9$  and  $\Delta H_{\text{H}_2\text{S}}=79.9$ , instead of  $\Delta H_{\text{H}_2\text{O}}=284.7$ , all in kJ/mol).

Generally, hydrogen is classified as an intermediate fuel, since it is produced from other primary sources and then is burnt or converted to electrical energy. As a result, it is known more as an 'energy carrier', rather than an energy source. H<sub>2</sub> can be produced from a wide range of sources, such as natural gas, gasoline, coal, methanol, ethanol, biomass and water, via multiple methodologies, like thermochemical, biological and electrochemical, as shown in Figure 2.4.

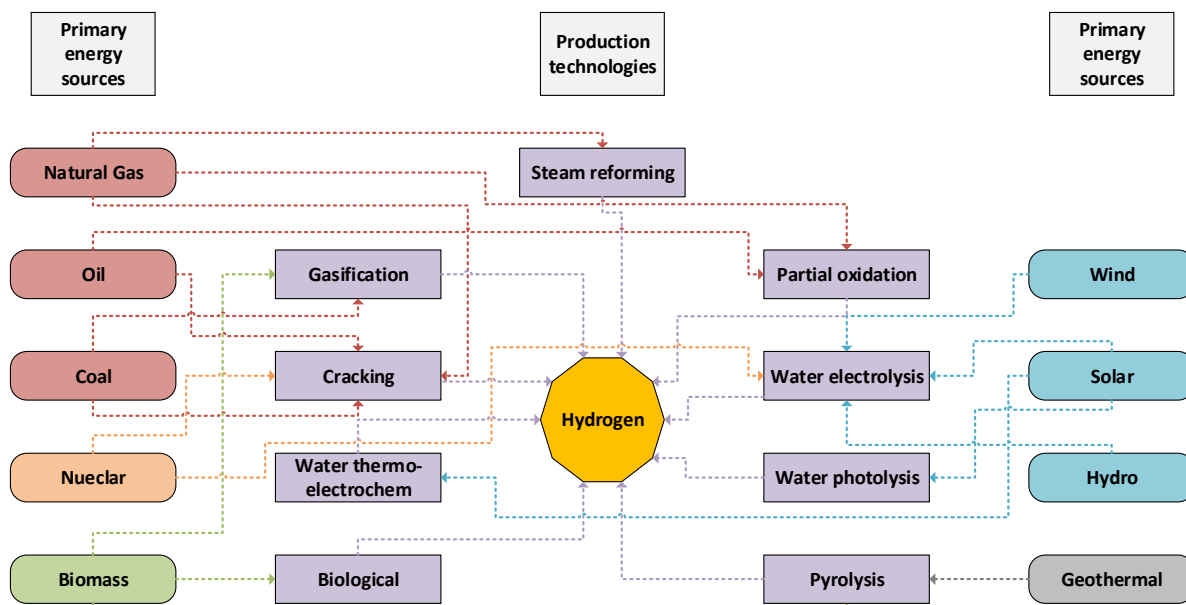


**Figure 2.4:** Hydrogen primary energy sources and production technologies.

### 2.3.1. Hydrogen: Characteristics, Benefits and Drawbacks

Hydrogen is an odorless, colorless, tasteless, non-toxic and non-metallic gas. In standard temperature (273.15 K) and pressure (101.325 kPa) conditions, it presents a low density value (0.0899 kg/m<sup>3</sup>), while it can be in liquid state below temperatures of 20.3 K (Cai et al.,

2014). Regarding its high heating value (HHV), hydrogen contains three times more energy per mass unit, compared to gasoline (141.9 MJ/kg). Respectively, the low heating value of hydrogen (LHV) dominates over the LHV of other fuels, as it is clearly depicted in Table 2.1. On the contrary, due to its low density, the heating value on a volumetric basis is only 11.89 MJ/m<sup>3</sup>, approximately one third of the respective value of natural gas (Sivasubramanian et al., 2007).

**Table 2.1:** Comparison of hydrogen HHV and LHV with fossil fuels.

Fuel	HHV in kJ/kg (at 25 °C/1 atm)	LHV in kJ/kg (at 25 °C/1 atm)
Hydrogen	141.86	119.93
Methane	55.53	50.02
Propane	50.36	45.60
Gasoline	47.50	44.50
Diesel	44.80	42.50
Methanol	19.96	18.05

Hydrogen is a clean energy carrier with no NO<sub>x</sub>, CO<sub>x</sub>, SO<sub>x</sub> and particulate matter, formed when it is combusted. Concerning the combustion properties, its minimum ignition energy is 0.017 MJ, in a wide range of ignition limits (to 4-75%). Thus, hydrogen is highly flammable and can form explosive mixtures with air, within this wide concentration range. Moreover, it possesses high burning velocity and a self-ignition temperature equal to 858 K (Midilli et al., 2005a; Midilli et al., 2005b; Midilli et al., 2008; Muldera et al., 2007). In the extreme and unaccustomed circumstance of an explosion, where H<sub>2</sub>, O<sub>2</sub> and an ignition source (e.g., spark, high heat or sunlight) are mixed up, H<sub>2</sub> has a very low explosive energy contained within the mixture; gasoline vapors contain approximately 22 times more explosive energy, given the same volumetric amount (Midilli et al., 2008; Muldera et al., 2007).

As an energy carrier, hydrogen presents excellent advantages, which in general are:

- It is easily obtainable, as it is abundantly found as a component of numerous compounds.
- Its combustion is environmentally sustainable and generates clean by-products.
- It is a renewable and ample energy source with limited risk of extinction.
- It is more efficient than traditional sources of energy.

It is in general difficult to estimate the global hydrogen production capacity; an estimation for 2010 suggested that H<sub>2</sub> production was in the order of 50-60 million metric tons or 400-500 billion cubic meters. Beyond energy, H<sub>2</sub> is primarily used in ammonia production, chemical industry, petroleum refining and in more special applications, like the aerospace industry. As a result, the demand for H<sub>2</sub> is constantly on the rise. In order to address the above demands and satisfy in the same time the criteria of sustainability, the hydrogen productivity levels should be increased by using non-fossil based feedstock. On the other hand, H<sub>2</sub> can be widely accessible, since it can be produced anywhere, provided that water and power are available.

With the potential of a decentralized source of energy, hydrogen can be used with oxygen in fuel cells, with water being the only by-product. As a result, H<sub>2</sub> in the transportation sector is a completely emission-free energy carrier. Recently, the Energy Information Administration (EIA) estimated for 2050 that the consumption of petroleum and CO<sub>2</sub> emissions in the transportation sector can be reduced between 37.1-84.1% and 8.8-83.8%, respectively, if H<sub>2</sub>-powered fuel cell vehicles enter the market (Energy Information Administration, 2008). Despite that the benefits from H<sub>2</sub> will depend on the actual level of fuel cell vehicle penetration, this concept is an excellent example of the H<sub>2</sub> potential to replace fossil fuels. Nevertheless, there are still some drawbacks, regarding the technical challenges in hydrogen production, namely, the cost of transportation and storage. As H<sub>2</sub> is the lightest gas (H<sub>2</sub> density is approximately 7% that of air) and its condensation temperature at atmospheric pressure is 20 K (Pant and Gupta, 2009), major limitations in transportation and storage arise, which need to be addressed before hydrogen meets the intended applications.

### 2.3.2. Hydrogen as an Energy Vector

As discussed earlier, H<sub>2</sub> is a primary feedstock for the petroleum and chemical industries. Petroleum refineries have changed their role from major producers to consumers of H<sub>2</sub>, due to the strict environmental regulations, regarding emission control for automobiles, requiring less benzene and sulfur compounds in gasoline (Armor, 1999). Therefore, more H<sub>2</sub> is needed for further processing of heavy hydrocarbons and desulfurization. In the chemical industry, H<sub>2</sub> is vastly consumed in ammonia synthesis (approximately 40% of the total world consumption) (Scholz, 1993). Smaller amounts are used in methanol synthesis, food

processing and electronic industries. Moreover, as H<sub>2</sub> has the highest energy-to-weight ratio of any fuel, it is extensively used in the space industry as a fuel propellant. Hydrogen is also an ideal feedstock to extend the life span of fossil fuels; for instance, when coal is gasified to produce H<sub>2</sub>, it becomes more usable and environmentally acceptable. Finally, H<sub>2</sub>-powered fuel cells are getting great attention because of their potential to generate pollution-free electricity. As an example, H<sub>2</sub> fuel cells are utilized on space shuttles to power life support systems and computers, while producing drinkable water as a co-product (Fang et al., 2015).

The major routes for the conversion of H<sub>2</sub> to energy are (Sivasubramanian et al., 2007): internal combustion engines, pure oxygen supply systems for steam production, catalysts for heat generation, and electrochemical methods. Hydrogen combustion (Reaction 2.1) is an exothermic process that releases heat and energy. An energy input is required to commence the reaction and overpower the forces between the atoms and the molecules, while an efficient energy amount is also generated from the break of chemical bonds (Rigden, 2003).



As can be seen, H<sub>2</sub>O vapor and heat are the only combustion products.

By utilizing the already existing technology of electrolysis towards H<sub>2</sub> production, especially when renewable energy sources (solar, wind, etc.) are also utilized, hydrogen is considered as the ideal energy carrier in the transportation sector or for temporary storage. However, due to the high production cost, hydrogen is not utilized yet as a fuel itself. Furthermore, as the combustion of fossil fuels contributes a large part of the global CO<sub>2</sub> emissions (approximately 30% of CO<sub>2</sub> emissions comes from transportation fuels), the widespread use of cars and mass transit vehicles powered by hydrogen-based fuel cells or hydrogen-fueled internal combustion engines will help mitigate climate change. In the future, H<sub>2</sub> could also be a premier energy carrier in the electricity sector, capable of storing, moving and delivering energy in a usable form. Without any doubt, H<sub>2</sub> has the potential to alter and replace the present energy infrastructure, although not until far in the future.

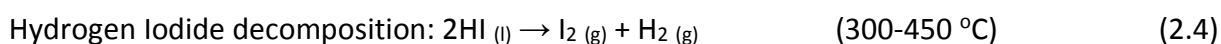
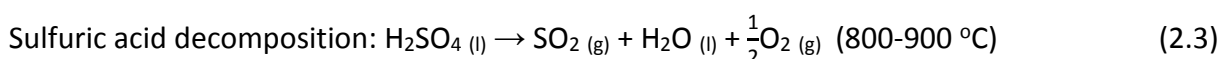
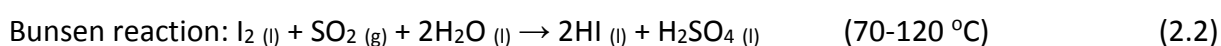
### 2.3.3. Hydrogen Production Methods

Despite being one of the most plentiful elements, H<sub>2</sub> does not exist naturally as a gas and is always combined with other elements. As a result, several methods of H<sub>2</sub> production from

hydrogen-containing compounds have been developed, including thermal, thermochemical, photochemical, photoelectrochemical, plasmachemical, biomass and electrolysis processes, according to specific technical and economic criteria. In what follows, a brief analysis of each production method is presented.

**Thermal:** It is well known that at temperatures well above 2,000 °C H<sub>2</sub>O can be decomposed into O<sub>2</sub> and H<sub>2</sub>, without the need for electrolysis or the presence of a catalyst or any other intermediary chemical. For example, when exposing water to sun radiation, in order to gain the desired temperature, water decomposition occurs in principle, though with a very low efficiency (approximately 1%). As a result, this process has no significant practical implementation, except for the case of solar-thermochemical dissociating processes.

**Thermochemical:** H<sub>2</sub> can be also produced by the decomposition of H<sub>2</sub>O, H<sub>2</sub>S, or any other hydrogen-containing compound via the thermochemical process, involving specific chemical reactions. Typical temperatures for this method are 650-1,100 °C, usually accomplished by concentrated solar collectors or nuclear reactors. The efficiency of the thermochemical dissociation is yet at low levels, thus more advanced methods have been proposed (Sivasubramanian et al., 2007). For example, the Sulfur-Iodine (S-I) thermochemical cycle is a promising technology, with an estimated average efficiency of 56% (Licht, 2005). The reactions occurring in a S-I cycle are:



The S-I cycle occurs in H<sub>2</sub>O under high temperatures, especially the Reactions 2.3 and 2.4. Notice that the exothermic Reaction 2.2 describes the operating principle of the Bunsen reactor, in which two immiscible liquid acid compounds are produced (Banerjee et al., 2006). As can be seen, beyond H<sub>2</sub> and O<sub>2</sub>, no harmful by-products are produced. Nevertheless, there is the drawback of the necessary treatment of the produced sulfuric and hydroiodic acids, as they are extremely corrosive and, generally, a significant threat to the equipment. In Figure 2.5 the total process of the Sulfur-Iodine cycle is depicted (Russ, 2009).

Another thermochemical technology, widely used for H<sub>2</sub> production, is Steam Reforming of Methane (SRM), which is presently considered as the leading technology in petrochemical

compounds refining. The main stages of SRM include the: i) pretreatment of the raw material for the removal of sulfur and other contaminants; ii) feedstock heating at high temperatures and medium pressures to convert it to syngas (i.e., mixture of CO, CO<sub>2</sub> and H<sub>2</sub>); iii) heat recapture from the produced syngas via CO shift reactions; and iv) purification of H<sub>2</sub> from CO, CO<sub>2</sub> and CH<sub>4</sub> via pressure swing adsorption (PSA).

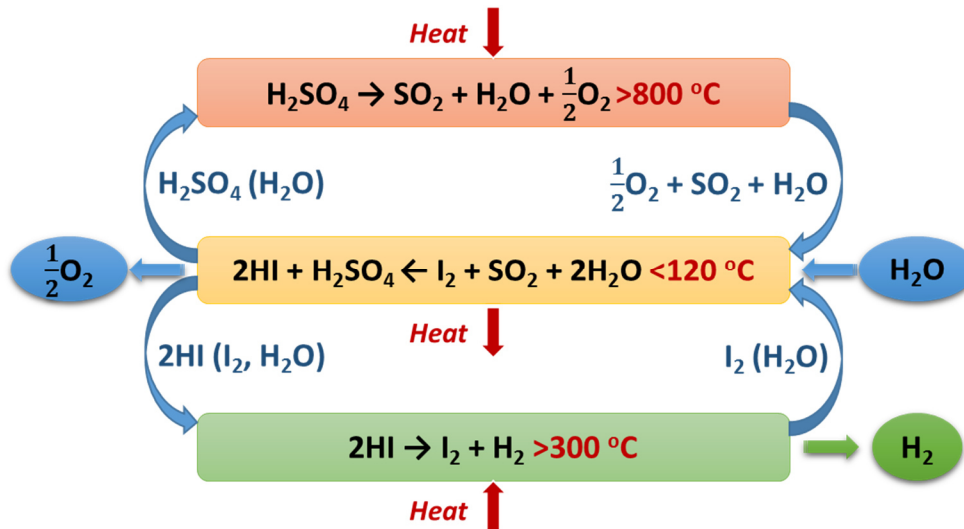


**Figure 2.5:** Schematic representation of the Sulfur-Iodine thermodynamic cycle.

Figure 2.6 illustrates the operational flowsheet of the SRM technology. Partial oxidation (POX) is an additional thermochemical process for H<sub>2</sub> production, which mainly deals with heavy petroleum feedstock (hydrocarbons to heavy oils and solids). Fuel, steam and air (or pure O<sub>2</sub> to enhance the process) react with the presence of a suitable catalyst, depending on the feedstock and process type. Compared to the SRM, POX is less expensive, though the investment in the oxygen availability and desulfurization process steps make it also capital intensive. Autothermal reforming (AR) is a process that combines both SRM and POX, where fuel, steam and air (or oxygen) pass through a mixed catalyst bed that supports both reactions. The heat produced from the POX reaction supplies the heat required by the endothermic SRM. Therefore an external burner or heat source is not needed.

In another thermochemical approach, H<sub>2</sub> can be produced via coal gasification. The reaction mechanism is similar to POX, except that it is applied specifically for solid fuels, which are pulverized and then partially oxidized with steam (or oxygen). The gas product, which

contains CO, CO<sub>2</sub>, H<sub>2</sub>, H<sub>2</sub>O and H<sub>2</sub>S (removed by purification), is quenched using H<sub>2</sub>O to remove ash, and subsequently fed to a gas shift reactor for further conversion of CO to CO<sub>2</sub> and production of additional H<sub>2</sub>. The effluent gas stream is purified via a PSA or scrubbing process to obtain pure H<sub>2</sub>. Coal gasification for H<sub>2</sub> production is the least cost-effective among the thermochemical processes, due to the large capital investment and the low energy recovery. Finally, H<sub>2</sub> can be produced by thermal cracking of natural gas in a high temperature pyrolysis unit. Hydrogen is generated from the direct cracking of methane (without CO<sub>2</sub> formation), and carbon black, the primary by-product, can be utilized in the rubber industry.

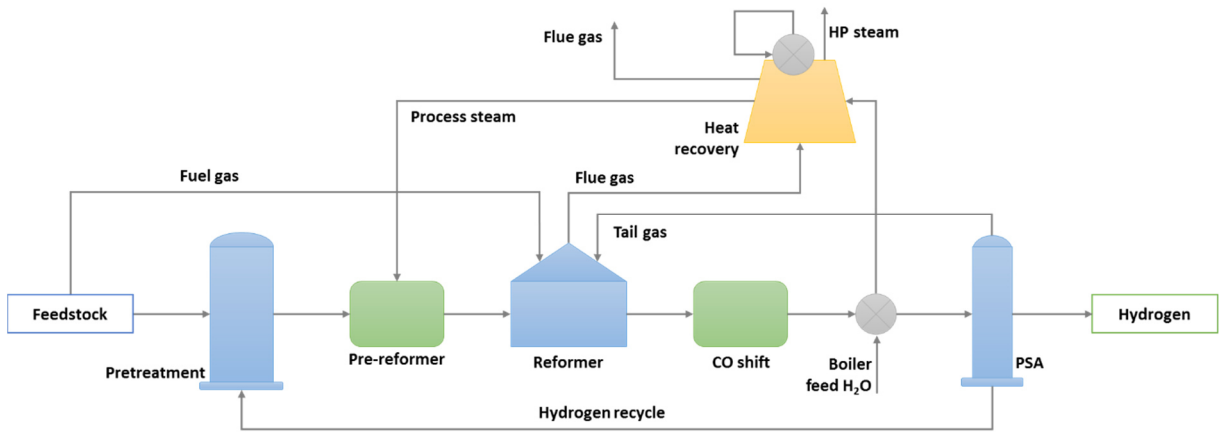


**Figure 2.6:** Generic process flowsheet of the Steam Reforming of Methane (SRM) technology.

**Photoelectrochemical:** In the photoelectrochemical method, photovoltaic (PV) systems and electrolysis processes are combined to dissociate H<sub>2</sub>O in H<sub>2</sub> and O<sub>2</sub>. The technology depends on two semiconductor electrodes, one of which is exposed to solar radiation to receive the demanded energy (photoanode). Within the photoanode, the generation of electrons in the conduction band and positively charged electrons (known as ‘holes’ and being responsible for the H<sub>2</sub>O dissociation) in the valence band takes place. Thereupon, the generated H<sub>2</sub> ions are transferred to the cathode:



On the other hand, the produced in the photoanode electrons migrate to the cathode through the external circuit, where they form hydrogen:



The generated voltage for this kind of dissociation is approximately 1.23 V, while the minimum required band gap for the semiconductor is approximately to 1.8 V.

**Photochemical:** The major difference between the photochemical and the photoelectrochemical method is that the former is based on the implementation of a suspension of semiconductors, instead of separate electrodes (in the latter) (Amouyal, 1995). In addition, molecules having the capacity to induce the reaction via sunlight absorption (photosensitizer particles) in an aqueous solution, are also utilized in the photochemical method. At the photosensitizers surface, specific reduction and oxidation reactions take place, in the presence of catalysts, to accelerate the overall redox mechanism:



Notice that the photochemical method for H<sub>2</sub> production is not widely used, because of the low efficiency (approximately 10%).

**Plasmochemical:** Plasma is a state of matter formed from ionized gases during nuclear reactions or electrical and microwave discharges. It can be also formed artificially, when electrical current passes through a dielectric gas or fluid. It is well known that to generate and sustain a plasma formation large amounts of energy are required (Zaman and Chakma, 1995). This novel method of H<sub>2</sub> production is superior to the conventional methods, regarding the efficiency of the process. The plasmochemical technology has been proposed to directly dissociate seawater and subsequently utilize the produced H<sub>2</sub>, in a process with many advantages: smaller energy cost than electrolysis, no catalyst presence and no harmful by-products formation.

**H<sub>2</sub> production from biomass:** As biomass represents a renewable and CO<sub>2</sub>-neutral feedstock for H<sub>2</sub> production, the implementation of thermochemical processes (fast pyrolysis and thermal gasification) and biological conversion processes (fermentation and biophotolysis) is of significance importance (Ni et al., 2006). To begin with, the process of rapidly heating biomass under high temperatures, in absence of air, so that vapor, bio-oil and H<sub>2</sub> are produced, describes the pyrolysis conversion route. If proper conditions are implemented (i.e., high temperatures and adequate residence time), then hydrogen can be directly formed (Ni et al., 2006):



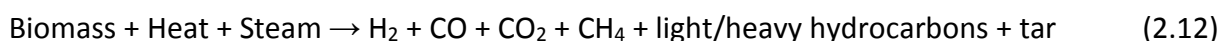
The generated hydrocarbons, like methane, can be further reformed for additional hydrogen production:



Thereupon, CO is converted to CO<sub>2</sub> along with H<sub>2</sub> production via the water gas shift reaction:



On the other hand, H<sub>2</sub> production via biomass thermal gasification at the temperature range 600-800 °C is performed in a three-step process. Initially, biomass particles are gasified with the aid of an air/steam agent, producing H<sub>2</sub>, CO, CO<sub>2</sub>, CH<sub>4</sub>, ash, tar and H<sub>2</sub>O; any undesired particles are removed through a cyclone technology. The second step is the compression of the product mixture and the final step is the treatment of tar and residual hydrocarbons with steam and catalysts (Ni et al., 2006). The overall process scheme can be written as:



Afterwards, the produced CO is reformed to further produce CO<sub>2</sub> and H<sub>2</sub>, through the water gas shift reaction:



Finally, the PSA process is also adopted here to separate and purify H<sub>2</sub>.

Regarding the biological methods, bacterial fermentation refers to a process in which organic matter is converted to H<sub>2</sub> and CO<sub>2</sub> under anaerobic conditions, without the need for solar radiation. In the biophotolysis process, a population of algae and/or cyanobacteria is employed to produce H<sub>2</sub>, along with the contribution of water and sunlight. Presently, the above methods are in the research level, due to their small efficiencies.

**Electrolysis:** In general, electrolysis is a 'green' process with no CO<sub>2</sub> emissions, which can utilize renewable energy sources and accomplish relatively high efficiency levels, up to 70% (Mazloomi et al., 2012). Because of the cost of electrical power, electrolysis is practical only when electricity is cost-efficiently derived from nuclear and solar energy or hydropower. It is based on the utilization of an electrolysis cell and a proper electrolyte (e.g., soluble salts, alkali solutions, acids). For water electrolysis the overall reaction can be described:



One of the widely used technologies for H<sub>2</sub>O electrolysis is the alkaline electrolyzer cell, which involves an electrode based on sodium or potassium hydroxide:



In addition, the proton electrolyte membrane electrolyzer is another technology used, which is based on a solid plastic material, acting as the electrolyte. Initially, it was developed (in 1960) to overcome the technical barriers of the previous alkaline electrolysis method. A Solid Polymer Electrolyte (SPE) enables the conduction of the produced protons from the anode to cathode, while the produced electrons circulate through an external circuit:



**Comparison of methods:** It is obvious that each one of the above described methods presents distinct advantages and disadvantages. For instance, SRM is the dominant technology to generate H<sub>2</sub> with high efficiency (70-85%) (Holladay, 2009), thus it is now used for the production most of the globally available H<sub>2</sub> from fossil feedstock (natural gas and coal). SRM, combined with POX and coal gasification, represent approximately 96% of the present H<sub>2</sub> production. The remaining 4% is produced via conventional electrolysis, in which the energy efficiency is still lower compared to SRM. More specifically, the natural gas SRM is the most cost-favorable process, because of the large thermal efficiency and the small capital investment. Beyond these large-scale methodologies, smaller-scale production plants for vehicle refueling stations and stationary fuel cells in buildings are currently being developed. In the near future, it is expected that H<sub>2</sub> produced from biomass, wind and solar sources will be also part of the energy sector. Without any doubt, the production of H<sub>2</sub> via a clean method has many technical challenges, a fact that explains why 96% of H<sub>2</sub> is still produced from non-renewable resources: 48% from natural gas, 30% from oil, 18% from coal, as shown in Figure 2.7. Of this amount, approximately 49% is used in ammonia production, 37% in petroleum refining, 8% in methanol production and the remaining 6% in other miscellaneous smaller-volume uses.

## 2.4. PRODUCTION OF HYDROGEN FROM HYDROGEN SULFIDE

Over the last centuries, hydrogen sulfide has been considered a liability. Only in recent years, H<sub>2</sub>S was proposed as a high value compound (Naman, 2008). In general, H<sub>2</sub>S is a fairly

abundant resource whose potential is not being fully utilized by the industry. An alternative route for the utilization of H<sub>2</sub>S is to develop novel methods to decompose it in H<sub>2</sub> and S. To this direction, the recent efforts which have been made through a diverse variety of technologies were successful up to a level.

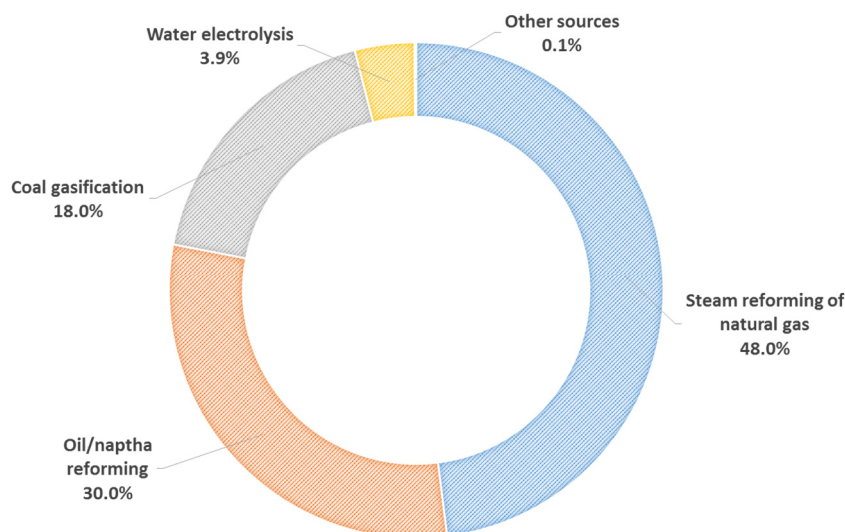


**Figure 2.7:** Global hydrogen production from primary energy sources.

#### 2.4.1. H<sub>2</sub>S Properties and Characteristics

Hydrogen sulfide (molecular weight 34.08 g/mol) is a colorless and flammable gas, having the foul odor of rotten eggs. Its structural formula is similar to water (i.e., H-S-H), in which is also soluble (1 g per 242 ml of H<sub>2</sub>O at 20 °C), forming a weakly acidic solution (dissociation into H<sup>+</sup> and HS<sup>-</sup>). Both pH and temperature of the solution have a strong impact on the H<sub>2</sub>S concentration. For example, at 20 °C and pH=7.4, it exists approximately 30-33% as H<sub>2</sub>S and 67-70% as HS<sup>-</sup>, with negligible S<sup>2-</sup>. However, at 37 °C and same pH value less than 20% H<sub>2</sub>S exists in its undissociated form. The major properties of H<sub>2</sub>S can be seen in Table 2.2.

H<sub>2</sub>S has been known for more than 300 years as a highly toxic and poisonous gas, having a strong impact on the environmental and human health. Molecular H<sub>2</sub>S is lipid soluble and is capable of crossing biological membranes and dissociate into HS<sup>-</sup> and H<sup>+</sup>, inducing multiple effects in the cell due to the presence of HS<sup>-</sup> (Mathai et al., 2009). More specifically, the human nervous system is the most often intoxicated; acute inhalation of H<sub>2</sub>S (500-1,000 ppm) causes neurotoxic effects such as headache, dizziness, amnesia and even

unconsciousness, due to the direct toxic effect on the brain. These effects are usually reversible and the sufferer can completely recover, if the exposure is rapidly removed. However, if the exposure is more pronounced (over 1,000 ppm) or prolonged, fatal respiratory paralysis may occur and even lead to death. Death may come instantly, when the concentration of H<sub>2</sub>S is higher than 5,000 ppm (Baykara et al., 2007; Naman et al., 2008).

**Table 2.2:** Major hydrogen sulfide properties.

Chemical formula	H <sub>2</sub> S
Molar mass	34.08 g/mol
Appearance	Colourless gas
Odour	Rotten eggs
Density	1.363 g/l
Melting point	-82 °C (-116 °F; 191 K)
Boiling point	-60 °C (-76 °F; 213 K)
Solubility in water	4 g/l (at 20 °C)
Vapour pressure	1740 kPa (at 21 °C)
Acidity (pK <sub>a</sub> ) / Basicity (pK <sub>b</sub> )	7.0 / 12.9
Specific heat capacity (C)	1.003 J/(K·g)
Std molar entropy (S <sup>o</sup> <sub>298</sub> )	206 J/(mol·K)
Std formation enthalpy (ΔH <sub>f</sub> <sup>o</sup> <sub>298</sub> )	-21 kJ/mol
EU classification (Dangerous Substances Directive, DSD)	 F+: Extremely flammable  T+: Very toxic  N: Dangerous for the environment
Standard System for the Identification of the Hazards of Materials for Emergency Response (NFPA 704)	 <p><b>Health hazard:</b> 4: very short exposure could cause death or serious residual injury even though prompt medical attention was given</p> <p><b>Fire hazard:</b> 4: will rapidly or completely vaporize at normal pressure and temperature, or is readily dispersed in air and will burn readily</p> <p><b>Reactivity:</b> 0: normally stable, even under fire exposure conditions, and not reactive with water</p>
Flash point	-82.4 °C (-116.3 °F; 190.8 K)
Auto-ignition temperature	232 °C (450 °F; 505 K)
Explosive limits	4.3-46%

Notice that the human nose is very sensitive to H<sub>2</sub>S and can detect the unpleasant smell as low as 0.02 ppm. However, this is only true at low concentrations, since at higher concentrations (up to 100 ppm), the H<sub>2</sub>S smell disappears and it emerges as an odorless gas, greatly increasing the risk of poisoning. Over exposure to H<sub>2</sub>S is often in the oil and gas industry as it is a large component of natural gas (Baldelli et al., 1993). In the majority of the European countries, the current safe occupational exposure for H<sub>2</sub>S is 5 ppm (8 h time weighted average) and 10 ppm (15 min, short term exposure limit). The threshold for the perception of the H<sub>2</sub>S odor is in the range of 0.02-0.13 ppm (Costigan, 2003).

#### 2.4.2. H<sub>2</sub>S Sources

H<sub>2</sub>S is a byproduct of a number of industrial processes (e.g., pulp manufacture in paper mills, leather processing in tanneries, coal liquefaction, sewage treatment, oil refineries), can be found in volcanic emissions and hot springs and is formed by bacteria upon the decomposition of organic materials (Haklıdır et al., 2006). It is generally believed that volcanoes (both active and inactive) have the major contribution of H<sub>2</sub>S to the atmosphere through lava flows, domes, fumaroles, erupting lava and submarine hydrothermal areas. These gas flows primarily consist of H<sub>2</sub>O, SO<sub>2</sub>, CO<sub>2</sub> and HCl, containing also secondary components, like N<sub>2</sub>, H<sub>2</sub>, CO, H<sub>2</sub>S, HF and HBr. The exact gas composition strongly depends on the location of the source and the individual geochemistry and eruption nature.

In the biogeochemical cycle, H<sub>2</sub>S exists as the product of the anaerobic oxidation by sulfur-reducing bacteria (Haklıdır et al., 2006). These bacteria are tolerant to a wide range of pH, pressure, temperature and salinity conditions. Their metabolic regulation towards the decomposition of organic matter to H<sub>2</sub>S is favored by low-oxygen and anaerobic environments, such as in swamps and sewage. Moreover, small amounts of H<sub>2</sub>S can be found in crude petroleum and larger volumes in natural gas. Approximately 10% of total global H<sub>2</sub>S emissions originate from industrial activities and processes, such as petroleum refineries, coke ovens, paper mills and tanneries. It should be noted that the normal concentration of H<sub>2</sub>S in clean air is in the range 100-200 ppb (Selene and Chou, 2003).

As a response to its toxic effect and environmental impact, different technologies, based on wet/dry adsorption and oxidation, have been used for the removal of H<sub>2</sub>S from flue gases on

a commercial scale. First of all, the well-known Claus process is the major process implemented for the recovery of elemental sulfur from gaseous  $\text{H}_2\text{S}$  (see Figure 2.8) (Elsner et al., 2003; Manenti et al., 2013). Moreover, dry catalytic processes, based on the selective catalytic oxidation of  $\text{H}_2\text{S}$  to elemental sulfur, have been also developed to overcome the equilibrium limitations of the wet Claus process: Mobil's direct-oxidation process and Comprimo's Super-Claus process. They both rely on the single-step recovery of S from tail gas, according to the catalytic oxidation of  $\text{H}_2\text{S}$ :



The key-process parameters presenting the major impact on the process efficiency are the volume, temperature and pressure of the influent gas, the space velocity, the selected process specifications (i.e., selectivity, sulfur recovery), the types and concentrations of impurities, the surface characteristics and regeneration capabilities, etc. The Claus process efficiency ranges between 94%-97%, while the environmental impact is minimal, provided that the process will be integrated with a tail gas treatment unit. Recently, this process was further improved, with respect to the operation cost, via process intensification (Manenti et al., 2013).

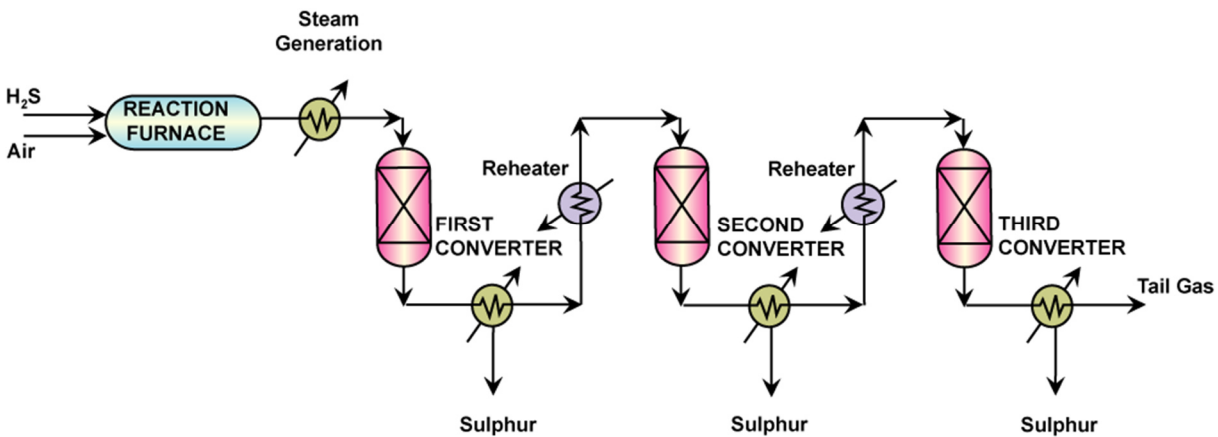


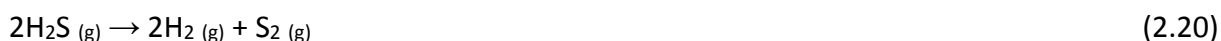
**Figure 2.8:** Flowsheet of the Claus process for sulfur removal from  $\text{H}_2\text{S}$ .

### 2.4.3. Methods for Hydrogen Production from $\text{H}_2\text{S}$

A suitable technology for the production of hydrogen from hydrogen sulfide should fulfil the trinity of waste minimization, resource utilization and environmental pollution reduction. In the following paragraphs, an overview of the current technologies is performed to identify

what can be presently achieved and what can be accomplished in the near future, in order to fully utilize H<sub>2</sub>S.

**Thermal decomposition:** When heated, H<sub>2</sub>S decomposes into H<sub>2</sub> and S. Specifically at low temperatures, molecules of one to eight sulfur atoms and many sulfane species (H<sub>2</sub>S<sub>2</sub> to H<sub>2</sub>S<sub>8</sub>) may be formed. In the temperature range 973-1123 K and pressure range 101-405 kPa, the molecules of S<sub>2</sub> are more than 99.8% of the total sulfur molecules (Zaman and Chakma, 1995). Overall, as the conversion is efficient over 1000 K, the produced sulfur will be necessarily diatomic. As a result, the thermal decomposition of H<sub>2</sub>S can be written as:



Presently, focus on the thermal decomposition of H<sub>2</sub>S is given on the development of superior catalysts, strategies to enhance the conversion by equilibrium shift, and single-through efficient processes, based on solar furnaces for high temperature and sub-atmospheric pressure operation (Raymont, 1974; Kaloidas and Papayannakos, 1989; Fletcher et al., 1984; Yang and Kung, 1994).

**Thermochemical methods:** As a great number of thermochemical cycles exist for the energy demanding H<sub>2</sub>O decomposition and, in principle, H<sub>2</sub>S decomposition is less energetically intensive, several thermochemical cycles has been examined for the production of H<sub>2</sub> from H<sub>2</sub>S (Zaman and Chakma, 1995). In a first approach, the two-step decomposition of H<sub>2</sub>S in the presence of metal or lower metal sulfides can be described by the following reactions:



Secondly, the two-step closed thermochemical cycle with CO follows the mechanism:



Similarly, the two-step closed thermochemical cycle with iodine can be written as:



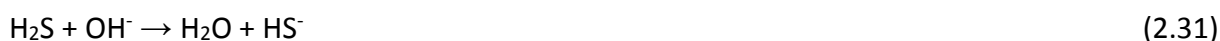
Finally, in the two-step open thermochemical cycle with metals, the latter are initially sulfided liberating  $H_2$  and, subsequently, the sulfides are oxidized to regenerate the metal and produce  $SO_2$ :



In all the above thermochemical cycles, the parameters that present the major effect on the process efficiency are the catalyst type and the operating conditions (e.g., temperature) (Noring and Fletcher, 1982).

**Electrochemical methods:** The already available technologies for  $H_2O$  electrolysis, such as the advanced alkaline water electrolysis (AWE), the inorganic membrane alkaline water electrolysis (IME), the solid polymer electrolysis (SPE), the high temperature electrolysis (HTE) and the intermediate temperature electrolysis (ITE) can be implemented also for the electrolysis of  $H_2S$  (Zaman and Chakma, 1995). Towards this direction, over the last years three distinct routes have emerged: direct electrolysis, indirect electrolysis and high temperature electrolysis.

Firstly, the direct electrolysis of  $H_2S$  presents limitations due to the low solubility and electrical conductance of  $H_2S$  as a liquid. The reaction is carried out in acidic or preferably in basic solutions. Despite the low energy demands of the electrochemical decomposition of  $H_2S$ , the process is challenging, due to sulfur passivation of electrodes, difficulties in sulfur handling and removal and occurrence of undesirable secondary electrochemical reactions. Several of remedies for the mitigation or elimination of the sulfur deposition on the anode have been attempted, including the use of organic solvents, porous electrodes, high temperatures and high concentrations of the alkaline solution (Zaman and Chakma, 1995). In general, when  $H_2S$  is dissolved in an alkaline solution, sulfide ion is formed:

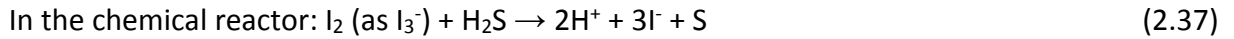


Subsequently, S is formed at the anode and  $H_2$  is produced at the cathode according to:



Secondly, regarding the indirect electrolysis, an electrochemical process based on the oxidation of iodide in aqueous hydriodic acid at high current densities, is implemented

(Zaman and Chakma, 1995). H<sub>2</sub> is produced concurrently with triiodide to yield an impure sulfur product:



Lastly, the high temperature electrochemical process presents the advantage of converting H<sub>2</sub>S directly to H<sub>2</sub> and S. In more detail, H<sub>2</sub> follows the major process stream, while S is condensed and collected. Thus, no waste gas treatment plant is needed. As the hot gas flows past the cathode (consisting of carbon, cobalt sulfide or nickel sulfide), the below electrochemical reaction takes place:

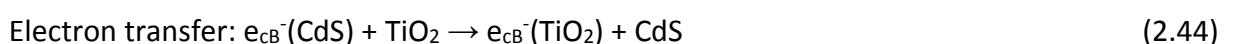


As H<sub>2</sub> remains at the cathode, S<sup>2-</sup> follows the electric potential gradient and moves to the anode, through a molten salt electrolyte suspended in an inert ceramic matrix:



**Photochemical methods:** The technology, originally developed for the photolytic decomposition of H<sub>2</sub>O, has been successfully applied also for the decomposition of H<sub>2</sub>S (Zaman and Chakma, 1995; Reverberi et al., 2016). The used catalysts can be semiconductor electrodes, semiconductor particles, colored redox species (dyes and metal complexes), or colored redox species adsorbed on semiconductor electrodes. In the former case, the process is often defined as a photoelectrochemical process (see below). On the other hand, when powder semiconductors are used, the process is called photochemical or photocatalytic.

As a successful example, H<sub>2</sub> can be produced with high rate when RuO<sub>2</sub>-loaded CdS particles are dispersed in aqueous solutions of H<sub>2</sub>S and illuminated with visible light. The different process steps can be described by the following mechanism:





The overall rate of the photochemical process involves also a mass transfer step, which takes into account the diffusion of  $\text{H}_2$  from the catalyst surface to the bulk liquid phase and further transport to the gas stream.

**Photoelectrochemical methods:** The major advantage of photoelectrochemical technologies is that, beyond  $\text{H}_2$ , electricity can be also produced (Zaman and Chakma, 1995). As an example, in a relevant photoelectrolytic cell, composed of a CdSe deposited film as the photoanode, a Pt-based cathode, a nation membrane to separate the anode and cathode compartments and a NaOH solution electrolyte, the photo-induced generation of 'holes' at the anode surface enables the oxidization of sulfide ions to polysulfide:



The formed electrons pass through the semiconductor and the external resistor to the cathode, where they reduce  $\text{H}_2\text{O}$  to  $\text{H}_2$ :



**Plasma methods:** A large amount of work on plasma decomposition of  $\text{H}_2\text{S}$  has been carried out, based on technologies like low power microwave installations and ozonizers, coupled with atmospheric rotating glow discharges (Zaman and Chakma, 1995). The proposed reactions mechanism is:



**Comparison of methods:** As of today, there is no commercial technology for the production of  $\text{H}_2$  and S from the decomposition of  $\text{H}_2\text{S}$ . Photochemical and plasmochemical methods are still in the development stage; they are not mature enough to be applied in the industrial-scale. Furthermore, none of the thermal methods stands out as the most promising one. The severe thermal and chemical environmental conditions act as strong inhibitors. Novel ceramic membranes may offer possibilities in the future in this respect. The closed cycle

thermochemical processes present the potential to produce H<sub>2</sub> at less severe conditions. Though, since none of them has been known to be commercialized or even piloted, additional research effort should be invested. On the other hand, the electrochemical technology, despite being established in other applications, its implementation to H<sub>2</sub>S requires further development. Moreover, both thermochemical and electrochemical technologies provide promising routes to generate H<sub>2</sub> from H<sub>2</sub>S hydrogen sulfide. Their success strongly depends on improving the performance of the employed catalyst and the individual cell, respectively. The aspects of scale-up, conceptual design and process intensification of reactor/cell modules should also be emphasized.

## 2.5. PRODUCTION OF HYDROGEN FROM BLACK SEA H<sub>2</sub>S

During the last decades, the Black Sea region has attracted the interest of the scientific community as a unique place of exploitation, due to its uncommon natural features, resources biodiversity and unique characteristics (Baykara et al., 2007). One of these characteristics is the high amounts hydrogen sulfide contained in the Black Sea waters (Baykara et al., 2011). Taking into account that with the application of modern technologies H<sub>2</sub>S can be considered more as an energy source than an environmental threat, the extraction of H<sub>2</sub> from H<sub>2</sub>S via an efficient, low-cost and environmental friendly process would definitely be of paramount importance for the environmental salvation and economic development of the wider region.

### 2.5.1. Black Sea

The Black Sea is considered as one of the newest seas of Europe, since it was formed approximately 8,000 years ago. After the rise of the Mediterranean Sea level, water passed through the Bosphorus straits, filling the Black Sea valley. The bottom Black Sea layers contain amounts of water with larger salinity, compared to the upper layers, where the inflow of many rivers occurs. As a result, a density gradient was formed between the salty water on the sediment of the Black Sea and the waters in the upper surface.

Morphologically, the Black Sea is an elliptical basin which covers an area of approximately 423,000 km<sup>2</sup> (average depth 1264 m and maximum depth 2212 m). With geographical coordinates of 40°55'N to 46°32'N latitude and 27°27'E to 41°42'E longitude, it is connected with the Sea of Marmara through the Bosphorus straits and with the Mediterranean Sea through the Dardanelles (see Figure 2.9). The coastal zone of the Black Sea is formed by 6 in total countries, namely, Turkey, Georgia, Russia, Ukraine, Romania and Bulgaria, while 17 more countries are intimately linked with the sea via the rivers flows (Borysova et al., 2005).



**Figure 2.9:** The Black Sea region.

With a total volume of 550,000 km<sup>3</sup>, the Black Sea annually accepts a large river draining, estimated at 350 km<sup>3</sup>. Combined with the deeper inflow from the Bosphorus Sea, these flows significantly affect the water salinity and cause unsuitable life conditions for the majority of the marine animals. More specifically, the water salinity of the upper layers of the Black Sea is really low (17‰), when the typical salinity in ocean waters is 35‰. Moreover, a unique characteristic of the Black Sea is that more than 90% of the water is under anaerobic conditions (Neretin et al., 2001). Under these extreme environmental conditions, no life is present, excluding specific anaerobic bacteria, which can grow on sulfate and utilize it as

their oxygen source (Haklidir et al., 2009). As explained before, these bacteria produce a series of gases (i.e., CH<sub>4</sub>, N<sub>2</sub>, CO<sub>2</sub> and H<sub>2</sub>S) via the decomposition of organic matter at the bottom sediments (Deuser, 1974). In Figure 2.10, the variation of the most important characteristics of the Black Sea with respect to the water depth is presented.

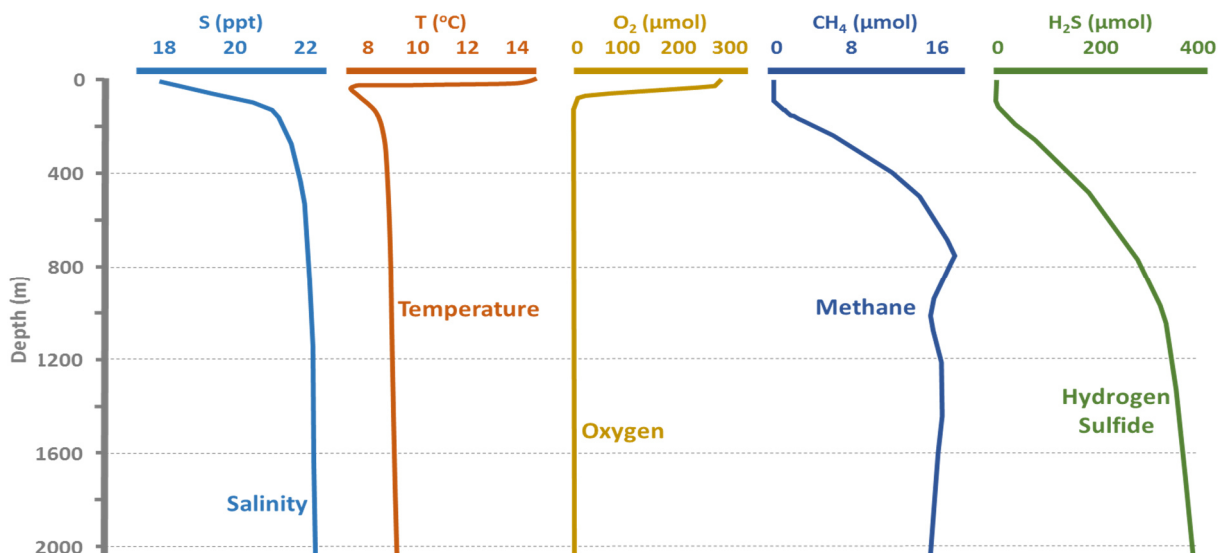


**Figure 2.10:** Major Black Sea characteristics in relation to the water depth.

### 2.5.2. H<sub>2</sub>S in Black Sea Waters

Black Sea is the largest water body of the world that contains large H<sub>2</sub>S quantities in a non-ideal state, i.e., a gas-liquid solution. It has been theoretically calculated that the average production of H<sub>2</sub>S per day is 10,000 tons, resulting in a total amount of H<sub>2</sub>S contained in Black Sea waters equal to 4,587 billion tons (Naman et al., 2008). Ideally, if the available H<sub>2</sub>S is completely recovered and converted, 270 Mtoe of H<sub>2</sub> can be produced (corresponding to  $3.83 \cdot 10^{19}$  thermal energy or  $8.97 \cdot 10^{15}$  electrical energy). To cover those thermal and electrical demands from fossil fuels, 808 Mtoe of gasoline and 766 Mtoe of natural gas should be consumed (Naman et al., 2008).

As depicted in Figure 2.11, H<sub>2</sub>S appears at approximately 100 m below the Black Sea surface. Its concentration increases gradually until 1,000 m (0.36 mmol/l). Below this depth, the rate decreases and from 1,500 m depth and below remains practically constant. The concentration of H<sub>2</sub>S at the sediment of the Black Sea is 0.40 mmol/l (Haklidir et al., 2009). However, the clear boundary of the H<sub>2</sub>S zone cannot be predicted accurately, since it

strongly depends on seasonal and annual fluctuations. For instance, the boundary is shallower during spring and deeper during summer, due to significant diversification in circulation, mainly caused from seasonal atmospheric variations (Deuser, 1974). As can be seen also in Figure 2.11 (Naman et al., 2008), the H<sub>2</sub>S concentration in the Black Sea varies with the water depth. At the basin surface, the absence of H<sub>2</sub>S indicates the existence of Sulfur Oxidizing Bacteria (SOB), which metabolize any H<sub>2</sub>S quantity comes from the lower layers to SO<sub>4</sub><sup>2-</sup>. On the other hand, at the Black Sea sediment, there is a population of Sulfur Reducing Bacteria (SRB), which produce H<sub>2</sub>S by metabolizing sulfur and SO<sub>4</sub><sup>2-</sup>.

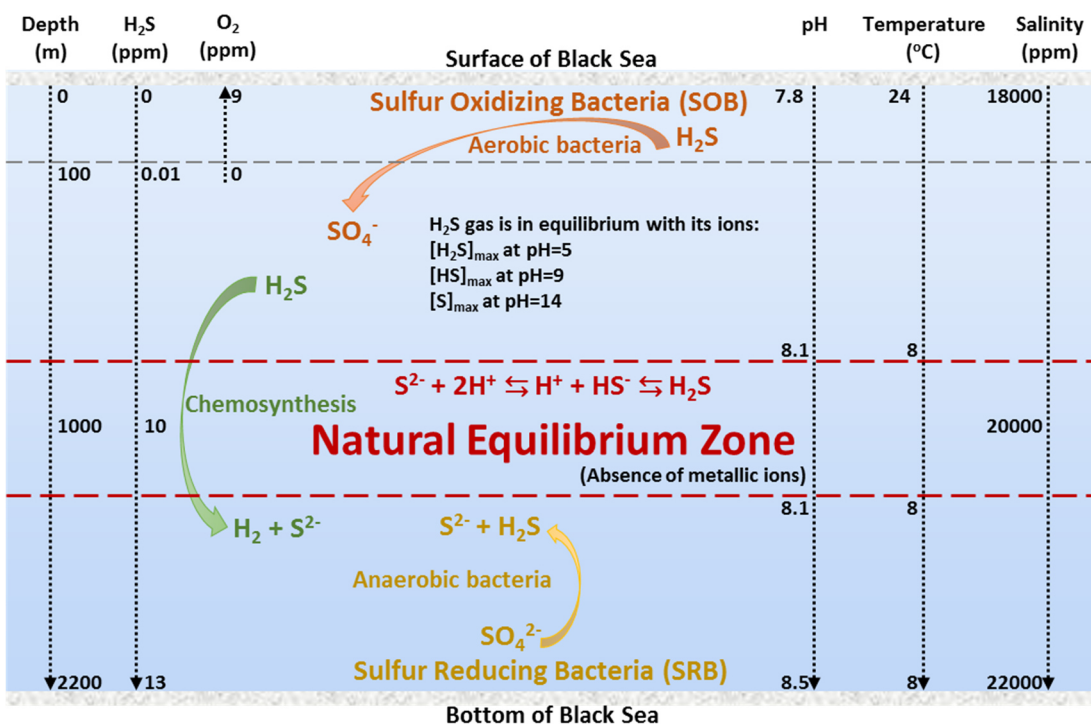


Figure 2.11: The Natural Equilibrium Zone in Black Sea waters.

### 2.5.3. H<sub>2</sub>S Production in Black Sea Waters

Depending on the oxygen concentration, three levels can be distinguished in Black Sea:

- Firstly, an oxic zone until 100 m depth. This first layer is well oxygenated due to the vertical stratification from the rivers and the Bosphorus inflow. The concentration of oxygen arises to 8 to 9 ppm in the surface, with a gradual reduction to zero ppm (James et al., 2005)

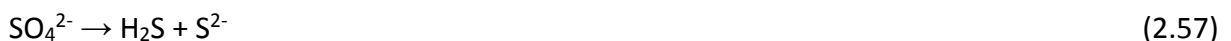
- Secondly, the suboxic zone, which is more a transition layer between the oxic zone and the deep sulfide layer. It is difficult to determine with accuracy the boundaries of this layer, due to the annual fluctuations of both O<sub>2</sub> and H<sub>2</sub>S concentrations. In general, it is defined as the layer where O<sub>2</sub> decreases near to zero and H<sub>2</sub>S starts to appear. In this zone, a significant number of bacterial populations contributes to the microbial production of H<sub>2</sub>S, through the chemosynthetic process (Veziroğlu and Tsitskishvili, 2012).
- Finally, the anoxic zone is present from 1,500 m down to the sediment of the sea, in which the lack of dissolved oxygen and the existence of hydrogen sulfide at 13 ppm concentration are the main characteristics.

The Sulfur Oxidizing Bacteria (SOB) that exist in the oxic zone, prevail the formation of H<sub>2</sub>S, as they are capable to oxidize it to elemental sulfur (S) or sulfate (SO<sub>4</sub><sup>2-</sup>):



The SOB also utilize the dissolved oxygen to decompose the organic components in the sea. As the dissolved oxygen concentration decreases, the bacteria use alternative oxygen sources, such as nitrates, nitrites, carbon dioxide and water (Haklıdır et al., 2009).

In the anoxic zone, the SRB convert the sulfide ions to H<sub>2</sub>S gas (Naman et al., 2008):



Those two bacteria types (SOB and SRB) can be found in equilibrium at a depth of approximately 1000 m (Figure 2.11). In this region, known as the 'Natural Equilibrium Zone', the concentration of H<sub>2</sub>S is estimated at 10 ppm, the salinity concentration is 20,000 ppm and the temperature is 8 °C.

#### 2.5.4. H<sub>2</sub>S Contribution to Environmental Degradation in Black Sea

Without any doubt, H<sub>2</sub>S is the main reason for the life decrease in Black Sea waters. As the increase of the eutrophication rate will gradually lead to the rise of the H<sub>2</sub>S layer in the Black Sea, it is important to minimize, if not extinguish, the rising concentrations of H<sub>2</sub>S in the sea waters. The danger of an environmental disaster is present for this region, unless proper security measures are soon adopted. Nonetheless, if an environmental disaster occurs, indications of the ecosystem degradation will be seen at the upper layers of the sea.

Moreover, H<sub>2</sub>S will gradually lead the maritime life in death and therefore in extinction of many species and loss of the biodiversity. Beyond the water level, it is possible that H<sub>2</sub>S will be mixed with air and cause environmental pollution in the atmospheric air of the wider region, threatening in extent the population of the coastal zone regions (Haklidir and Kapkin, 2005). Additionally, if the accumulation of H<sub>2</sub>S continues without control the fire or even explosion hazard is possible. Even if H<sub>2</sub>S is just mixed with air, the maritime population will be contaminated, making it unsuitable for human consumption. As can be concluded, it is of paramount importance to remove this lethal gas from Black Sea for two reasons: (i) to secure the environmental sustainability of the region, the maritime life and the living population; and (ii) to introduce an innovative source of hydrogen, an energy carrier that can cover the demands of the countries and act as an economic asset for the development of the region.

Apart from the contribution of H<sub>2</sub>S to its environmental degradation, the Black Sea faces many additional severe environmental issues that make it one of the most polluted, closed basins worldwide. During the last decades, the pollution caused by anthropogenic factors and natural causes, lead to adverse life conditions for the marine ecosystem (Edwards et al., 2011). Moreover, the extended water contamination poses health risks to the inhabitants and tourists of the area. Furthermore, industrial activity, overfishing, mining, untreated sewage and the Chernobyl accident conducted to the sea's degradation. It is highlighted by the European Environmental Agency (EEA) that the Black Sea environmental issues concern (Ragaini, 1999): contamination of the coastal zone, eutrophication, resources over-exploitation, ineffective catchment management and oil pollution.

One of the major ecological concerns is eutrophication, caused by the inflow of nutrients like phosphorus and nitrogen and other pollutants, coupled with the poor replenishment of water. It is estimated that 70% of those nutrients have a human origin, while the remaining 30% comes from bacterial populations (Petrov, 2011). Until now, eutrophication has led to disastrous consequences including the deterioration of the water quality in the Black Sea, the growth of low-nutritious species, the gradual elimination of marine life and the development of hypoxic conditions.

#### 2.4.5. Environmental Security Policy in Black Sea

In 1990, national organizations and the countries that form the coastal zone of the Black Sea motivated to act towards the protection of the sea from its severe ecological problems. 'The Bucharest Convection', which was the first well-organized attempt for the protection of the Black Sea, was signed in 1992, ratified in 1993 and implemented in 1994. The primary objectives of this convection were (Petrov et al., 2011): i) prevention and protection from land-based pollution; ii) prevention, reduction and control of marine environment pollution caused from oil; iii) prevention, reduction and control of marine environment pollution caused from dumping and untreated hazardous waste disposal; and iv) control of the illegal traffic in the Black Sea region. In 1993, the 'Ministerial Declaration on the Protection of the Black Sea' was signed to reinforce the above goals and also to found Regional Activity Centers in the framework of the Black Sea Regional Energy Centre (BSREC). Incentives for the BSREC were the protection of the prosperity and the reinforcement of the economic stability of the wider coastal region of the Black Sea (Ragaini, 1999). However, the most important environmental endeavor is the 'Black Sea Environmental Programme' (BSEP), established also in 1993 to serve specific goals: i) reinforcement of the endeavors for the Black Sea ecosystem protection; ii) implementation of a proper legal policy for the appraisal; iii) protection against further pollution; iv) enhancement of the existing biodiversity ecosystem; and v) elaboration of future environmental investments.

The above activities are now complemented with additional actions, measurements and policies, such as, the 'Black Sea Strategic Action Plant' (BSSAP) and several declarations by the Ministers of Environment of the relevant counties.

#### 2.5.6. Extraction and Utilization of Hydrogen Sulfide from Black Sea waters

There are four main methods for the extraction of H<sub>2</sub>S from seawater: adsorption, aeration, reverse osmosis and ozonation. In what follows, the above methods are briefly described.

**Adsorption:** For the H<sub>2</sub>S adsorption from the Black Sea waters, the major step is to decrease the pH level from 8 to 4, in order to secure proper conditions. Then, the extracted H<sub>2</sub>S/H<sub>2</sub>O solution (from approximately 1500 m depth) is lead to a suitable absorption column. By the utilization of activated carbon and further enrichment with NaOH, H<sub>2</sub>S is separated from

water with the simultaneous production of  $\text{HS}^-$  and  $\text{NaOH}$ . Subsequently, this solution is guided to an evaporator to increase its concentration, before entering into an electrolyzer that will generate  $\text{H}_2$  and polysulfide molecules. The complete process (Figure 2.12) can be described by the following simplified mechanism (Petrov et al., 2011):

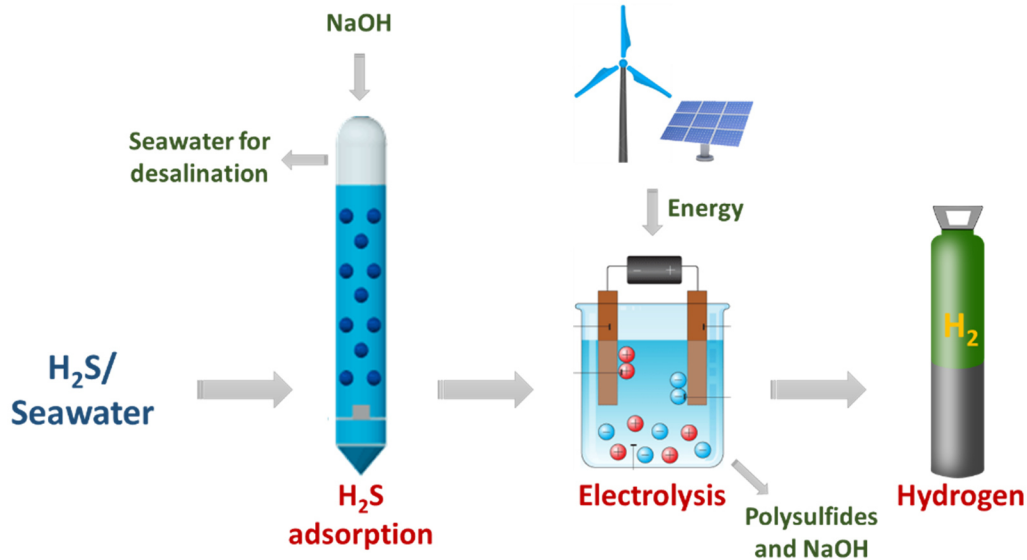


**Figure 2.12:** Process flowsheet for the adsorption and electrolysis of  $\text{H}_2\text{S}$  from seawater.

**Aeration:** Based on the existing technology, there are two main aeration processes that can be proposed for the removal of  $\text{H}_2\text{S}/\text{H}_2\text{O}$  mixtures from the Black Sea, depending on whether the process is located outside or inside the sea. The steps of both processes involve (Naman et al., 2008; Petrov et al., 2011): i) pumping of sea water; ii) extraction and separation of  $\text{H}_2\text{S}/\text{H}_2\text{O}$  to its components, to utilize  $\text{H}_2\text{S}$ ; iii) increase  $\text{H}_2\text{S}$  concentration from 10 ppm to 10,000 ppm; and iv) decomposition of  $\text{H}_2\text{S}$  to produce S and  $\text{H}_2$ . Depending on the selection of the key-process parameters, such as temperature and pH, the efficiency range of the process is 80-98% (Naman et al., 2008; Petrov et al., 2011). A significant drawback of the process, when located outside of water, is that a fraction of the extracted  $\text{H}_2\text{S}$  is oxidized in the atmospheric air, forming sulfide ions ( $\text{SO}_4^{2-}$ ). Also, there is the risk that even small amounts of  $\text{H}_2\text{S}$  can escape from the process to the environment. On the other hand, when the process is located inside the water, the extraction of the  $\text{H}_2\text{S}/\text{H}_2\text{O}$  mixture is carried out in the sea, thus, the only pumping system that is required is for transportation to the

surface. Additionally, no settling tank for storage is required. As a result, the operational cost can be significantly reduced, nominating the process as a potential cost-effective solution for H<sub>2</sub>S extraction. However, the economic impact of this kind of processes is yet under investigation, since the technology is at an early stage of development (Naman et al., 2008; Petrov et al., 2011). Typical units for the in- and out-water extraction processes can be seen in Figure 2.13.

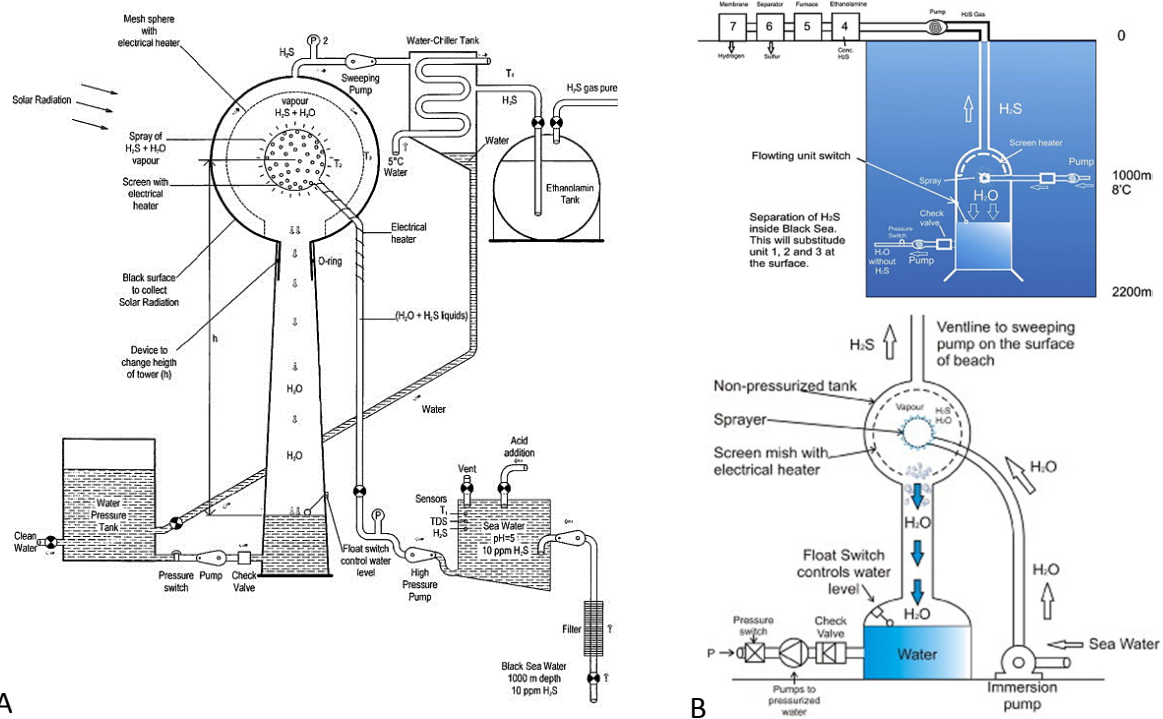


**Figure 2.13:** A) Out of water H<sub>2</sub>S extraction unit; B) In water H<sub>2</sub>S extraction units (Naman et al., 2008).

**Reverse osmosis:** It is possible to separate H<sub>2</sub>S from seawaters by using a semi permeable membrane that allows the solute to stay at the pressurized side, while the solvent passes to the other side of the membrane. For example, the recovery of H<sub>2</sub>S Black Sea water, along with iron-containing phosphotungstate heteropoly compounds, has been proposed (Ilinich et al., 1994):



**Ozonation:** H<sub>2</sub>S can be oxidized from the ozone molecules initially to elemental sulfur. Further oxidation leads to the production of sulfite and, subsequently, to sulfate. The use of

metal catalysts (e.g., MgO, ZnO, TiO<sub>2</sub>, Al<sub>2</sub>O<sub>3</sub>, Pr/Al<sub>2</sub>O<sub>3</sub>, Co/Al<sub>2</sub>O<sub>3</sub>, TiO<sub>2</sub>/silica gel, TiO<sub>2</sub>/Al<sub>2</sub>O<sub>3</sub>) has an effective impact on the H<sub>2</sub>S ozonation process. However, the major drawback of this technology is the high operational cost, compared to the previous extraction processes.

**Conversion of H<sub>2</sub>S to H<sub>2</sub>:** Upon its separation from Black Sea waters, the exploitation of H<sub>2</sub>S towards H<sub>2</sub> production can be realized using existing technologies, such as, thermal, thermochemical, photochemical, photoelectrochemical, plasmochemical and electrolysis processes. Consequently, several H<sub>2</sub> production processes have been proposed, based on specific technological and economic criteria, and were discussed in the previous sections.

## REFERENCES

- Amouyal E. (1995). Photochemical production of hydrogen and oxygen from water: A review and state of the art. *Solar Energy Materials and Solar Cells*, 38: pp. 249-276.
- Armor J.N. (1999). Striving for catalytically green processes in the 21<sup>st</sup> century. *Applied Catalysis A: General*, 189: pp. 153-162.
- Baldelli R.J., Green F.H., Auer R.N. (1993). Sulfide toxicity: mechanical ventilation and hypotension determine survival rate and brain necrosis. *Journal of Applied Physiology*, 75: pp. 1348-1353.
- Banerjee A.M., Bhattacharyya K., Pai M.R., Tripathi A.K., Kamble V.S., Bharadwaj S.R., Kulshreshtha S.K. (2006). Studies on Sulfur-Iodine thermochemical cycle for hydrogen production, *International Symposium on Materials Chemistry*, BARC, Mumbai.
- Barelli L., Bidini G., Gallorini F., Servili S. (2008). Hydrogen production through sorption-enhanced steam methanereforming and membrane technology: A review. *Energy*, 33: pp. 554-570.
- Barreto L., Makihiro A., Riahi K. (2003). The hydrogen economy in the 21<sup>st</sup> century: a sustainable development scenario. *International Journal of Hydrogen Energy*, 28: pp. 267-284.
- Baykara SZ. (2011). Black Sea and hydrogen sulphide. In: Ryann A.L., Perkins N.J., editors. *The Black Sea: dynamics, ecology and conservation*. New York: Nova Science Publishers.
- Baykara S.Z., Figen E.H., Kale A., Veziroglu T.N. (2007). Hydrogen from hydrogen sulphide in the Black Sea. *International Journal of Hydrogen Energy*, 32: pp. 1246-1250.
- Borysova O., Kondakov A., Paleari S., Rautalahti-Miettinen E., Stolberg F., Daler D. (2005). *Eutrophication in the Black Sea region; Impact assessment and Causal chain analysis*” University of Kalmar, Kalmar, Sweden.
- BP Statistical Review of World Energy, June 2016, 65<sup>th</sup> Edition. Available at: <https://www.bp.com/content/dam/bp/pdf/energy-economics/statistical-review-2016/bp-statistical-review-of-world-energy-2016-full-report.pdf>. Accessed: 02/04/2017.
- Cai Q., Adjiman C.S., Brandon N.P. (2014). Optimal control strategies for hydrogen production when coupling solid oxide electrolyzers with intermittent renewable energies. *Journal of Power Sources*, 268: pp. 212-224.
- Chauhan N.S., Singh V.K. (2009). Fundamentals and use of hydrogen as a fuel. *Journal of Mechanical Engineering*, 6: pp. 63-68.

- College of the Desert, SunLine Transit Agency. (2001). Hydrogen fuel cell engines and related technologies. Energy Technology Training Center.
- Costigan M.G. (2003). Hydrogen sulfide: UK occupational exposure limits. *Occupational and Environmental Medicine*, 60: pp. 308-312.
- Collodi G., Wheeler F. (2010). Hydrogen production via steam reforming with CO<sub>2</sub> capture.
- Deuser W.G. (1974). Evolution of anoxic conditions in Black Sea during holocene. In: Degens E.T., Ross D.A., editors. *The Black Sea geology, chemistry and biology*. Tulsa-Oklahoma: American Association of Petroleum Geologists.
- Dincer I. (1999). Environmental impacts of energy. *Energy Policy*, 27: pp. 845-854.
- Dorokhina A., Tessema D. (2011) World Energy and Population: trends to 2050. Advanced Research Project. MBA International Business Management, Virginia International University: 627.
- Dutta S. (2014). A review on production, storage of hydrogen and its utilization as an energy resource. *Journal of Industrial and Engineering Chemistry*, 20: pp. 1148-1156.
- Edwards S., Alharthi R., Ghaly A.E. (2011). Removal of hydrogen sulphide from water. *American Journal of Environmental Sciences*, 7: pp. 295-305.
- Elsner M.P., Menge M., Müller C., Agar D.W. (2003). The Claus process: teaching an old dog new tricks, *Catalysis Today*, 79–80: pp. 487-494.
- Energy Information Administration. (2008). The impact of increased use of hydrogen on petroleum consumption and carbon dioxide emissions. Tech. Rep. SR/OIAFCNEAF/ 2008-04, *Energy Information Administration*, Office Energy Statistics from the US Government.
- European Commission, Community Research. (2006). Introducing hydrogen as an energy carrier: safety, regulatory and public acceptance issues. Directorate General for Research Sustainable Energy Systems. *European Community*.
- European Parliament Directive 2009/28/EC of the Council of 23 April 2009 on the promotion of the use of energy from renewable sources and amending and subsequently repealing Directives 2001/77/EC and 2003/30/EC. Available at: <http://eur-lex.europa.eu/legal-content/EN/TXT/PDF/?uri=CELEX:32009L0028&from=en>. Accessed: 05/04/2017.
- European Parliament Directive Directive (EU) 2015/1513 of the Council of 9 September 2015 amending Directive 98/70/EC relating to the quality of petrol and diesel fuels and amending Directive 2009/28/EC on the promotion of the use of energy from renewable sources. Available at: <http://eur-lex.europa.eu/legal-content/EN/TXT/PDF/?uri=CELEX:32015L1513&from=en>. Accessed: 05/04/2017.
- Fletcher E.A., Noring J.E., Murray J.P. (1984). Hydrogen sulfide as a source of hydrogen. *International Journal of Hydrogen Energy*, 9: pp. 587-593.
- Goltsov V.A., Veziroglu T.N., Goltsova L.F. (2006). Hydrogen civilization of the future-a new conception of the IAHE. *International Journal of Hydrogen Energy*, 31: pp. 153-159.
- Haklıdır M., Servin F., Kapkin S. (2006). Possibilities of production and storage of hydrogen in the Black Sea. *16<sup>th</sup> World Hydrogen Energy Conference*, 4: pp. 3072-3079.
- Haklıdır M., Şule K. (2005). Black Sea, A Hydrogen Source. *International Hydrogen Energy Congress and Exhibition, IHEC*.
- Holladay J.D., Hu J., King D.L., Wang Y. (2009). An overview of hydrogen production technologies, *Catalysis Today*, 139: pp. 244-260.
- Ilinich O.M., Semin G.L., Vetchinova Yu.S., Zamaraev K.I. (1994). Reverse osmosis for separation of reaction solutions in homogenous catalysis. *Journal of Membrane Science*, 86: pp. 37-45.

- James O.O., Maity S., Mesubi M.A., Ogunniran K.O., Siyanbola T.O., Sahu S., Chaubey R. (2011). Towards reforming technologies for production of hydrogen exclusively from renewable resources. *Green Chemistry*, 13: pp. 2272-2284.
- Kaloidas V.E., Papayannakos N.G. (1989). Kinetics of thermal non-catalytic decomposition of hydrogen sulphide. *Chemical Engineering Science*, 44: pp. 2493-2500.
- Kaltschmitt M., Streicher W. (2007). Introduction. In: Renewable Energy Technology, Economics, and Environment. Kaltschmitt M. & Streicher W. (Eds.), Berlin, Springer: pp. 1-19.
- Kleijn R., Der Voet E.V. (2010). Resource constraints in a hydrogen economy based on renewable energy sources: An exploration. *Renewable Sustainable Energy Review*, 14: pp. 2784-2795.
- Lein A.Y., Ivanov M.V. (1991). On the sulphur and carbon balances in the Black Sea. In: Izdar E., Murray J.W. (Eds.), Black Sea Oceanography, *NATO-ASI Series C*, 351: pp. 307-318.
- Licht S. (2005). Thermochemical solar hydrogen generation. *Chemical Communications*, 37: pp. 4635-4646.
- Manenti F., Papasidero D., Bozzano G., Pierucci S., Ranzi E., Ferraris G.B. (2013). Total plant integrated optimization of sulfur recovery and steam generation for Claus processes using detailed kinetic schemes, 23<sup>rd</sup> European Symposium on Computer Aided Process Engineering – ESCAPE 23, Lappeenranta, Finland, pp. 811-816.
- Mathai J.C., Missner A., Kugler P., Saparov S.M., Zeidel M.L., Lee J.K., Pohl P. (2009). No facilitator required for membrane transport of hydrogen sulfide. *Proceedings of National Academic Science USA*, 106: pp. 16633-16638.
- Mazloomi K., Sulaiman N., Moayedi H. (2012). Electrical efficiency of electrolytic hydrogen production. *International Journal of Electrochemistry Science*, 7: pp. 3314-3326.
- Meng N., Leung D.Y.C., Leung M.K.H., Sumathy K. (2006). An overview of hydrogen production from biomass. *Fuel Processing Technology*, 87: pp. 461-472.
- Midilli A., Ay M., Dincer I., Rosen M.A. (2005a). On hydrogen and hydrogen energy strategies I: current status and needs, *Renewable Sustainable Energy Review*, 9: pp. 255-271.
- Midilli A., Ay M., Dincer I., Rosen M.A. (2005b). On hydrogen and hydrogen energy strategies II: future projections affecting global stability and unrest, *Renewable and Sustainable Energy Reviews*, 9: pp. 273-287.
- Midilli A., Ay M., Kale A., Veziroglu T.N. (2007). A parametric investigation of hydrogen energy potential based on H<sub>2</sub>S in Black Sea deep waters. *International Journal of Hydrogen Energy*, 32: pp. 117-124.
- Midilli A., Dincer I. (2008). Hydrogen as a renewable and sustainable solution in reducing global fossil fuel consumption, *International Journal of Hydrogen Energy*, 33: pp. 4209-4222.
- Mulder G., Hetland J., Lenaers G. (2007). Towards a sustainable hydrogen economy: Hydrogen pathways and infrastructure. *International Journal of Hydrogen Energy*, 32: pp. 1324-1331.
- Murray J.W., Jannasch H.W., Honjo S., Anderson R.A., Reeburg W.S., Top Z. (1989). Unexpected changes in the oxic-anoxic interface in the Black Sea. *Nature*, 338: pp. 411-413.
- Naman S.A., Ture E.I., Veziroglu T.N. (2008). Industrial extraction pilot plant for stripping H<sub>2</sub>S gas from Black Sea water. *International Journal of Hydrogen Energy*, 33: pp. 6577-6585.
- Neretin L.N., Volkov I.I., Bottcher M.E., Grinenko V.A. (2001). Sulfur budget for the Black Sea anoxic zone. *Deep-Sea Resources*, 48: pp. 2569-2593.
- Noring J.E., Fletcher E.A. (1982). High temperature solar thermochemical processing-hydrogen and sulfur from hydrogen sulfide. *Energy*, 7: pp. 651-667.

- Ohta T. (2006). Some thoughts about the hydrogen civilization and the culture development. *International Journal of Hydrogen Energy*, 31: pp. 161-166.
- Paris Climate Change Conference - November 2015, Decisions. Available at: [http://unfccc.int/meetings/paris\\_nov\\_2015/meeting/8926/php/view/decisions.php#c](http://unfccc.int/meetings/paris_nov_2015/meeting/8926/php/view/decisions.php#c). Accessed: 08/04/2017.
- Petrov K., Baykara S.Z., Ebrasu D., Gulin M., Veziroglu A. (2011). A brief assessment of hydrogen production from H<sub>2</sub>S in Black Sea waters. *International Journal of Hydrogen Energy*, 36: pp. 8936-8942.
- Ragani R.C. (1999). Environmental security issues in the Black Sea region. *Environmental Protection Department*.
- Rand D.A.J., Dell R.M. (2007). Hydrogen energy challenges and prospects, *RSC Energy Series*.
- Raymont M.E.D. (1974). Hydrogen sulfide thermal decomposition. Ph.D. Thesis, University of Calgary, Calgary, Canada.
- Reverberi A.P., Klemes J.J., Varbanov P.S., Fabiano B. (2016). A review on hydrogen production from hydrogen sulphide by chemical and photochemical methods. *Journal of Cleaner Production*. 136: pp. 72-80.
- Rigden J.S. (2004). Hydrogen: The essential element. *Journal of Chemical Education*, 81: pp. 36.
- Russ B. (2009). Sulfur-Iodine process summary for the hydrogen technology down-selection. *General Atomics*, Technical Report.
- Selene C.H., Chou J. (2003). Hydrogen Sulfide: Human Health Aspects. World Health Organization, Geneva.
- Scholz W.H. (1993). Processes for industrial production of hydrogen and associated environmental effects. *Gas Separation and Purification*, 7: pp. 131-139.
- Sivasubramania P.K., Ramasamy R.P., Freire F.J., Holland C.E., Weidner J.W. (2007). Electrochemical hydrogen production from thermochemical cycles using a proton exchange membrane electrolyzer. *International Journal of Hydrogen Energy*, 32: pp. 463-468.
- Stambouli A.B., Traversa E. (2002). Fuel cells an alternative to standard sources of energy. *Renewable Sustainable Energy Review*, 6: pp. 295-304.
- Uslu O. (2013). Resilience of ecological systems. In: Humboldt Kolleg: Innovative and eco-friendly future energy technologies and use of regional resources of Turkey and the European Union, Istanbul.
- Veziroğlu A., Tsitskishvili M. (2012). *Proceedings of the NATO Advanced Research Workshop on The Black Sea: Strategy for addressing its energy resource development and hydrogen energy problems, Batumi, Georgia*.
- Yang B.L., Kung H.H. (1994). Hydrogen recovery from hydrogen sulfide by oxidation and by decomposition. *Industrial and Engineering Chemistry Research*, 33: pp. 1090-1097.
- Zaman J., Chakma A. (1995). Production of hydrogen and sulfur from hydrogen sulfide. *Fuel Processing Technology*, 41: pp. 159-198.



# CHAPTER

# 3

## PROTON CONDUCTORS

Contents	Page
3.1. Introduction.	55
3.2. Solid electrolytes: definition and types.	55
3.3. Proton conductors, $H^+$ .	58
3.4. Proton conductor membrane reactors: operation and design.	65
3.5. Applications of proton conductor membrane reactors.	66
3.6. Conclusions.	86
References.	87



### 3.1. INTRODUCTION

Proton conducting materials have become the subject of intensive research due to their potential to reduce the operating temperature of solid oxide fuel cells, thus allowing the use of inexpensive materials. In 1981, Iwahara et al. reported that specific perovskite-type materials, based on  $\text{SrCeO}_3$ , exhibited high protonic conductivity at relatively large temperatures (500-1,000 °C). Since then, an extensive number of proton conducting ceramics has been synthesized and the relevant proton conduction properties have been studied (Iwahara et al., 1988; Scherban, 1989; Bonanos et al., 1991; Slade, 1993; Kreuer and Schonherr, 1994; Iwahara, 1995). In addition to their standard applications, i.e., sensors, separators, fuel cells and hydrogen pumps (Iwahara, 1995; Pal'guev, 1998; Matsumoto et al., 1999; Schober, 2003; Iwahara et al., 2004), high temperature proton conductors have been also used in the fabrication of proton conducting membrane cell reactors, in which catalytic hydro- and dehydro-genations are optimized in terms of their yield and/or selectivity to the desired product. Chapter 3 provides a brief description of the above applications and focuses specifically to the proton conducting membrane reactors (PCMRs), by presenting the major findings in the field during the last 30 years. It should be noted that due to the lack of a strict and clear classification of the above applications, it is possible that one work may be distributed to more than one category. For example, the steam reforming reaction of hydrocarbons may take place at the anode of a PCMR, with the simultaneous separation of the produced hydrogen from the reacting mixture. Also, a hydrogen separator, in which  $\text{H}_2$  is immediately used as a reactant, may be considered as a PCMR, as well. Therefore, the criterion used to include studies herein is the central goal of each PCMR: the production of a compound through a chemical or electrochemical reaction. Note also that emphasis is given in the catalytic studies of  $\text{H}_2\text{S}$  decomposition via a proton conducting membrane reactor.

### 3.2. SOLID ELECTROLYTES: DEFINITION AND TYPES

Solid electrolytes are solid-state materials, which under specific conditions can exhibit high ionic conductivity and are ideally impermeable for non-charged reaction species. These materials act as electrochemical cells, where the oxidation and reduction reactions are coupled and carried out separately on catalysts/electrodes layers, located on the opposite

sides of the electrolyte. Since any solid has non-zero ionic and electronic conductivity, it has been established that the solid electrolytes, in which the transference number for ions is two or more orders of magnitude higher than that for electrons, are called as “pure” ionic conductors. On the other hand, if the ionic and electronic transference numbers are of comparable magnitude, then the solids electrolytes are called as “mixed” conductors (Sundmacher et al., 2005; Garagounis et al., 2011). Thus,  $H^+$  or  $O_2^-$  conductors may under certain conditions display conduction of both these ions simultaneously. In a similar manner, mixed ionic-electronic conductivity may be exhibited by a material only in a suitable temperature range (e.g., gadolinia-doped-ceria becomes mixed conductor above 700 °C (Liu and Weppner, 1999)) or under certain gas phase compositions (e.g., doped barium cerates under dry vs. wet  $H_2$  (Coors, 2007)). Note that, the ionic conductivity of solid electrolytes is not a result of their porosity. Both purely ionic and mixed conductors are dense materials, and their conductivity is based on ionic displacement through their lattice. Figure 3.1 presents the conductivity of solid electrolytes compared to other categories of materials.

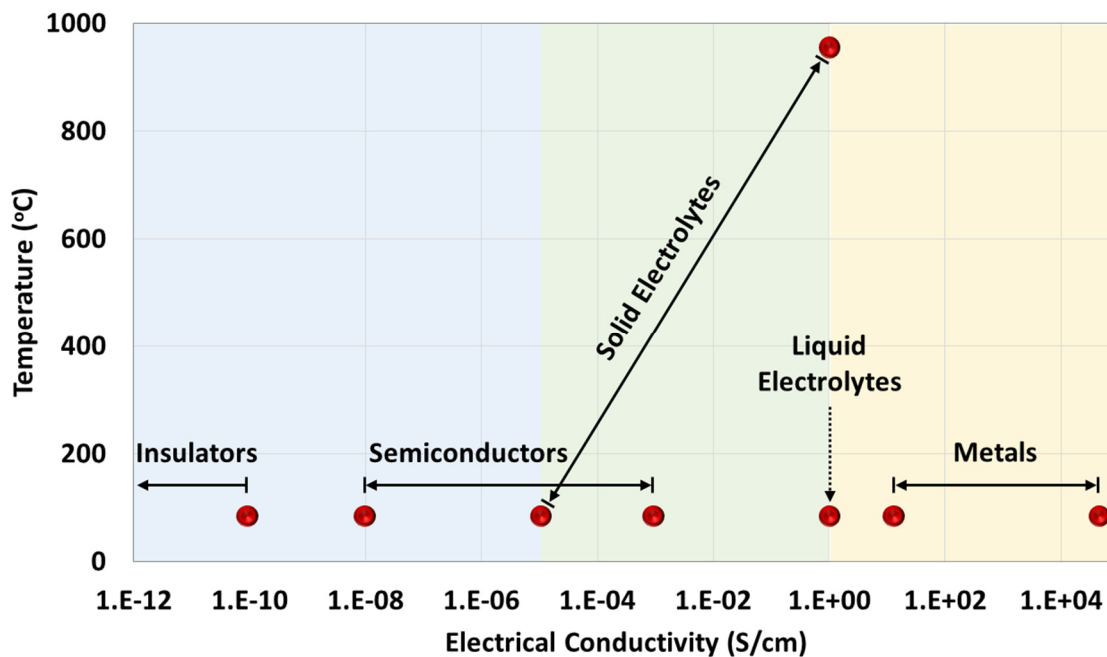


**Figure 3.1:** Electrical conductivity comparability graph for various materials.

As illustrated in Figure 3.1, the conductivity of solid electrolytes is larger than that of semiconductors ( $10^{-8}$ - $10^{-3}$  S/cm) and smaller than that of metals ( $10$ - $10^5$  S/cm). Also, when the operating temperature of the solid electrolyte is increased by few hundred degrees,

their conductivity increases significantly; for some materials is comparable to that of liquid electrolytes. Heat-resistant solid electrolytes can be oxides or mixtures of metal oxides (operating temperatures >1000 °C), as well as polymeric membranes (operating temperatures slightly >100 °C).

The classification of solid electrolytes can be performed according to the main conducting ion (anion or cation), the operating temperature or the material itself. When classified by the operation temperature, solid electrolytes can be separated into low, intermediate and high temperature conductors. There is no precisely defined boundary between the temperature ranges, however, the range 300-700 °C is considered as a good approximation for intermediate temperatures. Moreover, the range of operation of each electrolyte depends on the material. Thus, polymer electrolytes can be used at room temperature, though only up to about 120-150 °C, solid salt electrolytes can be used roughly between 150-300 °C and molten salts or solid oxides above 300 °C. The operation range of O<sup>2-</sup>, F<sup>-</sup>, H<sup>+</sup>, K<sup>+</sup>, Na<sup>+</sup>, Cu<sup>+</sup>, Ag<sup>+</sup>, and Li<sup>+</sup> based conductors is presented in Figure 3.2 (Rickert, 1978; Bates et al., 1982; Hibino et al., 1995; Hibino et al., 1996; Gellings and Bouwmeester, 1997).

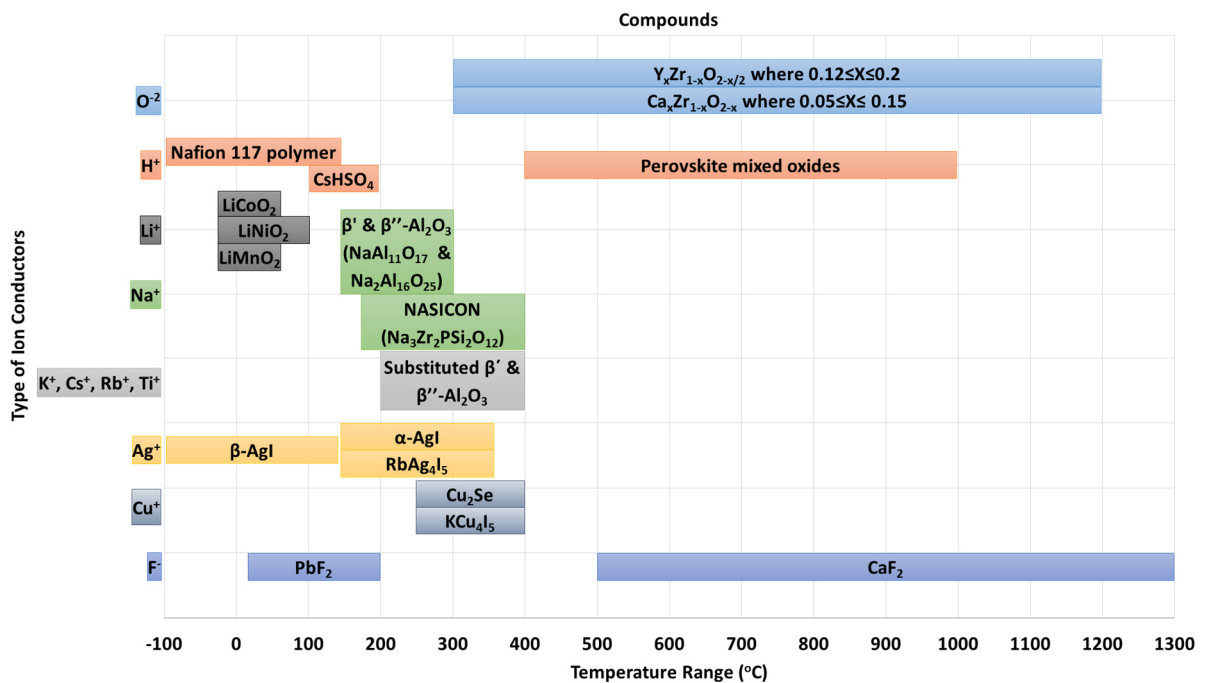


Figure 3.2: The main solid electrolytes categories based on the conducting ion, their major compounds and operation temperature range.

Because of their industrial importance in catalytic oxidation and hydrogenation processes, oxygen ion ( $O^{2-}$ ) and proton ( $H^+$ ) conductors are widely used. The most commonly used type of solid electrolytes, in the range of intermediate to high temperatures, are the solid oxide oxygen conducting ions ( $O^{2-}$ ). They are solid solutions of oxides of divalent or trivalent cations ( $Y_2O_3$ ,  $CaO$ ,  $Yb_2O_3$ ) in oxides of tetravalent metals ( $ZrO_2$ ,  $ThO_2$ ,  $CeO_2$ ). Due to its chemical stability and mechanical strength, the most popular and widely used  $O^{2-}$  conductor is 6-10 mol%  $Y_2O_3$  in  $ZrO_2$ , yttria-stabilized zirconia, YSZ. Though, gadolinia doped ceria (GDC or CGO) and various perovskite-based electrolytes present similar advantages. In the present chapter focus is given on high temperature proton conductors ( $H^+$ ), namely perovskite-type oxides, as well as, on their operation and application as membrane reactors.

### 3.3. PROTON CONDUCTORS, $H^+$

The development of new materials for solid oxide fuel cells (SOFCs), to be operated at low temperatures, is vital for the effective reduction of SOFC technologies cost (Singhal, 2000; Su et al., 2008). Proton conductors are usually defined as the materials in which protons, in the form of positively charged ions, can be transferred through the solid electrolyte and be converted to hydrogen gas at the cathode. Generally, beyond protons ( $H^+$ ), other conducting species that are able to transfer ions are:  $OH^-$ ,  $H_2O$ ,  $H_3O^+$ ,  $NH_4^+$ ,  $HS^-$ , etc. In principle, proton conducting electrolyte materials present a good alternative to the oxide ion conducting ones at intermediate temperatures. Thus, proton conductors are promising electrolytes, because of their lower activation energy (Kreuer, 1999; Katahira et al., 2000; Kreuer, 2003; Yamazaki et al., 2008; Shim et al., 2008) and larger conductivity at lower temperatures than oxide ion conductors (Kreuer, 1997; Norby and Larring, 1997).

Protonic conductors can be classified in a variety of ways, such as according to the preparation method, structural dimensionality, chemical composition, cost or conductivity mechanism (Colomban, 1992). As far as the preparation method is concerned, there are two major categories: direct synthesis or ion exchange. The former is usually used for hydrates, while the latter substitutes conducting ions with superionic conductors, by immersing the sample in a molten salt or an acidic solution. In the following subsections, protonic conducting materials are classified and discussed briefly, according to the temperature range

(emphasis is given to high temperature proton conductors), in which they can be efficiently used in technological applications (Alberti and Casciola, 2001):

- Low temperature proton conductors ( $T < 100$  °C);
- Proton conductors in the temperature range of 100-190 °C;
- Proton conductors in the temperature range of 190-350 °C;
- High temperature proton conductors ( $T > 400$  °C).

### 3.3.1. Low Temperature Proton Conductors

It should be noted that the upper temperature limit of this class of proton conductors was selected due to their ability to fully maintain hydration below 100 °C. In general, the majority of them presents conductivities larger than  $10^{-3}$  S/cm. The proton conductivity (at 25 °C) and the activation energy of the main representatives of low temperature proton conductors are reported in Table 3.1.

**Table 3.1:** Proton conductivity ( $\sigma$ ) at 25 °C and activation energy ( $E_a$ ) of the main representatives of low temperature proton conductors (Alberti and Casciola, 2001).

Categories	Proton Conductors	$\sigma$ (S/cm)	$E_a$ (eV)
Sulfonated polymers	Sulfonated polybenzimidazole (S-PBI)	$1 \cdot 10^{-2}$	-
Heteropolyacids	$H_4SiW_{12}O_{40} \cdot 28 H_2O$	$2 \cdot 10^{-2}$	0.40
Hydrated oxides	$SnO_2 \cdot 2 H_2O$	$4 \cdot 10^{-4}$	0.20
Three-dimensional structure	$H_2Sb_4O_{11} \cdot 3H_2O$	$2 \cdot 10^{-3}$	0.42
Layered structure	$\alpha\text{-Zr}(\text{HPO}_4)_2 \cdot n\text{H}_2\text{O}$	$10^{-4}$	0.3

### 3.3.2. Proton Conductors in the Temperature Range of 100-190 °C

The materials which can reach the temperature range of 100-190 °C under hydrated conditions are classified here, with the exception of acidic  $CsHSO_4$ . As this compound is crystalline and water-soluble, it is in general not suitable for the preparation of membranes (Baranov et al., 1982). Since the tendency of a material to lose hydrating water increases with increasing temperature, the maintenance of high values of relative humidity (r.h.) at high temperature requires high applied pressures. Notice that the upper limit of 190 °C was

not selected due to the thermal degradation of the organic network of the materials or due to the large water pressures over this temperature value, but due to the thermal instability of the SO<sub>3</sub>H groups of the conducting polymers and the degradation of SO units over 190 °C. Moreover, as the operational conditions (i.e., temperature and r.h.) are of primary importance for the performance of these materials, their conductivity values must always be accompanied by the relevant conditions values. Table 3.2 reports the major representatives of the proton conductors belonging at this class and their conductivity values at specific operating conditions.

**Table 3.2:** Proton conductivity ( $\sigma$ ) of the major proton materials at the temperature range of 100-190 °C (Alberti and Casciola, 2001).

Proton Conductors	T (°C)	% r.h.	$\sigma$ (S/cm)
$\gamma$ -Zr(PO <sub>4</sub> )(H <sub>2</sub> PO <sub>4</sub> ) $\cdot$ 2H <sub>2</sub> O	100	95	$3 \cdot 10^{-4}$
Nafion	100	100	$1.6 \cdot 10^{-1}$
	150	75	$5 \cdot 10^{-2}$
S-PEEK-1.6 <sup>a</sup>	100	100	$5 \cdot 10^{-2}$
	150	75	$3 \cdot 10^{-3}$
S-PEEK-2.48 <sup>b</sup>	150	75	$3 \cdot 10^{-2}$
	150	0	$5 \cdot 10^{-3}$
CsHSO <sub>4</sub>	150	0	$5 \cdot 10^{-3}$
$\alpha$ -Zr(HPO <sub>4</sub> ) <sub>2</sub> $\cdot$ H <sub>2</sub> O	100	97	$1.5 \cdot 10^{-4}$

<sup>a</sup> S-PEEK-2.48: sulfonated polyether ether ketone with ion exchange capacity of 2.48 mEq/g.

<sup>b</sup> S-PEEK-1.6: sulfonated polyether ether ketone with ion exchange capacity of 1.6 mEq/g.

### 3.3.3. Proton Conductors in the Temperature Range of 190-350 °C

As discussed in the previous section, ionomers containing SO<sub>3</sub>H groups are not classified in the temperature range 190-350 °C, as the degradation of SO units initiates at 190 °C, while the decomposition of the organic backbone usually takes place at temperatures higher than 250 °C. Generally, at temperatures higher than 200-250 °C, it is difficult to perform conductivity measurements at high r.h. values, therefore, the materials are usually studied in anhydrous conditions or under small r.h. values. Note that, since at low r.h. values the condensation of acid groups also takes place, there is the risk that the conductivity will eventually decrease.

### 3.3.4. High Temperature Proton Conductors ( $T > 400$ °C)

Despite that there are numerous excellent proton conductors at small temperatures, they are unstable at temperatures above 300 °C. To this end, during the last years an ever-growing interest has been directed towards high temperature (>400-450 °C) proton conductors (HTPCs) as electrolytes. The first report on oxide material as high-temperature proton conductors dates back to early 1980s, when Iwahara et al. (1981) reported that specific perovskites, namely,  $\text{SrCeO}_3$ ,  $\text{SrZrO}_3$ ,  $\text{BaCeO}_3$  and  $\text{BaZrO}_3$  exhibited efficient proton conductivity at large temperatures (500-1,000 °C), when exposed to hydrogen and/or water vapor containing atmospheres (Iwahara et al., 1993). Upon more than 30 years of active research, the perovskite-type cerates and zirconates have become well-established proton conducting systems. The crystal structure of these materials is based on the perovskite structure (described below), while the largest proton conductivities observed so far are those of  $\text{BaZrO}_3$  or  $\text{BaCeO}_3$  perovskite-structured oxides. In this class of proton conductors, barium zirconate exhibits the lowest distortion with respect to the ideal cubic structure, as the volume of the crystallographic unit cell is the largest. These structural parameters play an important role in the formation of proton charge carriers and their mobility (Kreuer, 1999). Comprehensive reviews detailing the progress over the years have been compiled by Iwahara (1996), Bonanos et al. (1995), Kreuer (2003) Fabbri et al. (2010), Souza and Muccillo (2010), Malavasi et al. (2010), and Reijers and Jaije (2008).

The first mineral perovskite was discovered in the Ural Mountains, Russia, by Gustav Rose, in 1839, and received this name in tribute to the Russian mineralogist Lev Aleksevich von Perovski. Although the name perovskite was originally used to describe the mineral  $\text{CaTiO}_3$ , currently it is commonly employed to name the specific group of oxides with the general formula  $\text{ABO}_3$  and similar crystal structure. This structural family is extremely important in terms of diversity of composition and abundance, since it is estimated that over 50% of the volume of the earth is composed of perovskite minerals (Navrotsky and Weidner, 1989). Compared to other oxide families, such as pyrochlore, compounds of perovskite structure can be obtained from a wide variety of combinations of chemical elements. Generally, the perovskite structure has two sites for cations of different sizes; site A for large cations and site B for cations of smaller size. Furthermore, the distortion of the regular cubic structure facilitates the incorporation of cations of different sizes in the unit cell. A-site can be filled

either by cations of the family of alkaline and alkaline-earth metals or rare earth metals, such as,  $M^+$  (Na, K),  $M^{2+}$  (Ca, Sr, Ba), or  $M^{3+}$  (La, Fe), while B-site can be occupied by cations of the family of transition metals or rare earth elements, such as  $M^{5+}$  (Nb, W),  $M^{4+}$  (Ce, Ti), or  $M^{3+}$  (Mn, Fe, Co, Ga). In addition to structural distortion and as a result of the combination of different ions, perovskite compounds may present large variations to their properties values (Ramadass, 1978): ionic conduction (Huang et al., 1997), proton conduction (Iwahara et al., 1981), superconducting, or semiconducting electronic. The  $ABO_3$  perovskite structure allows the formation of protonic defects in the temperature range of 400-700 °C, as a result of water absorption. The latter phenomenon requires the presence of oxygen ion vacancies in the material's network. Therefore, the large concentration of oxygen vacancies in a material, specifically a perovskite, will enhance its proton conductivity in the presence of steam (Bjørheim et al., 2010). To maintain a sufficient proton density even at small r.h., the oxygen sub-lattice should be strongly basic to form upstanding OH bonds. As a result, the material will be unstable in an atmosphere containing acidic or even amphoteric molecules, such as,  $H_2O$ ,  $CO_2$ ,  $H_2S$ ,  $SO_2$ , and  $SO_3$ , and will eventually form hydroxides, carbonates, sulfides, sulfites, or sulfates. In principle, there are two mechanisms describing the proton conduction. The first is called the Grotthus-mechanism, in which the proton jumps between adjacent oxygen ions, while the second mechanism is the hydroxyl ion migration, which is called the "vehicle" mechanism.

In dry reducing conditions,  $H^+$  dissolve directly to oxygen anions:



Protonic defects can be formed via the reaction between water molecules and oxygen vacancies (Bonanos, 2001; Haile et al., 2001; Kreuer, 2003) according to:



where, two effectively positive hydroxyl-groups on regular oxygen positions are formed, while protonic defects are formed by the dissociative absorption of water at the surface, which requires the presence of oxide-ion vacancies. Gas phase water dissociates into a hydroxide ion and a proton, with the hydroxide ion filling an oxide-ion vacancy and the proton forming a covalent bond with lattice oxygen. Because of the exothermic nature of this reaction (Sherban et al., 1993; Kreuer, 2003), proton conduction dominates at low temperatures. At elevated temperatures, where water desorption is favored (Stevenson et

al., 1993), electronic (p-type) or oxygen-ion conductivity increases (Bonanos, 1992; Schober et al., 1996; Song et al., 2003; Kharton et al., 2006; Pasierb et al., 2007; Fabbri et al., 2009). Furthermore, the incorporation of water in doped systems is more exothermic than that in undoped systems. An example of the impact of water vapor (pressure) can be seen Figure 3.3. Within the examined range of steam pressures,  $6.6 \cdot 10^{-2}$ - $2.3 \cdot 10^3$  Pa, the current efficiency was almost equal to one, up to current density values of 450-600 mA/cm<sup>2</sup>, and approximately 10 times larger than the current efficiency of the dry carrier gas case.

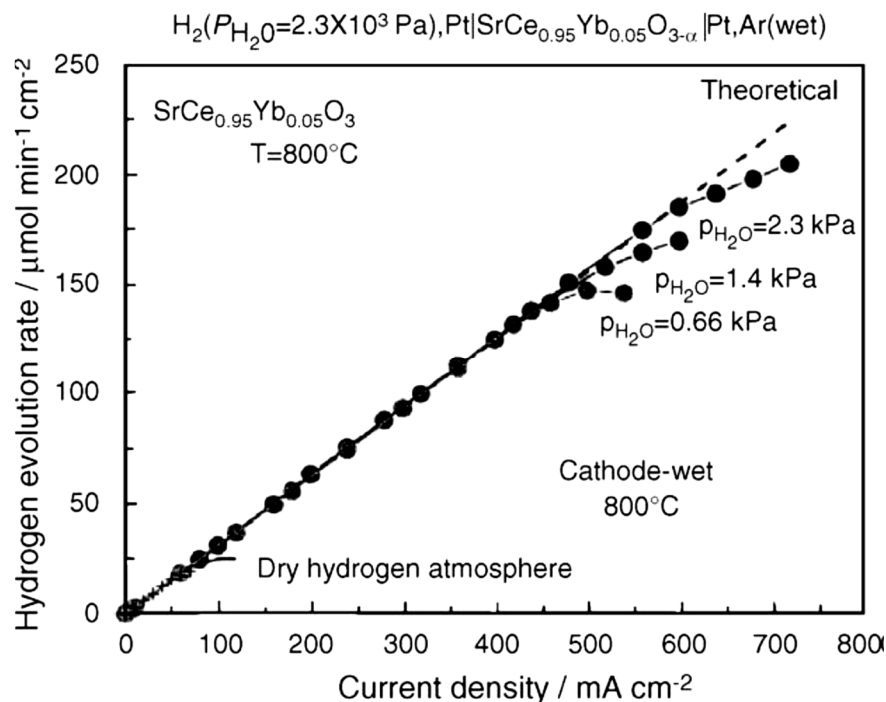


**Figure 3.3:** Hydrogen pumping using proton-conducting ceramic materials:  $\text{H}_2$  evolution rate at cathode vs. cell current density (Matsumoto et al., 2001).

The temperature for the initiation of the dehydration is strongly related to the HTPC composition. Generally, highly basic oxides, such as barium cerates, are better at stabilizing protonic defects, thus dehydration occurs above 600 °C, whereas less basic oxides, such as barium zirconates, start dehydrating above 400 °C (Kreuer, 2003). The optimal temperature range for proton conduction is a compromise between sample hydration and proton mobility; generally peaks between 400-600 °C. Among the HTPC electrolytes, Y-doped barium cerate (BCY) distinguishes for its high proton conductivity (Taniguchi et al., 1992; Shima and Haile, 1997; Ma et al., 1998; Katahira et al., 2000), but suffers from poor chemical

stability, as it easily reacts with acidic gases (e.g.,  $\text{CO}_2$  and  $\text{SO}_2$ ) and steam (Chen et al., 1997; Bhide and Virkar, 1999; Zakawsky et al., 2005). Compared with doped cerates, doped zirconates present better chemical stability but smaller conductivity value for practical applications, due to the presence of a large volume of poorly conductive grain boundaries, induced by the poor sinterability of BZY. The stability of doped-barium cerates could be improved by the introduction of Zr at B site in order to attain high proton conductivity and sufficient chemical stability in fuel cell operating conditions. A review article originally discussed the structural and chemical parameters of a solid solution of  $\text{Y}:\text{BaZrO}_3\text{-BaCeO}_3$  system that determine the formation and mobility of proton defects and renewed the interest in  $\text{BaZr}_{1-x}\text{Y}_x\text{Ce}_y\text{O}_3$  as a chemically stable, high temperature proton conductor (Kreuer, 2003). In Figure 3.4, different proton conducting ceramics and their relevant conductivities are presented.

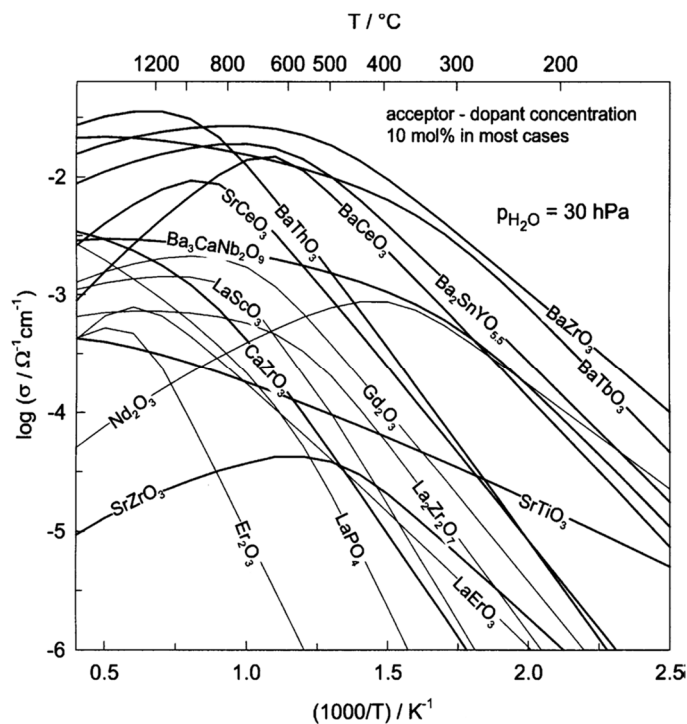


**Figure 3.4:** Examples of different proton conductivities of various oxides. Conductivities of oxides with perovskite-type structure are shown by bold lines (Kreuer, 2003).

Up to date, HTPC have found many electrochemical applications: i) high temperature fuel cells; ii) hydrogen sensors; iii) hydrogen gas separators; iv) proton conducting membrane

reactors; and v) steam electrolysis. In what follows, a survey on the studies and applications of proton conducting membrane reactors is presented.

### 3.4. PROTON CONDUCTOR MEMBRANE REACTORS: OPERATION AND DESIGN

Proton conducting materials can be used as membrane in chemical reactors for several catalytic processes. A schematic diagram of a PCMR is shown in Figure 3.5. The overall reaction that takes place can be written as:



where A and B are the reactant and product of the reaction, respectively.

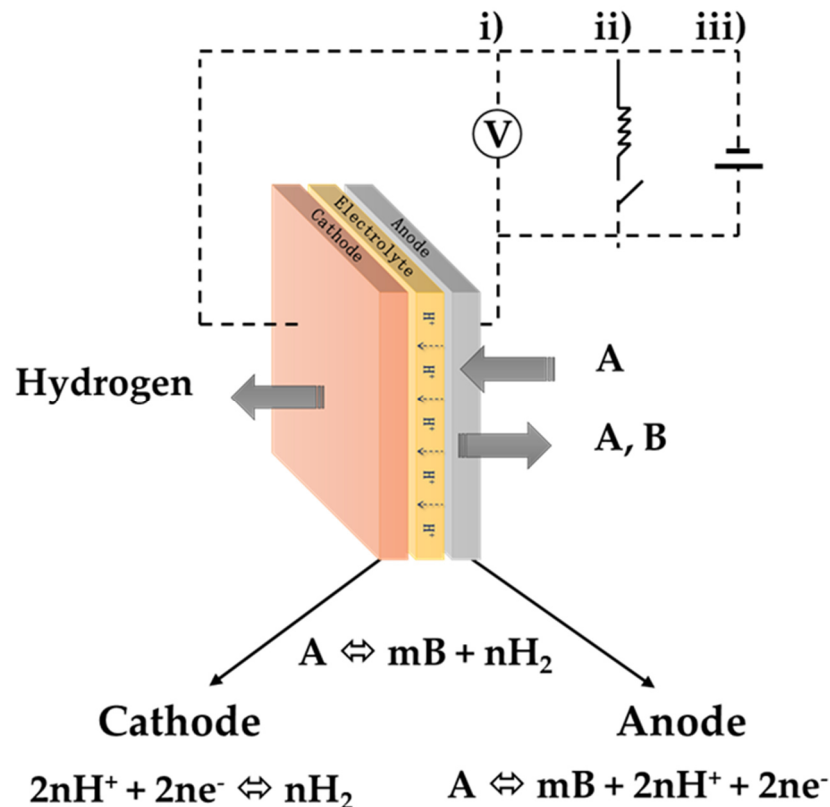


**Figure 3.5:** Schematic of a proton conducting membrane reactor: i) open circuit, ii) fuel cell mode and iii) H<sup>+</sup> pumping mode.

The membrane is sandwiched between two porous electrodes which can be connected to a voltmeter (case i), an external resistive load (case ii), or to an external power source (case

iii). The open-circuit voltage (case i)) provides information on the difference in chemical potential, allowing the investigation of the catalytic properties and reaction mechanisms. In the fuel cell mode (case ii)), chemical energy can be converted directly into electrical energy. By the application of an electrical current (case iii)), the cell acts as an electrochemical hydrogen pump.

In cases ii) and iii), the partial reactions are:



occurring at the anode and cathode, respectively, and resulting into the overall Reaction 3.3 when added by parts. The difference between cases ii) and iii) is that in the former the  $H^+$  ions flow at the direction favored by the chemical potential difference, whereas in the latter, they are forced to flow at the opposite direction. Case iii) mode is therefore called hydrogen pumping, and can be used, amongst other applications, to concentrate the hydrogen concentration at the  $H_2$ -rich side of the membrane. In general, two reactor designs exist: double-chamber or single chamber reactors, depending on if the two electrodes are gas-tight separated from each other or not. If the electrode at the reactant side (working electrode) serves also as the catalyst for the reaction, protons can be pumped to or away from the catalyst, during the reaction. This may affect the catalytic activity and/or the selectivity of the reaction. Usually, the rate at which the reactant(s) are converted to products is equal to the half of the rate at which protons are pumped to or from the catalyst. In this case, the reaction enhancement (if it actual occurs), is defined as Faradaic. In some cases though, the conversion rate can exceed the proton pumping rate, even by orders of magnitude, in an effect called NEMCA (Non-Faradaic Electrochemical Modification of Catalytic Activity).

### 3.5. APPLICATIONS OF PROTON CONDUCTOR MEMBRANE REACTORS

Proton Conducting Membrane Reactors (PCMRs) have been widely used to study a large number of catalytic reactions. Depending on the reaction system and based on the differences between a PCMR and a conventional catalytic reactor, the primary objectives of

these studies are: a) to take advantage of the selective conduction of ions; b) to improve the yield to the desired product via closed circuit operation; and c) to co-generate electricity and value-added chemical compounds via fuel cell mode operation. Examples for each case are described below.

### 3.5.1. Selective Conduction of Ions

The earlier applications of PCMRs in catalytic research aimed at the advantageous selective conduction of ions in these systems. Figure 3.6 represents the use of an  $H^+$  conductor for the reduction of NO by steam (Kobayashi et al., 2000; Kobayashi et al., 2002). At the anode, steam is electrolyzed according to the reaction (Garagounis et al., 2011):



while at the cathode, NO reacts with protons to produce molecular nitrogen:



The overall cell reaction is:

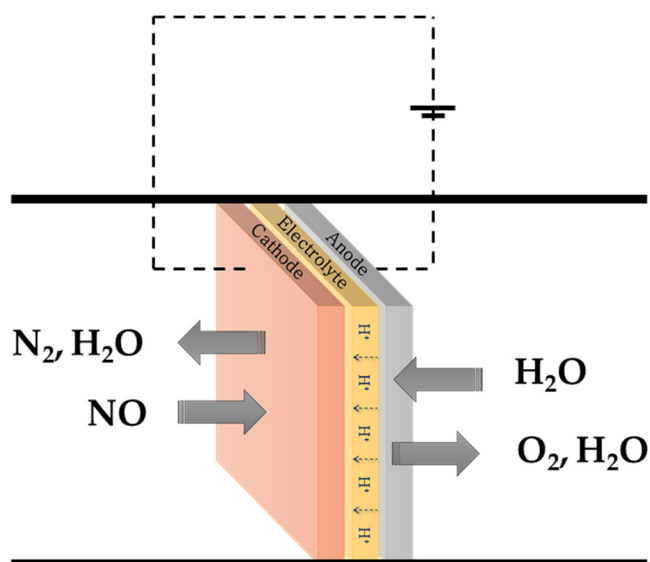


**Figure 3.6:** Schematic diagram of a PCMR used for NO reduction by steam.

As can be seen in Figure 3.6, steam is regenerated at the cathode and  $N_2$ -free  $O_2$  is produced at the anode. The selective conduction of ions offers also an additional advantage; poisonous impurities that may be present along with one of the reactants cannot transfer

through the solid electrolyte. For example, in the industrial production of ammonia, a large fraction of the operating cost is coupled with the preparation and purification of synthesis gas, as trace amounts of sulfur or oxygen cause irreversible poisoning of the used catalyst. More specifically, Figure 3.7 illustrates the synthesis of ammonia from steam and nitrogen (Skodra and Stoukides, 2009), where steam is electrolyzed at the anode to produce protons and oxygen. Subsequently, protons transport to the cathode, react with nitrogen to finally generate ammonia.

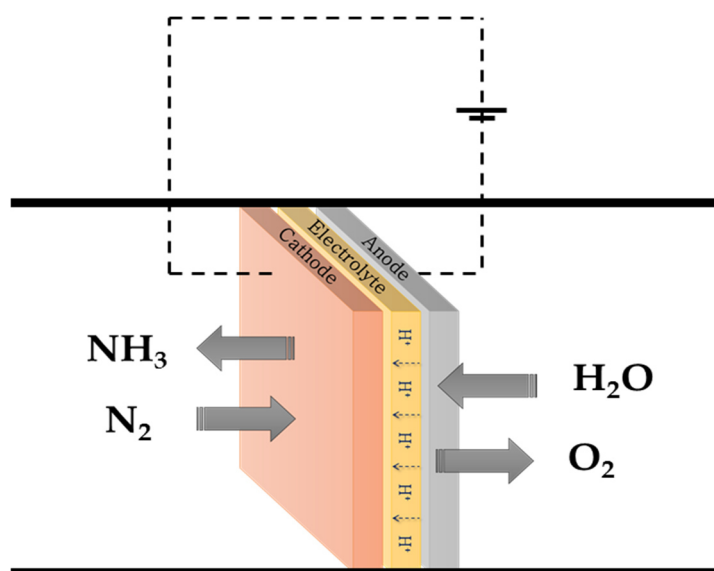


**Figure 3.7:** Schematic diagram of a PCMR used for  $\text{NH}_3$  synthesis from  $\text{N}_2$  and  $\text{H}_2\text{O}$ .

### 3.5.2. Electrochemical Promotion of Catalytic Reactions

PCMRs can be used to electrochemically promote catalytic reaction rates. In more detail, if the catalyst to be promoted is one of the electrodes, protons can be pumped to or away from it during the reaction. This can significantly affect the catalytic activity and/or selectivity of the reaction. The effect of electrochemical pumping can be quantitatively expressed by the use of two dimensionless numbers (Vayenas and Koutsodontis, 2008):

$$\Lambda = \Delta r / (I / 2F) \quad (3.9)$$

$$\rho = r / r_0 \quad (3.10)$$

where  $I$  is the imposed current,  $F$  is Faraday's constant,  $r$  is the catalytic reaction rate obtained at the closed circuit,  $r_0$  is the open circuit catalytic rate, and  $\Delta r = r - r_0$ .

If  $\Lambda=1$ , the effect is faradaic, that is, the increase in the reaction rate equals the rate of proton transport through the electrolyte. In many cases, a strong non-faradaic effect has been observed, where  $\Lambda$  values are in the order of  $10^5$  and  $\rho$  values in the order of  $10^3$  (Vayenas and Koutsodontis, 2008). As explained above, this is the non-faradaic electrochemical modification of catalytic activity (NEMCA) phenomenon, also called electrochemical promotion of catalysis (EPOC). Since the discovery of this phenomenon, several catalytic reaction systems have been reported to exhibit the NEMCA. According to the majority of experimental findings and theoretical calculations, it is due to the introduction of charged species from the solid electrolyte to the catalyst/gas interface. As a result, an overall neutral double layer is formed. This double layer, in turn, modifies the operation function of the catalyst surface and the chemisorptive bond strength of the reacting species, resulting in a reversible effect on the reaction rate. NEMCA can have a significant impact on catalytic research because a) the catalyst surface modification can be monitored electrochemically, that is, unlike gas phase or solid surface promoters, solid electrolytes offer dynamic manipulation of the catalyst properties; b) under a strong NEMCA effect, the product yield and/or selectivity can be maximized by imposing an ionic flux, orders of magnitude smaller than the stoichiometrically demanded; and c) the catalytic activity or selectivity can be optimized by using the single-chamber cell, which does not require the reactants to be separated.

### 3.5.3. Chemical Cogeneration

One of the advantages of PCMRs is that they can operate in a temperature range within numerous reactions can attain rate values of practical interest. Today, as the majority of chemicals are produced via exothermic catalytic pathways, the enthalpy of the relevant reaction, which is conducted in a conventional reactor, is converted into heat. Though, such as process would be much more attractive, provided that the cogeneration of electrical energy along with the targeted products could take place. An example of simultaneous production of useful chemicals and electricity, so called “chemical cogeneration,” is schematically shown in Figure 3.8, where hydrogen sulfide is used as a fuel (Peterson and Winnick, 1996). More specifically, at the anode  $\text{H}_2\text{S}$  is converted into  $\text{S}_2$  and protons:



while at the cathode, protons react with oxygen to produce steam:



Thus resulting in the overall reaction:

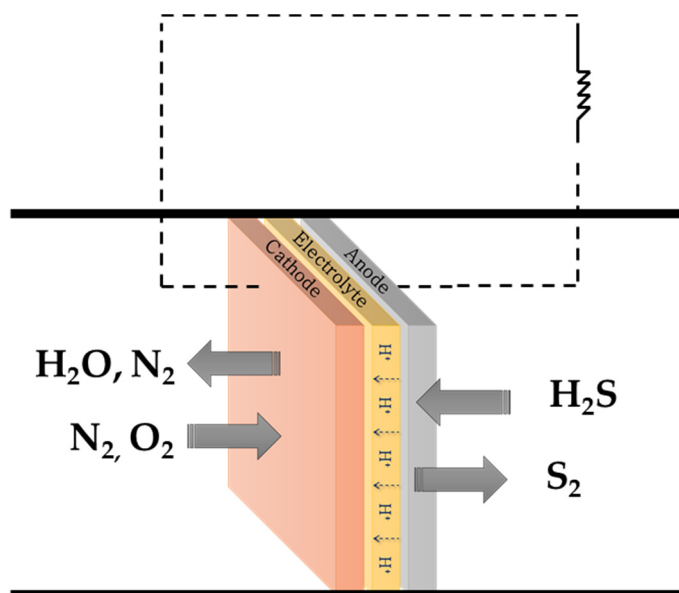


**Figure 3.8:** Schematic diagram of chemical co-generative  $\text{H}_2\text{S}$  fuel cell.

A list of available in the open literature chemical cogeneration studies conducted in PCMRs is presented in Table 3.3. The left-hand column shows the material used as the working electrode (WE, catalyst). The next two columns list the reactants and products of each catalytic system and the corresponding references.

In what follows, Tables 3.4 to 3.12 contain brief details about the catalytic reaction systems that have been studied using PCMRs up to date. The first column on the left-hand side contains the types of used HTPC. The second column lists the used catalysts, which are also the working electrodes (WEs) of the PCMRs. Notice that in some studies, since the HTPC was a mixed conductor (e.g.,  $\text{H}^+$  and  $\text{e}^-$ ) and therefore the cell was self-short-circuited, a working electrode was a prerequisite. The next two columns show the reactants and products formed on the WEs and the counter electrodes (CEs), respectively. It should be highlighted that in the majority of the listed studies, the reaction of interest was catalyzed on the anodic electrode, i.e., where protons are produced. Finally, the last column contains the

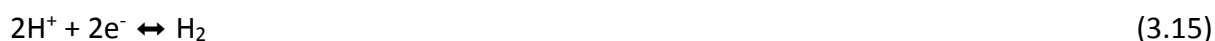
reference(s) of each work, while a summary of the most important findings for each reaction system is given below.

**Table 3.3:** Studies of chemical cogeneration in PCMRs

Working Electrode	Reactants and Products	References
Pt, thiospinels	$\text{H}_2\text{S}, \text{O}_2 \rightleftharpoons \text{S}, \text{SO}_2, \text{H}_2\text{O}$	Kirk and Winnick (1993) Peterson and Winnick (1996)
LSCF Perovskite	$\text{CH}_4, \text{H}_2\text{O}, \text{O}_2 \rightleftharpoons \text{C}_2\text{H}_4, \text{C}_2\text{H}_6, \text{CO}, \text{H}_2$	Kyriakou et al. (2012)
Pt	$\text{C}_2\text{H}_6, \text{O}_2 \rightleftharpoons \text{C}_2\text{H}_4, \text{H}_2\text{O}$	Iwahara et al. 1986)
Ag/Li <sub>2</sub> SO <sub>4</sub> , metal sulfides	$\text{H}_2\text{S}, \text{O}_2 \rightleftharpoons \text{S}_2, \text{H}_2\text{O}$	Zhong et al. (2006) Chuang et al. (2008)
Pt	$\text{C}_2\text{-C}_4 \text{ hydrocarbons}, \text{O}_2 \rightleftharpoons \text{C}_6\text{-C}_8, \text{CO}_2, \text{H}_2\text{O}$	Li et al. (2008)
Pt, Ni	$\text{CH}_4, \text{H}_2\text{O}, \text{O}_2 \rightleftharpoons \text{CO}, \text{H}_2$	Iwahara et al. (1989) Iwahara et al. (1990)

### 3.5.4. Methane Conversion to C<sub>2</sub> Hydrocarbons

The direct conversion of methane to versatile industrial intermediates and end-products, such as ethane or ethylene, is advantageous and financially profitable only when high C<sub>2</sub> yields are attained. In the 1980s, numerous investigators searched for the appropriate catalyst that would favor the oxidative coupling of methane, by successfully suppressing the complete oxidation to CO<sub>2</sub> and H<sub>2</sub>O. Several alternatives to the traditional reaction of gaseous methane and oxygen were examined, including the utilization of PCMRs (Liu et al., 2001; Kokkofitis et al., 2007b; Garagounis et al., 2010). The discovery of HTPCs led several research groups into a different research orientation, which was based on the methane dimerization via dehydrogenation rather than its partial oxidation. In this case, the reactions assumed to occur at the anode and the cathode of a PCMR are, respectively:



The first reports of methane dimerization in a PCMR were published in 1987 by Mori and Lmai and Mori and Lida. They used a SCYb (SrCe<sub>0.95</sub>Yb<sub>0.05</sub>O<sub>3-α</sub>) HTPC and Pt electrodes and by imposing a current through the cell, H<sub>2</sub> was abstracted from the methane stream and was

electrochemically transported to the cathode. At the same time, methane was dimerized to ethylene. As a result, two products were concomitantly produced and separated, hydrogen at the cathode and ethylene at the anode. Iwahara et al. (1989) used Pt electrodes to operate the PCMR as a chemical co-generative fuel cell at 800-1,000 °C. A mixture of steam and methane was fed at the anode and was partially converted to C<sub>2</sub> hydrocarbons. At the cathode, hydrogen was oxidized to water by oxygen. Other research groups (Chiang et al., 1991; Woldman and Sokolovskii, 1991; Chiang et al., 1992; Hamakawa et al., 1993; Hamakawa et al., 1994) also studied the conversion of methane to C<sub>2</sub> hydrocarbons using PCMRs as H<sup>+</sup> pumps. It should be noted that, in principle, the proton transference numbers of Sr-Ce and Ba-Ce perovskites may vary and generally depend on the partial pressures of hydrogen and oxygen. These types of membranes may exhibit almost pure protonic (Mori, 1987; Iwahara et al., 1989; Chiang et al., 1991), mixed protonic-electronic (Hamakawa et al., 1994; Langguth et al., 1997; White et al., 1998), or even mixed oxygen ion-protonic-electronic (Langguth et al., 1997) conductivity. Hence, mixed conducting membranes, coupled with (Hamakawa et al., 1994; Langguth et al., 1997) or without electrodes (White et al., 1998; Terai et al., 1999; Liu et al., 2006), have been applied to achieve efficient yields to C<sub>2</sub> products. It is also worth noticing that several mixed conducting perovskites (e.g., strontium cerates) were proved to be very efficient methane coupling catalysts and have been used such in regular catalytic reactors (Chen et al., 1997). In all cases, however, low C<sub>2</sub> yields were reported (less than 2%). One of the reasons behind this is that at the absence of oxygen, methane pyrolysis inevitably takes place via the reaction:



The partial oxidation of methane was also studied in a PCMR in the presence of steam (Kyriakou et al., 2012) serving a dual scope: a) to produce hydrogen and C<sub>2</sub> hydrocarbons and simultaneously separate H<sub>2</sub> from the reacting mixture (with the reactor operating in the pumping mode), and b) to cogenerate C<sub>2</sub>S and electricity (with the reactor operating in the fuel cell mode). In this process, methane-steam mixtures were fed to the anode, while hydrogen, in the form of H<sup>+</sup>, was pumped from the anode to the cathode. The presence of steam at the anode not only diminished carbon formation but also considerably increased the production of hydrogen (Kyriakou et al., 2012).

**Table 3.4:** Catalytic studies on methane conversion to C<sub>2</sub> hydrocarbons via proton conducting membrane reactors.

HTPC	Catalyst (WE)	Reactants and Products on WE	Reactants and Products on CE	References
SrCe <sub>0.95</sub> Yb <sub>0.05</sub> O <sub>3-α</sub>	Pt	CH <sub>4</sub> ⇌ H <sup>+</sup> , C <sub>2</sub> H <sub>4</sub> , C <sub>2</sub> H <sub>6</sub> , e <sup>-</sup>	e <sup>-</sup> , H <sup>+</sup> ⇌ H <sub>2</sub>	Mori and Lmai (1987) Terai et al. (1999)
SrCe <sub>0.95</sub> Yb <sub>0.05</sub> O <sub>3-α</sub>	Pt	CH <sub>4</sub> (H <sub>2</sub> O) ⇌ H <sup>+</sup> , C <sub>2</sub> H <sub>4</sub> , C <sub>2</sub> H <sub>6</sub> (+CO), e <sup>-</sup>	e <sup>-</sup> , H <sup>+</sup> , O <sub>2</sub> ⇌ H <sub>2</sub> O	Iwahara et al. (1989) Hamakawa et al. (1994)
SrCe <sub>0.95</sub> Yb <sub>0.05</sub> O <sub>3-α</sub>	La <sub>0.6</sub> Sr <sub>0.4</sub> MnO <sub>3</sub>	CH <sub>4</sub> (H <sub>2</sub> O) ⇌ H <sup>+</sup> , C <sub>2</sub> H <sub>4</sub> , C <sub>2</sub> H <sub>6</sub> (+CO), e <sup>-</sup>	e <sup>-</sup> , H <sup>+</sup> (O <sub>2</sub> ) ⇌ H <sub>2</sub> (H <sub>2</sub> O)	Woldman and Sokolovskii (1991)
SrCe <sub>0.95</sub> Yb <sub>0.05</sub> O <sub>3-α</sub>	Ag	CH <sub>4</sub> ⇌ H <sup>+</sup> , C <sub>2</sub> H <sub>4</sub> , C <sub>2</sub> H <sub>6</sub> , e <sup>-</sup>	e <sup>-</sup> , H <sup>+</sup> (O <sub>2</sub> ) ⇌ H <sub>2</sub> (H <sub>2</sub> O)	Hamakawa et al. (1993) Chiang et al. (1991) Chiang et al. (1992)
SrCe <sub>0.95</sub> Yb <sub>0.05</sub> O <sub>3-α</sub>	Ag	CH <sub>4</sub> ⇌ H <sup>+</sup> , C <sub>2</sub> H <sub>4</sub> , C <sub>2</sub> H <sub>6</sub> , e <sup>-</sup>	e <sup>-</sup> , H <sup>+</sup> ⇌ H <sub>2</sub>	Langguth et al. (1997)
BaCe <sub>0.95</sub> Mn <sub>0.05</sub> O <sub>3-α</sub>	-	CH <sub>4</sub> ⇌ H <sup>+</sup> , C <sub>2</sub> H <sub>4</sub> , C <sub>2</sub> H <sub>6</sub> , e <sup>-</sup>	e <sup>-</sup> , H <sup>+</sup> (O <sub>2</sub> ) ⇌ H <sub>2</sub> (H <sub>2</sub> O)	White and Sammells (1998)
SrCe <sub>0.95</sub> Yb <sub>0.05</sub> O <sub>3-α</sub>	SrTi <sub>0.4</sub> Mg <sub>0.6</sub> O <sub>3</sub>	CH <sub>4</sub> , H <sub>2</sub> O ⇌ H <sup>+</sup> , C <sub>2</sub> H <sub>4</sub> , C <sub>2</sub> H <sub>6</sub> , CO <sub>x</sub> , e <sup>-</sup>	e <sup>-</sup> , H <sup>+</sup> , O <sub>2</sub> ⇌ H <sub>2</sub> O	Terai et al. (1999)
SrCe <sub>0.95</sub> Yb <sub>0.05</sub> O <sub>3-α</sub>	-	CH <sub>4</sub> ⇌ H <sup>+</sup> , C <sub>2</sub> H <sub>4</sub> , C <sub>2</sub> H <sub>6</sub> , e <sup>-</sup>	e <sup>-</sup> , H <sup>+</sup> , O <sub>2</sub> ⇌ H <sub>2</sub> O	Liu et al. (2006)
SrCe <sub>0.95</sub> Yb <sub>0.05</sub> O <sub>3-α</sub>	LSCF, Au-CNW	CH <sub>4</sub> , H <sub>2</sub> O ⇌ H <sup>+</sup> , C <sub>2</sub> H <sub>4</sub> , C <sub>2</sub> H <sub>6</sub> , CO <sub>x</sub> , e <sup>-</sup>	e <sup>-</sup> , H <sup>+</sup> (O <sub>2</sub> ) ⇌ H <sub>2</sub> (H <sub>2</sub> O)	Kyriakou et al. (2012)

### 3.5.5. Other Reactions of Methane Activation

The conversion of methane into synthesis gas (CO and H<sub>2</sub>) was investigated by Iwahara et al. (1989) by using Nd-doped barium cerate as the HTPC and Pt the electrodes of a mixed-conducting PCMR. Mixtures of methane in steam were fed in the PCMR at 900-1,000 °C, resulting in high conversion yield to syngas. At the cathode, H<sup>+</sup> and O<sub>2</sub> reacted towards the production of H<sub>2</sub>O. The significant advantage of this specific cell is that both conducting ions contribute to the formation of products. Moreover, Mori (1987) used a SCYb HTPC and Pt electrodes for the decomposition of CH<sub>4</sub> to C and H<sub>2</sub> at the anode and then the transfer and production of H<sub>2</sub> at the cathode. In other works, Belyaev et al. (1995) used a PCMR with Pt electrodes to oxidize CH<sub>4</sub>-O<sub>2</sub> mixtures to CO<sub>2</sub> at the cathode and simultaneously electrolyze steam at the anode. In a similar configuration, Hibino et al. (1994) fed CH<sub>4</sub>-CO<sub>2</sub> mixtures to

the anode and pumped  $H^+$  to accelerate both the reforming of methane and its conversion to  $C_2$  hydrocarbons. Coors (2004; 2006) studied the methane steam reforming reaction in a 10% yttrium-barium cerate PCMR, operating in the fuel cell mode. The ambipolar permeation of steam from the cathode to the anode eliminated the need for an injection process step. Finally, Yamaguchi et al. (2005) converted  $CH_4$ - $O_2$  mixtures to  $CO_2$  and  $H^+$  at the anode, with the latter transported through the HTPC to produce pure  $H_2$  at the cathode.

**Table 3.5:** Catalytic studies on other reactions of methane activation via proton conducting membrane reactors.

HTPC	Catalyst (WE)	Reactants and Products on WE	Reactants and Products on CE	References
$SrCe_{0.95}Yb_{0.05}O_{3-\alpha}$	Pt	$CH_4 \rightleftharpoons H^+, C, e^-$	$e^-, H^+ \rightleftharpoons H_2$	Mori (1987)
$SrCe_{0.95}Yb_{0.05}O_{3-\alpha}$	Pt	$CH_4, H_2O \rightleftharpoons H^+, CO, e^-$	$e^-, H^+, O_2 \rightleftharpoons H_2$	Iwahara et al. (1989)
$BaCe_{0.9}Nd_{0.105}O_{3-\alpha}$	Pt	$CH_4, H_2O \rightleftharpoons H^+, CO, e^-$	$e^-, H^+, O_2 \rightleftharpoons H_2$	Iwahara et al. (1990)
$SrCe_{0.95}Yb_{0.05}O_{3-\alpha}$	Pt	$H^+, CH_4, CO_2, e^- \rightleftharpoons CO_2, H_2O, C_2O, C_2H_4, C_2H_6$	$H_2 \rightleftharpoons e^-, H^+$	Hibino et al. (1994)
$SrCe_{0.92}Dy_{0.08}O_{3-\alpha}$	Pt	$H^+, CH_4, CO_2, e^- \rightleftharpoons CO_2, H_2O, C_2O, C_2H_4, C_2H_6$	$H_2O \rightleftharpoons e^-, H^+, O_2$	Belyaev et al. (1995)
$BaCe_{0.90}Y_{0.10}O_{3-\alpha}$	Ag	$CH_4, H_2O \rightleftharpoons H^+, CO_2, e^-$	$e^-, H^+ \rightleftharpoons H_2$	Yamaguchi et al. (2005)
$BaCe_{0.90}Y_{0.10}O_{3-\alpha}$	Pt	$CH_4 (H_2O) \rightleftharpoons H^+, CO_2, e^-$	$e^-, H^+, O_2 \rightleftharpoons H_2O$	Coors (2003) Coors (2004)
$SrCe_{0.95}Yb_{0.05}O_3$	Pt	$CH_4, \rightleftharpoons H^+, C_2H_4, C_2H_6, e^-$	$e^-, H^+, O_2 \rightleftharpoons H_2O$	Liu et al. (2006)
$BaCe_{0.85}Y_{0.15}O_3$	Pd	$CH_4 \rightleftharpoons H^+, C, e^-$	$e^-, H^+ \rightleftharpoons H_2$	Han et al. (2013)
$SrCe_{0.95}Yb_{0.05}O_3$	LSCF	$CH_4, \rightleftharpoons H^+, C_2H_4, C_2H_6, e^-$	$e^-, H^+ \rightleftharpoons H_2$	Kyriakou et al. (2012)
$SrCe_{0.95}Yb_{0.05}O_3$	Au-CNW	$CH_4, \rightleftharpoons H^+, C_2H_4, C_2H_6, e^-$	$e^-, H^+ \rightleftharpoons H_2$	Kyriakou et al. (2012)
$BaZr_{0.7}Ce_{0.2}Y_{0.15}O_{2.9}$	Ni-BZCY72	$CH_4, \rightleftharpoons H^+, CO, CO_2, e^-$	$e^-, H^+ \rightleftharpoons H_2$	Kyriakou et al. (2016)
$BaZr_{0.7}Ce_{0.2}Y_{0.15}O_{2.9}$	(Cu)-Mo/ MCM-22	$CH_4, \rightleftharpoons H^+, C_6H_6, e^-$	$e^-, H^+ \rightleftharpoons H_2$	Morejudo et al. (2016)

### 3.5.6. Decomposition of Alcohols

In a couple of older studies Iwahara et al. (1986 and 1989) examined the fuel cell operational mode of a PCMR, in which methanol-steam or ethanol-steam mixtures were decomposed at the anode and  $H^+$  reacted with  $O_2$  at the cathode to produce  $H_2O$ . Strontium- and barium-doped cerates were tested as HTPCs to discover that the overall conductivity of barium cerates was larger but, at the same time, they exhibited mixed  $H^+$  and  $O_2$  conductivity.

**Table 3.6:** Catalytic studies on decomposition of alcohols via proton conducting membrane reactors.

HTPC	Catalyst (WE)	Reactants and Products on WE	Reactants and Products on CE	References
$SrCe_{0.95}Yb_{0.05}O_{3-\alpha}$	Pt	$C_2H_5OH \Rightarrow H^+, CO, H_2, e^-$	$e^-, H^+, O_2 \Rightarrow H_2O$	Iwahara et al. (1986)
$SrCe_{0.95}Yb_{0.05}O_{3-\alpha}$ , $BaCe_{0.9}Nd_{0.105}O_{3-\alpha}$	Pt	$CH_3OH \Rightarrow H^+, CO, H_2, e^-$	$e^-, H^+, O_2 \Rightarrow H_2O$	Iwahara et al. (1989)

### 3.5.7. Reactions of Alkanes and Alkenes

The performance of a PCMR, in which ethane was converted to ethylene with simultaneous generation of electrical energy, was initially studied by Iwahara et al. (1986). The cell operation was performed in the temperature range 800-1000 °C, while the selected anode materials were platinum and nickel. It was found that by the addition of water vapor to the ethane feeding stream, the performance of the PCMR was improved (Iwahara et al., 1986). More recently, Karagiannakis et al. (2005 and 2006) studied the conversion of propane to propene and hydrogen at the anode of a SCYb PCMR, where hydrogen was separated from the reacting mixture. The addition of steam resulted to the reduction of carbon, thus avoiding its undesirable deposition on the anodic electrode. In similar studies, a PCMR operated in the fuel cell mode in order to co-produce propylene and electricity from propane (Feng et al., 2007; Feng et al., 2008). It was discovered that under the fuel cell operation, the carbon deposition on the Cr(III)-based anode catalyst was significantly smaller than under the open-circuit operation (Feng et al., 2008).

**Table 3.7:** Catalytic studies on reactions of alkanes and alkenes via proton conducting membrane reactors.

HTPC	Catalyst (WE)	Reactants and Products on WE	Reactants and Products on CE	References
BZY	Pt	$C_2H_4, O_2 \rightleftharpoons H^+, CO_2, H_2O, e^-$	$e^-, H^+, O_2 \rightleftharpoons H_2O$	Poulidi et al. (2003)
$SrCe_{0.95}Yb_{0.05}O_{3-\alpha}$	Pt, Ni	$C_2H_6 \rightleftharpoons H^+, C_2H_4, H_2, e^-$	$e^-, H^+, O_2 \rightleftharpoons H_2O$	Iwahara et al. (1986)
$CaZr_{0.90}In_{0.1}O_{3-\alpha}$	Pt	$C_2H_4, O_2 \rightleftharpoons H^+, CO_2, H_2O, e^-$	$e^-, H^+, O_2 \rightleftharpoons H_2O$	Makri et al. (1996)
$BaCa_{1.18}Nb_{1.82}O_{3-\alpha}$	Pt	$C_2H_4, O_2 \rightleftharpoons H^+, CO_2, H_2O, e^-$	$e^-, H^+, O_2 \rightleftharpoons H_2O$	Thursfield et al. (2003)
$SrCe_{0.95}Yb_{0.05}O_{3-\alpha}$	Pt, Pd	$C_3H_8 \rightleftharpoons H^+, C_3H_6, H_2, e^-$	$e^-, H^+ \rightleftharpoons H_2$	Karagiannakis et al. (2005)
$SrCe_{0.95}Yb_{0.05}O_{3-\alpha}$	Pd	$C_3H_8, H_2O \rightleftharpoons H^+, C_3H_6, H_2, e^-$	$e^-, H^+ \rightleftharpoons H_2$	Karagiannakis et al. (2006)
$BaCe_{0.9}Y_{0.1}O_3$	Pt	$C_2H_6 \rightleftharpoons H^+, C_2H_4, H_2, e^-$	$e^-, H^+, O_2 \rightleftharpoons H_2O$	Feng et al. (2007) Feng et al. (2008)
$BaCe_{0.85}Y_{0.15}O_3$	Pt	$C_2H_6 \rightleftharpoons H^+, C_2H_4, H_2, e^-$	$e^-, H^+, O_2 \rightleftharpoons H_2O$	Wang et al. (2007) Shi et al. (2008)
Poly-benzimidazole (PBI)/ $H_3PO_4$	Pt/C	$C_2H_6 \rightleftharpoons H^+, C_2H_4, H_2, e^-$	$e^-, H^+, O_2 \rightleftharpoons H_2O$	Chen et al. (2009)
$BaCe_{0.85}Y_{0.15}O_3$	Pt	$C_2H_6 \rightleftharpoons H^+, C_2H_4, H_2, e^-$	$e^-, H^+, O_2 \rightleftharpoons H_2O$	Fu et al. (2010)
$BaCe_{0.8}Y_{0.15}Nd_{0.05}O_3$	$Cr_2O_3$	$C_2H_6 \rightleftharpoons H^+, C_2H_4, H_2, e^-$	$e^-, H^+, O_2 \rightleftharpoons H_2O$	Fu et al. (2011)
$BaCe_{0.7}Zr_{0.1}Y_{0.2}O_3$	$Cr_2O_3, WC$	$C_2H_6 \rightleftharpoons H^+, C_2H_4, H_2, e^-$	$e^-, H^+, O_2 \rightleftharpoons H_2O$	Cui et al. (2014)
$BaCe_{0.7}Zr_{0.1}Y_{0.2}O_3$	$La_{0.2}Sr_{0.7}TiO_3$	$C_2H_6 \rightleftharpoons H^+, C_2H_4, H_2, e^-$	$e^-, H^+, O_2 \rightleftharpoons H_2O$	Liu et al. (2015)
Nafion	Pt/C	$C_2H_6 \rightleftharpoons H^+, C_2H_4, H_2, e^-$	$e^-, H^+, O_2 \rightleftharpoons H_2O$	Chen et al. (2011)
$BaCe_{0.7}Zr_{0.1}Y_{0.2}O_3$	$(Pr_{0.4}Sr_{0.6})_3(Fe_{0.85}Mo_{0.15})_2O_7$	$C_2H_6 \rightleftharpoons H^+, C_2H_4, H_2, e^-$	$e^-, H^+, O_2 \rightleftharpoons H_2O$	Liu et al. (2016)

As ethylene is a key chemical with increasing global demand and ethane is the most competitive feedstock for its production (Liu et al., 2015), the development of a PCMR that allows the conversion of ethane to ethylene with simultaneous generation of electrical energy is of highly importance. To this end, current research efforts focus on the identification of effective anode-catalysts. Liu et al. (2015) studied the performance of a PCMR consisting of a  $\text{BaCe}_{0.7}\text{Zr}_{0.1}\text{Y}_{0.2}\text{O}_{3-\delta}$  perovskite as the electrolyte and a  $(\text{Pr}_{0.4}\text{Sr}_{0.6})_3(\text{Fe}_{0.85}\text{Mo}_{0.15})_2\text{O}_7$  double-layered perovskite as the anode. When the cell operated at 750 °C with ethane feed, the power output was equal to  $348.8 \text{ mW}\cdot\text{cm}^{-2}$ , a value comparable to that obtained with hydrogen feed (i.e.,  $496.2 \text{ mW}\cdot\text{cm}^{-2}$ ). At the same time, the  $\text{C}_2\text{H}_4$  selectivity exceeded 90%, resulting to an ethylene yield as high as 41.5% (Liu et al., 2016). Upon the employment of a lanthanum-strontium-titanate anode the same research group reported a stable long-term electrochemical operation of the cell, i.e., 100 h at 700 °C (Liu et al., 2015).

### 3.5.8. Forward and Reverse Water Gas Shift

The water gas shift (WGS) reaction ( $\text{CO} + \text{H}_2\text{O} \rightleftharpoons \text{CO}_2 + \text{H}_2$ ) is a key process for purifying hydrogen, obtained either by steam reforming or by partial oxidation of hydrocarbons. PCMRs can be used to selectively remove hydrogen from the reacting mixture and, at the same time, shift the reaction equilibrium to the right for larger conversions (Matsumoto et al., 2002; Karagiannakis et al., 2003; Coors, 2004). Iwahara et al. (1986) and Matsumoto et al. (2002) used SCYb and Pt electrodes to operate the developed PCMRs as a fuel cell and a hydrogen separator, respectively. This solid electrolyte, however, was not adequate because of the reaction with  $\text{CO}_2$ . Matsumoto et al. (2006) tested zirconate-based electrolytes, which present durability to  $\text{CO}_2$ , and also proposed alternatives to the expensive Pt electrodes. Kokkofitis et al. (2007a) studied the same reaction in a SZY ( $\text{SrZr}_{0.9}\text{Y}_{0.1}\text{O}_{3-\alpha}$ ) PCMR, in which the working (cathodic) electrode was Pd. A moderate NEMCA effect was observed, which resulted in maximum  $\rho$  and  $\Lambda$  obtained values equal to 2.0 and 8.0, respectively. Finally, Karagiannakis et al. (2003) explored the reverse WGS reaction on Cu electrodes in a SZY-based PCMR. It was discovered that upon “pumping” protons to the Cu surface, the intrinsic catalytic activity of the cell was increased up to an order of magnitude.

**Table 3.8:** Catalytic studies on forward and reverse water gas shift reaction via proton conducting membrane reactors.

HTPC	Catalyst (WE)	Reactants and Products on WE	Reactants and Products on CE	References
SrCe <sub>0.95</sub> Yb <sub>0.05</sub> O <sub>3-α</sub>	Pt	CO, H <sub>2</sub> O ⇌ H <sup>+</sup> , CO <sub>2</sub> , H <sub>2</sub> , e <sup>-</sup>	e <sup>-</sup> , H <sup>+</sup> , O <sub>2</sub> ⇌ H <sub>2</sub> O	Iwahara et al. (1986)
SrCe <sub>0.95</sub> Yb <sub>0.05</sub> O <sub>3-α</sub>	Pt	CO, H <sup>+</sup> , H <sub>2</sub> O ⇌ CO <sub>2</sub> , H <sub>2</sub> , e <sup>-</sup>	e <sup>-</sup> , H <sup>+</sup> ⇌ H <sub>2</sub>	Matsumoto et al. (2002)
SrZr <sub>0.90</sub> Y <sub>0.1</sub> O <sub>3-α</sub>	Cu	CO <sub>2</sub> , H <sup>+</sup> , e <sup>-</sup> ⇌ CO, H <sub>2</sub>	H <sub>2</sub> ⇌ e <sup>-</sup> , H <sup>+</sup>	Karagiannakis et al. (2003)
SrCe <sub>0.95</sub> Yb <sub>0.05</sub> O <sub>3-α</sub>	Pd	CO, H <sub>2</sub> O ⇌ H <sup>+</sup> , CO <sub>2</sub> , H <sub>2</sub> , e <sup>-</sup>	e <sup>-</sup> , H <sup>+</sup> ⇌ H <sub>2</sub>	Kokkofitis et al. (2007a)
BaCe <sub>0.90</sub> Y <sub>0.10</sub> O <sub>3-α</sub>	Pt	CO (H <sub>2</sub> O) ⇌ H <sup>+</sup> , CO <sub>2</sub> , e <sup>-</sup>	e <sup>-</sup> , H <sup>+</sup> , O <sub>2</sub> ⇌ H <sub>2</sub> O	Coors (2004)

### 3.5.9. Steam Electrolysis

Regarding the application of HTPC in high temperature electrolysis of water, Iwahara (1989) and Iwahara et al. (2000) used different PCMRs for steam electrolysis and hydrogen separation and discussed the advantages of using pure H<sup>+</sup> and O<sup>2-</sup> or mixed conductor. Moreover, Guan et al. (1997) utilized a mixed conductor to examine its performance as a hydrogen separator, which operates at relatively low temperatures (500-800 °C). On the other hand, Iwahara et al. (1996) tested the operation of a PCMR as an electrochemical steam pump. In more detail, during the PCMR operation H<sub>2</sub>O decomposed at the anode, while H<sup>+</sup> transported through the SCYb electrolyte and reacted with oxygen at the cathode to regenerate H<sub>2</sub>O. The targeted application for this reactor was the extraction of water vapor traces from gaseous streams (Iwahara et al., 2000). Finally, steam electrolysis was also studied by Kobayashi et al. (2001) and Matsumoto et al. (2006) in an effort to increase the process efficiency by investigating novel materials as HTPCs.

### 3.5.10. Ammonia Synthesis and Decomposition

For the past 100 years, the Haber-Bosch process, which involves the reaction of gaseous N<sub>2</sub> and H<sub>2</sub> at large pressures (100-150 bar) and relatively small temperatures (400-500 °C) in the presence of a Fe-based catalyst (Liu and Chin, 2014), remains the dominant route to the

production of  $\text{NH}_3$ . Ammonia has been also produced at ambient conditions in nature for millions of years, via the reaction of atmospheric nitrogen with protons and electrons with the aid of metalloenzymes (Kyriakou et al., 2016). It was this natural practice of protons and electrons utilization that motivated the solid state electrochemical approach for ammonia synthesis. In this context, the electrochemical production of ammonia in a solid state proton conducting cell was first experimentally demonstrated by Marnellos and Stoukides (1998). Since then, numerous relevant studies on electrochemical ammonia synthesis have been reported. The major findings and breakthroughs of these works have been analyzed in great depth in several recent reviews (Amar et al., 2011; Giddey et al., 2013). Thus, the interest for the electrochemical synthesis of ammonia remains until now at the highest level, though, there are still significant obstacles that need to be overcome so that it can be competitive to the Haber-Bosch process. Without any doubt, the most important issue is that the working electrode (i.e., cathode) should be not only electrocatalytically active towards ammonia synthesis, but also an electronic conductor. Recently, transition metal nitride catalysts have been identified, by using the DFT methodology, as promising cathode materials. It was found that the Faradaic Efficiency (FE) of the tested electrodes, i.e., the fraction of protons that is converted to ammonia, is in principle small and increases with temperature (Kyriakou et al., 2016). On the contrary, as the reverse reaction of ammonia decomposition dominates over the synthesis reaction at high temperatures, a trade off solution should be identified.

**Table 3.9:** Catalytic studies on steam electrolysis via proton conducting membrane reactors.

HTPC	Catalyst (WE)	Reactants and Products on WE	Reactants and Products on CE	References
$\text{SrCe}_{0.95}\text{Yb}_{0.05}\text{O}_{3-\alpha}$	Pt	$\text{H}_2\text{O} \rightleftharpoons \text{H}^+, \text{O}_2, \text{e}^-$	$\text{H}^+, \text{e}^- \rightleftharpoons \text{H}_2$	Matsumoto et al. (2002) Iwahara (1988)
$\text{SrCe}_{0.95}\text{Yb}_{0.05}\text{O}_{3-\alpha}$	Pt	$\text{H}_2\text{O} \rightleftharpoons \text{H}^+, \text{O}_2, \text{e}^-$	$\text{H}^+, \text{e}^-, \text{O}_2 \rightleftharpoons \text{H}_2\text{O}$	Iwahara et al. (1996)
$\text{BaCe}_{0.90}\text{Y}_{0.10}\text{O}_{3-\alpha}$	Pt, Ag	$\text{H}_2\text{O} \rightleftharpoons \text{H}^+, \text{O}_2, \text{e}^-$	$\text{H}^+, \text{e}^- \rightleftharpoons \text{H}_2$	Guan et al. (1997)
SCY, $\text{SrZr}_{0.90}\text{Yb}_{0.1}\text{O}_{3-\alpha}$	Pt	$\text{H}_2\text{O} \rightleftharpoons \text{H}^+, \text{O}_2, \text{e}^-$	$\text{H}^+, \text{e}^- \rightleftharpoons \text{H}_2$	Iwahara et al. (2000) Kobayashi et al. (2001)
$\text{SrCe}_{0.95}\text{Yb}_{0.05}\text{O}_{3-\alpha}$ , $\text{SrZr}_{0.90}\text{Y}_{0.1}\text{O}_{3-\alpha}$	Pt	$\text{H}_2\text{O} \rightleftharpoons \text{H}^+, \text{O}_2, \text{e}^-$	$\text{H}^+, \text{e}^- \rightleftharpoons \text{H}_2$	Matsumoto et al. (2006)

**Table 3.10:** Catalytic studies on ammonia synthesis and decomposition via proton conducting membrane reactors.

HTPC	Catalyst (WE)	Reactants and Products on WE	Reactants and Products on CE	References
SrZ <sub>0.9</sub> Y <sub>0.1</sub> O <sub>3-α</sub>	Fe	NH <sub>3</sub> ⇌ H <sup>+</sup> , N <sub>2</sub> , e <sup>-</sup>	e <sup>-</sup> , H <sup>+</sup> ⇌ H <sub>2</sub>	Pitselis et al. (1997)
SrCe <sub>0.95</sub> Yb <sub>0.05</sub> O <sub>3-α</sub>	Pd	H <sup>+</sup> , N <sub>2</sub> , e <sup>-</sup> ⇌ NH <sub>3</sub>	H <sub>2</sub> ⇌ e <sup>-</sup> , H <sup>+</sup>	Marnellos et al. (2000)
SrZ <sub>0.9</sub> Y <sub>0.1</sub> O <sub>3-α</sub>	Fe	H <sup>+</sup> , N <sub>2</sub> , e <sup>-</sup> ⇌ NH <sub>3</sub>	H <sub>2</sub> ⇌ e <sup>-</sup> , H <sup>+</sup>	Yokari et al. (2000)
La <sub>1.9</sub> Ca <sub>0.1</sub> Zr <sub>2</sub> O <sub>6.95</sub>	Pd-Ag	H <sup>+</sup> , N <sub>2</sub> , e <sup>-</sup> ⇌ NH <sub>3</sub>	H <sub>2</sub> ⇌ e <sup>-</sup> , H <sup>+</sup>	Xie et al. (2004)
BaCa <sub>1.18</sub> Nb <sub>1.82</sub> O <sub>3-α</sub> , BaCe <sub>0.8</sub> Gd <sub>0.2</sub> O <sub>3-α</sub>	Pd-Ag	H <sup>+</sup> , N <sub>2</sub> , e <sup>-</sup> ⇌ NH <sub>3</sub>	H <sub>2</sub> ⇌ e <sup>-</sup> , H <sup>+</sup>	Li et al. (2005)
Ce <sub>0.8</sub> M <sub>0.2</sub> O <sub>2-α</sub> (M=La, Y, Ga, Sm)	Pd-Ag	H <sup>+</sup> , N <sub>2</sub> , e <sup>-</sup> ⇌ NH <sub>3</sub>	H <sub>2</sub> ⇌ e <sup>-</sup> , H <sup>+</sup>	Liu et al. (2006)
SrCe <sub>0.95</sub> Yb <sub>0.05</sub> O <sub>3-α</sub>	Ru	NH <sub>3</sub> ⇌ H <sup>+</sup> , N <sub>2</sub> , e <sup>-</sup>	e <sup>-</sup> , H <sup>+</sup> ⇌ H <sub>2</sub>	Skodra et al. (2006)
La <sub>0.9</sub> Sr <sub>0.1</sub> Ga <sub>0.8</sub> Mg <sub>0.2</sub> O <sub>3-α</sub>	Ag-Pd	H <sup>+</sup> , N <sub>2</sub> , e <sup>-</sup> ⇌ NH <sub>3</sub>	H <sub>2</sub> ⇌ e <sup>-</sup> , H <sup>+</sup>	Zhang et al. (2007)
BaZr <sub>0.8</sub> Y <sub>0.2</sub> O <sub>3-6</sub>	Ag	H <sup>+</sup> , N <sub>2</sub> , e <sup>-</sup> ⇌ NH <sub>3</sub>	H <sub>2</sub> ⇌ e <sup>-</sup> , H <sup>+</sup> , O <sub>2</sub>	Yun et al. (2015)
BaZr <sub>0.8</sub> Y <sub>0.2</sub> O <sub>3-6</sub>	Pt	H <sup>+</sup> , N <sub>2</sub> , e <sup>-</sup> ⇌ NH <sub>3</sub>	H <sub>2</sub> ⇌ e <sup>-</sup> , H <sup>+</sup> , O <sub>2</sub>	Yun et al. (2015)
BaZr <sub>0.8</sub> Y <sub>0.2</sub> O <sub>3-6</sub>	La <sub>0.6</sub> Sr <sub>0.4</sub> Co <sub>0.2</sub> Fe <sub>0.8</sub> O <sub>3-6</sub> (LSCF)	H <sup>+</sup> , N <sub>2</sub> , e <sup>-</sup> ⇌ NH <sub>3</sub>	H <sub>2</sub> ⇌ e <sup>-</sup> , H <sup>+</sup> , O <sub>2</sub>	Yun et al. (2015)
BaCe <sub>0.9</sub> Y <sub>0.1</sub> O <sub>3-6</sub>	La <sub>0.5</sub> Sr <sub>0.5</sub> Ti <sub>0.6</sub> Ru <sub>0.4</sub> O <sub>3</sub> (LSTR40)	H <sup>+</sup> , N <sub>2</sub> , e <sup>-</sup> ⇌ NH <sub>3</sub>	H <sub>2</sub> ⇌ e <sup>-</sup> , H <sup>+</sup>	Otomo et al. (2015)
BaCe <sub>0.9</sub> Y <sub>0.1</sub> O <sub>3-6</sub>	Ag-Pd	H <sup>+</sup> , N <sub>2</sub> , e <sup>-</sup> ⇌ NH <sub>3</sub>	H <sub>2</sub> ⇌ e <sup>-</sup> , H <sup>+</sup>	Otomo et al. (2015)
SrZr <sub>0.9</sub> Y <sub>0.1</sub> O <sub>3-α</sub>	Fe, Ag	H <sup>+</sup> , N <sub>2</sub> , e <sup>-</sup> ⇌ NH <sub>3</sub>	H <sub>2</sub> ⇌ e <sup>-</sup> , H <sup>+</sup>	Ouzounidou et al. (2007)
SrZr <sub>0.9</sub> Y <sub>0.1</sub> O <sub>3-α</sub>	Fe	H <sup>+</sup> , N <sub>2</sub> , e <sup>-</sup> ⇌ NH <sub>3</sub>	H <sub>2</sub> ⇌ e <sup>-</sup> , H <sup>+</sup>	Ouzounidou et al. (2007)
BaCe <sub>0.85</sub> Y <sub>0.15</sub> O <sub>3-α</sub>	Ag-Pd	H <sup>+</sup> , N <sub>2</sub> , e <sup>-</sup> ⇌ NH <sub>3</sub>	H <sub>2</sub> ⇌ e <sup>-</sup> , H <sup>+</sup>	Guo et al. (2009)

BaZr <sub>0.7</sub> Ce <sub>0.2</sub> Y <sub>0.1</sub> O <sub>3-δ</sub>	Ni-BZCY72	H <sup>+</sup> , N <sub>2</sub> , e <sup>-</sup> ⇌ NH <sub>3</sub>	H <sub>2</sub> ⇌ e <sup>-</sup> , H <sup>+</sup>	Vasileiou et al. (2016)
BaZr <sub>0.7</sub> Ce <sub>0.2</sub> Y <sub>0.1</sub> O <sub>3-δ</sub>	Ni-BZCY72	H <sub>2</sub> , H <sup>+</sup> , N <sub>2</sub> , e <sup>-</sup> ⇌ NH <sub>3</sub>	H <sub>2</sub> ⇌ e <sup>-</sup> , H <sup>+</sup>	Vasileiou et al. (2016)
Ba <sub>0.98</sub> Ce <sub>0.8</sub> Y <sub>0.2</sub> O <sub>3-α</sub> + 0.04ZnO	Ag-Pd	H <sup>+</sup> , N <sub>2</sub> , e <sup>-</sup> ⇌ NH <sub>3</sub>	H <sub>2</sub> ⇌ e <sup>-</sup> , H <sup>+</sup>	Zhang et al. (2011)
BaCe <sub>0.85</sub> Y <sub>0.15</sub> O <sub>3-α</sub>	Ba <sub>0.5</sub> Sr <sub>0.5</sub> Co <sub>0.8</sub> Fe <sub>0.2</sub> O <sub>3-δ</sub> (BSCF)	H <sup>+</sup> , N <sub>2</sub> , e <sup>-</sup> ⇌ NH <sub>3</sub>	H <sub>2</sub> ⇌ e <sup>-</sup> , H <sup>+</sup>	Wang et al. (2010)
Ce <sub>0.8</sub> Y <sub>0.2</sub> O <sub>1.9</sub> - Ca <sub>3</sub> (PO <sub>4</sub> ) <sub>2</sub> , K <sub>3</sub> PO <sub>4</sub>	Ag-Pd	H <sup>+</sup> , N <sub>2</sub> , e <sup>-</sup> ⇌ NH <sub>3</sub>	CH <sub>4</sub> ⇌ e <sup>-</sup> , H <sup>+</sup> , C <sub>2</sub> H <sub>6</sub>	Liu et al. (2006)
Ce <sub>0.8</sub> Sm <sub>0.2</sub> O <sub>1.9</sub>	Ag-Pd	H <sup>+</sup> , N <sub>2</sub> , e <sup>-</sup> ⇌ NH <sub>3</sub>	H <sub>2</sub> ⇌ e <sup>-</sup> , H <sup>+</sup>	Liu et al. (2006)
Ce <sub>0.8</sub> La <sub>0.2</sub> O <sub>1.9</sub>	Ag-Pd	H <sup>+</sup> , N <sub>2</sub> , e <sup>-</sup> ⇌ NH <sub>3</sub>	H <sub>2</sub> ⇌ e <sup>-</sup> , H <sup>+</sup>	Liu et al. (2006)
Ce <sub>0.8</sub> La <sub>0.2</sub> O <sub>1.9</sub>	Ag-Pd	H <sup>+</sup> , N <sub>2</sub> , e <sup>-</sup> ⇌ NH <sub>3</sub>	H <sub>2</sub> ⇌ e <sup>-</sup> , H <sup>+</sup>	Liu et al. (2006)
Ce <sub>0.8</sub> La <sub>0.2</sub> O <sub>1.9</sub>	Ag-Pd	H <sup>+</sup> , N <sub>2</sub> , e <sup>-</sup> ⇌ NH <sub>3</sub>	H <sub>2</sub> ⇌ e <sup>-</sup> , H <sup>+</sup>	Chen et al. (2009)
La <sub>0.9</sub> Ba <sub>0.1</sub> Ga <sub>0.8</sub> Mg <sub>0.2</sub> O <sub>3-α</sub>	Ag-Pd	H <sup>+</sup> , N <sub>2</sub> , e <sup>-</sup> ⇌ NH <sub>3</sub>	H <sub>2</sub> ⇌ e <sup>-</sup> , H <sup>+</sup>	Chen et al. (2009)
La <sub>0.9</sub> Ba <sub>0.1</sub> Ga <sub>0.8</sub> Mg <sub>0.2</sub> O <sub>3-α</sub>	Ag-Pd	H <sup>+</sup> , N <sub>2</sub> , e <sup>-</sup> ⇌ NH <sub>3</sub>	H <sub>2</sub> ⇌ e <sup>-</sup> , H <sup>+</sup>	Chen et al. (2009)
La <sub>0.9</sub> Ba <sub>0.1</sub> Ga <sub>0.8</sub> Mg <sub>0.2</sub> O <sub>3-α</sub>	Ag-Pd	H <sup>+</sup> , N <sub>2</sub> , e <sup>-</sup> ⇌ NH <sub>3</sub>	H <sub>2</sub> ⇌ e <sup>-</sup> , H <sup>+</sup>	Chen and Ma (2008)
La <sub>0.9</sub> Ba <sub>0.1</sub> Ga <sub>0.8</sub> Mg <sub>0.2</sub> O <sub>3-α</sub>	Ag-Pd	H <sup>+</sup> , N <sub>2</sub> , e <sup>-</sup> ⇌ NH <sub>3</sub>	H <sub>2</sub> ⇌ e <sup>-</sup> , H <sup>+</sup>	Chen and Ma (2009)
BaCe <sub>0.85</sub> Gd <sub>0.15</sub> O <sub>3-α</sub>	Ag-Pd	H <sup>+</sup> , N <sub>2</sub> , e <sup>-</sup> ⇌ NH <sub>3</sub>	H <sub>2</sub> ⇌ e <sup>-</sup> , H <sup>+</sup>	Wang et al. (2011)
BaCe <sub>0.7</sub> Zr <sub>0.2</sub> Sm <sub>0.1</sub> O <sub>3-α</sub>	Ag-Pd	H <sup>+</sup> , N <sub>2</sub> , e <sup>-</sup> ⇌ NH <sub>3</sub>	H <sub>2</sub> ⇌ e <sup>-</sup> , H <sup>+</sup>	Liu et al. (2010)
BaCe <sub>0.9</sub> Ca <sub>0.1</sub> O <sub>3-α</sub>	Ag-Pd	H <sup>+</sup> , N <sub>2</sub> , e <sup>-</sup> ⇌ NH <sub>3</sub>	H <sub>2</sub> ⇌ e <sup>-</sup> , H <sup>+</sup>	Wang et al. (2010)
(Li,Na,K) <sub>2</sub> CO <sub>3</sub> - Ce <sub>0.8</sub> Sm <sub>0.2</sub> O <sub>2-δ</sub>	La <sub>0.6</sub> Sr <sub>0.4</sub> Fe <sub>0.8</sub> Cu <sub>0.2</sub> O <sub>3-δ</sub> (LSFCu)-SDC	H <sup>+</sup> , N <sub>2</sub> , e <sup>-</sup> ⇌ NH <sub>3</sub>	H <sub>2</sub> ⇌ e <sup>-</sup> , H <sup>+</sup>	Amar et al. (2011)
LiAlO <sub>2</sub> - ((Li/Na/K) <sub>2</sub> CO <sub>3</sub> )	Fe <sub>3</sub> Mo <sub>3</sub> N-Ag	H <sup>+</sup> , N <sub>2</sub> , e <sup>-</sup> ⇌ NH <sub>3</sub>	H <sub>2</sub> ⇌ e <sup>-</sup> , H <sup>+</sup>	Amar et al. (2015)
LiAlO <sub>2</sub> -	Co <sub>3</sub> Mo <sub>3</sub>	H <sup>+</sup> , N <sub>2</sub> , e <sup>-</sup> ⇌ NH <sub>3</sub>	H <sub>2</sub> ⇌ e <sup>-</sup> , H <sup>+</sup>	Amar et al.

$((\text{Li}/\text{Na}/\text{K})_2\text{CO}_3)$	N-Ag				(2015)
$\text{LiAlO}_2$ - $((\text{Li}/\text{Na}/\text{K})_2\text{CO}_3)$	$\text{CoFe}_2\text{O}_4$ -Ag	$\text{H}^+, \text{N}_2, \text{e}^- \rightleftharpoons \text{NH}_3$	$\text{H}_2 \rightleftharpoons \text{e}^-, \text{H}^+$		Amar et al. (2011)
$\text{BaZr}_{0.7}\text{Ce}_{0.2}\text{Y}_{0.1}\text{O}_{3-\delta}$	Ni-BZCY72	$\text{H}_2, \text{H}^+, \text{N}_2, \text{e}^- \rightleftharpoons \text{NH}_3$	$\text{H}_2 \rightleftharpoons \text{e}^-, \text{H}^+$		Vasileiou et al. (2015)
$\text{SrZr}_{0.9}\text{Y}_{0.1}\text{O}_{3-\alpha}$	Ru	$\text{H}^+, \text{N}_2, \text{e}^- \rightleftharpoons \text{NH}_3$	$\text{H}_2 \rightleftharpoons \text{e}^-, \text{H}^+, \text{O}_2$		Skodra et al. (2009)
$\text{BaCe}_{0.9}\text{Sm}_{0.1}\text{O}_{3-\delta}$	Ag-Pd	$\text{H}^+, \text{N}_2, \text{e}^- \rightleftharpoons \text{NH}_3$	$\text{H}_2 \rightleftharpoons \text{e}^-, \text{H}^+$		Li et al. (2007)
$\text{BaCe}_{0.8}\text{Gd}_{0.1}\text{Sm}_{0.1}\text{O}_{3-\delta}$	Ag-Pd	$\text{H}^+, \text{N}_2, \text{e}^- \rightleftharpoons \text{NH}_3$	$\text{H}_2 \rightleftharpoons \text{e}^-, \text{H}^+$		Li et al. (2007)
$\text{BaZr}_{0.7}\text{Ce}_{0.2}\text{Y}_{0.1}\text{O}_{3-\delta}$	Ni-BZCY72	$\text{H}^+, \text{N}_2, \text{e}^- \rightleftharpoons \text{NH}_3$	$\text{H}_2 \rightleftharpoons \text{e}^-, \text{H}^+$		Vasileiou et al. (2015)

### 3.5.11. Decomposition and Reduction of $\text{NO}_x$

Kobayashi et al. (2000 and 2002) studied the reduction of  $\text{NO}_x$  in PCMRs, where steam was electrolyzed at the cell anode, while the produced  $\text{H}^+$  reacted with  $\text{NO}_x$  at the cathode to produce  $\text{N}_2$  and  $\text{H}_2\text{O}$ . Strontium cerates and strontium zirconates were tested as high temperature proton conductor materials. When Pt-based catalysts ( $\text{Pt}/\text{Ba}/\text{Al}_2\text{O}_3$  or  $\text{Pt}/\text{Sr}/\text{Al}_2\text{O}_3$ ) were used as working electrodes, they succeeded to reduce  $\text{NO}_x$ , even in the presence of excess  $\text{O}_2$  (Kobayashi et al., 2000; Kobayashi et al., 2002).

### 3.5.12. Hydrogen Sulfide Decomposition

As it was discussed in detail in the previous chapters, hydrogen sulfide ( $\text{H}_2\text{S}$ ) is a toxic compound, globally produced in large quantities (>50 million tons per year). More specifically,  $\text{H}_2\text{S}$  is contained in small or larger quantities in different industrial waste streams, oil and natural gas reserves, geothermal and volcanic activity areas, oceans, and maritime deep waters (Fakuda et al., 1978). In addition,  $\text{H}_2\text{S}$  that is abundantly found in Black Sea waters (produced by sulfur reducing bacteria), hails as a potential  $\text{H}_2$  source, while its removal from the Black Sea waters will contribute to the sufficient environmental protection of the surrounding ecosystem (Ipsakis et al., 2015).

**Table 3.11:** Catalytic studies on decomposition and reduction of  $\text{NO}_x$  via proton conducting membrane reactors.

HTPC	Catalyst (WE)	Reactants and Products on WE	Reactants and Products on CE	References
$\text{SrZr}_{0.90}\text{Yb}_{0.1}\text{O}_{3-\alpha}$	$\text{Sr}/\text{Al}_2\text{O}_3$	$\text{H}^+, \text{NO}, \text{e}^- \rightleftharpoons \text{N}_2, \text{H}_2\text{O}$	$\text{H}_2\text{O} \rightleftharpoons \text{e}^-, \text{H}^+, \text{O}_2$	Kobayashi et al. (2000)
$\text{SrCe}_{0.95}\text{Yb}_{0.05}\text{O}_{3-\alpha}$ , $\text{SrZr}_{0.90}\text{Yb}_{0.1}\text{O}_{3-\alpha}$	$\text{Pt}/\text{Ba}/\text{Al}_2\text{O}_3$	$\text{H}^+, \text{NO}, \text{e}^- \rightleftharpoons \text{N}_2, \text{H}_2\text{O}$	$\text{H}_2\text{O} \rightleftharpoons \text{e}^-, \text{H}^+, \text{O}_2$	Kobayashi et al. (2000) Kobayashi et al. (2002)

The current industrial practice for  $\text{H}_2\text{S}$  management involves the well-known Claus process, which is a partial oxidation treatment that allows the recovery of elemental sulphur ( $\text{S}_n$ ) at the expense of hydrogen consumption to water (Chuang et al., 2008). Several alternatives processes have been proposed for the production of  $\text{H}_2\text{S}$  from  $\text{H}_2\text{S}$  decomposition, which are currently at different stages of development, involving thermochemical, photochemical, plasm-chemical and electrochemical methods. The majority of these approaches present certain disadvantages, coupled with the particular high energy requirements and the low efficiencies, thus rendering their commercialization doubtful. Recently, the electrochemical approach was proposed to efficiently generate and separate, in a single step, pure  $\text{H}_2$  from  $\text{H}_2\text{S}$  electrolysis at high temperatures, by employing a proton conducting ceramic membrane reactor (Li et al., 2006; Slavov et al., 1998; Fabbri et al., 2010; Malavasi et al., 2010). It should be noticed that the operation of these PCMRs in the fuel cell mode offered the possibility not only to remove  $\text{H}_2\text{S}$  from gaseous mixtures, but also to generate electricity:



Most research groups conducted the  $\text{H}_2\text{S}$  decomposition experiments in oxide ion solid electrolytes (Manoj et al., 2008; Arnstein et al., 2007), while some other groups used proton conductors (Tomita et al., 2006; Jinxia et al., 2006). However, the utilization of  $\text{O}^{2-}$  cells revealed that in addition to elemental sulfur, sulfur oxides were also produced. This leads to an in general counterproductive process, especially if the aim is to remove sulfur from a gaseous stream. Though, in a PCMR, sulfur oxides are not produced, as oxygen is efficiently

separated from the sulfur species. As a result, during the last decade, the performance of various  $H^+$  fuel cells has been widely tested at temperatures as low as 65 °C and as high as 800 °C (Zhong et al., 2006; Li et al., 2006; Chuang et al., 2008; Tan et al., 2009; Duysebaev et al., 2014). Despite that the generated power densities in these systems were promising (approximately  $70 \text{ mW}\cdot\text{cm}^{-2}$  at 750 °C), in most cases the cells were unable to operate stably because of the rapid deactivation of the anodic electrode and/or the electrolyte. For example, strontium and barium cerates, which are in principle very promising proton conductors, suffered from their gradual degradation and the generation of sulfates or sulfides (Kokkofitis et al., 2007b; Chuang et al., 2008). Furthermore, the deposition of solid sulfur on the anode or its reaction with the metal or oxide components of the electrode also renders these materials unsuitable for long term applications. Despite their disadvantages in comparison to the PCMRs, the  $O^{2-}$  cells are more stable as they are more tolerant to sulfur poisoning. Thus, current research efforts focus on the development of either proton or oxide ion  $H_2S$  fuel cells (Vincenta et al., 2012; Zhou et al., 2014). In this framework, the improvement of the protonic conductivity of barium zirconates, which are generally stable perovskites, could be a considerable step forward, when scaling-up the  $H_2S$  fuel cell (Li et al., 2008; Ipsakis et al., 2015; Kraia et al., 2016).

However, one of the major challenges of  $H_2S$  decomposition is the optimal selection of cell materials and especially for the anode electrode, which will be exposed to a  $H_2S$ -containing reacting mixture and generate the protons to be transported through the  $H^+$  conducting solid electrolyte to the cathode, where in turn pure hydrogen will be formed. The anode material has to exhibit high electro-catalytic activity towards  $H_2S$  decomposition, high electronic/ionic conductivity, good adherence on the solid electrolyte surface, and tolerance to  $H_2S$  rich environments (Vorontsov et al., 2008; Gong et al., 2007). To this direction, Pt, Ni, and other valuable metals were first used as anode catalysts. It was found that these catalysts were easily deactivated under the corrosive atmosphere of  $H_2S$ , thus affecting the conductivity of anode materials and the electro-catalysis in the three-phase interface (Mohtadi et al., 2005). Moreover, several sulphides, oxides and metals have been investigated for the same purpose. Among the various sulfur resistant anode materials, thiospinels and metal sulfides are the most promising for  $H_2S$  oxidation fuel cells; however their time-consuming and complex synthesis procedure, along with their rather low electro-

catalytic activity and insufficient chemical stability, limit their applicability in real processes. As a result, some metal sulfides, advanced by Chuang et al. (2008), such as  $\text{CoS}_{1.035}$ ,  $\text{MoS}_2$ ,  $\text{WS}_2$ ,  $\text{NiS}$ , and  $\text{Li}_2\text{S}/\text{CoS}_{1.035}$ , were proposed to be more suitable for a sulfur-tolerant anode in the fuel cell (Slavov et al., 1998; Mingyang et al., 2007).

**Table 3.12:** Catalytic studies on  $\text{H}_2\text{S}$  decomposition via proton conducting membrane reactors.

HTPC	Catalyst (WE)	Reactants and Products on WE	Reactants and Products on CE	References
$\text{SrCe}_{0.95}\text{Yb}_{0.05}\text{O}_{3-\alpha}$ , $\text{Li}_2\text{SO}_4$	Pt	$\text{H}_2\text{S} \rightleftharpoons \text{H}^+, \text{S}, \text{e}^-$	$\text{e}^-, \text{H}^+ \rightleftharpoons \text{H}_2$	Kirk and Winnick (1993) Peterson and Winnick (1995)
$\text{Li}_2\text{SO}_4/\text{Al}_2\text{O}_3$	Metal Sulfides	$\text{H}_2\text{S} \rightleftharpoons \text{H}^+, \text{S}, \text{e}^-$	$\text{e}^-, \text{H}^+, \text{O}_2 \rightleftharpoons \text{H}_2\text{O}$	Zhong et al. (2006)
$\text{Li}_2\text{SO}_4/\text{Al}_2\text{O}_3$	$\text{MoS}_2\text{-NiS}$	$\text{H}_2\text{S} \rightleftharpoons \text{H}^+, \text{S}, \text{e}^-$	$\text{e}^-, \text{H}^+, \text{O}_2 \rightleftharpoons \text{H}_2\text{O}$	Li et al. (2006)
$\text{Li}_2\text{SO}_4/\text{Al}_2\text{O}_3$	Mo-S-Ni-Ag-YSZ	$\text{H}_2\text{S} \rightleftharpoons \text{H}^+, \text{S}, \text{e}^-$	$\text{e}^-, \text{H}^+, \text{O}_2 \rightleftharpoons \text{H}_2\text{O}$	Chuang et al. (2008)
Y-doped $\text{Ba}(\text{Ce},\text{Zr})\text{O}_3$	$\text{LaCrO}_3\text{-VO}_x\text{-YSZ}$	$\text{H}_2\text{S} \rightleftharpoons \text{H}^+, \text{S}, \text{e}^-$	$\text{e}^-, \text{H}^+, \text{O}_2 \rightleftharpoons \text{H}_2\text{O}$	Chuang et al. (2008)
$\text{MoS}_2\text{-BaCe}_{0.425}\text{Zn}_{0.475}\text{Y}_{0.1}\text{O}_{3-\text{Ag}}$	$\text{BaCe}_{0.425}\text{Zn}_{0.475}\text{Y}_{0.1}\text{O}_3$	$\text{H}_2\text{S} \rightleftharpoons \text{H}^+, \text{S}, \text{e}^-$	$\text{e}^-, \text{H}^+, \text{O}_2 \rightleftharpoons \text{H}_2\text{O}$	Tan et al. (2009)
Nafion	Pd-graphite	$\text{H}_2\text{S} \rightleftharpoons \text{H}^+, \text{S}, \text{e}^-$	$\text{e}^-, \text{H}^+, \text{O}_2 \rightleftharpoons \text{H}_2\text{O}$	Duysebaev et al. (2014)

Ceria-based mixed oxides have also recently gained considerable attention, due to their sufficient electrochemical performance and resistance to poisons. For instance,  $\text{Co}_3\text{O}_4\text{-CeO}_2$  materials have been extensively applied in solid oxide fuel cells (SOFCs), as they combine enhanced electronic conductivity and electro-catalytic activity (Konsolakis, 2016; Atkinson et al., 2004; Kraia et al., 2016). Recently, the superior catalytic performance of  $\text{Co}_3\text{O}_4\text{-CeO}_2$  composites towards  $\text{H}_2\text{S}$  decomposition to  $\text{H}_2$  in both dry and wet (90 v/v%) atmospheres was also demonstrated. Following these developments, in the present thesis, the application of several types of metals on a proton conducting membrane reactor  $\text{BaZr}_{0.7}\text{Ce}_{0.2}\text{Y}_{0.1}\text{O}_3$  (BZCY72) was examined. Complete details can be found in Chapter 8.

### 3.6. CONCLUSIONS

A large number of industrially important reactions have been studied in PCMRs and several promising results have been obtained. The increased need for energy conservation and cleaner technologies motivated many research groups to exploit the advantageous characteristics of PCMRs, which can be summarized as follows:

- PCMRs can operate as catalytic membrane reactors to produce the desired compound and simultaneously separate it from the reacting mixture.
- Electrical power can be cogenerated with the desired product by direct conversion of the reaction free energy into electricity.

On the other hand, as already discussed in previous reviews (Liu et al., 2001; Sanchez Marcano and Tsotsis, 2004; Kokkofitis et al., 2007b; Garagounis et al., 2010), there are several hurdles that PCMRs have to overcome on their way to commercialization. In addition to the traditional techno-economic criteria, new parameters, such as the environmental cost, should be included in the sustainability assessment of these systems. Hence, in the last decade, a number of applications, disregarded in the past, were revisited and the possibility for further developments was examined.

Hydrogen, if derived from carbon-free energy resources, is worldwide acknowledged as an environmental friendly energy vector, which can support future energy developments. Therefore, processes that involve hydrogen production-separation, together with the production of an industrially important compound, may be advanced near to commercialization in the years to come.

Another powerful option of chemical co-generation in PCMRs is provided by the  $H_2S$  decomposition to  $H_2$  process (Zhong et al., 2006); a process that is under study in the present thesis. Generally, huge amounts of  $H_2S$  are generated, primarily as by-products of the petroleum and natural gas industries, geothermal and volcanic activity areas, oceans, and Black Sea waters. The effects of  $H_2S$  on human health and the environment impel its removal from all effluent streams. Without any doubt, the elimination of a harmful compound like  $H_2S$ , coupled with the simultaneous production of electric power constitutes a very interesting and attractive process, with substantial economic and environmental impact.

## REFERENCES

- Alberti G., Casciola M. (2001). Solid state protonic conductors, present main applications and future prospects. *Solid State Ionics*, 145: pp. 3-16.
- Amar I.A., Petit C.T.G., Zhang L., Lan R., Skabara P.J., Tao S. (2011). Electrochemical synthesis of ammonia based on doped-ceria-carbonate composite electrolyte and perovskite cathode. *Solid State Ionics*, 201: pp. 94-100.
- Amar I.A., Lan R., Petit C.T.G., Tao S. (2015). Electrochemical Synthesis of Ammonia Based on  $\text{Co}_3\text{Mo}_3\text{N}$  Catalyst and  $\text{LiAlO}_2\text{-(Li,Na,K)}_2\text{CO}_3$  Composite. *Electrocatalysis*, 6: pp. 286-294.
- Amar I.A., Lan R., Petit C.T.G., Tao S. (2015). Electrochemical Synthesis of Ammonia Using  $\text{Fe}_3\text{Mo}_3\text{N}$  Catalyst and Carbonate-Oxide Composite Electrolyte. *International Journal of Electrochemical Science*, 10: pp. 3757-3766.
- Amar I.A., Lan R., Petit C.T.G., Arrighi V., Tao S. (2011). Electrochemical synthesis of ammonia based on a carbonate-oxide composite electrolyte. *Solid State Ionics*, 182: pp. 133-138.
- Amezawa K., Kjelstrup S., Norby T., Ito Y. (1998). Protonic and native conduction in Sr-substituted  $\text{LaPO}_4$  studied by thermoelectric power measurements. *Journal of Electrochemical Society*, 145: pp. 3313-3319.
- Amezawa K., Maekawa H., Tomii Y., Yamamoto N. (2001). Protonic conduction and defect structures in Sr-doped  $\text{LaPO}_4$ . *Solid State Ionics*, 145: pp. 233-240.
- Arnstein N., Ivar W., Markus B., Hustad J.E., Arild V. (2007). Experiments studies on the influence of  $\text{H}_2\text{S}$  on SOFC performance at 800 °C. *Energy and Fuels*, 21: pp. 1098-1101.
- Asano K., Hibino T., Iwahara H. (1995). A novel solid oxide fuel cell system using the partial oxidation of methane. *Journal of Electrochemical Society*, 142: pp. 3241-3245.
- Atkinson A., Barnett S., Gorte R.J., Irvine J.T.S, McEvoy A.J., Mogensen M., Singhal S.C., Vohs J. (2004). Advanced anodes for high-temperature fuel cells. *Natural Materials*, 3: pp. 17-27.
- Baranov Al., Shuvalov L.A., Shagina N.M. (1982). Superior conductivity and phase transitions in  $\text{C}_5\text{HSO}_4$  and  $\text{C}_5\text{HSeO}_4$  crystals. *JETPh Letters*, 36: pp. 459-62.
- Bates J.B., Wang J.C., Dudney N.J. (1982). Solid electrolytes-the beta aluminas. *Physics Today*, 35: pp. 46.
- Belyaev V.D., Gal'Vita V.V., Gorelov V.P., Sobyenin V.A. (1994). Oxidation of methane over platinum in a solid proton-conducting electrolyte cell. *Catalysis Letters*, 30: pp. 151-158.
- Belyaev, V.D., Sobyenin V.A., Gorelov V.P., Gal'Vita V.V. (1995). Effect of hydrogen pumping on the rate of methane oxidation over a platinum electrode. *Catalysis Today*, 24: pp.301-303.
- Bhide S.V., Virkar A.V. (1999). Stability of  $\text{BaCeO}_3$ -Based proton conductors in water-containing atmospheres. *Journal of Electrochemical Society*, 146: pp. 2038-2044.
- Bjørheim T.S., Stølena S., Norby T. (2010). Ab initio studies of hydrogen and acceptor defects in rutile  $\text{TiO}_2$ . *The Journal of Physical Chemistry*, 12: pp. 6817-6825.
- Bonanos N. (1992). Transport properties and conduction mechanism in high-temperature protonic conductors. *Solid State Ionics*, 53-56: pp. 967-974.
- Bonanos N. (2001). Oxide-based protonic conductors: point defects and transport properties. *Solid State Ionics*, 145: pp. 265-274.
- Bonanos N., Ellis B., Mahmood M.N. (1991). Construction and operation of fuel cells based on the solid electrolyte  $\text{BaCeO}_3\text{:Gd}$ . *Solid State Ionics*, 44: pp. 305-311.
- Bonanos N., Knight K.S., Ellis B. (1995). Perovskite solid electrolytes: structure, transport properties and fuel cell applications. *Solid State Ionics*, 79: pp. 161-170.

- Chen C., Sorensen O.T., Meng G., Peng D. (1997). Chemical stability study of  $\text{BaCe}_{0.9}\text{Nd}_{0.1}\text{O}_{3-\alpha}$  high-temperature proton-conducting ceramic. *Journal of Materials Chemistry*, 7: pp. 481-485.
- Chen C., Ma J. (2009). Proton conduction in  $\text{BaCe}_{1-x}\text{Gd}_x\text{O}_{3-\alpha}$  at intermediate temperature and its application to synthesis of ammonia at atmospheric pressure. *Journal of Alloys and Compounds*, 485: pp. 69-72.
- Chen C., Ma J. (2008). Preparation, proton conduction, and application in ammonia synthesis at atmospheric pressure of  $\text{La}_{0.9}\text{Ba}_{0.1}\text{Ga}_{1-x}\text{Mg}_x\text{O}_{3-\alpha}$ . *Journal of Materials Science*, 43: pp. 5109-5114.
- Chen C., Zhong L., Luo J., Chuang K. (2011). *Chinese Journal of Inorganic Chemistry*, 27: pp. 421-427.
- Chen C., Zhong L., Chuang K. (2010). *Chinese Journal of Inorganic Chemistry*, 26: pp. 132-137.
- Chen C., Hong P.J., Dai S.S., Zhang C.C. (1997). Effect of lithium addition on the performance of proton conducting catalysts for oxidative coupling of methane under microwave irradiation. *Reaction Kinetics and Catalysis Letters*, 61: pp. 181-185
- Chiang P.H., Eng D., Stoukides M. (1991). Electrocatalytic methane polarization with a Yb-doped  $\text{SrCeO}_3$  solid electrolyte. *Journal of Electrochemical Society*, 138: pp. L11-L12.
- Chiang P.H., Eng D., Alqahtany H., Stoukides M. (1992). Non oxidative methane coupling with the aid of solid electrolytes. *Solid State Ionics*, 53-56: pp. 135-141.
- Chuang K.T., Sanger A.R., Slavova S.V., Donini J.C. (2001). A proton-conducting solid state  $\text{H}_2\text{S}-\text{O}_2$  fuel cell. Operation using  $\text{H}_2\text{S}$ -hydrogen mixtures as anode feed. *International Journal of Hydrogen Energy*, 26: pp. 103-108.
- Chuang K.T., Luo J. (2008). Evolution of fuel cells powered by  $\text{H}_2\text{S}$ -containing gases. *Chemical Industry & Chemical Engineering Quarterly*, 14: pp. 69-76.
- Colomban (Ed.). (1992). Proton Conductors. *Cambridge University Press*.
- Coors W.G. (2007). Protonic ceramic steam-permeable membranes. *Solid State Ionics*, 178: pp. 481-485.
- Coors W.G. (2003). Protonic ceramic fuel cells for high-efficiency operation with methane. *Journal of Power Sources*, 118: pp. 150-156.
- Coors W.G. (2004). Steam reforming and water-gas shift by steam permeation in a protonic ceramic fuel cell. *Journal of Electrochemical Society*, 151: pp. A994-A997.
- Duysebaev B., Abramov A., Berstenev S., Ryspanov N., Sokolov A.Y., Shkolnik V., Umirov N., Bakenov Z. (2014). Investigation of using sulfur-containing gases in low-temperature fuel cell at sulfuric acid production site. *Eurasian Chemico-Technological Journal*, 16: pp. 271-275.
- Fabbri E., Pergolesi D., Traversa E. (2010). Materials challenges toward proton-conducting oxide fuel cells: a critical review. *Chemical Society Review*, 39: pp. 339-359.
- Fabbri E., Oh T., Licoccia S., Traversa E., Wachsman E.D. (2009). Chemical and structural properties of a TaN/ $\text{HfO}_2$  gate stack processed using atomic vapor deposition dielectric science and materials. *Journal of Electrochemical Society*, 156: pp. B38-B45.
- Fukuda K., Dokiya M., Kameyama T., Kotera Y. (1978). Catalytic decomposition of hydrogen sulfide. *Industrial & Engineering Chemistry Fundamentals*, 17: pp. 243-247.
- Feng Y., Luo J.L., Chuang K.T. (2008). Propane dehydrogenation in a proton-conducting fuel cell. *Journal of Physical Chemistry C*, 112: pp. 9943-9949.
- Feng Y., Luo J.L., Chuang K.T. (2007). Carbon deposition during propane dehydrogenation in a fuel cell. *Journal of Power Sources*, 167: pp. 486-490.
- Garagounis I., Kyriakou V., Anagnostou C., Bourganis V., Papachristou I., Stoukides M. (2011). Solid electrolytes: applications in heterogeneous catalysis and chemical cogeneration. *Industrial & Engineering Chemistry Research*, 50: pp. 431-472.

- Guan J., Dorris S.E., Balachandran U., Liu M. (1997). Transport properties of  $\text{BaCe}_{0.95}\text{Y}_{0.05}\text{O}_{3-\alpha}$  mixed conductors for hydrogen separation. *Solid State Ionics*, 100: pp. 45-52.
- Gong M., Liu X., Tremblay J., Johnson C. (2007). Sulfur-tolerant anode materials for solid oxide fuel cell application, *Journal of Power Sources*, 168: pp. 289-298.
- Haile S.M., Staneff G., Ryu K.H. (2001). Non-stoichiometry, grain boundary transport and chemical stability of proton conducting perovskites. *Journal of Materials Science*, 36: pp. 1149-1160.
- Hamakawa S., Hibino T., Iwahara H. (1993). Electrochemical methane coupling using protonic conductors. *Journal of Electrochemistry Society*, 140: pp. 459-462.
- Hamakawa S., Hibino T., Iwahara H. (1994). Electrochemical hydrogen permeation in a proton-hole mixed conductor and its application to a membrane reactor. *Journal of Electrochemistry Society*, 141: pp. 1720-1725.
- Han K.S., Kim J.H., Kim H.K., Hwang K.T. (2013). Direct methane cracking using a mixed conducting ceramic membrane for production of hydrogen and carbon. *International Journal of Hydrogen Energy* 38: pp. 16133-16139.
- Hibino T., Masegi A., Iwahara H., (1995). Electrocatalytic oxidation of methane to  $\text{C}_2$  hydrocarbons using a  $\text{Li}^+$  ion conductor. *Journal of Electrochemistry Society*, 142: pp. L72-L73.
- Hibino T., Ushiki K., Kuwahara Y., Masegi A., Iwahara H. (1996). Oxidative coupling of  $\text{CH}_4$  using alkali-metal ion conductors as a solid electrolyte. *Journal of the Chemical Society, Faraday Transactions*, 92: pp. 2393-2396.
- Hibino T., Hamakawa S., Suzuki T., Iwahara H. (1994). Recycling of carbon dioxide using a proton conductor as a solid electrolyte. *Journal of Applied Electrochemistry*, 24: pp. 126-130.
- Hibino T., Ushiki K., Sato T., Kuwahara Y. (1995). A novel cell design for simplifying SOFC system. *Solid State Ionics*, 81: pp. 1-3.
- Hibino T., Ushiki K., Kuwahara Y. (1996). New concept for simplifying SOFC system. *Solid State Ionics*, 91: pp. 69-74.
- Huang, K., Feng M., Goodenough J.B. (1997). Electrode performance test on single ceramic fuel cells using as electrolyte Sr- and Mg-doped  $\text{LaGaO}_3$ . *Journal of Electrochemistry Society*, 144: pp. 3620-3624.
- Ipsakis D., Kraia Tz., Marnellos G.E., Ouzounidou M., Voutetakis S., Dittmeyer R., Dubbe A., Haas-Santo K., Konsolakis M., Figen H.E., Guldal N.O., Baykara S.Z. (2015). An electrocatalytic membrane-assisted process for hydrogen production from  $\text{H}_2\text{S}$  in Black Sea: Preliminary results. *International Journal of Hydrogen Energy*, 40: pp. 7530-7538.
- Iwahara H. (1988). High temperature proton conducting oxides and their applications to solid electrolyte fuel cells and steam electrolyzer for hydrogen production. *Solid State Ionics*, 28-30, Part 1: pp. 573-578.
- Iwahara H. (1996). Proton conducting ceramics and their applications. *Solid State Ionics*, 86-88, Part 1: pp. 9-15.
- Iwahara H., Uchida H., Ono K., Ogaki K. (1988). Proton conduction in sintered oxides based on  $\text{BaCeO}_3$ . *Journal of Electrochemical Society*, 135: pp. 529-533.
- Iwahara H., Uchida H., Morimoto K., Hosogi S. (1989). High-temperature  $\text{C}_1$ -gas fuel cells using proton-conducting solid electrolytes. *Journal of Applied Electrochemistry*, 19: pp. 448-452.
- Iwahara H., Esaka T., Uchida H., Maeda N. (1981). Proton conduction in sintered oxides and its application to steam electrolysis for hydrogen production. *Solid State Ionics*, 3-4: pp. 359-363.
- Iwahara H., Yajima T., Hibino T., Ozaki K., Suzuki H. (1993). Protonic conduction in calcium, strontium and barium zirconates. *Solid State Ionics*, 61: pp. 65-69.

- Iwahara H., Matsumoto H., Takeuchi K. (2000). Electrochemical dehumidification using proton conducting ceramics. *Solid State Ionics*, 136-137: pp. 133-138.
- Iwahara H., Uchida H., Morimoto K. (1990). High temperature solid electrolyte fuel cells using perovskite-type oxide based on BaCeO<sub>3</sub>. *Journal of Electrochemical Society*, 137: pp. 462-465.
- Iwahara H., Uchida H., Tanaka S. (1986). High temperature-type proton conductive solid oxide fuel cells using various fuels. *Journal of Applied Electrochemistry*, 16: pp. 663-668.
- Iwahara H., Hibino T., Sunano T. (1996). An electrochemical steam pump using a proton conducting ceramic. *Journal of Applied Electrochemistry*, 26: pp. 829-832.
- Iwahara H. (1995). Technological challenges in the application of proton conducting ceramics. *Solid State Ionics*, 77: pp. 289-298.
- Iwahara H., Esaka T., Uchida H., Maeda N. (1981). Proton conduction in sintered oxides and its application to steam electrolysis for hydrogen production. *Solid State Ionics*, 3-4: pp. 359-363.
- Iwahara H., Asakura Y., Katahira K., Tanaka M. (2004). Prospect of hydrogen technology using proton-conducting ceramics. *Solid State Ionics*, 168: pp. 299-310.
- Jinxia L., Jing L., Chuang K.T., Sanger A.R. (2006). Proton conductivity and chemical stability of Li<sub>2</sub>SO<sub>4</sub> based electrolyte in a H<sub>2</sub>S-air fuel cell. *Journal of Power Sources*, 160: pp. 909-914.
- Karagiannakis G., Kokkofitis C., Zisekas S., Stoukides M. (2005). Catalytic and electrocatalytic production of H<sub>2</sub> from propane decomposition over Pt and Pd in a proton-conducting membrane-reactor. *Catalysis Today*, 104: pp. 219-224.
- Karagiannakis G., Zisekas S., Kokkofitis C., Stoukides M. (2006). Effect of H<sub>2</sub>O presence on the propane decomposition reaction over Pd in a proton conducting membrane reactor. *Applied Catalysis A*, 301: pp. 265-271.
- Karagiannakis G., Zisekas S., Stoukides M. (2003). Hydrogenation of carbon dioxide on copper in a H<sup>+</sup> conducting membrane-reactor. *Solid State Ionics*, 162-163: pp. 313-318.
- Katahira K., Kohchi Y., Shimura T., Iwahara H. (2000). Protonic conduction in Zr-substituted BaCeO<sub>3</sub>. *Solid State Ionics*, 138: pp. 91-98.
- Kharton V.V., Marozau I.P., Mather G.C., Naumovich E.N., Frade J.R. (2006). Transport numbers and oxygen permeability of SrCe(Y)O<sub>3</sub>-based ceramics under oxidizing conditions. *Electrochimica Acta*, 51: pp. 6389-6399.
- Kirk T.J., Winnick J. (1993). A hydrogen sulfide solid oxide fuel cell using ceria-based electrolytes. *Journal of Electrochemical Society*, 140: pp. 3494-3496.
- Kobayashi T., Abe K., Ukyo Y., Iwahara H. (2000). Reduction of nitrogen oxide by steam electrolysis cell using a protonic conductor SrZr<sub>0.9</sub>Yb<sub>0.1</sub>O<sub>3-α</sub> and the catalyst Sr/Al<sub>2</sub>O<sub>3</sub>. *Solid State Ionics*, 134: pp. 241-247.
- Kobayashi T., Abe K., Ukyo Y., Matsumoto H. (2001). Study on current efficiency of steam electrolysis using a partial protonic conductor SrZr<sub>0.9</sub>Yb<sub>0.1</sub>O<sub>3-α</sub>. *Solid State Ionics*, 138: pp. 243-251.
- Kobayashi T., Abe K., Ukyo Y., Iwahara H. (2002). Performance of electrolysis cells with proton and oxide-ion conducting electrolyte for reducing nitrogen oxide. *Solid State Ionics*, 154: pp. 699-705.
- Kokkofitis C., Ouzounidou M., Skodra A., Stoukides M. (2007a). Catalytic and electrocatalytic production of H<sub>2</sub> from the water gas shift reaction over Pd in a high temperature proton-conducting cell-reactor. *Solid State Ionics*, 178: pp. 475-480.
- Kokkofitis C., Ouzounidou M., Skodra A., Stoukides M. (2007b). High temperature proton conductors: applications in catalytic processes. *Solid State Ionics*, 178: pp. 507-513.
- Köleli F., Röpke T. (2006). Electrochemical hydrogenation of nitrogen to ammonia on a polyaniline electrode. *Applied Catalysis B: Environmental*, 62: pp. 306-310.

- Konsolakis M. (2016). The role of Copper–Ceria interactions in catalysis science: Recent theoretical and experimental advances. *Applied Catalysis B: Environmental*, 198: pp. 49-66.
- Kordali V., Kyriacou G., Lambrou C. (2000). Electrochemical synthesis of ammonia at atmospheric pressure and low temperature in a solid polymer electrolyte cell. *Chemical Community*, 0: pp. 1673-1674.
- Kraia Tz., Konsolakis M., Marnellos G.E. (2016). H<sub>2</sub>S in Black Sea: Turning an environmental threat to an opportunity for clean H<sub>2</sub> production via an Electrochemical Membrane Reactor. Research progress in H<sub>2</sub>S-PROTON Project, *MATEC Web Conference*, 41: pp. 04002.
- Kreuer K.D. (1999). Aspects of the formation and mobility of protonic charge carriers and the stability of perovskite-type oxides. *Solid State Ionics*, 125: pp. 285-302.
- Kreuer K.D. (2003). Proton-conducting oxides. *Annual Review of Materials Research*, 33: pp. 333-359.
- Kreuer K.D. (1997). On the development of proton conducting materials for technological applications. *Solid State Ionics*, 97: pp. 1-15.
- Kyriakou V., Garagounis I., Vourros A., Vasileiou E., Manerbino A., Coors W.G., Stoukides M. (2016). Methane steam reforming at low temperatures in a BaZr<sub>0.7</sub>Ce<sub>0.2</sub>Y<sub>0.1</sub>O<sub>2.9</sub> proton conducting membrane reactor. *Applied Catalysis B: Environmental*, 186: pp. 1-9.
- Kyriakou V., Athanasiou C., Garagounis I., Stoukides M. (2012). Production of C<sub>2</sub> hydrocarbons and H<sub>2</sub> from CH<sub>4</sub> in a proton conducting cell. *Solid State Ionics*, 225: pp. 219-222.
- Langguth J., Dittmeyer R., Hofmann H., Tomandl G. (1997). Studies on oxidative coupling of methane using high-temperature proton-conducting membranes. *Applied Catalysis A*, 158: pp. 287-305.
- Li J., Luo J.L., Chuang K.T., Sanger A.R. (2006). Proton conductivity and chemical stability of Li<sub>2</sub>SO<sub>4</sub> based electrolyte in a H<sub>2</sub>S-air fuel cell, *Journal of Power Sources*, 160: pp. 909-914.
- Li J., Luo J.L., Chuang K.T., Sanger A.R. (2008). Chemical stability of Y-doped Ba(Ce,Zr)O<sub>3</sub> perovskites in H<sub>2</sub>S-containing H<sub>2</sub>. *Electrochimica Acta*, 53: pp. 3701-3707.
- Li J., Liu R.Q., Wang J.D., Xu Z., Xie Y.H., Wang B.H. (2007). Preparation of double-doped BaCeO<sub>3</sub> and its application in the synthesis of ammonia at atmospheric pressure. *Science and Technology of Advanced Materials*, 8: pp. 566-570.
- Liu H., Weppner W. (1999). Electronic conductivity measurement of gadolinia doped ceria by DC-partial-polarization. *Ionics*, 5: pp. 115-121.
- Liu H., Chin J. (2014). Ammonia synthesis catalyst 100 years: Practice, enlightenment and challenge, *Journal of Catalysis*, 35: pp. 1619-1640.
- Liu S., Tan X., Li K., Hughes R. (2001). Methane coupling using catalytic membrane reactors. *Catalysis Reviews*, 43: pp. 147-198.
- Liu Y., Tan X., Li K. (2006). Non oxidative methane coupling in aSrCe<sub>0.95</sub>Yb<sub>0.05</sub>O<sub>3-α</sub> (SCYb) hollow fiber membrane reactor. *Industrial & Engineering Chemistry Research*, 45: pp. 3782-3790.
- Liu R.Q., Xie Y.H., Wang J.D., Li S.Z., Wang B.H. (2006). Synthesis of ammonia at atmospheric pressure with Ce<sub>0.8</sub>M<sub>0.2</sub>O<sub>2-δ</sub> (M = La, Y, Gd, Sm) and their proton conduction at intermediate temperature. *Solid State Ionics*, 177: pp. 73-76.
- Ma G., Shimura T., Iwahara H. (1998). Ionic conduction and non-stoichiometry in Ba<sub>x</sub>Ce<sub>0.9</sub>OY<sub>0.10</sub>O<sub>3-α</sub>. *Solid State Ionics*, 110: pp. 103-110.
- Makri M., Buekenhoudt A., Luyten J., Vayenas C.G. (1996). Non-Faradaic electrochemical modification of the catalytic activity of Pt using a CaZr<sub>0.9</sub>In<sub>0.1</sub>O<sub>3-α</sub> proton conductor. *Ionics*, 2: pp. 282-288.

- Malavasi L., Fisher C.A.J., Islam M.S. (2010). Oxide-ion and proton conducting electrolyte materials for clean energy applications: structural and mechanistic features. *Chemical Society Reviews*, 39: pp. 4370-4387.
- Manoj R.P., Ilwon K., David M. B., Barnett S.A. (2008). Fuel-flexible operation of a solid oxide fuel cell with  $\text{Sr}_{0.8}\text{La}_{0.2}\text{TiO}_3$  support. *Journal of Power Sources*, 185: pp.1086-1093.
- Marnellos G., Athanasiou C., Tsiakaras P., Stoukides M. (1996). Modelling of solid oxide proton conducting reactor-cells: thermodynamics and kinetics. *Ionics*, 2: pp. 412-420.
- Matsumoto H., Okubo M, Hamajima S., Katahira K., Iwahara H. (2002). Extraction and production of hydrogen using high-temperature proton conductor. *Solid State Ionics*, 152-153: pp. 715-720.
- Matsumoto H., Shimura T., Iwahara H., Higuchi T., Yashiro K., Kaimai A., Kawada T., Mizusaki J. (2006). Hydrogen separation using proton conducting perovskites. *Journal of Alloys and Compounds*, 408-412: pp. 456-462.
- Matsumoto H., Takeuchi K., Iwahara H. (1999). Electromotive force of  $\text{H}_2\text{-D}_2$  gas cell using high-temperature proton conductors. *Solid State Ionics*, 125: pp. 377-381.
- Mingyang G., Xingbo L., Jason T. (2007). Sulfur-tolerant anode materials for solid oxide fuel cell application. *Journal of Power Sources*, 168: pp. 289-298.
- Mohtadi R., Lee W.K., Zee J.W. (2005). The effect of temperature on the adsorption rate of hydrogen sulfide on Pt anodes in a PEMFC. *Applied Catalysis B: Environmental*, 56: pp. 37-42.
- Mori K., Lida K. (1987). Method for decomposing methane. JPS62139889, Japan Patent.
- Mori K., Lmai T. (1987). Method for reforming Methane, JPS62128901, Japan Patent.
- Navrotsky A., Weidner D.J. (1989). Perovskite: a structure of great interest to geophysics and materials science. Geophysical Monograph Series. American Geophysical Union, 45.
- Norby T., Christiansen N. (1995). Proton conduction in Ca- and Sr-substituted  $\text{LaPO}_4$ . *Solid State Ionics*, 77: pp. 240-243.
- Norby T., Larring Y. (1997). Concentration and transport of protons in oxides. *Current Opinion in Solid State and Materials Science*, 2: pp. 593-599.
- Otomo J., Noda N., Kosaka F. (2015). Electrochemical synthesis of ammonia with proton conducting solid electrolyte fuel cells at intermediate temperatures. *ECS Transactions*, 68: pp. 2663-2670.
- Pal'guez SF. (1998). High-temperature protonic solid electrolytes (review). *Russian Journal of Applied Chemistry*, 71: pp. 5.
- Pasier P., Wierzbick M., Komornicki S., Rekas M. (2007). Structural, electrical and transport properties of yttrium-doped proton-conducting strontium cerates. *Journal of Power Sources*, 173: 681-687.
- Peterson D., Winnick J. (1996). A hydrogen sulfide fuel cell using a proton-conducting solid electrolyte. *Journal of Electrochemical Society*, 143: pp. L55-L56.
- Ramadass N. (1978).  $\text{ABO}_3$ -type oxides: their structure and properties; a bird's eye view. *Material Science Engineering*, 36: pp. 231-239.
- Reijers R., Haije W. (2008). Literature review on high temperature proton conducting materials. Electrolyte for fuel cell or mixed conducting membrane for  $\text{H}_2$  separation. *Energy Research Centre of the Netherlands*.
- Rickert H.A. (1978). Solid ionic conductors: Principles and applications. *Angewandte Chemie International Edition*, 17: pp. 37-46.
- Sanchez Marcano J.G., Tsotsis T.T. (2004). Membrane bioreactors, in: Catalytic membranes and membrane reactors, Wiley-VCH Verlag GmbH & Co. KGaA. pp. 133-168.
- Scherban T., Villeneuve R., Albello L., Lucazeau G. (1993). Raman scattering study of acceptor-doped  $\text{BaCeO}_3$ . *Solid State Ionics*, 61: pp. 93-98.

- Scherban T., Nowick A.S. (1989). Bulk protonic conduction in Yb-doped SrCeO<sub>3</sub>. *Solid State Ionics*, 35: pp. 189-94.
- Schober T., Schilling W., Wenzl H. (1996). Defect model of proton insertion into oxides. *Solid State Ionics*, 86-88: pp. 653-658.
- Schober T. (2003). Applications of oxidic high-temperature proton conductors. *Solid State Ionics*, 162-163: pp. 277-281.
- Shi Luo J., Wang S., Sanger A.R., Chuang K.T. (2008). Protonic membrane for fuel cell for co-generation of power and ethylene. *Journal Power Sources*, 176: pp. 122-127.
- Shim J.H., Gur T.M., Prinz F.B. (2008). Proton conduction in thin film yttrium-doped barium zirconate. *Applied Physics Letters*, 92: 253115.
- Shima D., Haile S.M. (1997). The influence of cation non-stoichiometry on the properties of undoped and gadolinia-doped barium cerate. *Solid State Ionics*, 97: pp. 443-455.
- Singhal S.C. (2000). Advances in solid oxide fuel cell technology. *Solid State Ionics*, 135: pp. 305-313.
- Skodra A., Stoukides M. (2009). Electrocatalytic synthesis of ammonia from steam and nitrogen at atmospheric pressure. *Solid State Ionics*, 180: pp. 1332-1336.
- Slade R.C.T., Singh N. (1993). The perovskite-type proton-conducting solid electrolyte BaCe<sub>0.90</sub>Y<sub>0.10</sub>O<sub>3-α</sub> in high temperature electrochemical cells. *Solid State Ionics*, 61: pp. 111-114.
- Slavov S.V., Chuang K.T., Sanger A.R., Donini J.C., Kot J., Petrovic S. (1998). A proton-conducting solid state H<sub>2</sub>S-O<sub>2</sub> fuel cell. 1. Anode catalysts, and operation at atmospheric pressure and 20-90 °C, *International Journal of Hydrogen Energy*, 23: pp. 1203-1212
- Song S.J., Wachsman E.D., Dorris S.E., Balachandran U. (2003). Electrical properties of p-type electronic defects in the protonic conductor SrCe<sub>0.95</sub>Eu<sub>0.05</sub>O<sub>3-δ</sub>. *Journal of Electrochemical Society*, 150: pp. A790-795.
- Souza E.C.C., Muccillo R. (2010). Properties and applications of perovskite proton conductors. *Journal of Material Research*, 13: pp. 385-394.
- Stevenson D.A., Jiang N., Buchanan R.M., Henn F.E.G. (1993). Characterization of Gd, Yb and Nd doped barium cerates as proton conductors. *Solid State Ionics*, 62: pp. 279-285.
- Su P.C., Chao C.C., Shim J.H., Fasching R., Prinz F.B. (2008). Solid oxide fuel cell with corrugated thin film electrolyte. *Nano Letters*, 8: pp. 2289-2292.
- Sundmachera K., Rihko-Struckmanna L.K., Galvita V. (2005). Solid electrolyte membrane reactors: Status and trends. *Catalysis Today*, 104: pp. 185-199.
- Tan W.Y, Zhong Q., Miao M.S., Qu H.X. (2009). H<sub>2</sub>S solid oxide fuel cell based on a modified Barium cerate perovskite proton conductor. *Ionics*, 15: pp. 385-388.
- Taniguchi N., Nishimura C., Kato J. (2001). Endurance against moisture for protonic conductors of perovskite-type ceramics and preparation of practical conductors. *Solid State Ionics*, 145: pp. 349-355.
- Terai T., Li X., Tomishige K., Fujimoto K. (1999). Development of catalyst-membrane system for oxidative coupling of methane by water. *Chemical Letters*, 4: pp. 323-324.
- Thursfield A., Brosda S., Pliangos C., Schober T., Vayenas C.G. (2003). Electrochemical promotion of an oxidation reaction using a proton conductor. *Electrochimica Acta*, 48: pp. 3779-3788.
- Tomita A., Tsunekawa K., Hibino T., Teranishi S., Tachi Y., Sano M. (2006). Chemical and redox stabilities of a solid oxide fuel cell with BaCe<sub>0.8</sub>Y<sub>0.2</sub>O<sub>3-α</sub> functioning as an electrolyte and as an anode. *Solid State Ionics*, 177: pp. 2951-2956.

- Vasileiou E., Kyriakou V., Garagounis I., Vourros A., Manerbino A., Coors W.G., Stoukides M. (2016). Electrochemical enhancement of ammonia synthesis in a  $\text{BaZr}_{0.7}\text{Ce}_{0.2}\text{Y}_{0.1}\text{O}_{2.9}$  solid electrolyte cell. *Solid State Ionics*, 288: pp. 357-362.
- Vasileiou E., Kyriakou V., Garagounis I., Vourros A., Stoukides M. (2015). Ammonia synthesis at atmospheric pressure in a  $\text{BaCe}_{0.2}\text{Zr}_{0.7}\text{Y}_{0.1}\text{O}_{2.9}$  solid electrolyte cell. *Solid State Ionics*, 275: pp. 110-116.
- Vayenas C.G., Koutsodontis C.G. (2008). Non-Faradaic electrochemical activation of catalysis. *The Journal of Chemical Physics*, 128: pp. 182506-182513.
- Vorontsov V., Luo J.L., Sanger A.R., Chuang K.T. (2008). Synthesis and characterization of new ternary transition metal sulphide anodes for  $\text{H}_2\text{S}$ -powered solid oxide fuel cell. *Journal of Power Sources*, 183: pp. 76-83.
- Wang S., Luo J.L., Sanger A.R., Chuang K.T. (2007). Performance of ethane/oxygen fuel cells using yttrium-doped barium cerate as electrolyte at intermediate temperatures. *Journal of Physical Chemistry C*, 111: pp. 5069-5074.
- Wang W.B., Cao X.B., Gao W.J., Zhang F., Wang H.T., Ma G.L. (2010). Ammonia synthesis at atmospheric pressure using a reactor with solid electrolyte  $\text{BaCe}_{0.85}\text{Y}_{0.15}\text{O}_{3-\alpha}$ . *Journal of Membrane Science*, 360: pp. 397-403.
- Woldman L.S., Sokolovskii V.D. (1991). Electrocatalytic methane coupling in the absence of oxygen on a high-temperature proton conducting electrolyte. *Catalysis Letters*, 8: pp. 61-66.
- Yamaguchi S., Yamamoto S., Tsuchiya B., Nagata S., Shishido T. (2005). Construction of fuel reformer using proton conducting oxides electrolyte and hydrogen-permeable metal membrane cathode. *Journal of Power Sources*, 145: pp. 712-715.
- Yamazaki Y., Babilo P., Haile S.M. (2008). Defect chemistry of yttrium-doped barium zirconate: A thermodynamic analysis of water uptake. *Chemical Materials*, 20: pp. 6352-6357.
- Zakowsky N., Williamson S., Irvine J.T.S. (2005). Elaboration of  $\text{CO}_2$  tolerance limits of  $\text{BaCe}_{0.9}\text{Y}_{0.1}\text{O}_{3-\delta}$  electrolytes for fuel cells and other applications. *Solid State Ionics*, 176: pp. 3019-3026.
- Zhang F., Yang Q., Pan B., Xu R., Wang H., Ma G. (2007). Proton conduction in  $\text{La}_{0.9}\text{Sr}_{0.1}\text{Ga}_{0.8}\text{Mg}_{0.2}\text{O}_{3-\alpha}$  ceramic prepared via micro emulsion method and its application in ammonia synthesis at atmospheric pressure. *Material Letters*, 61: pp. 4144-4148.
- Zhong L., Qi M., Wei G., Luo J., Chuang K. (2006). An intermediate-temperature  $\text{H}_2\text{S}$  fuel cell with a  $\text{Li}_2\text{SO}_4$ -based proton-conducting membrane. *Chinese Journal of Chemical Engineering*, 14: pp.51-55.
- Zhu B. (1999). Advanced environmental/energy technology: desulfurization and fuel cell cogeneration. *Fuel Cells Bulletin*, 2: pp. 9-12.
- Zhu B., Tao S. (2000). Chemical stability study of  $\text{Li}_2\text{SO}_4$  in a  $\text{H}_2\text{S}/\text{O}_2$  fuel cell. *Solid State Ionics*, 127: pp. 83-88.

# PART

## H<sub>2</sub>S CATALYTIC DECOMPOSITION IN H<sub>2</sub>O ABSENCE/PRESENCE



Contents	Page
I.1. Introduction. . . . .	97
References. . . . .	104
Chapter 4: Materials and methods. . . . .	107
Chapter 5: H <sub>2</sub> S Catalytic decomposition in the absence of H <sub>2</sub> O. . . . .	131
Chapter 6: H <sub>2</sub> S Catalytic decomposition in the presence of H <sub>2</sub> O. . . . .	175



## I.1. INTRODUCTION

World energy demands have been historically increasing due to the population growth, technological development and living standards. Presently, the production of energy is mainly based on non-renewable sources, e.g., coal, petroleum, natural gas. The extensive use of these non-renewable sources is responsible for the following socioeconomic and environmental implications: i) energy deficit, i.e., shortage of fossil fuels, ii) environmental pollution, e.g., global warming, iii) aridity, poverty, decline of human health, food supply, etc., and iv) local, regional and global conflicts. In order to partially ameliorate or completely address the above problems, nowadays, the worldwide society is called to utilize renewable and non-polluting energy resources and establish novel technologies, as essential requirements for sustainable growth and development, towards a “cleaner” world (Midilli et al., 2007).

Hydrogen economy is believed to be an important part of the future energy mix. More specifically, H<sub>2</sub>, if derived from carbon-free energy resources, is worldwide acknowledged as an environmental friendly energy vector, which can support future energy developments. Such an approach could be the production of hydrogen from hydrogen sulfide (H<sub>2</sub>S) decomposition, by using the excess of intermittent renewable energy sources (RES). In general, H<sub>2</sub>S is a poisonous, flammable and acidic gas, as well as, a corrosive refinery product of the hydrodesulphurization process, which is generally considered as an environmental threat. Due to its toxicity and harmful effects on human health and environment, H<sub>2</sub>S is necessary to be removed or reduced to acceptable levels from all effluent streams and ecosystems, before its disposal (Selene and Chou, 2003; Bahadori, 2014; Garry and Handwerk, 2001).

The current industrial practice for H<sub>2</sub>S management is the Claus process, a partial oxidation treatment (Kaloidas and Papayanakos, 1987), which allows the recovery of elemental sulfur, at the expense of H<sub>2</sub>, which is consumed for H<sub>2</sub>O (Kohl and Nielsen, 1997; Elsner et al., 2003; Manenti et al., 2013). In contrast to water, H<sub>2</sub> is only loosely bound to the H<sub>2</sub>S molecule ( $\Delta H_f^0_{298} = -4.82$  kcal/mol), thus, the decomposition of H<sub>2</sub>S has recently become a process of great importance towards the production of two saleable products, i.e., hydrogen and sulfur.

It is believed that H<sub>2</sub>S, which is abundantly found in Black Sea deep waters, where nearly 90% of the water is anoxic (Baykara et al., 2007; Baykara, 2011) with a total sulphide pool of 4.6×10<sup>9</sup> tons, could be an inexhaustible source of hydrogen (Neretin et al., 2001). The ecological background for this reasoning is as follows: H<sub>2</sub>S in Black Sea is produced as a result of a complex microbial sulphur cycle involving a simultaneous carbon cycle (Deuser, 1974), which is replenished by organic and inorganic carbon sources in the basin (Murray et al., 1989). Below an oxygenated top water layer, an interface layer exists, where H<sub>2</sub>S from the anoxic region is converted by dissolved O<sub>2</sub> into sulphate. In the anoxic region, the H<sub>2</sub>S concentration steadily increases with depth until a constant level of 9.5 mg/l at around 1500 m (Neretin et al., 2001). Caused by the depletion of oxygen in the top layer, the depth level of the interface layer is rising steadily at an increasing rate (Lein and Ivanov, 1991), with the possible risk that the thickness of the upper aerobic zone may diminish and sulphide-rich waters will force their way to the surface of the Marmara and Mediterranean seas (Lein and Ivanov, 1991). This would threaten the ecosystem, especially the fish population, and the economy in the Black Sea region, especially if the Channel Istanbul (parallel to Bosphorus) is opened (Uslu, 2013).

Apart from the harmful effects due to H<sub>2</sub>S presence in the Black Sea, i.e., human health and ecological problems that arise from air and water pollution, Black Sea H<sub>2</sub>S may serve as a future energy source. From theoretical calculations it has been found that it will be possible to produce:

- H<sub>2</sub> fuel (almost 1.3 Mio. tons or 1.84·10<sup>17</sup> J) from the H<sub>2</sub>S layer in 100-200 m depth of the Black Sea coastal parts. The maximum potential of H<sub>2</sub> can be estimated at 86.4 Mio. tons from 1469 Mio. tons of H<sub>2</sub>S in a layer of 1000-1500 m width. The total H<sub>2</sub> potential is estimated at 270 Mio. tons (Midilli et al., 2007; Zaman and Chakma, 1995).
- 3.83·10<sup>19</sup> J of thermal or 8.97·10<sup>15</sup> Wh of electrical energy, by using 270 Mio. tons of the total H<sub>2</sub>, based on the total H<sub>2</sub>S potential. This H<sub>2</sub> amount corresponds to 808 Mio. tons of gasoline or 766 Mio. tons of natural gas (Midilli et al., 2007; Baykara et al., 2007).

As a consequence, if H<sub>2</sub> is produced from the Black Sea H<sub>2</sub>S, the energy demands of the regional countries can be partially compensated and surplus H<sub>2</sub> fuel can be transported to Europe. Notice that methods for extracting H<sub>2</sub>S from seawaters are already well-known: adsorption and stripping processes (Naman et al., 2008; Petrov et al., 2011).

Several alternatives have been proposed for the production of hydrogen from H<sub>2</sub>S decomposition, which are currently at different stages of development, involving thermochemical, photochemical, plasmachemical and electrochemical methods (Zaman and Chakma, 1995; Luinstra, 1996; Raymont, 1975; Revereberi et al., 2016). The majority of these approaches present certain disadvantages attributed to the particular high energy requirements and low efficiencies, rendering their commercialization still in doubt. The most commonly employed direct method is the thermal decomposition of H<sub>2</sub>S (Zaman and Chakma, 1995), which however takes place at high temperatures in order to achieve conversions exceeding 80%. Breaking up the H<sub>2</sub>S molecule into its constituent elements require substantial amount of energy since the thermal decomposition process of H<sub>2</sub>S, given in Equation I.1, is an endothermic reaction and this is considered as the major drawback of the method (Chivers and Lau, 1987a).



The resulting S<sub>2</sub> further reacts with excess H<sub>2</sub>O:



The overall reaction of the process is:



resulting in a threefold amount of hydrogen per mole of H<sub>2</sub>S, compared with the corresponding decomposition in the absence of H<sub>2</sub>O. It should be noted that the kinetics of the direct thermal decomposition of H<sub>2</sub>S (see Equation I.1) are already well-described (Karan et al., 1999; Binoist et al., 2003).

The decrease of the activation energy of the above reaction is possible by using a suitable catalyst in order to increase the conversion of hydrogen sulfide and to enhance hydrogen yield. There are several studies found in literature attempting to make this process feasible by using various techniques and utilizing several types of catalysts. In the literature, there are studies where numerous metal oxide or metal sulfide catalysts (Chivers and Lau, 1987b; Kaloidas and Papayannakos, 1987; Bandermann and Harder, 1982; Fukuda et al., 1978; Chivers et al., 1980; Chivers et al., 1980; Bishara et al., 1987; Salman et al., 1987; Al-Shamma et al., 1989; Sugioka and Aomura, 1984; Kiuchi et al., 1982; Kiuchi et al., 1984; Moffat et al., 1996; Startsev et al., 2013; Guldal et al., 2015) containing Co, Cr, Cu, Fe, Mo, Ni, V, Al<sub>2</sub>O<sub>3</sub>, W, have been utilized to enhance H<sub>2</sub>S conversion.

Recently, researchers suggested that the H<sub>2</sub>S decomposition using a proton-conducting, ceramic electrolysis cell (Chuang et al., 2008; Gong et al., 2007; Li et al., 2006; Athanassiou et al., 2007; Mbah et al., 2008) constitutes a promising alternative process for H<sub>2</sub>S decomposition towards H<sub>2</sub> production. However, one of the most challenging tasks of this concept is to identify the optimum cell materials, and especially the selection of the material, employed as anode in the H<sup>+</sup> conducting high temperature proton conductor membrane reactor, is crucial for the successful operation of the proposed process. For this specific application, the conductive anode electrode should exhibit, among others properties: i) high catalytic activity towards H<sub>2</sub>S/H<sub>2</sub>O decomposition, ii) high electronic conductivity, iii) good adherence on solid electrolyte, and iv) tolerance to H<sub>2</sub>S rich environments (Gong et al., 2007; Vorontsov et al., 2008).

In general, the S-tolerant electrodes are categorized to: thiospinels and metal sulphides (MoS<sub>2</sub>, CoS<sub>2</sub>), metal cermets, and mixed ionic and electronic conductors (MIEC). Thiospinels and metal sulfides are favorable for H<sub>2</sub>S oxidation fuel cells, however, their time-consuming and complex synthesis procedure, along with their inadequate stability, limit their applicability in real-scale processes (Gong et al., 2007). In parallel, several relevant studies have focused on Cu- and Co-CeO<sub>2</sub> cermets, showing promising electrochemical performance and stable behavior. Materials like alumina, titania, zirconia and CeO<sub>2</sub> can serve as supporting carriers. Regarding the catalyst support, it should possess adequate chemical and mechanical properties to provide the required activity and stability under the reaction conditions. Most importantly, supporting composites should provide strong metal-support interactions and high oxygen mobility, preserving the active phase from sintering. CeO<sub>2</sub> is a technologically important material, which has been so far employed for various applications in chemical catalysis, including the water gas shift reaction (Polychronopoulou et al., 2011), NO<sub>x</sub> reduction (Ilieva et al., 2007; Baudin et al., 2004), oxidation or partial oxidation of hydrocarbons (De Lima et al., 2008), hydrocarbons reforming (Laosiripojana and Assabumrungrat, 2006), etc., and solid oxide fuel cells, owed to its excellent redox properties and oxygen storage capacity, via the oxidation change from Ce<sup>4+</sup> to Ce<sup>3+</sup> in redox cycles. Doped or undoped CeO<sub>2</sub>, tends to be a common choice as a sulfur tolerant component in metal anodes, due to their good performance and lower cost.

In this context, and prior to electrochemical tests, a series of metal catalysts were synthesized, via the wet impregnation method, and evaluated, in terms of their catalytic activity and stability, for H<sub>2</sub>S decomposition, in the absence (see Chapter 5)/presence (see Chapter 6) of H<sub>2</sub>O. In addition, characterization studies, involving BET, XRD, SEM/EDX, XPS measurements and sulfur elemental analysis of both the “fresh”, “aged” and “sulfated” samples, were performed in both H<sub>2</sub>S reaction conditions to reveal the impact of the structural and surface characteristics of the employed catalysts, on the H<sub>2</sub>S decomposition performance and, thus, to gain insight into possible structure-activity relationships.

Afterwards, the catalytic activity and stability experiments were performed in an automated apparatus consisting of the feeding unit, the fixed bed quartz U-shaped tube reactor, the heating system of the reactor and the gas analysis unit. In H<sub>2</sub>O-free experiments, a mixture of H<sub>2</sub>S/Ar (typically 1 v/v%) was fed in the reactor through two mass flow controllers. When H<sub>2</sub>O (typically 90 v/v%) was co-fed to the reactor, a separate system for water supply was involved, consisting of a double-distilled H<sub>2</sub>O storage tank and a water syringe pump. Then, liquid water was evaporated to steam in a preheater and mixed with the gaseous feeding streams before entering the reactor. The experiments were carried out at the temperature range of 550-850 °C, at ambient pressure and mass catalyst equal to 250 mg, while the total volumetric flow was kept constant to 100 cm<sup>3</sup>/min. Before entering the analysis system, which was an on-line gas chromatographer, equipped with a TCD detector, the effluents were introduced in a condenser to remove any residual steam and subsequently fed in a sulphur scrubber. For comparison purposes, the thermodynamic H<sub>2</sub>S conversion as a function of temperature and feed concentration, and inert/steam addition and the product molar fraction at the exit as a function of feed concentration, were also examined and presented below.

### 1.1.1. Thermodynamic Calculations

The method of thermodynamic analysis based on the minimization of Gibbs free energy is performed in most chemical processes in order to identify the limits of catalysts activity, prior or in parallel with the conducted experiments. In principle, thermodynamic calculations can provide indications on optimal feed ratios and operating temperatures. The system can

be considered as ideal and the total Gibbs function is given by (notice that  $i$  are the components):

$$G^t = \sum_{i=1}^N n_i \overline{G}_i = \sum_{i=1}^N n_i \overline{\mu}_i = \sum_{i=1}^N n_i G_i^o + RT \sum_{i=1}^N n_i \ln \frac{\phi_i y_i P}{P_i^o} \quad (1.4)$$

where  $G$  denotes the Gibbs energy in J,  $n$  the moles of the component,  $\mu$  the chemical potential,  $R$  the ideal gas constant in J/(mol·K),  $T$  the temperature in K,  $\phi$  the fugacity,  $y$  the component molar fraction,  $P$  the overall pressure and  $P_i$  the component partial pressure in bar. The symbol (dash) above each variable denotes average values, while  $G_i$  at initial state is set equal to zero for all components.

The minimum Gibbs free energy of each gaseous species and that of the total system can be expressed from Equations 1.5 and 1.6, with the Lagrange's ( $\lambda$  and  $\alpha$  are the relevant parameters) undetermined multiplier method (Wang et al., 2011):

$$\Delta G_{f_i}^o + RT \sum \ln \frac{\phi_i y_i P}{P_i^o} + \sum_k \lambda_k a_{ik} = 0 \quad (1.5)$$

$$\sum_{i=1}^N n_i (\Delta G_{f_i}^o + RT \sum \ln \frac{\phi_i y_i P}{P_i^o} + \sum_k \lambda_k a_{ik}) = 0 \quad (1.6)$$

The primary species involved in the analysis are  $H_2S$ ,  $H_2$ ,  $S$  (in various forms),  $SO_2$ ,  $H_2O$ ,  $Ar$  and  $O_2$ . The thermodynamic calculations were performed in the temperature range 550-950 °C, at atmospheric pressure and  $H_2S$  inlet concentration in the range 0-5%. The thermodynamic equilibrium calculations were accomplished with the use of Aspen Plus. Figures I.1A and I.1B present, respectively, the effect of inert ( $Ar$ ) and water (steam) addition at the anode, as a function of temperature and feed concentration.

As expected, and independently of  $Ar$  (Figure I.1A)/steam addition (Figure I.1B), the increase of temperature promotes the decomposition of  $H_2S$  (endothermic reaction), while in all cases, the addition of  $Ar/H_2O$  at the feed stream, promotes  $H_2$  production. Lower  $H_2S$  concentrations lead to larger conversions that can reach almost 100% in the case of steam addition. The comparison between  $Ar$  and steam addition, reveals that for  $H_2S > 2.5\%$  the effect of  $Ar$  as inert is more significant than of steam, but for lower concentrations, steam significantly favours  $H_2S$  conversion.

Similarly, Figure I.2A illustrates the combined effect of  $Ar$  and steam addition, where it is verified that steam addition promotes more than  $Ar$  the decomposition of  $H_2S$ . The

## H<sub>2</sub>S CATALYTIC DECOMPOSITION IN H<sub>2</sub>O ABSENCE/PRESENCE

calculated product compositions for various feed gas mixtures (H<sub>2</sub>S/H<sub>2</sub>O) at 850 °C (Figure I.2B) shows that in the presence of H<sub>2</sub>O the formation of SO<sub>2</sub> is favored against elemental S generation. Hydrogen, which is derived from H<sub>2</sub>S dissociation is increasing upon increasing the H<sub>2</sub>S content. On the other hand, the molar fraction summation of the sulphur containing products, i.e., SO<sub>2</sub> and elemental S, which are derived only from H<sub>2</sub>S decomposition, is decreasing with increasing H<sub>2</sub>S concentration, indicating a reduced H<sub>2</sub>S conversion.

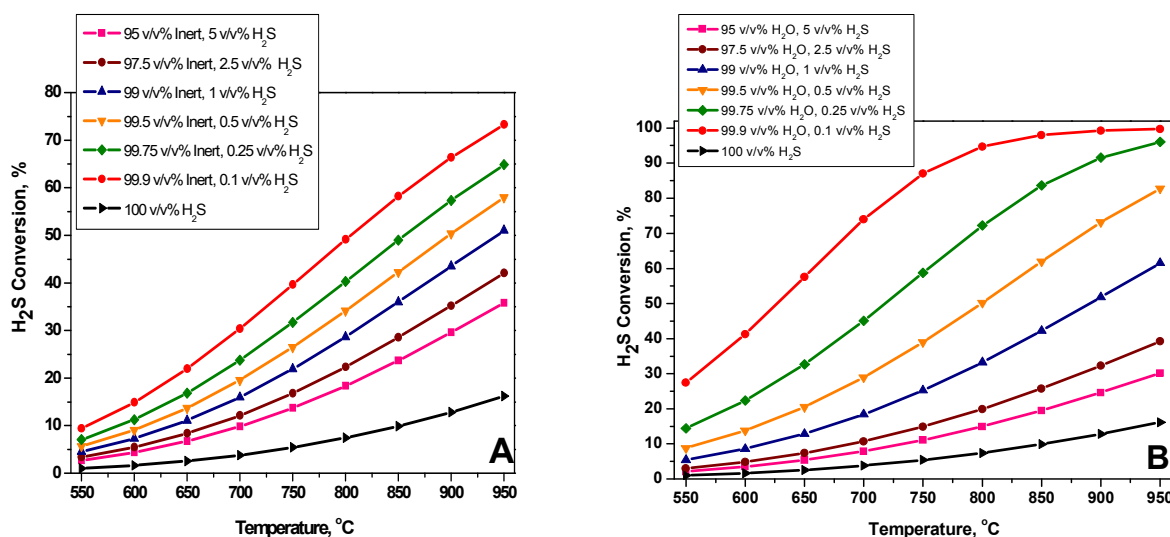


**Figure I.1:** H<sub>2</sub>S conversion as a function of temperature and feed concentration: A) inert (Ar) addition and B) steam addition.

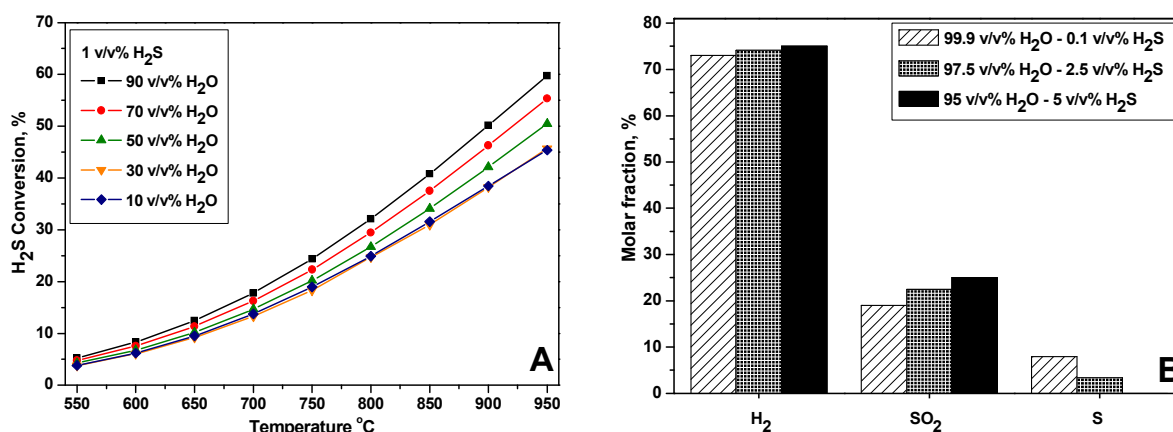


**Figure I.2:** A) Calculated equilibrium H<sub>2</sub>S conversion as a function of temperature and inlet H<sub>2</sub>O concentration for H<sub>2</sub>S/H<sub>2</sub>O/Ar feed gases with constant H<sub>2</sub>S inlet concentration of 1 v/v%.; B) product molar fractions at the exit as a function of feed concentration.

## REFERENCES

- Al-Shamma L.M., Naman S.A. (1989). Kinetic study for thermal production of hydrogen from H<sub>2</sub>S by heterogeneous catalysis of vanadium sulfide in a flow system. *International Journal of Hydrogen Energy*, 14: pp. 173-179.
- Athanassiou C., Pekridis G., Kaklidis N., Kalimeri K., Vartzoka S., Marnellos G. (2007). Hydrogen production in solid electrolyte membrane reactors (SEMRs). *International Journal of Hydrogen Energy*, 32: pp. 38-54.
- Bahadori A. (2014). Natural gas processing. Technology and engineering design. *Gulf Professional Publishing*, Waltham, U.S.A.
- Bandermann F., Harder K.B. (1982). Production of H<sub>2</sub> via thermal decomposition of H<sub>2</sub>S and separation of H and HS by pressure swing adsorption. *International Journal of Hydrogen Energy*, 7: pp. 471-475.
- Baudin F., da Costa P., Thomas C., Calvo S., Lendresse Y., Schneider S., Delacroix F., Plassat G., Mariadassou G.D. (2004) NO<sub>x</sub> reduction over CeO<sub>2</sub>-ZrO<sub>2</sub> supported iridium catalyst in the presence of propanol. *Topics in Catalysis*, 30: pp. 97-101.
- Baykara S.Z., Figen E.H., Kale A., Veziroglu T.N. (2007). Hydrogen from hydrogen sulphide in the Black Sea. *International Journal of Hydrogen Energy*, 32: pp. 1246-1250.
- Baykara S.Z. (2011). Black Sea and hydrogen sulphide, in *The Black Sea: dynamics, ecology and conservation*. Ryann A.L., Perkins N.J. (Eds.), *Nova Science Publishers*, New York, U.S.A.
- Binoist M., Labégorre B., Monnet F., Clark P.D., Dowling N.I., Huang M., Archambault D., Plasari E., Marquaire P.-M. (2003). Kinetic study of the pyrolysis of H<sub>2</sub>S. *Industrial and Engineering Chemistry Research*, 42: pp. 3943-3951.
- Bishara A., Salman O.A., Khraishi N., Marafi A. (1987). Thermochemical decomposition of hydrogen sulfide by solar energy. *International Journal of Hydrogen Energy*, 12: pp. 679-685.
- Chivers T., Hyne J.B., Lau C. (1980). The thermal decomposition of hydrogen sulfide over transition metal sulfides. *International Journal of Hydrogen Energy*, 5: pp. 499-506.
- Chivers T., Lau C. (1987a). The thermal decomposition of hydrogen sulfide over vanadium and molybdenum sulfides and mixed sulfide catalysts in quartz and thermal diffusion column reactors. *International Journal of Hydrogen Energy*, 12: pp. 235-243.
- Chivers T., Lau C. (1987b). The use of thermal diffusion column reactors for the production of hydrogen and sulfur from the thermal decomposition of hydrogen sulfide over transition metal sulfides. *International Journal of Hydrogen Energy*, 12: pp. 561-569.
- Chuang K.T., Luo J., Sanger A.R. (2008). Evolution of fuel cells powered by H<sub>2</sub>S-containing gases. *Chemical Industry and Chemical Engineering Quarterly*, 14: pp. 69-76.
- De Lima S.M., da Cruz I.O., Jacobs G., Davis B.H., Mattos L.V., Noronha F.B. (2008). Steam reforming, partial oxidation, and oxidative steam reforming of ethanol over Pt/CeZrO<sub>2</sub> catalyst. *Journal of Catalysis*, 257: pp. 356-368.
- Deuser W.G. (1974). Evolution of anoxic conditions in Black Sea during holocene, in *The Black Sea-geology, chemistry and biology*. Degens E.T., Ross D.A. (Eds.). American Association of Petroleum Geologists, Tulsa-Oklahoma, U.S.A.
- Elsner M.P., Menge M., Müller C., Agar D.W. (2003). The Claus process: teaching an old dog new tricks. *Catalysis Today*, 79-80: pp. 487-494.
- Fukuda K., Dokiya M., Kameyama T., Kotera Y. (1978). Catalytic decomposition of hydrogen sulfide. *Industrial and Engineering Chemistry Fundamentals*, 17: pp. 243-248.

- Garry J.H., Handwerk G.E. (2001). Petroleum refining, technology and economics, fourth ed. *Marcel Dekker Inc.*, New York, U.S.A.
- Gong M., Liu X., Tremblay J., Johnson C. (2007). Sulfur-tolerant anode materials for solid oxide fuel cell application. *Journal of Power Sources*, 168: pp. 289-298.
- Guldal N.O., Figen H.E., Baykara S.Z. (2015). New catalysts for hydrogen production from H<sub>2</sub>S: preliminary results. *International Journal of Hydrogen Energy*, 40: pp. 7452-7458.
- Ilieva L., Pantaleo G., Sobczak J.W., Ivanov I., Venezia A.M., Andreev D. (2007). NO reduction by CO in the presence of water over gold supported catalysts on CeO<sub>2</sub>Al<sub>2</sub>O<sub>3</sub> mixed support, prepared by mechanochemical activation. *Applied Catalysis B: Environmental*, 76: pp. 107-114.
- Kaloidas V.E., Papayannakos N.G. (1987). Hydrogen production from the decomposition of hydrogen sulphide. Equilibrium studies on the system H<sub>2</sub>S/H<sub>2</sub>/S<sub>i</sub>, (i=1,...,8) in the gas phase. *International Journal of Hydrogen Energy*, 12: pp. 403-409.
- Karan K., Mehrotra A.K., Behie L.A. (1999). On reaction kinetics for the thermal decomposition of hydrogen sulphide. *AIChE Journal*, 45: pp. 383-389.
- Kiuchi H., Nakamura T., Funaki K., Tanaka T. (1982). Recovery of hydrogen from hydrogen sulfide with metals or metal sulfides. *International Journal of Hydrogen Energy*, 7: pp. 477-482.
- Kiuchi H., Funaki K., Nakai Y., Tanaka T. (1984). Thermochemical decomposition cycle of H<sub>2</sub>S with nickel sulfide. *International Journal of Hydrogen Energy*, 9: pp. 701-705.
- Kohl A., R. Nielsen. (1997). Gas purification, fifth ed. *Gulf Publishing Co.*, Houston, U.S.A.
- Laosiripojana N., Assabumrungrat S. (2006). Catalytic steam reforming of ethanol over high surface area CeO<sub>2</sub>: The role of CeO<sub>2</sub> as an internal pre-reforming catalyst. *Applied Catalysis B: Environmental*, 66: 29-39.
- Lein A.Y., Ivanov M.V. (1991). On the sulphur and carbon balances in the Black Sea, in Black Sea Oceanography, NATO-ASI Series C, vol. 351, Izdar E., Murray J.W. (Eds.), *Kluwer Academic Publishers*, Boston, U.S.A.
- Li J., Luo J.L., Chuang K.T., Sanger A.R. (2006). Proton conductivity and chemical stability of Li<sub>2</sub>SO<sub>4</sub> based electrolyte in a H<sub>2</sub>S-air fuel cell. *Journal of Power Sources*, 160: pp. 909-914.
- Luinstra E. (1996). H<sub>2</sub>S: a potential source for hydrogen. *Sulphur*, 244: pp. 37-47.
- Manenti F., Papisidero D., Bozzano G., Pierucci S., Ranzi E., Ferraris G.B. (2013). Total plant integrated optimization of sulfur recovery and steam generation for Claus processes using detailed kinetic schemes. *Computer Aided Chemical Engineering*, 32: pp. 811-816.
- Mbah J., Krakow B., Stefanakos E., Wolan J. (2008). Electrolytic splitting of H<sub>2</sub>S using CsHSO<sub>4</sub> membrane. *Journal of The Electrochemical Society*, 155: pp. E166-E170.
- Midilli A., Ay M., Kale A., Veziroglu T.N. (2007). A parametric investigation of hydrogen energy potential based on H<sub>2</sub>S in Black Sea deep waters. *International Journal of Hydrogen Energy*, 32: pp. 117-124.
- Moffat S.C., Adesina AA. (1996). The dissociation kinetics of H<sub>2</sub>S over an alumina supported Co-Mo sulphide catalyst. *Catalysis Letters*, 37: pp. 167-172.
- Murray J.W., Jannasch H.W., Honjo S., Anderson R.A., Reeburg W.S., Top Z., Friederich G.E., Codispoti L.A., Izdar E. (1989). Unexpected changes in the oxic-anoxic interface in the Black Sea. *Nature* 1989; 338: pp. 411-413.
- Naman S.A., Ture E.I., Veziroglu T.N. (2008). Industrial extraction pilot plant for stripping H<sub>2</sub>S gas from Black Sea water. *International Journal of Hydrogen Energy*, 33: pp. 6577-6585.
- Neretin L.N., Volkov I.I., Bottcher M.E., Grinenko V.A. (2001). Sulfur budget for the Black Sea anoxic zone. *Deep Sea Research Part I: Oceanographic Research Papers*, 48: pp. 2569-2593.

- Petrov K., Baykara S.Z., Ebrasu D., Gulin M., Veziroglu A. (2011). A brief assessment of hydrogen production from H<sub>2</sub>S in Black Sea waters. *International Journal of Hydrogen Energy*, 36: pp. 8936-8942.
- Polychronopoulou K., Kalamaras C.M., Efstathiou A.M. (2011). Ceria-based materials for hydrogen production via hydrocarbon steam reforming and water-gas shift reactions. *Recent Patents on Materials Science*, 4: pp. 122-145.
- Raymont M.E.D. (1975). Make hydrogen from hydrogen sulphide. *Hydrocarbon Processing*, 54: pp. 139-142.
- Reverberi A.P., Klemes J.J., Varbanov P.S., Fabiano B. (2016). A review on hydrogen production from hydrogen sulphide by chemical and photochemical methods. *Journal of Cleaner Production*, 136(B): pp. 72-80.
- Salman O.A., Bishara A., Marafi A. (1987). An alternative to the Claus process for treating hydrogen sulfide, *Energy*, 12: pp. 1227-1232.
- Sugioka M., Aomura K. (1984). A possible mechanism for catalytic decomposition of hydrogen sulfide over molybdenum disulfide. *International Journal of Hydrogen Energy*, 9: pp. 891-894.
- Selene C.H., Chou J. (2003). Hydrogen sulfide: human health aspects. *World Health Organization*, Geneva, Switzerland.
- Startsev A.N., Kruglyakova O.V., Chesalov Y.A., Ruzankin S.P., Kravtsov E.A., Larina T.V., Paukshtis E.A. (2013). Low temperature catalytic decomposition of hydrogen sulfide into hydrogen and diatomic gaseous sulfur. *Topics in Catalysis*, 56: pp. 969-980.
- Uslu O. (2013). Resilience of ecological systems, in: Innovative and eco-friendly future energy technologies and use of regional resources of Turkey and the European Union, *Humboldt Kolleg*, Istanbul, Turkey.
- Vorontsov V., Luo J.L., Sanger A.R., Chuang K.T. (2008). Synthesis and characterization of new ternary transition metal sulphide anodes for H<sub>2</sub>S-powered solid oxide fuel cell. *Journal of Power Sources*, 183: pp. 76-83.
- Zaman J., Chakma A. (1995). Production of hydrogen and sulfur from hydrogen sulfide. *Fuel Processing Technology*, 41:159-198.

# CHAPTER

# 4

## MATERIALS AND METHODS

Contents	Page
4.1. Introduction. . . . .	109
4.2. Catalysts preparation. . . . .	110
4.3. Materials. . . . .	114
4.4. Characterization methods. . . . .	116
4.5. Experimental equipment and sample preparation. . . . .	118
References. . . . .	129



## 4.1. INTRODUCTION

Catalysis, in chemistry, is the acceleration of a chemical reaction due to the participation of an additional substance called catalyst, without itself being consumed or affected by the overall reaction. Hence, catalysts can assist reactions that would not run without their presence, or perform them much faster, or even at lower temperatures. This means that the catalysts permit a different energy pathway for a chemical reaction, which presents lower activation energy (see Figure 4.1).

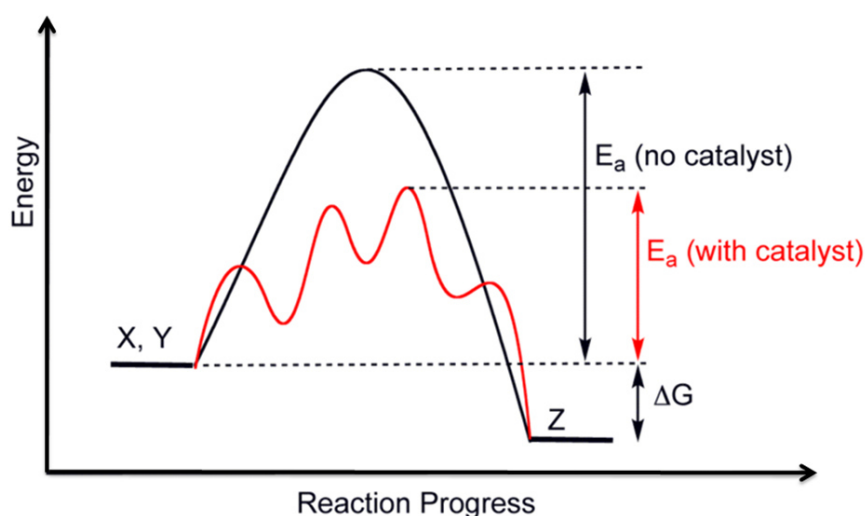


**Figure 4.1:** Generic potential energy diagram showing the effect of a catalyst in a hypothetical exothermic chemical reaction  $X + Y$  to give  $Z$ . The presence of the catalyst opens a different reaction pathway (shown in red) with lower activation energy.

In general, catalysts play a vital role in sustaining the competitiveness of the modern chemical industry. If they are selective, stable and have high activity under the selected conditions of the process, they are suitable for industrial processes such as oil refining, chemical processing and pharmaceuticals production. In heterogeneous catalytic reactions, a catalyst is highly active if it has the capacity, through its large inner surface, to adsorb large amounts of the reaction gases. Moreover, beyond the actual catalytic actions these materials can serve multiple objectives. In this sense, the materials used in this work were employed for two different roles, i.e., as catalysts to promote the hydrogen sulfide catalytic decomposition reaction and as anodic electrodes in  $H_2S$  electrolytic cells. Several reasons can be mentioned for their selection, such as that they combine the electronic conductivity

of the metal phase with the ionic conductivity of the CeO<sub>2</sub> support, which is significantly important for fuel cell anodes. Furthermore, the reducibility of ceria can have a beneficial effect on both the catalytic and electrocatalytic activity of such materials.

Chapter 4 discusses the materials used and the synthesis routes employed for the preparation of catalysts, along with the experimental methods conducted for their evaluation. It also briefly touches upon the various physicochemical characterization studies carried out to determine the physical and chemical properties of the catalysts, as well as, addresses the detailed development of the fixed-bed catalytic reactor and the relevant experimental procedure followed to carry out the hydrogen sulfide decomposition reaction. More specifically, upon a small introduction (Section 4.1) the catalysts that were used in the experiments (presented in the subsequent chapters of this thesis) and their preparation methods are explained in Sections 4.2 and 4.3, respectively, while the techniques used for their characterization are presented in Section 4.4. Finally, the employed experimental apparatus is described in Section 4.5.

## 4.2. CATALYSTS PREPARATION

There are diverse methods for catalysts preparation and different researchers use different procedures for preparing them. However, the principle methods of catalyst development and design criteria do not change and usually involve several quite similar successive steps. The selection of the process to be used for catalysts preparation depends on parameters, which are critical for the characteristics and properties of the catalyst, such as (Perego and Villa, 1997):

- Aggregate morphology of the used carrier, if any;
- Quantities used (solutions and carrier);
- Concentrations;
- Stirring conditions (shape and volume of vessel are also important);
- Temperature;
- Sequence and duration of all options.

Additionally, the catalyst preparation methodology plays a major role, because it affects the dispersion of the active metal on the carrier surface and finally determines the catalytic

behavior. Most industrial catalysts are made either by precipitation, when the active phase and support are produced and precipitated together, or by impregnation of an active phase on a preformed support. The majority of metal and oxide catalysts are prepared by the succession of impregnation, drying, calcination and grinding. In the framework of this thesis the wet impregnation method was selected for the preparation of the catalysts.

#### 4.2.1. Impregnated Catalysts

Impregnation, as one of the most commonly used methods for catalysts preparation, is a simple and economic process, with reproducible results in the production of samples. The preparation of a catalyst via the impregnation method is performed by introducing a solid support material, with high surface area, to a liquid solution, which contains dissolved an oxide precursor. Common precursors include inorganic metal salts, such as metal sulfates, carbonates, chlorides, nitrates, or acetates, and organic metal complexes, such as metal acetylacetonates. The most widely used solvent for inorganic salts is water, due to its high solubility for the majority of the precursors. Two main impregnation methods can be distinguished, namely, wet impregnation (WI), whereby an excess amount of solution is used, and pore volume impregnation (PVI), in which an amount to just fill the pore volume of the support is used. The latter method is also known as incipient wetness impregnation (IWI) or dry impregnation (DI), because the impregnated material maintains a dry character at a macroscopic scale. Regardless of the specific impregnating method used, the most important variables of this process are (Haber et al., 1995):

- Impregnation temperature;
- Type and amount of the precursor;
- Type of used solvent;
- Type and quantity of the additives;
- Impregnation time.

The above parameters often specify the active phase structure, dispersion and distribution of the active element along a carrier particle (Munnik et al., 2015). An increase of the impregnation temperature also increases the solubility of the precursor compound and mainly solves the problem of deposition on sparingly soluble salts. If there are no specific requirements, the impregnation can take place at room temperature. The type and amount

of the precursor is also important, as it will determine to some extent the properties of the active phase (Schwarz, 1995). On the other hand, the impregnation time is a parameter that substantially determines the distribution of the precursor into the carrier pores. As it has been already proved, the increase of the impregnation time leads to a more uniform distribution of the precursor compound into the liquid phase. The completion of the impregnation step is followed by the steps of drying, calcination and finally grinding, in order to prepare the final material. In this thesis, the catalyst preparation initiated with the dissolution of the support precursor in double-distilled water. The solution was then heated to 125 °C, under stirring (250 rpm) for complete water evaporation.

#### 4.2.2. Drying

Regardless of the method used for the deposition of the active metal oxide to the carrier, the manufacturing process of any catalytic material comprises also the step of drying, which takes place right after the deposition of the active phase elements to the surface of the carrier. It should be noted that the drying of the impregnated supports may change the distribution of the active components, unless these components are strongly absorbed to the support. During the drying stage the process steps that are carried out are the following:

- Evaporation of the solvent;
- Transportation of the liquid phase into the porous of the carrier system;
- Diffusion of the solution through the porous of the carrier.

The evaporation initiates from the surface of the catalyst particles and continues preferentially towards the interior, in which the vapor pressure is higher. High catalyst surface area and porosity can be achieved by carefully controlling the drying process. This process has a strong effect on the size of the metal particles and can lead to a fine distribution of the metal over the support material (Richardson, 1989; Regalbuto, 2006). The most important parameters of the drying step are the heating rate, final temperature, period of processing and type of atmosphere, where it takes place. In the present work, the drying step was carried out in an oven at a constant temperature of 100 °C, where the samples remained for 15-18 hours. In the next step, the impregnated and dried catalysts were calcined in air, thus converting the soluble salt into the respective insoluble oxide.

### 4.2.3. Calcination

As already mentioned above, the drying step is followed by the calcination of the catalysts, which is the most important step in their preparation. Thus, the catalyst is exposed to high temperatures for the final formation of metal oxides. The calcination process can be achieved by using one of the following thermal energy sources: microwave oven, electric oven, or gas fired furnace. The calcination may be performed in the presence of an oxidizing or reducing agent, as well as, in any environment, and at a temperature slightly above the projected operating temperature of the catalyst. In principle, calcination can be defined as the process of the active phase creation, which results from the decomposition of the precursor salt, starting from the surface, as well as, the removal of any contaminants, which may exist in the carrier due to the previous preparation process. Thus, the main aim of calcination is to stabilize the physical, chemical and catalytic properties of the catalyst. The role of the calcination process can be summarized in the following points (Richardson, 1989; Regalbuto, 2006):

- Decomposition of thermally unstable compounds (carbonates, nitrates, hydroxides and organic salts) under gas evolution and conversion to oxides;
- Removal of poisons, such as sulphides and halides, from the catalyst surface;
- Control of the crystalline phase and the size of the support grain and surface oxides;
- Generation of the active phase.

Specifically, the calcination step was carried out in an electrical furnace by placing the catalyst samples into a crucible. The temperature of the furnace was increased to 600 °C (heating rate of 5 °C/min) and maintained at this value in static air for 2 hours. After calcination and before grinding, the catalyst was allowed to remain inside the switched-off furnace to cool down slowly to room temperature.

### 4.2.4. Grinding

In general, catalysts grinding is an essential process step following the calcination process, and is used to form catalyst particles of a desired size. Grinding may take place in the absence (dry) or presence (wet) of a liquid/solvent, usually water. In this thesis, the grinding was carried out with the aid of a mortar, in the absence of water.

## 4.3. MATERIALS

As it is reported in detail in Table 4.1, a series of catalysts based on Cu and supported on different pure oxides of rare earth-REOs ( $\text{CeO}_2$ ,  $\text{Sm}_2\text{O}_3$ ,  $\text{La}_2\text{O}_3$ ,  $\text{Gd}_2\text{O}_3$ ,  $\text{Pr}_6\text{O}_{11}$  and  $\text{Nd}_2\text{O}_3$ ), as well as on  $\text{Ce}_{1-x}\text{Sm}_x\text{O}_6$  catalysts, were prepared by the wet impregnation method. Furthermore, for the catalytic experiments, transition metal catalysts (Co, Fe, Ni and Cu) supported on  $\text{CeO}_2$  and  $\text{Cu}_{20-x}\text{Co}_x/\text{CeO}_2$  bimetallic catalysts, were also prepared. Finally, catalysts with different Co loadings (0-100 wt.%) were produced, in order to examine the catalytic efficiency of the  $\text{H}_2\text{S}$  and  $\text{H}_2\text{S}/\text{H}_2\text{O}$  decomposition reactions. The process steps for the preparation of the catalysts (listed in Table 4.1) are schematically described in Figure 4.2.

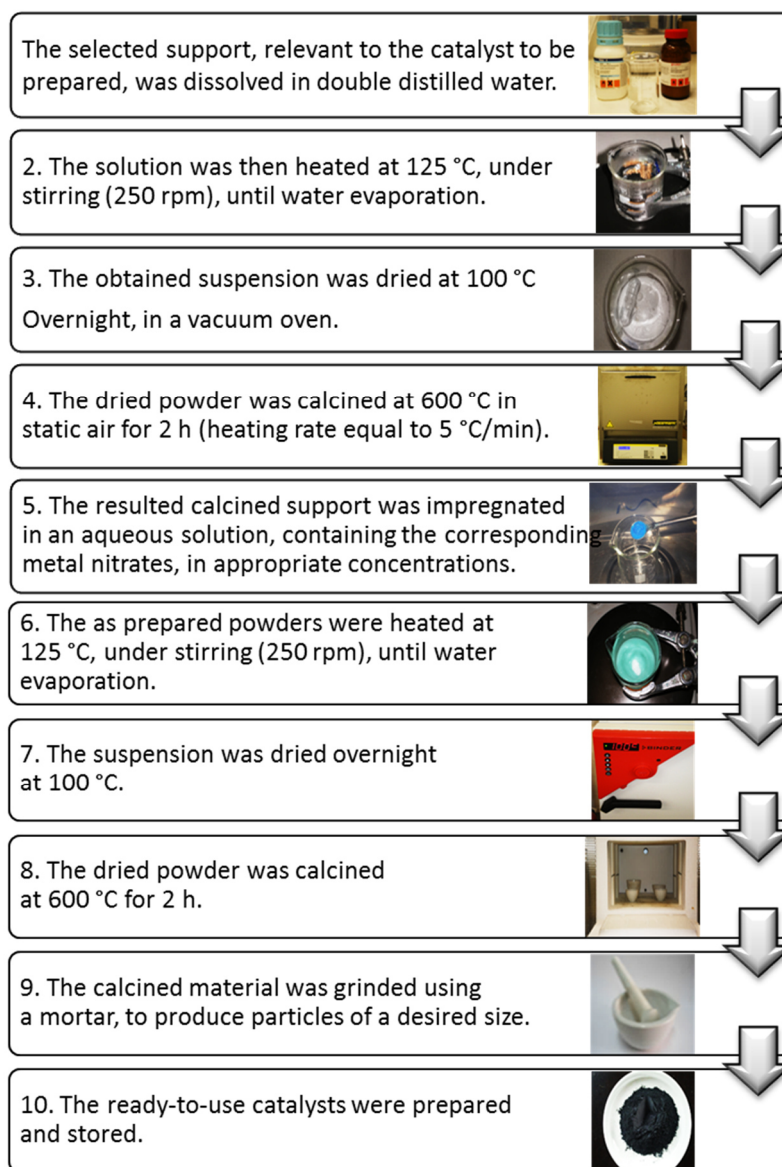


**Figure 4.2:** The catalysts preparation procedure.

**Table 4.1:** List of prepared catalysts.

Samples	Raw materials
<b>Cu supported on REOs catalysts</b>	
1. 20 wt.% Cu/Nd <sub>2</sub> O <sub>3</sub>	Nd(NO <sub>3</sub> ) <sub>3</sub> ·6H <sub>2</sub> O, Cu(NO <sub>3</sub> ) <sub>2</sub> ·3H <sub>2</sub> O
2. 20 wt.% Cu/Sm <sub>2</sub> O <sub>3</sub>	Sm(NO <sub>3</sub> ) <sub>3</sub> ·6H <sub>2</sub> O, Cu(NO <sub>3</sub> ) <sub>2</sub> ·3H <sub>2</sub> O
3. 20 wt.% Cu/Gd <sub>2</sub> O <sub>3</sub>	Gd(NO <sub>3</sub> ) <sub>3</sub> ·6H <sub>2</sub> O, Cu(NO <sub>3</sub> ) <sub>2</sub> ·3H <sub>2</sub> O
4. 20 wt.% Cu/Pr <sub>6</sub> O <sub>11</sub>	Pr(NO <sub>3</sub> ) <sub>3</sub> ·6H <sub>2</sub> O, Cu(NO <sub>3</sub> ) <sub>2</sub> ·3H <sub>2</sub> O
5. 20 wt.% Cu/La <sub>2</sub> O <sub>3</sub>	La(NO <sub>3</sub> ) <sub>3</sub> ·6H <sub>2</sub> O, Cu(NO <sub>3</sub> ) <sub>2</sub> ·3H <sub>2</sub> O
6. 20 wt.% Cu/CeO <sub>2</sub>	Cu(NO <sub>3</sub> ) <sub>2</sub> ·3H <sub>2</sub> O, Ce(NO <sub>3</sub> ) <sub>3</sub> ·6H <sub>2</sub> O
<b>Cu supported on Sm-doped Ceria (SDC) catalysts</b>	
7. 20 wt.% Cu/Ce <sub>0.75</sub> Sm <sub>0.25</sub> O <sub>2</sub>	Cu(NO <sub>3</sub> ) <sub>2</sub> ·3H <sub>2</sub> O, Ce(NO <sub>3</sub> ) <sub>3</sub> ·6H <sub>2</sub> O, Sm(NO <sub>3</sub> ) <sub>3</sub> ·6H <sub>2</sub> O
8. 20 wt.% Cu/Ce <sub>0.5</sub> Sm <sub>0.5</sub> O <sub>2</sub>	Cu(NO <sub>3</sub> ) <sub>2</sub> ·3H <sub>2</sub> O, Ce(NO <sub>3</sub> ) <sub>3</sub> ·6H <sub>2</sub> O, Sm(NO <sub>3</sub> ) <sub>3</sub> ·6H <sub>2</sub> O
9. 20 wt.% Cu/Ce <sub>0.25</sub> Sm <sub>0.75</sub> O <sub>2</sub>	Cu(NO <sub>3</sub> ) <sub>2</sub> ·3H <sub>2</sub> O, Ce(NO <sub>3</sub> ) <sub>3</sub> ·6H <sub>2</sub> O, Sm(NO <sub>3</sub> ) <sub>3</sub> ·6H <sub>2</sub> O
<b>Supports</b>	
10. Co <sub>3</sub> O <sub>4</sub>	Co(NO <sub>3</sub> ) <sub>2</sub> ·3H <sub>2</sub> O
11. CeO <sub>2</sub>	Ce(NO <sub>3</sub> ) <sub>3</sub> ·6H <sub>2</sub> O
<b>Transition metal catalysts</b>	
12. 20 wt.% Co/CeO <sub>2</sub>	Co(NO <sub>3</sub> ) <sub>2</sub> ·3H <sub>2</sub> O, Ce(NO <sub>3</sub> ) <sub>3</sub> ·6H <sub>2</sub> O
13. 20 wt.% Ni/CeO <sub>2</sub>	Ni(NO <sub>3</sub> ) <sub>2</sub> ·6H <sub>2</sub> O, Ce(NO <sub>3</sub> ) <sub>3</sub> ·6H <sub>2</sub> O
14. 20 wt.% Fe/CeO <sub>2</sub>	Fe(NO <sub>3</sub> ) <sub>3</sub> ·9H <sub>2</sub> O, Ce(NO <sub>3</sub> ) <sub>3</sub> ·6H <sub>2</sub> O
<b>Cu<sub>20-x</sub>Co<sub>x</sub>/CeO<sub>2</sub> Bimetallic catalysts</b>	
15. 5 wt.% Cu-10 wt.% % Co/CeO <sub>2</sub>	Cu(NO <sub>3</sub> ) <sub>2</sub> ·3H <sub>2</sub> O, Co(NO <sub>3</sub> ) <sub>2</sub> ·3H <sub>2</sub> O, Ce(NO <sub>3</sub> ) <sub>3</sub> ·6H <sub>2</sub> O
16. 10 wt.% Cu-10 wt.% % Co/CeO <sub>2</sub>	Cu(NO <sub>3</sub> ) <sub>2</sub> ·3H <sub>2</sub> O, Co(NO <sub>3</sub> ) <sub>2</sub> ·3H <sub>2</sub> O, Ce(NO <sub>3</sub> ) <sub>3</sub> ·6H <sub>2</sub> O
17. 10 wt.% Cu-5 wt.% % Co/CeO <sub>2</sub>	Cu(NO <sub>3</sub> ) <sub>2</sub> ·3H <sub>2</sub> O, Co(NO <sub>3</sub> ) <sub>2</sub> ·3H <sub>2</sub> O, Ce(NO <sub>3</sub> ) <sub>3</sub> ·6H <sub>2</sub> O
<b>Catalysts with different Co loadings</b>	
18. 15 wt.% Co/CeO <sub>2</sub>	Co(NO <sub>3</sub> ) <sub>2</sub> ·3H <sub>2</sub> O, Ce(NO <sub>3</sub> ) <sub>3</sub> ·6H <sub>2</sub> O
19. 25 wt.% Co/CeO <sub>2</sub>	Co(NO <sub>3</sub> ) <sub>2</sub> ·3H <sub>2</sub> O, Ce(NO <sub>3</sub> ) <sub>3</sub> ·6H <sub>2</sub> O
20. 30 wt.% Co/CeO <sub>2</sub>	Co(NO <sub>3</sub> ) <sub>2</sub> ·3H <sub>2</sub> O, Ce(NO <sub>3</sub> ) <sub>3</sub> ·6H <sub>2</sub> O
21. 40 wt.% Co/CeO <sub>2</sub>	Co(NO <sub>3</sub> ) <sub>2</sub> ·3H <sub>2</sub> O, Ce(NO <sub>3</sub> ) <sub>3</sub> ·6H <sub>2</sub> O
22. 50 wt.% Co/CeO <sub>2</sub>	Co(NO <sub>3</sub> ) <sub>2</sub> ·3H <sub>2</sub> O, Ce(NO <sub>3</sub> ) <sub>3</sub> ·6H <sub>2</sub> O
23. 60 wt.% Co/CeO <sub>2</sub>	Co(NO <sub>3</sub> ) <sub>2</sub> ·3H <sub>2</sub> O, Ce(NO <sub>3</sub> ) <sub>3</sub> ·6H <sub>2</sub> O

## 4.4. CHARACTERIZATION METHODS

Prior and upon their use, the synthesized catalysts should be characterized and evaluated, under the reaction conditions. The main reasons for characterizing catalysts are to i) identify the modifications in their morphology, structure and chemical composition, taking place during each step of catalysts preparation, ii) determine the catalysts' characteristics, responsible for their performance and obtain possible structure-activity correlations and iii) use these characterizations as feedback during the subsequent stages for catalyst design to improve their performance (Idem, 1995). Thus, the characteristics of "fresh" and "aged" samples should be determined in order to understand the catalyst behavior before and after the reaction, which will also give a useful insight for catalysts improvement. Finally, the study of the surface properties of the catalysts is necessary to understand and explain the catalytic behavior of these materials, under the reaction conditions.

In the present thesis, for the physicochemical characterization of the fresh and aged catalytic materials, the following techniques were employed:

- Textural characterization (BET);
- Structural characterization (XRD);
- Morphological characterization (SEM);
- Surface characterization (XPS);
- Chemical analysis.

### 4.4.1. Textural Characterization (BET)

In order to determine the catalytic surface area and average pore size of fresh and spent catalysts, the samples were analyzed by the nitrogen adsorption-desorption method. This technique assisted in understanding the physical changes to the catalyst structure, as well as in probing and quantifying the sintering effects, in terms of changes to the surface area. More specifically, the specific surface area of the catalysts was determined in a Tristar Micromeritics 3000 flow apparatus, using the multipoint Brunauer-Emmett-Teller (BET) analysis technique, under N<sub>2</sub>-adsorption/desorption isotherms at -196 °C, at a relative pressure between 0.005 and 0.99. The total pore volume was calculated based on the nitrogen adsorbed volume at the highest relative pressure, whereas the average pore

diameter was determined by the Barrett-Joyner-Halenda (BJH) method. The samples were degassed at 250 °C overnight prior to measurements.

#### 4.4.2. Structural Characterization (XRD)

In general, powder X-ray diffraction (XRD) offers a method to characterize materials via their constituent crystal structures. When a crystal, containing regular repeating arrays of atoms, is irradiated by a monochromated X-ray beam, it generates a unique fingerprint in the form of diffraction peaks. Through this diffraction process a powder diffractogram can be used to identify the crystalline components of the studied sample. The application of the diffraction process to a grinded powder material for phase identification is a common routine, when using optimized diffraction hardware and analysis software (Clearfield et al., 2008). In this work, XRD measurements were carried out in a Siemens D 500 X-ray diffractometer, using Cu K<sub>a</sub> radiation ( $\lambda = 0.154$  nm) and operating at 40 kV and 30 mA. Diffractograms were recorded in the  $2\theta = 10-80^\circ$  range at a scanning rate equal to  $0.04^\circ$  per 2 s. The Scherrer equation was employed to determine the crystal size of different phases, based on the most intense diffraction peaks.

#### 4.4.3. Morphological Characterization (SEM)

Scanning electron microscopy (SEM), with the aid of a JEOL 6300 microscope, was used to examine the morphology of the synthesized and used catalysts. This analysis was coupled with energy dispersive X-ray analysis (EDX, Oxford Link ISIS-2000), in order to determine the elemental distribution of the catalytic mixtures.

#### 4.4.4. Surface Characterization (XPS)

X-ray photoelectron spectroscopy (XPS) is a surface-sensitive quantitative spectroscopic technique that measures the elemental composition at the parts per thousand range, the empirical formula, the chemical state and the electronic state of the elements that exist within a material. XPS spectra are obtained by irradiation of a material with a beam of X-rays, while simultaneously measuring the kinetic energy and number of electrons that

escape from the top 0 to 10 nm of the material being analyzed (Castle, 1996). XPS measurements were carried out in MAX200 analysis chamber at  $\sim 10^{-8}$  mbar pressure, using non-monochromatic  $\text{MgK}\alpha$  X-rays and a Hemispherical Electron Energy Analyser (SPECS EA200) with Multi-Channel Detection, properly calibrated according to ISO15472 and ISO24237 standards. The analyzer operated under conditions optimized for better signal intensity (constant pass energy of 100 eV, maximum lens aperture and analysis along the specimen surface normal). The analyzed specimen area was a 4.7 mm<sup>2</sup> rectangle, placed near the center of each specimen surface on an Al plate sample holder.

#### 4.4.5. Chemical Analysis

All aged samples, after reaction in  $\text{H}_2\text{S}$ -containing environments, were chemically characterized by means of elemental analysis (S wt.% content) according to the UOP 703 method, using a LECO CHNS-932 analyzer for sulfur.

### 4.5. EXPERIMENTAL EQUIPEMENT AND SAMPLE PREPARATION

In this section, the experimental setup and the safety precautions taken before, during and after the experiments are described. More specifically, Section 4.5.1 presents the design requirements, Section 4.5.2 provides the description of the individual parts of the unit, Section 4.5.3 describes the overall procedure, Section 4.5.4 explains the need of testing the experimental set up before use, and finally Section 4.5.5 mentions the safety precautions taken during the conduction of the experiments.

#### 4.5.1. Design Considerations

Since hydrogen sulfide is one of the most difficult species one can deal with in the chemical world, the development of a system for its treatment at high temperatures is demanding and challenging. Taking this into account, a suitable experimental apparatus was designed and constructed to carry out the study of the catalytic decomposition of hydrogen sulfide towards hydrogen production. The important factors to be considered in the design of the apparatus were:

- Hydrogen sulfide, the raw material, is a highly toxic gas, corrosive and its mixtures with air are flammable;
- The reaction carried out at high temperatures;
- Hydrogen sulfide also vigorously attacks at stainless steel, at high temperatures.

All the previous factors were taken into consideration for the design of the apparatus and the selection of tubing materials and other auxiliaries. A schematic diagram of the experimental apparatus is shown in Figure 4.3.

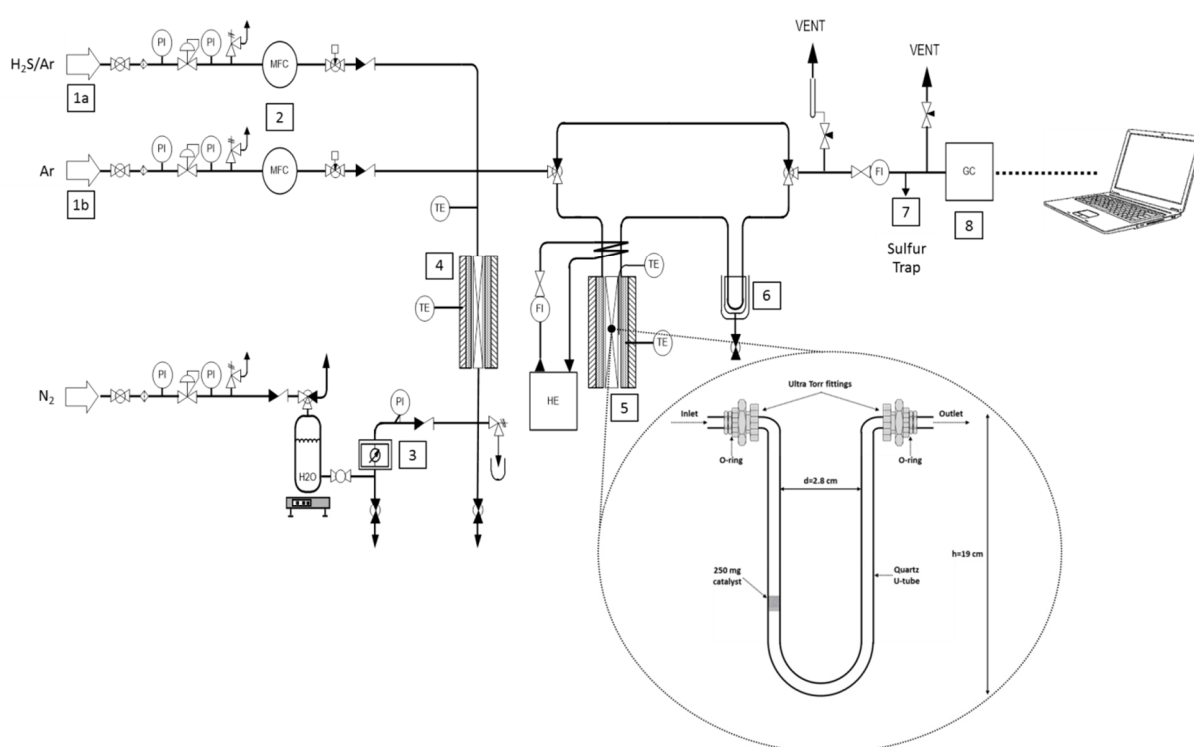


**Figure 4.3:** Schematic flowsheet for high temperature decomposition of  $H_2S$  to  $H_2$ . **Feed section:** (1) feedstock units: a)  $H_2S$  cylinder, b) Ar cylinder; (2) MFC: mass flow controllers for  $H_2S$  and Ar; (3) pump; (4) preheater. **Reaction section:** (5) furnace and U-tube quartz reactor; (6) condenser; (7) sulfur trap. **Analysis section:** (8) GC: gas chromatograph Shimadzu 14B. PI: pressure indicator; FI: flow indicator; TE: temperature indicator; HE: heat exchanger.

Consequently, the apparatus was constructed from stainless steel. More specifically, the 316 stainless steel type was selected as it can withstand moderately high temperatures and corrosion and is widely commercially available. The same material was also used for all the connections. The fittings used to connect the various pieces, were either of brass or steel. Brass fittings were used only in those places where small or no corrosion could occur, and

the chances of failure were minimal. Pyrex glass was used for the flasks in the  $H_2S$  absorber. Because of the gases flammability, the room was well ventilated, during the conduction of the experiments. Thus, a large fan was installed in the room, and more specifically on the top of the unit, to aid ventilation. The experimental set-up was also thoroughly leak tested to withstand gas pressures, in larger values than those encountered during the experiment. The actual experimental unit and setup can be seen in the images of the Figure 4.4.



**Figure 4.4:** Experimental setup for high temperature decomposition of  $H_2S$  to  $H_2$  production (PSDI Laboratory, CPERI/CERTH Institute).

#### 4.5.2. Description of Individual Units

The system used for the H<sub>2</sub>S decomposition in the absence/presence of H<sub>2</sub>O towards H<sub>2</sub> production, can be divided into three main sections, namely:

1. Feedstock Section;
2. Reaction Section;
3. Analysis Section.

In what follows, the major parts of the individual units of the process are described, according to the classification and numbering of Figure 4.3.

##### 4.5.2.1. Feedstock Section

**[1a,b]:** Gases were stored in high pressure cylinders, connected with pressure regulators to control the inline pressure of the feed and purge streams. The H<sub>2</sub>S source consisted of a 50 L cylinder of 10 v/v% hydrogen sulfide/argon (Air Liquide). The regulator was further fitted with a stainless steel needle valve, to control the flow rate. The Ar source consisted of a 50 L cylinder of 99.998 v/v% Argon (Linde). A stainless steel Tescom regulator was used in both cases.

**[2]:** Initially, the mass flow controllers (MFC) were calibrated in the range of the used flows, under the selected feed conditions, using the actual gas reactants. The range of the mass flow controllers for the H<sub>2</sub>S/Ar mixture is 0-20 ml/min, with an accuracy of 1%, while for Argon is 0-100 ml/min, also with an accuracy of 1%. Flow rates are controlled using Brooks Instruments MFC, which were pre-calibrated by the manufacturer over the specified flow rate ranges and recalibrated by the user before the experimental run. The mass flow meters provided also the efficient control of multiple flow rates, by the use of individual control loop modules. The actual flow rates are additionally measured at the outlet of the MFC, with the aid of a digital flow bubble meter (Optiflow 520). If necessary, relevant correction factors for the displayed by the mass flow meter values were used to readjust the flows. The correction factors vary, in principle, for different gases. The correction factors, provided by the manufacturer of the flowmeter, were 0.85 for hydrogen sulfide and 1.395 for argon. Moreover, Swagelok check valves are placed right after the MFC to prevent any back flow, due to possible pressure fluctuations during the course of the experiments. A

Swagelok pressure relief valve is also installed in a side stream near the U-tube quartz reactor inlet to protect the system against excessive pressure.

**[3]:** An HPLC 305 Pump (GILSON) was used to control the flow of the liquid water into the system. The pump can operate in a flow range of 0.135 to 25 ml/min, with an accuracy of 0.001 ml/min. The water flowrate was maintained at 0.0495 ml/min (for 90 v/v% H<sub>2</sub>O) throughout the experiments. The outlet of the HPLC pump was connected to microbore tubing, in order to create sufficient pressure drop and the selected amount of liquid can be injected. The gases and water enter the reactor through different process lines. 1/4 inch lines were used both for gases and liquid. Each line was fitted with non-return valves to avoid any back flow, due to any pressure build up in the system. Pressure gauges were also installed to each line to monitor the pressure. The temperature of all feeding lines, when H<sub>2</sub>O introduced into the system, was controlled at 130 °C, by a K-type thermocouple. **[4]:** The vaporized water (at 130 °C) and preheated gases were mixed in a cross connection near the reactor inlet point.

#### 4.5.2.2. Reaction Section

**[5]:** The U-tube quartz reactor was contained in a 10 12 CE567 model electrical furnace (Pantothermiki). This 240 volt furnace featured a temperature controller that could hold the reactor temperature  $\pm 1$  °C of the controller set-point. The power rating of the furnace was 1,350 watts and could operate as high as 1,500 °C. To reduce the amount of heat losses from the furnace in the vertical direction, an insulating material (fine quartz wool) was installed on the top of the furnace. To verify and, if necessary correct, the reaction temperature, a thermocouple was used to monitor and record the actual temperature at the exact height of the catalyst bed. Furthermore, lab-scale reactors for H<sub>2</sub>S decomposition were employed to evaluate the activity and stability of the catalysts for hydrogen production. The type of the employed reactor depends on several pre-determined factors, such as reactor feed, temperature, pressure and expected product distribution. Thus, the catalysts performance was determined using a U-tube quartz reactor. Figure 4.5 presents the U-tube reactor in greater detail. The reactor has a capacity of approximately 20 g solid and a maximum temperature limit of 1,200 °C. Quartz was chosen as the reactor material, since it is able to withstand the high operating temperatures of the experiments (up to 850 °C), and it does

not react with hydrogen sulfide. It should be noted that strength properties (e.g., large mechanical stress) are not a major prerequisite for the reactor, since the system operates at atmospheric pressure. Two silicone O-rings, capable of withstanding temperatures up to 200 °C, were placed in between the Ultra-Torr parts in the inlet and outlet provisions of the reactor, for gas tightness.

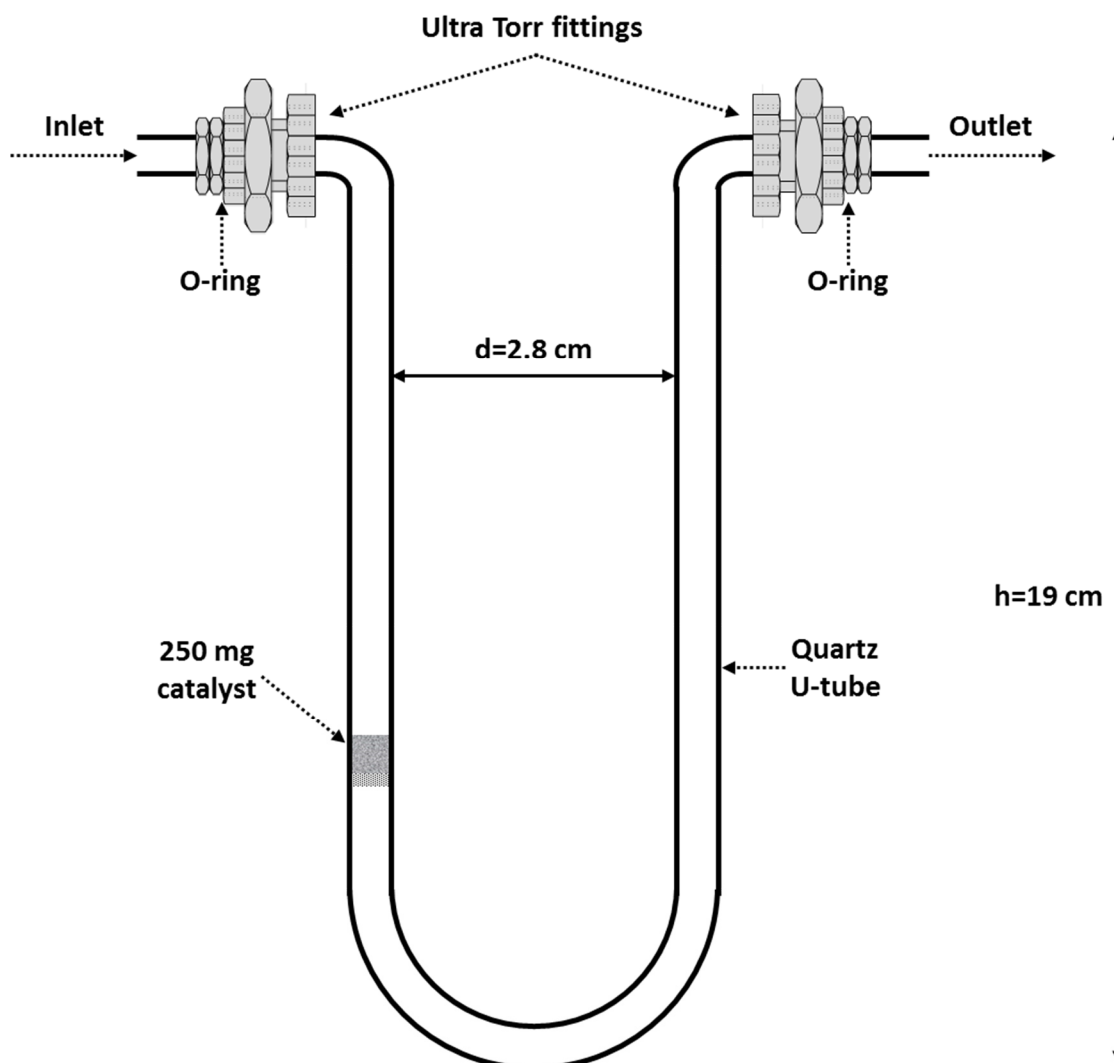


**Figure 4.5:** Graphical representation of the U-tube quartz reactor and Ultra-Torr parts.

**Catalyst loading:** In this work, the reactor was loaded with 250 mg of catalyst in the form of powder, diluted with equal amount of quartz beads (MERCK). The total length of the bed was maintained at  $h=16$  cm and it was placed exactly at the first half of the U-reactor, just upon the quartz frit. Notice that great care was taken to obtain an ideal fixed bed reactor

system. This fixed bed configuration requires the catalyst bed to be stable, fixed in height, placed on top of a flat surface and to have a flat top. For this reason, the catalyst bed was placed on the top of a filterpor (10 mm). Maintaining the location of the catalyst bed within the reactor was critical for reproducible reaction conditions. The reactor temperature was controlled and maintained by a JUMO iTRON Compact microprocessor temperature controller. As a safety measure, the controller automatically shuts down the furnace, if the temperature exceeds 1,000 °C.

**[6]:** A condenser immersed in an ice bath was installed to condense and remove any unreacted water that comes out of the reactor. Thus, the outlet stream, containing as well the product gases, passed through the condenser to remove any residual steam. The dry gases were then directed to the online GC for analysis, using a 1/8 inch SS 316 line.

**[7]:** The sulfur trap (H<sub>2</sub>S absorber) consisted of a Pyrex glass bottle with removable stainless steel fittings to facilitate cleaning and refilling. The absorbent was a saturated solution of KOH. The bottle was filled with a fresh 5 M KOH solution, every five activity or stability experiments. The solution was prepared by dissolving 280.55 grams of KOH pellets (MERCK) in 1 L of double distilled water. Then, it was continuously stirred and cooled (in an ice bath) to prevent the overheating of the solution. The spent KOH solution was collected and treated as waste.

The line which connects the reaction and the analysis sections, right after the sulfur trap, provides an extra auxiliary exit, where the volumetric flowrate of the gas stream can be measured (with the aid of a bubble-flow meter), either directly from the mass flow meters (by-pass) or after passing through the reactor (set the three-way valves). The flowrate was always measured to make sure that there were no leaks, which would be indicated by a drop in the volumetric flowrate.

#### 4.5.2.3. Analysis Section

**[8]:** The composition analysis of the gas outflow, free of residual H<sub>2</sub>O and H<sub>2</sub>S, was performed by an online gas chromatograph (GC). More specifically, for the measurement of the produced H<sub>2</sub> in the H<sub>2</sub>S decomposition experiments, a SHIMADZU GC-14B chromatograph, equipped with Molecular Sieve 5A and argon as the carrier gas, was used

(10 ppm accuracy). Gas chromatography measurements are in general based on two operating principles, one for separating the injected mixture and the other for quantifying the individual gases. As gas chromatograph (GC) generally operates at above ambient temperatures (usually in the range of 40-180 °C), where many compounds that are at liquid state at room temperature (e.g., light alcohols and aldehydes, benzene and medium alkanes) can be also measured in their gas state.

For the separation, the injected gas was fed to a column (packed or capillary), where each component of the mixture interacts differently with the separating medium. These interactions depend both on the material of this medium and on the specifications of the molecules, i.e., the size of molecules relative to that of the pores and their affinity with the material (intermolecular forces), especially in packed columns. A constant flow of carrier gas pushes the gases through the column. Depending on the strength of each compound's interaction with the column material, it will be pushed through more or less readily, resulting in its separation from the other compounds. For a given column (subject to ageing and chemical weathering), operating at a certain temperature and carrier gas flow rate, a given compound will require a specific amount of time (retention time) to reach the column end. Using standard gas mixtures, the retention times of each compound of interest can be pre-established. At the end of the column there are one or more detectors, which quantify the individual gases.

The operating principle of the detector can vary, depending on the type of compounds chosen to be measured. In the present work, a thermal conductivity detector (TCD) was used (Kitson et al., 2000). As indicated by its name, it measures the difference in thermal conductivity between the carrier gas (reference) and the gas being analyzed. This is achieved by preheating both the column effluent and a stream of pure carrier gas to the same temperature, while maintaining a thin thermally conductive membrane at a different one. These gas streams flow on either side of this membrane and, depending on their thermal conductivities, cool (or heat) the membrane differently, causing it to deform. The deformation is converted to an electrical signal, which is portrayed in the chromatogram as a positive or negative peak, whose area is directly proportional to the amount (concentration) of the compound. Calibration of peak areas, carried out with the use of standard gases, can provide accurate measurements of the concentration of the desired compounds. For the

needs of the present thesis, the product gas samples were injected every 15-30 minutes until steady state, i.e., constant chromatogram areas for all the components.

### 4.5.3. Procedure

The gas flow experimental test-rig, elaborated to study the H<sub>2</sub>S decomposition reaction, is schematically presented in Figure 4.3 and the experimental procedure followed for the course of these experiments is given below.

#### 4.5.3.1. Initiation of the Experiment

The steps followed for the initiation of the experiment are:

- The “empty” reactor was washed with acetone and dried or calcined with air at 1000 °C after each experiment. Subsequently, it was placed in the experimental setup and all necessary connections were restored.
- The hydrogen sulfide absorbers were filled with a fresh, potassium hydroxide solution.
- A quartz U-tube reactor (Figure 4.5) was loaded with 250 mg of the catalyst, admixed with an equal amount of quartz pellets of similar particle size. Taking into account that the internal diameter of the quartz tube was approximately 9.6 mm, the overall total bed volume was equal to 0.45 cm<sup>3</sup>, corresponding to a gas hourly space velocity (GHSV) of 13,500 h<sup>-1</sup>. The isothermal operation of the catalyst bed was controlled by the thermocouple placed inside the reactor tube.
- The argon carrier gas, as well as the air cylinder for the gas chromatograph and valves, respectively, were switched on. The power of the chromatograph was also switched on, and the column was allowed to warm up. When the oven temperature reached 50 °C, the chromatograph recorder was activated and was ready for the first run.

In general, for H<sub>2</sub>O-free experiments, a mixture of H<sub>2</sub>S/Ar (typically 1 v/v%) was fed in the reactor through two mass flow controllers. On the other hand, when H<sub>2</sub>O was co-fed to reactor, a separate system for water supply was involved, consisting of a double distilled H<sub>2</sub>O storage tank and a water syringe pump, employing N<sub>2</sub> as carrier gas. The fed liquid water was evaporated to steam in a preheater and then mixed with the gaseous feeding streams, before entering the reactor.

#### 4.5.3.2. Process Operation

The steps followed for the process operation are:

- The flow connections were made and checked for leakage (with a bubble flowmeter). Thereupon, the inlet valve of the reactor was opened and argon gas was allowed to pass through the reactor as a purge gas.
- The thermocontroller of the furnace was set to the selected set-point. The furnace was then allowed a minimum of one hour to attain the steady state.
- After argon passed through the reactor for sufficient time and temperature reached the selected set-point, the valve connecting the hydrogen sulfide tank was opened. A flow of pure argon, employed as diluent agent, was mixed with hydrogen sulfide supplied from a 10 v/v% H<sub>2</sub>S/Ar high pressure gas cylinder, at appropriate flow rates, so as to prepare an H<sub>2</sub>S/Ar feed mixture containing 1 v/v% H<sub>2</sub>S concentration.
- After a period of at least three quarters of an hour the reactions were started.
- Both activity and stability catalytic experiments were performed at atmospheric pressure and the total volumetric feed flow passing through the catalytic fixed bed zone was kept constant at 100 cm<sup>3</sup>/min. The pressure of the inlet and outlet streams of the reactor, were monitored and recorded, in order to secure the operation of the H<sub>2</sub>S trap.
- The reactor temperature was continuously checked throughout each experimental run and was found to maximum deviate  $\pm 1$  °C from the reported value. Further, the flow rate of hydrogen sulfide was continuously monitored and corrected, when necessary, in an effort to ensure the consistency of the derived experimental data. Since the system was designed to operate at ambient conditions, any flow pressure gauge recorded indicated a plugged tube. Upon that, the hydrogen sulfide flow was immediately switched off and the U-tube reactor was disassembled.
- Before gas analysis, the effluent gas mixture passed through the sulfur trap (KOH) to remove any S-containing species and protect the GC from H<sub>2</sub>S traces.
- The quantification of produced H<sub>2</sub> was carried out by the on-line installed GC unit.

#### 4.5.3.3. Completion of the Experiment

The steps followed for the completion of the experiment are:

- Right after switching off the furnace, H<sub>2</sub>S flow was shut off and argon passed through the reactor again to purge the system from H<sub>2</sub>S. When dealing with a mixture of gases both valves were shut off, prior to the feeding of argon.
- The chromatograph was switched off and cooled, in preparation for the next run. The pressure of the regulator of the hydrogen sulfide tank was carefully discharged to eliminate the possibility of seepage. Then, the laboratory was thoroughly ventilated before leaving the apparatus.

During the catalytic activity experiments, the temperature was stepwisely increased by 50 °C, in the temperature range 550-850 °C, while during the stability experiments the system heated up directly to the selected temperature. At each temperature step the system was allowed to reach a steady state (45 min), before the effluent gas analysis was performed. For comparison reasons, blank experiments (without catalyst) were also carried out under identical reaction conditions. Several experiments with H<sub>2</sub>S were repeated to ensure the reproducibility of the results.

In this work, the catalytic performance of the employed samples is expressed in terms of hydrogen sulfide conversion ( $X_{H_2S}$ ):

$$X_{H_2S}(\%) = \frac{\text{Moles of produced } H_2 \text{ at the outlet}}{H_2S \text{ moles fed to the inlet}} \times 100 \quad (4.1)$$

In all cases, the calculation of the H<sub>2</sub> production rate ( $r_{H_2}$ ) was based on its v/v% concentration in the effluent stream, according to the following equation:

$$r_{H_2}(\text{mol/s}) = \frac{\text{Concentration}(v/v\%) \cdot F_T(\text{cm}^3/\text{min})}{100 \cdot 60(\text{s}/\text{min}) \cdot v_m(\text{cm}^3/\text{mol})} \quad (4.2)$$

where  $F_T$  is the total flow rate and  $v_m$  is the gas molar volume at STP conditions (25 °C and 1 bar).

The gas hourly space velocity (GHSV) is defined as the ratio of the imported reactants (total volumetric inlet flow) to the reactor volume (or the volume of the catalyst bed):

$$\text{GHSV} = \frac{\text{Total volumetric inlet flow } (\frac{\text{L}}{\text{h}})}{\text{Catalyst bed volume (L)}} \quad (4.3)$$

According to Equation 4.3, for a total volumetric inlet flow equal to 100 cm<sup>3</sup>/min and catalyst bed diameter and height equal to 9.6 mm and 0.6 cm, respectively, the GHSV is equal to 13,500 h<sup>-1</sup>.

#### 4.5.4. Testing of the Experimental Set-up

Before each experimental run, the apparatus was examined under maximum rate of argon passing through it. A soap solution was painted around all jointed surfaces for leakage test. Since the reactor would only operate under ambient pressure, this system testing was considered satisfactory. The equipment was set up as shown in the flow diagram of Figure 4.3. Any detected leaks were removed by sealing the connection with a suitable sealant.

#### 4.5.5. Safety Precautions

Since hydrogen sulfide is highly flammable, toxic and extremely poisonous, even in small quantities, strict safety precautions were taken, during the conduction of the experiments. General and specific lab safety precautions were followed throughout this work to minimize the associated to H<sub>2</sub>S risks. Additionally, a local powered exhaust was used to remove any combustion products from the vicinity of the apparatus. A hydrogen sulfide sensor was used to periodically check for hydrogen sulfide in the laboratory air. In addition, all the connections were tested for leaks. The outlet gases passed through H<sub>2</sub>S scrubbers, connected in series, to absorb any traces of unreacted hydrogen sulfide. A specific gas mask was used when disconnecting the H<sub>2</sub>S gas pipeline connections. Personal protection devices, including goggles, face shield and heat resistant gloves, were used when necessary.

## REFERENCES

- Castle J.E. (1996). Practical surface analysis, Auger and X-ray photoelectron spectroscopy. 2<sup>nd</sup> ed. Briggs D., Seah M.P. (Eds.), *John Wiley & Sons*, Chichester, U.K.
- Clearfield A., Reibenspies J.H., Bhuvanesh N. (2008). Principles and applications of powder diffraction, *Wiley-Blackwell Publishing*, New York, U.S.A.
- Haber J., Block J.H., Delmon B. (1995). Manual of methods and procedures for catalyst characterization. *Pure and Applied Chemistry*, 67: pp. 1257-1306.
- Idem R.O. (1995). Production of hydrogen from the low temperatures steam reforming of methanol. PhD thesis, *University of Saskatchewan*, Canada.
- Kitson F.G., Larsen B.S., McEwen C.N. (2000). Gas chromatography and mass spectrometry. *Academic Press*, San Diego, California, U.S.A.
- Munnik P., Jongh P.E., Jongh K.P. (2015). Recent development in the synthesis of supported catalysts. *Chemical Reviews*, 115: pp. 6087-6718.
- Perego C., Villa P. (1997). Catalyst preparation methods. *Catalysis Today*, 34: pp. 281-305.

## CHAPTER 4

### 4

Regalbuto J. (2006). Catalyst preparation: science and engineering. *CRC Press, Taylor & Francis Group*, London, U.K.

Richardson J.T. (1989). Principles of catalyst development. *Springer Publishing*, New York, U.S.A.

Schwarz J.A., Contescu C., Contescu A. (1995). Methods for preparation of catalysts materials. *Chemical Reviews*, 95: pp. 477-510.

# CHAPTER

# 5

## H<sub>2</sub>S CATALYTIC DECOMPOSITION IN THE ABSENCE OF H<sub>2</sub>O

Contents	Page
5.1. Introduction.	133
5.2. H <sub>2</sub> S catalytic decomposition over 20 wt.% Cu/ REOs catalysts.	133
5.3. H <sub>2</sub> S catalytic decomposition over 20 wt.% Cu/Ce <sub>1-x</sub> Sm <sub>x</sub> O <sub>8</sub> catalysts.	142
5.4. H <sub>2</sub> S catalytic decomposition over ceria supported transition metal (Co, Ni, Fe and Cu) catalysts.	145
5.5. H <sub>2</sub> S catalytic decomposition over bimetallic (Cu <sub>20-x</sub> Co <sub>x</sub> /CeO <sub>2</sub> ) (x = 0, 5, 10, 15, 20 wt.%) catalysts.	155
5.6. Stability tests over optimum 20 wt.% Co/CeO <sub>2</sub> catalyst.	163
References.	171



## 5.1. INTRODUCTION

As it was discussed in the previous chapters, the selection of the material to be employed as the anode in the H<sup>+</sup> proton conducting membrane reactor/fuel cell is crucial for the successful operation of the proposed system. In this context and prior to the electrochemical tests (see Chapter 8), a series of catalysts, namely, i) 20 wt.% Cu supported REOs (Cu/REOs), ii) 20 wt.% Cu supported Ce<sub>1-x</sub>Sm<sub>x</sub>O<sub>8</sub> (20 wt.% Cu/Ce<sub>1-x</sub>Sm<sub>x</sub>O<sub>8</sub>), iii) ceria supported transition metal (Co, Ni, Fe and Cu) and iv) bimetallic (Cu<sub>20-x</sub>Co<sub>x</sub>/CeO<sub>2</sub>) (x = 0, 5, 10, 15, 20 wt.%), were synthesized via the wet impregnation method and evaluated in terms of their activity and stability towards H<sub>2</sub>S decomposition in the absence of H<sub>2</sub>O. In all cases, the experimental results are accompanied by the corresponding thermodynamic calculations. Moreover, both “fresh” and “aged” catalyst samples were characterized in terms of their chemical composition and microstructure (BET, XRD, SEM, XPS, TPR and sulfur elemental analysis).

## 5.2. H<sub>2</sub>S CATALYTIC DECOMPOSITION OVER 20 wt.% Cu/REOs

Cu-based catalysts have recently attracted great attention both in catalysis and electrocatalysis fields, due to their excellent catalytic performance and low cost. The present section aims to initially investigate the performance of Cu catalysts, supported on rare earth oxides (REOs) for the H<sub>2</sub>S decomposition reaction activity towards H<sub>2</sub> production, by employing 1 v/v% H<sub>2</sub>S/Ar as feedstock mixture. Extensive characterization studies, involving the multipoint Brunauer-Emmett-Teller (BET) analysis method, X-ray powder diffraction (XRD), scanning electron microscopy (SEM), X-ray photoelectron spectroscopy (XPS) and temperature programme reduction (TPR) studies were conducted to reveal the textural, structural, morphological and surface properties of the employed catalysts and to gain insight into possible structure activity relationships.

### 5.2.1. Textural and Structural Characterization (BET and XRD Analysis) of 20 wt.% Cu/REOs Catalysts

The textural characteristics (BET surface area, total pore volume, average pore diameter) of 20 wt.% Cu/REOs catalysts are listed in Table 5.1. The superiority of the 20 wt.% Cu/CeO<sub>2</sub>

catalyst in terms of surface area ( $44.6 \text{ m}^2/\text{g}$ ) and total pore volume ( $0.15 \text{ cm}^3/\text{g}$ ) is clearly depicted. The remaining REOs-supported catalysts exhibited significantly smaller BET areas and total pore volumes, according to the following order: 20 wt.% Cu/CeO<sub>2</sub> > 20 wt.% Cu/Gd<sub>2</sub>O<sub>3</sub> > 20 wt.% Cu/Pr<sub>6</sub>O<sub>11</sub> > 20 wt.% Cu/Sm<sub>2</sub>O<sub>3</sub> > 20 wt.% Cu/La<sub>2</sub>O<sub>3</sub> > 20 wt.% Cu/Nd<sub>2</sub>O<sub>3</sub>. Moreover, it should be highlighted that the addition of Cu to the bare supports had a detrimental effect on the textural characteristics of the catalysts; obviously shown for CeO<sub>2</sub>.

**Table 5.1:** Textural characteristics of 20 wt.% Cu/REOs catalysts.

Cu/REOs catalysts	S <sub>BET</sub> (m <sup>2</sup> /gr)	Total pore volume (cm <sup>3</sup> /gr)	Average pore diameter (nm)
20 wt.% Cu/Nd <sub>2</sub> O <sub>3</sub>	6.5	0.03	16.3
20 wt.% Cu/Sm <sub>2</sub> O <sub>3</sub>	13.3	0.06	17.0
20 wt.% Cu/Gd <sub>2</sub> O <sub>3</sub>	20.9	0.10	19.8
20 wt.% Cu/Pr <sub>6</sub> O <sub>11</sub>	15.0	0.08	22.7
20 wt.% Cu/La <sub>2</sub> O <sub>3</sub>	11.3	0.06	23.5
20 wt.% Cu/CeO <sub>2</sub>	44.6	0.15	13.1
CeO <sub>2</sub>	71.5	0.27	15.4

Figure 5.1 illustrates the XRD spectra of 20 wt.% Cu/REOs catalysts calcined at 600 °C, while Table 5.2 depicts the detected phases for each catalyst sample, their lattice parameters, as well as, their approximate crystallite sizes, determined by Scherrer analysis. Despite that this analysis is not the most accurate methodology to estimate the crystallite size of catalysts, a general insight to the impact of the support on the structural characteristics can be obtained. As can be seen, copper crystallized as CuO tenorite of monoclinic structure in all 20 wt.% Cu/REOs catalysts. However, the respective crystallite size strongly depends on the support type; the following order was identified: La<sub>2</sub>O<sub>3</sub> > CeO<sub>2</sub> > Pr<sub>6</sub>O<sub>11</sub> > Nd<sub>2</sub>O<sub>3</sub> > Sm<sub>2</sub>O<sub>3</sub> > Gd<sub>2</sub>O<sub>3</sub>. In general, the CuO crystallite size followed an identical with the size of rare earth elements pattern, implying an intense interaction of Cu with the oxide carrier. Also, it should be noticed that the size of CuO is about five-fold larger than the size of CeO<sub>2</sub>, denoting the copper species segregation by the formation of large CuO particles over the catalyst surface. Under these conditions, a significant decrease of the surface area at low Cu loading, due to the blockage of support pores, is expected (Gamarra et al., 2007).

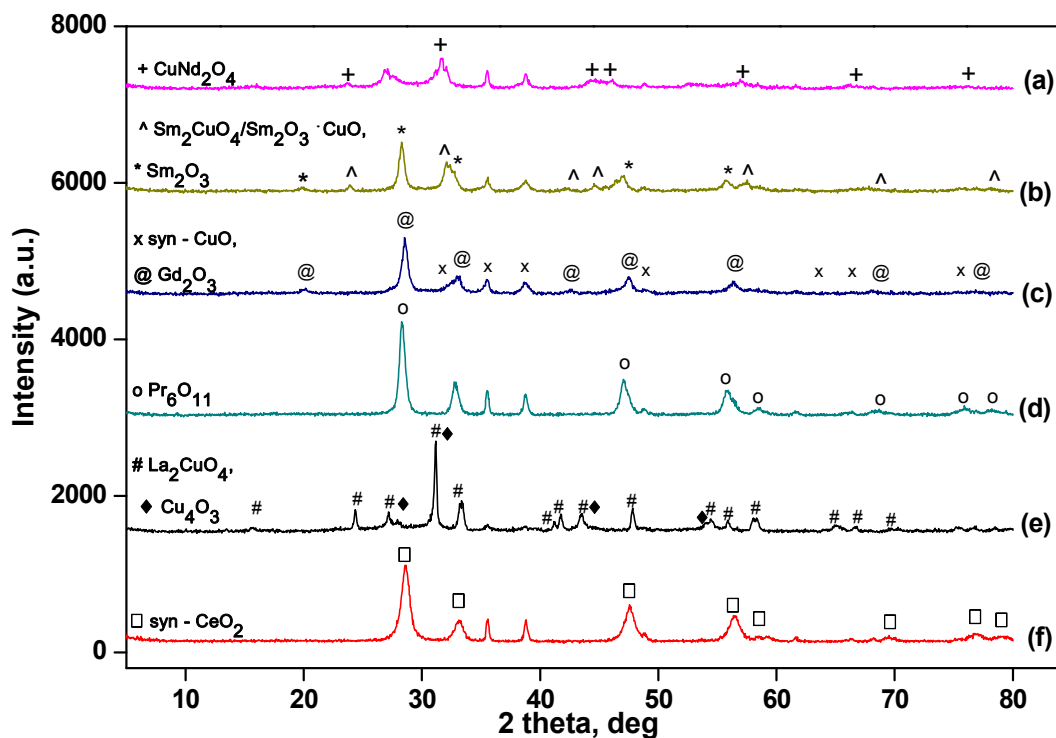


**Figure 5.1:** X-ray diffraction patterns of a) 20 wt.% Cu/Nd<sub>2</sub>O<sub>3</sub>, b) 20 wt.% Cu/Sm<sub>2</sub>O<sub>3</sub>, c) 20 wt.% Cu/Gd<sub>2</sub>O<sub>3</sub>, d) 20 wt.% Cu/Pr<sub>6</sub>O<sub>11</sub>, e) 20 wt.% Cu/La<sub>2</sub>O<sub>3</sub>, and f) 20 wt.% Cu/CeO<sub>2</sub> catalysts.

Furthermore, the REOs carriers, namely, ceria, praseodymia, gadolinia and samaria were crystallized as pure oxides in cubic structures, i.e., CeO<sub>2</sub>, Pr<sub>6</sub>O<sub>11</sub>, Gd<sub>2</sub>O<sub>3</sub> and Sm<sub>2</sub>O<sub>3</sub>, respectively. For the 20 wt.% Cu/REOs catalysts with low surface area, a strong interaction between Cu and the oxide carrier probably occurred, resulting in the formation of Ln<sub>2</sub>CuO<sub>4</sub> mixed phases (Ln: Nd, La, Sm). Their crystallite sizes follow the same order as the sizes of the corresponding rare earth elements. Interestingly, in the case of the neodymia and lanthana based catalysts, the crystal structures of the respective bare oxides were not identified by the XRD spectra (Figure 5.1).

### 5.2.2. Surface Characterization (XPS Analysis) of 20 wt.% Cu/REOs Catalysts

XPS measurements were also carried out for the 20 wt.% Cu/REOs samples to obtain information about the elemental chemical states and surface composition. Figure 5.2 depicts the XPS spectra in the Cu2p region for the Cu/REOs catalysts. The spectrum of Cu/PrO<sub>2</sub> is not included in the figure due to the overlap of the Cu2p and Pr3d peaks. All spectra are characterized by two principal peaks of Cu2p<sub>1/2</sub> at 953 eV and Cu2p<sub>3/2</sub> at 933.8, along with

shake-up satellites at 942.2-944.9 eV, which can be attributed to fully oxidized Cu<sup>2+</sup> species (Ayastuy et al., 2012; Mai et al., 2011; Liu and Stephanopoulos, 1995; Kundakovic et al., 1998).

**Table 5.2:** XRD characterization of 20 wt.% Cu/REOs catalysts.

20 wt.% Cu/REOs	Detected phase	Crystallite size (nm)	Lattice	Lattice parameters
Cu/Nd <sub>2</sub> O <sub>3</sub>	CuO	33.47	Monoclinic	a=0.468830 nm, b=0.342290 nm, c=0.513190 nm, β=99.506°
	Nd <sub>2</sub> CuO <sub>4</sub>	21.55	Tetragonal	a=0.394366 nm, b=0.394366 nm, c=1.216930 nm, β=90°
Cu/Sm <sub>2</sub> O <sub>3</sub>	CuO	16.52	Monoclinic	a=0.468830 nm, b=0.342290 nm, c=0.513190 nm, β=99.506°
	Sm <sub>2</sub> O <sub>3</sub>	14.64	Cubic	a=1.093060 nm, β=90°
	Sm <sub>2</sub> CuO <sub>4</sub>	13.30	Tetragonal	a=0.390500 nm, b=0.390500 nm, c=1.193800 nm, β=90°
Cu/Gd <sub>2</sub> O <sub>3</sub>	CuO	15.11	Monoclinic	a=0.468830 nm, b=0.342290 nm, c=0.513190 nm, β=99.506°
	Gd <sub>2</sub> O <sub>3</sub>	12.77	Cubic	a=1.081300 nm, β=90°
Cu/Pr <sub>6</sub> O <sub>11</sub>	CuO	38.37	Monoclinic	a=0.468830 nm, b=0.342290 nm, c=0.513190 nm, β=99.506°
	Pr <sub>6</sub> O <sub>11</sub>	13.40	Cubic	a=0.546950 nm, β=90°
	CuO	47.11	Monoclinic	a=0.468830 nm, b=0.342290 nm, c=0.513190 nm, β=99.506°
Cu/La <sub>2</sub> O <sub>3</sub>	La <sub>2</sub> CuO <sub>4</sub>	38.63	Orthorhombic	a=0.535560 nm, b=0.540110 nm, c=1.314900 nm, β=90°
	Cu <sub>4</sub> O <sub>3</sub>	8.70	Tetragonal	a=0.583700 nm, b=0.583700 nm, c=0.993200 nm, β=90°
Cu/CeO <sub>2</sub>	CuO	43.49	Monoclinic	a=0.468830 nm, b=0.342290 nm, c=0.513190 nm, β=99.506°
	CeO <sub>2</sub>	9.32	Cubic	a=0.541134 nm; β=90°

According to relevant studies, Cu2p<sub>3/2</sub> binding energies (BE) at ca. 933-934.2 eV, in combination with the appearance of shake-up peaks, are distinct characteristics of CuO (Ayastuy et al., 2012; Mai et al., 2011; Liu and Stephanopoulos, 1995; Kundakovic et al.,

1998). Thus, the majority of Cu species in 20 wt.% Cu/REOs samples was presented as Cu<sup>2+</sup>, independently from the support type. This is consistent with the absence of Cu<sup>+</sup> species on pre-oxidized 20 wt.% Cu/CeO<sub>2</sub> samples (Hardacre et al., 1994; Lamonier et al., 1996). The divalent state of Cu is also in accordance with the XRD results, which imply that in 20 wt.% Cu/REOs samples copper exists either as bare oxide (CuO) or as rare earth cuprate (Ln<sub>2</sub>CuO<sub>4</sub>). The findings of additional XPS studies on La, Nd and Pr cuprates (Ionov, 2001) are also in accordance with the present results, demonstrating Cu2p states with remarkable satellites, typical for the divalent copper.

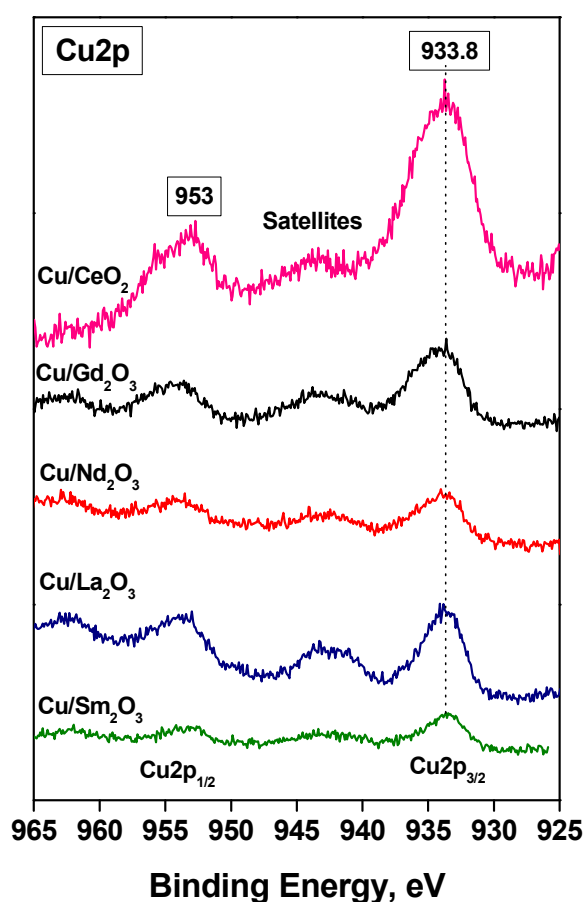


**Figure 5.2:** Core-level Cu2p spectra of 20 wt.% Cu/REOs catalysts.

The surface composition of 20 wt.% Cu/REOs samples, obtained by XPS analysis, is analyzed in Table 5.3. Bulk atomic concentration data are also included in the table. The comparison between the XPS and the nominal values of Cu reveals a significant decrease in the Cu surface species for all samples. This can be mainly ascribed to the high 20 wt.% Cu loading

and the agglomeration of Cu particles during the catalyst preparation. The atomic concentration (at.%) of surface copper is within the range of 7.5-11.2 at.% for almost all samples. However, a much smaller atomic concentration value (2.77 at.%) was found for Cu/Pr<sub>6</sub>O<sub>11</sub>. This may be explained by the enrichment of the catalyst surface due to the presence of praseodymium oxide, as suggested by the larger Pr and O fractions on the outer surface, compared to the corresponding bulk concentrations (Ioakeimidis et al., 2014).

**Table 5.3:** Bulk and surface (XPS) atomic concentrations (at.%) for 20 wt.% Cu/REOs catalysts.

Cu/REOs catalysts	XPS			Bulk		
	Cu	Lanthanide	O	Cu	Lanthanide	O
Cu/Nd <sub>2</sub> O <sub>3</sub>	7.52	31.35	61.13	20.93	31.63	47.44
Cu/Sm <sub>2</sub> O <sub>3</sub>	7.58	36.1	56.32	21.53	31.39	47.08
Cu/Gd <sub>2</sub> O <sub>3</sub>	8.34	32.05	59.61	22.19	31.12	46.68
Cu/Pr <sub>6</sub> O <sub>11</sub>	2.77	34.60	62.63	20.60	31.76	47.63
Cu/La <sub>2</sub> O <sub>3</sub>	11.21	22.42	66.37	20.40	31.84	47.76
Cu/CeO <sub>2</sub>	8.16	34.01	57.83	18.41	27.19	54.40

### 5.2.3. Reducibility Studies (H<sub>2</sub>-TPR) of 20 wt.% Cu/REOs Catalysts

Temperature-programmed reduction studies were performed to gain insight into the impact of the support on the reducibility of Cu/REOs catalysts. Figure 5.3 depicts the thermoreduction profiles of Cu supported on REOs in terms of hydrogen uptake as a function of temperature. Cu oxide presents two reduction peaks at ca. 300 °C, which correspond to the reduction of CuO and Cu<sub>2</sub>O to metallic Cu (Carabineiro et al., 2011). The presence of two reduction signals is also sometimes attributed to the stepwise reduction of copper oxide (Cu<sup>2+</sup>→Cu<sup>+</sup>→Cu<sup>0</sup>) (Breen et al., 1999) or to the presence of Cu species with different reducibility (Turco et al., 2007). In contrast, bare REOs are characterized by lower reducibility and reduction peaks at higher temperatures. For example, Pr, Sm and La oxides show TPR profiles with maximum rates of reduction at ca. 500, 750 and 800 °C, respectively (Liu et al., 1991; Haneda et al., 2002), whereas CeO<sub>2</sub> (Caputo et al., 2008; Carabineiro et al., 2010) is characterized by two reduction peaks at ca. 550 and 800 °C. The low temperature

peak is related to the surface-shell reduction of ceria, whereas the high temperature peak corresponds to the reduction of bulk oxygen and the formation of lower oxides of cerium (Carabineiro et al., 2010). However, metal incorporation into CeO<sub>2</sub> facilitates the surface-shell reduction, thus, shifting TPR peaks to lower temperatures (Carabineiro et al., 2010). Based on the above, the overlapping peaks observed over Cu/CeO<sub>2</sub> catalysts can be mainly assigned to the reduction of surface oxygen of the support along with the reduction of Cu oxide species. In this context, the low-temperature peak at 133 °C has been ascribed to the reduction of Cu species interfaced with CeO<sub>2</sub>, whereas the overlapping peaks at 215 and 267 °C have been attributed to Cu species non strongly associated with ceria (Papavasiliou et al., 2007).

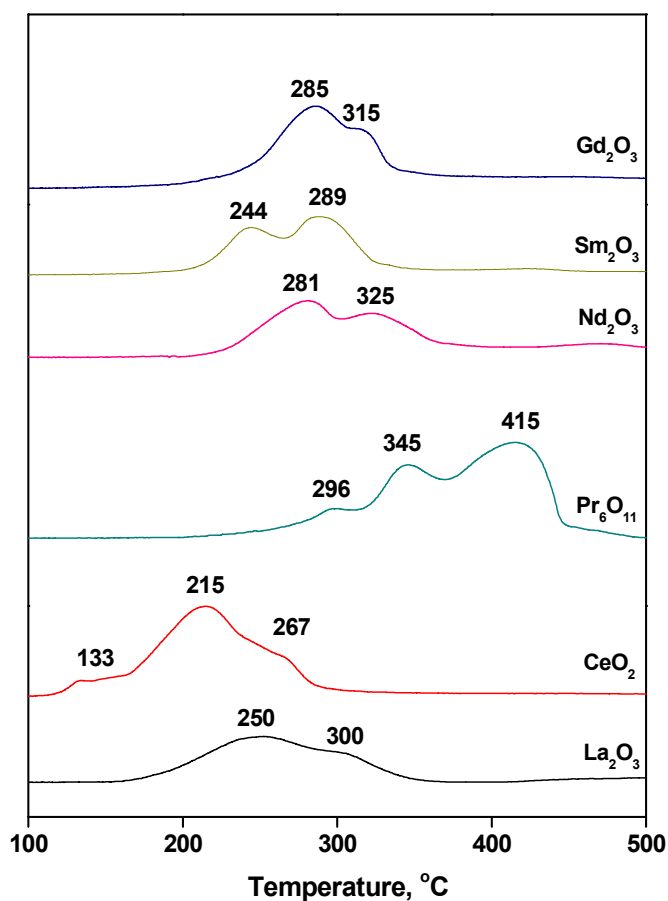


**Figure 5.3:** TPR profiles of 20 wt.% Cu/REOs catalysts.

### 5.2.4. Surface Morphology (SEM/EDAX) of 20 wt.% Cu/CeO<sub>2</sub> Catalysts

In Figure 5.4, the SEM micrograph of the “fresh” 20 wt.% Cu/CeO<sub>2</sub> catalyst (at different magnifications), along with the corresponding elemental mapping, can be seen. The size of the particles ranges from 2 to 50 μm, whereas it ranges in majority between 2 and 10 μm. The elemental mapping on the microstructure of the sample reveals that the distribution of Cu and Ce species is, in principle, uniform.

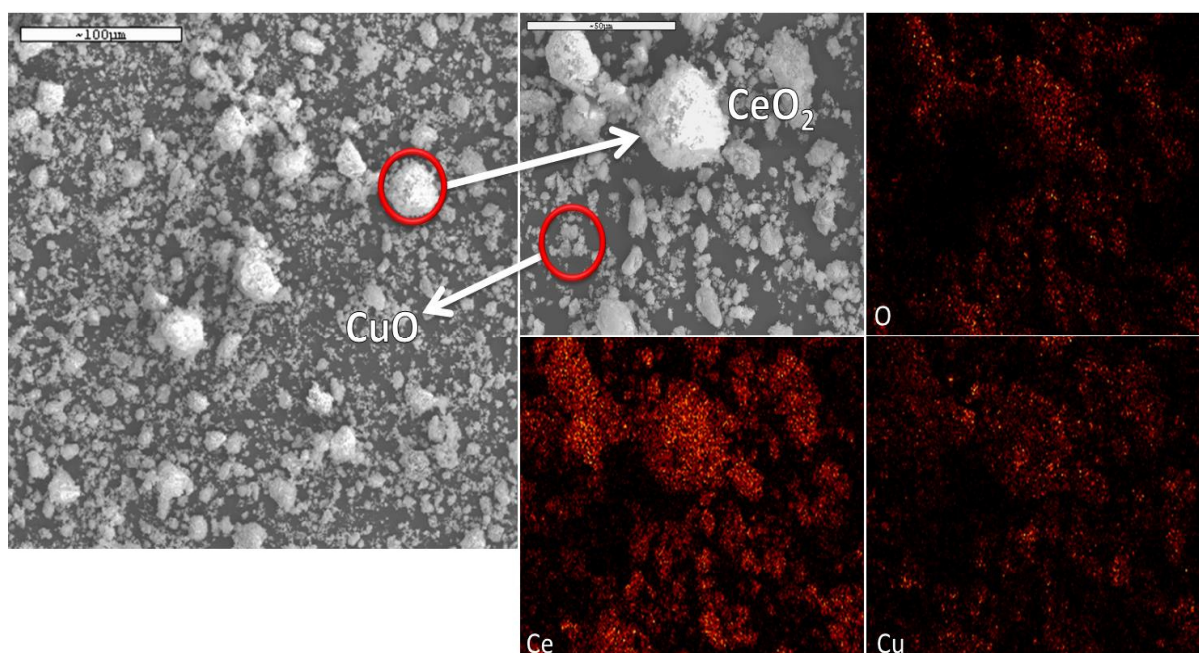


**Figure 5.4:** SEM picture and elemental mapping of the 20 wt.% Cu/CeO<sub>2</sub> catalyst.

### 5.2.5. Catalytic Activity Studies - Effect of Support Type (REOs)

Figure 5.5 depicts the effect of temperature on the H<sub>2</sub>S conversion, over 20 wt.% Cu catalysts supported on REOs, i.e., CeO<sub>2</sub>, Sm<sub>2</sub>O<sub>3</sub>, La<sub>2</sub>O<sub>3</sub>, Pr<sub>6</sub>O<sub>11</sub>, Nd<sub>2</sub>O<sub>3</sub>, and Gd<sub>2</sub>O<sub>3</sub>, at the temperature range 550-850 °C and under 1 v/v% H<sub>2</sub>S supply. By comparing these results, it is evident that the most promising performance is demonstrated by the 20 wt.% Cu/Sm<sub>2</sub>O<sub>3</sub> and 20 wt.% Cu/CeO<sub>2</sub> catalysts; the corresponding H<sub>2</sub>S conversion values are 11.0% and 10.0%, at T = 700 °C. The following order, in terms of H<sub>2</sub>S conversion, is obtained: Sm<sub>2</sub>O<sub>3</sub> > CeO<sub>2</sub> > Gd<sub>2</sub>O<sub>3</sub> > Pr<sub>6</sub>O<sub>11</sub> > La<sub>2</sub>O<sub>3</sub> > Nd<sub>2</sub>O<sub>3</sub> (Figure 5.4).

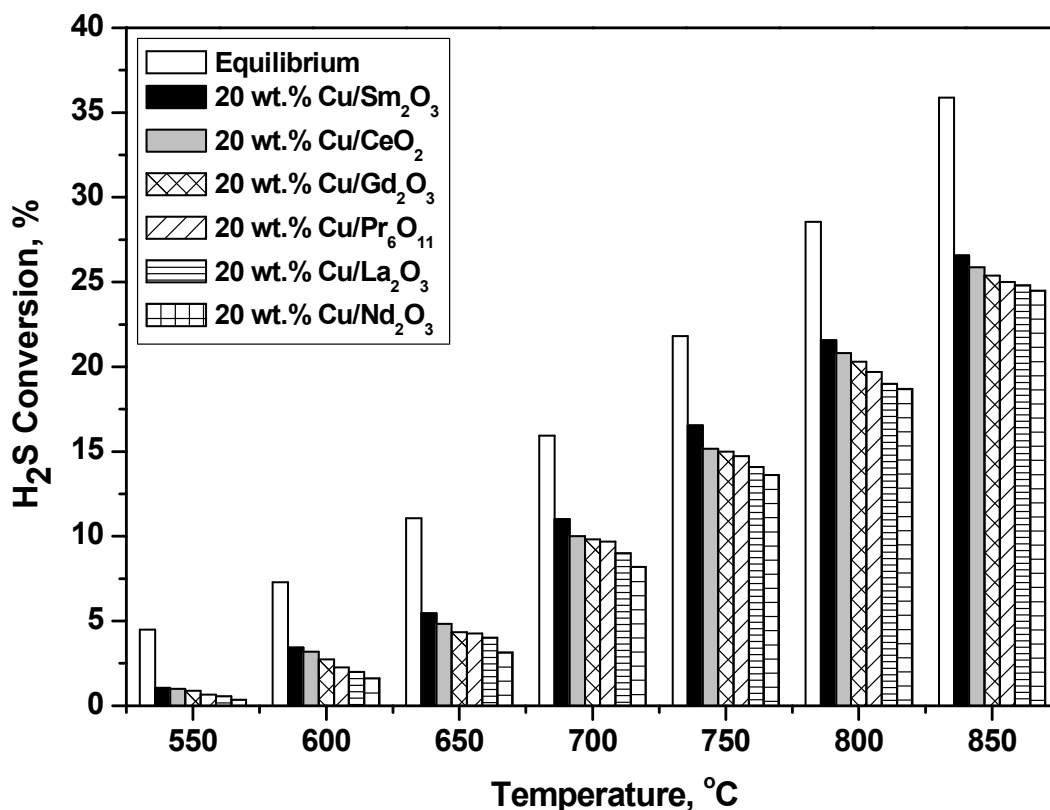


**Figure 5.5:** Effect of the support type on H<sub>2</sub>S conversion by Cu/Nd<sub>2</sub>O<sub>3</sub>, Cu/Sm<sub>2</sub>O<sub>3</sub>, Cu/Gd<sub>2</sub>O<sub>3</sub>, Cu/Pr<sub>6</sub>O<sub>11</sub>, Cu/La<sub>2</sub>O<sub>3</sub>, and Cu/CeO<sub>2</sub> catalysts at the temperature range of 550-850 °C. Reaction conditions: 1 v/v% H<sub>2</sub>S, balanced with Ar; Total flow rate = 100 cm<sup>3</sup>/min; Catalysts mass = 250 mg; GHSV = 13500 h<sup>-1</sup>.

In general, it can be concluded that, upon the examination of H<sub>2</sub>S decomposition towards H<sub>2</sub> production over 20 wt.% Cu/REOs catalysts, the optimal performance is identified for the Sm<sub>2</sub>O<sub>3</sub>- and CeO<sub>2</sub>-supported catalysts, as they demonstrated H<sub>2</sub>S conversion values equal to 11.0% and 10.0%, at T = 700 °C respectively. Note that, the optimal performance of both Sm<sub>2</sub>O<sub>3</sub>- and CeO<sub>2</sub>-supported catalysts is also revealed by the XPS and TPR analysis. As can be seen, the respective reduction peaks shift to smaller temperatures, compared to the rest catalysts and the atomic concentrations (at.%) for the corresponding lanthanides are higher. The remaining Cu-based catalysts exhibited smaller H<sub>2</sub>S conversion values, with the following order of performance: Sm<sub>2</sub>O<sub>3</sub> > CeO<sub>2</sub> > Gd<sub>2</sub>O<sub>3</sub> > Pr<sub>6</sub>O<sub>11</sub> > La<sub>2</sub>O<sub>3</sub> > Nd<sub>2</sub>O<sub>3</sub>. In the sequence, in order to improve the achieved performance of the optimum 20 wt.% Cu/Sm<sub>2</sub>O<sub>3</sub> catalyst on mixed Ce<sub>1-x</sub>Sm<sub>x</sub>O<sub>δ</sub> (where x = 0, 0.25, 0.5, 0.75 and 1) carriers, was examined.

### 5.3. H<sub>2</sub>S CATALYTIC DECOMPOSITION OVER 20 wt.% Cu/Ce<sub>1-x</sub>Sm<sub>x</sub>O<sub>δ</sub> CATALYSTS

The present section investigates the H<sub>2</sub>S decomposition performance of 20 wt.% Cu/Ce<sub>1-x</sub>Sm<sub>x</sub>O<sub>δ</sub> catalysts, when feeding 1 v/v% H<sub>2</sub>S/Ar gas mixtures. More specifically, the physicochemical properties of Cu entities were modified by employing ceria-based mixed oxides (Ce<sub>1-x</sub>Sm<sub>x</sub>O<sub>δ</sub>) as supporting carriers. The relevant characterization study, via BET and XRD, reveal that significant modifications on the physicochemical properties of Cu sites can be induced by replacing CeO<sub>2</sub> with Sm<sub>2</sub>O<sub>3</sub> in the support.

#### 5.3.1. Textural and Structural Characterization (BET and XRD Analysis)

The textural properties of all Cu catalysts supported on Ce<sub>1-x</sub>Sm<sub>x</sub>O<sub>δ</sub> mixed oxides, in terms of their BET area, cumulative pore volume and average pore diameter, are summarized in Table 5.4. As can be seen, the 20 wt.% Cu/CeO<sub>2</sub> supported catalyst presented again the largest BET surface area (44.63 m<sup>2</sup>/g), pore volume (0.15 cm<sup>3</sup>/g) and average pore diameter (10.05 nm), compared to the rest 20 wt.% Cu/Ce<sub>1-x</sub>Sm<sub>x</sub>O<sub>δ</sub> (x = 0, 0.25, 0.5, 0.75, 1). The latter observation implies that the addition of samarium had a detrimental effect on the textural characteristics, almost proportional to the samaria loading, thus resulting in smaller BET surface areas and pore volumes. These differences in BET areas and pore volumes can be explained by taking into account the textural characteristics of the parent oxides, as well as, the different crystallite sizes of the different phases, formed due to Sm addition.

**Table 5.4:** Textural properties of 20 wt.% Cu/Ce<sub>1-x</sub>Sm<sub>x</sub>O<sub>δ</sub> catalysts.

20 wt.% Cu/Ce <sub>1-x</sub> Sm <sub>x</sub> O <sub>δ</sub> catalysts	S <sub>BET</sub> (m <sup>2</sup> /gr)	BJH desorption cumulative pore volume (cm <sup>3</sup> /gr)	BJH desorption average pore diameter (nm)
20 wt.% Cu/CeO <sub>2</sub>	44.63	0.15	10.05
20 wt.% Cu/Ce <sub>0.75</sub> Sm <sub>0.25</sub> O <sub>1.875</sub>	19.74	0.08	11.37
20 wt.% Cu/Ce <sub>0.5</sub> Sm <sub>0.5</sub> O <sub>1.75</sub>	18.72	0.08	12.67
20 wt.% Cu/Ce <sub>0.25</sub> Sm <sub>0.75</sub> O <sub>1.625</sub>	6.13	0.04	15.97
20 wt.% Cu/Sm <sub>2</sub> O <sub>3</sub>	13.26	0.06	11.81

Figure 5.6 illustrates the XRD spectra of 20 wt.% Cu/Ce<sub>1-x</sub>Sm<sub>x</sub>O<sub>δ</sub> catalysts, while Table 5.5 lists the detected phases along with their crystallite sizes, as they were determined by Scherrer analysis. More specifically, CuO tenorite was identified in all samples, while CeO<sub>2</sub> cerianite was also present in Ce-containing samples. On the other hand, Sm-containing phases were detected mostly in samples with  $x \geq 0.5$ . In these samples, both a tetragonal Sm<sub>2</sub>CuO<sub>4</sub> phase and a cubic Sm<sub>2</sub>O<sub>3</sub> type phase were revealed, as it was expected from the relevant Sm<sub>2</sub>O<sub>3</sub>/CuO phase diagram (Takeda et al., 2000).

It is important to notice that only in the case of the 20 wt.% Cu/Ce<sub>0.75</sub>Sm<sub>0.25</sub>O<sub>1.875</sub> catalyst, all phases were detected, i.e., CeO<sub>2</sub> cerianite, CuO tenorite, cubic Sm<sub>2</sub>O<sub>3</sub> and tetragonal Sm<sub>2</sub>CuO<sub>4</sub> (Table 5.5). This probably implies the non-effective packing of the different phases, which in turn can result to the decrease of the surface area, as indeed observed in Table 5.4. Hence, it can be concluded that the amount of Sm doping, coupled with the crystallite size of different detected phases in each catalyst, should be accounted for the determination of textural characteristics.

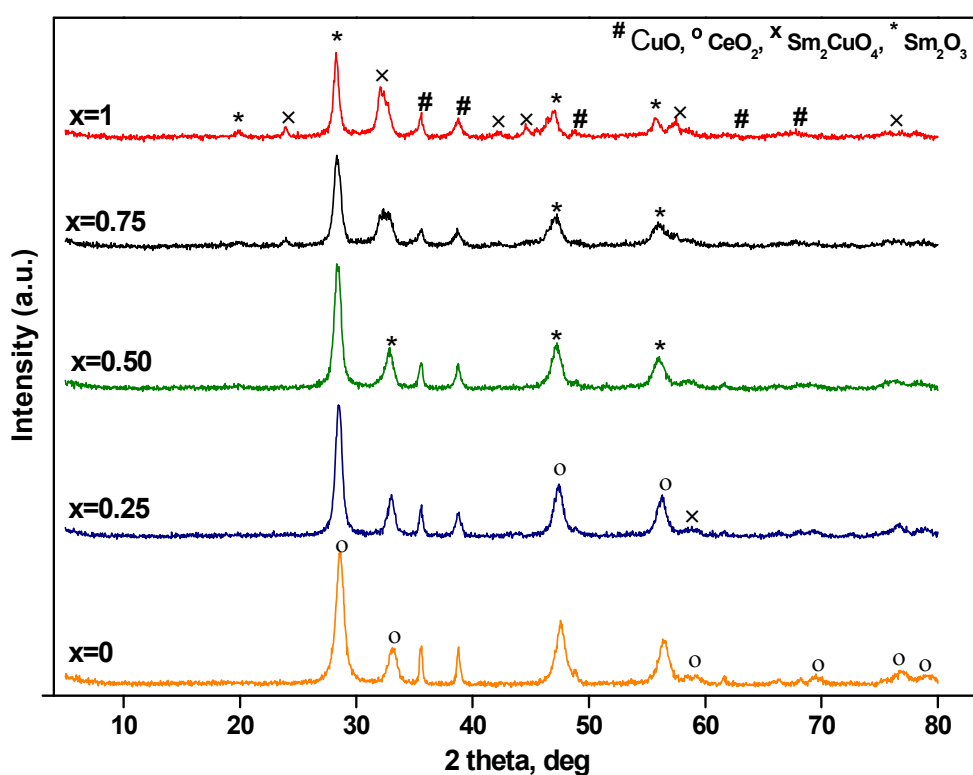


**Figure 5.6:** X-ray patterns of 20 wt.% Cu/Ce<sub>1-x</sub>Sm<sub>x</sub>O<sub>δ</sub> catalysts at different Ce/Sm atomic ratios ( $x = 0, 0.25, 0.5, 0.75, 1$ ).

**Table 5.5:** XRD characteristics of 20 wt.% Cu/Ce<sub>1-x</sub>Sm<sub>x</sub>O<sub>δ</sub> catalysts.

20 wt.% Cu/Ce <sub>1-x</sub> Sm <sub>x</sub> O <sub>δ</sub> catalysts	Detected phase	Crystallite size (nm)
20 wt.% Cu/CeO <sub>2</sub>	CeO <sub>2</sub>	9.32
	CuO	43.49
20 wt.% Cu/Ce <sub>0.75</sub> Sm <sub>0.25</sub> O <sub>1.875</sub>	CeO <sub>2</sub>	12.79
	CuO	27.69
	Sm <sub>2</sub> O <sub>3</sub>	13.62
20 wt.% Cu/Ce <sub>0.5</sub> Sm <sub>0.5</sub> O <sub>1.75</sub>	CeO <sub>2</sub>	10.54
	CuO	25.92
	Sm <sub>2</sub> O <sub>3</sub>	11.83
20 wt.% Cu/Ce <sub>0.25</sub> Sm <sub>0.75</sub> O <sub>1.625</sub>	CeO <sub>2</sub>	9.55
	CuO	19.72
	Sm <sub>2</sub> O <sub>3</sub>	13.66
	Sm <sub>2</sub> CuO <sub>4</sub>	11.00
20 wt.% Cu/Sm <sub>2</sub> O <sub>3</sub>	CuO	16.52
	Sm <sub>2</sub> O <sub>3</sub>	13.3
	Sm <sub>2</sub> CuO <sub>4</sub>	14.64

### 5.3.2. Catalytic Activity Studies

The catalytic performance of 20 wt.% Cu/Ce<sub>1-x</sub>Sm<sub>x</sub>O<sub>δ</sub> catalysts, towards H<sub>2</sub>S decomposition, is presented in Figure 5.7. It can be seen that the most active sample was once more the 20 wt.% Cu/Sm<sub>2</sub>O<sub>3</sub>; the respective conversion value was as high as 26.6%, at T = 850 °C. It is also clearly revealed that the addition of Ce has a significant effect on the catalytic activity. More specifically, as the Ce fraction in the catalyst increases, the conversion of H<sub>2</sub>S to H<sub>2</sub> decreases, all over the operational temperature range (550-850 °C). Nevertheless, it should be noted that all samples seem to facilitate the H<sub>2</sub>S decomposition towards H<sub>2</sub> production under the present conditions.

On the basis of the present findings, it can be inferred that the support nature/composition can exert a profound influence on the H<sub>2</sub>S decomposition performance of Cu-based catalysts. Among the Cu/REOs catalysts, the optimum deH<sub>2</sub>S performance was observed by Cu/Sm<sub>2</sub>O<sub>3</sub>.

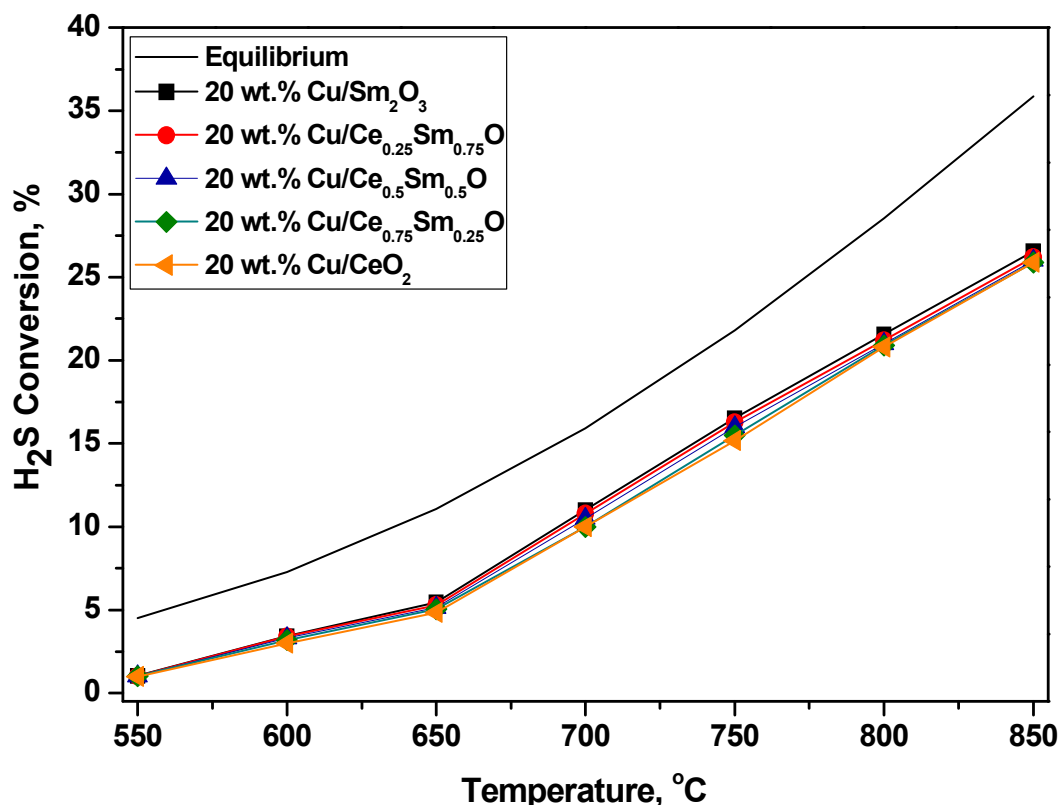


**Figure 5.7:** H<sub>2</sub>S conversion, as a function of temperature (550-850 °C), of 20 wt.% Cu/Ce<sub>1-x</sub>Sm<sub>x</sub>O<sub>8</sub> catalysts ( $x = 0, 0.25, 0.5, 0.75, 1$ ). Reaction conditions: 1 v/v% H<sub>2</sub>S, balanced with Ar; Total flow rate = 100 cm<sup>3</sup>/min; Catalysts mass = 250 mg; GHSV = 13500 h<sup>-1</sup>.

In an effort to optimize the deH<sub>2</sub>S behavior, the catalytic properties of Cu/Ce<sub>1-x</sub>Sm<sub>x</sub>O<sub>8</sub> mixed oxides were also explored. It was found, however, that Ce addition to Sm<sub>2</sub>O<sub>3</sub> support has always a relatively small effect, despite its pronounced impact on the textural properties (Table 5.4). Hence, it can be concluded that the superiority of Sm<sub>2</sub>O<sub>3</sub>- and CeO<sub>2</sub>-based samples can be mainly ascribed to the intrinsic characteristics of these particular carriers in conjunction to the presence of copper rather than to their textural characteristics.

#### 5.4. H<sub>2</sub>S CATALYTIC DECOMPOSITION OVER CERIA SUPPORTED TRANSITION METAL (Co, Ni, Fe and Cu) CATALYSTS

In the present section, a series of transition metal catalysts (Co, Ni, Fe and Cu) supported on CeO<sub>2</sub> were prepared and evaluated, initially with respect to their catalytic performance during the H<sub>2</sub>S decomposition reaction. The effect of various parameters, namely, i) metal entity (Fe, Co, Ni, Cu), ii) metal loading (15-30 wt.%), and iii) operation temperature (550-850

°C), and iv) H<sub>2</sub>S feed (v/v%): 0.25, 0.5, 0.75, 1, 1.5, 2, on the catalytic performance, were thoroughly studied. Similarly with the previous sections, the physicochemical and morphological characteristics of these catalytic systems were also determined by using the BET, XRD, XPS and SEM methods.

#### 5.4.1. Textural and Structural Characterization (BET and XRD Analysis)

The major textural properties (in terms of BET surface area, total pore volume and average pore diameter) and structural characteristics (in terms of the detected crystal structures and their approximate sizes, calculated by the Scherrer equation), of the prepared catalysts are displayed in Tables 5.6 and 5.7, respectively. It is obviously seen that the addition of transition metals to the bare ceria carrier decreases the BET surface area. The surface area of Co/CeO<sub>2</sub> catalysts is exacerbated, as the Co content of the catalyst increases. However, the BET area does not decrease linearly with the cobalt content of the catalyst. This can be attributed to the different crystallite sizes of the Co<sub>3</sub>O<sub>4</sub> and CeO<sub>2</sub> phases in the Co/CeO<sub>2</sub> catalysts, as determined by the XRD analysis (Table 5.7), which is presented in the following paragraphs.

**Table 5.6:** Textural characterization of bare CeO<sub>2</sub> and 20 wt.% M/CeO<sub>2</sub> (M: Co, Ni, Fe and Cu) catalysts.

Catalysts	Surface Area (m <sup>2</sup> /g)	Pore volume (cm <sup>3</sup> /g)	Average Pore Diameter (nm)
CeO <sub>2</sub>	71.5	0.27	15.4
20 wt.% Co/CeO <sub>2</sub>	33.4	0.13	16.0
20 wt.% Ni/CeO <sub>2</sub>	57.6	0.54	37.7
20 wt.% Fe/CeO <sub>2</sub>	57.0	0.26	18.3
20 wt.% Cu/CeO <sub>2</sub>	44.6	0.15	13.1
15 wt.% Co/CeO <sub>2</sub>	64.2	0.28	17.8
25 wt.% Co/CeO <sub>2</sub>	42.2	0.19	18.2
30 wt.% Co/CeO <sub>2</sub>	44.9	0.21	18.7

Figure 5.8 depicts the XRD spectra of the “fresh” M/CeO<sub>2</sub> catalysts, whereas, Figure 5.9 presents the corresponding spectra of Co-based catalysts of different metal loadings (15-30 wt.%), all calcined at 600 °C. As can be seen, all metals were crystallized in the form of the respective oxides, i.e., cobalt as Co<sub>3</sub>O<sub>4</sub>, nickel as NiO, iron as Fe<sub>2</sub>O<sub>3</sub>, and copper as CuO, while non mixed metal oxide/CeO<sub>2</sub> phases were also identified. Moreover, the Scherrer analysis indicated that the average crystallite size of metal oxides follows the order of: CuO > Co<sub>3</sub>O<sub>4</sub> > Fe<sub>2</sub>O<sub>3</sub> > NiO (Table 5.7). The sizes of CeO<sub>2</sub> crystallites increase as the sizes of the corresponding metal oxide phases decrease. Notice that in the Co-based catalysts of different metal content, cobalt is again met in the form of its Co<sub>3</sub>O<sub>4</sub>, regardless of the Co weight loading. The crystallite size of CeO<sub>2</sub> remains almost constant, despite the increase of the Co content. Additionally, the size of the Co<sub>3</sub>O<sub>4</sub> phase increases from 30.8 to 37.7 nm as the Co content increases from 15 to 20 wt.%. However, no further increase was observed for higher Co loadings, confirming the stabilization of BET area values above this specific Co loading value.

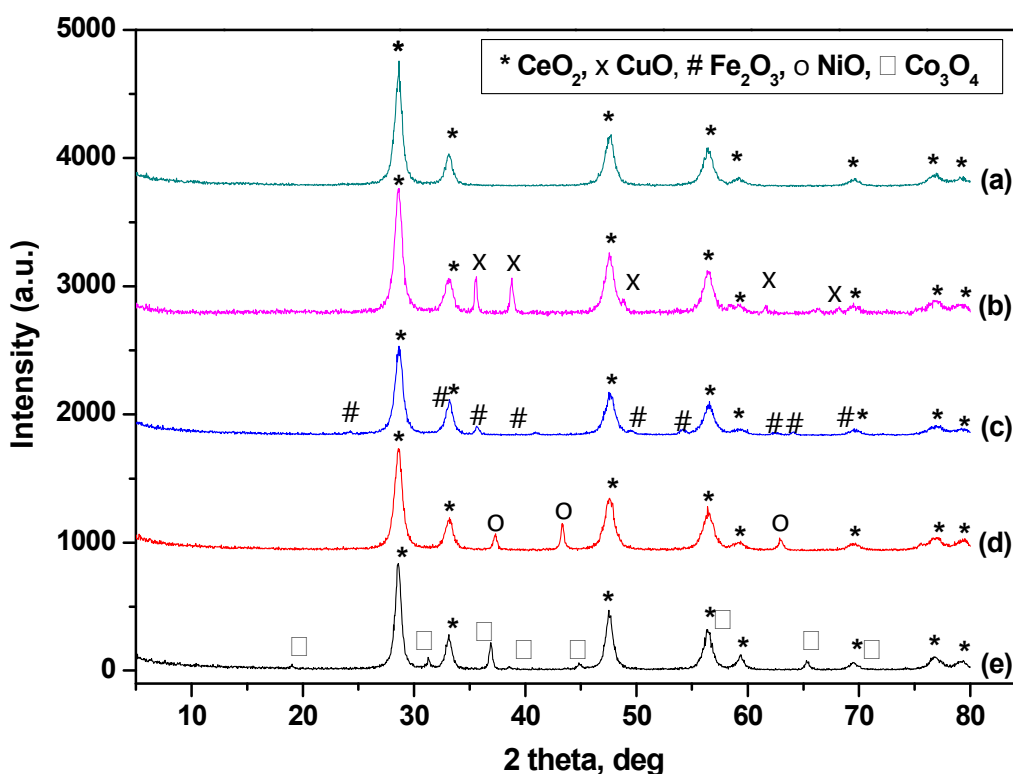


**Figure 5.8:** XRD patterns of ceria supported transition metal (Co, Ni, Fe and Cu) catalysts: a) bare CeO<sub>2</sub>, b) Cu, c) Fe, d) Ni, and e) Co, supported on CeO<sub>2</sub> catalysts.

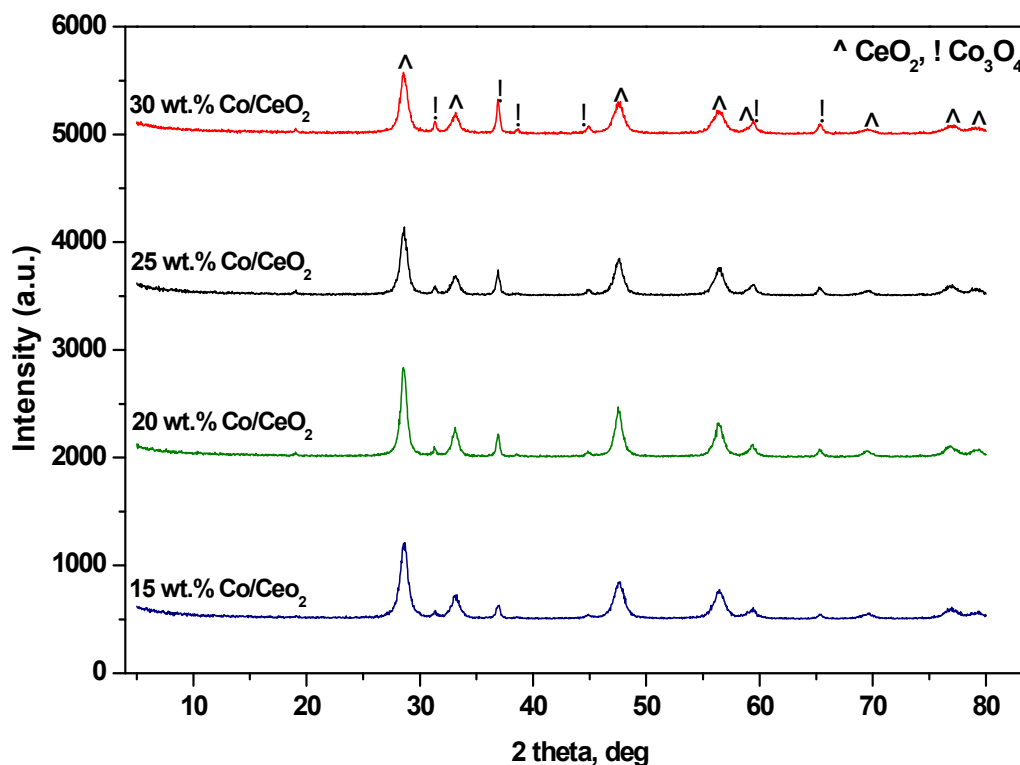


**Figure 5.9:** XRD patterns of Co/CeO<sub>2</sub> catalysts with 15, 20, 25, 30 wt.% Co loading.

It should be noted also that the size of Co<sub>3</sub>O<sub>4</sub> is approximately 3-fold larger than CeO<sub>2</sub>, a strong indication that the cobalt species segregate over the catalyst surface (Table 5.7). Thus, a significant decrease of bare ceria surface area (71.5 m<sup>2</sup>/g) is expected, upon increasing the Co loading, due to the blockage of ceria pores. However, this decrease could not be monotonic, since above a specific Co content, the formation of large Co<sub>3</sub>O<sub>4</sub> particles obstructs the dispersion of Co<sub>3</sub>O<sub>4</sub> entities into the CeO<sub>2</sub> pores and, consequently, any further decrease of the BET area.

A similar trend, upon the increase of the Cu content in Cu/CeO<sub>2</sub> catalysts, was also observed by Gamarra et al. (2007). Regarding the M/CeO<sub>2</sub> catalysts with a constant metal loading (20 wt.%), Ni- and Fe-based catalysts possess the higher BET areas (approximately 57 m<sup>2</sup>/g), while the Cu- and Co-based samples exhibit significantly lower surface area values, i.e., 44.6 and 33.4 m<sup>2</sup>/g, respectively. These variations in the textural characteristics of the catalysts can be related with the different crystallite size of the metal oxides formed in each case, as it will be discussed later.

**Table 5.7:** Structural characteristics of ceria supported transition metal (Co, Ni, Fe and Cu) catalysts and Co/CeO<sub>2</sub> catalysts with 15, 20, 25, 30 wt.% Co loading.

Catalysts	Detected phase / Lattice	Crystallite size
20 wt.% Co/CeO <sub>2</sub>	CeO <sub>2</sub> / Cubic	10.2
	Co <sub>3</sub> O <sub>4</sub> / Cubic	37.7
20 wt.% Ni/CeO <sub>2</sub>	CeO <sub>2</sub> / Cubic	11.2
	NiO / Cubic	23.2
20 wt.% Fe/CeO <sub>2</sub>	CeO <sub>2</sub> / Cubic	10.6
	Fe <sub>2</sub> O <sub>3</sub> / Rhombohedral	34.1
20 wt.% Cu/CeO <sub>2</sub>	CeO <sub>2</sub> / Cubic	9.3
	CuO / Monoclinic	43.5
15 wt.% Co/CeO <sub>2</sub>	CeO <sub>2</sub> / Cubic	11.5
	Co <sub>3</sub> O <sub>4</sub> / Cubic	30.8
25 wt.% Co/CeO <sub>2</sub>	CeO <sub>2</sub> / Cubic	13.6
	Co <sub>3</sub> O <sub>4</sub> / Cubic	32.3
30 wt.% Co/CeO <sub>2</sub>	CeO <sub>2</sub> / Cubic	10.4
	Co <sub>3</sub> O <sub>4</sub> / Cubic	37.7

#### 5.4.2. Surface Characterization of M/CeO<sub>2</sub> Catalysts

XPS measurements were carried out next to obtain insights into the elemental oxidation states and surface composition. In the case of the Fe/CeO<sub>2</sub> sample, peaks in the region of 709-713 eV with satellites at ca. 725 eV appear. Curve-fitting revealed the contribution of Fe<sup>2+</sup> and Fe<sup>3+</sup> ions at 709-711 eV and 711-713 eV, respectively (Galvez et al., 2014; Reddy et al., 2011). The presence of a certain amount of Fe<sup>2+</sup> ions probably implies the co-existence of Fe<sub>2</sub>O<sub>3</sub> (as indicated by XRD) with lower valence iron oxides (FeO/Fe<sub>3</sub>O<sub>4</sub>). The Co2p spectrum of Co/CeO<sub>2</sub> catalyst is characterized by a main peak at 780.6 eV accompanied by a low intensity satellite and a spin-orbit doublet Co2p<sub>1/2</sub>-Co2p<sub>3/2</sub> of 15.2 eV. These characteristics point to the formation of Co<sup>3+</sup> species in Co<sub>3</sub>O<sub>4</sub>-like phase (Zhang et al., 2014). The Ni2p<sub>3/2</sub> can be analyzed into two components corresponding to different Ni chemical states. The peak at ca. 854 eV is usually assigned to NiO, whereas the higher BE peak at 855-856 eV to Ni bonded with OH groups (Zyryanova et al., 2014; Nesbitt et al., 2000). The spectrum of the

Cu/CeO<sub>2</sub> sample is characterized by a Cu2p<sub>3/2</sub> band at 933.8 eV and shake-up satellites at ca. 944.0 eV, typical characteristics of Cu<sup>2+</sup> species in CuO-like phase (Kundakovic et al., 1998; Li et al., 1995; Ayastuy et al., 2012; Lamonier et al., 1996; Mai et al., 2011). The above assignments are in line with the XRD findings, which revealed the formation of the corresponding metal oxides in M/CeO<sub>2</sub> samples (Table 5.9).

Curve-fitting of the O1s spectra of M/CeO<sub>2</sub> catalysts, based on a mixture of Lorentzian and Gaussian curves, revealed three components. The low binding energy peak (OI) at ~529 eV can be ascribed to lattice oxygen, the intermediate peak (OII) at ~531 eV to surface O, OH groups and oxygen vacancies and the high energy band (OIII) at ~534 eV to adsorbed water (Ayastuy et al., 2012; Rao et al., 2011; Santos et al., 2014). In the case of Ni/CeO<sub>2</sub> the low BE peak at ca. 527 eV could be due to the differential charging of the oxide. Based on the area of OI, OII and OIII envelopes, a relative comparison between the M/CeO<sub>2</sub> samples could be obtained (Table 5.8). It is evident that the ratio between the lattice oxygen to the sum of surface oxygen species notably changes with the metal type. Co/CeO<sub>2</sub> catalysts possess the highest amount of OI species (70%), which are related to lattice oxygen in ceria and cobalt oxides. These differences in the population of surface oxygen species are expected to affect the H<sub>2</sub>S decomposition reaction as shown in the sequence.

**Table 5.8:** Percentage of surface oxygen species on M/CeO<sub>2</sub> catalysts.

Catalysts	%		
	O <sub>I</sub>	O <sub>II</sub>	O <sub>III</sub>
20 wt.% Co/CeO <sub>2</sub>	70	24	6
20 wt.% Ni/CeO <sub>2</sub>	58	42	0
20 wt.% Fe/CeO <sub>2</sub>	48	45	7
20 wt.% Cu/CeO <sub>2</sub>	38	55	7

The surface composition of M/CeO<sub>2</sub> samples obtained by XPS analysis, along with the bulk atomic concentrations (at. %), is presented in Table 5.9. Comparison of the XPS and nominal values of transition metal (Co, Ni, Fe and Cu) atomic concentrations reveals a decrease in metal surface species for all samples. These findings can be understood to a good extent considering surface characterization studies over Co-Ce binary oxides (Konsolakis et al.,

2015), where it was demonstrated the impoverishment of catalyst surface in Co species during the calcination procedure. The latter has been mainly attributed to the low surface energy of cobalt compared to ceria, resulted in a localization of ceria on the outer surface. In a similar manner, it has been revealed that the surface concentration of metal ions (such as Ni and Co) supported on ceria-based materials can be notably decreased due to the incorporation of metal ions into the support lattice (Varga et al., 2015; Santos et al., 2014; Vari et al., 2015). This particular configuration, involving the coexistence of metal ions in the outer surface and inside the support structure, could largely favor the oxygen mobility, with large consequences in the catalytic activity (Ocampo et al., 2009).

**Table 5.9:** Bulk and surface-X-ray Photoelectron Spectroscopy (XPS)-atomic concentrations (at%) for 20 wt.% M/CeO<sub>2</sub> catalysts.

Catalysts	XPS			Bulk		
	M	Ce	O	M	Ce	O
20 wt.% Co/CeO <sub>2</sub>	10.97	25.51	63.52	15.52	21.26	63.22
20 wt.% Ni/CeO <sub>2</sub>	15.22	23.42	61.36	16.41	22.39	61.19
20 wt.% Fe/CeO <sub>2</sub>	7.69	29.58	62.72	15.64	20.30	64.06
20 wt.% Cu/CeO <sub>2</sub>	8.16	34.01	57.83	15.55	22.96	61.48

#### 5.4.3. Surface Morphology (SEM/EDAX) of 20 wt.% Co/CeO<sub>2</sub> Catalysts

As can be seen in Figure 5.10, the SEM analysis of the “fresh” 20 wt.% Co/CeO<sub>2</sub> catalyst revealed that its particle sizes range from 1 to 10 μm, substantially smaller than the respective sizes of the 20 wt.% Cu/CeO<sub>2</sub> “fresh” catalyst (see Figure 5.3). Furthermore, the EDS and elemental mapping analyses showed a uniform Co and Ce distribution in the catalyst sample.

#### 5.4.4. Catalytic Activity Studies – Effect of Metal Type in H<sub>2</sub>S Decomposition

The performance of bare CeO<sub>2</sub> and 20 wt.% Co/CeO<sub>2</sub> catalysts, in terms of the obtained H<sub>2</sub>S conversion, are compared in Figure 5.11, where the predicted by thermodynamics (equilibrium) conversion, as well as, the conversion in the absence of catalyst (blank tests),

are also included. Note that the blank experiment was conducted in the reactor, under the same operational conditions (i.e., 1 v/v% H<sub>2</sub>S diluted in argon, at a constant flow rate of 100 cm<sup>3</sup>/min), in order to verify and compare the H<sub>2</sub>S conversion without the catalyst presence. In addition, the impact of the catalysts type (Co, Ni, Fe, Cu) and the operation temperature (550-850 °C) on the direct H<sub>2</sub>S decomposition reaction is presented in Figure 5.12. In all cases, the H<sub>2</sub>S conversion values increased with temperature, while the beneficial effect of the catalyst presence is more intense at higher temperatures. Thus, the pronounced effect and importance of both temperature and catalyst presence on H<sub>2</sub>S decomposition is clearly revealed.

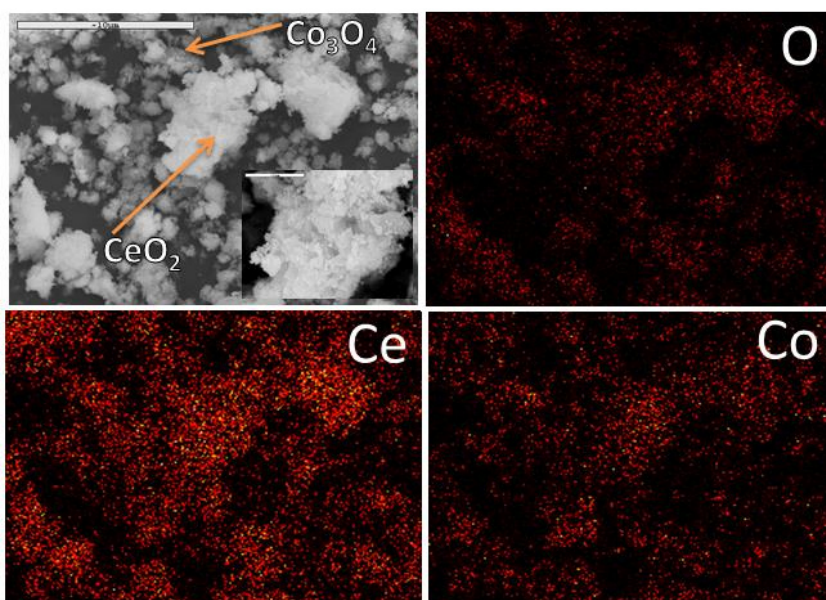


**Figure 5.10:** SEM image and respective elemental mapping of the 20 wt.% Co/CeO<sub>2</sub> catalyst.

Through the investigation of the individual transition metal catalysts performance (Figure 5.12), it can be highlighted that the 20 wt.% Co/CeO<sub>2</sub> catalyst exhibited the optimum behavior over the entire range of temperatures, followed by the Ni-, Fe- and Cu-based catalysts. Specifically, in the temperature range of 550-650 °C, the 20 wt.% Co/CeO<sub>2</sub> and 20 wt.% Ni/CeO<sub>2</sub> catalysts presented approximately identical activity values, while at higher temperatures, the 20 wt.% Co/CeO<sub>2</sub> catalyst was more efficient than the rest transition metal catalysts.

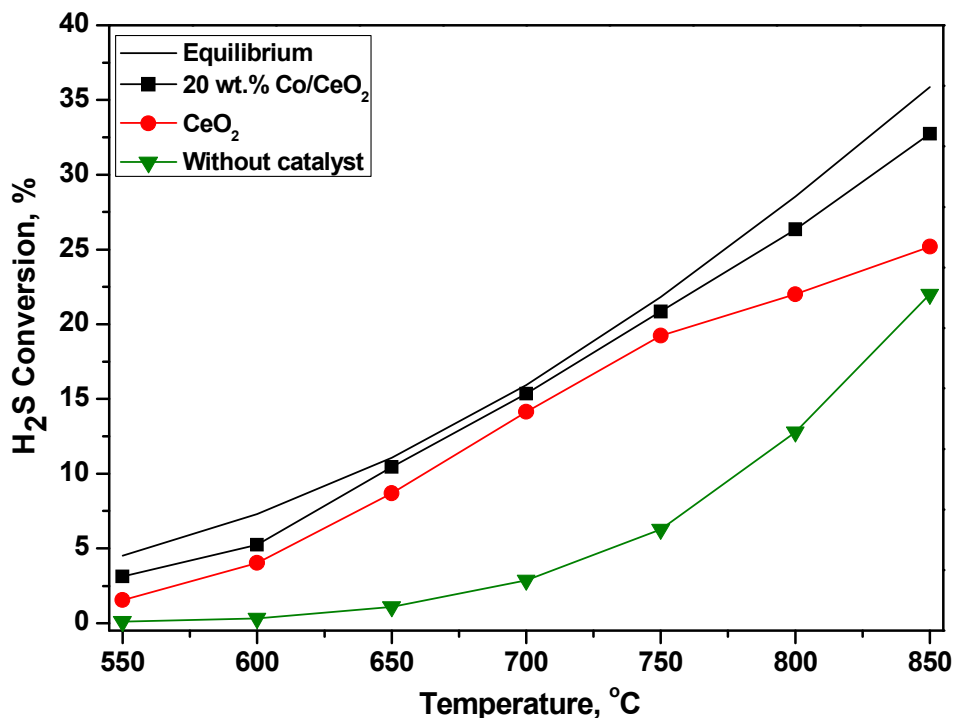


**Figure 5.11:** H<sub>2</sub>S conversion as a function of the reaction temperature (550-850 °C). Reaction conditions: 1 v/v% H<sub>2</sub>S, balanced with Ar; Total flow rate = 100 cm<sup>3</sup>/min; Catalysts mass = 250 mg; GHSV = 13,500 h<sup>-1</sup>.

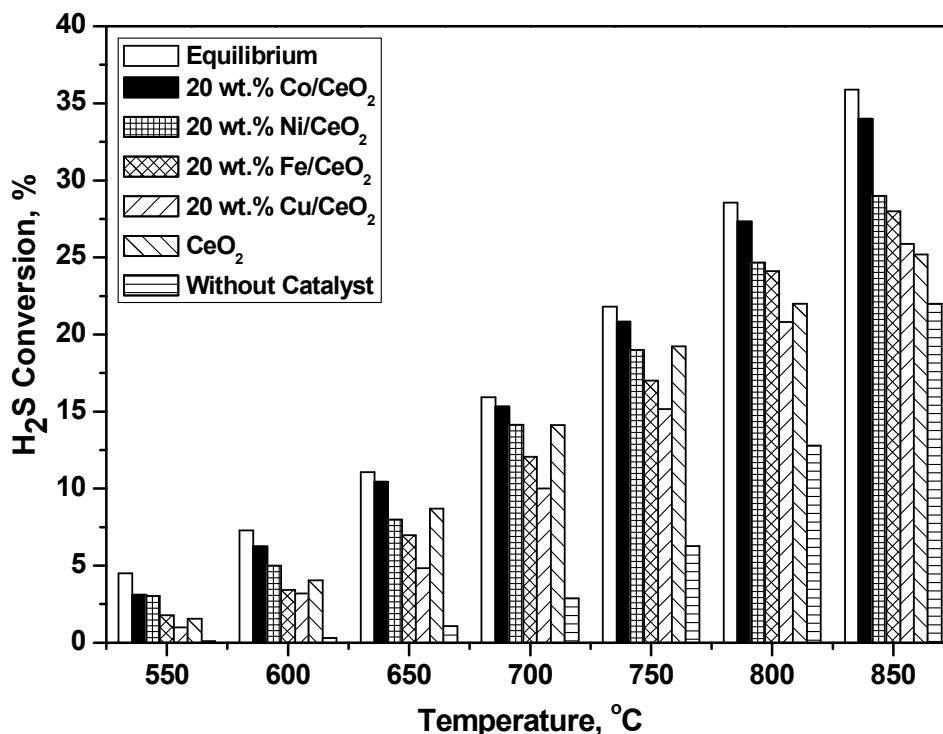


**Figure 5.12:** H<sub>2</sub>S conversion as a function of the reaction temperature (550-850 °C) over ceria supported transition metal (Co, Ni, Fe and Cu) catalysts. Reaction conditions: 1 v/v% H<sub>2</sub>S, balanced with Ar; Total flow rate = 100 cm<sup>3</sup>/min; Catalysts mass = 250 mg; GHSV = 13,500 h<sup>-1</sup>.

The beneficial effect of transition metals to ceria, as well as, the observed trend in catalytic activity was further verified by the relevant kinetic experiments, performed at  $P_{\text{H}_2\text{S}}=1$  kPa and differential conditions ( $\text{H}_2\text{S}$  conversion smaller than 25%). More specifically, by plotting the logarithm of the  $\text{H}_2\text{S}$  decomposition rate versus the absolute inverse temperature, the apparent activation energy ( $E_{\text{act}}$ ) was calculated by the slope of the produced curve. Under homogeneous reaction conditions the  $E_{\text{act}}$  was equal to 36.4 kcal/mol, while in the presence of 20 wt.% Co-, Ni-, Fe-, and Cu-CeO<sub>2</sub> catalysts, the apparent activation energy substantially decreased to 15.6, 15.3, 18.7, and 23.8 kcal/mol, respectively, indicating once again the pronounced role of the M/CeO<sub>2</sub> catalysts in the  $\text{H}_2\text{S}$  decomposition reaction.

In addition, as the reaction temperature increases, the catalytic rates of all catalyst types approach the equilibrium  $\text{H}_2\text{S}$  conversion value; specifically, the  $\text{H}_2\text{S}$  decomposition rate of the 20 wt.% Co/CeO<sub>2</sub> sample at 850 °C is practically identical to the equilibrium value. Moreover, the results highlight the importance of the CeO<sub>2</sub> support, since its catalytic behavior is comparable with the transition metal supported catalysts, especially at low temperatures.

Following the above analysis, the Co/CeO<sub>2</sub> catalyst is selected as the most promising one for the next studies. Moreover, by investigating the effect of Co loading (in the range 15-30 wt.%), the 20 wt.% Co/CeO<sub>2</sub> sample presented again the optimal performance (data not shown); thus, it was decided hereinafter to focus on this catalyst. It should be noted that this particular range of relatively high metal loadings is dictated by the required high electrical conductivity of the materials, employed as anode materials in proton conducting electrochemical membrane reactors.

In more detail, for the case of the optimum 20 wt.% Co/CeO<sub>2</sub> catalyst, and by keeping the operation temperature constant at 700 °C, the reaction order for  $\text{H}_2\text{S}$  decomposition was calculated from kinetic experiments, in which the feed  $\text{H}_2\text{S}$  partial pressure varied from 0.25 to 2 kPa. By combining the aforementioned findings, the following rate expression for the  $\text{H}_2\text{S}$  decomposition reaction in the case of the 20 wt.% Co/CeO<sub>2</sub> catalyst, was revealed:

$$r_{\text{H}_2\text{S}} = 15.3 \cdot 10^7 \exp(15,600/RT) \cdot C_{\text{H}_2\text{S}}^2 \quad (5.1)$$

where the rate of  $\text{H}_2\text{S}$  decomposition,  $r_{\text{H}_2\text{S}}$ , is expressed in kmol/m<sup>3</sup>·hr, the  $\text{H}_2\text{S}$  concentration,  $C_{\text{H}_2\text{S}}$ , in kmol/m<sup>3</sup> and the pre-exponential factor is equal to  $15.3 \cdot 10^7$  m<sup>3</sup>/kmol·hr. The rate expression and the respective energy activation and pre-exponential

factors are in full agreement with relevant studies in literature (Karan et al., 1999; Binoist, 2003).

In summary, the 20 wt.% Co/CeO<sub>2</sub> sample demonstrated the optimum activity performance under the present conditions, achieving similar conversion values to that predicted by the reaction equilibrium. However, since the 20 wt.% Co/CeO<sub>2</sub> exhibited a catalytic performance almost identical to that predicted by thermodynamics at higher temperatures, in an effort to further improve the efficiency of the catalytic system at lower temperature range (i.e., 550-650 °C), the Co active phase was chosen to be enhanced by the presence of a second transition metal entity, namely, copper. To this end, bimetallic Cu<sub>20-x</sub>Co<sub>x</sub>/CeO<sub>2</sub> (x = 0, 5, 10, 15 and 20) catalysts were prepared, via the wet impregnation method, and investigated in the next section.

## 5.5. H<sub>2</sub>S CATALYTIC DECOMPOSITION OVER BIMETALLIC (Cu<sub>20-x</sub>Co<sub>x</sub>/CeO<sub>2</sub>) (x = 0, 5, 10, 15, 20 wt.%) CATALYSTS

The feasibility of tailoring the H<sub>2</sub>S conversion activity of Cu/CeO<sub>2</sub> catalysts through the use of a second active metal (Cu<sub>20-x</sub>Co<sub>x</sub>, where x = 0, 5, 10, 15, 20 wt.%) was investigated, after the preparation of a series of Cu<sub>20-x</sub>Co<sub>x</sub>/CeO<sub>2</sub> bimetallic catalysts. The impact of several parameters, namely, the operating temperature and the Cu/Co ratio on H<sub>2</sub>S conversion, were investigated. Furthermore, the study of the Cu/Co ratio was extended to its effect on the structural, morphological and surface characteristics of the Cu<sub>20-x</sub>Co<sub>x</sub>/CeO<sub>2</sub> catalysts, via various characterization methods (BET, XRD, SEM/EDX, XPS), to potentially identify a close structure-activity correlation.

### 5.5.1. Textural and Structural Characterization (BET and XRD Analysis) of Bimetallic Cu<sub>20-x</sub>Co<sub>x</sub>/CeO<sub>2</sub> (x = 0, 5, 10, 15, 20 wt.%) Catalysts

Table 5.10 summarizes the textural characteristics of all Cu<sub>20-x</sub>Co<sub>x</sub>/CeO<sub>2</sub> (x = 0, 5, 10, 15, 20 wt.%) catalysts, in terms of their BET surface area, total pore volume and average pore diameter. It can be seen that the 20 wt.% Cu/CeO<sub>2</sub> catalyst possesses the highest BET area (44.63 m<sup>2</sup>/g) and pore volume (0.15 cm<sup>3</sup>/g), compared to the rest Cu<sub>20-x</sub>Co<sub>x</sub>/CeO<sub>2</sub> catalysts.

The latter observation implies the detrimental effect of the Cu phase substitution by Co (Cu-Co bimetallic catalysts) on the textural characteristics. It should be highlighted that the monometallic 20 wt.% Co/CeO<sub>2</sub> catalyst demonstrated the lowest BET area (33.36 m<sup>2</sup>/g). The observed differences in the textural characteristics of the bimetallic composites, compared to the monometallic catalysts, are probably due to the formation of mixed oxides in bimetallic samples and the different CuO and Co<sub>3</sub>O<sub>4</sub> crystallite sizes (Table 5.11).

**Table 5.10:** Textural characteristics of Cu<sub>20-x</sub>Co<sub>x</sub>/CeO<sub>2</sub> (x = 0, 5, 10, 15, 20 wt.%) catalysts.

Cu <sub>20-x</sub> Co <sub>x</sub> /CeO catalysts	S <sub>BET</sub> (m <sup>2</sup> /g)	Total pore volume (cm <sup>3</sup> /g)	Average pore diameter (nm)
20 wt.% Co/CeO <sub>2</sub>	33.36	0.13	16.00
5 wt.% Cu-15wt.% Co/CeO <sub>2</sub>	33.85	0.12	13.78
10 wt.% Cu-10 wt.% Co/CeO <sub>2</sub>	34.43	0.13	15.12
15 wt.% Cu-5 wt.% Co/CeO <sub>2</sub>	44.54	0.14	12.78
20 wt.% Cu/CeO <sub>2</sub>	44.63	0.15	13.11

Furthermore, Figure 5.13 illustrates the XRD spectra of the Cu<sub>20-x</sub>Co<sub>x</sub>/CeO<sub>2</sub> catalysts and Table 5.11 summarizes the phases that were detected in the samples, as well as, their approximate crystallite sizes, as determined by the Scherrer analysis. As mentioned above, despite that the Scherrer analysis does not provide an accurate estimation of the crystallite sizes, a qualitative assessment of the impact of the active phase (Cu-Co) composition on the structural characteristics could be obtained. In the monometallic composites (20 wt.% Co/CeO<sub>2</sub> and 20 wt.% Cu/CeO<sub>2</sub>), the cobalt diffraction peaks were assigned to the Co<sub>3</sub>O<sub>4</sub> cubic structure and the copper peaks to the monoclinic CuO tenorite structure (Murata et al., 2004). In both samples, Ce crystallized in the cubic structure. In addition to the aforementioned structures, in bimetallic samples (Cu<sub>20-x</sub>Co<sub>x</sub>/CeO<sub>2</sub>), the formation of a spinel Cu<sub>x</sub>Co<sub>3-x</sub>O<sub>4</sub> structure phase was also identified. The bimetallic catalyst with the lowest Cu content (i.e., 5 wt.% Cu - 15 wt.% Co/CeO<sub>2</sub>) showed diffraction peaks for the spinel structure (Cu<sub>x</sub>Co<sub>3-x</sub>O<sub>4</sub>) alone, while, no peaks assigned to CuO were detected. This suggests that, at a Cu/Co weight ratio equal to 1/3, Cu<sup>2+</sup> may completely replace Co<sup>2+</sup> in the Co<sub>3</sub>O<sub>4</sub> cubic structure (Li et al., 2009).

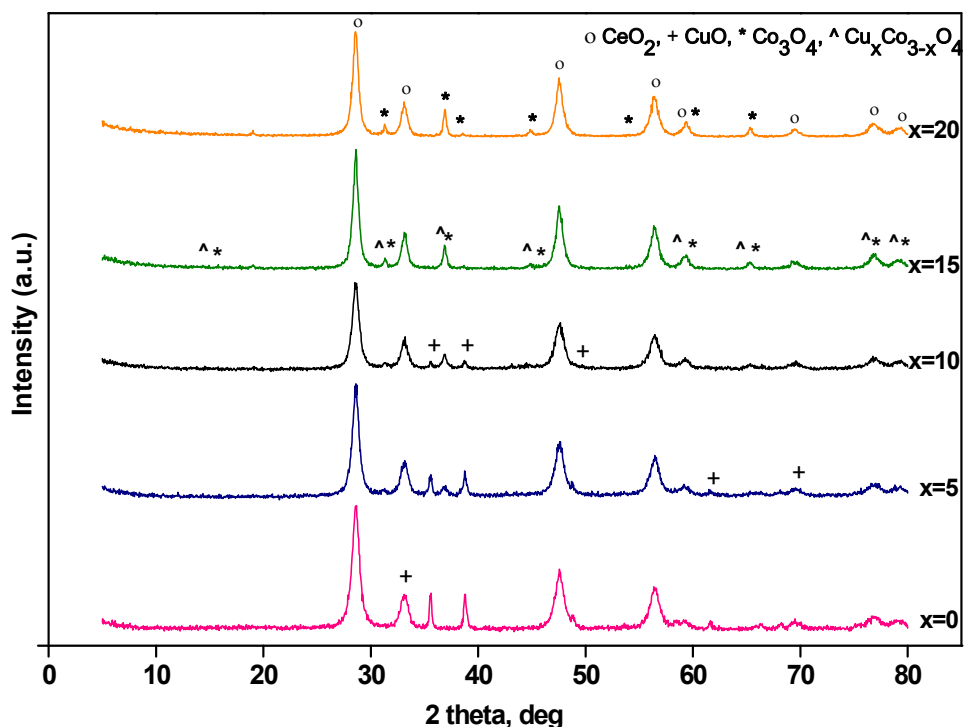


**Figure 5.13:** XRD diffraction spectra of Cu<sub>20-x</sub>Co<sub>x</sub>/CeO<sub>2</sub> ( $x = 0, 5, 10, 15, 20$  wt.%) catalysts.

**Table 5.11:** Detected crystal phases and their crystallite sizes for the Cu<sub>20-x</sub>Co<sub>x</sub>/CeO<sub>2</sub> ( $x = 0, 5, 10, 15, 20$  wt.%) catalysts.

Cu <sub>20-y</sub> Co <sub>y</sub> /CeO catalysts	Detected phase / Lattice	Crystallite size (nm)
20 wt.% Co/CeO <sub>2</sub>	CeO <sub>2</sub> / Cubic	10.2
	Co <sub>3</sub> O <sub>4</sub> / Cubic	37.7
5 wt.% Cu - 15wt.% Co/CeO <sub>2</sub>	CeO <sub>2</sub> / Cubic	14.41
	Cu <sub>x</sub> Co <sub>3-x</sub> O <sub>4</sub> / Cubic	30.00
	Co <sub>3</sub> O <sub>4</sub> / Cubic	59.33
10 wt.% Cu - 10 wt.% Co/CeO <sub>2</sub>	CeO <sub>2</sub> / Cubic	11.16
	CuO / Cubic	47.33
	Cu <sub>x</sub> Co <sub>3-x</sub> O <sub>4</sub> / Cubic	25.51
	Co <sub>3</sub> O <sub>4</sub> / Cubic	20.00
15 wt.% Cu - 5 wt.% Co/CeO <sub>2</sub>	CeO <sub>2</sub> / Cubic	10.84
	CuO / Cubic	45.12
	Cu <sub>x</sub> Co <sub>3-x</sub> O <sub>4</sub> / Cubic	9.59
	Co <sub>3</sub> O <sub>4</sub> / Cubic	13.50
20 wt.% Cu/CeO <sub>2</sub>	CeO <sub>2</sub> / Cubic	9.32
	CuO / Cubic	43.49

Moreover, the crystallite sizes of  $\text{CeO}_2$  and  $\text{CuO}$  slightly increased with increasing Co content. On the contrary, a significant increase of the  $\text{Cu}_x\text{Co}_{3-x}\text{O}_4$  crystallite size is obtained upon increasing the Co loading. Notice also that the crystallite size of the  $\text{Co}_3\text{O}_4$  phase attains its maximum value in the 5 wt.% Cu - 15 wt.% Co/ $\text{CeO}_2$  sample. However, in the monometallic Co/ $\text{CeO}_2$  sample a smaller  $\text{Co}_3\text{O}_4$  crystallite size of is observed, compared to the 5 wt.% Cu - 15 wt.% Co/ $\text{CeO}_2$  sample.

### 5.5.2. Surface Characterization of Bimetallic $\text{Cu}_{20-x}\text{Co}_x/\text{CeO}_2$ ( $x = 0, 5, 10, 15, 20$ wt.%) Catalysts

To obtain information about the elemental chemical states and surface composition of the studied catalysts, XPS measurements were also performed. Figure 5.14A depicts the XPS spectra, in the  $\text{Cu}2\text{p}$  region, of the  $\text{Cu}_{20-x}\text{Co}_x/\text{CeO}_2$  catalysts. The  $\text{Cu}/\text{CeO}_2$  sample showed a 933.8 eV  $\text{Cu}2\text{p}_{3/2}$  band and shake-up satellites at ca. 944.0 eV, which are typical characteristics for  $\text{Cu}^{2+}$  species in a  $\text{CuO}$ -like phase (Liu and Flytzani-Stephanopoulos, 1995; Kundakovic and Flytzani-Stephanopoulos, 1998; Ayastuy et al., 2006; Mai et al., 2011). Upon decreasing the Cu content to 15 and 10 wt% (i.e., 15 wt.% Cu - 5 wt.% Co/ $\text{CeO}_2$  and 10 wt.% Cu - 10 wt.% Co/ $\text{CeO}_2$ , respectively), the  $\text{Cu}2\text{p}_{3/2}$  peak intensity decreased without any significant shift, denoting the decrease of the  $\text{Cu}^{2+}$  species on the catalyst surface. However, as the Cu/Co weight ratio decreased, a slight though obvious broadening of the low energy side was observed, revealing a lower binding energy (BE) band contribution. By further decreasing the Cu/Co weight ratio to 1/3 (i.e., 5 wt.% Cu - 15 wt.% Co/ $\text{CeO}_2$ ), the band at high BE values (933.8 eV) and the shake-up satellites notably attenuated, whereas, a low intensity band at ca. 933.1 eV also appeared. According to literature,  $\text{Cu}2\text{p}_{3/2}$  BE at ca. 933-934.2 eV, in combination with the presence of shake-up peaks, are typical characteristics of  $\text{CuO}$ . On the other hand,  $\text{Cu}2\text{p}_{3/2}$  at ca. 932-933 eV and the absence of shake-up peaks are characteristics of reduced copper species, primarily  $\text{Cu}_2\text{O}$  (Liu and Flytzani-Stephanopoulos, 1995; Kundakovic and Flytzani-Stephanopoulos, 1998; Ayastuy et al., 2006; Mai et al., 2011). Accordingly, the low energy broadening and the  $\text{Cu}^{2+}$  attenuation in the 15 wt.% Cu - 5 wt.% Co/ $\text{CeO}_2$  and 10 wt.% Cu - 10 wt.% Co/ $\text{CeO}_2$  samples imply that  $\text{Cu}_2\text{O}$  coexists with  $\text{CuO}$ . Moreover, in the catalyst with the smaller copper content (15 wt.% Cu - 5 wt.% Co/ $\text{CeO}_2$ ) the 933.8 eV peak ( $\text{Cu}^{2+}$ ) notably decreased, the shake-up peaks weakened and were broadened,

and the low BE peak intensity at ca. 933.1 eV (Cu<sup>+</sup>) increased. Therefore, it can be concluded that the Cu species in the bimetallic catalysts are in a reduced state, while the Cu oxidation state decreases upon the increase of the Co content. These findings are consistent with the XRD results (Table 5.9) that indicate the formation of Cu<sub>x</sub>Co<sub>3-x</sub>O<sub>4</sub> spinel structures at the expense of single oxides in the bimetallic catalysts.

The core-level Co2p spectra of the Cu<sub>20-x</sub>Co<sub>x</sub>/CeO<sub>2</sub> catalysts are shown in Figure 5.14B, where the Co2p spectrum of the monometallic 20 wt.% Co/CeO<sub>2</sub> catalyst is characterized by a main peak at 780.6 eV, with low intensity satellites, and a Co2p<sub>1/2</sub>-Co2p<sub>3/2</sub> spin-orbit doublet of 15.2 eV.

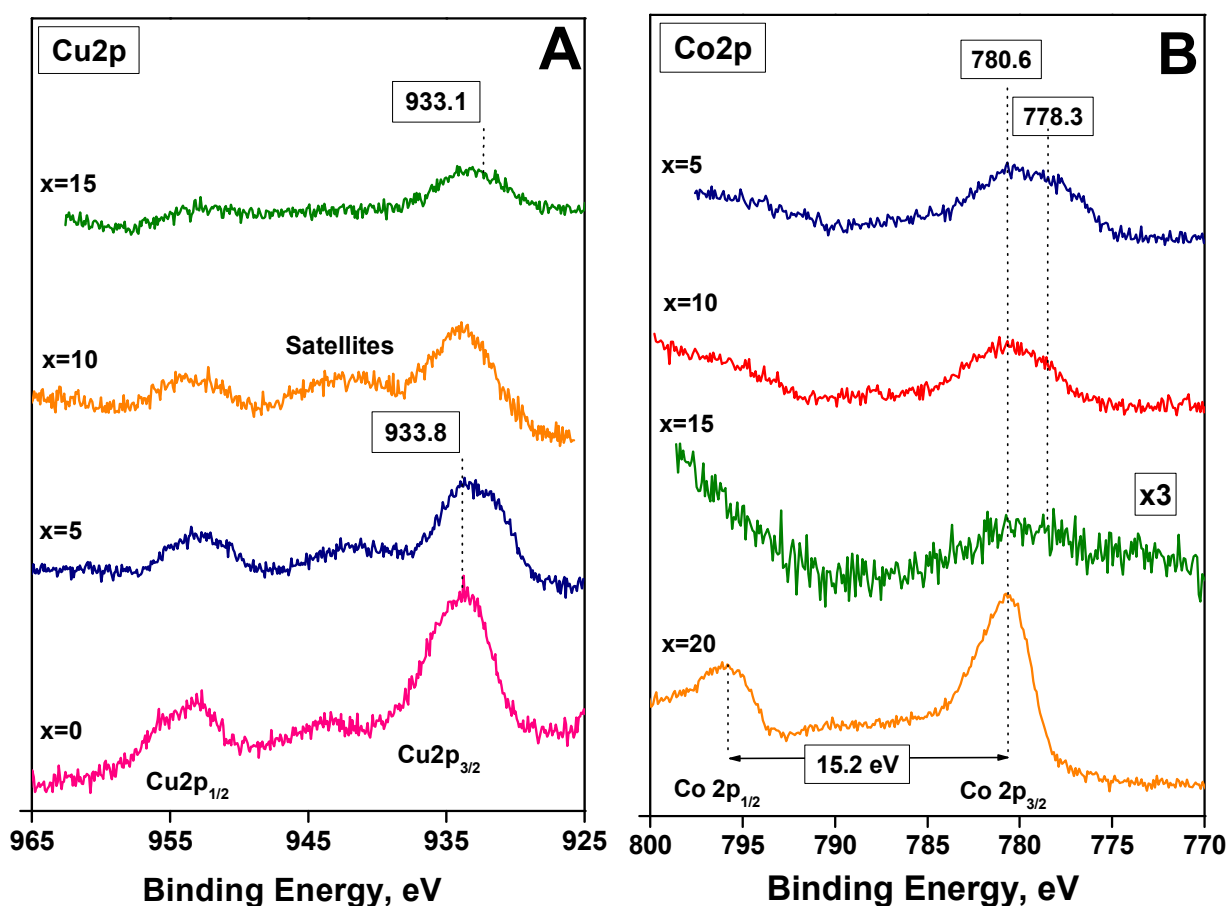


**Figure 5.14:** Core-level A) Cu2p and B) Co2p spectra of Cu<sub>20-x</sub>Co<sub>x</sub>/CeO<sub>2</sub> ( $x = 0, 5, 10, 15, 20$  wt.%) catalysts.

Despite that both Co<sup>2+</sup> and Co<sup>3+</sup> BE values are similar; the cobalt oxidation states can be discriminated by the presence or absence of shake-up satellites (Gomez et al., 2013). In

contrast to  $\text{Co}^{2+}$ , the  $\text{Co}^{3+}$  species is in a low spin state; therefore, energy is not sufficiently transferred to any unpaired electrons, thus preventing the formation of satellite peaks for  $\text{Co}^{3+}$  species (Gomez et al., 2013; Liotta et al., 2006; Pietrogiacomini et al., 2003). Specifically, the very small shake-up satellite intensity in the 20 wt.%  $\text{Co}/\text{CeO}_2$  sample, coupled with the main 780.6 eV band, indicates the formation of  $\text{Co}^{3+}$  species in a  $\text{Co}_3\text{O}_4$ -like phase. This assignment is consistent with the XRD findings that suggest the formation of a  $\text{Co}_3\text{O}_4$  phase in the 20 wt.%  $\text{Co}/\text{CeO}_2$  sample (Table 5.11). In the  $\text{Co}2p$  spectra of the bimetallic catalyst, a band at ca. 778.3 eV appears, resulting in low energy side broadening. According to literature, this peak can be specifically assigned to metallic Co (Bechara et al., 2001). Interestingly, the low energy 778.3 eV band intensity increased as the Cu content of the bimetallic catalysts also increased, thus a higher metallic cobalt contribution to the intensity can be supposed. Given the XPS analysis of the mono- and bi-metallic  $\text{Cu}_{20-x}\text{Co}_x/\text{CeO}_2$  catalysts, important conclusions can be drawn: i) in monometallic 20 wt.%  $\text{Cu}/\text{CeO}_2$  or 20 wt.%  $\text{Co}/\text{CeO}_2$  catalysts, the transition metal (M) is in a high oxidation state ( $\text{Cu}^{2+}$ ,  $\text{Co}^{3+}$ ), and ii) in bimetallic  $\text{Cu}_{20-x}\text{Co}_x/\text{CeO}_2$  catalysts, a combination of oxidized metal species with more reduced entities ( $\text{Cu}^0$  and  $\text{Co}^0$ ) can be found, due to the strong metal-metal interactions. The latter observation is consistent with the XRD spectra of the bimetallic catalysts that suggest the formation of a spinel  $\text{Cu}_x\text{Co}_{3-x}\text{O}_4$  structure, at the expense of the single oxides ( $\text{CuO}$  and  $\text{Co}_3\text{O}_4$ ).

Furthermore, the comparison of the surface atomic ratios (namely,  $\text{Cu}/\text{Ce}$ ,  $\text{Co}/\text{Ce}$ ,  $\text{Co}/\text{Cu}$  and  $\text{O}/\text{Ce}$ ), along with the bulk ratios of the  $\text{Cu}_{20-x}\text{Co}_x/\text{CeO}_2$  samples, is performed in Table 5.12. In all cases, the surface  $\text{Cu}/\text{Ce}$  and  $\text{Co}/\text{Ce}$  ratios are smaller than the nominal ones, probably due to the agglomeration of metal species during the calcination process. Moreover, notice that the surface  $\text{Co}/\text{Cu}$  ratio notably decreases when the Co content increases, suggesting the catalyst surface enrichment in copper. In the bimetallic 5 wt.% Cu - 15 wt.%  $\text{Co}/\text{CeO}_2$  sample with the larger Co content, the  $\text{Co}/\text{Cu}$  surface ratio is approximately 20 times smaller than the bulk ratio, implying the strong impoverishment of the catalyst surface in cobalt, due to the lower surface energy of copper, when compared with cobalt, and the preferential localization of copper species at the outer surface of the sample (Konsolakis and Ioakeimidis, 2014). In conjunction with the formation of spinel  $\text{Cu}_x\text{Co}_{3-x}\text{O}_4$  structure in the 5 wt.% Cu - 15 wt.%  $\text{Co}/\text{CeO}_2$  catalyst, it can be suggested that the incorporation of  $\text{Cu}^{2+}$  into  $\text{Co}_3\text{O}_4$  inhibits

the localization of Co species at the outer catalyst surface. Furthermore, it should be pointed out that the monometallic 20 wt.% Co/CeO<sub>2</sub> catalyst exhibits the largest O/Ce surface ratio (equal to 2.49), denoting a high concentration of surface oxygen groups, due to the intense synergistic metal-support interaction. The latter is of major importance in catalysis, since the beneficially impact of considerably accessible oxygen on the catalytic activity is well established (Yu et al., 2014).

**Table 5.12:** XPS and bulk atomic ratios for Cu<sub>20-x</sub>Co<sub>x</sub>/CeO<sub>2</sub> (x = 0, 5, 10, 15, 20 wt.%) catalysts.

Cu <sub>20-x</sub> Co <sub>x</sub> /CeO catalysts	XPS				Bulk			
	Co/Ce	Co/Cu	Cu/Ce	O/Ce	Co/Ce	Co/Cu	Cu/Ce	O/Ce
20 wt.% Co/CeO <sub>2</sub>	0.43	-	0	2.49	0.72	-	0	2.0
5 wt.% Cu - 15wt.% Co/CeO <sub>2</sub>	0.03	0.20	0.15	1.72	0.54	3.17	0.54	2.0
10 wt.% Cu - 10 wt.% Co/CeO <sub>2</sub>	0.09	0.33	0.27	1.85	0.36	1.05	0.34	2.0
15 wt.% Cu - 5 wt.% Co/CeO <sub>2</sub>	0.13	0.31	0.41	1.93	0.18	0.35	0.51	2.0
20 wt.% Cu/CeO <sub>2</sub>	0	0	0.24	1.70	0	0	0.68	2.0

### 5.5.3. Catalytic Activity Studies - Effect of the Surface Support of Cu<sub>20-x</sub>Co<sub>x</sub>/CeO<sub>2</sub> (x = 0, 5, 10, 15, 20 wt.%) Catalysts

In order to improve the efficiency of the 20 wt.% Co/CeO<sub>2</sub> catalysts towards the H<sub>2</sub>S decomposition, the Co active phase of the catalysts was enhanced, along with the presence of a second transition metal, i.e., copper. The experimental results of the activity tests, in terms of H<sub>2</sub>S conversion, are presented in Figure 5.15. As can be seen, the progressive substitution of Co by Cu decreases the H<sub>2</sub>S conversion, which is an effect exactly opposite to the one on the respective BET surface area, implying that the textural properties do not affect the catalytic performance. Therefore, upon the surface support of the Co/CeO<sub>2</sub> catalysts, it was again confirmed that 20 wt.% Co/CeO<sub>2</sub> is the optimum catalyst for the

studied process, probably due to this highest O/Ce surface ratio compared to the other Co-Cu bimetallic catalysts.

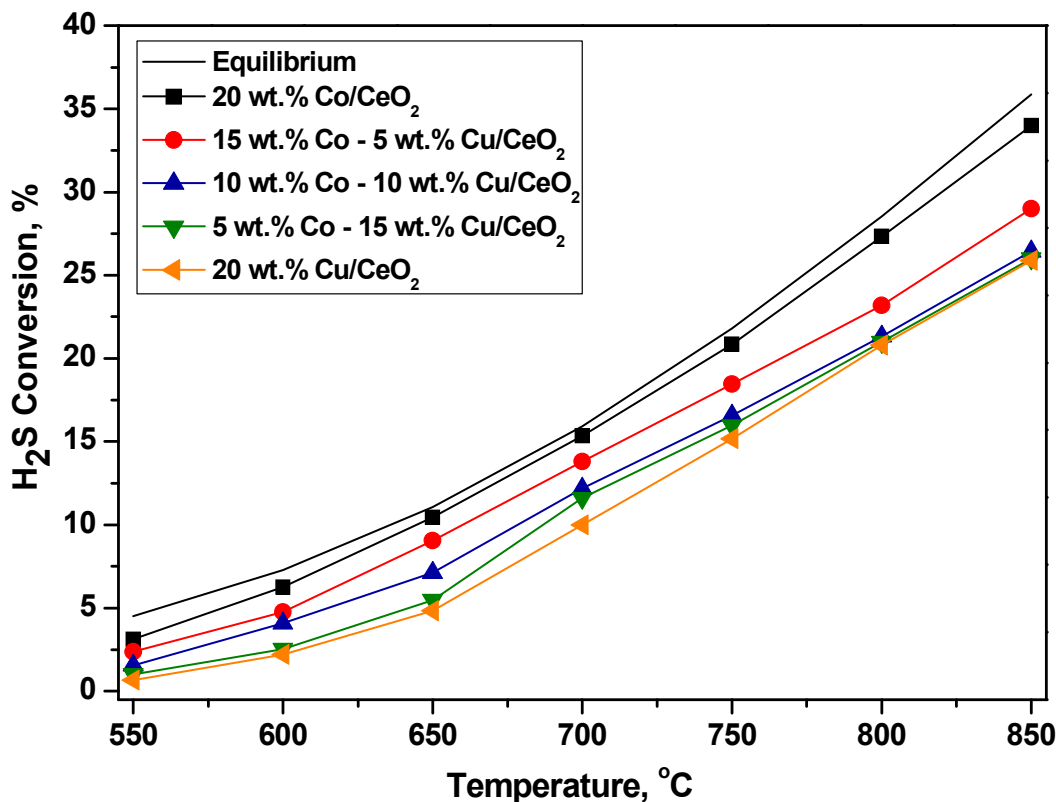


**Figure 5.15:**  $H_2S$  conversion, as a function of temperature (550–850 °C), over bimetallic  $Cu_{20-x}Co_x/CeO_2$  ( $x = 0, 5, 10, 15, 20$  wt.%) catalysts. Reaction conditions: 1 v/v%  $H_2S$ , balanced with Ar; Total flow rate = 100  $cm^3/min$ ; Catalysts mass = 250 mg; GHSV = 13,500  $h^{-1}$ .

It should be noted that through the investigation of the catalytic performance of bimetallic  $Cu_{20-x}Co_x/CeO_2$  ( $x = 0, 5, 10, 15, 20$  wt.%) catalysts during the  $H_2S$  decomposition reaction, under identical operation conditions, the 20 wt.% Co/ $CeO_2$  sample demonstrated again the most promising performance; the maximum achieved  $H_2S$  conversion was 34% at  $T = 850$  °C. On the other hand, a notable lower conversion (25.89%) was achieved in the case of the 20 wt.% Cu/ $CeO_2$  sample. In light of the characterization studies and the activity results, the superior catalytic performance of Co/ $CeO_2$  catalysts could be ascribed to their better resistance to reduction, associated with the formation of  $Co^{3+}$  species in a  $Co_3O_4$ -like phase and the highest O/Ce surface reaction. This may also contribute to the enhanced sulfur tolerance of Co-based catalysts.

## 5.6. STABILITY TESTS OVER OPTIMUM 20 wt.% Co/CeO<sub>2</sub> CATALYST

Having established, by the previous experimental activity results, the superiority of the 20 wt.% Co/CeO<sub>2</sub> catalysts, long-term (24 h) stability tests, were carried out at two different operation temperatures (700 and 850 °C) to assess their lifetime characteristics (Figure 5.16). In these experiments, the catalysts were first heated up to 700 and 850 °C (3 °C/min) under pure Ar atmosphere, remained at the selected temperature for 1 hr, and then the standard feed mixture ( $P_{\text{H}_2\text{S}} = 1$  kPa, with Ar as a diluent), identical to the one used in the activity tests, was introduced into the reactor (“Aged” sample). It is obvious that for the studied 20 wt.% Co/CeO<sub>2</sub> sample, the initial conversion (at  $t = 0$  h) is rather small (less than 0.5% and 2.7% at 700 and 850 °C, respectively), however it progressively increases with time on stream. In all cases, after an initial “activation period” and depending on the reaction temperature, a stable conversion performance was attained close to the conversion value achieved in the activity experiments. This H<sub>2</sub>S conversion remained constant until the end of the test period.

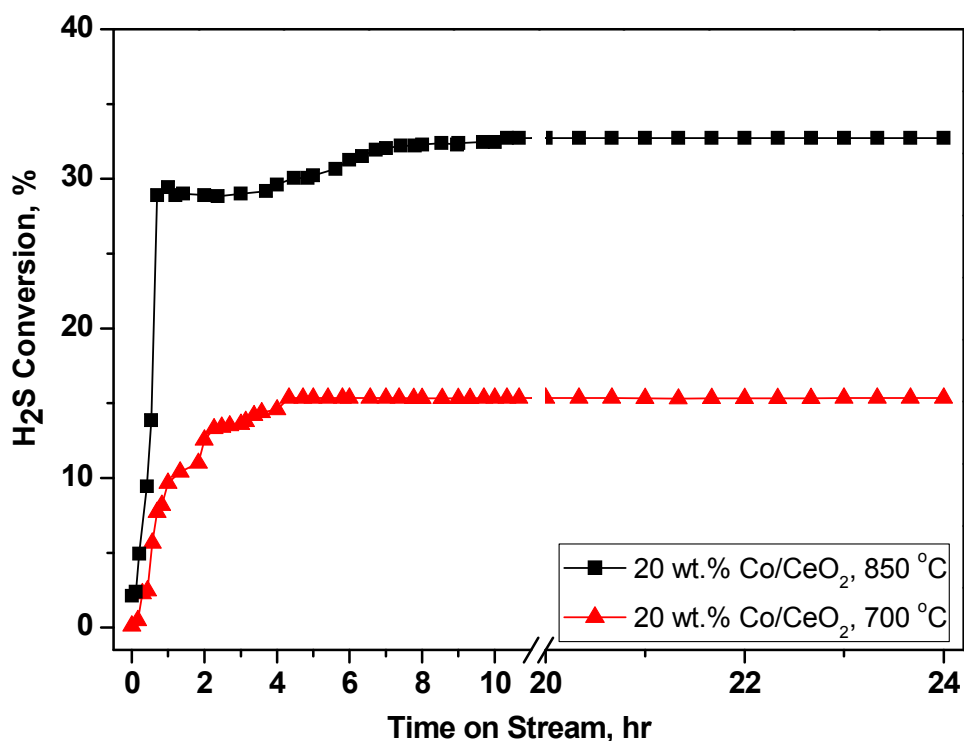


**Figure 5.16:** Stability performance (H<sub>2</sub>S conversion vs. time on stream) at  $T = 700$  and  $850$  °C of the optimum “Aged” 20 wt.% Co/CeO<sub>2</sub> catalysts, during the H<sub>2</sub>S decomposition reaction. Reaction conditions: 1 v/v% H<sub>2</sub>S, balanced with Ar; Total flow rate = 100 cm<sup>3</sup>/min; Catalysts mass = 250 mg; GHSV = 13,500 h<sup>-1</sup>.

In more detail, the  $\text{H}_2\text{S}$  conversion at  $T = 700\text{ }^\circ\text{C}$  increased from 0.5% at  $t = 0\text{ h}$  to 15.3% at  $t = 3\text{ h}$ , and remained stable at this value till the end of the corresponding experiment. On the other hand, the requested activation period at  $850\text{ }^\circ\text{C}$  was significantly shorter. Approximately 1 h after switching from pure Ar to the reacting mixture, a stable value for  $\text{H}_2\text{S}$  conversion was measured (34%). This value was constant for the entire 24 h testing period, thus, the system presented once more an impressive stability. These findings strongly suggest the in-situ induced beneficial effect of the reaction environment on the  $\text{H}_2\text{S}$  decomposition process. Additionally, the optimum catalyst sample was also studied in a step-change experiment at  $T = 850\text{ }^\circ\text{C}$ , where the  $\text{H}_2\text{S}$  concentration in the feedstock stream was progressively increased to 1 v/v%, 2 v/v% and 4 v/v%, and remained at each step constant for three hours (Figure 5.17). It can be observed that in all cases, even in the extreme case where the catalyst was exposed to a 4 v/v%  $\text{H}_2\text{S}/\text{Ar}$  mixture, the performance of the  $\text{Co}/\text{CeO}_2$  sample remained unaffected without any significant variations.

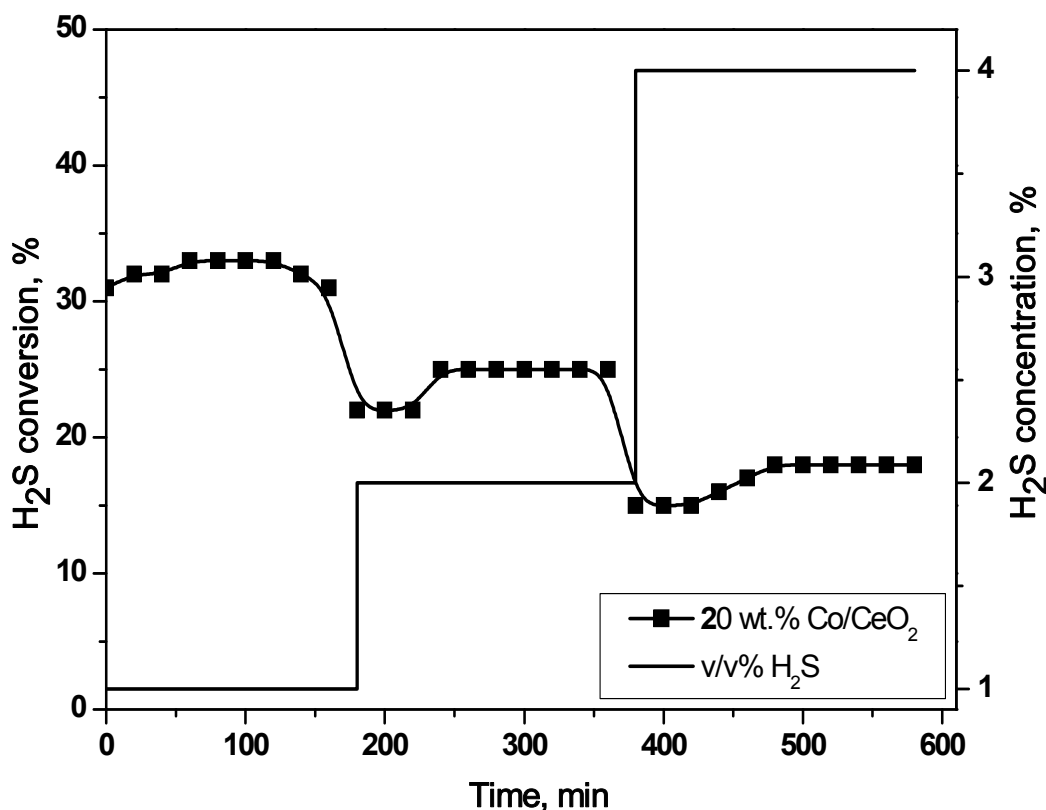


**Figure 5.17:**  $\text{H}_2\text{S}$  conversion, as a function of the reaction time and the stepwise changes (3 h) in the  $\text{H}_2\text{S}$  concentration (1 v/v%, 2 v/v% and 4 v/v%), at  $T = 850\text{ }^\circ\text{C}$ , when studying the optimum 20 wt.%  $\text{Co}/\text{CeO}_2$  catalyst. Reaction conditions: Total flow rate =  $100\text{ cm}^3/\text{min}$ ; Catalysts mass = 250 mg; GHSV =  $13,500\text{ h}^{-1}$ .

Taking into account that under the employed reaction conditions H<sub>2</sub>S is decomposed to H<sub>2</sub> and elemental sulfur, the initial activation phase could be related, either to the in-situ reduction of the catalyst by the generated H<sub>2</sub>, or to the catalyst in-situ sulfation, both favored at increased temperatures. These two processes, separately or in synergy, alter the surface chemistry of the catalyst and, in extent, the deH<sub>2</sub>S performance of the 20 wt.% Co/CeO<sub>2</sub> catalysts. To clarify more the aforementioned complex phenomena, the H<sub>2</sub>S stability performance of:

- i) "Aged" sample [the catalyst is initially exposed to pure argon, during the reactor heat-up to the set-point temperature (850 °C) and then at t = 0 min (Figure 5.18) exposed to the standard feed mixture (1 v/v% H<sub>2</sub>S, balanced with Ar), for 10 hr].
- ii) "Reduced" sample [the catalyst is initially exposed to reducing conditions (i.e., 10 v/v% H<sub>2</sub>, balanced with argon), inside the reactor while the temperature steadily increased up to 850 °C, with a heating rate of 3 °C/min. When the selected temperature is reached, the catalyst is continuously exposed to reducing conditions (10 v/v% H<sub>2</sub>, balanced with argon) for 1 h at T = 850 °C and then at t = 0 min the sample was also subjected to the long term stability experiment (10 h at 850 °C with 1 v/v%, balanced with Ar)].
- iii) "Sulfated" sample [the catalyst is exposed to 1 v/v% H<sub>2</sub>S, balanced with Ar reaction mixture, for 10 h at 850 °C and at t = 0 min the sample is subjected to the long term stability experiment with 1 v/v% H<sub>2</sub>S, balanced with Ar for 10 h at 850 °C].

20 wt.% Co/CeO<sub>2</sub> catalysts was investigated in long-term stability tests (Figure 5.16), using the identical protocol of the respective experiments presented in Figure 5.15. As it is clearly illustrated in Figure 5.18, especially for the stability experiments at T = 700 °C, where the "reduction" and "sulfation" processes proceed at lower rates, the activation period is strongly affected by the different pretreatment processes. The fastest activation period is achieved for the "sulfated" samples; the requested periods for catalyst activation are equal to 80 and 20 min for the stability tests performed at T = 700 and 850 °C, respectively. On the other hand, the activation period of the "reduced" samples is longer, compared to the "sulfated" ones. Thus, approximately 160 and 42 min for the tests conducted at T = 700 and 850 °C, respectively, are needed; a time-period that is however again clearly shorter than the time required for the activation of the fresh samples (260 and 100 min for the experiments employed at T = 700 and 850 °C, respectively). Note that for all cases and independently of the pretreatment process, the final H<sub>2</sub>S conversion values converge to the

same stable  $\text{H}_2\text{S}$  conversion value (15.3% at  $T = 700\text{ }^\circ\text{C}$  and 34% at  $T = 850\text{ }^\circ\text{C}$ ). These findings clearly point out that both the in-situ reduction and sulfation of the catalyst, from the  $\text{H}_2$  and elemental S, in-situ generated by the  $\text{H}_2\text{S}$  decomposition reaction, affect the catalyst's activity; the latter pretreatment method appears to be more critical to the overall activity and stability performance of the 20 wt.% Co/CeO<sub>2</sub> catalyst.

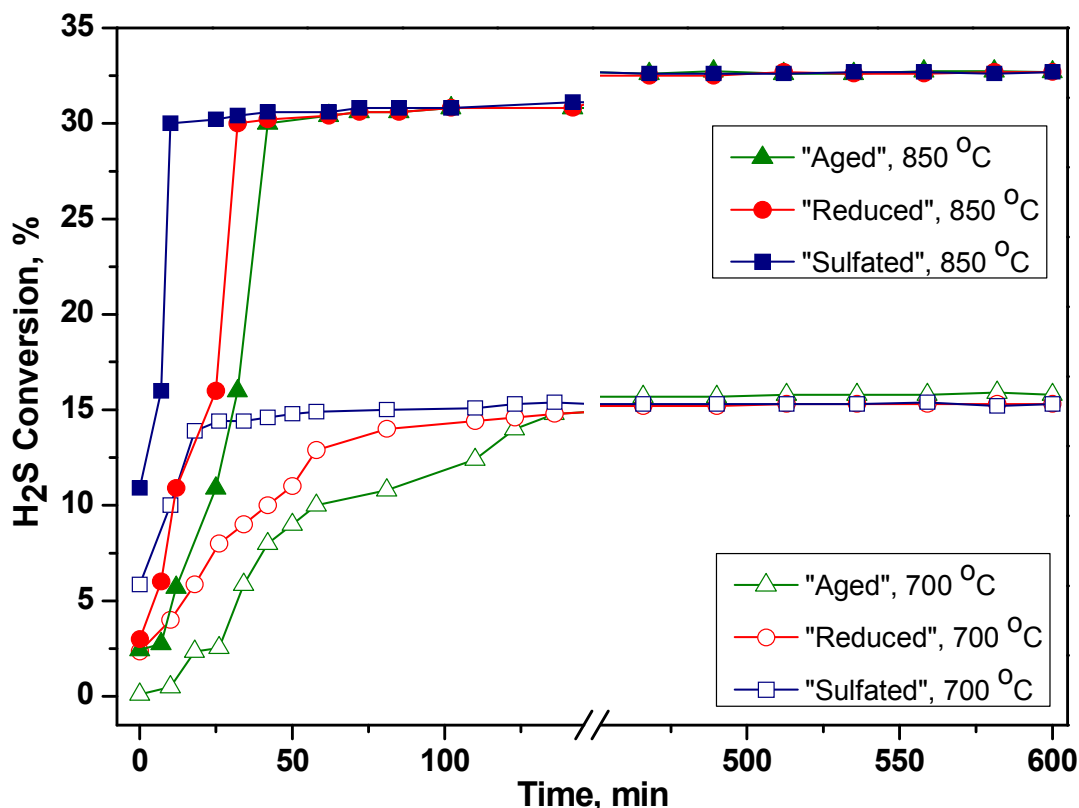


**Figure 5.18:** Stability performance ( $\text{H}_2\text{S}$  conversion vs. time on stream) at  $T = 700$  and  $850\text{ }^\circ\text{C}$  over "Aged", "Reduced" and "Sulfated" optimum 20 wt.% Co/CeO<sub>2</sub> catalysts, during the  $\text{H}_2\text{S}$  decomposition reaction. Reaction conditions: 1 v/v%  $\text{H}_2\text{S}$ , balanced with Ar; Total flow rate =  $100\text{ cm}^3/\text{min}$ ; Catalysts mass = 250 mg; GHSV =  $13,500\text{ h}^{-1}$ .

## 5.7 "AGED" OPTIMUM 20 wt.% Co/CeO<sub>2</sub> CATALYSTS CHARACTERIZATION

For further investigation, a complementary characterization study using BET, XRD, SEM, XPS and elemental analyses, was carried out over the "aged" catalysts (the catalyst is initially exposed to pure argon, during the reactor heat-up to the set-point temperature ( $850\text{ }^\circ\text{C}$ ) and then at  $t = 0\text{ min}$  (Figure 5.16) exposed to the standard feed mixture (1 v/v%  $\text{H}_2\text{S}$ , balanced

with Ar, for 10 hr). It should be highlighted that the catalyst “sulfation” under the above reaction conditions resulted in the pore catalyst structure to practically collapse. More specifically, the BET area and the pore volume values of the “Aged” 20 wt.% Co/CeO<sub>2</sub> catalyst decreased to about 0.9 m<sup>2</sup>/g and 0.04 cm<sup>3</sup>/g, respectively, from 33.4 m<sup>2</sup>/g and 0.1 cm<sup>3</sup>/g, which are the respective values of the “Fresh” catalyst (as prepared). In direct correlation with the previously discussed remarkable stability of the “Aged” or “Sulfated” 20 wt.% Co/CeO<sub>2</sub> catalysts, the above results clearly indicate that additional factors, beyond the textural characteristics, could govern the overall catalytic performance.

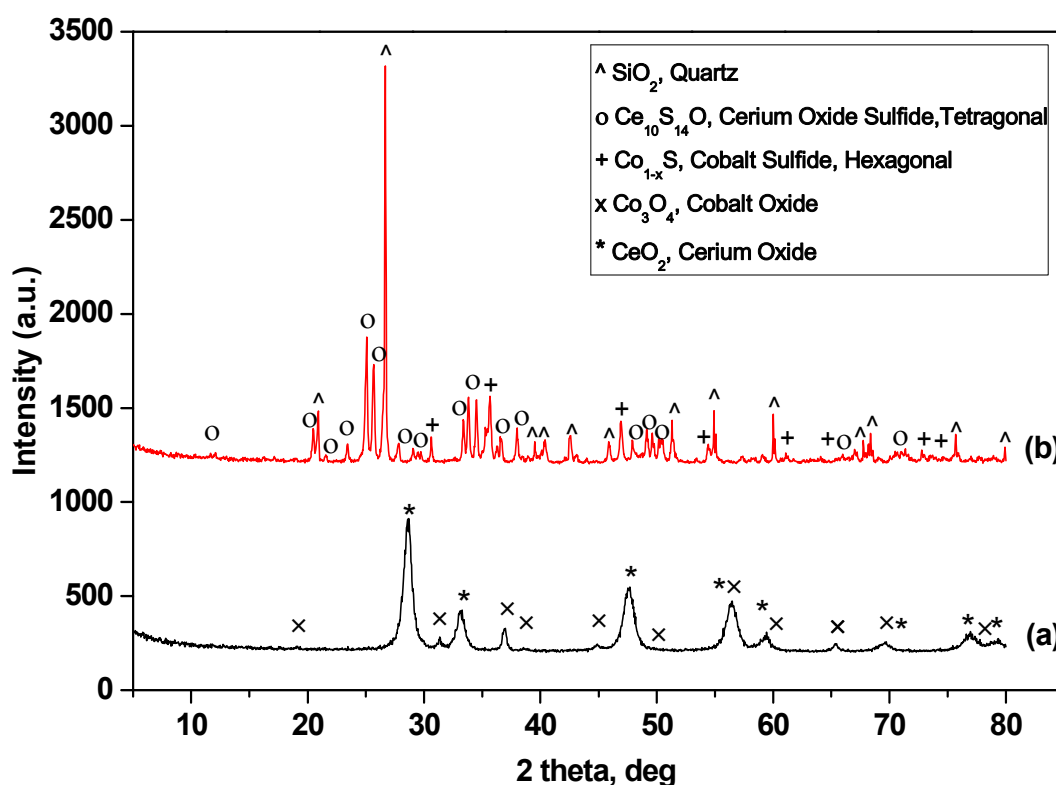


**Figure 5.19:** X-ray diffraction patterns of the a) “Fresh” and b) “Aged” optimum 20 wt.% Co/CeO<sub>2</sub> catalysts, exposed for 10 h in a reaction mixture containing 1 v/v% H<sub>2</sub>S, balanced with Ar, at T = 850 °C.

By the comparison of the XRD spectra of “Fresh” and “Aged” 20 wt.% Co/CeO<sub>2</sub> catalysts, as they are depicted in Figure 5.19, it can be clearly identified that totally new crystal structures are formed during the H<sub>2</sub>S decomposition reaction, which are absent from the “Fresh” samples. Specifically, cobalt oxide (Co<sub>3</sub>O<sub>4</sub>) and cerium oxide (CeO<sub>2</sub>) were converted into Co<sub>1-x</sub>S<sub>y</sub> of hexagonal structure and Ce<sub>10</sub>S<sub>14</sub>O<sub>y</sub> of tetragonal structure, respectively. These

modifications were further verified by the SEM images, illustrated in Figure 5.20. As can be seen, the size of the “aged” particles slightly increased, compared to the “fresh” catalyst particles, potentially implying the mild sintering of the catalyst. Furthermore, the EDS analysis and the relevant elemental mapping revealed a significant amount of sulfur, present in the catalyst sample (Figure 5.21). The latter could be accounted for the excellent performance of 20 wt.% Co/CeO<sub>2</sub> catalyst under reaction conditions at 850 °C for 10 h (Figure 5.16).

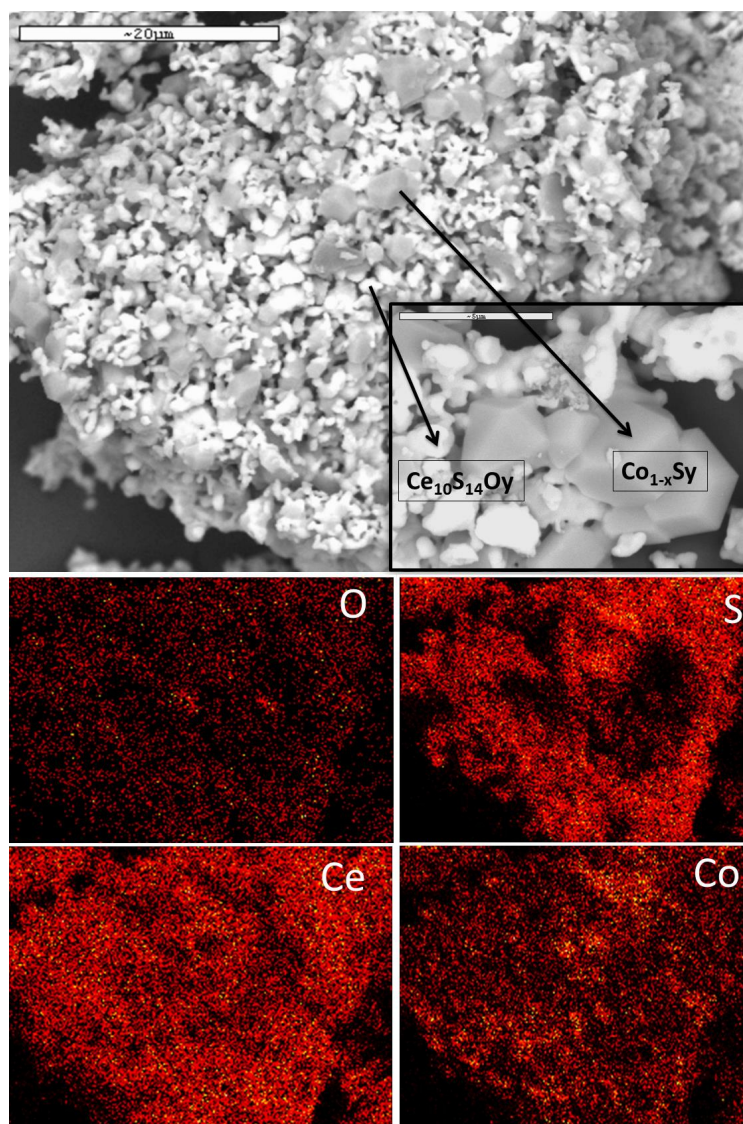


**Figure 5.20:** SEM images and elemental mapping of the “Aged” optimum 20 wt.% Co/CeO<sub>2</sub> catalyst, exposed for 10 h in a reaction mixture containing 1 v/v% H<sub>2</sub>S, balanced with Ar, at T = 850 °C.

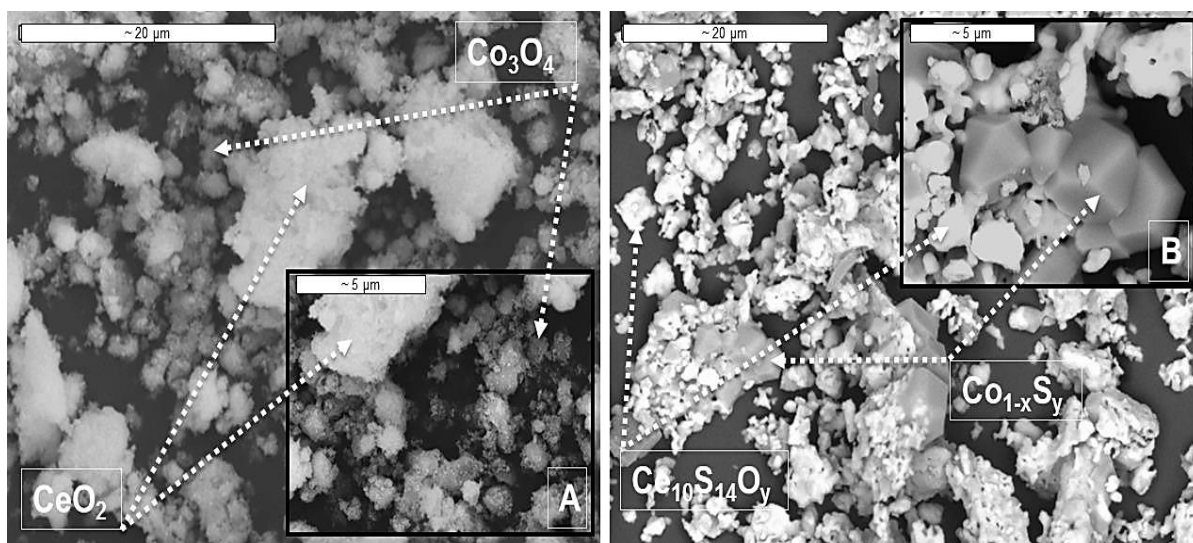


**Figure 5.21:** SEM images of the A) “fresh” and B) “aged” optimum 20 wt.% Co/CeO<sub>2</sub> catalyst, exposed for 10 h in a reaction mixture containing 1 v/v% H<sub>2</sub>S, balanced with Ar, at 850 °C.

In addition, the in-situ formation of the cobalt- and ceria-sulfated phases was also confirmed by the comparison of the XPS spectra of the “fresh” and “aged” 20 wt.% Co/CeO<sub>2</sub> samples. More specifically, Figure 5.22(a) depicts the Ce3d spectra of “fresh” (as-prepared) and “aged” (exposed to the reaction mixture, consisting of 1 v/v% H<sub>2</sub>S/Ar for 10 h, at 850 °C) 20 wt.% Co/CeO<sub>2</sub> catalysts. Through the automatic curve-fitting eight species, which correspond to Ce3d<sub>3/2</sub> (u peaks) and Ce3d<sub>5/2</sub> (v peaks) spin-orbit components, were identified. The peaks labeled as v, v' and v''' correspond to the 3d<sub>5/2</sub> level of Ce<sup>4+</sup>, while the u, u' and u''' peaks are assigned to the 3d<sub>3/2</sub> level of Ce<sup>4+</sup>. On the other hand, the v' and u' peaks are related to one of the two possible electron configurations of the final state of the Ce<sup>3+</sup> species. As can be seen, the exposure of the “fresh” sample to the H<sub>2</sub>S-containing stream (“Aged” catalyst) resulted in a considerable increase of v' (886 eV) and u' (905 eV) doublets, attributed to the Ce<sup>3+</sup> species, at the expense of Ce<sup>4+</sup> components. This clearly demonstrates the interaction of H<sub>2</sub>S with CeO<sub>2</sub>, towards the formation of sulfates, resulting also in the reduction of Ce<sup>4+</sup> surface cations to Ce<sup>3+</sup>. Similar results have been also reported previously, when investigating the interaction of SO<sub>2</sub>/O<sub>2</sub> gas mixtures with bare ceria (Ferrizz et al., 2002) or Co<sub>3</sub>O<sub>4</sub>/CeO<sub>2</sub> mixed oxides (Xiaoyan et al., 2014). Moreover, Figure 5.22(b) presents the corresponding Co2p spectra of the catalyst samples. The spectrum of the 20 wt.% Co/CeO<sub>2</sub>-“fresh” sample is characterized by a main Co2p<sub>3/2</sub> peak at ca. 781 eV, accompanied by a low intensity satellite and a spin-orbit Co2p<sub>1/2</sub>-Co2p<sub>3/2</sub> splitting of about 15 eV. These

characteristic features can be attributed to the presence of the  $\text{Co}_3\text{O}_4$  phase (Konsolakis et al., 2015). Furthermore, the effect of  $\text{H}_2\text{S}$  on the 20 wt.%  $\text{Co}/\text{CeO}_2$  catalyst results in the shifting of the  $\text{Co}2p_{3/2}$  peak to ca. 779 eV, which clearly indicates the formation of cobalt sulfide (Mingyang et al., 2015; Jong et al., 1996).

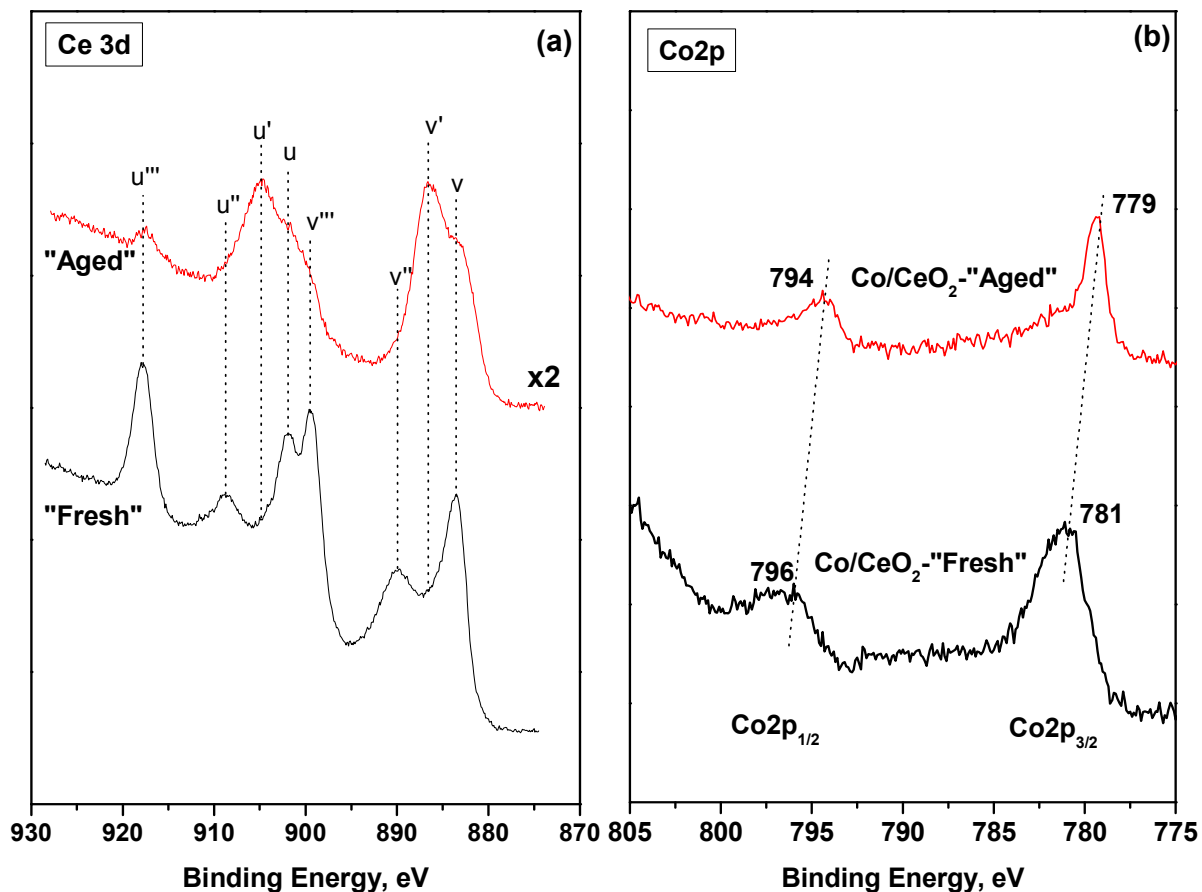


**Figure 5.22:** Ce3d (a) and Co2p (b) spectra of “fresh” and “aged” optimum 20 wt.%  $\text{Co}/\text{CeO}_2$  catalysts.

To further explore the dynamic of the sulfation process, the sulfur content of “aged” catalyst samples, under different exposure time periods to the reacting mixture, was also determined. It was found that for the catalyst used in the stability experiments (exposure times equal to 4 and 8 h), the S content approximately doubled from 7.2% to 15.9%, respectively, suggesting that initially the sulfation process is linearly progressed. However, this linear correlation was not verified upon the catalyst exposure to the  $\text{H}_2\text{S}$ -containing reacting mixture for 24 h. In this case, the S content was equal to 18.2%, indicating that its deposition on the catalyst surface is not linearly dependent on the exposure time, though

interacts with both catalysts' counterparts, as it was already suggested by the XRD, SEM and XPS findings. As a result, it can be concluded that the produced elemental sulfur is not simply deposited on the catalyst surface, but interacts with the catalyst's components, thus, forming new active and stable phases that contribute to the superior performance of the 20 wt.% Co/CeO<sub>2</sub> catalysts. In addition, the positive effect of the in-situ catalyst reduction by the generated hydrogen, could further improve the activity and stability performance of the 20 wt.% Co/CeO<sub>2</sub> catalysts, during the H<sub>2</sub>S decomposition reaction.

## REFERENCES

- Al-Musa A., Al-Saleh M., Ioakeimidis Z.C., Ouzounidou M., Yentekakis I.V., Konsolakis M., Marnellos G.E. (2014). Hydrogen production by iso-octane steam reforming over Cu catalysts supported on rare earth oxides (REOs). *International Journal of Hydrogen Energy*, 39: pp. 1350-1363.
- Ayastuy J.L., Gurbani A., Gonzalez-Marcos M.P., Gutierrez- Ortiz M.A. (2012). Selective CO oxidation in H<sub>2</sub> streams on CuO/Ce<sub>x</sub>Zr<sub>1-x</sub>O<sub>2</sub> catalysts: correlation between activity and low temperature reducibility. *International Journal of Hydrogen Energy*, 37: pp. 1993-2006.
- Bechara R., Balloy D., Vanhove D. (2001). Catalytic properties of Co/Al<sub>2</sub>O<sub>3</sub> system for hydrocarbon synthesis. *Applied Catalysis A: General*, 207: pp. 343-353.
- Binoist M., Labégorre B., Monnet F., Clark P.D., Dowling N.I., Huang M., Archambault D., Plasari E., Marquaire P.-M. (2003). Kinetic study of the pyrolysis of H<sub>2</sub>S. *Industrial and Engineering Chemistry Research*, 42: pp. 3943-3951.
- Breen B., Ross J.R.H. (1999). Methanol reforming for fuel-cell applications: development of zirconia-containing Cu-Zn-Al catalysts. *Catalysis Today*, 511: pp. 521-533.
- Caputo T., Lisi L., Pirone R., Russo G. (2008). On the role of redox properties of CuO/CeO<sub>2</sub> catalysts in the preferential oxidation of CO in H<sub>2</sub>-rich gases. *Applied Catalysis A: General*, 348: pp. 42-53.
- Carabineiro S.A.C., Bastos S.S.T., Orfao J.J.M., Pereira M.F.R., Delgado J.J., Figueiredo J.L. (2010). Exotemplated ceria catalysts with gold for CO oxidation. *Applied Catalysis A: General*, 381: pp. 150-160.
- Carabineiro S.A.C., Bogdanchikova N., Avalos-Borja M., Pestryakov A., Tavares .B., Figueiredo J.L. (2011). Gold supported on metal oxides for carbon monoxide oxidation. *Nano Research*, 4: pp. 180-193.
- Gálvez M.E., Ascaso S., Stelmachowski P., Legutko P., Kotarba A., Moliner R., Lázaro M.J. (2014). Influence of the surface potassium species in Fe-K/Al<sub>2</sub>O<sub>3</sub> catalysts on the soot oxidation activity in the presence of NO<sub>x</sub>. *Applied Catalysis B*, 152-153: pp. 88-98.
- Gamarrá D., Munuera G., Hungria A.B., Fernandez-Garcia M., Conesa J.C., Midgley P.A., Wang X.Q., Hanson J.C., Rodríguez J.A., Martínez-Arias A. (2007). Structure-activity relationship in nanostructured copper-ceria-based preferential CO oxidation catalysts. *The Journal of Physical Chemistry C*, 111: pp. 11026-11038.
- Ferrizz R.M., Gorte R.J., Vohs J.M. (2002). TPD and XPS Investigation of the Interaction of SO<sub>2</sub> with Model Ceria Catalysts. *Catalysis Letters*, 82: pp. 123-129.

- Gomez L.E., Boix A.V., Miro E.E. (2013). Co/ZrO<sub>2</sub>, Co/CeO<sub>2</sub> and MnCoCe structured catalysts for COPrO<sub>x</sub>. *Catalysis Today*, 216: pp. 246-253.
- Haneda M., Kintaichi Y., Hamada H. (2002). Surface reactivity of pre reduced rare earth oxides with nitric oxide: new approach for NO decomposition. *Physical Chemistry Chemical Physics*, 4: pp. 3146-3151.
- Hardacre C., Ormerod R.M., Lambert R.M. (1994). Platinum-promoted catalysis by ceria. A study of carbon monoxide oxidation over Pt (111)/CeO<sub>2</sub>. *The Journal of Physical Chemistry*, 98: pp. 10901-10905.
- Ionov A.M. (2001). Clean “as grown” surfaces of Ln<sub>2</sub>CuO<sub>4</sub> and (LnM)<sub>2</sub>CuO<sub>4</sub>(001) single crystals: atomic and electronic structure. *Physics of Low-Dimensional Structures*, 12: pp. 143-154.
- Jong A.M., (San) de Beer V.H.J., Rob van Veen J.A., (Hans) Niemantsverdriet J.W. (1996). Surface science model of a working cobalt-promoted molybdenum sulfide hydrodesulfurization catalyst: characterization and reactivity. *The Journal of Physical Chemistry*, 100: pp. 17722-17724.
- Karan K., Mehrotra A.K., Behie L.A. (1999). On reaction kinetics for the thermal decomposition of hydrogen sulphide. *AIChE Journal*, 45: pp. 383-389.
- Konsolakis M., Ioakeimidis Z. (2014). Surface/structure functionalization of copper-based catalysts by metal-support and/or metal-metal interactions. *Applied Surface Science*, 320: pp. 244-255.
- Konsolakis M., Sgourakis M., Carabineiro S.A.C. (2015). Surface and redox properties of cobalt–ceria binary oxides: On the effect of Co content and pretreatment conditions. *Applied Surface Science*, 341: pp. 48-54.
- Kundakovic L., Flytzani-Stephanopoulos M. (1998). Reduction characteristics of copper oxide in cerium and zirconium oxide systems. *Applied Catalysis A*, 171: pp. 13-29.
- Lamonier C., Bennani A., D’Huysser A., Aboukais A., Wrobel G. (1996). Evidence for different copper species in precursors of copper-cerium oxide catalysts for hydrogenation reactions: An X-ray diffraction, EPR and X-ray photoelectron spectroscopy study. *Journal of the Chemical Society, Faraday Transactions*, 92: pp. 131-136.
- Li D., Liu X., Zhang Q., Wang Ye., Wan H. (2009). Cobalt and copper composite oxides as efficient catalysts for preferential oxidation of CO in H<sub>2</sub>-rich stream. *Catalysis Letters*, 127: pp. 377-385.
- Liotta L.F., Di Carlo G., Pantaleo G., Venezia A.M., Deganello G. (2006). Co<sub>3</sub>O<sub>4</sub>/CeO<sub>2</sub> composite oxides for methane emissions abatement: relationship between Co<sub>3</sub>O<sub>4</sub>-CeO<sub>2</sub> interaction and catalytic activity. *Applied Catalysis B: Environmental*, 66: pp. 217-227.
- Liu W., Flytzani-Stephanopoulos M. (1995). Total oxidation of carbon monoxide and methane over transition metal-fluorite oxide composite catalysts I. Catalyst composition and activity. *Journal of Catalysis*, 153: pp. 304-316.
- Liu X., Yang Y., Zhang J. (1991). Temperature programmed reduction and desorption studies of praseodymium promoted platinum/alumina catalysts. *Applied Catalysis*, 71: pp. 167-184.
- Mai H., Zhang D., Shi L., Li H. (2011). Highly active Ce<sub>1-x</sub>Cu<sub>x</sub>O<sub>2</sub> nanocomposite catalysts for the low temperature oxidation of CO. *Applied Surface Science*, 257: pp. 7551-7559.
- Mingyang X., Helin N., Jinjing H., Jiming S., Changjie M., Shengyi Z., Chengfeng Z., Changle C. (2015). Facile synthesis of graphene-like Co<sub>3</sub>S<sub>4</sub> nanosheet/Ag<sub>2</sub>S nanocomposite with enhanced performance in visible-light photocatalysis, *Applied Surface Science*, 351: pp. 374-381.
- Murata K., Wang L., Saito M., Inaba M., Takahara I., Mimura N. (2004). Hydrogen production from steam reforming of hydrocarbons over alkaline-earth metal-modified Fe- or Ni-based catalysts. *Energy Fuels*, 18: pp. 122-126.

- Nesbitt H.W., Legrand D., Bancroft G.M. (2000). Interpretation of Ni2p XPS spectra of Ni conductors and Ni insulators. *Physics and Chemistry of Minerals*, 27: pp. 357-366.
- Ocampo F., Louis B., Roger A.C. (2009). Methanation of carbon dioxide over nickel-based Ce<sub>0.72</sub>Zr<sub>0.28</sub>O<sub>2</sub> mixed oxide catalysts prepared by sol-gel method. *Applied Catalysis A*, 369: pp. 90-96.
- Papavasiliou J., Avgouropoulos G., Ioannides Th. (2007). Effect of dopants on the performance of CuO-CeO<sub>2</sub> catalysts in methanol steam reforming. *Applied Catalysis B: Environmental*, 69: pp. 226-234.
- Pietrogiacomini D., Campa M.C., Tut S., Indovina V. (2003). CoO<sub>x</sub>/ sulphated-ZrO<sub>2</sub> and CoSO<sub>4</sub>/ZrO<sub>2</sub> as catalysts for the abatement of NO with C<sub>3</sub>H<sub>6</sub> in the presence of excess O<sub>2</sub>. *Applied Catalysis B: Environmental*, 41: pp. 301-312.
- Rao K.N., Venkataswamy P., Reddy B.M. (2011). Structural characterization and catalytic evaluation of supported Copper-Ceria catalysts for soot oxidation. *Industrial & Engineering Chemistry Research*, 50: pp. 11960-11969.
- Reddy G.K., Boolchand P., Smirniotis P.G. (2011). Sulfur tolerant metal doped Fe/Ce catalysts for high temperature WGS reaction at low steam to CO ratios-XPS and Mössbauer spectroscopic study. *Journal of Catalysis*, 282: pp. 258-269.
- Santos V.P., Carabineiro S.A.C., Bakker J.J.W., Soares O.S.G.P., Chen X., Pereira M.F.R., Órfão J.J.M., Figueiredo J.L., Gascon J., Kapteijn F. (2014). Stabilized gold on cerium-modified cryptomelane: highly active in low-temperature CO oxidation. *Journal of Catalysis*, 309: pp. 58-65.
- Takeda H., Okuno M., Ohgaki M., Yamashita K., Matsumoto T. (2000). Crystal growth and structure analysis of Sm<sub>2-x</sub>Ce<sub>x</sub>CuO<sub>4</sub>. *Journal of Materials Research*, 15: pp. 1905-1910.
- Turco M., Bagnasco G., Cammarano C., Senese P., Costantino U., Sisani M. (2007). Cu/ZnO/Al<sub>2</sub>O<sub>3</sub> catalysts for oxidative steam reforming of methanol: the role of Cu and the dispersing oxide matrix. *Applied Catalysis B: Environmental*, 77: pp. 46-57.
- Xiaoyan S., Yunbo Y., Li X., Hong H. (2014). Effect of sulfur poisoning on Co<sub>3</sub>O<sub>4</sub>/CeO<sub>2</sub> composite oxide catalyst for soot combustion. *Chinese Journal of Catalysis*, 35: pp. 1504-1510.
- Yu S.W., Huang H.H., Tang C.W., Wang C.B. (2014). The effect of accessible oxygen over Co<sub>3</sub>O<sub>4</sub>-CeO<sub>2</sub> catalysts on the steam reforming of ethanol. *International Journal of Hydrogen Energy*, 39: pp. 20700-20711.
- Varga E., Pusztai P., Óvári L., Oszkó A., Erdohelyi A., Papp C., Steinrück H.P., Kónya Z., Kiss J. (2015). Probing the interaction of Rh, Co and bimetallic Rh-Co nanoparticles with the CeO<sub>2</sub> support: Catalytic materials for alternative energy generation. *Physical Chemistry Chemical Physics*, 17: pp. 27154-27166.
- Vári G., Óvári L., Papp C., Steinrück H.P., Kiss J., Kónya Z. (2015). The interaction of cobalt with CeO<sub>2</sub>(111) prepared on Cu(111). *Journal of Physical Chemistry C*, 119: pp. 9324-9333.
- Zhang C., Li S., Wu G., Gong J. (2014). Synthesis of stable Ni-CeO<sub>2</sub> catalysts via ball-milling for ethanol steam reforming. *Catalysis Today*, 233: pp. 53-60.
- Zyryanova M.M., Snytnikov P.V., Gulyaev R.V., Amosov Yu I., Boronin A.I., Sobyanin V.A. (2014). Performance of Ni/CeO<sub>2</sub> catalysts for selective CO methanation in hydrogen-rich gas. *Chemical Engineering Journal*, 238: pp. 189-197.



# CHAPTER

# 6

## H<sub>2</sub>S CATALYTIC DECOMPOSITION IN THE PRESENCE OF H<sub>2</sub>O

Contents	Page
6.1. Introduction. . . . .	177
6.2. Characterization studies. . . . .	177
6.3. Catalytic evaluation studies. . . . .	178
6.4. Stability tests over the optimum catalytic system. . . . .	182
6.5. 30 wt.% Co/CeO <sub>2</sub> "Sulfated" catalyst characterization. . . . .	186
6.6. References. . . . .	190



## 6.1. INTRODUCTION

In Chapter 6, and prior to the electrochemical tests, the evaluation of the optimum (i.e., efficient and stable) catalytic system, which will be applied as the anode electrode in the proton H<sup>+</sup> conducting solid electrolyte electrochemical membrane reactor, is performed. More specifically, the H<sub>2</sub>S decomposition reaction towards H<sub>2</sub> production is examined in the presence of excess H<sub>2</sub>O, under the proposed and simulated Black Sea conditions. In this context, a series of CeO<sub>2</sub>-supported Co catalysts (Co/CeO<sub>2</sub>), were synthesized and evaluated, in terms of their catalytic activity and stability, during the H<sub>2</sub>S decomposition reaction towards hydrogen in the presence of H<sub>2</sub>O (90 v/v%). The effects of key parameters, namely, i) feed stream composition, ii) temperature (550-850 °C), and iii) Co loading (0-100 wt.%) on the activity and stability of Co/CeO<sub>2</sub> catalysts, were thoroughly investigated. Furthermore, the selected as optimum catalysts were examined in kinetic experiments, in order to estimate the apparent activation energy and the partial reactions orders. In addition, characterization studies, involving BET, XRD, SEM/EDX, XPS and sulfur elemental analysis were performed over both the “Fresh” and “Sulfated” samples, to gain insight into potential structure-activity correlations.

## 6.2. CHARACTERIZATION STUDIES

The main textural (BET surface area, total pore volume and average pore diameter) characteristics of the as prepared Co/CeO<sub>2</sub> catalysts, with different Co loadings (0-100 wt.%) are displayed in Table 6.1. As can be seen, the superiority of the CeO<sub>2</sub> catalyst, in terms of its BET surface area (71.5 m<sup>2</sup>/g) and total pore volume (0.27 cm<sup>3</sup>/g) values, is clear. It is obvious that the incorporation of Co into the ceria support presents a detrimental effect on both BET surface and pore volume. More specifically, the 30 wt.% Co/CeO<sub>2</sub> catalyst possesses the optimum textural characteristics (largest surface area, 44.9 m<sup>2</sup>/g, and total pore volume, 0.21 cm<sup>3</sup>/g). The progressive addition of cobalt at loadings higher than 30 wt.%, results in the decrease of the catalyst BET surface area and total pore volume. In the case of 60 and 100 wt.% Co-based catalysts, the measured values of surface area (i.e., 15.1 and 2.93 m<sup>2</sup>/g, respectively) and total pore volume (i.e., 0.07 and 0.01 cm<sup>3</sup>/g, respectively) were the lowest ones. The observed trend in textural characteristics can be attributed to the different

crystallite sizes of  $\text{Co}_3\text{O}_4$  and  $\text{CeO}_2$  phases determined by the XRD analysis, which differ by changing the Co loadings, and are both present in the Co/ $\text{CeO}_2$  catalysts, as they were determined by the XRD analysis.

**Table 6.1:** Textural properties of Co/ $\text{CeO}_2$  catalysts, with different Co loadings (0-100 wt.%).

Catalysts	Surface Area ( $\text{m}^2/\text{g}$ )	Total pore volume ( $\text{cm}^3/\text{g}$ )	Average pore diameter (nm)
$\text{CeO}_2$	71.5	0.27	15.4
20 wt.% Co/ $\text{CeO}_2$	33.4	0.13	16.0
30 wt.% Co/ $\text{CeO}_2$	44.9	0.21	18.7
40 wt.% Co/ $\text{CeO}_2$	28.4	0.10	14.7
60 wt.% Co/ $\text{CeO}_2$	15.1	0.07	19.3
$\text{Co}_3\text{O}_4$	2.93	0.01	17.8

Figure 6.1 depicts the XRD spectra of Co-based catalysts of different Co loadings (0-100 wt.%), while Table 6.2 lists the phases that were detected for each sample and the approximate crystallite sizes, as determined through the Scherrer analysis. In principle, all catalysts crystallized in the form of their respective oxides. Moreover, in the Co-based catalysts of different metal contents, cobalt was also present in the form of oxide ( $\text{Co}_3\text{O}_4$ ), regardless of the Co loading. The 100 wt.% Co loading constitutes an exception, as both  $\text{Co}_3\text{O}_4$  and  $\text{CoO}$  phases were detected in the catalyst sample. It should be noted that the crystallite size of  $\text{CeO}_2$  remains approximately constant upon the increase of the Co content. On the other hand, the size of the  $\text{Co}_3\text{O}_4$  phase increased from 37.7 to 42.4 nm along with the increase of the Co content from 20 to 60 wt.%, implying the partial segregation of Co metal entities, as the Co loading increases.

## 6.3. CATALYTIC EVALUATION STUDIES

### 6.3.1. Effect of the Reaction Conditions

Initially, as can be seen in Figure 6.2, blank (i.e., without the presence of a catalyst) experiments were performed using two different feedstock compositions (i.e., 1 v/v%  $\text{H}_2\text{S}$ ,

90 v/v% H<sub>2</sub>O, balanced with Ar, and 90 v/v% H<sub>2</sub>O, balanced with Ar) at the temperature range of 550-850 °C. In these experiments, the monitored parameter was the production rate of H<sub>2</sub>, while, for comparison purposes, the H<sub>2</sub> production rate obtained in the absence of excess H<sub>2</sub>O (i.e., 1 v/v% H<sub>2</sub>S, balanced with Ar), was also included in the figure. It is clearly revealed that the H<sub>2</sub>O conversion was negligible, both in the absence or presence of the catalyst (bare CeO<sub>2</sub>), for the 90 v/v% H<sub>2</sub>O feedstock composition. However, it can be stated that the combined presence of H<sub>2</sub>S and H<sub>2</sub>O in the reaction feedstock mixture (1 v/v% H<sub>2</sub>S, 90 v/v% H<sub>2</sub>O balanced with Ar), enhances the production rate of H<sub>2</sub>, as it was already predicted by the thermodynamic simulations (Figure I.2.A, Part I).

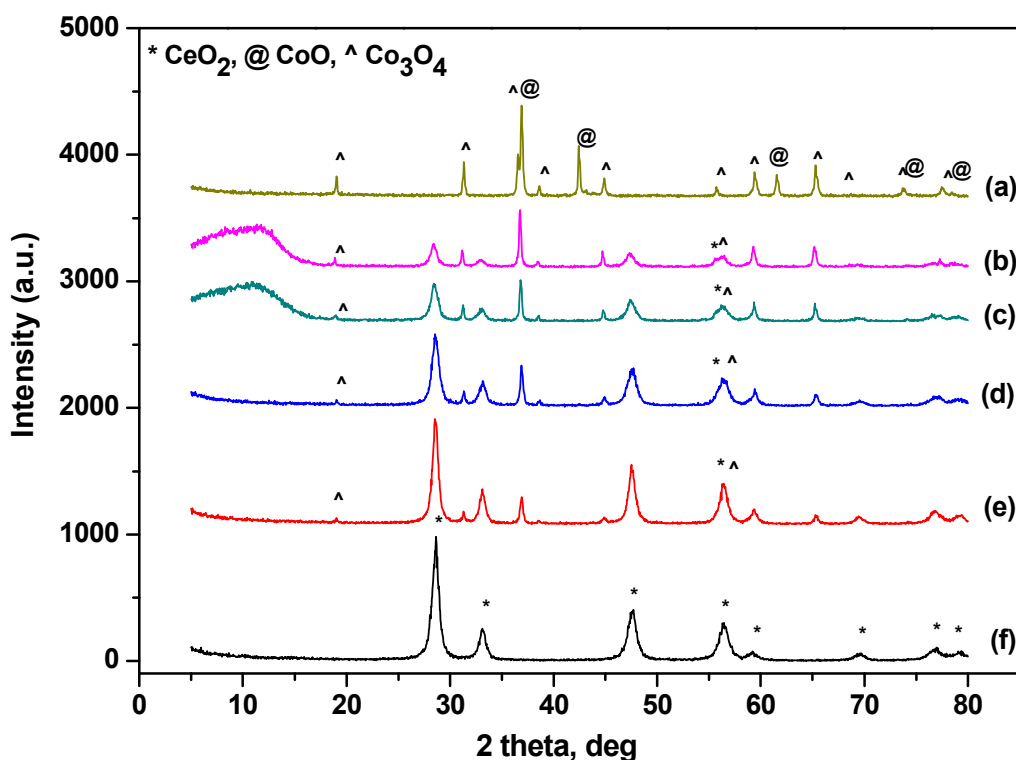


**Figure 6.1:** X-ray powder diffraction patterns of Co/CeO<sub>2</sub> catalysts with 100 (a), 60 (b), 40 (c), 30 (d), 20 (e), 0 (f), wt.% Co loading.

### 6.3.2. Effect of Co-Loading (0-100 wt.%)

Figure 6.3 illustrates the effect of the Co loading on the H<sub>2</sub> production rate (μmol/s·g) at the temperature range of 600-850 °C. It is evident that in the selected temperature range, the H<sub>2</sub> production rate strongly depends on Co loading and temperature. Note that in the absence of Co (bare CeO<sub>2</sub>), the H<sub>2</sub> production rate (at 600-700 °C) was significantly smaller than the

respective H<sub>2</sub> production rate, when Co/CeO<sub>2</sub> catalysts were employed. Moreover, the superior behavior of the 30 wt.% Co/CeO<sub>2</sub> catalyst, in the entire temperature range, should be highlighted. Finally, in the cases of 40 wt.% and 60 wt.% Co loading the catalytic performance was similar, while in the case of 100 wt.% Co loading (bare Co<sub>3</sub>O<sub>4</sub>), the H<sub>2</sub> production rate was substantially decreased; e.g., at T = 750 °C it is approximately 50% of the maximum value, obtained with the optimum 30 wt.% Co/CeO<sub>2</sub> catalyst.

**Table 6.2:** Structural characteristics of Co/CeO<sub>2</sub> catalysts with different Co loadings (0-100 wt.%).

Catalysts	Detected phase	Crystallite size (nm)
CeO <sub>2</sub>	CeO <sub>2</sub>	11.0
20 wt.% Co/CeO <sub>2</sub>	CeO <sub>2</sub>	10.2
	Co <sub>3</sub> O <sub>4</sub>	37.7
30 wt.% Co/CeO <sub>2</sub>	CeO <sub>2</sub>	10.4
	Co <sub>3</sub> O <sub>4</sub>	37.9
40 wt.% Co/CeO <sub>2</sub>	CeO <sub>2</sub>	10.5
	Co <sub>3</sub> O <sub>4</sub>	41.7
60 wt.% Co/CeO <sub>2</sub>	CeO <sub>2</sub>	10.5
	Co <sub>3</sub> O <sub>4</sub>	42.2
Co <sub>3</sub> O <sub>4</sub>	Co <sub>3</sub> O <sub>4</sub>	50.7
	CoO	52.7

### 6.3.3. Comparison of Optimum Catalytic Systems in the Absence/Presence of H<sub>2</sub>O

In Figure 6.4, the H<sub>2</sub> production rate of bare CeO<sub>2</sub> is compared with the rate of the 20 and 30 wt.% Co/CeO<sub>2</sub> catalysts, both in the absence and presence of excess H<sub>2</sub>O. The results clearly indicate the superiority of Co/CeO<sub>2</sub> catalysts, under both dry and wet conditions. More specifically, the 20 wt.% Co/CeO<sub>2</sub> catalyst exhibited the optimum performance in the absence of H<sub>2</sub>O, being, however, similar to that obtained by 30 wt.% Co/CeO<sub>2</sub>. On the other hand, the 30 wt.% Co/CeO<sub>2</sub> clearly demonstrated the optimum performance in the presence of H<sub>2</sub>O. This suggests that a specific Co loading is required to achieve the optimum performance, depending on the reactions conditions.

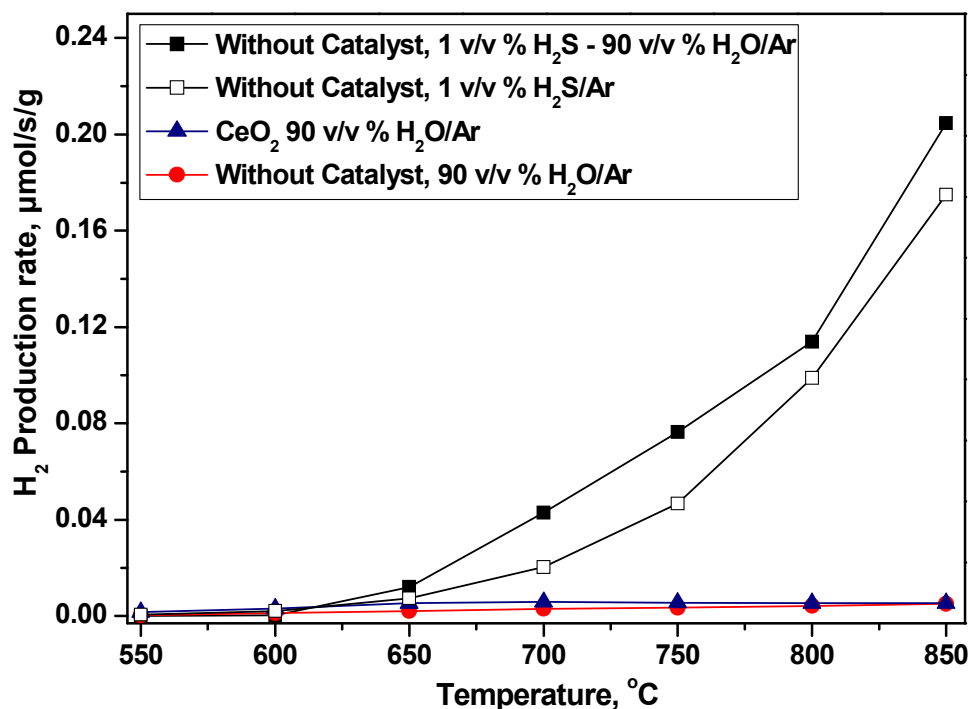


**Figure 6.2:** Hydrogen production rate as a function of temperature and feedstock composition for blank experiments (without catalyst) and bare CeO<sub>2</sub> catalyst. Reaction conditions: **Without H<sub>2</sub>O:** 1 v/v% H<sub>2</sub>S, balanced with Ar, and **H<sub>2</sub>O Addition:** 1 v/v% H<sub>2</sub>S - 90 v/v% H<sub>2</sub>O, balanced with Ar and 90 v/v% H<sub>2</sub>O, balanced with Ar; Catalyst mass = 250 mg; Total flow rate = 100 cm<sup>3</sup>/min.

Generally, as it was already highlighted previously (see Figure 6.2), the catalytic performance of all samples was notably enhanced in the presence of H<sub>2</sub>O, in line with the thermodynamic calculations (Marrocchelli and Yilidiz, 2012; Carroll et al., 1991; Lee et al., 1977). The latter can be ascribed to the additional amount of H<sub>2</sub>, which is produced via the reaction (Luinstra, 1996):



Thus, H<sub>2</sub> is derived from the thermal and catalytic H<sub>2</sub>S decomposition reactions, both favored by excess H<sub>2</sub>O.

Interestingly, the comparison of the 20 and 30 wt.% Co/CeO<sub>2</sub> catalysts with bare CeO<sub>2</sub>, reveals their similar performance, especially under “dry” conditions (Figure 6.4). As a result, it can be concluded that CeO<sub>2</sub> plays a major role in the deH<sub>2</sub>S process (Laosiripojana and Assabumrungrat, 2006; Konsolakis et al., 2015; Xiaoyan et al., 2014). However, taking into account that the selected catalyst will be applied as anodic electrode in the proton conducting membrane reactor, the incorporation of the Co phase into the catalyst is

considered necessary to ensure the high electronic conductivity of the electrode (Gang et al., 2007; Kaklidis et al., 2011; Chivers et al., 1980). Moreover, under “wet” conditions the superiority of Co-loaded catalysts is evident, justifying their selection as anodic electrodes.

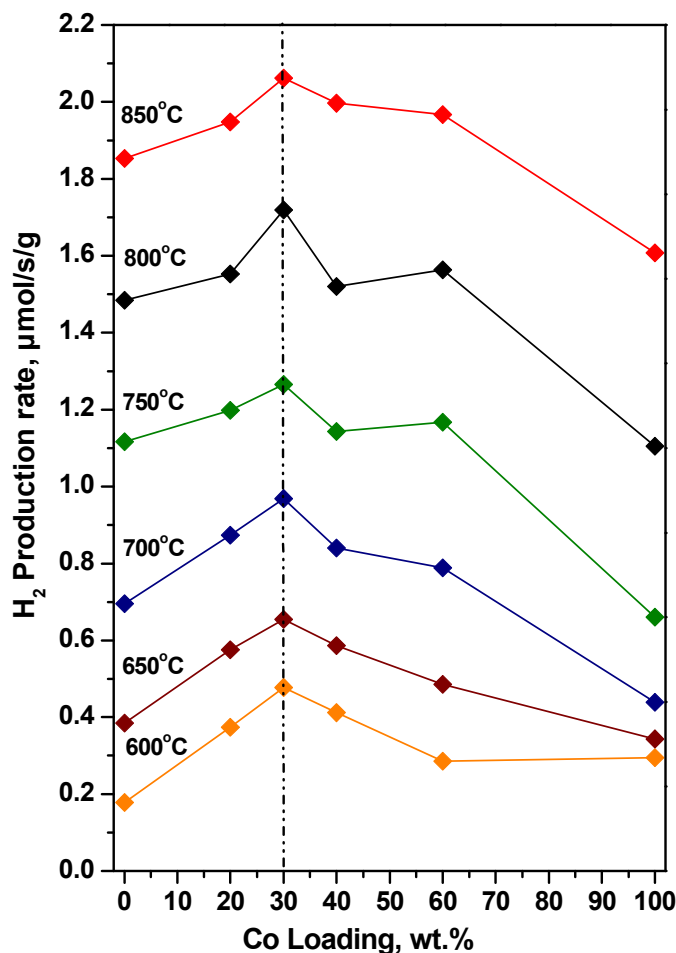


**Figure 6.3:** Hydrogen production rate as a function of temperature and catalyst Co-loading. Reaction conditions: 1 v/v%  $H_2S$  - 90 v/v%  $H_2O$ , balanced with Ar; Catalyst mass = 250 mg; Total flow rate =  $100\text{ cm}^3/\text{min}$ .

#### 6.4. STABILITY TESTS OVER THE OPTIMUM CATALYTIC SYSTEM

Having established, through the activity tests in excess  $H_2O$  presence, the superiority of the 30 wt.% Co/ $CeO_2$  catalyst, long term (10 h) stability experiments were then carried out to assess the impact of time on stream on the “Aged”, “Reduced” and “Sulfated” catalysts lifetime characteristics. In this regard, the  $H_2$  production rate was continuously monitored as a function of time on stream. All experiments were carried out at  $T = 850\text{ °C}$  under exactly the

same conditions (1 v/v% H<sub>2</sub>S - 90 v/v% H<sub>2</sub>O, balanced with Ar), used in the activity experiments. In these experiments, “Aged” refers to the catalyst which was initially exposed to pure argon, during the reactor heat-up to the set-point temperature (850 °C) and then at t = 0 min (Figure 6.5) is pre-sulfated by its exposure to the standard feedstock mixture (1 v/v% H<sub>2</sub>S - 90 v/v% H<sub>2</sub>O, balanced with Ar) inside the reactor. As can be seen in Figure 6.5, after the initial activation period (approximately 3 h), the H<sub>2</sub> production rate over the optimum “Aged” 30 wt.% Co/CeO<sub>2</sub> catalyst was stabilized at 2.4 μmol/g·s, a value similar to the one indicated by the activity experiments (Figure 6.3), and remained stable until the end of the 10 h period of the experiment. The respective results obtained with bare CeO<sub>2</sub> were also included to identify the individual role of Co and CeO<sub>2</sub> in the process. Despite the larger initial H<sub>2</sub> production rate observed for bare CeO<sub>2</sub>, the catalyst activity was not stable during the stability test. The activity followed a slightly downward trend vs. time on stream, thus implying the major effect of cobalt entities on the stability of the catalytic system.

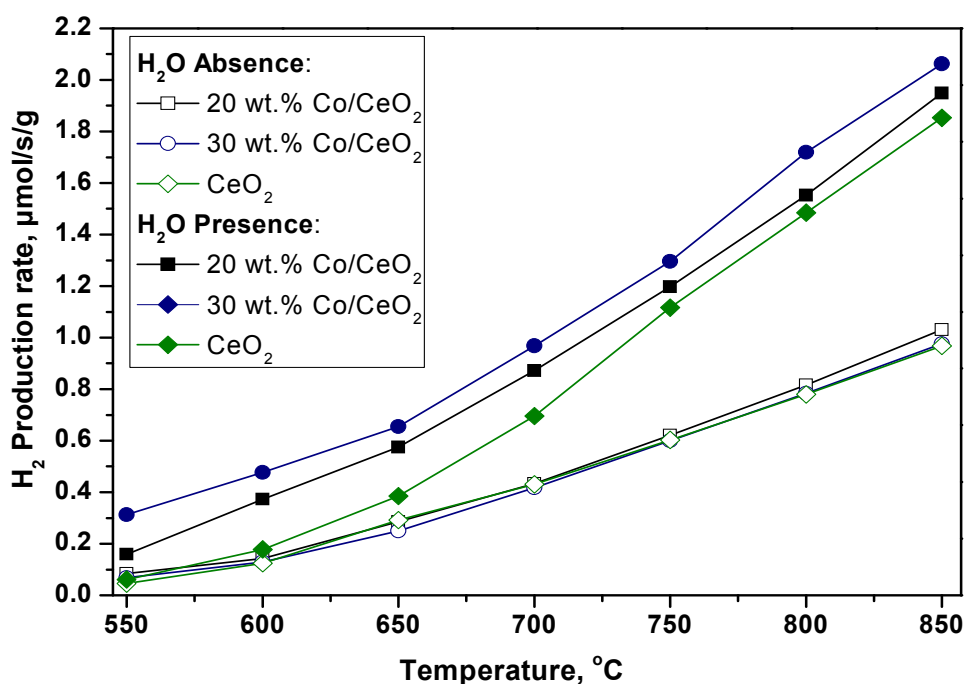


**Figure 6.4:** H<sub>2</sub> production rate as a function of temperature for 20, 30 wt.% Co/CeO<sub>2</sub> and CeO<sub>2</sub> catalysts. Reaction conditions: **Dry:** 1 v/v% H<sub>2</sub>S, balanced with Ar, and **Wet:** 1 v/v% H<sub>2</sub>S - 90 v/v% H<sub>2</sub>O, balanced with Ar; Catalyst mass = 250 mg; Total flow rate = 100 cm<sup>3</sup>/min.

In an attempt to clarify whether the initial activation period (3 h) of the “Aged” 30 wt.% Co/CeO<sub>2</sub> catalyst was due to the in-situ sulfation or reduction of the catalyst during the

reaction, two additional long-term (10 h) experiments were also carried out (Figure 6.6). It should be noted that “Sulfated” refers to 30 wt.% Co/CeO<sub>2</sub> catalyst which was initially pre-sulfated to 1 v/v% H<sub>2</sub>S - 90 v/v% H<sub>2</sub>O, balanced with Ar reaction mixture, for 10 h at T = 850 °C inside the reactor and at t = 0 min the “Sulfated” sample was subjected to the long term stability experiment (10 h at T = 850 °C with 1 v/v% H<sub>2</sub>S - 90 v/v% H<sub>2</sub>O, balanced with Ar). On the other hand, “Reduced” refers to the 30 wt.% Co/CeO<sub>2</sub> catalyst which was initially exposed to reducing conditions (i.e., 10 v/v% H<sub>2</sub>, balanced with argon), inside the reactor while the temperature steadily increased up to the set-point value (850 °C), with a heating rate of 3 °C/min. When the selected temperature was attained and after the application of additional reducing pre-treatment (10 v/v% H<sub>2</sub>, balanced with argon) for 1 h at T = 850 °C, the sample at t = 0 min was also subjected to the long term stability experiment (10 h at T = 850 °C with 1 v/v% H<sub>2</sub>S - 90 v/v% H<sub>2</sub>O, balanced with Ar).

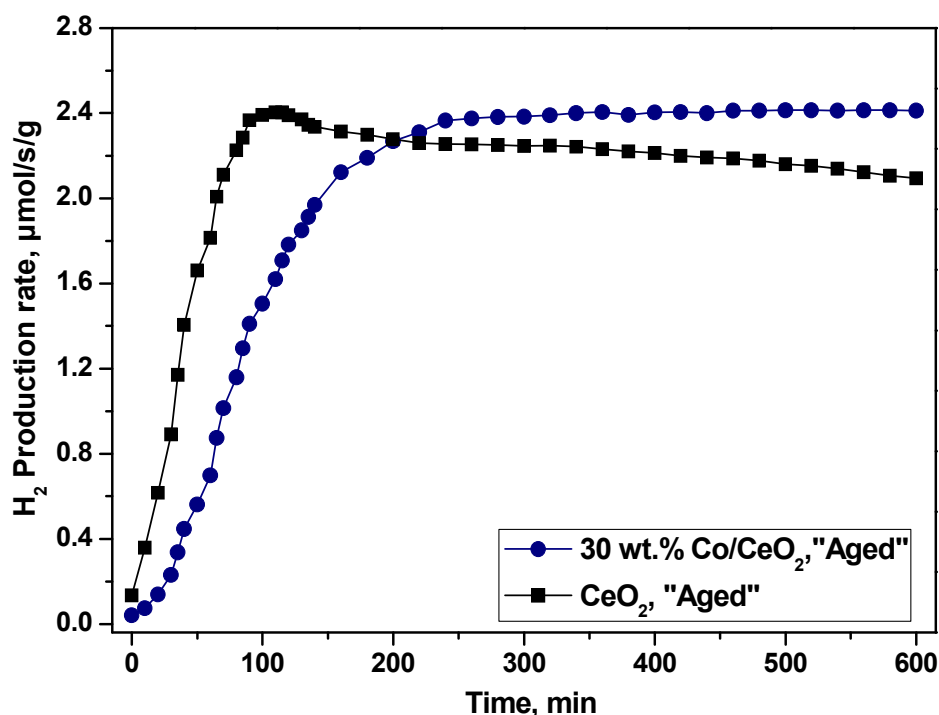


**Figure 6.5:** Hydrogen production rate vs. time on stream (10 h) for “Aged” 30 wt.% Co/CeO<sub>2</sub> and bare CeO<sub>2</sub> catalysts. Reaction conditions = 1 v/v% H<sub>2</sub>S - 90 v/v% H<sub>2</sub>O, balanced with Ar; Catalyst mass = 250 mg; Total flow rate = 100 cm<sup>3</sup>/min.

In general, the comparison of the pretreated catalysts revealed the remarkable behavior of the “Sulfated” 30 wt.% Co/CeO<sub>2</sub> catalyst. It was observed that the initially activation period

of approximately 3 h of the “Aged” 30 wt.% Co/CeO<sub>2</sub> catalyst may be reduced to less than 1.5 h, when the “Sulfated” catalyst was used. This observation indicates that the remarkable stability of the catalyst can be attributed to the in-situ sulfation of the catalyst under the reaction atmosphere. On the other hand, the “Reduced” catalyst required almost 2 h to achieve steady state. Note that, in both cases (“Sulfated” and “Reduced” 30 wt.% Co/CeO<sub>2</sub> catalysts) the H<sub>2</sub> production rate attained a stable value, similar to that indicated by the activity experiments and remained stable until the end of the 10 h duration of the experiment.

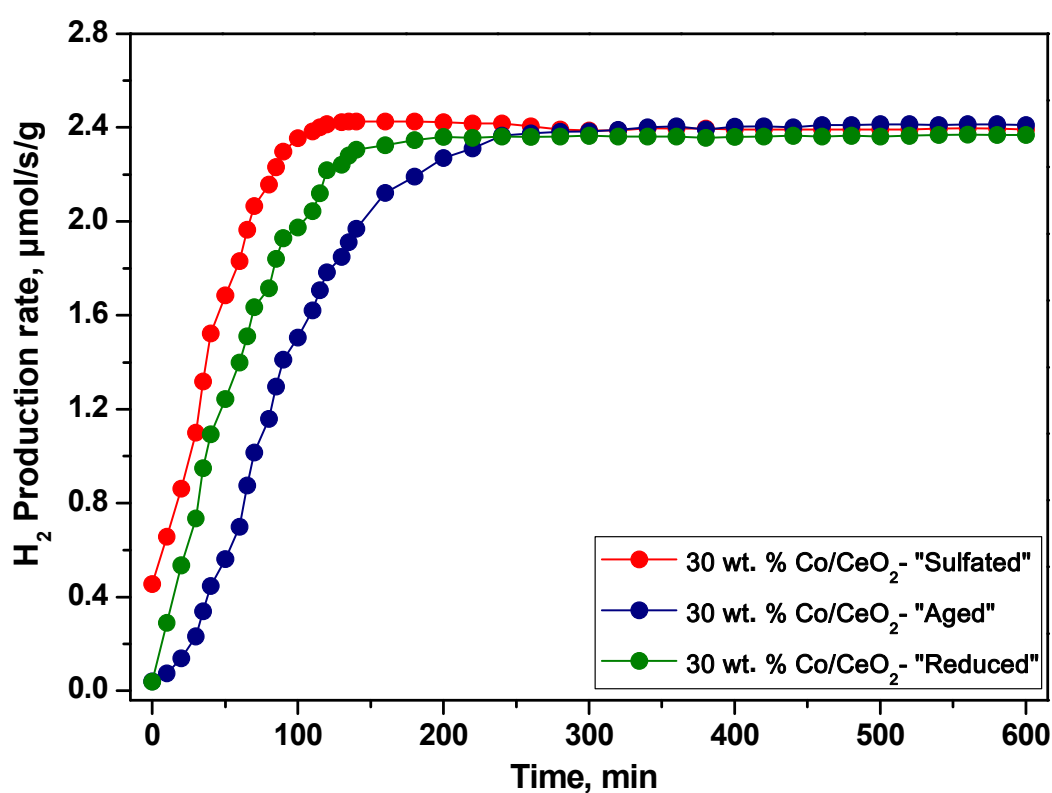


**Figure 6.6:** Hydrogen production rate vs. time on stream (10 h) for “Aged”, “Sulfated” and “Reduced” 30 wt.% Co/CeO<sub>2</sub> catalysts. Reaction conditions = 1 v/v% H<sub>2</sub>S - 90 v/v% H<sub>2</sub>O, balanced with Ar; Catalyst mass = 250 mg; Total flow rate = 100 cm<sup>3</sup>/min.

Based on the above results, it can be concluded that the progressive catalysts sulfation rather than the in-situ reduction was responsible for the initial activation period, as well as, for the remarkable stability which was demonstrated throughout the duration (10 h) of the stability experiments.

## 6.5. 30 wt.% Co/CeO<sub>2</sub> "SULFATED" CATALYST CHARACTERIZATION

In order to gain insight on the impact of the reaction conditions on the textural, structural, morphological and surface features of the employed catalysts, as well as, to identify potential structure-activity correlations, a complementary characterization study of samples, prior and after the stability experiments (BET, XRD, SEM, XPS and sulfur elemental analysis), was carried out. In terms of the textural characteristics, it is worth noticing that the catalysts sulfation under the selected reaction conditions resulted in the collapse of the pore structure; the BET surface area and the pore volume of the "Sulfated" 30 wt.% Co/CeO<sub>2</sub> catalyst decreased to about 2.4 m<sup>2</sup>/g and 0.04 cm<sup>3</sup>/g from 44.9 m<sup>2</sup>/g and 0.21 cm<sup>3</sup>/g of the "Fresh" catalyst (as prepared), respectively. Coupled with the excellent activity and stability performance of the "Sulfated" 30 wt.% Co/CeO<sub>2</sub> catalyst, the deterioration of its morphology clearly indicates that other factors, beyond the textural characteristics, could govern the overall catalytic performance of the system.

By comparing the XRD spectra of the "Fresh" and "Sulfated" 30 wt.% Co/CeO<sub>2</sub> catalysts, as illustrated in Figure 6.7, it can be clearly identified that new crystal structures are formed during the reaction, which were absent from the "Fresh" samples. The XRD spectrum of the "Fresh" sample presents reflections that correspond only to the Co<sub>3</sub>O<sub>4</sub> and CeO<sub>2</sub> oxides, thus verifying that no chemical transformations or interactions between these two oxides occurred up to 600 °C. Moreover, the broad Co<sub>3</sub>O<sub>4</sub>-related peaks observed in the "Fresh" 30 wt.% Co/CeO<sub>2</sub> catalyst indicate that Co<sub>3</sub>O<sub>4</sub> was well distributed on the CeO<sub>2</sub> support. However, the XRD patterns of the "Sulfated" 30 wt.% Co/CeO<sub>2</sub> catalysts were totally different, due to the formation of new crystalline sulfate species during the catalyst sulfidation.

Finally, in the case of the "Sulfated" sample, the CoO phase was also appeared; probably it was formed during the reduction of cobalt oxide by the in-situ produced H<sub>2</sub>, as it is described by the following reaction scheme:



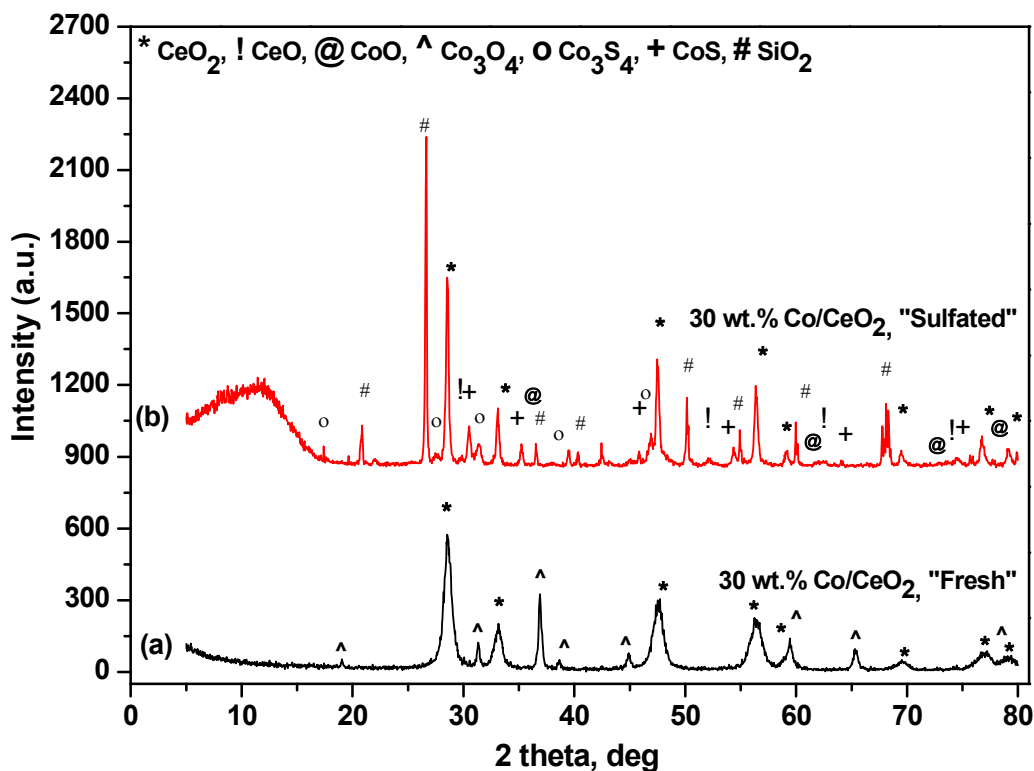


**Figure 6.7:** X-ray diffraction patterns of the a) “Fresh” and b) “Sulfated” optimum 30 wt.% Co/CeO<sub>2</sub> catalysts, exposed for 10 h in a reaction mixture containing 1 v/v% H<sub>2</sub>S - 90 v/v% H<sub>2</sub>O, balanced with Ar, at T = 850 °C.

These surface and structure modifications of the catalysts were further investigated by the SEM images of Figure 6.8, where the micrographs of the “Fresh” and “Sulfated” 30 wt.% Co/CeO<sub>2</sub> catalysts are presented at different magnifications. By comparing the SEM images of the “Fresh” (Figure 6.8A and 6.8B) and “Sulfated” (Figure 6.8C and 6.8D) samples, it is evident that the “Sulfated” catalyst has undergone significant morphological modifications, leading to the formation of new phases and to a larger porosity, as a result of its exposure in H<sub>2</sub>S-containing environments at high temperatures. In particular, the average size of the cobalt containing particles of the “Sulfated” catalyst increased, compared to the “Fresh” catalyst, due to its mild sintering, leading to the formation of polygon-like shapes (cobalt sulfide) and sponge-like shapes (cerium oxide particles). Moreover, a significant amount of sulfur was also detected via the EDX analysis (data not shown), as a result of the considerable formation and deposition of sulfur on the catalyst surface, even in the presence of excess H<sub>2</sub>O (90 v/v%). Notice that the relevant elemental mapping of the same sample showed that the sulfur formation and deposition was favored in Co-depleting areas, while S

species was not traced in  $\text{CeO}_2$  areas. In view of the above findings, the already established superiority of the 30 wt.%  $\text{Co/CeO}_2$  catalyst for the  $\text{H}_2\text{S}$  decomposition reaction under extremely “wet” (90 v/v%  $\text{H}_2\text{O}$ ) conditions, should be directly related with the in-situ sulfation of the catalyst’s active counterparts ( $\text{Co}_3\text{O}_4$  to  $\text{Co}_3\text{S}_4$  and  $\text{CoS}$ ), during its exposure to the reaction atmosphere.

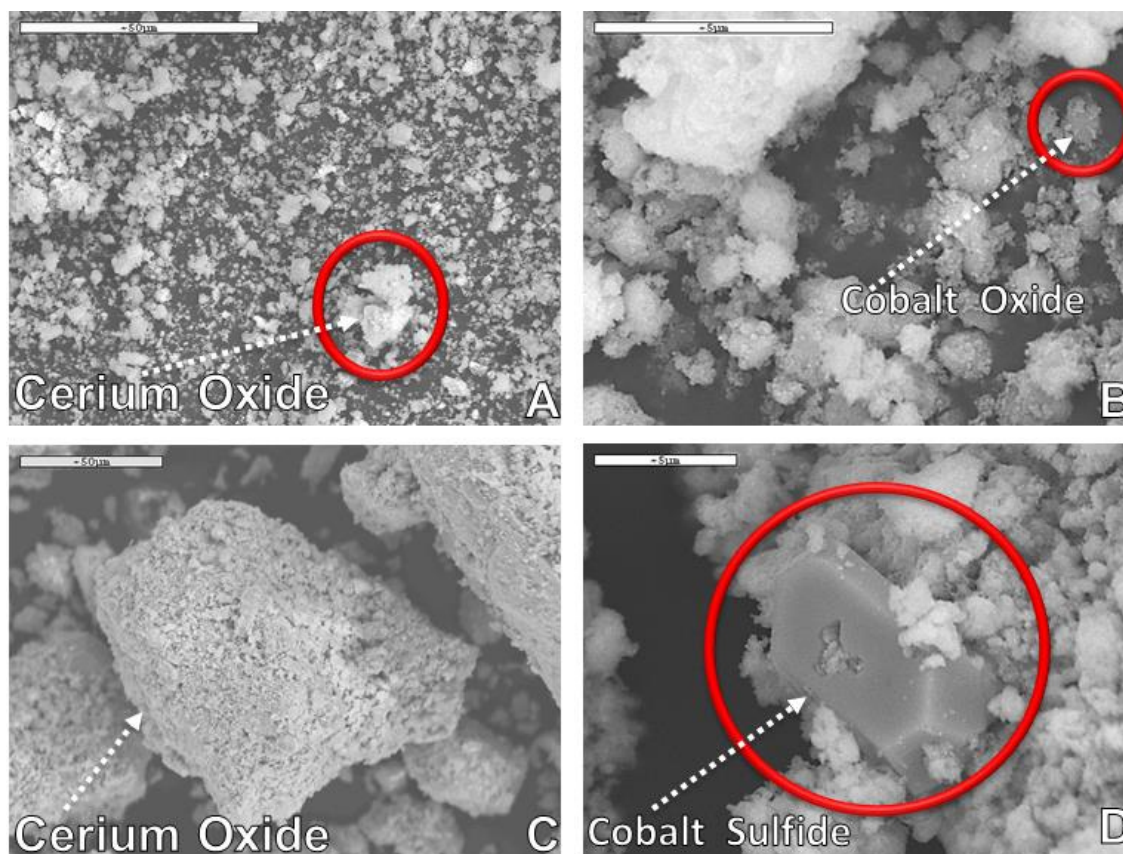


**Figure 6.8:** SEM images of the “Fresh” (A) and (B), and “Sulfated” (C) and (D), optimum 30 wt.%  $\text{Co/CeO}_2$  catalysts, exposed for 10 h in a reaction mixture containing 1 v/v%  $\text{H}_2\text{S}$  - 90 v/v%  $\text{H}_2\text{O}$ , balanced with Ar, at  $T = 850^\circ\text{C}$ .

To further explore the dynamic evolution of the sulfation process, the S content of the “Aged” (1 v/v%  $\text{H}_2\text{S}$ , balanced with Ar) and “Sulfated” (1 v/v%  $\text{H}_2\text{S}$  - 90 v/v%  $\text{H}_2\text{O}$ , balanced with Ar) catalyst samples was also determined. It was found that for the catalyst used in the “dry” stability experiments (10 h exposure at  $T = 850^\circ\text{C}$ ), the S content was approximately 13.13%, while, in excess  $\text{H}_2\text{O}$  presence, the S content was approximately decreased in half (Table 6.3), implying the particular importance of the selected reaction conditions on the sulfur deposition process.

**Table 6.3:** Sulfur elemental analysis for the optimum 30 wt.% Co/CeO<sub>2</sub> catalysts at different reaction conditions in the absence/presence of excess H<sub>2</sub>O.

Sample/Reaction conditions	S (%)
“Aged” 30 wt.% Co/CeO <sub>2</sub> , 850 °C, 10 h, 1 v/v% H <sub>2</sub> S, balanced with Ar	13.13%
“Sulfated” 30 wt.% Co/CeO <sub>2</sub> , 850 °C, 10 h, 1 v/v% H <sub>2</sub> S - 90 v/v% H <sub>2</sub> O, balanced with Ar	6.5%

The in-situ formation of the sulfated phases was also confirmed by the comparison of the XPS spectra of the “Fresh” and “Sulfated” 30 wt.% Co/CeO<sub>2</sub> samples. More specifically, Figure 6.9A depicts the Ce3d spectra of “Fresh” and “Sulfated” 30 wt.% Co/CeO<sub>2</sub> catalysts. Figure 6.9B presents the corresponding Co2p spectra. Both figures characteristics reveal the significant attenuation of Co and Ce surface species as well as their reduction upon “Sulfated” process, in line with the formation of sulfated compounds (Ferrizz et al., 2002; Mingyang et al., 2015; Xiaoyan et al., 2014; Jong et al., 1996). More details about the interpretation of XPS results can be found at Chapter 5, Section 5.7.

Without any doubt, the previous analysis leads to the conclusion that during the catalytic decomposition of H<sub>2</sub>S in the presence of H<sub>2</sub>O, the 30 wt.% Co/CeO<sub>2</sub> catalyst demonstrates the optimum activity performance and, in the same time, a remarkably stable behaviour. This stability can be safely attributed to the in-situ sulfation of the catalysts’ active components, during their exposure to feedstock mixture. As a result, the produced elemental sulfur is not simply deposited on the catalyst surface, but interacts with the catalyst’s counterparts to create new active and stable phases. Furthermore, by taking into account the small relative differences in the structural and textural characteristics of Co/CeO<sub>2</sub> catalysts with different Co loadings, the superiority of the 30 wt.% Co/CeO<sub>2</sub> sample can be related to the intrinsic characteristics of the Co and CeO<sub>2</sub> phases and to the nature of the metal-carrier interactions. These factors affect both the type and quantity of the produced Co- and CeO<sub>2</sub>-based sulfur compounds, as well as, the surface characteristics of the catalysts (i.e., oxidative state, oxygen mobility, surface structure, etc.). These promising findings could pave the way for the development of active and stable catalytic materials to be applied as anode electrodes, in a proton H<sup>+</sup> conducting solid electrolyte electrochemical

membrane reactor, able to effectively manage the H<sub>2</sub>S-containing sources towards hydrogen production, such as the proposed H<sub>2</sub>S quantities found in Black Sea waters.

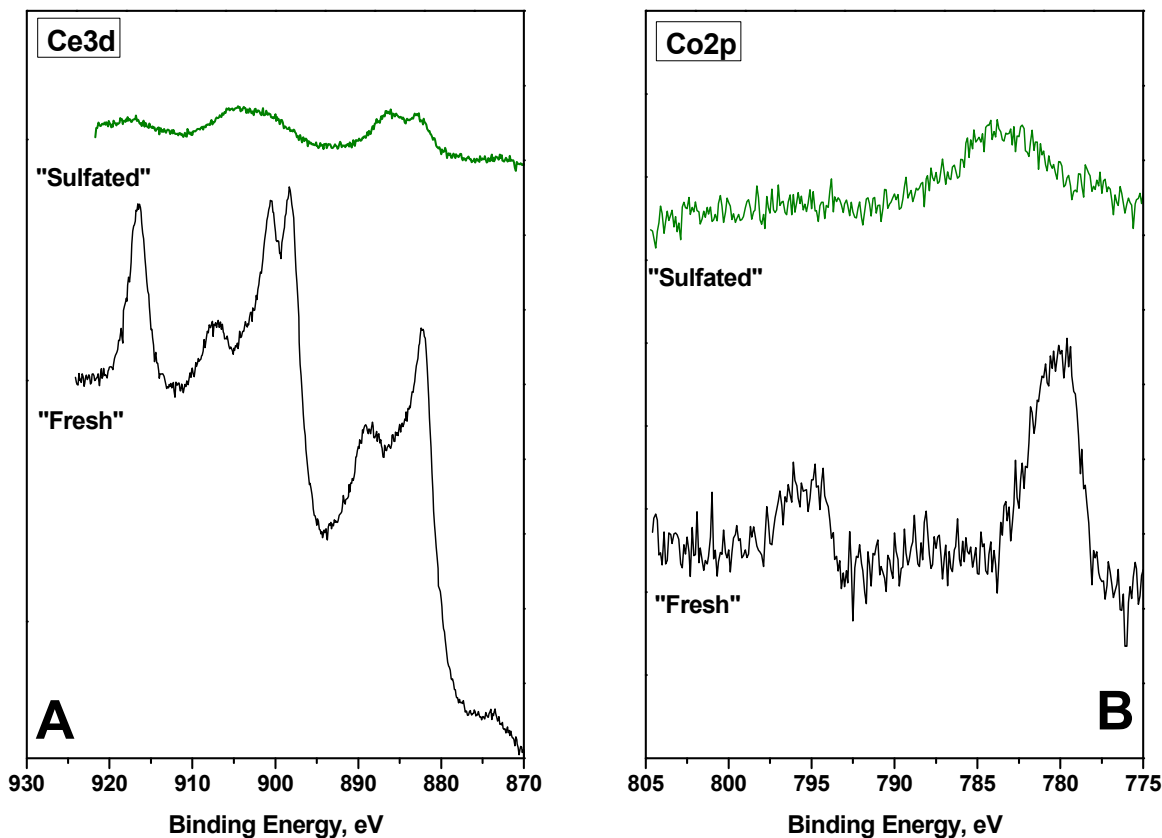


**Figure 6.9:** A) Ce3d and B) Co2p spectra of the "Fresh" and "Sulfated" optimum 30 wt.% Co/CeO<sub>2</sub> catalyst.

## REFERENCES

- Carroll J.J., Mather A.E. (1991). Phase equilibrium in the system water-hydrogen sulphide: Hydrate-forming conditions. *The Canadian Journal of Chemical Engineering*, 69: pp.1206-1212.
- Chivers T., Hyne J.B., Lau C. (1980). The thermal decomposition of hydrogen sulfide over transition metal sulfides. *International Journal of Hydrogen Energy*, 5: pp. 499-506.
- Ferrizz R.M., Gorte R.J., Vohs J.M. (2002). TPD and XPS investigation of the interaction of SO<sub>2</sub> with model ceria catalysts. *Catalysis Letters*, 82: pp. 123-129
- Gong M., Liu X., Tremblay J., Johnson C. (2007). Sulfur-tolerant anode materials for solid oxide fuel cell application. *Journal of Power Sources*, 168: pp. 289-298.
- Jong A.M., (San) de Beer V.H.J., Rob van Veen J.A., (Hans) Niemantsverdriet J.W. (1996). Surface science model of a working cobalt-promoted molybdenum sulfide hydrodesulfurization catalyst: characterization and reactivity. *The Journal of Physical Chemistry*, 100: pp. 17722-17724.
- Kaklidis N., Pekridis G., Athanasiou C., Marnellos G.E. (2011). Direct electro-oxidation of iso-octane in a solid electrolyte fuel cell. *Solid State Ionics*, 192: pp. 435-443.

- Konsolakis M., Sgourakis M., Carabineiro S.A.C. (2015). Surface and redox properties of cobalt-ceria binary oxides: On the effect of Co content and pretreatment conditions. *Applied Surface Science*, 341: pp. 48-54.
- Laosiripojana N., Assabumrungrat S. (2006). Catalytic steam reforming of ethanol over high surface area CeO<sub>2</sub>: The role of CeO<sub>2</sub> as an internal pre-reforming catalyst. *Applied Catalysis B: Environmental*, 66: pp. 29-39.
- Lee J.I., Mather A.E. (1977). Solubility of hydrogen sulfide in water. *The Journal of Physical Chemistry*, 81: pp. 1020-1023.
- Luinstra E. (1996). H<sub>2</sub>S: a potential source for hydrogen. *Sulphur*, 244: pp. 37-47.
- Marrocchelli D., Yildiz B. (2012). First-principles assessment of H<sub>2</sub>S and H<sub>2</sub>O reaction mechanisms and the subsequent hydrogen absorption on the CeO<sub>2</sub> (111) surface. *Journal of Physical Chemistry C*, 116: pp. 2411-2424.
- Mingyang X., Helin N., Jinjing H., Jiming S., Changjie M., Shengyi Z., Chengfeng Z., Changle C. (2015). Facile synthesis of graphene-like Co<sub>3</sub>S<sub>4</sub> nanosheet/Ag<sub>2</sub>S nanocomposite with enhanced performance in visible-light photocatalysis, *Applied Surface Science*, 351: pp. 374-381.
- Xiaoyan S., Yunbo Y., Li X., Hong H. (2014). Effect of sulfur poisoning on Co<sub>3</sub>O<sub>4</sub>/CeO<sub>2</sub> composite oxide catalyst for soot combustion. *Chinese Journal of Catalysis*, 35: pp. 1504-1510.



# PART

## DEVELOPMENT OF PROTON CONDUCTING ELECTROCHEMICAL CELLS FOR H<sub>2</sub>S ELECTROLYSIS



Contents	Page
II.1. Introduction. . . . .	195
References. . . . .	199
Chapter 7: Experimental methods, equipment and techniques. . . . .	201
Chapter 8: Electrochemical experiments. . . . .	235



## II.1. INTRODUCTION

Nowadays, the constantly emerging energy and environmental concerns force the global society to utilize “clean” fuel resources and efficient energy conversion technologies (Midilli et al., 2007). Initiatives, like the global Paris Agreement (2015), point to the need for a massive penetration of intermittent renewable power sources (IRES) to form the backbone for a sustainable future. However, in order to use that green power, efficient energy storage solutions, such as the use of hydrogen, should be developed to power all needs and applications that society now takes for granted, from heating to transportation.

Hydrogen, if derived from carbon-free energy resources, is worldwide acknowledged as an environmental friendly energy vector, which can support future energy developments. Among the different sustainable approaches for hydrogen production, the decomposition of hydrogen sulphide (H<sub>2</sub>S), when using the excess electricity of IRES, is of particular interest. It is well known that H<sub>2</sub>S is present in various quantities in industrial waste streams, oil and natural gas reserves, geothermal and volcanic activity areas, oceans, and maritime deep waters (Fukuda et al., 1978). In addition, H<sub>2</sub>S that is abundantly found in Black Sea waters (produced by sulfur reducing bacteria), hails as a potential H<sub>2</sub> source, while its removal from the Black Sea waters and conversion to H<sub>2</sub>, through an efficient process, will contribute to the sufficient environmental protection of the surrounding ecosystem (Ipsakis et al., 2015). The process steps of a potential H<sub>2</sub> production technology from H<sub>2</sub>S contained into Black Sea waters are as follows (the proposed process in the present thesis): a) pumping sea water, containing H<sub>2</sub>S (0.36 mmol/l at 1,000 m depth), to the surface, b) extraction of H<sub>2</sub>S from water (Naman et al., 2008), and c) decomposition of H<sub>2</sub>S to H<sub>2</sub> and sulphur.

To date, several alternatives have been proposed for the production of hydrogen via H<sub>2</sub>S decomposition, which are currently at different stages of development, involving thermochemical, photochemical, plasmochemical and electrochemical methods (Luinstra, 1996; Zaman and Chakma, 1995). The majority of these approaches present certain disadvantages attributed to their particular high energy requirements and low efficiencies, rendering their commercialization still in doubt. Recently, researchers suggested an electrochemical approach at high temperatures to efficiently generate and separate, in a single step, pure H<sub>2</sub> from H<sub>2</sub>S electrolysis, employing a proton conducting ceramic membrane reactor (Li et al., 2006; Slavov et al., 1998; Fabbri et al., 2010; Malavasi et al.,



2010). However, one of the major challenges of this technology, is the optimal selection of cell materials, especially of the anode electrode, which will be exposed to the H<sub>2</sub>S-containing reacting mixture and generate the protons to be transported through the H<sup>+</sup>-conducting solid electrolyte to the cathode, where pure hydrogen will be formed. To this direction, the anode material has to exhibit high electro-catalytic activity towards H<sub>2</sub>S decomposition, high electronic/ionic conductivity, good adherence on the solid electrolyte surface, and tolerance to H<sub>2</sub>S rich environments (Vorontsov et al., 2008; Gong et al., 2007). Several sulphides, oxides and metals have been investigated for this purpose, successfully reviewed in Gong et al. (2007). Among the various sulphur resistant anode materials, thiospinels and metal sulphides are favourable for H<sub>2</sub>S-oxidating fuel cells, however their time-consuming and complex synthesis procedure, along with their rather low electro-catalytic activity and insufficient chemical stability, limit their applicability in real processes (Vorontsov et al., 2008).

Recently, ceria-based mixed oxides have gained considerable attention in the field of electro-catalysis due to their efficient electrochemical performance and resistance to poisons. For instance, Co<sub>3</sub>O<sub>4</sub>/CeO<sub>2</sub> materials have been extensively applied in the field of solid oxide fuel cells (SOFCs), since they combine enhanced electronic conductivity and electro-catalytic activity (Konsolakis, 2016; Atkinson et al., 2004). In addition, the superior catalytic performance of Co<sub>3</sub>O<sub>4</sub>/CeO<sub>2</sub> composites towards H<sub>2</sub>S decomposition to H<sub>2</sub>, in both “dry” and “wet” (i.e., 90 v/v% H<sub>2</sub>O) atmospheres was also revealed (Kraia et al., 2016).

In general, the mechanism of the electrochemical oxidation of H<sub>2</sub>S in solid electrolyte cells has been thoroughly investigated (Yentekakis and Vayenas, 1989; Chuang et al., 2008; Li et al., 2006; Gong et al., 2007; Slavov et al., 1998) and simulated (Yentekakis and Vayenas, 1989; Monder et al., 2010). The H<sub>2</sub>S decomposition by electrochemical membrane reactors (Athanasidou et al., 2007) and electrolysis using proton conductors (Mbah et al., 2008) and molten sulphide electrolytes (Lim et al., 1984) have been also well studied. Furthermore, the effect of the fuel feedstock composition and flow rate on the developed Open Circuit Voltage (OCV) of H<sub>2</sub>S-fed oxygen anion (O<sub>2</sub>) conducting SOFCs has been already examined in detail, through fuel cell experiments and thermodynamic calculations (Monder et al., 2012; Aguilar et al., 2004). More specifically, Aguilar et al. (2004) studied the performance of a LSV/YSZ/LSM-YSZ (LSV: La<sub>x</sub>Sr<sub>1-x</sub>VO<sub>3-δ</sub>) cell, fed with 5 v/v% H<sub>2</sub>S - 95 v/v% N<sub>2</sub> and 5 v/v% H<sub>2</sub>S -

95 v/v% H<sub>2</sub>, at 1,000 °C. The authors calculated theoretical OCV values, by employing the Nernst's equation, and compared them with the experimentally observed OCV values. The equilibrium model and experimental data were in good agreement, when the fuel feedstock mixture consisted of 5 v/v% H<sub>2</sub>S - 95 v/v.% N<sub>2</sub>. However, when N<sub>2</sub> was substituted by H<sub>2</sub> in the feedstock, the experimental OCV values were approximately 90% of the theoretical OCV values. This deviation was attributed to the preferential adsorption of sulphur species onto the LSV anode. Moreover, Monder et al. (2012) observed an unusual dependence of the cell performance and the relevant OCV on the fuel composition and flow rate. Through fuel cell experiments and thermodynamic calculations, the authors suggested that H<sub>2</sub>S, instead of H<sub>2</sub> (produced from H<sub>2</sub>S dissociation), was preferentially electro-oxidized on the three-phase boundaries (tpb) of the anode.

In the present section of this thesis, the H<sub>2</sub>S decomposition is carried out in a proton-conducting ceramic electrochemical membrane reactor (Figure II.1). In more detail, the anode of the cell reactor is exposed to 0.1-1 v/v% in H<sub>2</sub>S mixtures, in excess H<sub>2</sub>O (i.e., 90 v/v% H<sub>2</sub>O), to mimic the feedstock mixture, as it would be delivered upon the pumping and pre-concentration of Black Sea water from 1,000 m depth (Naman et al., 2008). In addition, the anode catalyzes the H<sub>2</sub>S decomposition to H<sup>+</sup> and S, while the cathode is exposed to oxidizing conditions. The reactor is in principle operated at the temperature range 700-850 °C. When an anodic overpotential is applied, the protons (H<sup>+</sup>), formed during the H<sub>2</sub>S/H<sub>2</sub>O electrolysis, are transferred through the solid electrolyte to the cathode, where they are converted to:

- H<sub>2</sub> (membrane reactor operation mode), or
- H<sub>2</sub>O, generating at the same time electrical power (fuel cell operation mode).

As a result, pure H<sub>2</sub> is generated and separated in a single stage.

As mentioned above, one of the major challenges in such a complex process is the optimal selection of cell materials. More specifically, the electrolyte must allow ions to migrate rapidly from the one electrode to the other and must have negligible electronic conductivity. Notice that both the anode and cathode consist of catalysts that cause the fuel feedstock to oxidize and generate positively charged hydrogen ions and electrons. Moreover, as it is highlighted previously, special attention should be given to the anode electrode, due to its exposure on H<sub>2</sub>S-containing conditions.

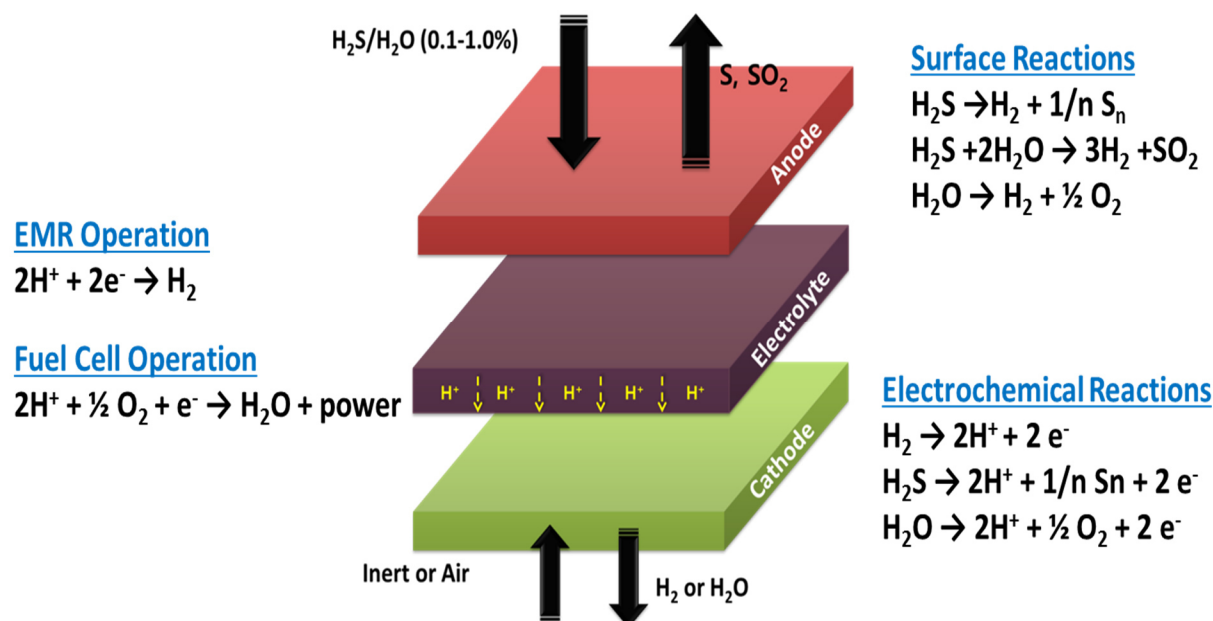


**Figure II.1:** Principle of the electrochemical reactor, based on a proton-conducting membrane, for the production of  $\text{H}_2$  via the electrolysis of  $\text{H}_2\text{S}$  and  $\text{H}_2\text{O}$  (EMR operation) or  $\text{H}_2\text{O}$  and energy (fuel cell operation).

Starting at Chapter 7, several methods and thermal treatments were examined to fabricate an efficient conductive cell, while the experimental results are integrated with the physicochemical characterization of the materials via XRD and SEM methods. As the applied feedstock (i.e.,  $\text{H}_2\text{S}/\text{H}_2\text{O}$ ) is considered to be especially troublesome, since it promotes corrosion, poses a health and environmental threat, and can be converted to even more toxic and environmentally hazardous compounds (e.g.,  $\text{SO}_2$  or  $\text{H}_2\text{SO}_4$ ), the optimization of the selected materials will be a fundamental step for the development of a competitive fuel cell. To avoid the general challenges that  $\text{H}_2\text{S}$  creates, i.e., poisoning and/or decomposition of cell electrodes, especially Ni, which is a common anode component, the cell materials development in this thesis includes the following compounds:

- $\text{BaZr}_{0.7}\text{Ce}_{0.2}\text{Y}_{0.1}\text{O}_3$  (BZCY72): A BZCY (NorECs, 2016) disk is selected as the  $\text{H}^+$ -conducting solid electrolyte/membrane, where the cathode and anode materials will be deposited (see Section 7.2.1).
- $\text{Co}_3\text{O}_4/\text{CeO}_2$  powders are selected, as they are consistent with the electronic conductivity and resistance to  $\text{SO}_2/\text{H}_2\text{S}/\text{H}_2\text{O}$  atmospheres demands of the cell (see Section 7.2.2).
- $\text{BaGd}_{0.8}\text{La}_{0.2}\text{Co}_2\text{O}_{6.6}$  (BGLC): BGLC (Strandbakke et al., 2015) is chosen as the cathode material (see Section 7.2.3).

## DEVELOPMENT OF PROTON CONDUCTING ELECTROCHEMICAL CELLS FOR H<sub>2</sub>S ELECTROLYSIS

Note that the above described technology greatly relies on the tailor-made synthesis and assembly of the selected materials (electrolyte and electrodes).

In Chapter 8, the impact of pH<sub>2</sub>, pH<sub>2</sub>O and temperature on the electrochemical performance of the symmetrical cell Co<sub>3</sub>O<sub>4</sub>/CeO<sub>2</sub>-BZCY72-Co<sub>3</sub>O<sub>4</sub>/CeO<sub>2</sub> was initially examined by measuring its electrical properties, like its conductivity (see Section 8.1). Subsequently, the electrochemical performance and stability of Co<sub>3</sub>O<sub>4</sub>/CeO<sub>2</sub> composite electrodes, in H<sub>2</sub>S atmospheres containing excess H<sub>2</sub>O (90 v/v%), is examined in a single-chamber proton conducting ceramic symmetrical cell, when employing BaZr<sub>0.7</sub>Ce<sub>0.2</sub>Y<sub>0.1</sub>O<sub>3</sub> (BZCY72) as a proton conducting solid electrolyte material (see Section 8.2). Finally, the H<sub>2</sub>S electrolysis is carried out in a proton-conducting ceramic electrochemical membrane reactor BZCY72 of double chamber (see Section 8.3). In more detail, H<sub>2</sub>S (diluted in excess H<sub>2</sub>O) is fed at the anode Co<sub>3</sub>O<sub>4</sub>/CeO<sub>2</sub>, while the cathode BGLC is exposed to oxidizing conditions.

## REFERENCES

- Aguilar L., Zha S., Cheng Z., Winnick J., Liu M. (2004). A solid oxide fuel cell operating on hydrogen sulfide (H<sub>2</sub>S) and sulfur containing fuels. *Journal of Power Sources*, 135: pp. 17-24.
- Athanassiou C., Pekridis G., Kaklidis N., Kalimeri K., Vartzoka S., Marnellos G. (2007). Hydrogen production in solid electrolyte membrane reactors (SEMRs). *International Journal of Hydrogen Energy*, 32: pp. 38-54.
- Atkinson A., Barnett S., Gorte R.J., Irvine J.T.S., McEvoy A.J., Mogensen M., Singhal S.C., Vohs J. (2004). Advanced anodes for high-temperature fuel cells. *Nature Materials*, 3: pp. 17-27.
- Fabbri E., Pergolesi D., Traversa E. (2010). Materials challenges toward proton-conducting oxide fuel cells: a critical review. *Chemical Society Reviews*, 39: pp. 339-359.
- Fukuda K., Dokiya M., Kameyama T., Kotera Y. (1978). Catalytic decomposition of hydrogen sulfide. *Industrial & Engineering Chemistry Research*, 17: pp. 243-247.
- Gong M., Liu X., Tremblay J., Johnson C. (2007). Sulfur-tolerant anode materials for solid oxide fuel cell application. *Journal of Power Sources*, 168: pp. 289-298.
- Ipsakis D., Kraia Tz., Marnellos G.E., Ouzounidou M., Voutetakis S., Dittmeyer R., Dubbe A., Haas-Santo K., Konsolakis M., Figen H.E., Güldal N.O., Baykara S.Z. (2015). An electrocatalytic membrane-assisted process for hydrogen production from H<sub>2</sub>S in Black Sea: preliminary results, *International Journal of Hydrogen Energy*, 40: pp. 7530-7538.
- Konsolakis M. (2016). The role of copper–ceria interactions in catalysis science: recent theoretical and experimental advances. *Applied Catalysis B Environmental*, 198: pp. 49-66.
- Kraia Tz., Konsolakis M., Marnellos G.E. (2016). H<sub>2</sub>S in Black Sea: turning an environmental threat to an opportunity for clean H<sub>2</sub> production via an electrochemical membrane reactor, In: Research Progress in H<sub>2</sub>S-PROTON Project. *MATEC Web Conference*, 41: 04002.

- Li J., Luo J.L., Chuang K.T., Sanger A.R. (2006). Proton conductivity and chemical stability of  $\text{Li}_2\text{SO}_4$  based electrolyte in a  $\text{H}_2\text{S}$ -air fuel cell. *Journal of Power Sources*, 160: pp. 909-914.
- Lim H.S., Winnick J. (1984). Electrochemical removal and concentration of hydrogen sulfide from coal Gas. *Journal of Electrochemical Society*, 131: pp. 562-568.
- Luinstra E. (1996).  $\text{H}_2\text{S}$ : a potential source for hydrogen. *Sulphur*, 244: pp. 37-47.
- Malavasi L., Fisher C.A.J., Islam M.S. (2010). Oxide-ion and proton conducting electrolyte materials for clean energy applications. Structural and mechanistic features. *Chemical Society Reviews*, 39: pp. 4370-4387.
- Mbah J., Krakow B., Stefanakos E., Wolan J. (2008). Electrolytic splitting of  $\text{H}_2\text{S}$  using  $\text{CsHSO}_4$  membrane. *Journal of Electrochemical Society*, 155: pp. E166-E170.
- Midilli A., Ay M., Kale A., Veziroglu T.N. (2007). A parametric investigation of hydrogen energy potential based on  $\text{H}_2\text{S}$  in Black Sea deep waters. *International Journal of Hydrogen Energy*, 32: pp. 117-124.
- Monder D.S., Vorontsov V., Luo J., Chuang K.T., Nandakumar K. (2012). An investigation of fuel composition and flow-rate effects in a  $\text{H}_2\text{S}$  fueled SOFC: experiments and thermodynamic analysis. *The Canadian Journal of Chemical Engineering*, 90: pp. 1033-1042.
- Naman S.A., Ture E.I., Veziroglu T.N. (2008). Industrial extraction pilot plant for stripping  $\text{H}_2\text{S}$  gas from Black Sea water. *International Journal of Hydrogen Energy*, 33: pp. 6577-6585.
- NorECs, Norwegian Electro Ceramics AS, in: <http://www.norecs.com>, <http://www.norecs.com/index.php?page=Newsletter+154>. Accessed: 08/12/2016.
- Paris Agreement, United Nations Framework Convention on Climate Change, in: [http://unfccc.int/files/essential\\_background/convention/application/pdf/english\\_paris\\_agreement.pdf](http://unfccc.int/files/essential_background/convention/application/pdf/english_paris_agreement.pdf), 2015. Accessed: 10/12/2016.
- Slavov S.V., Chuang K.T., Sanger A.R., Donini J.C., Kot J., Petrovic S. (1998). A proton-conducting solid state  $\text{H}_2\text{S-O}_2$  fuel cell. 1. Anode catalysts, and operation at atmospheric pressure and 20-90 °C. *International Journal of Hydrogen Energy*, 23: pp. 1203-1212.
- Vorontsov V., Luo J.L., Sanger A.R., Chuang K.T. (2008). Synthesis and characterization of new ternary transition metal sulphide anodes for  $\text{H}_2\text{S}$ -powered solid oxide fuel cell. *Journal of Power Sources*, 183: pp. 76-83.
- Yentekakis I.V., Vayenas C.G. (1989). Chemical cogeneration in solid electrolyte cells: the oxidation of  $\text{H}_2\text{S}$  to  $\text{SO}_2$ . *Journal of Electrochemical Society*, 136: pp. 996-1002.
- Zaman J., Chakma A. (1995). Production of hydrogen and sulphur from hydrogen sulphides. *Fuel Processing Technology*, 41: pp. 159-198.
- Strandbakke R., Cherepanov V.A., Zuev A.Y., Tsvetkov D.S., Argirusis C., Sourkouni G., Prãente S., Norby T. (2015). Gd- and Pr-based double perovskite cobaltites as oxygen electrodes for proton ceramic fuel cells and electrolyzer cells. *Solid State Ionics*, 278: pp. 120-132.

# CHAPTER

## EXPERIMENTAL METHODS, EQUIPMENT AND TECHNIQUES

# 7

Contents	Page
7.1. Introduction. . . . .	203
7.2. Cell fabrication. . . . .	203
7.3. Efficient electrode deposition on BZCY72 techniques. . . . .	206
7.4. Characterization studies. . . . .	213
7.5. Experimental set-up, reactor design and procedure. . . . .	217
7.6. Theory. . . . .	229
References. . . . .	233



## 7.1. INTRODUCTION

Chapter 7 presents the synthesis, characterization and evaluation of selected materials for the development of the solid electrolyte and electrodes, in parallel with the construction of the electrochemical reactor. These objectives involve the implementation of relevant physicochemical and, especially, electrochemical methodologies, as well as, the fabrication and assembly of the complete proton conductor electrochemical membrane reactor. Note that great effort was initially devoted to the improvement and optimization of the selected materials and methodologies towards the efficient electrodes deposition and cell operation, under realistic conditions. More specifically, the reactor cell (electrodes and electrolyte) and its preparation methods are described in detail in Sections 7.2 and 7.3, while the techniques used for its characterization in Section 7.4. Finally, the experimental equipment and the theory used for the electrochemical measurements are presented in Sections 7.5 and 7.6, respectively.

## 7.2. CELL FABRICATION

Several preparation methods and thermal treatment protocols were examined to effectively fabricate the conductive cell reactor. Subsequently, the cell was characterized regarding its physicochemical (using XRD and SEM) and electrochemical (using EIS) properties. It is well known that H<sub>2</sub>S/H<sub>2</sub>O mixtures are considered especially troublesome, since they promote equipment corrosion, pose a threat to health and environment, and can be converted to other toxic and environmentally hazardous compounds, such as SO<sub>2</sub>. In this case, H<sub>2</sub>S presents a challenge, since it can be poisonous and lead to the decomposition of the electrodes (especially Ni, a common anode component). Thus, the optimization of suitable electrode materials is a fundamental step in the development of tolerant and efficient cells.

More specifically, the cell (Figure 7.1) materials development includes the following steps:

- BaZr<sub>0.7</sub>Ce<sub>0.2</sub>Y<sub>0.1</sub>O<sub>3</sub> (BZCY72): A BZCY72 (NorECs) disk was selected as the H<sup>+</sup> conducting solid electrolyte/membrane, where the cathode and anode materials were deposited (see Section 7.2.1).

- $\text{Co}_3\text{O}_4/\text{CeO}_2$  powders were selected as the anode, after the completion of the  $\text{H}_2\text{S}$  catalytic decomposition experiments in the absence (Chapter 5)/presence (Chapter 6) of  $\text{H}_2\text{O}$ , towards  $\text{H}_2$  production (see Section 7.2.2).
- $\text{BaGd}_{0.8}\text{La}_{0.2}\text{Co}_2\text{O}_{6.6}$  (BGLC): BGLC was chosen as the cathode material (see Section 7.2.3).

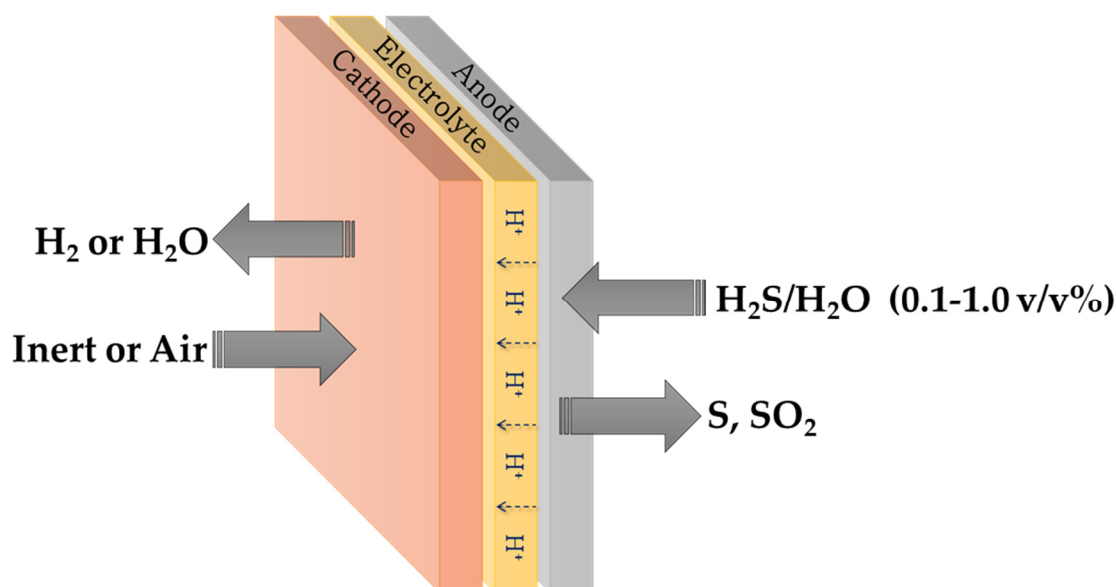


**Figure 7.1:** Schematic of the electrochemical reactor, consisting of the proton conducting membrane, anode and cathode for the production of  $\text{H}_2$  and  $\text{SO}_2$ , via  $\text{H}_2\text{S}$  electrolysis in the presence of water.

Note that the above described technology greatly relies on the tailor-made synthesis and assembly of the selected and optimized materials (electrolyte and electrodes).

### 7.2.1. $\text{H}^+$ Conducting Solid Electrolyte/Membrane, $\text{BaZr}_{0.7}\text{Ce}_{0.2}\text{Y}_{0.1}\text{O}_3$ (BZCY72)

In general, the  $\text{H}^+$  conducting solid electrolytes have to exhibit: i) high ionic conductivity at moderate temperatures, so that less expensive materials can be used (Marnellos et al., 2008), ii) chemical stability to  $\text{H}_2\text{S}$ , and iii) mechanical strength. The most frequently used  $\text{H}^+$  conducting oxide electrolytes are  $\text{CeO}_2$ -doped and Sr-doped zirconia perovskite oxides (Iwahara, 1995). Although high  $\text{H}^+$  conductivity has been reported for many perovskite and non-perovskite oxides in humid atmospheres (Norby, 1999), the combination of high  $\text{H}^+$  conductivity and stability, which is a major prerequisite for their successful application, has

not been satisfactorily demonstrated yet. In the open literature, only few studies have dealt with the use of  $H^+$  conducting membranes in  $H_2S$ -containing mixtures (Li et al., 2008). A relevant comparison between perovskite and non-perovskite oxides revealed that the former are superior in terms of their ionic conductivity (Shimura et al., 2001). Among the different perovskite oxides,  $BaCe_{1-x}Y_xO_{3-\delta}$  exhibited the largest ionic conductivity (Iwahara, 1995), however its chemical stability still was a critical issue. Moreover, several perovskite structured solid oxide electrolytes can be hydrated by water vapors to become proton conducting materials below  $700\text{ }^\circ\text{C}$ . On the other hand, BZY-based materials are considered as potential candidates for proton conducting membrane reactors (PCMRs), due to their high proton conductivity and chemical stability to  $H_2O$  and  $H_2S$  containing atmospheres, but suffer until now from poor sinterability and high grain boundary resistance. Recently however,  $BaZrO_3$ -derivatives have gained increased interest, upon the introduction of sintering aids, such as  $NiO$ ,  $ZnO$  and  $CoO$ . Both sinterability and grain boundary conductivity were improved, without severely affecting the overall stability, by substituting on the B-site of the material a fraction of Ce with Zr. Presently, the challenging goal is to develop novel complex perovskites based on  $BaCe_{1-x}(Zr,Y,Zn,Fe)_xO_{3-\delta}$  for their application in intermediate temperature  $H^+$  conducting cells; they should exhibit high stability and electrochemical performance, when operating with  $H_2S$ . More specifically, a new  $H^+$  conductor, based on  $BaCe_{0.5}Zr_{0.3}Y_{0.16}Zn_{0.04}O_{3-\delta}$ , which presented in wet 5 v/v%  $H_2$  a total conductivity of  $3.14\text{ mS/cm}$  at  $T = 400\text{ }^\circ\text{C}$ , has been already developed (Tao and Irvine, 2006). Furthermore, Li et al. (2008) found that yttrium-doped barium zirconate exhibited high stability in dilute  $H_2S$  mixtures at a temperature range of  $700\text{-}1000\text{ K}$ .

### 7.2.2. Anode Electrode, $Co_3O_4$ Supported on $CeO_2$ Catalysts ( $Co_3O_4/CeO_2$ )

The selection of the anode material in a  $H^+$  conducting high temperature membrane reactor is crucial for the successful operation of the cell reactor. For this specific application, the anodic electrode has to exhibit: i) high catalytic activity and selectivity towards  $H_2S/H_2O$  decomposition, ii) high electronic conductivity, iii) good adherence to the solid electrolyte, and iv) corrosion tolerance to  $H_2S$  and sulfur compounds (Gong et al., 2007). To this direction, the majority of studies deal with sulfur tolerant electrodes in  $O^{2-}$  SOFCs. More specifically, the physical absorption of sulfur, blocking the active sites, and the chemical

reaction that generates sulphides are the main studied degradation mechanisms (Gong et al., 2007). In general, the sulfur tolerant electrodes are categorized to thiospinels and metal sulphides, active for H<sub>2</sub>S decomposition, metal cermets, and mixed ionic and electronic conductors (MIEC) (Mbah et al., 2010). To address the above phenomena, the combined application of materials through proper design and enhancement using surface/structure modifiers can be effective to achieve the desired balance between stability and efficiency (Gong et al., 2007). Moreover, it is well known that the implementation of carriers in catalysis enables the modification of its electronic properties and, as a consequence, assists in adjusting the strength of the chemisorptive bonds. To this end, upon the evaluation of the catalytic activity and stability of a series of catalysts (see Chapters 5 and 6), Co<sub>3</sub>O<sub>4</sub> supported on CeO<sub>2</sub> catalysts were selected as the most promising ones to be utilized in H<sub>2</sub>S decomposition towards H<sub>2</sub> production experiments, in the absence/presence of H<sub>2</sub>O.

### 7.2.3. Counter Electrode, BaGd<sub>0.8</sub>La<sub>0.2</sub>Co<sub>2</sub>O<sub>6-δ</sub> (BGLC)

In principle, a suitable for this kind of applications counter electrode should exhibit: i) electro-catalytic activity towards H<sub>2</sub> and H<sub>2</sub>O formation, ii) high electronic conductivity, iii) good adherence to the solid electrolyte surface, iv) extended active electrochemical zone (Three Phase Boundary, TPB), and v) low over-potential towards H<sub>2</sub> formation and H<sup>+</sup> oxidation. In a previous study, BaGd<sub>0.8</sub>La<sub>0.2</sub>Co<sub>2</sub>O<sub>6-δ</sub> (BGLC) was identified as a very promising electrode material for SOFCs and electrolyzers with respect to the above characteristics. As it exhibits conductivity values and polarization resistances in the order of 1000 S/cm and 10<sup>-2</sup> cm<sup>2</sup> (at a temperature range of 500-700 °C), respectively, BGLC is in-line to surpass the current state-of-the-art materials. Accordingly, BGLC was selected as the cathode material and was deposited on the one side of the BZCY72 electrolyte, for the fuel cell mode. It should be noted that the only available study on BGLC was recently published by Strandbakke et al. (2015).

## 7.3. EFFICIENT ELECTRODE DEPOSITION ON BZCY72 TECHNIQUES

Generally, electrodes should be thin enough (1-10 μm) to prevent significant (gas) mass transport limitations, especially under large reaction rates; though, in some cases it can be

up to 50  $\mu\text{m}$  thick. Furthermore, the purity, particle size and size distribution of the selected material play major role to its final microstructure and properties (mechanical, thermal, electrical and chemical resistances). To overcome the above constraints, a number of mild synthesis methodologies has been used for the preparation of key-process materials. For example, as the the film porosity is of paramount importance, since it determines the catalyst's active surface area and hence the reaction rate, the catalyst's active area should be 30 to 3000 times larger than its superficial area and can be adjusted by the calcination and sintering protocols. Higher calcination temperatures cause extensive sintering, leading to lower layer's porosities, which further reduce the catalyst's active area. The opposite effect is observed at lower calcination temperatures.

### 7.3.1. Basic Principle

The prerequisite of the adopted in the present thesis deposition technique is to have available a casting knife (blade) and a flat substrate (BZCY72 button cell), on which the layer will be deposited (see Figure 7.2). The basic principle is based on the coating of a ceramic ink through a specific handmade screen, while the shape of this screen determines the shape of the coating that will be printed on the support.

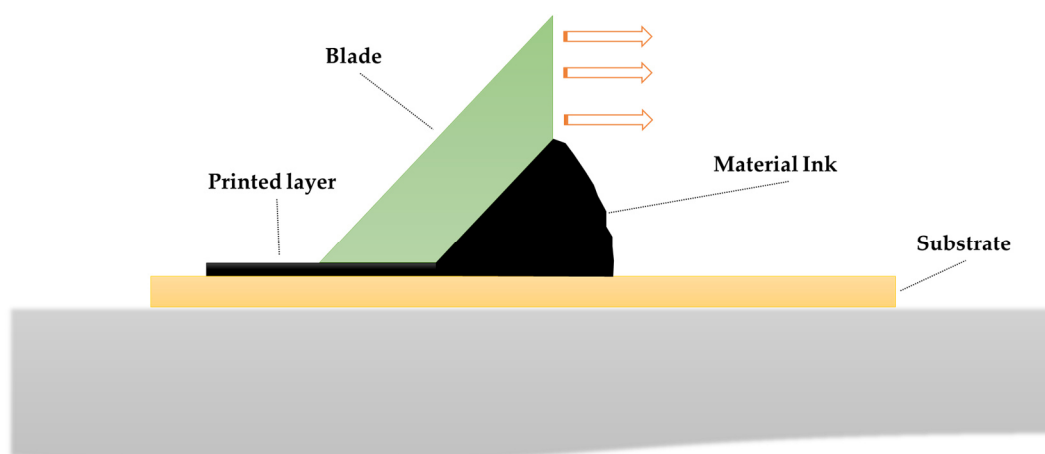


**Figure 7.2:** Schematic of the principle of the blade-based printing process.

The ink is composed from a mixture of ceramic powders and organic compounds. The thickness of the layer is related to the gap between the blade and the button cell and the

number of deposits, while the density of the layer is linked to the solid loading (ratio between powders and organics) and the heat treatment protocol. A drying step is necessary to let the solvent evaporate, leaving a dry membrane to finally form a flat and homogeneous electrode (Williams, 1976; Mintler et al., 1978).

### 7.3.1.1. Ink Formulation

In the present work, three types of ink were examined: a) PVC-based, b) water-based and c) organic-based. The latter inks are generally more suitable for applications like protonic ceramic coatings, since, as discussed also in Chapter 3, their basicity enhances the phase hydrolysis in the presence of water (Thorel, 2010; Costa et al., 2009). The printing ink should present a thixotropic behavior, meaning that the viscosity of the ink will decrease proportionally with the applied mechanical stress. Moreover, the viscosity should be small enough to facilitate the easy casting, but also large enough to maintain the ink geometry. As a result, the stability of the slurry is one of the major characteristics, as any instability of the mixture will introduce heterogeneities, which will lead to the formation of defects on the printed layer (cracks, bubbles, etc.). As the solid/liquid ratio increases, the densities of the printed layer and the final substrate also increase. Consequently, this ratio will tailor the final microstructure and density of the material (Mistler and Twinaime, 2006).

Furthermore, the composition of the ink and the treatment protocol are of significant importance to obtain the desired final properties (Lengwiler, 2013). Moreover, the granulometry of the used powder is a key parameter affecting the final microstructure of the layer. A wide variety of compounds can be coated onto substrates, from active anode materials, like cermet, to electrolytes and cathode materials. Among them, a mixture of a ceramic powder and an ethylcellulose-terpineol vehicle is commonly reported in the literature as one of the best options (Dailly et al., 2010; Bi et al., 2009; Dailly and Marrony, 2013). It should be also noted that prior to the final coating step, an one-hour milling step in a suitable mortar is needed to homogenize the mixture (Meng et al., 2000). Further milling in a three-roll mill is applied to improve the quality and the viscosity of the ink (Dimarcello et al., 1972; Rahaman, 2006). As the selected powder is the most important compound of the ink, the main parameters to be controlled are the powder particle size, distribution and shape, its surface area and density. The amount of organic additives is directly linked with

these parameters due to the the interactions between the powder and the other components of the slurry. For example, if the powder particles size is too small, the sintering effects become large, leading to a very dense final material (incompatible with anode layers), or to cracks and defects.

### 7.3.1.2. Drying Step

The drying step, and more specifically the drying rate is an additional crucial parameter of the proposed methodology, as the employed solvent should be able to evaporate as quickly as possible. Nevertheless, a rapid drying step results in the formation of a skin on the surface of the layer, blocking this way the evaporation of organics and inducing cracks and defects (Lostec, 1997). During the drying step, the solvent is removed from the printed layer, following two main mechanisms, i.e., solvent transport to the drying surface through the layer and surface evaporation.

### 7.3.1.3. Sintering Step

Upon drying, the following sintering step should be well defined and controlled, in order to attain the desired material microstructure and to prevent any cell damage. Similarly with the previous process steps, the parameters affecting the sintering step are strongly related with the selected material and the desired microstructure. In this work, the sintering cycle is implemented in three steps: 1) A first slow heating ramp up to an intermediate temperature level initiates the evaporation of organic compounds; the evaporation is almost completed after few hours. 2) Subsequently, the heating rate increases to the high sintering temperature. 3) During the sintering step, all the layers are subjected to identical temperature, duration and atmosphere, meaning that the selected temperature is necessarily a compromise among the sintering temperatures of all layers. This compromise can be smoothed by modifying the sintering protocol (by decreasing the temperature, though applied for an extended time period). It should be noted that it is important to apply a relatively slow heating ramp in order to complete the combustion of organics at the lowest possible temperature. The complete heat treatment mechanism presents in general a second order behavior, with respect to the heating and cooling rates, plateaus, etc. More

specifically, the heating and cooling ramps do not affect equally the printed layer. At the beginning of the treatment, as the substrate is in a powder form, it is not capable of transferring the elastic stress through the ceramic material. On the other hand, during the cooling step, the material is rigid and sensitive to the elastic stress originating from the unique thermal expansion of each layer.

### 7.3.2. Anode Electrode, $\text{Co}_3\text{O}_4$ Supported on $\text{CeO}_2$ Catalysts ( $\text{Co}_3\text{O}_4/\text{CeO}_2$ )

Commercially available powders of cobalt oxide,  $\text{Co}_3\text{O}_4$  (Sigma Aldrich) and cerium oxide,  $\text{CeO}_2$  (Alfa Aesar), were used as the starting materials. Initially, the oxides were separately milled in isopropanol with the aid of a planetary ball mill, using agate grinding balls and cups (4 h, at 300 rpm). The resulted powders were subsequently mixed in a weight ratio of 1:1, without any sintering agent, and milled in isopropanol for 40 min at 200 rpm, using zirconium balls and cups, to homogenize the composite mixture. The final slurry was subsequently left to dry at  $T = 100\text{ }^\circ\text{C}$  overnight.

Then, the  $\text{Co}_3\text{O}_4/\text{CeO}_2$  oxides ink was prepared by mixing the dried composite oxide powders with a commercial (NexTech Materials) organic ink vehicle VEH at a 1:2 weight ratio (400 rpm, overnight). The optimal thin film layers preparation procedure was achieved by applying the resulted viscous suspension in two steps. In the first step, one layer was printed symmetrically on both sides of the dense electrolyte, with the aid of a blade, and dried for 30 min at  $T = 100\text{ }^\circ\text{C}$ . The same procedure was repeated for the second layer deposition step. The mass gain was calculated by measuring the weight of the total cell before and after each deposition step. The deposited films weight on both sides of the disk was equal to 100-110 mg, resulting in an apparent area for each electrode equal to  $0.25\text{ cm}^2$ . When the development of the layer was successful, the cell was ready to be heated up to the desired temperature in ambient air, followed by cooling to room temperature at a constant rate.

It is worth mentioning that great effort was spent on several electrode deposition techniques. Thus, electrodes were applied to the pellets in numerous ways, investigating at the same time various parameters (number of layer depositions, calcination temperature, heating/cooling rates and calcination duration). After trial and error tests, due to serious cracking of specimens, it was revealed that these cracks were likely to happen during the

calcination step. To address this issue and optimize the calcination step, instead of heating up directly to the desired calcination temperature, an intermediate heating stage at  $T = 600$  °C for 1 h was employed to completely remove polyvinyl butyral (PVB) and to reduce the thermal stress applied to the electrode layer. As a result, the electrode layers were successfully sintered by the protocol graphically displayed in Figure 7.3.

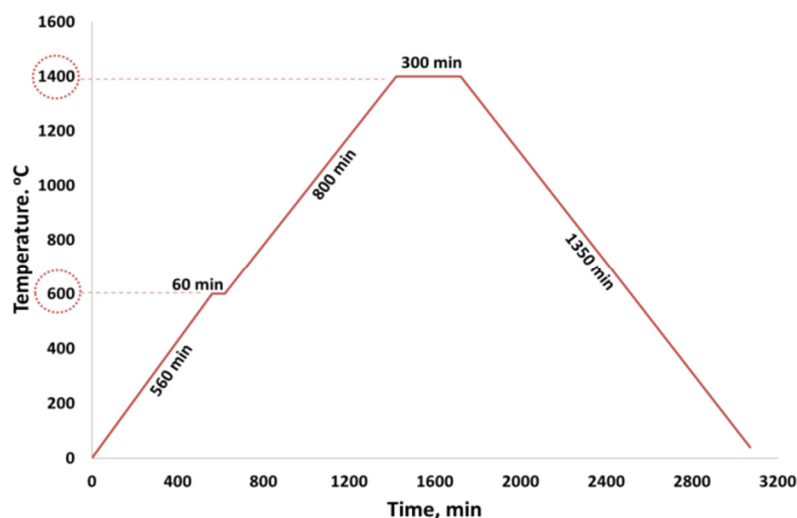


**Figure 7.3:** Heating/cooling protocol for the optimized sintering treatment of  $\text{Co}_3\text{O}_4/\text{CeO}_2$  electrode on BZCY72, 1 mm thick pellet.

### 7.3.3. Counter Electrode, $\text{BaGd}_{0.8}\text{La}_{0.2}\text{Co}_2\text{O}_{6-\delta}$ (BGLC)

Initially,  $\text{BaGd}_{0.8}\text{La}_{0.2}\text{Co}_2\text{O}_{6-\delta}$  powder samples of nominal compositions were selected and prepared via the glycerol-nitrate method, using  $\text{Gd}_2\text{O}_3$ ,  $\text{La}(\text{NO}_3)_3 \cdot 6\text{H}_2\text{O}$ ,  $\text{BaCO}_3$ , and Co, as the starting materials. A stoichiometric mixture of the precursor materials was dissolved in a concentrated nitric acid solution and the required volume of glycerol was added to serve as a complexing agent. The solution was continuously heated at  $T = 100$  °C, till water evaporation, termination and pyrolysis of the dried precursor. The resulted material was subsequently calcined at  $T = 1,100$  °C for 10 h to obtain the desired double perovskite powder. The phase composition of the powder samples was studied (at room temperature) by X-ray diffraction (XRD), with the aid of an Equinox 3000 diffractometer; XRD showed no indication for the presence of a second phase in the prepared samples. Afterwards, BGLC powder suspensions for the electrode functional layer deposition on BZCY72 (NorECs) electrolyte were prepared by ball milling 1 g of electrode material powder and 0.09 g of

polyvinylpyrrolidone K15 dispersion agent in isopropanol (250 rpm, 18 h). The powder suspension was left for a minimum of two hours for the larger particles to sink. Finally, BGLC electrode inks were prepared by mixing the respective dried BGLC powders with a commercial (NexTech Materials) organic ink vehicle VEH at a 1:1.5 weight ratio (400 rpm, overnight). The optimized process steps for BGLC electrode deposition on the cathode side of BZCY72 are:

- The BGLC suspension was dripped onto the pellet top surface using the proper amount, i.e., approximately 11 droplets with 30 min evaporation (100 °C) in between, until a uniform covering layer of sub-micron grained powder was achieved.
- When the development of the “dropping” layer was successful, the pellet was heated at  $T = 1,150$  °C for 5 h (10.5 h ramp up, 6 h ramp down).
- The optimal thin film layers preparation was achieved by applying the resulted viscous suspension in three steps. Thus, three layers were printed on the one side of the dense BZCY72 electrolyte, by using a suitable blade and having a 30 min evaporation step (100 °C) in between.
- When the development of all layers was successful, the pellet was heated at  $T = 1,150$  °C for 5 h (10.5 h ramp up, 6 h ramp down).

#### 7.3.4. Final Electrodes Processing Methods

Prior to electrodes deposition, the BZCY72 disk was ground with SiC paper to obtain good adherence of the electrode on the electrolyte surface. Thereupon, the BZCY72 disc was heated up to 120 °C for 30 min and weighted. The heating process was necessary to remove any disc humidity. Finally, two porous electrode layers were deposited on both sides of the BZCY72 disk. It should be also noted that during the deposition procedure, the produced electrodes (anode and cathode) were tested and considered successful only if the total in-plane resistance was within the order of hundreds of Ohms and the developed layer did not peel of or scratched easily. If these conditions were not fulfilled, one or both layers were removed and prepared again, or additional layer(s) were deposited on top of them. After the successful electrode deposition and for the cell completion, a fine-masked gold mesh was pressed down on the electrode to act as the current collector, while gold wires was also used to serve as current leads (Figure 7.4).



**Figure 7.4:** Symmetrical gold mesh and gold wires deposition on  $\text{Co}_3\text{O}_4/\text{CeO}_2$  electrode surface.

## 7.4. CHARACTERIZATION STUDIES

### 7.4.1. $\text{H}^+$ Conducting Solid Electrolyte/Membrane, $\text{BaZr}_{0.7}\text{Ce}_{0.2}\text{Y}_{0.1}\text{O}_3$ (BZCY72)

BZCY72 (NorECs, Oslo, Norway) in the form of a disk (ca. 2 cm diameter and 1 mm thickness), was employed as the proton conducting ceramic solid electrolyte, having less than 100 ppm Ni content and an estimated density of ca. 99% (Table 7.1).

**Table 7.1:** Typical characteristics of a commercial BZCY72 disc (NorECs, Oslo, Norway).

Sample Specification	BZCY72
Type	$\text{BaZr}_{0.7}\text{Ce}_{0.2}\text{Y}_{0.1}\text{O}_3$
Ni content (ppm)	<100
Diameter (mm)	20
Thickness (mm)	10
Grain size ( $\mu\text{m}$ )	~5
Estimated density (%)	99
Proton conductivity, 600 °C, wet $\text{H}_2$ (S/cm)	$\sim 1.2 \cdot 10^{-3}$

Upon sintering, a flat ceramic disc with black color (as presented in Figure 7.5) was obtained and weighted to determine the electrodes weight.

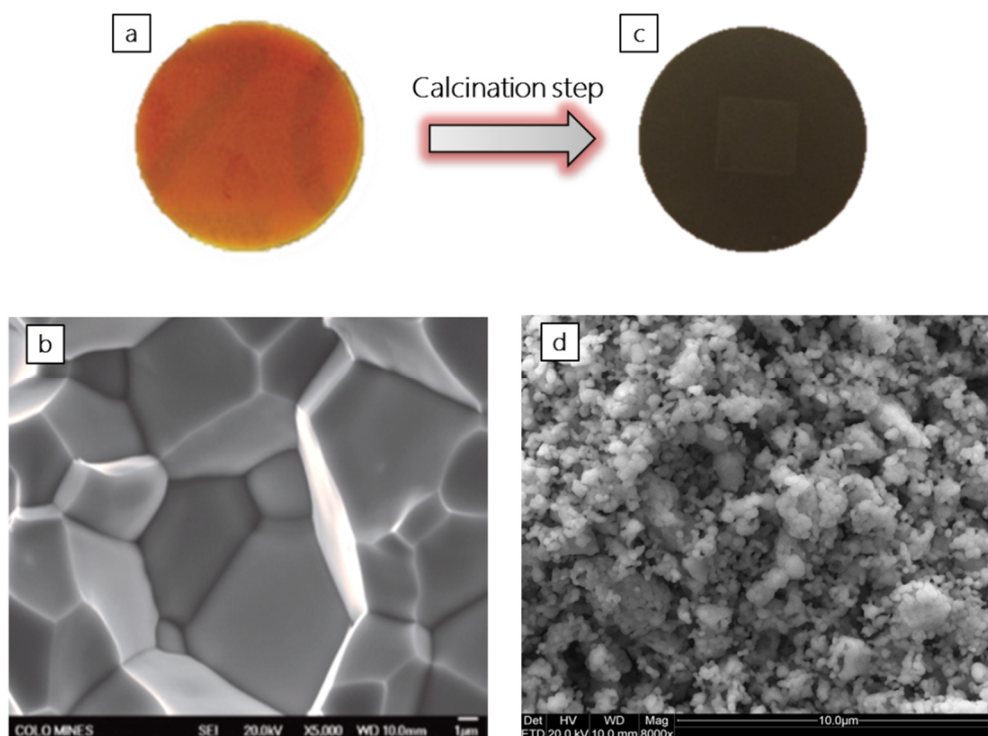


**Figure 7.5:** Representative sample characteristics: a) Commercial BZCY72, NorECs, disc; b) Fractured disc microstructure, magnification bar: 1  $\mu\text{m}$  (NorECs, Oslo, Norway); c) BZCY72, disc, 1,400  $^{\circ}\text{C}$ , 5 h; d) Treated disc under reducing conditions (800  $^{\circ}\text{C}$ , 12 h, 10 v/v%  $\text{H}_2$ /90 v/v% Ar) microstructure, magnification bar: 10  $\mu\text{m}$ .

#### 7.4.2. Anode Electrode, $\text{Co}_3\text{O}_4$ Supported on $\text{CeO}_2$ Catalysts ( $\text{Co}_3\text{O}_4/\text{CeO}_2$ )

Scanning electron microscopy (SEM) analysis was performed to visualize, evaluate and verify the microstructure of the developed layers. The microstructure of the deposited  $\text{Co}_3\text{O}_4/\text{CeO}_2$  layers were examined before and after the electrochemical tests, supported also by energy dispersive X-ray spectroscopy (EDS), using a FEI Quanta 200 FEG-ESEM electron microscope in high vacuum mode.

The sample was attached to a metal sample holder using carbon tape and coated with a thin gold layer. SEM-inspection of electrodes after firing at  $T = 1,400\text{ }^{\circ}\text{C}$  showed a well sintered grain structure of 5  $\mu\text{m}$  grains for both layers. The anode electrode oxide grains were well connected to each other and a porous network with good electronic conductivity was formed. Figure 7.6 presents the top view micrographs of the printed  $\text{Co}_3\text{O}_4/\text{CeO}_2$  layer after a) calcination at  $T = 1,400\text{ }^{\circ}\text{C}$ , and b) reduction for 10 h (10 v/v%  $\text{H}_2$ /90 v/v% Ar) at  $T = 850\text{ }^{\circ}\text{C}$ , overnight.

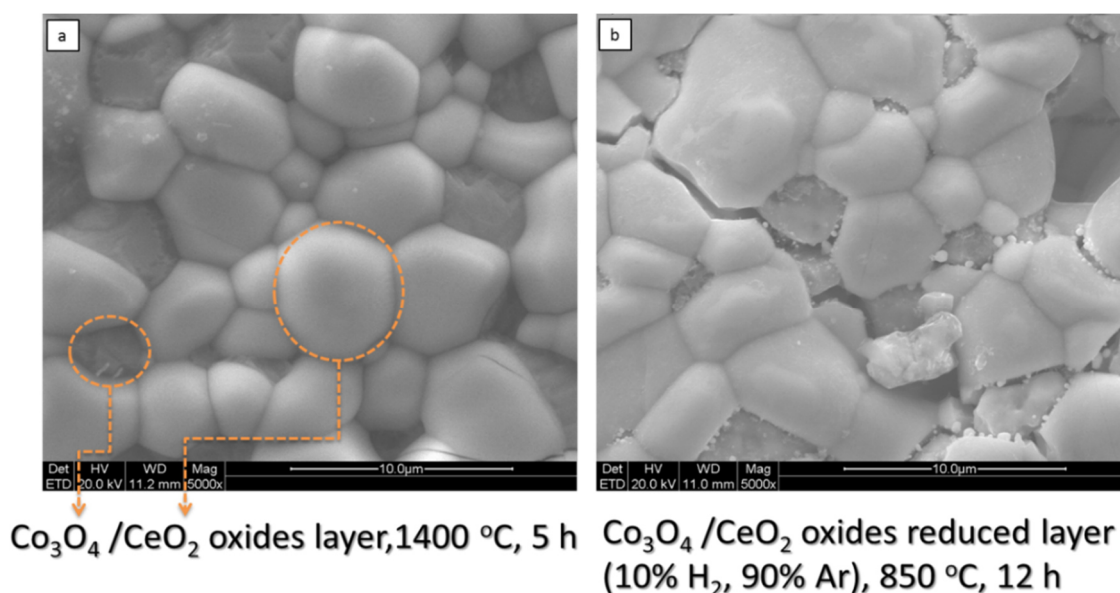


**Figure 7.6:** Top view micrographs of the screen-printed  $\text{Co}_3\text{O}_4/\text{CeO}_2$  layer after a) calcination at  $T = 1,400\text{ }^\circ\text{C}$ , and b) reduction for 10 h (10 v/v%  $\text{H}_2/90\text{ v/v}\%$  Ar) at  $T = 850\text{ }^\circ\text{C}$ , overnight.

#### 7.4.3. Counter Electrode, $\text{BaGd}_{0.8}\text{La}_{0.2}\text{Co}_2\text{O}_{6-\delta}$ (BGLC)

The composition and phases of the BGLC electrode was studied via x-ray powder diffraction. More specifically, small samples of approximately 20 mg were suspended in isopropanol and then dripped onto suitable sample holders, where isopropanol was allowed to evaporate. The sample preparation was completed upon repeating these steps several times until the formation of a uniform film on the substrate. For the analysis, a Bruker D8 3-circle diffractometer, equipped with an area detector and a nitrogen cryostat, was employed. The x-rays were scanned at angles ranging from  $20^\circ$  to  $80^\circ$ .

As it was previously analyzed, BGLC powders were initially synthesized at  $T = 1,100\text{ }^\circ\text{C}$ . Subsequently, the temperature was reduced to  $T = 900\text{ }^\circ\text{C}$  to facilitate the formation of a more active body for sintering; the density of the sintered bodies was increased from 70-80% to an average value approximately equal to 93%. The density measurements were made using two micrometers (i.e., thickness and diameter) and an Archimedes setup. After powder calcination at  $T = 1,100\text{ }^\circ\text{C}$ , the obtained diffractograms (see Figure 7.7) revealed that no secondary phases were present, though a phase-pure product was formed. Moreover, the diffractogram taken at  $T = 25\text{ }^\circ\text{C}$  indicated a tetragonal system with a  $p4/mmm$  symmetry group; a similar structure to other double perovskites.

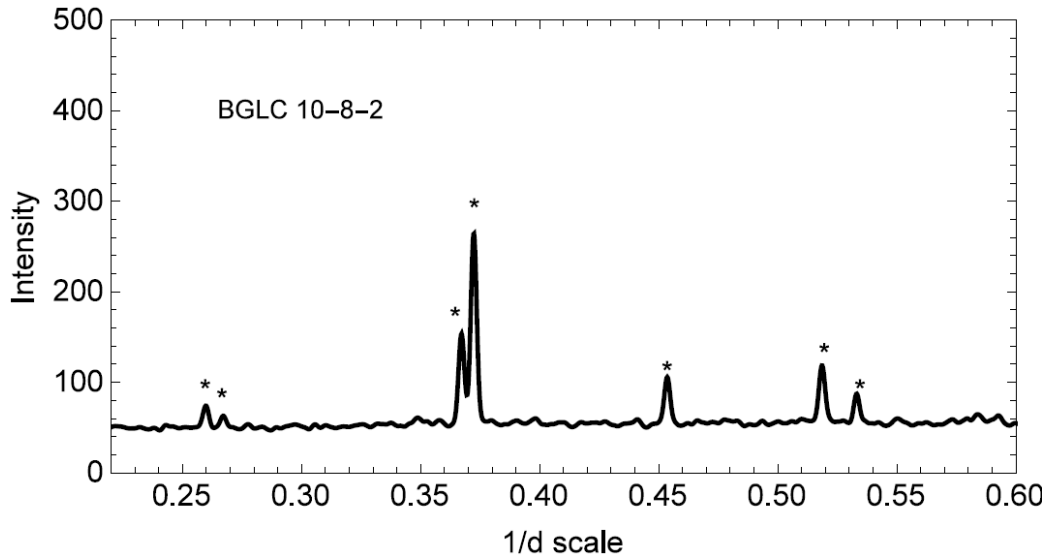


**Figure 7.7:** Diffractogram of a BGLC 10-8-2 sample taken at 25 °C. \*peaks taken from Strandbakke et al. (2015).

Typical Nyquist plots, produced via the Electrochemical Impedance Spectroscopy (EIS) methodology, are presented in Figure 7.8, regarding the BZCY72 electrolyte-BGLC electrode system, in wet oxygen at 550 °C.

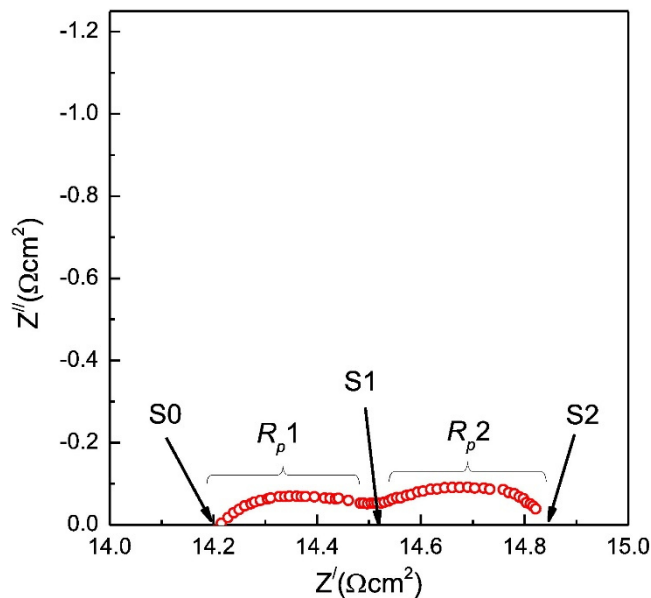


**Figure 7.8:** Nyquist plot with impedance sweep from 15 kHz to 1 mHz of BGLC electrodes in a symmetrical configuration, after correcting for electrode area, in wet oxygen at 550 °C (Strandbakke et al., 2015).

Two impedance arcs can be identified from the spectrum, while S0, S1, and S2 can be assigned to the resistances associated with the electrolyte, electrode charge transfer and electrode diffusion phenomena, respectively. It should be highlighted that BGLC presented the lowest polarization resistance for the selected temperature range (500 to 700 °C). Moreover, the electrodes showed in general a good performance, with the lowest total apparent polarization resistance for BGLC/BZCY72 being 0.05 and 10  $\Omega\cdot\text{cm}^2$  at  $T = 650$  and  $350$  °C, respectively (Strandbakke et al., 2015).

## 7.5. EXPERIMENTAL SETUP, REACTOR DESIGN AND PROCEDURE

### 7.5.1. Electrochemical Performance Employing Ideal ( $\text{H}_2/\text{H}_2\text{O}/\text{Ar}$ Mixtures) Reaction Conditions

Initially, the electrochemical performance of  $\text{Co}_3\text{O}_4/\text{CeO}_2$  mixed oxide electrodes, when exposed to  $\text{H}_2/\text{H}_2\text{O}/\text{Ar}$  mixtures, was examined by employing a proton conducting  $\text{BaZr}_{0.7}\text{Ce}_{0.2}\text{Y}_{0.1}\text{O}_3$  symmetrical cell. The impact of temperature,  $p_{\text{H}_2}$  and  $p_{\text{H}_2\text{O}}$  on the cell performance was thoroughly assessed by means of electrochemical impedance spectroscopy (EIS), upon employing a GAMRY References 3000 potentiostat, under open circuit conditions (frequency 0.5 MHz to 1  $\mu\text{Hz}$ , amplitude 25 RMS).

The apparatus used to examine the symmetrical cell performance under ideal conditions can be divided into three main parts, namely:

1. Gas flow and temperature control.
2. The reactor cell system.
3. Electrochemical measurements.

#### 7.5.1.1. Gas Flow and Temperature Control

In what follows, the protocol for the operation of the ProboStat™ system is described in detail. Initially, the flow connections were installed and checked for leakage (by using a bubble flowmeter). After the construction of the reactor and its installation into the furnace and prior to the experiments, the selected gas mixtures were delivered by an in-house built gas mixer, designed to efficiently control the composition of the reactant gas feedstock, as

well as, the water vapor pressure in the measurement cell, assisted by a two-step wetting step of the gas mixture at room temperature. Also before the experimental runs, the temperature was steadily increased up to the set point with the aid of a programmed temperature controller, while feeding pure argon as the carrier gas. During the experiments, the gas feedstock (consisted of H<sub>2</sub> and/or H<sub>2</sub>O gas mixtures, balanced if necessary with Ar) flow was fixed with appropriate mass flow controllers. After the cell chamber, the feed mixture passed through a saturated KBr aqueous solution. In more detail inert argon (99.999 v/v% purity, Air Liquide), with a flow rate of 50 cm<sup>3</sup>/min, was introduced into the cell reactor, while the temperature was steadily increased up to 850 °C (heating rate 3 °C /min). When the selected temperature was reached, 10 v/v% H<sub>2</sub> with a flow rate of 50 cm<sup>3</sup>/min, was introduced and fed overnight into the cell reactor; subsequently water vapor (2.5 v/v% H<sub>2</sub>O) was introduced to the cell reactor. After reaching steady state, appropriate H<sub>2</sub>/H<sub>2</sub>O/Ar mixtures were also introduced to the cell reactor; e.g., p<sub>H<sub>2</sub></sub> was kept constant, while p<sub>H<sub>2</sub>O</sub> was regulated from dry to wet conditions at both temperatures (600 and 850 °C).

### 7.5.1.2. The Reactor Cell System

The cell was mounted in a ProboStat™ measuring apparatus (NorECs, Oslo, Norway), as illustrated in Figure 7.9. It should be highlighted that the ProboStat™ patented system is in principle a cell for electrical measurements with a versatile construction and a broad range of accessories, based on years of development and experience in the Kofstad/Norby group at the University of Oslo. In this system, the sample rests on a 50 cm long alumina support tube, in the standard design for 20 mm diameter discs, inside a sealed outer tube of alumina or silica. The sample is in contact with the two electrodes of the button cell disc, via a spring-loaded alumina assembly. The system is equipped with electrode contact leads, two wire pairs (i.e., one for current and one for voltage) and thermocouple feedthroughs, as well as, gas inlet and outlet provisions for both inner and outer compartments.

The electrical connections are made via coax cables, suitable for standard impedance spectrometer connectors, and standard thermocouple compensation cables. Gases can be fed in single or dual chamber modes, directly onto or from electrodes, facilitating the experiments under controlled atmospheres, transport number measurements in gradients, and testing of cell components. The gas supply is performed via Swagelok quick-connects.

Thus, the environment, in which the sample is exposed, can be controlled with respect to temperature and partial pressures of the reactant gasses. The base unit is illustrated in Figure 7.10, while the schematic of the experimental setup and the in-house built gas mixer is presented in Figure 7.11.

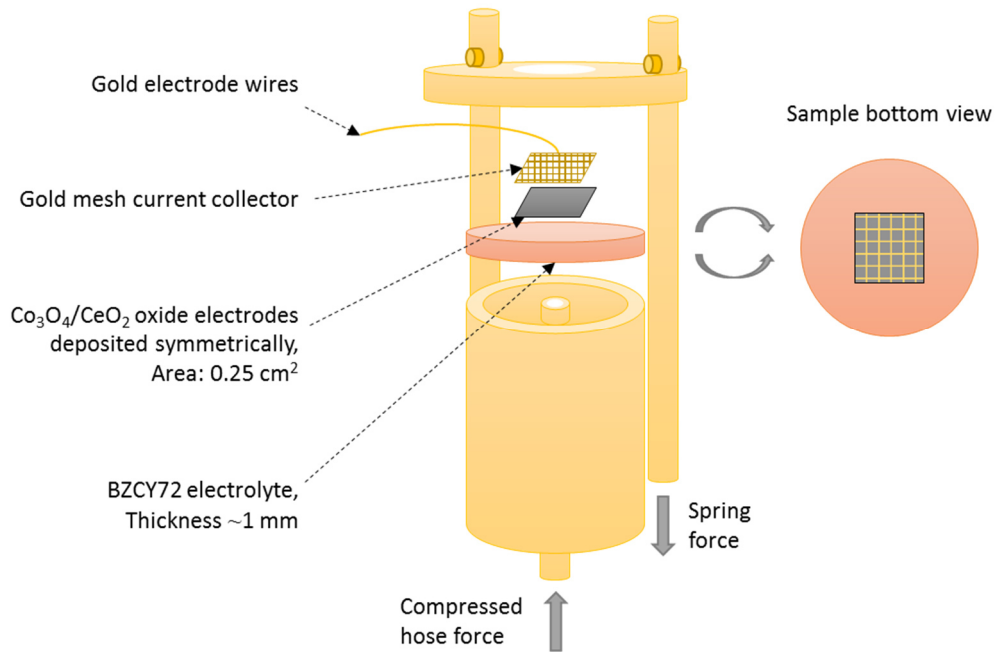


**Figure 7.9:** Example of the connection of disk samples for impedance measurements. The schematic presents the major characteristics of the cell (NorECs, Oslo, Norway).

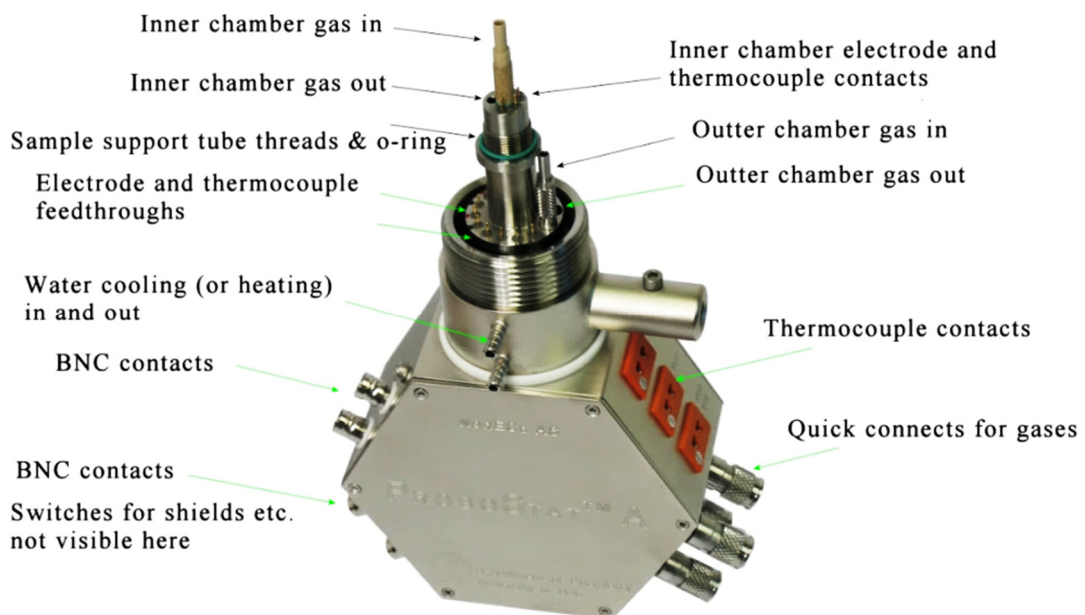


**Figure 7.10:** ProboStat™ base unit with feedthroughs (NorECs, Oslo, Norway).

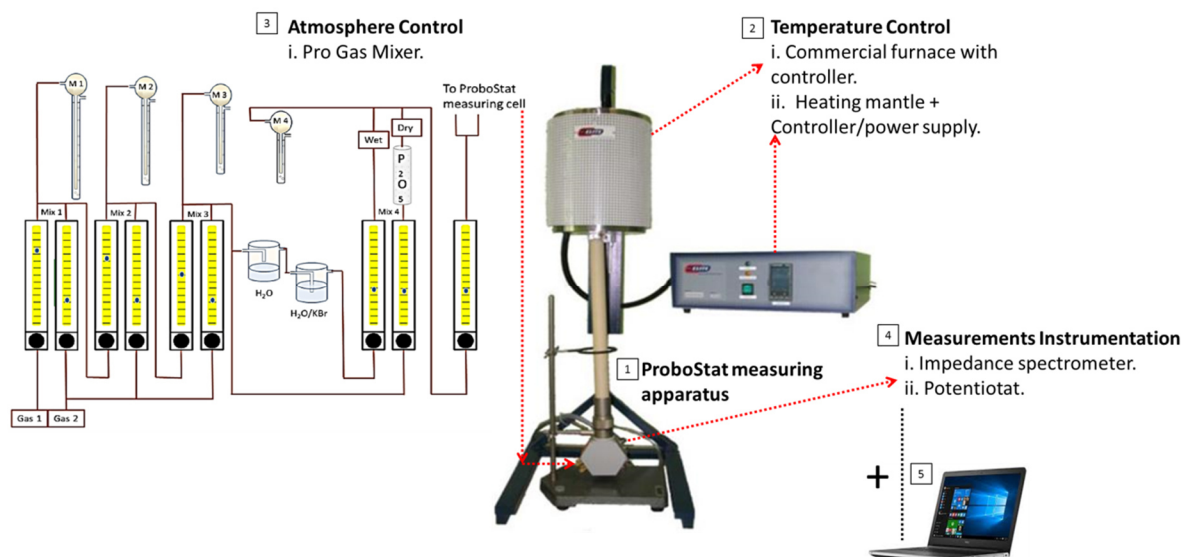


**Figure 7.11:** Schematic illustration of the experimental setup and the in-house built gas mixer.

### 7.5.1.3. Electrochemical Measurements

In order to evaluate the  $\text{Co}_3\text{O}_4/\text{CeO}_2$  electrode, AC impedance spectroscopy studies were performed at various temperatures (850-600 °C) and feed mixtures ( $\text{pH}_2$ ,  $\text{pH}_2\text{O}$ ) in a button cell (flat disk) configuration, employing the symmetrical cell  $\text{Co}_3\text{O}_4\text{-CeO}_2/\text{BZCY72}/\text{Co}_3\text{O}_4\text{-CeO}_2$ . In general, this analysis was conducted to enable the calculation of the polarization resistance, which is the outcome of the electrochemical reactions on the electrode/electrolyte interface. More specifically, after multiplying with the electrode surface area and dividing by two (due to the symmetrical configuration of the cell), all resistance values are expressed in this work as area specific resistances (ASR in  $\Omega\cdot\text{cm}^2$ ), and used to compare the electrodes electrochemical effectiveness.

All EIS experiments were conducted under atmospheric pressure, at temperatures between 600 and 850 °C and the total flow rate of the reacting mixture was equal to  $100\text{ cm}^3/\text{min}$ . Impedance measurements were performed in two-point configuration, where two wires (current lead and voltage probe) were linked to the top (working) and the bottom (counter, linked with the low current lead) electrodes. A single symmetrical cell was employed for all measurements and the spectra were acquired every 4 h, while each step duration was 45 min (different  $\text{H}_2$ ,  $\text{H}_2\text{O}$  feed concentrations and cell temperatures).

The impedance measurements were performed and analyzed with the aid of a GAMRY Reference 3000 potentiostat, by applying oscillating 25 mV RMS voltages in the frequency range from 0.5 MHz to 1  $\mu$ Hz. Since different temperatures and gas environments demand different voltages and frequency ranges, it was necessary to measure frequencies as low as 1  $\mu$ Hz. The voltage amplitude value was set as low as possible to avoid any impact by the applied voltage on the activation energy of the electrode reaction and, also, to prevent any mass transport limitation phenomena. The impedance data were deconvoluted by using the ZView software from Scribner Associates, Inc. The effect of temperature,  $p_{H_2}$  and  $p_{H_2O}$  on the electrical properties of the symmetrical cell, using the AC impedance method are described in detail in Chapter 8 (Section 8.1) of this thesis.

### 7.5.2. Electrochemical Performance of the Cell, Employing $H_2S/H_2O/Ar$ Reaction Conditions, Single Chamber

The electrochemical performance and stability of  $Co_3O_4$  catalysts, supported on  $CeO_2$  composite electrodes, in rich  $H_2S$  atmospheres containing excess  $H_2O$  (90 v/v%) was examined in a single chamber proton conducting ceramic symmetrical cell, employing  $BaZr_{0.7}Ce_{0.2}Y_{0.1}O_3$  (BZCY72) as the proton conducting solid electrolyte. The impact of temperature (850-700  $^{\circ}C$ ) and  $H_2S$  concentration in steam-rich atmospheres on the cell performance was thoroughly assessed by means of electrochemical impedance spectroscopy (EIS); the Versa Stat 4 workstation was employed in this case under open circuit conditions (frequency 0.5 MHz to 1  $\mu$ Hz, amplitude 25 mV RMS). The system used in the  $H_2S$  electrolysis experiments can be divided into three main parts, namely:

1. Gas flow and temperature control.
2. The reactor cell system.
3. Electrochemical measurements.

#### 7.5.2.1. Gas Flow and Temperature Control

Initially, the flow connections were installed and checked for leakage (using a bubble flowmeter). After the construction of the reactor, its installation into the furnace and prior to the experimental runs, the three way valves should be adjusted appropriately so that the

reactant stream is by-passing the reactor. Initially, inert argon (99.999 v/v% purity, Air Liquide), with a flowrate of 50 cm<sup>3</sup>/min, was introduced into the cell reactor, while the temperature was steadily increased up to the set point, with a heating rate 3 °C/min, regulated by a programmed temperature controller. When the selected temperature was reached and after the employment of reducing conditions (10 v/v% H<sub>2</sub> - 90 v/v% Ar) overnight, water vapor (90 v/v% H<sub>2</sub>O) was gradually introduced to the cell reactor with the aid of a liquid double-distilled H<sub>2</sub>O pump and a heater. After reaching the steady state, a 10 v/v% H<sub>2</sub>S, balanced with Ar mixture at the appropriate flow rate was also fed into the cell reactor to result in reaction mixtures containing 0-1 v/v% H<sub>2</sub>S - 90 v/v% H<sub>2</sub>O, balanced with Ar as a diluent. Notice that in case that the operation temperature was needed to be regulated at another set-point value, it was not necessary to switch the three way valves to the reactor by-pass position. On the other hand, when the reactants composition was about to change, the new feed was regulated and controlled while the stream was by-passing the reactor and upon that was driven into the reactor, as described previously.

### 7.5.2.2. The Reactor Cell System

With the exception of the reactor configuration, the gas flow experimental set-up, as well as, the experimental procedure followed to examine the electrochemical performance of the Co<sub>3</sub>O<sub>4</sub>-CeO<sub>2</sub>/BZCY72/Co<sub>3</sub>O<sub>4</sub>-CeO<sub>2</sub> symmetrical cell at H<sub>2</sub>S/H<sub>2</sub>O atmospheres, were identical to those described in detail in Chapter 4; the set-up briefly consisted of: 1) the gas feeding unit, including the cylinders of the employed gas mixtures: 1a) pure Ar and 1b) H<sub>2</sub>S/Ar, 2) the corresponding mass flow controllers, 3) the liquid H<sub>2</sub>O pump and 4) the heater for H<sub>2</sub>O vapor incorporation into the cell reactor, 5) the cell reactor, 6) the condenser, located just after the cell reactor, to remove the unreacted H<sub>2</sub>O, 7) the sulfur trap, located before the gas analysis system, to remove the S-containing chemical species, 8) the Gas Chromatograph to monitor the generated H<sub>2</sub> at the cell reactor effluent, and 9) the electrochemical workstation connected to the cell (addition of the present configuration). The apparatus configuration is shown in Figure 7.12 with the inset presenting the schematic of the cell reactor.

More details regarding the various parts of the custom-made single chamber reactor cell testing system are given in Figure 7.13.

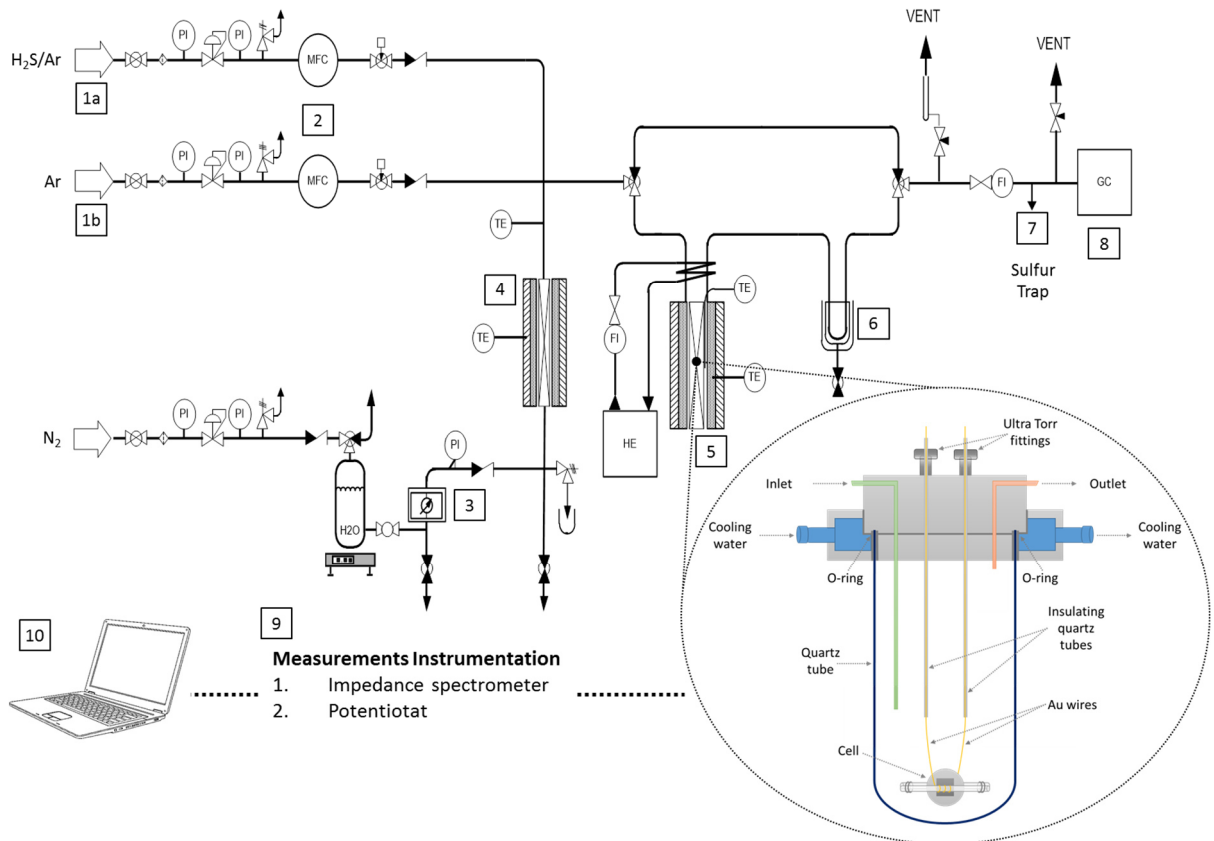


**Figure 7.12:** Gas flow experimental set-up for the examination of the electrochemical performance of the  $\text{Co}_3\text{O}_4\text{-CeO}_2/\text{BZCY72}/\text{Co}_3\text{O}_4\text{-CeO}_2$  symmetrical cell, employing  $\text{H}_2\text{S}/\text{H}_2\text{O}/\text{Ar}$  reaction conditions, in single chamber mode.

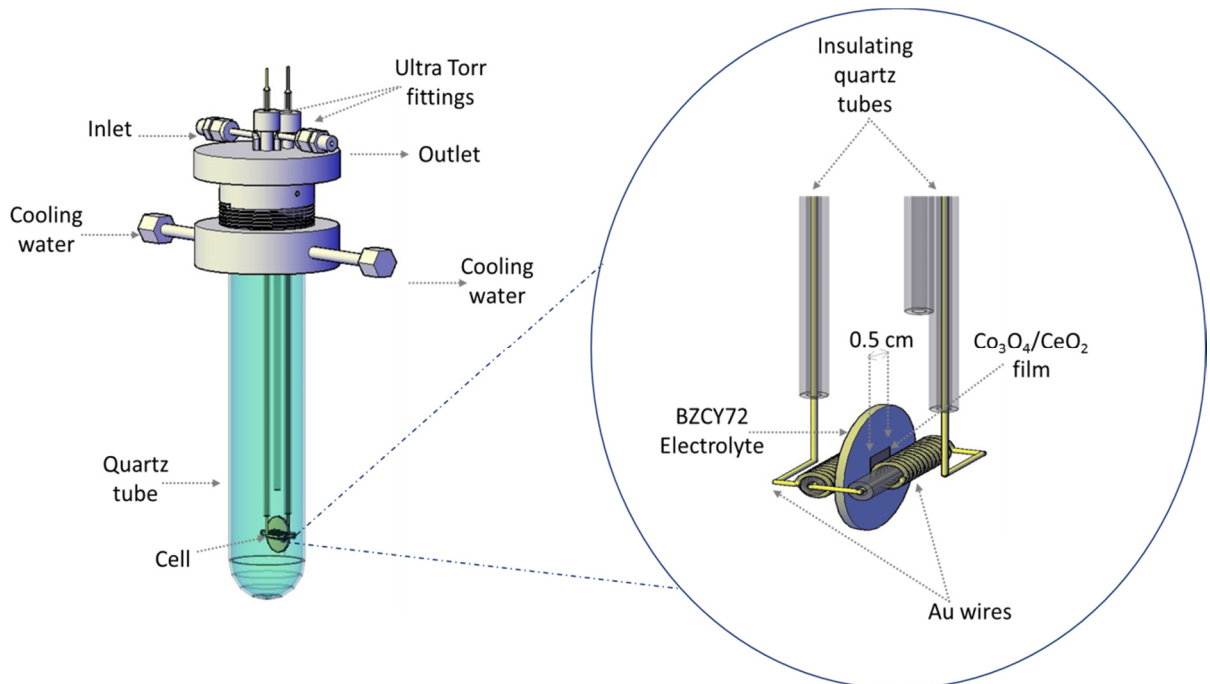


**Figure 7.13:** Schematic representation of the single chamber proton conducting ceramic symmetrical cell,  $\text{Co}_3\text{O}_4\text{-CeO}_2/\text{BZCY72}/\text{Co}_3\text{O}_4\text{-CeO}_2$ .

The system consists of a stainless steel head, which incorporates specific provisions for reactants feed and products removal, and to which a quartz tube (150 mm long, ID=37 mm, OD=40 mm) is accommodated. The quartz tube is equipped with a cooling ring (SS 316) and a Viton O-ring for sealing. The cell is located inside a quartz tube, and both electrodes are exposed to the same reaction atmosphere. Two thin Au wires in contact with the electrodes are used to hold the cell suspended inside the quartz tube and to electrically connect the cell to the Versa Stat 4 electrochemical workstation. Quartz tubes (ID=1 mm, OD =3 mm) are used to insulate the Au wires from the reactor head and Ultra Torr fittings hold the tubes in place. The top of these tubes were is sealed by placing and melting at open flame a small (about 1 cm long) piece of 1/8" polyethylene tube.

### 7.5.2.3. Electrochemical Measurements

As discussed above, all EIS experiments were conducted under atmospheric pressure, at temperatures between 850 and 700 °C, while the total flow rate of the reacting mixture was equal to 100 cm<sup>3</sup>/min. The pressure of the inlet and outlet streams of the reactor were monitored and recorded, in order to secure the operation of the H<sub>2</sub>S trap. Moreover, the impedance measurements were performed in two-point/four wire configurations. Two wires were linked to the top and the bottom electrodes. The impedance measurements were carried out with an oscillating 25 mV RMS voltage in the frequency range from 0.5 MHz to 1 μHz, using a Versa Stat 4 electrochemical workstation by Princeton Applied Research and the relevant software (Versa Studio) for data processing. A single symmetrical cell was employed for all measurements and the spectra were acquired every 30 min for a total duration of 3 h in each step (different H<sub>2</sub>S feed concentrations and cell temperatures). In all cases, the cell impedance was normalized by the geometric area of the symmetrical cell, thus all resistance values are expressed in Ω·cm<sup>2</sup>. The impedance data was deconvoluted by using the Z-view software from Scribner Associates and by applying a Randle's type of equivalent circuit, as presented in Figure 7.14. If necessary, the circuit was modified by including a Gerischer element, accounting for a distributed chemical-electrochemical reaction series and providing asymmetric impedance responses, such as drop-shaped semi-circles.

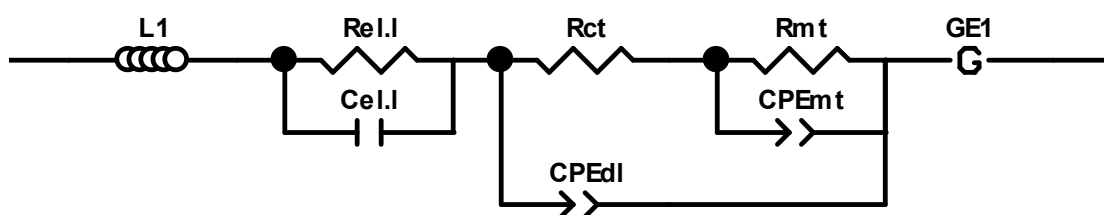


**Figure 7.14:** Equivalent circuit model, representing the i) electrolyte resistance ( $R_{eI.I}$ ), ii) capacitance ( $C_{eI.I}$ ), iii) charge transfer resistance ( $R_{ct}$ ), iv) double layer pseudo-capacitance ( $CPE_{dI}$ ), v) mass transfer resistance ( $R_{mt}$ ), vi) pseudo-capacitance ( $CPE_{mt}$ ), and vii) Gerischer impedance ( $GE1$ ).

When the Gerischer element is used for the deconvolution, the reported total mass transfer resistance is always defined as the sum of  $R_{mt}$  and  $R_G$ . Thus,  $R_G$  is the Gerischer resistance at DC, calculated as:

$$R_G(\omega = 0) = \frac{1}{Y_0 \sqrt{k}} \quad (7.1)$$

### 7.5.3. Electrochemical Performance of the Cell, Employing $H_2/Ar$ and $H_2S/H_2O/Ar$ Mixtures Reaction Conditions, Double Chamber

For the  $H_2S$  electrolysis process, implemented using a double chamber proton conducting cell, diluted  $H_2S$  in excess  $H_2O$  was fed at the anode, while the cathode was exposed to oxidizing conditions. In such a cell, as it is described in the previous sections, one of the major issues is the optimal selection of materials; thus,  $BaZr_{0.7}Ce_{0.2}Y_{0.1}O_3$  (BZCY72) was employed as the solid electrolyte, and  $Co_3O_4$  supported on  $CeO_2$  catalysts and  $BaGd_{0.8}La_{0.2}Co_2O_{6-\delta}$  (BGLC) were selected as the anode and cathode materials, respectively. The impact of temperature (800 °C) employing different reaction conditions i.e.,  $H_2$  concentration (1 v/v%) at dry conditions and  $H_2S$  concentration (1 v/v%) in steam-rich atmospheres (30 v/v%) on the cell performance was thoroughly assessed by means of EIS (use of the Versa Stat 4 workstation under open circuit conditions with 0.5 MHz to 1  $\mu$ Hz frequency and 25 mV RMS amplitude).

Similarly with the single chamber case, the experimental apparatus used for the double chamber case was identical to the one described in Chapter 4 (except the reactor). Thus, the

system used in the H<sub>2</sub>S electrolysis experiments can be divided into three main parts, namely:

1. Gas flow and temperature control.
2. The reactor cell system.
3. Electrochemical measurements.

### 7.5.3.1. Gas Flow and Temperature Control

Initially, the inlet valve of the reactor was switched on and argon was allowed to pass through the reactor as a purge gas. In each experimental run, upon the construction and installation of the reactor into the furnace, three way valves were adjusted appropriately, so that the reactant stream was by-passing the reactor. Moreover, a suitable temperature controller was programmed to control the temperature increase. As in many similar studies with YSZ electrolytes, where a typical 3-5 °C heating rate was applied, the cell was initially heated from room temperature to 800 °C at a heating rate of 3 °C/min. When the selected temperature set point was reached, the three way valves were switched so that the reactant feed passed through the reactor and reducing conditions (10 v/v% H<sub>2</sub> - 90 v/v% Ar) were employed overnight. Subsequently, water vapor (30 v/v% H<sub>2</sub>O) was gradually introduced to the cell reactor with the aid of a liquid double-distilled H<sub>2</sub>O pump and a heater. After Ar passed through the reactor for sufficient time, the valve connecting the hydrogen sulfide tank (containing 10 v/v% H<sub>2</sub>S, balanced with Ar mixture) was switched on and the appropriate flow was fed to the cell reactor to accomplish reaction mixtures with desired composition, i.e., 1 v/v% H<sub>2</sub> and 1 v/v% H<sub>2</sub>S - 30 v/v% H<sub>2</sub>O, with Ar as the diluent. The sweep gas was channeled into the anode chamber at a flowrate of 100 cm<sup>3</sup>/min, whereas the cathode was exposed to air at a flow rate of 50 cm<sup>3</sup>/min. Upon a time period of at least three quarters of an hour the experiments were initiated. Again, it was not necessary to switch the three way valves to the reactor by-pass mode, so that the operation temperature could be changed. On the contrary, the feed stream composition was altered only when it was by-passing the reactor.

### 7.5.3.2. The Reactor Cell System

In order to perform the  $\text{H}_2\text{S}$  electrolysis experiments, the same reaction system, gas flow experimental set-up and experimental procedure with the ones described in Chapter 4 were used, except for the reactor cell. The latter consisted of an Yttrium Stabilized Zirconia (YSZ) tube (1.2 mm thickness) as the main component of the double chamber reactor, opened at both ends. Since YSZ is considered as a classical oxygen ion conducting solid electrolyte, it was implemented to efficiently separate the two chambers of the reactor. More details on the various parts of the custom-made double chamber reactor cell testing system are described in the sequence and are presented in Figure 7.15. It consists of a stainless steel head (Figure 7.16), which incorporates specific provisions for the reactants feed and the products removal, and to which a quartz tube (150 mm long, ID = 37 mm, OD = 40 mm), is accommodated.

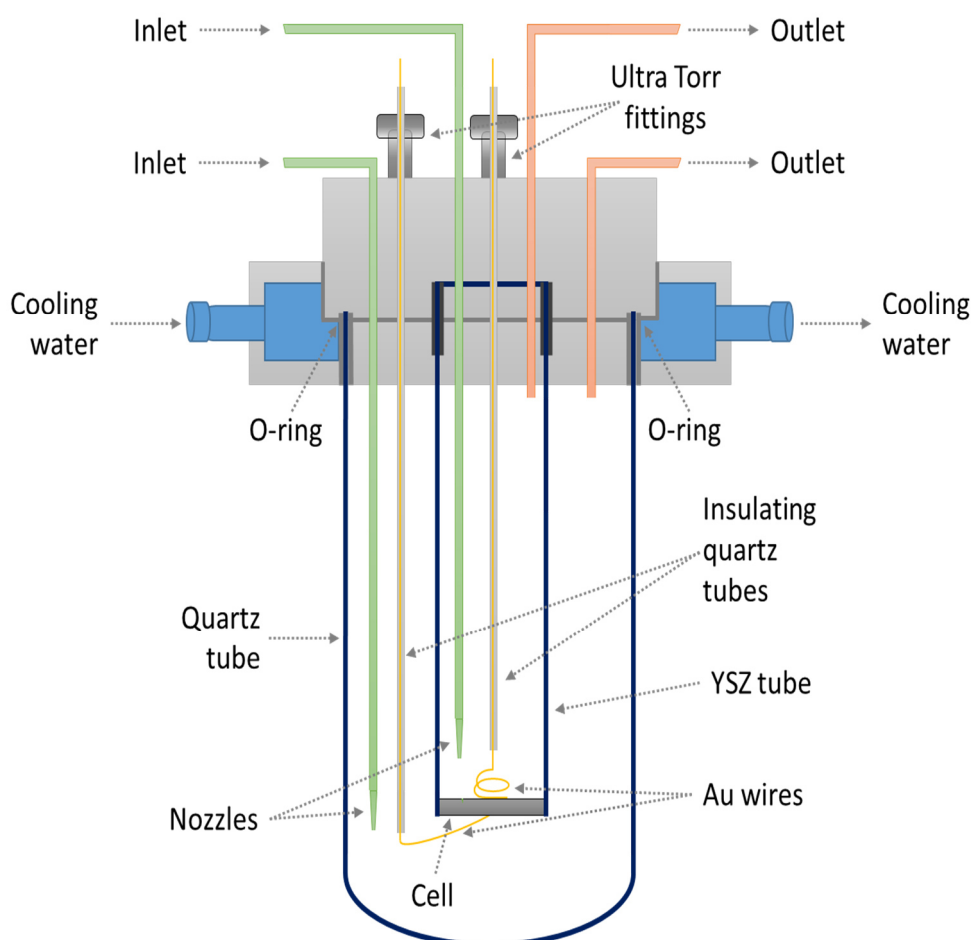


**Figure 7.15:** Schematic representation of the double chamber symmetrical proton conducting cell,  $\text{Co}_3\text{O}_4\text{-CeO}_2/\text{BZCY72}/\text{BGLC}$ , with the cathode exposed to air.

The main functions of the reactor head are to provide the:

- “Centerpiece” of the setup, the component which connects all the other parts.
- Tubes for the feed of reactants and the removal of products for both chambers.
- Gastight sealing of the YSZ tube; this is accomplished with the aid of Viton O-rings and Teflon tape, which have to be kept at fairly low temperature.
- Flow of the cooling water; this is necessary to maintain the temperature at safe levels (<60 °C). Water was circulated via two tubes at diametrically opposite positions.



**Figure 7.16:** Physical images of the stainless steel head of the double chamber reactor cell.

The quartz tube, closed at one end, was installed for the formation of the second chamber and was equipped with a cooling ring (SS 316) and an O-ring for sealing, which are both made of Viton (for high temperature operation). Two thin Au wires, in contact with the electrodes, were used to hold the cell suspended inside the quartz tube and to electrically connect the cell to the Versa Stat 4 electrochemical workstation. Quartz tubes open at both ends (ID = 1 mm, OD = 3 mm) were used to insulate the Au wires from the reactor head and Ultra Torr fittings held the tubes in place. The top of these tubes were sealed by placing and melting at open flame a small (about 1 cm long) piece of 1/8” polyethylene tube. A porous  $\text{Co}_3\text{O}_4/\text{CeO}_2$  and BGLC film, deposited on the inner and outer surface of the BZCY72 electrolyte, served as the anode and cathode electrodes, respectively. The manufacture and role of the electrodes were described in details in Sections 7.3.2 and 7.3.3.

### 7.5.3.3. Electrochemical Measurements

All EIS experiments were carried out under atmospheric pressure, in the temperature range 800 °C, while the total flow rate of the reacting mixture was equal to 100 cm<sup>3</sup>/min. The pressure of the inlet and outlet streams of the reactor were continuously monitored and recorded to secure the operation of the H<sub>2</sub>S trap. Two wires were linked to the top and the bottom electrodes. The cell voltage and the produced electrical current were also monitored by means of digital multi-meters (RE69). The impedance measurements were carried out with an oscillating 25 mV RMS voltage in the frequency range of 0.5 MHz to 1 μHz, using a Versa Stat 4 electrochemical workstation by Princeton Applied Research and the relevant software (Versa Studio) for data processing. A double symmetrical cell was employed for all measurements and the spectra were acquired every 30 min for a total duration of 4 h in each step (different H<sub>2</sub>/H<sub>2</sub>S feed concentrations). In all cases, the cell impedance was normalized by the geometric area of the symmetrical cell, thus all resistance values are expressed in Ω·cm<sup>2</sup>. The impedance data was deconvoluted by using the Z-view software from Scribner Associates.

## 7.6. THEORY

### 7.6.1. Electrochemical Impedance Spectroscopy (EIS)

In order to evaluate the ionic conductivity of electrochemical systems, voltammetry methods are conventionally used. The applied signal is in general an electrode potential of sufficient magnitude to provide a measurable DC response. The analysis of the current, as a function of the imposed electrode potential, is used to identify the characteristics and properties of the electrochemical system. However, the method based on DC bias does not generally allow to determine the different contributions (electrolyte interfaces, electrode reactions, etc.) in a solid-state electrochemical cell. In addition, this technique can induce concentration polarization and space charge in the electrodes, which can affect the electrochemical behavior of the materials. The application of a low amplitude alternating current may overcome these difficulties, since the currents flowing through the samples are small. In addition, for high frequencies, the effect of electrode polarization is negligible. Impedance spectroscopy allows such measurement conditions and also the separation or

the deconvolution of the various contributions of resistive and capacitive electrochemical responses. Thus, the characteristics of the electrolyte and the electrode materials can be analyzed and the different electrochemical processes can be specifically studied. The electrochemical characteristics of the cell are based on the point by point analysis of the response of the alternating current according to the frequency of the excitation signal.

Ohm's law defines the resistance,  $R$ , in terms of the applied voltage  $V$  and current  $I$ . Its use is limited to the ideal resistor for a DC system, which is independent of frequency. The relationship between the resistance, current and voltage can be generally expressed as:

$$R = VI \quad (7.2)$$

However, real electrochemical systems exhibit much more complex behaviors, as they are not simply resistive and the electrochemical double layer adds a capacitive term. Other electrode processes, such as diffusion, are time and/or frequency dependent. Therefore, for an actual electrochemical system, impedance is used instead of resistance. The impedance of an electrochemical system, in the present case a ceramic sample placed between two electrodes, defined as  $Z(\omega)$ , is the AC response of the system being studied under the application of an imposed AC signal. The form of the current/voltage relationship of the impedance in an electrochemical system can be expressed by:

$$Z(\omega) = V(t)I(t) \quad (7.3)$$

where  $V(t)$  and  $I(t)$  are the measurements of voltage and current in the AC system. The technique that measures the AC impedance of a circuit element or an electric circuit is called AC impedance spectroscopy. If AC impedance spectroscopy is used in an electrochemical system, the technique is generally called electrochemical impedance spectroscopy, known as EIS. The impedance of an electrochemical system can be also typically expressed in Cartesian coordinates:

$$Z(\omega) = Z_{\text{Re}}(\omega) - jZ_{\text{Im}}(\omega) \quad (7.4)$$

where  $Z_{\text{Re}}$  and  $Z_{\text{Im}}$  are the real and imaginary parts of the impedance, respectively.

In principle, the impedance spectrum of an electrochemical system can be expressed by Nyquist plots, which are graphical representations of the impedance as a function of frequency. A Nyquist plot is displayed for the experimental data set  $(Z(Z_{\text{Re}_i}, Z_{\text{Im}_i}, \omega_i))$ , for  $i = 1, 2, \dots, n$ ) of  $n$  points measured at different frequencies, with each point representing the real and imaginary parts of the impedance ( $Z_{\text{Re}_i} \sim Z_{\text{Im}_i}$ ) at a particular frequency  $\omega_i$ . Some

typical Nyquist plots for an electrochemical system are shown in Figure 7.17. The plots usually have a semicircle shape, where the high frequency area corresponds to the solution resistance (for a cell, mainly the membrane resistance) and the width of the semicircle corresponds to the charge-transfer resistance. The number and shape of the semicircles in a Nyquist plot depend on the working temperature and the cell configuration.

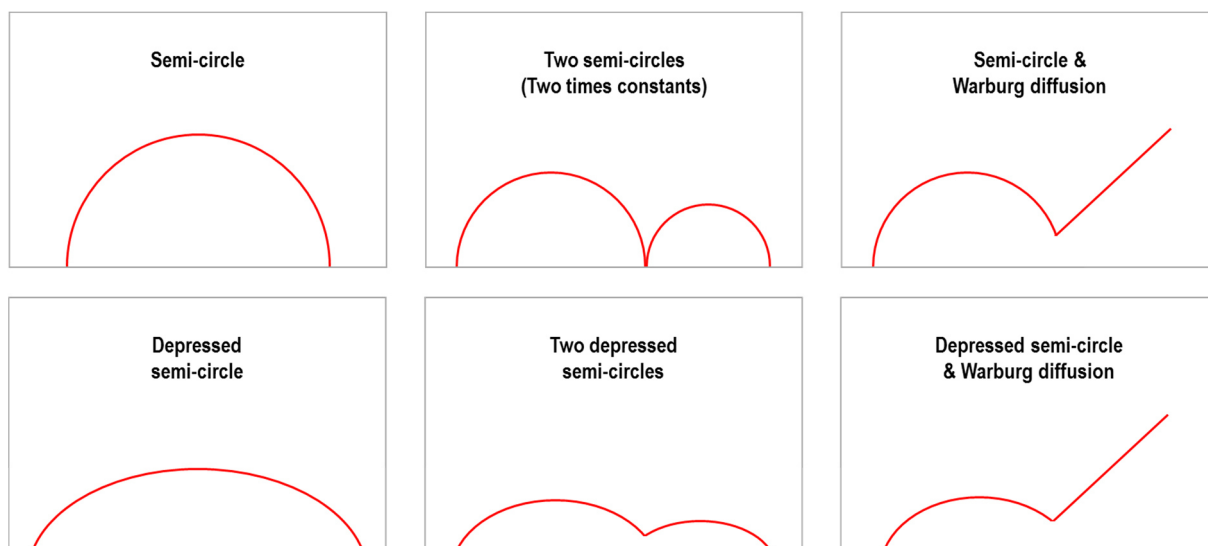


**Figure 7.17:** Typical Nyquist plots for electrochemical systems.

A classical solid-state electrochemical cell consists of two electrodes (currently metals or oxides) separated by an ionic conducting ceramic (a protonic conductor in this PhD thesis). The theoretical impedance diagram expected for such a system is presented in Figure 7.18. It consists of four semicircles: i) high frequency (HF): there are two contributions coming from the bulk and grain boundaries of the electrolyte (resistances  $R_b$  and  $R_{gb}$ , respectively), ii) medium frequency (MF): transfer of the  $H^+$  ions at the cathode/electrolyte interface ( $R_t$ ), iii) low frequency (LF): the phenomenal electrode (resistance  $R_e$ ) corresponding to the reduction of oxygen (adsorption, dissociation, etc.) and the distribution of the  $H^+$  ions. These four main contributions can be separated if the frequencies of relaxation phenomena,  $f_b$ ,  $f_{gb}$ ,  $f_t$  and  $f_e$ , are sufficiently different (ratio  $>50$ ). Notice that each semicircle can be modeled by a parallel RC circuit.

To identify the different contributions, it is convenient to use the Arrhenius diagram of relaxation frequencies. Indeed, this characteristic  $f_R$  is a sort of “identification sign” of

measured phenomena, as they do not depend on the geometrical characteristics of the sample. The relaxation frequencies corresponding to the various phenomena associated with proton-conducting cells are not always sufficiently different to be separated and well identified. The resistance of the electrolyte ( $R_s$ , corresponding to the first intersection of the diagram with the  $Z'$  axis) and the polarization resistance (equal to the difference of the total resistance from the electrolyte resistance,  $R_p = R_{tot} - R_s$ ) are the directly identified quantities.

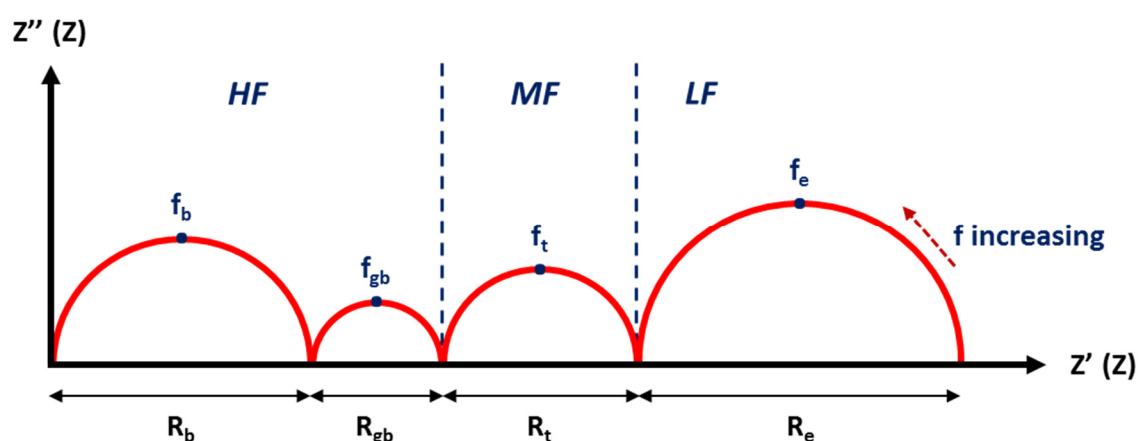


**Figure 7.18:** Theoretical impedance diagram of a cell reactor, consisting of one electrolyte and two electrodes.

### 7.6.2. Equivalent Circuit Models

EIS data analysis is commonly carried out by fitting the data to an equivalent electric circuit model. A circuit model is a combination of resistances, capacitances, and/or inductances, as well as, a few specialized electrochemical elements (such as Warburg diffusion elements and constant phase elements), which produces the same response with the electrochemical system, when the same excitation signal is imposed. Equivalent circuit models can be partially or completely empirical. In a relevant model, each circuit component comes from a physical process of the electrochemical cell and presents a characteristic impedance behavior. The shape of the model impedance spectrum is controlled by the type of the electrical elements in the model and the interconnections between them (series or parallel combinations). The size of each feature in the spectrum is affected by the circuit elements parameters. However, although powerful numerical analysis software, e.g., Zview, is available to fit the spectra and provide optimal values for equivalent circuit parameters, the

analysis of the impedance data can still be troublesome, because complicated and specialized electrochemical processes, such as Warburg diffusion or adsorption also contribute to the impedance. To set up a suitable model, a basic knowledge of the cell being studied and a fundamental understanding of the behavior of cell elements are required. The equivalent circuit should be as simple as possible to represent the electrochemical system and it should give the best possible match between the model impedance and the measured impedance of the system (experimental), whose equivalent circuit contains at least an electrolyte resistance, a double-layer capacity and the impedance of the Faradaic or non-Faradaic process.

## REFERENCES

- Bi L., Zhang S., Lin B., Fang S., Xia C., Liu W. (2009). Screen-printed  $\text{BaCe}_{0.8}\text{Sm}_{0.2}\text{O}_{3-\delta}$  thin membrane solid oxide fuel cells with surface modification by spray coating. *Journal of Alloys and Compounds*, 473: pp. 48-52.
- Costa R., Hafsaoui J., de Oliveira A.P.A., Grosjean A., Caruel M., Chesnaud A., Thorel A. (2009). Tape casting of proton conducting ceramic material. *Journal of Applied Electrochemistry*, 39: pp. 485-495.
- Dailly J., Fourcade S., Largeteau A., Mauvy F., Grenier J.C., Marrony M. (2010). Perovskite and  $\text{A}_2\text{MO}_4$ -type oxides as new cathode materials for protonic solid oxide fuel cells. *Electrochimica Acta*, 55: pp. 5847-5853.
- Dailly J., Marrony M. (2013). BCY-based proton conducting ceramic cell: 1000 h of long term testing in fuel cell application. *Journal of Power Sources*, 240: pp. 323-327.
- Dimarcello F.V., Key P.L., Williams J.C. (1972). Preferred Orientation in  $\text{Al}_2\text{O}_3$  Substrates. *Journal of the American Ceramic Society*, 55: pp. 509-514.
- Gong M., Liu X., Tremblay J., Johnson C. (2007). Sulfur-tolerant anode materials for solid oxide fuel cell application. *Journal of Power Sources*, 168: pp. 289-298.
- Iwahara H. (1995). Technological challenges in the application of proton conducting ceramics. *Solid State Ionics*, 77: pp. 289-298.
- Lengwiler G. (2013). A history of screen-printing. ST Publications, Cincinnati, U.S.A.
- Li J., Luo J.-L., Chuang K.T., Sanger A.R. (2008). Chemical stability of Y-doped  $\text{Ba}(\text{Ce,Zr})\text{O}_3$  perovskites in  $\text{H}_2\text{S}$ -containing  $\text{H}_2$ . *Electrochimica Acta*, 53: pp. 3701-3707.
- Lostec L. (1997). Elaboration par coulage en bande et caractérisation microstructurale et mécanique de composite  $\text{SiC}/\text{MAS-L}$ . PhD Thesis, Université de Limoges, France.
- Marnellos G.E., Athanasiou C., Makridis S.S., Kikkinides E.S. (2008). Integration of hydrogen energy technologies in autonomous power systems, in: Hydrogen based autonomous power systems. Lymberopoulos N., Zoulias E.I. (Eds.), pp. 23-82, Springer, London, U.K.
- Mbah J., Srinivasan S., Krakow B., Wolan J., Goswami Y., Stefanakos E., Appathurai N. (2010). Effect of  $\text{RuO}_2\text{-CoS}_2$  anode nanostructured on performance of  $\text{H}_2\text{S}$  electrolytic splitting system. *International Journal of Hydrogen Energy*, 35: pp. 10094-10101.

- Meng G., Wang P., Gu Y., Peng D. (2000). Preparation and characterization of barium cerate-based thick membranes using a screen printing process. *Solid State Ionics*, 136-137: pp. 209-213.
- Meulenberg W.A., Serra J.M., Schober T. (2006). Preparation of proton conducting  $\text{BaCe}_{0.8}\text{Gd}_{0.2}\text{O}_3$  thin films. *Solid State Ionics*, 177: pp. 2851-2856.
- Mintler R.E., Shanefield D.J., Runk R.B. (1978). Tape casting of ceramics, in: Ceramic processing before firing. Onoda G.Y, Hench L.L. (Eds.) John Wiley and Sons, New York, U.S.A.
- Mistler R.E., Twiname E.R. (2006). Tape casting: theory and practice, John Wiley and Sons, New York, U.S.A.
- Norby T. (1999). Solid-state protonic conductors: Principles, properties, progress and prospects. *Solid State Ionics*, 125: pp. 1-11.
- Rahaman M.N. (2006). Ceramic processing, CRC Press, Taylor & Francis Group, London, U.K.
- Shimura T., Fujimoto S., Iwahara H. (2001). Proton conduction in non-perovskite-type oxides at elevated temperatures. *Solid State Ionics*, 143: pp. 117-123.
- Strandbakke R., Cherepanov V.A., Zuev A.Y., Tsvetkov D.S., Argirusis C., Sourkouni G., Prunte S., Norby T. (2015). Gd- and Pr-based double perovskite cobaltites as oxygen electrodes for proton ceramic fuel cells and electrolyser cells. *Solid State Ionics*, 278: pp. 120-132.
- Taillades G., Dailly J., Taillades-Jacquin M., Mauvy F., Essouhmi A., Marrony M., Lalanne C., Fourcade S., Jones D.J., Grenier J.-C., Rozière J. (2010). Intermediate temperature anode-supported fuel cell based on  $\text{BaCe}_{0.9}\text{Y}_{0.1}\text{O}_3$  electrolyte with novel  $\text{Pr}_2\text{NiO}_4$  cathode. *Fuel Cells*, 10: pp. 166-173.
- Tao S.W., Irvine J.T.S. (2006). A stable, easily sintered proton-conducting oxide electrolyte for moderate-temperature fuel cells and electrolyzers. *Advanced Materials*, 18: pp. 1581-1584.
- Thorel A.S. (2010). Tape casting ceramics for high temperature fuel cell applications, in: *Ceramic materials*. Wunderlich W. (Ed.), pp. 49-67, Sciyo, Rijeka, Croatia.
- Williams J.C. (1976). Doctor-blade process. *Treatise on Materials Science and Technology*, 9: pp. 173-178.

# CHAPTER

## ELECTROCHEMICAL EXPERIMENTS

# 8

Contents	Page
8.1. Electrochemical characterization of $\text{Co}_3\text{O}_4/\text{CeO}_2$ mixed oxide electrode in a proton conducting solid oxide symmetrical cell. . . . .	237
8.2. Electrochemical performance of a $\text{Co}_3\text{O}_4\text{-CeO}_2/\text{BZCY72}/\text{Co}_3\text{O}_4\text{-CeO}_2$ proton conducting solid oxide symmetrical cell fed with $\text{H}_2\text{S}/\text{H}_2\text{O}$ mixtures. . . . .	246
References. . . . .	257

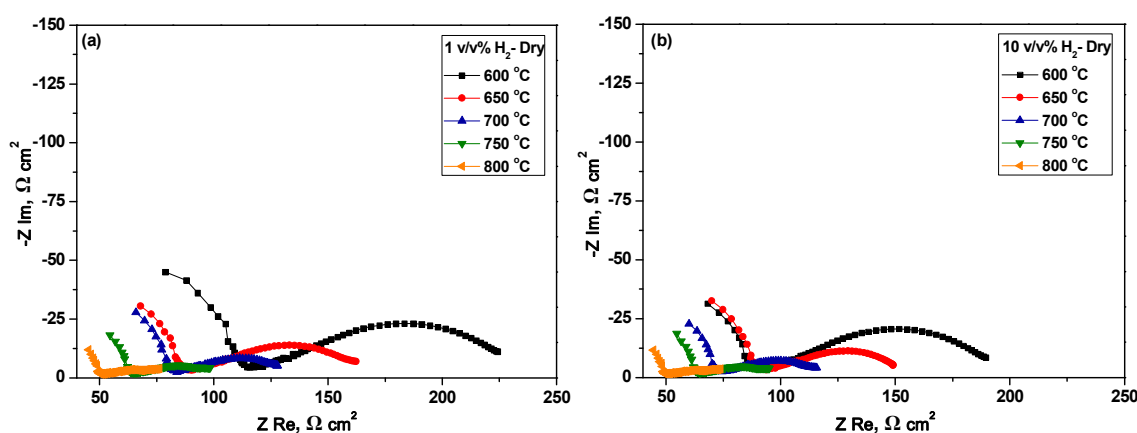


## 8.1. ELECTROCHEMICAL CHARACTERIZATION OF $\text{Co}_3\text{O}_4/\text{CeO}_2$ MIXED OXIDE ELECTRODE IN A PROTON CONDUCTING SOLID OXIDE SYMMETRICAL CELL

In the present section, the electrochemical performance of  $\text{Co}_3\text{O}_4/\text{CeO}_2$  mixed oxide electrode, when exposed to  $\text{H}_2/\text{Ar}$  mixtures, was examined employing a proton conducting  $\text{Co}_3\text{O}_4\text{-CeO}_2/\text{BaZr}_{0.7}\text{Ce}_{0.2}\text{Y}_{0.1}\text{O}_3$  symmetrical cell. The impact of cell temperature (600-850 °C) and hydrogen partial pressure,  $p_{\text{H}_2}=1\text{-}10$  kPa, at both dry and wet atmospheres ( $p_{\text{H}_2\text{O}}=0\text{-}2.5$  kPa) on the overall cell and electrode performance was thoroughly assessed by means of AC electrochemical impedance spectroscopy (EIS). Experiments showed that the temperature increases the cell and electrode conductivities, while it remains essentially unaffected by the hydrogen feed partial pressure both in dry/wet conditions.

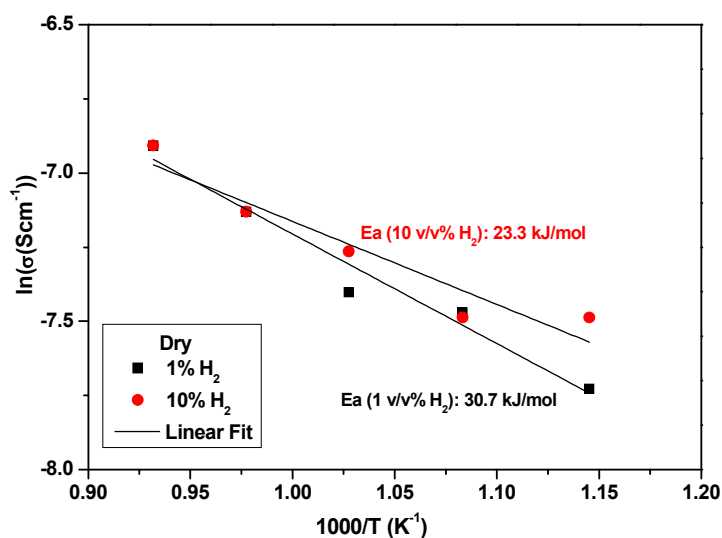
### 8.1.1. Effect of Cell Temperature at Dry and Wet Hydrogen Containing Mixtures

Figure 8.1 depicts the open circuit AC impedance spectra of the  $\text{Co}_3\text{O}_4\text{-CeO}_2/\text{BZCY72}/\text{Co}_3\text{O}_4\text{-CeO}_2$  cell at different operating temperatures (600-800 °C) and for a) 1 and b) 10 v/v%  $\text{H}_2/\text{Ar}$  mixtures. The values for overall cell conductivity and electrode processes polarization resistances along with the corresponding pseudo-capacitance values derived from fitting are listed in Table 8.1.



**Figure 8.1:** AC impedance spectra at different cell temperatures and for a) 1 and b) 10 v/v%  $\text{H}_2/\text{Ar}$  mixtures. Reaction conditions: 1 or 10 v/v%  $\text{H}_2$  diluted in Ar,  $F_t=100$   $\text{cm}^3/\text{min}$ ,  $T=600\text{-}800$  °C.

It is evident that the overall cell conductivity is improved upon temperature increase, while it remains essentially unaffected by the hydrogen feed partial pressure. In specific, the electrolyte conductivity,  $\sigma$ , increases from ca.  $0.5 \cdot 10^{-3}$  S/cm at 600 °C to  $1.0 \cdot 10^{-3}$  S/cm at 800 °C with apparent activation energies of 30.7 and 23.3 kJ/mol for 1 and 10 v/v% H<sub>2</sub>/Ar mixtures, respectively (Figure 8.2). Here it should be also noticed that the calculated pseudo-capacitance values was in the order of  $10^{-11}$  F/cm<sup>2</sup>, indicating the pure contribution by the solid electrolyte. A similar behavior was also observed for the electrode polarization resistance. By taking a more careful look on the shape of the AC impedance curves and aided by the fitting process, several electrode processes were identified by the features of the spectra, which are comprised of three arcs, one centered at high frequencies (HF), the second one at medium frequencies (MF) and the last one at very low frequencies (LF), with the MF contribution dominating the polarization resistance (Figure 8.3).



**Figure 8.2:** Arrhenius plots of cell conductivity,  $\sigma$ . Reaction conditions: 1 and 10 v/v% H<sub>2</sub> diluted in Ar,  $F_t = 100$  cm<sup>3</sup>/min,  $T = 600$ - $800$  °C.

The HF resistance shows a pseudo-capacitance value of  $10^{-6}$  F/cm<sup>2</sup> and is clearly decreasing with temperature ( $E_a = 62.2$  and  $50.0$  kJ/mol for 1 and 10 v/v% H<sub>2</sub>/Ar mixtures, respectively) and H<sub>2</sub> concentration increase, implying that could be assigned to the charge transfer process of hydrogen oxidation to H<sup>+</sup>,  $H_2 \rightarrow 2H^+ + 2e^-$ . The large MF arc presents pseudo-capacitance values ranging between  $10^{-4}$ - $10^{-3}$  F/cm<sup>2</sup> and the corresponding process resistance is clearly decreasing with temperature and slightly improved with  $P_{H_2}$ , with

apparent activation energies of 58.4 and 61.5 kJ/mol for 1 and 10 kPa feed hydrogen partial pressure, respectively. Taking into account the low  $P_{H_2}$  dependency as well as the range of pseudo-capacitance values, it could be assumed that the MF arc corresponds to diffusion processes and specifically to  $H^+$  mass transfer surface processes.

**Table 8.1:** Overall cell conductivity and electrode processes polarization resistances as a function of cell temperature (600-800 °C) for 1 and 10 v/v%  $H_2/Ar$  mixtures.

<b>1 v/v% <math>H_2</math> - Dry</b>					
Temperature (°C)	600	650	700	750	800
$\sigma$ (S·cm <sup>-1</sup> )	$4.4 \cdot 10^{-4}$	$5.7 \cdot 10^{-4}$	$6.1 \cdot 10^{-4}$	$8 \cdot 10^{-4}$	$1 \cdot 10^{-3}$
<b>Electrode polarization resistances</b>					
Rp2 ( $\Omega \cdot cm^2$ )	24.1	14.9	11.3	6.4	5
Rp3 ( $\Omega \cdot cm^2$ )	97.9	65.5	40	33.8	20.9
Rp4 ( $\Omega \cdot cm^2$ )	25	8.2	12.5	6.3	6.3
Rel ( $\Omega \cdot cm^2$ )	147	88.6	63.8	46.5	32.2
<b>Pseudo-capacitances</b>					
Cel (F/cm <sup>2</sup> )	$6.9 \cdot 10^{-11}$	$5.1 \cdot 10^{-11}$	$6 \cdot 10^{-11}$	$6.8 \cdot 10^{-11}$	$5.3 \cdot 10^{-11}$
C2 (F/cm <sup>2</sup> )	$8.6 \cdot 10^{-6}$	$7.8 \cdot 10^{-6}$	$5.4 \cdot 10^{-6}$	$2.4 \cdot 10^{-6}$	$4.7 \cdot 10^{-6}$
C3 (F/cm <sup>2</sup> )	$7 \cdot 10^{-4}$	$1.4 \cdot 10^{-3}$	$1.2 \cdot 10^{-3}$	$1.5 \cdot 10^{-3}$	$2.2 \cdot 10^{-3}$
C4 (F/cm <sup>2</sup> )	2.4	3.5	1.5	3.1	1.2
<b>10 v/v% <math>H_2</math> - Dry</b>					
Temperature (°C)	600	650	700	750	800
$\sigma$ (S·cm <sup>-1</sup> )	$5.6 \cdot 10^{-4}$	$5.6 \cdot 10^{-4}$	$7 \cdot 10^{-4}$	$8 \cdot 10^{-4}$	$1 \cdot 10^{-3}$
<b>Electrode polarization resistances</b>					
Rp2 ( $\Omega \cdot cm^2$ )	16.4	12.9	9.1	5.6	5
Rp3 ( $\Omega \cdot cm^2$ )	94.1	53.4	37.8	30.8	17.2
Rp4 ( $\Omega \cdot cm^2$ )	-	-	0.1	6.3	6.3
Rel ( $\Omega \cdot cm^2$ )	110	66.3	47.0	42.7	28.5
<b>Pseudo-capacitances</b>					
Cel (F/cm <sup>2</sup> )	$9.5 \cdot 10^{-11}$	$5.8 \cdot 10^{-11}$	$5.8 \cdot 10^{-11}$	$6.6 \cdot 10^{-11}$	$3 \cdot 10^{-11}$
C2 (F/cm <sup>2</sup> )	$7 \cdot 10^{-6}$	$6 \cdot 10^{-6}$	$4.2 \cdot 10^{-6}$	$2.2 \cdot 10^{-6}$	$9.3 \cdot 10^{-6}$
C3 (F/cm <sup>2</sup> )	$1.4 \cdot 10^{-3}$	$1.2 \cdot 10^{-3}$	$1.2 \cdot 10^{-3}$	$1.4 \cdot 10^{-3}$	$2.5 \cdot 10^{-3}$
C4 (F/cm <sup>2</sup> )	-	-	3	3.2	0.9

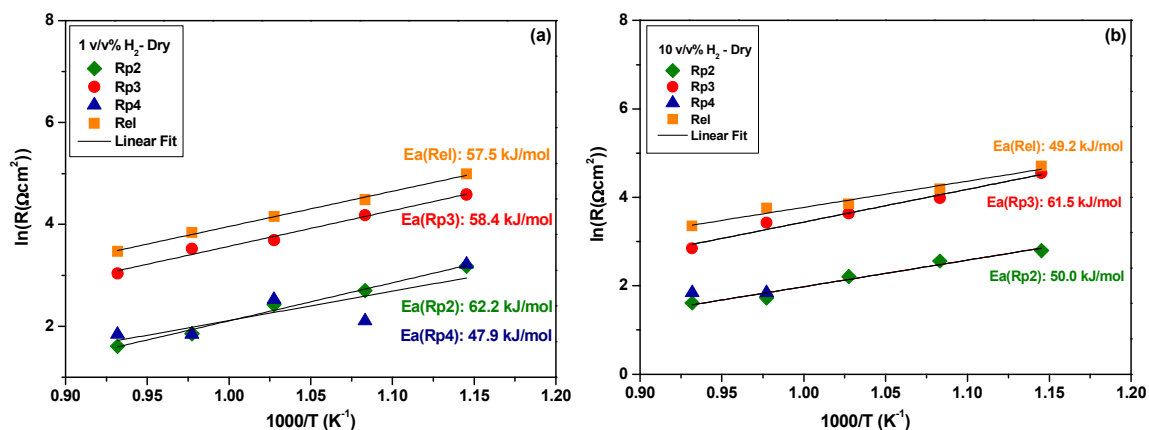


**Figure 8.3:** Arrhenius plots of electrode processes resistances. Reaction conditions: a) 1 and b) 10 v/v% H<sub>2</sub> diluted in Ar,  $F_t = 100 \text{ cm}^3/\text{min}$ ,  $T = 600\text{--}800 \text{ }^\circ\text{C}$ .

On the other hand, the LF process with the high chemical-like pseudo-capacitance of the order of  $10^0 \text{ F/cm}^2$ , is improved with the cell temperature (47.9 kJ/mol at 1 v/v% H<sub>2</sub>/Ar mixture), and it can be probably attributed either to gas phase diffusion or equally to the incorporation of hydrogen in the electrode material; in other words to the progressive reduction of Co<sub>3</sub>O<sub>4</sub>/CeO<sub>2</sub> electrodes by the hydrogen during operation.

Figure 8.3 also depicts the Arrhenius plots for the overall electrode resistance, which at 1 v/v% H<sub>2</sub>/Ar shows an apparent activation energy similar to Rp3 process and equal to 57.5 kJ/mol, while at 10 v/v% H<sub>2</sub>/Ar the apparent activation energy of the polarization resistance equals to 49.2 kJ/mol close to the corresponding value calculated for the Rp2 process. Thus, it could be argued that at 1 v/v% H<sub>2</sub>/Ar feed mixture the mass transfer of protons is prevailing the interfacial polarization resistance, while at 10 v/v% H<sub>2</sub>/Ar the charge transfer reaction of hydrogen oxidation to protons determines the overall mechanism of electrode conductivity.

Similar measurements were also elaborated with hydrogen containing wet mixtures (2.5 v/v% H<sub>2</sub>O), where again the effect of cell temperature on the overall cell conductivity and electrode polarization resistance was revealed. Figure 8.4 presents the open circuit impedance spectra of the symmetrical cell at various temperatures varying from 600 to 800 °C, employing two feed mixtures containing a) 1 v/v% H<sub>2</sub>, 2.5 v/v% H<sub>2</sub>O, diluted in Ar and b) 10 v/v% H<sub>2</sub>, 2.5 v/v% H<sub>2</sub>O, diluted in Ar.

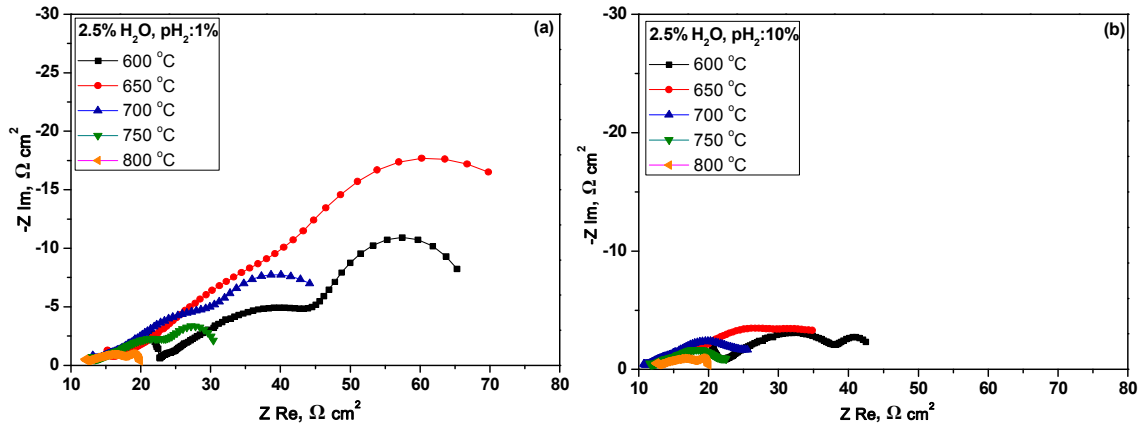


**Figure 8.4:** AC impedance spectra at different cell temperatures and for a) 1 and b) 10 v/v%  $H_2/Ar$  wet mixtures. Reaction conditions: 1 or 10 v/v%  $H_2$ , 2.5 v/v%  $H_2O$  diluted in  $Ar$ ,  $F_t = 100 \text{ cm}^3/\text{min}$ ,  $T = 600\text{-}800 \text{ }^\circ\text{C}$ .

In Table 8.2, the fitting values for overall cell conductivity, electrode polarization resistances and pseudo-capacitance values, are depicted. Notice that in comparison with the dry experiments, in the case of the feed mixture with 10 v/v%  $H_2$  a new contribution is revealed (Rp2b), which it seems to be favored at high  $H_2$  and  $H_2O$  partial pressures, where the transference of protons is enhanced. The pronounced effect of temperature is clear, increasing the electrolyte conductivity from  $2.3\text{-}2.6 \cdot 10^{-3} \text{ S/cm}$  at  $600 \text{ }^\circ\text{C}$  to  $4.3\text{-}4.1 \cdot 10^{-3} \text{ S/cm}$  at  $800 \text{ }^\circ\text{C}$ , for the 1 and 10 v/v%  $H_2/Ar$  wet mixtures, respectively. Moreover, the effect of  $H_2O$  presence is also pronounced, since it clearly increases the cell conductivity from ca.  $0.5 \cdot 10^{-3}$  and  $1.0 \cdot 10^{-3} \text{ S/cm}$  to  $2.3\text{-}2.6 \cdot 10^{-3}$  and  $4.3\text{-}4.1 \cdot 10^{-3} \text{ S/cm}$  at  $600$  and  $800 \text{ }^\circ\text{C}$ , respectively. Here it should be mentioned that two distinct regions were observed in the corresponding Arrhenius plots, one at the temperature range of  $600$  to  $750 \text{ }^\circ\text{C}$ , where the cell conductivity obviously increases with temperature and the other at higher temperatures, where the cell conductivity seems to level off with the cell temperature.

As shown in Figure 8.4, the features of the AC impedance spectra are similar to those observed at the corresponding experiments with the dry mixtures, although the electrode resistances are substantially improved by the  $H_2O$  presence. Also from Table 8.2, the pronounced effect of temperature is clearly seen except for the  $600\text{-}650 \text{ }^\circ\text{C}$  range (the partial resistances are increasing); thus for the wet mixtures all apparent activation energies have been calculated for the temperature range of  $650\text{-}800 \text{ }^\circ\text{C}$  (Figure 8.5).

**Table 8.2:** Overall cell conductivity and electrode processes polarization resistances as a function of cell temperature (600-800 °C) for 1 and 10 v/v% H<sub>2</sub>/Ar wet mixtures.

<b>pH<sub>2</sub> 1 v/v% - Wet</b>					
Temperature (°C)	600	650	700	750	800
$\sigma$ (S·cm <sup>-1</sup> )	$2.3 \cdot 10^{-3}$	$3.5 \cdot 10^{-3}$	$4 \cdot 10^{-3}$	$4 \cdot 10^{-3}$	$4.3 \cdot 10^{-3}$
<b>Electrode polarization resistances</b>					
Rp2 (Ω·cm <sup>2</sup> )	7.7	10.4	11.1	6.6	3.6
Rp3 (Ω·cm <sup>2</sup> )	23.8	44.5	21.7	8.8	3.7
Rp4 (Ω·cm <sup>2</sup> )	20	35.3	15.2	5.2	1.3
Rel (Ω·cm <sup>2</sup> )	51.5	90.2	48.0	20.6	8.6
<b>Pseudo-capacitances</b>					
Cel (F/cm <sup>2</sup> )	$9.7 \cdot 10^{-12}$	$7.9 \cdot 10^{-11}$	$5.6 \cdot 10^{-11}$	$5.1 \cdot 10^{-11}$	$3.8 \cdot 10^{-11}$
C2 (F/cm <sup>2</sup> )	$6.9 \cdot 10^{-6}$	$4 \cdot 10^{-5}$	$1.6 \cdot 10^{-4}$	$3.7 \cdot 10^{-5}$	$1 \cdot 10^{-5}$
C3 (F/cm <sup>2</sup> )	$4.9 \cdot 10^{-4}$	$4.6 \cdot 10^{-3}$	$2.6 \cdot 10^{-3}$	$2.6 \cdot 10^{-3}$	$1.3 \cdot 10^{-3}$
C4 (F/cm <sup>2</sup> )	0.1	0.1	0.2	0.4	0.9
<b>pH<sub>2</sub> 10 v/v% - Wet</b>					
Temperature (°C)	600	650	700	750	800
$\sigma$ (S·cm <sup>-1</sup> )	$2.6 \cdot 10^{-3}$	$3.9 \cdot 10^{-3}$	$4.7 \cdot 10^{-3}$	$4.3 \cdot 10^{-3}$	$4.1 \cdot 10^{-3}$
<b>Electrode polarization resistances</b>					
Rp2 (Ω·cm <sup>2</sup> )	-	4.7	4.8	3.4	2.1
Rp2b (Ω·cm <sup>2</sup> )	4.4	1.3	0.6	0.7	0.4
Rp3 (Ω·cm <sup>2</sup> )	17.7	14.5	8.1	6.4	4.6
Rp4 (Ω·cm <sup>2</sup> )	3.6	6.3	3.7	1.7	1.2
Rel (Ω·cm <sup>2</sup> )	25.7	26.8	17.2	12.2	8.3
<b>Pseudo-capacitances</b>					
Cel (F/cm <sup>2</sup> )	$7.8 \cdot 10^{-11}$	$5.5 \cdot 10^{-11}$	$3.6 \cdot 10^{-11}$	$4.1 \cdot 10^{-11}$	$4 \cdot 10^{-11}$
C2 (F/cm <sup>2</sup> )	-	$8.2 \cdot 10^{-5}$	$9.3 \cdot 10^{-5}$	$6.4 \cdot 10^{-5}$	$1.3 \cdot 10^{-5}$
C3 (F/cm <sup>2</sup> )	$1.9 \cdot 10^{-7}$	$5.5 \cdot 10^{-7}$	$5.4 \cdot 10^{-7}$	$3.7 \cdot 10^{-7}$	$6.6 \cdot 10^{-8}$
C4 (F/cm <sup>2</sup> )	$5.7 \cdot 10^{-4}$	$1 \cdot 10^{-2}$	$1.1 \cdot 10^{-2}$	$7.8 \cdot 10^{-3}$	$2 \cdot 10^{-3}$
Cel (F/cm <sup>2</sup> )	1.3	1.4	2.2	5.3	1

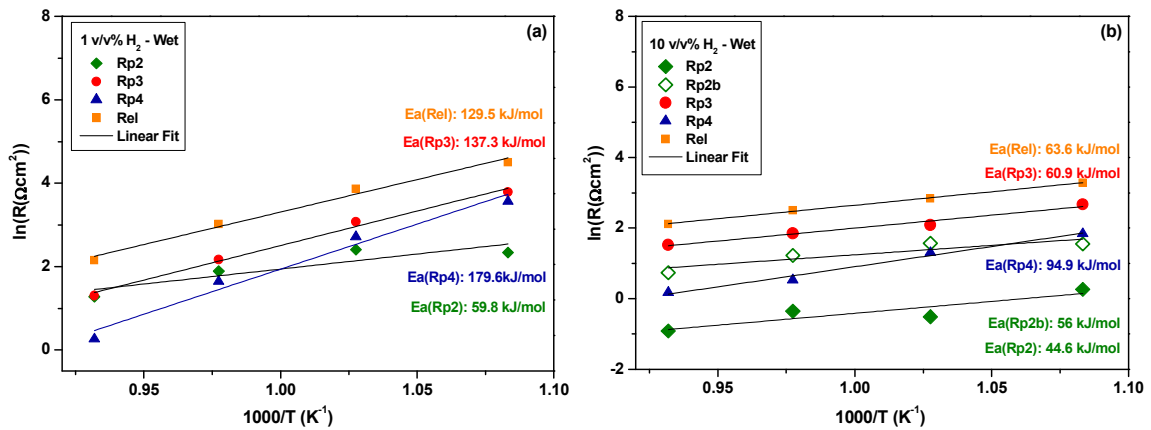


**Figure 8.5:** Arrhenius plots of electrode processes resistances. Reaction conditions: a) 1 and b) 10 v/v%  $\text{H}_2/\text{Ar}$  wet mixtures (2.5 v/v%  $\text{H}_2\text{O}$ ),  $F_t = 100 \text{ cm}^3/\text{min}$ ,  $T = 650\text{-}800 \text{ }^\circ\text{C}$ .

In the case of wet 1 v/v%  $\text{H}_2/\text{Ar}$ , the resistance of Rp2 process corresponding to the charge transfer reaction is decreasing with temperature with an apparent  $E_{\text{act}} = 59.8 \text{ kJ/mol}$  similar to the dry case (62.1 kJ/mol). The surface diffusion of protons or hydroxyls/hydroxides (R3) constitutes again the highest contribution to the interfacial polarization resistance and decreases with temperature with an apparent activation energy of 137.3 kJ/mol (close to the activation energy of the overall electrode resistance, 129.5 kJ/mol), almost double compared to the dry mixtures. Finally the resistance of the LF process, corresponding to gas phase diffusion, is also decreasing with temperature with the highest apparent activation energy (179.6 kJ/mol) compared to all other electrode sub-processes and is positively affected by the presence of  $\text{H}_2\text{O}$ .

On the other hand, at 10 v/v%  $\text{H}_2/\text{Ar}$  wet mixture, an additional electrode process is deconvoluted (Rp2b) by the fitting, which also corresponds to the charge transfer reaction at the electrode/electrolyte interface but with a lower pseudo-capacitance of ca.  $10^{-8}\text{-}10^{-7} \text{ F/cm}^2$  compared to Rp2 (ca.  $10^{-5} \text{ F/cm}^2$ ). Both Rp2 and Rp2b could be assigned to the charge transfer process and the resistance of  $\text{H}^+$  to be incorporated onto the solid electrolyte structure. Rp2b process with the lower pseudo-capacitance could be assigned to the space charge effect dominating at high  $P_{\text{H}_2}$  and  $P_{\text{H}_2\text{O}}$ ; an extra barrier for the charge transfer reaction to be overcome by the accumulated protons near the three phase boundary (tpb). Rp2 is the normal hydrogen oxidation to protons process taking place at tpb. Both processes are improved by increasing the cell temperature with apparent activation energies of 44.6 and 56 kJ/mol for the Rp2 and Rp2b processes, respectively. Moreover, the resistance of R3

and R4 processes are also improved by the cell temperature with activation energies of 60.9 and 94.9 kJ/mol, respectively, substantially lower compared to the case of 1 v/v% H<sub>2</sub>/Ar wet mixture. Finally, the overall electrode resistance is clearly decreasing with temperature presenting activation energy of 63.6 kJ/mol, close to the activation energy of R3 process, indicating its important role on the overall electrode performance.

### 8.1.2. Effect of Hydrogen Partial Pressure

In the following, the effect of hydrogen partial pressure in wet mixtures at 600 and 850 °C on the overall cell conductivity and electrode polarization resistance is examined. Figure 8.6 shows the corresponding AC impedance spectra, where again are comprised by the HF, MF and LF contributions.

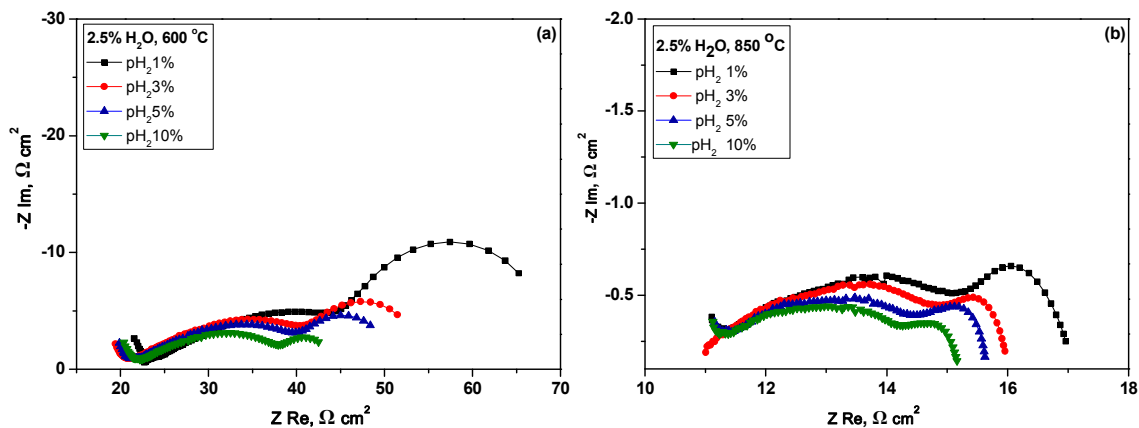


**Figure 8.6:** AC impedance spectra at different feed hydrogen partial pressures for a) 600 and b) 800 °C cell temperatures. Reaction conditions: 1, 3, 5 and 10 v/v% H<sub>2</sub>, 2.5 v/v% H<sub>2</sub>O diluted in Ar,  $F_t = 100 \text{ cm}^3/\text{min}$ .

Table 8.3 presents the cell conductivity, electrode processes resistances and the corresponding pseudo-capacitance values at different operation conditions. It can be obviously seen that the cell conductivity remains apparently stable by increasing the hydrogen feed concentration, while it increases by the increase in cell temperature, as was also observed in the corresponding temperature dependent experiments at standard feed mixtures under dry and wet atmospheres (see Tables 8.1 and 8.2).

**Table 8.3:** Overall cell conductivity and electrode processes polarization resistances as a function of hydrogen concentration (1-10 v/v% H<sub>2</sub>/Ar wet mixtures) for 600 and 850 °C.

<b>600 °C, Wet</b>				
pH <sub>2</sub>	1v/v% H <sub>2</sub>	3 v/v% H <sub>2</sub>	5 v/v% H <sub>2</sub>	10 v/v% H <sub>2</sub>
σ (S/cm)	2.4·10 <sup>-3</sup>	2.7·10 <sup>-3</sup>	2.7·10 <sup>-3</sup>	2.6·10 <sup>-3</sup>
<b>Electrode polarization resistances</b>				
Rp2 (Ω·cm <sup>2</sup> )	8.0	4.8	4.7	4.4
Rp3 (Ω·cm <sup>2</sup> )	24.0	23.9	21.6	17.7
Rp4 (Ω·cm <sup>2</sup> )	20.2	8.6	6.7	3.6
Rel (Ω·cm <sup>2</sup> )	52.2	37.3	33.0	25.7
<b>Pseudo-capacitances</b>				
Cel (F/cm <sup>2</sup> )	7.9·10 <sup>-11</sup>	7.7·10 <sup>-11</sup>	7.7·10 <sup>-11</sup>	7.5·10 <sup>-11</sup>
C2 (F/cm <sup>2</sup> )	3.4·10 <sup>-6</sup>	1.8·10 <sup>-7</sup>	1.5·10 <sup>-7</sup>	9.4·10 <sup>-8</sup>
C3 (F/cm <sup>2</sup> )	2.3·10 <sup>-4</sup>	3.9·10 <sup>-4</sup>	3.4·10 <sup>-4</sup>	2.8·10 <sup>-4</sup>
C4 (F/cm <sup>2</sup> )	0.07	0.2	0.3	0.7
<b>850 °C, Wet</b>				
pH <sub>2</sub>	1v/v% H <sub>2</sub>	3 v/v% H <sub>2</sub>	5 v/v% H <sub>2</sub>	10 v/v% H <sub>2</sub>
σ (S/cm)	4.6·10 <sup>-3</sup>	4.7·10 <sup>-3</sup>	4.6·10 <sup>-3</sup>	4.6·10 <sup>-3</sup>
<b>Electrode polarization resistances</b>				
Rp2 (Ω·cm <sup>2</sup> )	2.4	2.7	2.9	2.7
Rp3 (Ω·cm <sup>2</sup> )	2.9	2.3	1.4	1.4
Rp4 (Ω·cm <sup>2</sup> )	1.0	0.6	0.7	0.5
Rel (Ω·cm <sup>2</sup> )	6.3	5.6	5.0	4.6
<b>Pseudo-capacitances</b>				
Cel (F/cm <sup>2</sup> )	3.1·10 <sup>-11</sup>	1.5·10 <sup>-11</sup>	2.4·10 <sup>-11</sup>	2.5·10 <sup>-11</sup>
C2 (F/cm <sup>2</sup> )	3.8·10 <sup>-6</sup>	4·10 <sup>-6</sup>	6.3·10 <sup>-6</sup>	5.2·10 <sup>-6</sup>
C3 (F/cm <sup>2</sup> )	1.1·10 <sup>-3</sup>	9.6·10 <sup>-4</sup>	1.6·10 <sup>-3</sup>	1.5·10 <sup>-3</sup>
C4 (F/cm <sup>2</sup> )	0.5	0.9	0.6	0.9

The logarithmic dependence of the different electrode processes resistances along with the overall interfacial resistance by the hydrogen feed concentration is depicted in Figure 8.7. It can be seen that at T = 600 °C, the overall electrode resistance is improved by the hydrogen partial pressure (P<sub>H<sub>2</sub></sub><sup>-0.30</sup>) mainly due to the pronounced effect of hydrogen on Rp4 process

( $P_{H_2}^{-0.73}$ ) and secondly to Rp2 ( $P_{H_2}^{-0.26}$ ) and Rp3 ( $P_{H_2}^{-0.13}$ ) contributions, with the latter being almost unaffected by the hydrogen feed concentration.

On the other hand at  $T = 850$  °C, the effect of hydrogen is milder compared to  $T = 600$  °C. The overall interfacial resistance is only slightly improved by the increase of hydrogen partial pressure ( $P_{H_2}^{-0.14}$ ), with the main contributions being derived by the improvement of surface Rp3 ( $P_{H_2}^{-0.35}$ ) and gas phase Rp4 ( $P_{H_2}^{-0.27}$ ) diffusion processes. The resistance of the charge transfer process is not practically affected by the hydrogen presence.

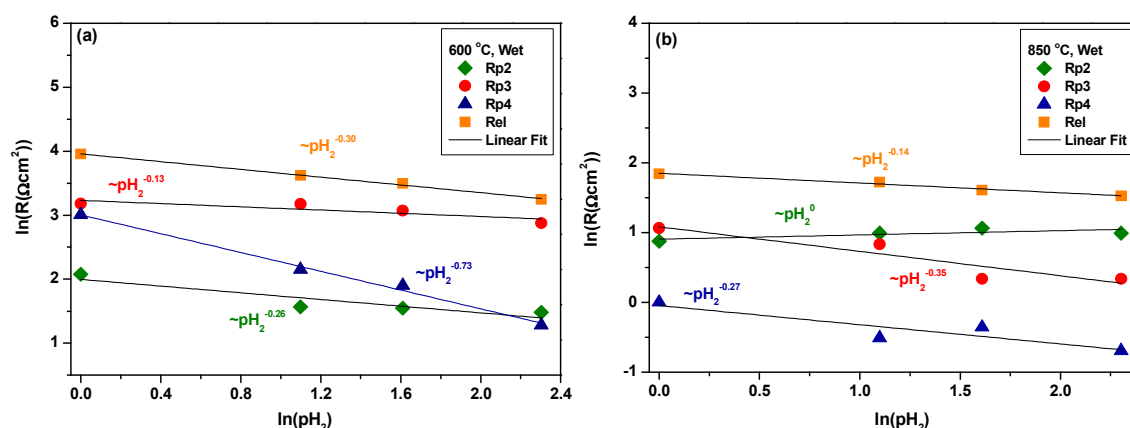


**Figure 8.7:** Logarithmic dependence of electrode processes resistances by the hydrogen feed concentration for a) 600 and b) 800 °C cell temperatures. Reaction conditions: 1, 3, 5 and 10 v/v%  $H_2$ , 2.5 v/v%  $H_2O$  diluted in Ar,  $F_t = 100$   $\text{cm}^3/\text{min}$ .

## 8.2. ELECTROCHEMICAL PERFORMANCE OF A $\text{Co}_3\text{O}_4$ - $\text{CeO}_2$ /BZCY72/ $\text{Co}_3\text{O}_4$ - $\text{CeO}_2$ PROTON CONDUCTING SOLID OXIDE CELL FED WITH $\text{H}_2\text{S}/\text{H}_2\text{O}$ MIXTURES

The electrochemical performance of  $\text{Co}_3\text{O}_4/\text{CeO}_2$  mixed oxide materials as electrodes, when exposed to  $\text{H}_2\text{S}/\text{H}_2\text{O}$  atmospheres, was examined employing a proton conducting symmetrical cell, with  $\text{BaZr}_{0.7}\text{Ce}_{0.2}\text{Y}_{0.1}\text{O}_3$  (BZCY72) as the solid electrolyte. The impact of temperature (700-850 °C) and  $\text{H}_2\text{S}$  concentration (0-1 v/v%) in steam-rich atmospheres (90 v/v%  $\text{H}_2\text{O}$ ) on the overall cell performance was thoroughly assessed by means of electrochemical impedance spectroscopy (EIS) studies. The performance of the  $\text{Co}_3\text{O}_4/\text{CeO}_2$  electrode was significantly enhanced by increasing the  $\text{H}_2\text{S}$  concentration and temperature. The obtained results were interpreted on the basis of EIS results and physicochemical

characterization (XRD, SEM) studies of fresh and used electrodes. Notably, it was found that the mass transport processes, mainly associated with the adsorption and diffusion of the intermediate species resulting by the chemical and half-cell reactions taking place during cell operation, dominate the electrode polarization resistance compared with the charge transfer processes. Upon increasing temperature and H<sub>2</sub>S concentration, the electrode resistance is substantially lowered, due to the in situ activation and morphological modifications of the electrode, induced by its interaction with the reactants (H<sub>2</sub>S/H<sub>2</sub>O) and products (H<sub>2</sub>/SO<sub>2</sub>) mixtures

### 8.2.1. Effect of H<sub>2</sub>S Feed Concentration

Figure 8.8 depicts the open circuit AC impedance spectra of the symmetrical cell, Co<sub>3</sub>O<sub>4</sub>-CeO<sub>2</sub>/BZCY72/Co<sub>3</sub>O<sub>4</sub>-CeO<sub>2</sub>, under different H<sub>2</sub>S concentrations (0-1 v/v% H<sub>2</sub>S) in the presence of excess H<sub>2</sub>O (90 v/v%) conditions, at T = 850 °C. The corresponding fitting curves, according to the equivalent circuit model are also shown. It should be noted here, that the experiments were carried out as 3 h step change tests, starting from H<sub>2</sub>S-free atmospheres (90 v/v% H<sub>2</sub>O diluted in Ar) to H<sub>2</sub>S-containing feed compositions by increasing stepwise the H<sub>2</sub>S concentration from 0.25 to 0.5 and finally 1.0 v/v%. The values for overall cell conductivity and electrode polarization resistance characteristics derived from fitting are listed in Table 8.4.

It is evident that the overall cell conductivity is improved upon addition of 0.25% H<sub>2</sub>S, although it is independent of further increased H<sub>2</sub>S concentration. In particular, the electrolyte conductivity,  $\sigma$ , increases from  $1.5 \cdot 10^{-3}$  S/cm in the absence of H<sub>2</sub>S to ca.  $1.8 \cdot 10^{-3}$  S/cm in H<sub>2</sub>S-containing environments. A similar picture is also obtained for the electrode polarization resistance; R<sub>p</sub> drastically decreases from 277  $\Omega \cdot \text{cm}^2$  in the absence of H<sub>2</sub>S to ca. 48  $\Omega \cdot \text{cm}^2$  in the presence of 0.25 v/v% H<sub>2</sub>S in the feed stream, then slightly decreasing by further increasing the H<sub>2</sub>S concentration to 0.5 and 1.0 v/v%.

The above findings can be well rationalized on the basis of chemical and electrochemical processes taking place on the symmetrical cell, Co<sub>3</sub>O<sub>4</sub>-CeO<sub>2</sub>/BZCY72/Co<sub>3</sub>O<sub>4</sub>-CeO<sub>2</sub>, when it is exposed to different H<sub>2</sub>S-H<sub>2</sub>O-Ar containing mixtures. At the gas phase and on the electrodes surface the following stoichiometries are carried out:



while at the anode three-phase-boundary (tpb) the produced  $\text{H}_2$  from reactions (1) and (2) along with the co-electrolysis of  $\text{H}_2\text{S}$  (4) and  $\text{H}_2\text{O}$  (5) could generate protons ( $\text{H}^+$ ), which are transported to the cathode tpb toward  $\text{H}_2$  evolution (6):

**Anode half-cell reactions:**



**Cathode half-cell reactions:**

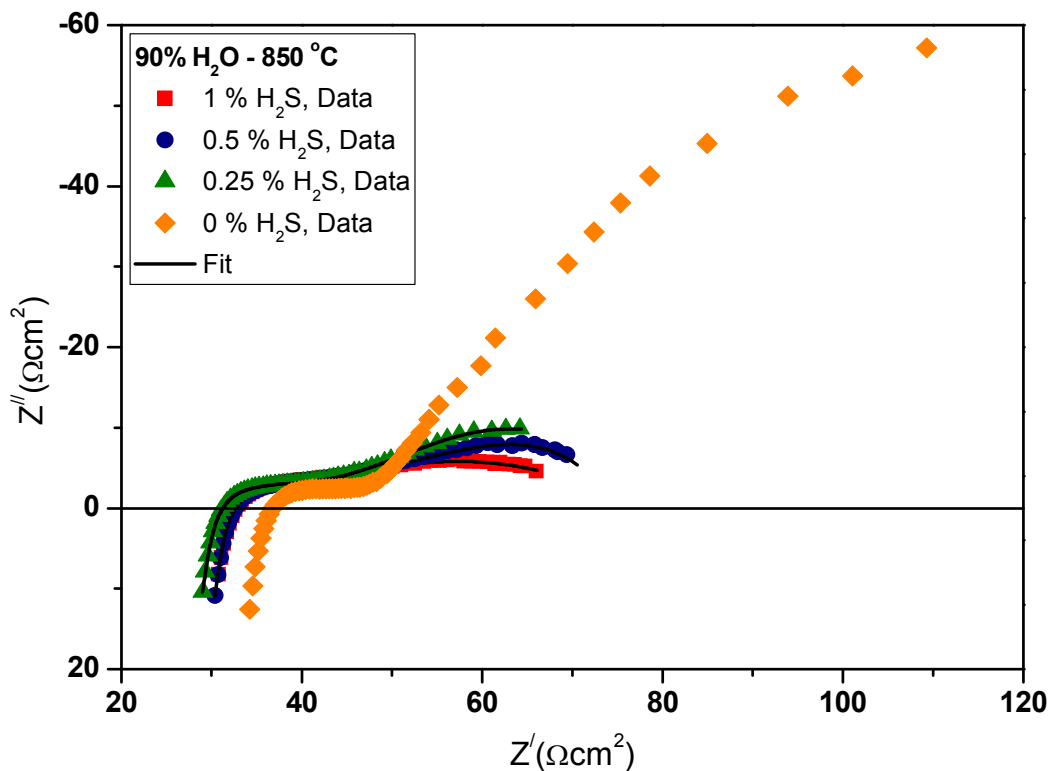
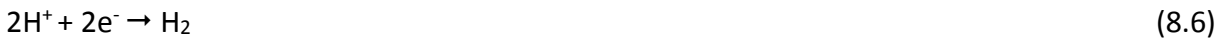


**Figure 8.8:** AC impedance spectra and corresponding fitting curves at different  $\text{H}_2\text{S}$  concentrations. Reaction conditions: 0-1 v/v%  $\text{H}_2\text{S}$ , 90 v/v%  $\text{H}_2\text{O}$  diluted in Ar,  $F_t = 100 \text{ cm}^3/\text{min}$ ,  $T = 850 \text{ }^\circ\text{C}$ .

The pronounced effect of  $\text{H}_2\text{S}$  addition can be, inter alia, assigned to the in situ generated  $\text{H}_2$  via the gas phase and surface reactions (8.1) and (8.2) and/or to the

structural/morphological modifications of the electrode induced by its interaction with the H<sub>2</sub>S/H<sub>2</sub>O reacting mixture and the associated reaction intermediates. Both parameters can enhance to a different extent the electrode kinetics, while the latter clearly affects the electrode in-plane conductivity by utilizing better more of the electrolyte. However, on the basis of the present results, no definitive conclusions in relation to the precise effect of each parameter on the electrochemical performance can be obtained.

**Table 8.4:** Overall cell conductivity and polarization resistance characteristics as a function of feed composition, at  $T = 850$  °C.

Feed mixtures	Overall electrolyte conductivity, $\sigma$ (S/cm)	Electrode polarization resistance, $R_p$ ( $\Omega \cdot \text{cm}^2$ )	Charge transfer resistance, $R_{ct}$ ( $\Omega \cdot \text{cm}^2$ )	Mass transfer resistance, $R_{mt}$ ( $\Omega \cdot \text{cm}^2$ )
90 v/v% H <sub>2</sub> O, balanced with Ar	$1.5 \cdot 10^{-3}$	277	16.3	260
0.25 v/v % H <sub>2</sub> S-90 v/v % H <sub>2</sub> O, balanced with Ar	$1.8 \cdot 10^{-3}$	49.7	14.7	35.0
0.50 v/v % H <sub>2</sub> S-90 v/v % H <sub>2</sub> O, balanced with Ar	$1.8 \cdot 10^{-3}$	47.7	15.7	32.0
1.00 v/v % H <sub>2</sub> S-90 v/v % H <sub>2</sub> O, balanced with Ar	$1.7 \cdot 10^{-3}$	47.5	14.1	33.4

In general, the features of the AC impedance spectra are comprised of two arcs, one entered at high frequencies (HF) and the other one at lower frequencies (LF), with the latter dominating the polarization resistance, as obviously seen for the 90 v/v% H<sub>2</sub>O/Ar mixture (Figure 8.8). Based on the pseudo-capacitance values, of  $10^{-6}$ - $10^{-5}$  and  $10^{-3}$ - $10^{-2}$  F/cm<sup>2</sup> for the HF and LF arcs, respectively, it can be safely assumed that the HF arc is attributed to charge transfer processes, while the LF arc is reflecting mass transfer limitations, associated with the adsorption/ diffusion of reactions (1) and (2) intermediates. From the corresponding values in Table 8.4 it is evident that the adsorption, diffusion and surface reaction steps are the main contributors to the overall electrode polarization resistance.

## 8.2.2. Effect of Cell Temperature

In the following, the same symmetrical cell was employed to assess the effect of temperature at a constant feed composition. It should be again mentioned that the duration of each temperature step was equal to 3 h and impedance spectra were acquired every 30 min. Figure 8.9 presents the open circuit impedance spectra and the corresponding deconvoluted fitting curves of the symmetrical cell at various temperatures ranging from 700 to 850 °C, with a standard feed mixture containing 1 v/v% H<sub>2</sub>S, 90 v/v% H<sub>2</sub>O, diluted in Ar.

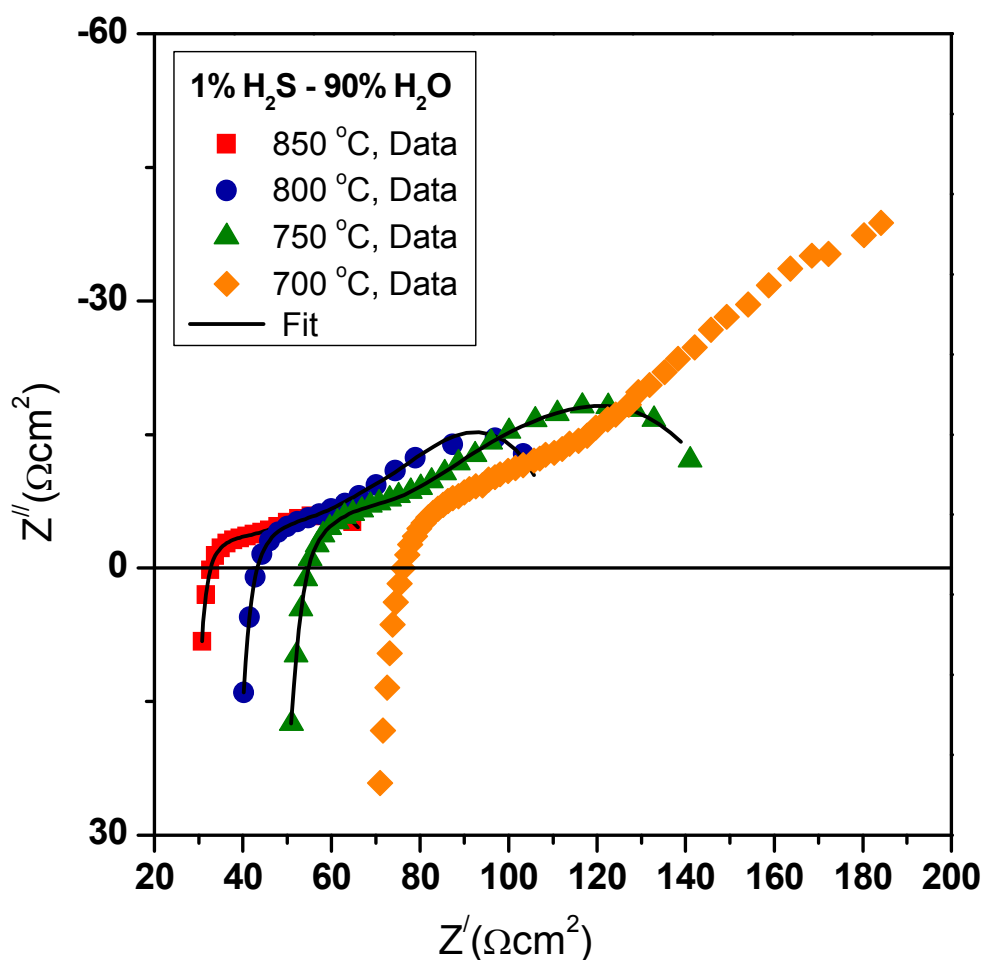


**Figure 8.9:** Impedance spectra and corresponding fitting curves as a function of cell temperature (700-850 °C). Reaction conditions: 1 v/v% H<sub>2</sub>S, 90 v/v% H<sub>2</sub>O diluted in Ar,  $F_t = 100 \text{ cm}^3/\text{min}$ .

In Table 8.5, the fitting values for cell conductivity, electrode polarization, charge transfer and mass transfer resistances, are listed. The pronounced effect of temperature is clear, increasing the electrolyte conductivity from  $0.7 \cdot 10^{-3}$  S/cm at  $T = 700$  °C to  $1.7 \cdot 10^{-3}$  S/cm at  $T = 850$  °C, with an activation energy, equal to 53.2 kJ/mol. Similar values of conductivity, i.e.,  $2.03 \cdot 10^{-3}$  S/cm, were also reported for the Pt/BaZr<sub>0.85</sub>Y<sub>0.15</sub>O<sub>3-δ</sub>/Pt cell at  $T = 650$  °C, when exposed to 0.5 v/v% H<sub>2</sub>S/H<sub>2</sub> mixtures (Li et al., 2008).

**Table 8.5:** Overall electrolyte conductivity and polarization resistance characteristics as a function of temperature at a constant feed composition of 1 v/v% H<sub>2</sub>S-90 v/v% H<sub>2</sub>O diluted in Ar.

Temperature (°C)	Overall electrolyte conductivity, $\sigma$ (S/cm)	Electrode polarization resistance, $R_p$ ( $\Omega \cdot \text{cm}^2$ )	Charge transfer resistance, $R_{ct}$ ( $\Omega \cdot \text{cm}^2$ )	Mass transfer resistance, $R_{mt}$ ( $\Omega \cdot \text{cm}^2$ )
700	$0.7 \cdot 10^{-3}$	191	41.0	150
750	$1.0 \cdot 10^{-3}$	112	35.3	77.2
800	$1.3 \cdot 10^{-3}$	74.5	29.1	45.4
850	$1.7 \cdot 10^{-3}$	47.5	14.1	33.4

Again, the dominant feature in the impedance spectra (Figure 8.9) is comprised of a small high frequency (HF) arc overlapped with a large arc at low frequencies (LF), while the size of both arcs, reflecting the electrode polarization resistance, decreases significantly by increasing the cell temperature. This is also reflected on the calculated values of  $R_p$ ,  $R_{ct}$  and  $R_{mt}$ , which are sufficiently improved as the cell temperature increases, with activation energies equaled to 83.3, 29.7 and 92.0 kJ/mol, respectively (Figure 8.10). From the acquired data, it is evident that as the temperature increases, the surface kinetics are faster and the contribution of the charge transfer processes becomes more critical on the overall cell performance, beginning with 20% at  $T = 700$  °C and reaching almost 40% of the overall electrode polarization at  $T = 800$  °C. The charge transfer contribution compared to mass transfer processes is lowered at  $T = 850$  °C, which could be attributed to the red-ox processes of intermediate reaction products (e.g., sulfur-containing species) or to the partial O<sup>2-</sup> transport of BZCY72 at high temperatures, as it has been observed in previous relevant

works (Strandbakke et al., 2015; Strandbakke et al., 2016). For this reason, the activation energy for  $R_{ct}$  (29.7 kJ/mol) has been calculated taking into account the corresponding values in the temperature range of 700-800 °C, thus excluding the point at  $T = 850$  °C.

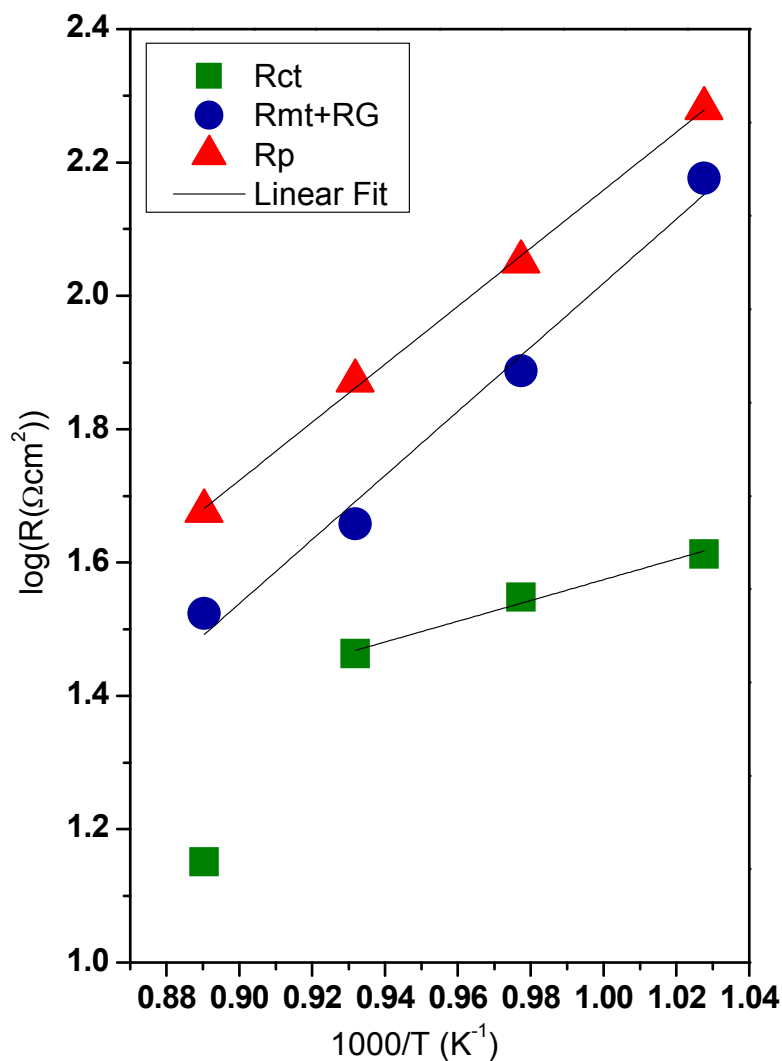


**Figure 8.10:** Arrhenius plots of electrode polarization,  $R_p$ , charge transfer,  $R_{ct}$ , and mass transfer,  $R_{mt}$ , resistances. Reaction conditions: 1 v/v%  $H_2S$ , 90 v/v%  $H_2O$  diluted in  $Ar$ ,  $F_T = 100$  cm<sup>3</sup>/min.

### 8.2.3 Physicochemical Characterization Studies

To gain insight into the impact of reaction atmosphere on the structural/ morphological features of cell constituents, and their consequent effect on the above described electrochemical performance, a SEM/EDS and XRD analysis of samples before and after measurements was carried out. Figure 8.11 shows SEM pictures of the fresh  $Co_3O_4/CeO_2$

electrode surface (Fig. 8.11A), as well as of the cross section image of the corresponding  $\text{Co}_3\text{O}_4$ - $\text{CeO}_2$ /BZCY72 interface (Figure 8.11B). Two distinct phases, i.e., cobalt oxide (darker features) and ceria (brighter features) were identified in the fresh sintered electrode, with a grain size of 1-5  $\mu\text{m}$ . In the cross section (Fig. 8.11B), a two layer structure, consisting of a dense electrolyte and a porous electrode with thickness of 20  $\mu\text{m}$ , is observed. The BZCY72 retained its dense and crack-free microstructure after electrode calcination, demonstrating that blade-aided electrode printing at  $T = 1,400^\circ\text{C}$  is a suitable method for the fabrication of  $\text{Co}_3\text{O}_4$ / $\text{CeO}_2$  supported cells, based on BZCY72 electrolytes.

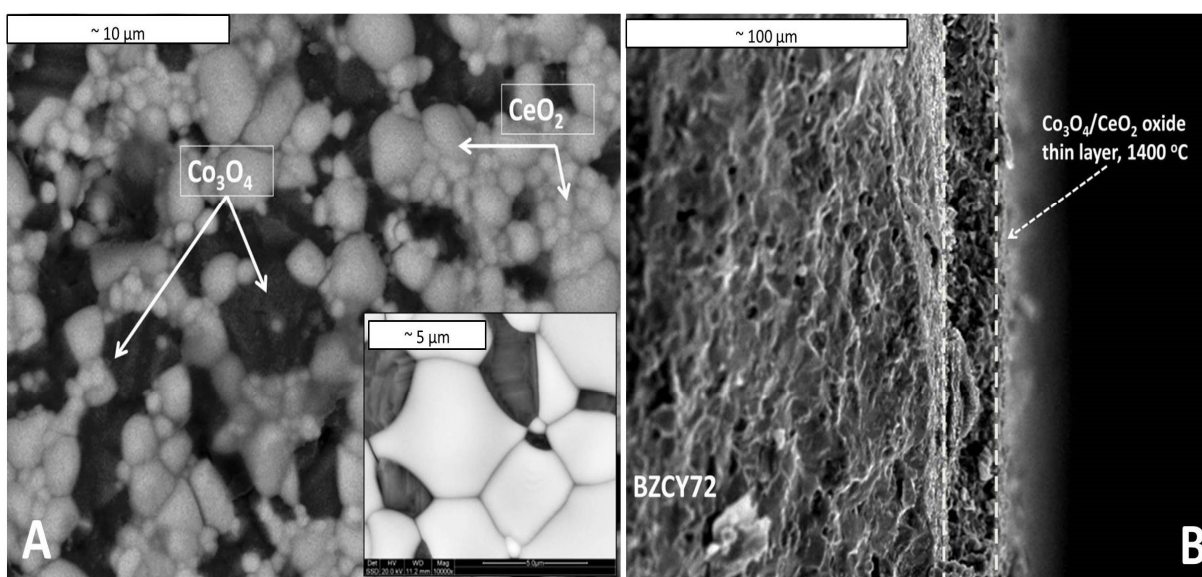


**Figure 8.11:** A) SEM pictures of the fresh calcined  $\text{Co}_3\text{O}_4$ / $\text{CeO}_2$  electrode surface at two different magnifications. B) Cross section image of the fresh  $\text{Co}_3\text{O}_4$ - $\text{CeO}_2$ /BZCY72 interface.

Moreover, it should be noticed that although a high sintering temperature was selected to obtain a good  $\text{Co}_3\text{O}_4$ / $\text{CeO}_2$  electrode layer adhesion on the BZCY72 surface, no chemical reactions at the electrode/electrolyte interface were observed, by the SEM and EDS studies.

The XRD spectrum (not shown) of the fresh sample revealed only reflections corresponding to  $\text{Co}_3\text{O}_4$ ,  $\text{CeO}_2$ , and BZCY72, verifying that no chemical transformations or interactions between the two oxides and the electrolyte occurred up to  $T = 1,400^\circ\text{C}$  in air. However, in the case of the aged sample, the  $\text{CoO}$  phase was additionally identified, indicating the reduction of cobalt oxide by the in situ produced  $\text{H}_2$  from reaction (8.1) and (8.2). On the

other hand, no change in BZCY72 structure was observed, verifying its chemical stability in  $\text{H}_2\text{S}$ -containing atmospheres (Polfus et al., 2015).

Corresponding SEM micrographs of the used electrode surface and cell cross section are shown in Figure 8.12.

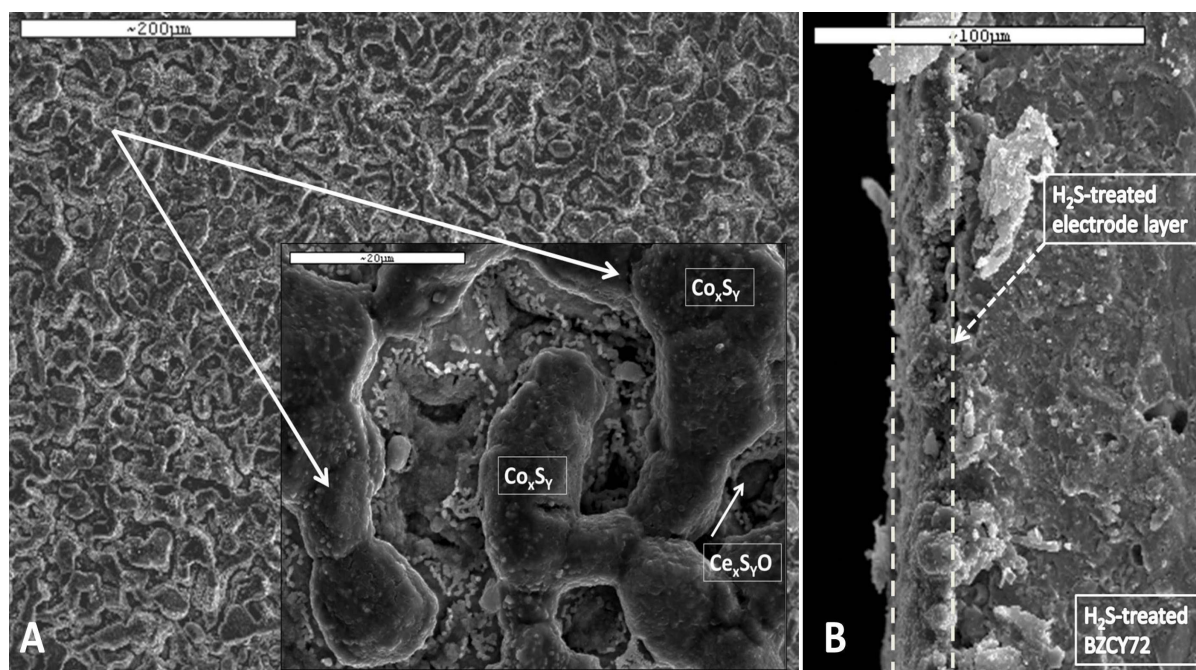


**Figure 8.12:** A) SEM pictures of the aged  $\text{Co}_3\text{O}_4/\text{CeO}_2$  electrode at two different magnifications. B) Cross section image of the aged  $\text{Co}_3\text{O}_4\text{-CeO}_2/\text{BZCY72}$  interphase.

By comparing the SEM pictures of the fresh (Figure 8.11A) and used (Figure 8.12A) samples, it is evident that the electrode has undergone significant morphological modifications, leading to new phases and a better porosity, as a result of its exposure in  $\text{H}_2\text{S}$ -containing environments at high temperatures. In particular, the average size of the cobalt containing particles increased to  $10\ \mu\text{m}$ , forming a worm-like shape, overlapping the smaller  $\text{CeO}_2$  particles which are located at the bottom edges of the cobalt species. Moreover, EDS analysis of the cobalt containing agglomerates revealed the existence of cobalt sulfides. In view of this fact, the superiority of  $\text{Co}_3\text{O}_4/\text{CeO}_2$  catalysts toward  $\text{H}_2\text{S}$  decomposition to  $\text{H}_2$  in both dry and wet (90 v/v%) atmospheres can be attributed to the in-situ sulfidation of catalysts active counterparts ( $\text{Co}_3\text{O}_4$  to  $\text{Co}_{1-x}\text{S}_y$  and  $\text{CeO}$  to  $\text{Ce}_{10}\text{S}_{14}\text{O}_y$ ) during the exposure under reaction conditions (Kraia et al., 2015). On the contrary, the BZCY72 pellet remained

dense and stable (Figure 8.12B), demonstrating its tolerance to H<sub>2</sub>S presence, a behavior also observed in (Li et al., 2008) and for BaCe<sub>0.8-x</sub>Zr<sub>x</sub>Y<sub>0.2</sub>O<sub>3-δ</sub> (with 0.4 ≤ x ≤ 0.8) after treatment with 10 v/v% H<sub>2</sub>S/Ar at T = 700 °C for 10 h (Medvedev et al., 2015).

At this point it may be noticed that only few studies have addressed the effect of H<sub>2</sub>S on the electrochemical performance of proton conducting ceramic cells, whereas most of these are mainly focused on the chemical stability of the solid electrolyte rather than the electrode (Li et al., 2008; Medvedev et al., 2015; Gong et al., 2007).

In light of the above, the present work was focused on the electrochemical performance and stability of Co<sub>3</sub>O<sub>4</sub>/CeO<sub>2</sub> electrodes exposed to H<sub>2</sub>S/H<sub>2</sub>O atmospheres, by employing a proton conducting symmetrical cell, with BZCY72 as the solid electrolyte. AC impedance measurements at different H<sub>2</sub>S feed concentrations and temperatures employing step change stability tests coupled with XRD and SEM studies of fresh and used electrodes, were employed to assess the electrochemical performance of Co<sub>3</sub>O<sub>4</sub>/CeO<sub>2</sub> composites. It was found that upon increasing temperature and H<sub>2</sub>S concentration, the overall cell conductivity, electrode resistance and as a consequence the electrochemical performance, although not sufficiently high for practical applications, is substantially improved, being remarkably stable even after the step change experiments at H<sub>2</sub>S-containing environments (of 21 h total duration).

The AC impedance spectra indicated two contributions attributed to the charge transfer and mass transport processes, with the latter being associated with the chemical steps (adsorption, diffusion, surface reaction) of reactions (1) and (2) intermediates. Moreover, the SEM and XRD studies of the aged electrodes showed that the Co<sub>3</sub>O<sub>4</sub>/CeO<sub>2</sub> electrode undergoes significant structural/morphological alterations, due to its exposure to H<sub>2</sub>S/H<sub>2</sub>O/Ar feed mixtures. In specific, part of the initial Co<sub>3</sub>O<sub>4</sub> is reduced to CoO by the in situ produced hydrogen, while both electrode counterparts (CeO<sub>2</sub> and Co<sub>3</sub>O<sub>4</sub>) have grown in size and transformed to sulfides by the interaction with the reactions (1) and (2) intermediates, simultaneously rearranged on the electrode surface. These modifications may be responsible for the improved electrochemical performance, since they can lead to i) more active electrode surfaces, ii) better distributed cobalt-rich particles enhancing the electrode in-plane conductivity and thus its electronic percolation and iii) better porosity, facilitating the mass transfer processes.

Concluding, the electrochemical behavior of  $\text{Co}_3\text{O}_4/\text{CeO}_2$  composite in  $\text{H}_2\text{S}$ -containing atmospheres under excess  $\text{H}_2\text{O}$  (90 v/v%) conditions was examined in a proton conducting ceramic symmetrical cell of the type  $\text{Co}_3\text{O}_4\text{-CeO}_2/\text{BZCY72}/\text{Co}_3\text{O}_4\text{-CeO}_2$ . AC impedance spectroscopy studies, at different  $\text{H}_2\text{S}$  feed concentrations (0-1 v/v%) and temperatures (700-850 °C), in conjunction with physicochemical characterization measurements of the fresh and aged (after  $\text{H}_2\text{S}$ -treatment) electrodes/ cells, were employed to systematically assess the electrochemical performance and stability behavior of the electrode. A promising stable electrochemical behavior was achieved, being favored as the  $\text{H}_2\text{S}$  feed composition and cell temperature increased. AC impedance spectra revealed contributions from charge transfer and mass transport steps, with the latter being in general more critical for the overall system, associated with the adsorption, diffusion and surface processes of the  $\text{H}_2\text{S} + 2 \text{H}_2\text{O} \rightleftharpoons 3 \text{H}_2 + \text{SO}_2$  and  $\text{H}_2\text{S}$  decomposition reactions intermediates. Although the electrolyte (BZCY72) itself was not affected by the  $\text{H}_2\text{S}$  treatment, significant modifications in the structural phases and morphology of the electrode were observed by the SEM and XRD studies of the used samples. The in situ reduction and sulfation of the electrode results in more active surfaces with higher porosity and better electronic conductivity, facilitating both the charge transfer and mass transport processes. The stable electrochemical performance of  $\text{Co}_3\text{O}_4/\text{CeO}_2$  composites under  $\text{H}_2\text{S}$ - $\text{H}_2\text{O}$  atmospheres may open new perspectives for the development of efficient, IRES powered, proton conducting ceramic  $\text{H}_2\text{S}$  and  $\text{H}_2\text{O}$  co-electrolysis cells toward “green” hydrogen production.

#### 8.2.4. Electrochemical Performance of a $\text{Co}_3\text{O}_4\text{-CeO}_2/\text{BZCY72}/\text{BGLC}$ Proton Conducting Solid Oxide Cell Fed with $\text{H}_2\text{S}/\text{H}_2\text{O}$ Mixtures

Figure 8.13 depicts the AC impedance spectra of the electrochemical cell consisting of Y-doped barium zirconate (BZCY72) as the solid electrolyte,  $\text{Co}_3\text{O}_4\text{-CeO}_2$  mixed oxide as the anode and  $\text{BaGd}_{0.8}\text{La}_{0.2}\text{Co}_2\text{O}_{6.6}$  (BGLC) perovskite as the cathode electrode. Two experiments were performed by feeding at the anode 1 v/v%  $\text{H}_2/\text{Ar}$  and 1 v/v%  $\text{H}_2\text{S}/30$  v/v%  $\text{H}_2\text{O}/\text{Ar}$  gas mixtures, while the cathode was always exposed to air flow. In the first case, the cell and electrode resistances were equal to 49 and 190  $\Omega\cdot\text{cm}^2$ , clearly higher values compared to the corresponding measurements with the symmetrical cell (approximately 65  $\Omega\cdot\text{m}^2$  electrode resistance). On the other hand, by switching to  $\text{H}_2\text{S}$ -containing atmospheres, the

electrochemical performance was slightly degraded showing cell and interfacial resistance values of 65 and 215  $\Omega\cdot\text{cm}^2$  but with a remarkable stable behavior for more than 5 hours. Again these values are higher compared to the corresponding experiments with the symmetrical cell confirming the contribution of cathode processes. This is also revealed by the shape of both AC impedance spectra, which are different compared to the spectra showed in the previous sections. Certainly, more experiments are required to come out with concrete conclusions regarding the electrochemical performance of the  $\text{Co}_3\text{O}_4\text{-CeO}_2/\text{BZCY72}/\text{BGLC}$  cell.

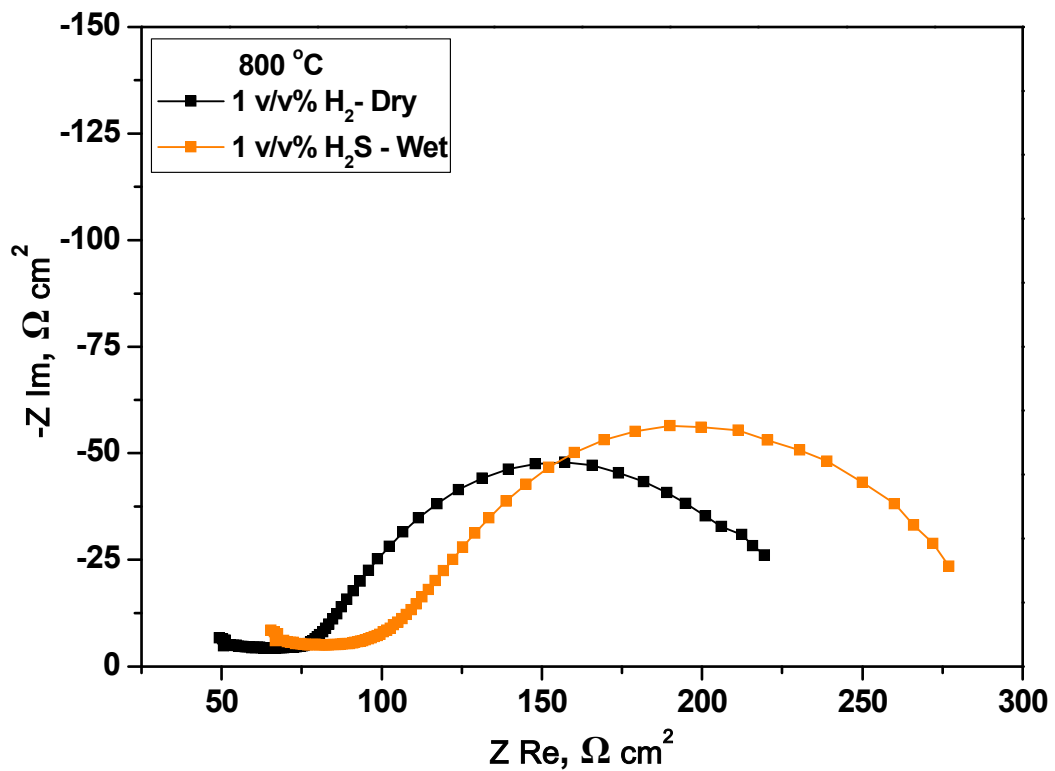


**Figure 8.13:** AC impedance spectra for a) 1 v/v%  $\text{H}_2/\text{Ar}$  and b) 1 v/v%  $\text{H}_2\text{S}/30$  v/v%  $\text{H}_2\text{O}/\text{Ar}$  feed mixtures at the anode. Cathode exposed to air flow. Reaction conditions:  $F_t=100$   $\text{cm}^3/\text{min}$  both at the anode and cathode,  $T = 800$   $^\circ\text{C}$ .

## REFERENCES

- Gong M., Liu X., Tremblay J., Johnson C. (2007). Sulfur-tolerant anode materials for solid oxide fuel cell application. *Journal of Power Sources*, 168: pp. 289-298.
- Kraia Tz., Konsolakis M., Marnellos G.E. (2016).  $\text{H}_2\text{S}$  in Black Sea: turning an environmental threat to an opportunity for clean  $\text{H}_2$  production via an electrochemical membrane

reactor, In: Research Progress in H<sub>2</sub>S-PROTON Project, *MATEC Web of Conferences*, 41: 04002.

Li J., Luo J.L., Chuang K.T., Sanger A.R. (2008). Chemical stability of Y-doped Ba(Ce,Zr)O<sub>3</sub> perovskites in H<sub>2</sub>S-containing H<sub>2</sub>. *Electrochemical Acta*, 53: pp. 3701-3707.

Medvedev D., Lyagaeva J., Plaskin S., Demin A., Tsiakaras P. (2015). Sulfur and carbon tolerance of BaCeO<sub>3</sub>-BaZrO<sub>3</sub> proton conducting materials, *Journal of Power Sources*, 273: pp. 716-723.

Polfus J.M., Norby T., Bredesen R. (2015). Protons in oxysulfides, oxysulfates, and sulfides: a first-principles study of La<sub>2</sub>O<sub>2</sub>S, La<sub>2</sub>O<sub>2</sub>SO<sub>4</sub>, SrZrS<sub>3</sub>, and BaZrS<sub>3</sub>. *The Journal of Physical Chemistry C*, 119: pp. 23875-23882.

Strandbakke R., Dyrllie O., Hage F.S., Norby T. (2016). Reaction kinetics of protons and oxide ions in LSM/lanthanum tungstate cathodes with Pt nanoparticle activation. *Journal of the Electrochemical Society*. 163: pp. 507-515.

Strandbakke R., Cherepanov V.A., Zuev A.Y., Tsvetkov D.S., Argirusis C., Sourkouni G., Prünke S., Norby T. (2015). Gd- and Pr-based double perovskite cobaltites as oxygen electrodes for proton ceramic fuel cells and electrolyzer cells. *Solid State Ionics*, 278: pp. 120-132.

# CHAPTER

## PRELIMINARY FEASIBILITY STUDY OF THE INTEGRATED APPROACH

# 9

Contents	Page
9.1. Introduction. . . . .	261
9.2. Process flow diagram development and brief description. . . . .	261
9.3. Mass and energy balances. . . . .	269
9.4. Economic evaluation and overall assessment. . . . .	272
References. . . . .	284



## 9.1. INTRODUCTION

As discussed in the previous chapters of this thesis, hydrogen presents the potential to be a clean and alternative to the fossil fuels energy carrier. This is especially true if H<sub>2</sub> production is coupled with the utilization of renewable resources (e.g., biomass) or the mitigation of severe environmental effects (e.g., the impact of H<sub>2</sub>S on the Black Sea territory). It is clear that during the last years the share of hydrogen in the energy market constantly increases, due to the implementation of innovative fuel cell systems and the growing demand for zero-emission fuels (Hamedani et al., 2016). Thus, in the following years, hydrogen production will need to keep pace with this growing market (Tremel et al., 2015). The here proposed technology for hydrogen production via the electrochemical decomposition of Black Sea H<sub>2</sub>S can be a promising route in terms of the environmental impact and economic feasibility. If the H<sub>2</sub> production process is integrated with the generation of significant amounts of electrical power and the concomitant production of a complementary product, like H<sub>2</sub>SO<sub>4</sub>, the potential is even larger, as a novel value chain is developed.

However, the present technologies for hydrogen production from alternative sources face significant technical and economic challenges, especially in the small-scale plants required for decentralized units (Ferrero et al., 2016). The major key to apply these technologies is to overcome the barriers associated with technical and economic aspects of pure H<sub>2</sub> production and, especially for large-scale plants, environmental acceptance (Becherif et al., 2014). For this reason, a plant once technically viable and environmentally friendly, requires to be economically favorable, so that the sustainability criterion is fulfilled (Hamedani et al., 2016). Towards this direction, a thorough techno-economic analysis is the unique route to conduct rational selections of appropriate research and development paths in this complex and rich technical area. For this purpose, the techno-economic analysis, carried out in the framework of the present thesis, is presented in the following sections.

## 9.2. PROCESS FLOW DIAGRAM DEVELOPMENT AND BRIEF DESCRIPTION

The technical and economic evaluation of the scaled-up and integrated plant, based on the operation of the process for the H<sub>2</sub> electrochemical production directly through the

utilization of the Black Sea water, is assessed via the development of two different process flow diagrams. Beyond  $H_2$ , which is the primary saleable product of the plant, the process is designed to generate electrical power, as a valuable secondary product. The difference between the two proposed operating schemes lies on the diversity on  $H_2SO_4$  production, which is the complementary product of the integrated plant. The production of  $H_2SO_4$  is facilitated due to the presence of the side-product  $SO_2$  (main feedstock for sulfuric acid production). Both flow diagrams consist of 4 distinct process steps (stages) and ultimately target the production of 100 kg/hr hydrogen (capacity operating goal) that is equivalent of refueling up to 50-60 articulated buses. It should be noted that an articulated bus consumes approximately 15.5 kg of  $H_2$  per 100 km to travel around 250-300 km/day. In detail, the 4 process stages are (Eudy and Post, 2014):

- i) Pumping Black Sea water from 1 km depth ( $H_2S$  concentration 14 ppm) and  $H_2S$  enrichment up to a concentration of 0.5 v/v%  $H_2S/H_2O$ .
- ii)  $H_2$  production through  $H_2S/H_2O$  electrolysis at  $T = 850\text{ }^\circ\text{C}$  and 2 bar. Notice that the pressure value equal to 2 bar was selected to allow a flexible removal of gases through the anode and cathode, with the aid of a small flow of inert gas (e.g.,  $N_2$  or Ar).
- iii) Purification and separation of the electrolyzer exit streams ( $H_2$  and  $SO_2$  products).
- iv)  $H_2SO_4$  production under two different options.

Notice that the production of electrical power in the plant takes place in more than one of the above stages, thus it is not considered as an individual process step. Moreover, the process flow diagram development, simulation and overall evaluation have been performed in the Aspen Plus software platform (Aspen Technology, 2000).

### 9.2.1. Process Flow Diagram 1 Description: Production of $H_2SO_4$ through $SO_3$ Absorption/Reaction in $H_2O$

Figure 9.1 illustrates the first proposed design configuration for the integrated plant that produces  $H_2$ , electricity and  $H_2SO_4$ , through  $SO_3$  absorption/reaction in  $H_2O$ . In what follows, a brief description of the flowsheet is presented according to the identified process steps.

**STEP 1:** A technically qualified pump (P-1) delivers 1,300 tn/hr of Black Sea water ( $H_2S$  concentration 14 ppm) from 1 km depth, pressure 101.8 bar and temperature  $4\text{ }^\circ\text{C}$ ,

containing NaCl and MgCl<sub>2</sub> as major mineral salts) at the sea level. In order to gasify and enrich the feedstock mixture in H<sub>2</sub>S up to a concentration of 0.5 v/v%, a series of heat exchangers is involved. Firstly, heat recovery from the hot (residual) water stream returning to the cold Black Sea at sea level, upon the intake, takes place at HX-1 (temperature increase of 80 °C). Next, further heating of the H<sub>2</sub>S/H<sub>2</sub>O mixture is conducted in the burner effluent. To this end, a natural gas burner receives as inlet: i) a high pressure (HP) natural gas (CH<sub>4</sub>) stream, delivered by a local supplier at T = 185 °C and 30-35 bar, and ii) air at a ratio 2.7 times the stoichiometrically demanded. The heat supply of the effluent (flue) gases takes place at HX-2 (temperature increase equal to 17 °C and also evaporation part of the liquid water phase for the enrichment of H<sub>2</sub>S). The hot outlet contains an equilibrium mixture of vapor-liquid that is separated (EQUIL-TANK) in two phases. Notice that EQUIL-TANK and HX-2 are assumed as a single unit equipment, connected in series, which allows the proper separation of vapor-liquid phases. As a result, the gas phase attains the 0.5 v/v% H<sub>2</sub>S/H<sub>2</sub>O concentration, whereas the hot liquid outlet from the tank constitutes the water return to the Black Sea that is heat exchanging in HX-1, as mentioned above. Since the H<sub>2</sub>S/H<sub>2</sub>O mixture needs to be further heated at T = 850 °C (i.e., the electrolyzer operating temperature), a two-stage heat exchanger is properly involved. In HX-3, the burner flue gases initially provide part of their heat (temperature increase 230 °C) and then are driven to a gas turbine (TUR-1) that is able to produce electrical power equal to 27 MW<sub>p</sub>. Sequentially, in the electrical heater ELEC-HX-1, the mixture is further heated (temperature increase 520 °C) up to the desired temperature of 850 °C.

**STEP 2:** The electrolyzer operates at 850 °C and 2 bar under an electrical supply of 6 MW (Pure energy center: Hydrogen Electrolyser, 2016). The total mass of the electrolyzer feedstock is 1,009 kg/hr of 0.5 v/v% H<sub>2</sub>S/H<sub>2</sub>O. Note that an inert N<sub>2</sub> stream also enters the reactor cathode, at the same temperature, in order to facilitate the purge of the produced gases. In the electrolyzer, the electrochemical decomposition of H<sub>2</sub>O and H<sub>2</sub>S takes place through the Reactions R1 and R2 of Table 9.1, while the production of SO<sub>2</sub> is also performed via the Reactions R3a/b. The anode outlet (which is pure H<sub>2</sub> at a capacity equal to 100 kg/hr) is cooled via an air cooler (HX-4, temperature decrease 350 °C) and a water cooler (HX-5, temperature decrease 470 °C) and stored for further use in gas cylinders under pressure. The regulation of the electrolyzer operating temperature at the desired set-point, due to the

endothermic nature of the decomposition reactions, is ensured through electrical heating units (ELEC-HX-2).

**STEP 3:** On the other hand, the cathode outlet stream from the electrolyzer is initially air cooled (HX-6, temperature decrease 400 °C) and then enters the SO<sub>2</sub> oxidizer reactor where the Reactions R4 and R5 (Table 9.1) take place at T = 450 °C. The outlet of this oxidation reactor is further water cooled (HX-7, temperature decrease of 380 °C) and is fed the absorber.

**STEP 4:** At the absorber, a concentrated feed of 98 v/v% H<sub>2</sub>SO<sub>4</sub>/H<sub>2</sub>O is introduced to suppress and regulate the highly exothermic Reaction R6 of H<sub>2</sub>SO<sub>4</sub> formation, due to SO<sub>3</sub> absorption in free water at 70 °C (King et al., 2013). The liquid outlet stream contains an enriched in H<sub>2</sub>SO<sub>4</sub> mixture (99 v/v% H<sub>2</sub>SO<sub>4</sub>/H<sub>2</sub>O concentration) that is water cooled at (HX-8 temperature decrease 40 °C) and then separated in the product stream (capacity equal to 31 kg/hr) and the recycled to the absorber stream (after diluted in the mixer with additional water). It should be highlighted that in HX-5 and HX-7, medium pressure steam (MP steam 1 and 2) is produced due to heat exchanging, which is fed to a two-stage turbine (TUR-2, TUR-3) for further production of electrical power equal to 50 kWp.

### 9.2.2. Process Flow Diagram 2 Description: Production of H<sub>2</sub>SO<sub>4</sub> through SO<sub>2</sub> and Iodine Cycle

The second proposed design configuration for the concomitant production of H<sub>2</sub>, electrical power and H<sub>2</sub>SO<sub>4</sub> from Black Sea H<sub>2</sub>S is presented in Figure 9.2. As can be seen, Steps 1 and 2 of the plant are exactly identical with the first configuration and the major modifications in the second flowsheet exist at the third and fourth step, dealing with the cathode outlet stream from the electrolyzer.

**STEP 3:** More specifically, the cathode outlet stream is initially air cooled (HX-6 temperature decrease 350 °C) and then water cooled (HX-7 temperature decrease 410 °C) before entering the H<sub>2</sub>SO<sub>4</sub> reactor (or the Bunsen reactor).

**STEP 4:** In the reactor, Reaction R7 takes place in the presence of fresh iodine (I<sub>2</sub>) to produce H<sub>2</sub>SO<sub>4</sub> at high concentration (Liberatore et al., 2012a; Liberatore et al., 2012b). The gas-liquid mixture stream, exiting the reactor, is separated at the following G-L separator. The liquid

phase is further separated in waste H<sub>2</sub>O and the 99 v/v% H<sub>2</sub>SO<sub>4</sub>/H<sub>2</sub>O product (capacity 31 kg/hr) in an L-L extractor (heavy and light phases), after being water cooled (HX-8 temperature decrease 55 °C). On the other hand, the gas-phase is heated in two stages via the flue gases of the burner (HX-9 temperature increase 240 °C) and in an electrical heater (ELEC-HX-3 temperature increase 80 °C) and then is fed to the HI decomposition reactor (also electrical power is demanded) for iodine recovery according to Reaction R8. The outlet of the decomposition reactor is water cooled (HX-10 temperature decrease 375 °C) and further separated to a waste gas stream and to the recovered iodine in an aqueous solution.

Finally, the produced medium pressure steam streams (MP steam 1, 2 and 3 in HX-5, -7 and -10, respectively) are led to a two-stage turbine for the production of electrical power equal to 84 kWp. Notice that the Reactions R9 of Table 9.1 refer to the electrochemical decomposition character of the previous reactions (modified as discussed above to be used in the Aspen calculations, due to the necessity of electron-free expressions). Moreover, the reaction conversions are calculated based on the first reactant of each equation, e.g., 35% of H<sub>2</sub>S is converted in R1, 60% in R3a, while 5% remains unconverted. Similar assumptions are made for the other components as well. The detailed description of the process equipment units, used in both flow diagrams 1 and 2, is listed in Table 9.2.

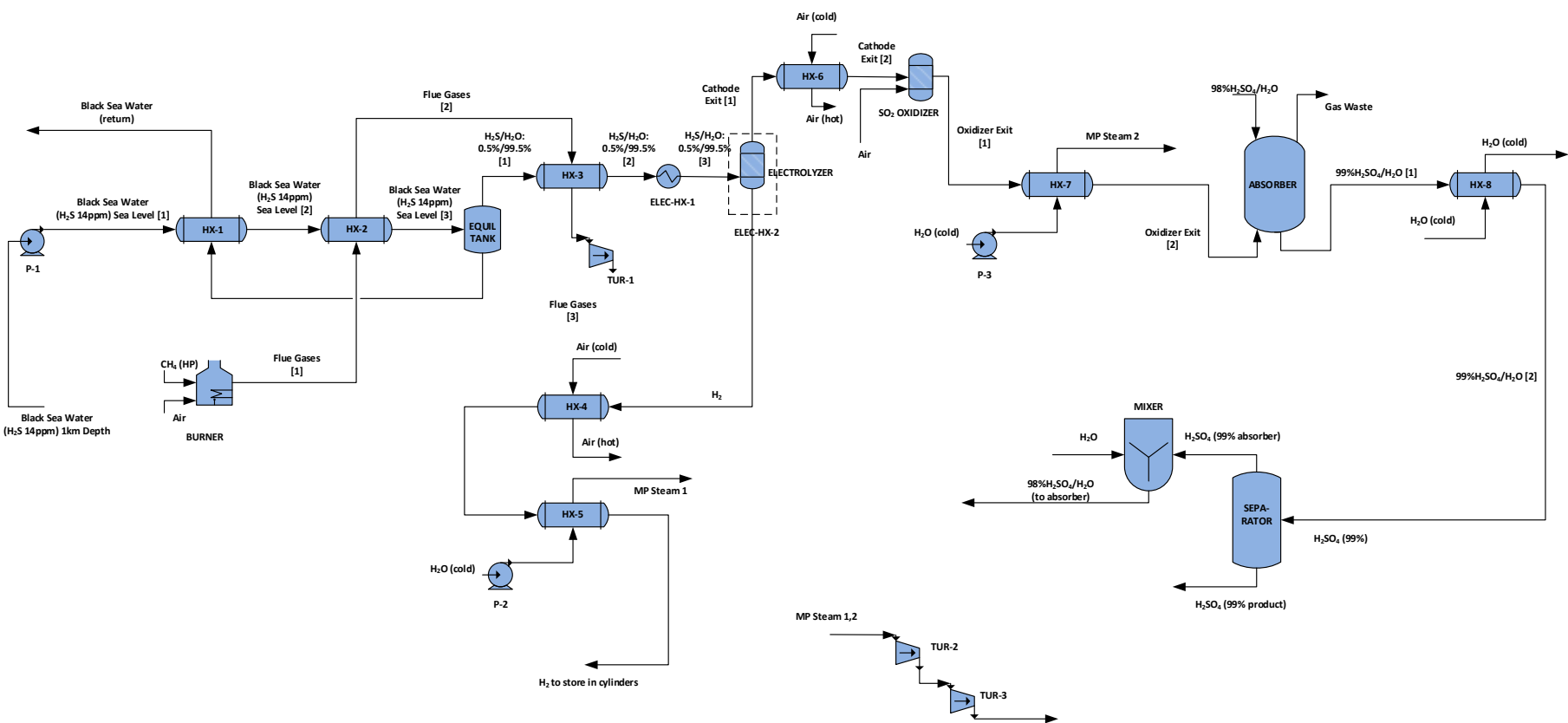
**Table 9.1:** Overall reaction scheme.

Description	Reaction	Conversion
Electrochemical H <sub>2</sub> S decomposition	R1: H <sub>2</sub> S → H <sub>2</sub> + S	35%
Electrochemical H <sub>2</sub> O decomposition	R2: H <sub>2</sub> O → H <sub>2</sub> + 0.5O <sub>2</sub>	85%
SO <sub>2</sub> formation	R3a: H <sub>2</sub> S + 2H <sub>2</sub> O → 3H <sub>2</sub> + SO <sub>2</sub>	60%
	R3b: S + O <sub>2</sub> → SO <sub>2</sub>	100%
H <sub>2</sub> S Oxidation	R4: H <sub>2</sub> S + O <sub>2</sub> → SO <sub>2</sub> + H <sub>2</sub>	100%
SO <sub>2</sub> Oxidation	R5: SO <sub>2</sub> + 0.5O <sub>2</sub> → SO <sub>3</sub>	100%
H <sub>2</sub> SO <sub>4</sub> formation	R6: SO <sub>3</sub> + H <sub>2</sub> O → H <sub>2</sub> SO <sub>4</sub>	100%
H <sub>2</sub> SO <sub>4</sub> formation	R7: SO <sub>2</sub> + 2H <sub>2</sub> O + I <sub>2</sub> → H <sub>2</sub> SO <sub>4</sub> + 2HI	100%
HI decomposition	R8: 2HI → H <sub>2</sub> + I <sub>2</sub>	100%
Electrochemical Reactions	R9a: H <sub>2</sub> S → 2H <sup>+</sup> + S + 2e <sup>-</sup>	
	R9b: H <sub>2</sub> O → 2H <sup>+</sup> + 0.5O <sub>2</sub> + 2e <sup>-</sup>	
	R9c: H <sub>2</sub> → 2H <sup>+</sup> + 2e <sup>-</sup>	

**Table 9.2:** Description of process equipment in flow diagrams 1 and 2.

Process equipment	Description
ABSORBER	Absorber tower for the absorption of SO <sub>2</sub> and further reaction with free water from a 98 v/v% H <sub>2</sub> SO <sub>4</sub> /H <sub>2</sub> O feed
BURNER	Natural gas burner
ELEC-HX-1	Electrical heater for heating H <sub>2</sub> S/H <sub>2</sub> O mixture to the electrolyzer operating temperature
ELEC-HX-2	Electrical heater for maintaining the electrolyzer operating temperature
ELEC-HX-3	Electrical heater
ELECTROLYZER	Proton-Conducting Solid Oxide Electrolysis Cell (PC-SOEC)
EQUIL-TANK	Equilibrium tank for H <sub>2</sub> S enrichment and vapor-liquid phase separation
G-L SEPARATOR	Gas-Liquid separator
H <sub>2</sub> SO <sub>4</sub> REACTOR	Reactor for H <sub>2</sub> SO <sub>4</sub> formation through H <sub>2</sub> O, SO <sub>2</sub> and I <sub>2</sub>
HI DECOMPOSITION REACTOR	Reactor for I <sub>2</sub> recovery
HX-1, HX-2, HX-3	Heat exchangers network for a) enriching H <sub>2</sub> S/H <sub>2</sub> O mixture at 0.5% concentration and b) further heating close to the electrolyzer operating temperature
HX-4, HX-6	Air cooled heat exchangers
HX-5, HX-7, HX-10	Water cooled heat exchangers (steam production)
HX-8	Water cooled heat exchanger
HX-9	Heat exchanger
L-L EXTRACTOR	Liquid-liquid extractor for the separation of H <sub>2</sub> SO <sub>4</sub> and H <sub>2</sub> O (heavy and light phases)
MIXER	Mixing of water and 99 v/v% H <sub>2</sub> SO <sub>4</sub> /H <sub>2</sub> O (dilution to 8 v/v%)
SO <sub>2</sub> OXIDIZER	Reactor for the oxidation of SO <sub>2</sub> (and H <sub>2</sub> S as well)
P-1	Electrical pump for the intake of Black Sea water from 1 km depth
P-2, P-3, P-4	Electrical pumps for ensuring high pressure water at heat exchangers (used for steam production)
SEPARATOR	Flow separation of 99 v/v% H <sub>2</sub> SO <sub>4</sub> /H <sub>2</sub> O
TUR-1	Gas turbine for electrical production
TUR-2, TUR-3	Series of steam turbines for electrical production

Figure 9.1: Process flow diagram 1 (PFD1): Production of  $H_2SO_4$  through  $SO_3$  and  $H_2O$ .



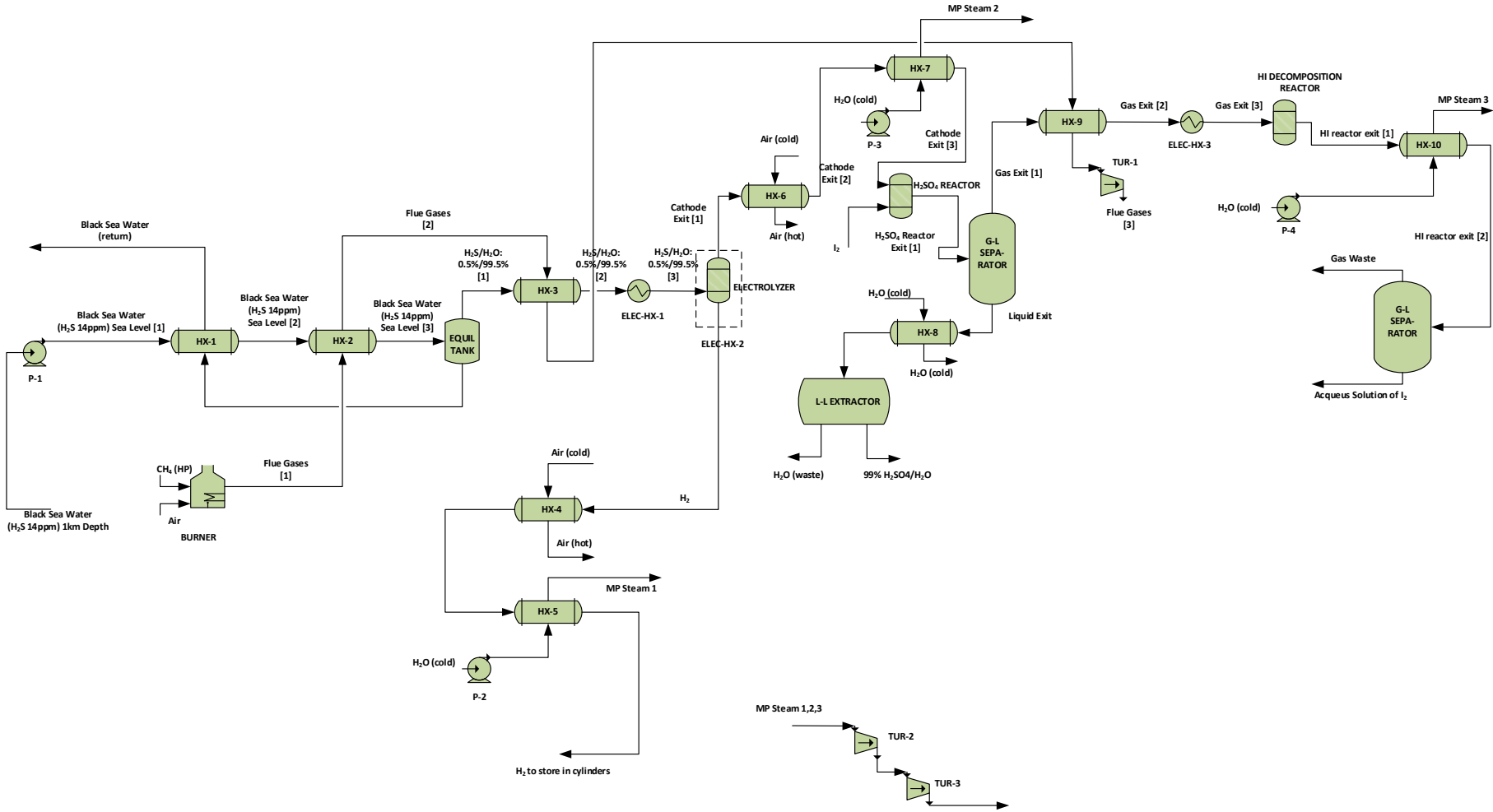


Figure 9.2: Process flow diagram 2 (PFD2): Production of H<sub>2</sub>SO<sub>4</sub> through SO<sub>2</sub> and Iodine Cycle.

### 9.3. MASS AND ENERGY BALANCES

Upon the development and description of the two main operating schemes (flowsheets), the detailed calculation of the complete mass and energy balances, along with the equipment sizing, is performed in Aspen Plus. In Tables 9.3 and 9.4, the overall material circulation and the consumption/production of electrical power for the operation of both schemes are presented in summary.

#### 9.3.1. Process Flow Diagram 1 Description: Production of H<sub>2</sub>SO<sub>4</sub> through SO<sub>3</sub> Absorption/Reaction in H<sub>2</sub>O

Overall, 1,300 tn/hr of Black Sea water are delivered at sea level and upon H<sub>2</sub>S enrichment and further heating in a series of heat exchangers, 1,009 kg/hr of a 0.5 v/v% H<sub>2</sub>S/H<sub>2</sub>O mixture is introduced in the electrolyzer at the operation temperature, i.e., 850 °C. The residual Black Sea water intake (1,299 tn/hr) returns back to a specific depth of the sea. The heat requirements in HX-2 and HX-3 are met by the flue gases produced in the natural gas burner (CH<sub>4</sub>: 6.7 tn/hr, Air: 311.6 tn/hr), which operates at a high pressure (32 bar). The total outlet flow of flue gases is equal to 318.3 tn/hr (composition: 7.45 v/v% H<sub>2</sub>O, 12.77 v/v% O<sub>2</sub>, 76.06 v/v% N<sub>2</sub>, 3.72 v/v% CO<sub>2</sub>). The H<sub>2</sub> product stream, exiting the electrolyzer and assumed to be in a pure state, is stored under pressure. The total flow of H<sub>2</sub> is 96.34 kg/hr. On the other hand, the total flow of the cathode exit stream from the electrolyzer is 912.93 kg/hr (composition: 25.04 v.v% H<sub>2</sub>O, 0.05 v.v% H<sub>2</sub>S, 73.96 v.v% O<sub>2</sub>, 0.95 v/v% SO<sub>2</sub>) and enters the SO<sub>2</sub> oxidizing reactor, along with 45.6 kg/hr of air. The cooled exit of the SO<sub>2</sub> oxidizer is introduced in the absorber, having a total flow of 958.52 kg/hr (composition: 23.96 v/v% H<sub>2</sub>O, 0.95 v/v% SO<sub>3</sub>, 0.05 v/v% H<sub>2</sub>, 71.27 v.v% O<sub>2</sub>, 3.76 v/v% N<sub>2</sub>), along with a 98 v/v% H<sub>2</sub>SO<sub>4</sub>/H<sub>2</sub>O stream of 4,550 kg/hr flow. The gas outlet (waste) of the absorber is released to the environment (802.42 kg/hr flow, with composition: 2.63 v/v% H<sub>2</sub>O, 0.06 v/v% H<sub>2</sub>, 92.42 v/v% O<sub>2</sub>, 4.89 v/v% N<sub>2</sub>). The 99 v/v% H<sub>2</sub>SO<sub>4</sub>/H<sub>2</sub>O stream, accounting for a capacity equal to 31 kg/hr, is also stored as a product. The total air requirement for air coolers is equal to 41.5 tn/hr, while cooling water demands are at 1.46 tn/hr.

With respect to the energy demands of the plant, the water pumps (P-2 and P-3) require 1.3 kWp, while the Black Sea water pumping step (P-1) demands 3.09 MWp. Furthermore, the

electrical power demands of the electrolyzer are: a) 6 MWp, regarding the electrical consumption for H<sub>2</sub> production, b) 9.07 MWp, regarding the electrical consumption for temperature maintenance (ELEC-HX-2), and c) 0.89 MWp for feedstock heating (ELEC-HX-1). However, during the plant operation, the production of electrical power is larger than the total demands. Under the operation of the proposed scheme, the total electrical power production from steam amounts to 50 kWp, while the respective production from flue gases, after heat exchanging, is 27.16 MWp. Hence, the integrated process operates with a net electrical power gain of 8.18 MWp.

### 9.3.2. Process Flow Diagram 2 Description: Production of H<sub>2</sub>SO<sub>4</sub> through SO<sub>2</sub> and Iodine Cycle

As discussed above, the first two process steps of flow diagrams 1 and 2 are identical. As a result, the material circulation up to the electrolyzer outlet is exactly the same. Thereupon, the cathode exit from the electrolyzer with a total flow of 912.93 kg/hr (composition: 25.04 v/v% H<sub>2</sub>O, 0.05 v/v% H<sub>2</sub>S, 73.96 v/v% O<sub>2</sub>, 0.95 v/v% SO<sub>2</sub>) enters the H<sub>2</sub>SO<sub>4</sub> reactor, along with 80.41 kg/hr of I<sub>2</sub>. The mass flow of the liquid exit stream of the reactor is equal to 31 kg/hr, containing 99 v/v% H<sub>2</sub>SO<sub>4</sub>/H<sub>2</sub>O. This mixture is stored as a complementary product of the plant, while the gas exit stream, with a total flow of 961.64 kg/hr (composition: 23.18 v/v% H<sub>2</sub>O, 0.05 v/v% H<sub>2</sub>S, 74.81 v/v% O<sub>2</sub>, 1.91 v/v% HI, 0.04 v/v% I<sub>2</sub>) subsequently enters the HI decomposition reactor. The waste gas outlet stream of the reactor absorber is released to the environment (total flow 765.98 kg/hr, with a composition: 2.52 v/v% H<sub>2</sub>O, 0.06 v/v% H<sub>2</sub>S, 96.12 v/v% O<sub>2</sub>, 1.28 v/v% H<sub>2</sub>). Moreover, the mass flow of the aqueous solution stream (4% iodine concentration) is 196 kg/hr. Finally, the total air requirement for air coolers amounts to 41.5 tn/hr, while the cooling water demands are 64.9 kg/hr.

Regarding the electrical demands of this case, the total power requirements in water pumps (P-2, P-3 and P-4) are 2.03 kWp, while the Black Sea water pumping step (P-1) demands 3.09 MWp of electrical power. Furthermore, the electrical requirements for the electrolyzer operation are: a) 6 MWp, regarding the electrical power consumption for H<sub>2</sub> production, b) 9.07 MWp, regarding the electrical power needed for temperature maintenance (ELEC-HX-2), and c) 0.89 MWp of power needed for the feedstock heating (ELEC-HX-1). Finally, the

electrical power demands for heating at ELEC-HX-3 are 64.8 kWp, with the respective requirements for HI decomposition amount to 40 kWp. On the other hand, the in-situ generation of electrical power is larger than the total demands, due to the 84 kWp of power produced from the total available steam and the 27.16 MWp of power recovered from the output flue gases, after heat exchanging, in TUR-1. Similarly to the first flowsheet, the integrated process operates with a net electrical power equal to 8.08 MWp. The comparison of the material circulation and utilities flows for the Process Flow Diagrams 1 (PFD1) and 2 (PFD2) are presented in Table 9.3, while the relevant electricity demands and power generation for both cases are listed in Table 9.4.

**Table 9.3:** Material circulation and utilities in PFD1/2.

<b>Material (kg/hr)</b>	<b>PFD1</b>	<b>PFD2</b>
Hydrogen production	96.3	96.3
H <sub>2</sub> SO <sub>4</sub> production	31	31
Air utilities at reactors	45.6	-
I <sub>2</sub> utilities at reactor	-	80.5
98 v/v% H <sub>2</sub> SO <sub>4</sub> /H <sub>2</sub> O	4,550	-
Air utilities at coolers	411,500	411,500
Water utilities at coolers	1,460	64.9
CH <sub>4</sub> at burner	6,700	6,700
Air at burner	311,600	311,600

**Table 9.4:** Power requirements/production in PFD1/2.

<b>Electrical power for/from (kW<sub>p</sub>)</b>	<b>PFD1</b>	<b>PFD2</b>
Black Sea water pumping	-3,090	-3,090
Water pumping	-1.30	-2.03
Electrolyzer power	-6,000	-6,000
Electrolyzer heating	-9,070	-9,070
Electrical heaters	-878	-943
HI decomposition	-	-40
Steam power production	+50	+84
Gas power production	+27,160	+27,160
Net power	+8,180	+8,080

## 9.4. ECONOMIC EVALUATION AND OVERALL ASSESSMENT

The evaluation and assessment of the economic potential of the two proposed operating schemes is described in what follows. More specifically, emphasis will be given in the following:

- Description of equipment sizing, cost and fixed capital investment.
- Evaluation of raw materials, utilities and overall production cost.
- Evaluation of secondary cost categories (labor, supervision, operating, etc.)

It should be noted that all calculations were performed based on steady-state simulations, according to the data presented in the previous section. As discussed, both flow diagrams consist of 4 distinct process steps and ultimately target towards the production of approximately 100 kg/hr of H<sub>2</sub> (operating goal). It is the objective of this section to assess the operating feasibility of both cases in terms of cost indices, even if the overall economics indicate a relatively small or even negative profit. In the latter case, a set of economic objectives will be formulated according to realistic scenarios, so that they will render the overall process promising.

### 9.4.1. Equipment Sizing, Dimensioning and Related Costs

In the present section, the sizing procedure of all process equipment, corresponding to the process flow diagrams of Figures 9.1 and 9.2, is presented. Specific dimensions and engineering details are provided wherever is considered as necessary.

#### 9.4.1.1. Reactors/Distillation Columns

Reactors and distillation columns are being used in both flow diagrams in order to process the cathode exit of the electrolyzer and to produce H<sub>2</sub>SO<sub>4</sub> of high purity. Their sizing is based on a) the inlet flow rate, b) the residence time of the reactant mixture and c) the related physicochemical properties (e.g., viscosity, mixture density). All reactors are constructed using stainless steel (316) so that they will present efficient resistant to wear and tear, as well as, to corrosion. The mechanical components and the general configuration of the reactors were equally selected, taking into account the high operating pressure and

temperature, therefore they are explosion proof. Notice that the relevant information on design and cost equations are rather empirical in nature and can be found in the open literature (Couper et al., 2003; Koukos, 2009; Kiparissides, 2008; Peters et al., 2006). In cases that heating and/or cooling equipment (e.g., jackets, condensers) are utilized, they all are included to the main reactor cost.

#### 9.4.1.2. Heat Exchangers

Heat exchangers are widely used in the proposed plants to efficiently transfer heat between two independent streams via convection. Shell and tubes heat exchangers are selected as they consist a common and well-known technology in chemical processing industries. Embedded within the design of a heat exchanger are numerous baffles, supporting the tubes and forcing the fluids to flow through several groups of parallel tubes, thus increasing the number of passes and creating enough friction for sufficient heat transfer. In the design process, the fouling factor is also considered to have an impact on the total heat transfer efficiency of the heat exchanger. In the present case, a fouling factor ( $F$ ) equal to 0.9 is used throughout, while the standard tube length and diameters are selected equal to 5 m and 0.02 m, respectively.

In more detail, the design of a single heat exchanger is performed according to the following procedures: a) calculation of the demanded heat duty, b) determination of the type of fluid that occupies the tubes and the shell (in most cases, it is preferable that the more corrosive and high pressure fluid passes through the tubes, while the less corrosive through the shell), c) selection of the tube diameter (nominal value 0.02 m), d) calculation of the logarithmic mean temperature difference, and e) calculation the required heat transfer area and the number of tubes (Stewart and Lewis, 2013, Paras, 2014). In all cases, the previously estimated data on feed flow rates, temperature differences and heat duties are utilized during cost estimation.

#### 9.4.1.3. Pumps

The primary use of pumps in the plants is to enable the flow of liquids due to pressure difference, obtained via the consumption of electrical energy. In general, pumps of different

types or models represent diverse operational functionalities. As centrifugal pumps present a wider application potential in chemical fluid industries, due to their low purchase cost and their ability to efficiently operate under a wide range of operating conditions, they are employed in the present analysis. The design variables in pump costs, as provided by the Aspen simulation data, are the power output (kW), the total developed head height (m) and the pressure difference (bar).

#### 9.4.1.4. Flash Tanks/Storage Vessels

As can be seen in both flow diagrams, flash tanks are required to enrich the  $\text{H}_2\text{S}/\text{H}_2\text{O}$  mixture and also to separate different components (e.g.,  $\text{H}_2\text{SO}_4$  for  $\text{I}_2$ ). In principle, flash drums operate under minimal pressure conditions (normally 1 atm), depending on the vapor and liquid phase contents. They are, in most cases, equipped with demister pads to effectively trap vapor droplets and increase the separation efficiency. In the design of storage tanks, specifications in accordance to specific recognized authorities, such as the American Society for Testing Materials (ASTM) and API, are met. For instance, the API 620 standard has already established the minimum requirements for material design, fabrication, erection and testing. Accordingly, depending on the volatility of the stored product, floating or cone roof tanks are employed (Baasel, 1976; American Petroleum Institute, 2002, Peters et al., 1991). The major variables in flash drum and storage tank design are the volumetric flow rate ( $\text{m}^3/\text{hr}$ ), the resident time ( $\text{sec}/\text{hr}$ ), the fill factor and the operating temperature/pressure.

#### 9.4.1.5. Compressors/Turbines

Usually, centrifugal compressors are widely employed in industrial chemical processes to increase the gas pressure by accelerating the gas velocity, as it flows radially out from the rotating impeller. The increase in velocity is then converted to increase in pressure, as the gas exits the compression stage. Notice that a centrifugal compressor, unlike other types of compressors, involves a constant flow through the compressor. The efficiency of a compressor is usually expressed as isentropic efficiency. The exact reversed operation is involved in turbines (Smith, 2005). The major variables considered in the compressors design are the power consumption and pressure difference.

#### 9.4.1.6. Furnace

A furnace unit is involved in both flow diagrams in order to provide the necessary heat duty, in cases where a significant temperature increase is required. The furnace is designed to operate using a mixture of CH<sub>4</sub>/air as inlet, while its sizing is performed based on the inlet gas flow and the related heat duty that the combustion provides.

#### 9.4.1.7. Electrolyzer

The cost of producing hydrogen via current electrolytic processes largely depends on the cost of electricity, the efficiencies of the systems, and the capital costs of the systems (e.g., materials for the construction of the anode, cathode, electrolyte, etc.). Because the process efficiency can be increased in only a limited amount, an increased efficiency will not reduce the cost as much as a significant reduction in the electricity price. Moreover, all electrolysis systems will benefit from a reduction in capital cost, as the hydrogen economy grows and these systems are mass produced; the smaller systems will benefit the most, as the largest percentage of their hydrogen cost contribution comes from capital costs. Moreover, cost projections for electrolyzer cells are based on limited experience and frequently on small-scale cells. As a result, since it is already established that the cost for electrical power is the major contributor to the overall cost of the electrolyzer, the estimation of its purchase cost is based on the calculated electricity demands (Penev, 2013).

#### 9.4.1.8. Purchased Equipment Cost

It should be noted that in all the previously described cases, the process equipment cost estimations were conducted using empirical relationships from literature studies, considering the selected equipment sizing parameters. A cost escalation was performed, taking into account the effect of time difference on cost variance, due to monetary and labor cost inflations. Specifically, Marshall and Swift (M&S) cost escalation indices were used to project equipment prices from a specific time period to the present. This method is widely recognized, accounting for monetary inflation and presents an acceptable margin of error. The monetary exchange rate was further utilized to express prices from one currency to another. In Table 9.5, the individual cost for the purchase of the major equipment is

presented. Moreover, Figures 9.3 and 9.4 illustrate the overall percentage share of individual equipment for both flow diagrams. As can be seen, the highest share is due to the compressors/turbines and the electrolyzer, both accounting for larger than 50% of the total fixed capital cost.

**Table 9.5:** Equipment cost for both flow diagrams.

Equipment	Cost in PFD1, €	Cost in PFD2, €
Reactors/distillation columns	121,737	118,005
Heat exchangers	3,771,321	3,904,507
Pumps	60,967	70,536
Compressors/turbines	7,310,434	7,370,868
Flash tanks/Storage vessels	3,057,691	3,170,998
Furnace	514,904	515,244
Electrolyzer	5,100,000	5,100,000
Major Equipment Cost (MEC in 2016)	19,937,054	20,250,158

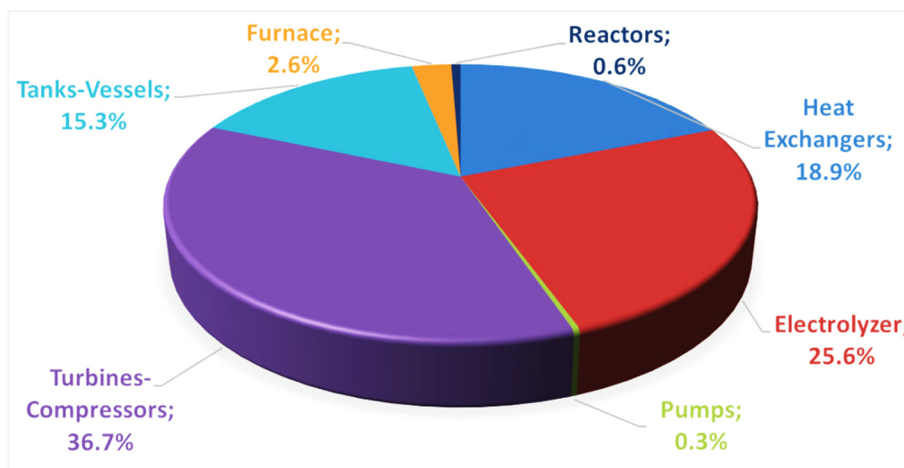


**Figure 9.3:** Percentage share of individual equipment for PFD1.

#### 9.4.2. Economic Analysis of the Overall Process

The proof of concept and the possibility of establishing a process plant for the utilization of H<sub>2</sub>S towards H<sub>2</sub> and electrical power production is equally dependent on the economic performance or economic criteria. These economic performance indicators reflect the sustainability and profitability of the entire venture throughout its projected useful life.

Therefore, analysis of the economic viability of the project will entail the use of empirical economic indices and apparent taxation policies in the land of installation. The useful life span of the project, in accordance to literature reviews on similar plants, is assumed to be within the range of 10 years (N=10), as such, the depreciation factor and the capital recovery factor are assumed equal (d=e) and defined as the reciprocal of the life span, i.e.,  $d=e=1/N$  or 10%. A total income tax of 26%, based on the net profit of the process plant and the prevailing economic indexes in most interested in this technology countries (surrounding the Black Sea) is adapted throughout the economic performance calculations. In addition, the allowable minimum rate of return (Reasonable Return on Investment) is 10% (considering the fact that the concept is new). In summary, the economic indices used in the performance and profitability analysis of the two proposed process plants are listed in Table 9.6.

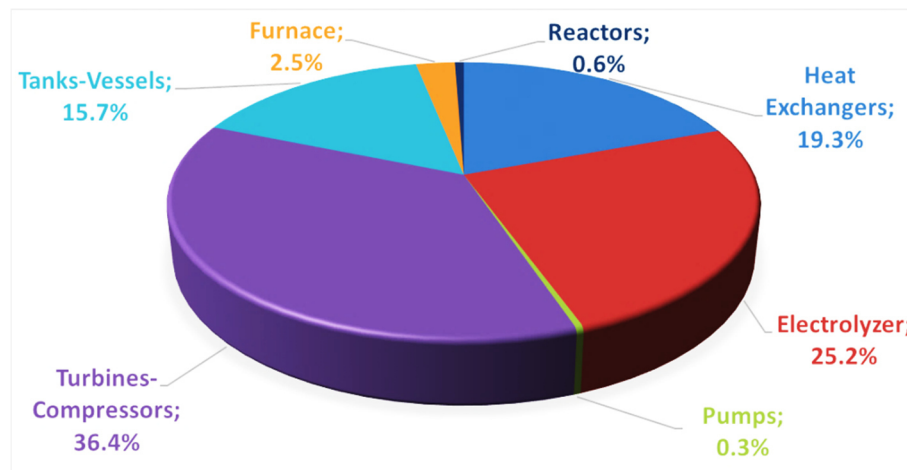


**Figure 9.4:** Percentage share of individual equipment for PFD2.

**Table 9.6:** Economic performance indexes.

Description of economic index	Selected value
Plant operation factor (%)	96
Plant useful life, N (years)	10
Income tax rate, t (% of Net Profit)	26
Reasonable Return on Investment, i (%)	10
Risk factor, h (%)	8
Depreciation, d (%)	10
Investment recovery factor, e (%)	10

## 9.4.2.1. Material/Energy Utilities and Product Related Costs

In both flow diagrams, the material and energy utilities refer to a) the required electrical energy (to supply heat exchangers, compressors, pumps, etc.), b) the cooling water utilities, c) the natural gas fed to the furnace/burner, d) the air used as a cooling agent and as a reactant and e) the used 98 v/v% H<sub>2</sub>SO<sub>4</sub>/H<sub>2</sub>O in PFD1 and I<sub>2</sub> in PFD2. It is important to highlight again that in both cases surplus electrical power exists and deemed as a saleable product. As can be seen in Table 9.7, the utility costs of PFD2 are nearly twice those of PFD1, due to the high cost of I<sub>2</sub> as raw material at H<sub>2</sub>SO<sub>4</sub> production.

**Table 9.7:** Raw materials and utilities costs for both flow diagrams.

Raw material or utility	Cost in PFD1, €/yr	Cost in PFD2, €/yr
Electrical energy (0.083 €/kWh)	-	-
Water (0.10 €/kg)	1,151,064	51,167
Natural gas (0.18 €/m <sup>3</sup> )	696,636	696,636
Air (0.1 €/tn)	570,092	570,092
98 v/v% H <sub>2</sub> SO <sub>4</sub> /H <sub>2</sub> O (0.25 €/kg)	896,805	-
I <sub>2</sub> (83.0 €/kg)	-	5,261,150
Total raw materials and utilities cost (2016)	3,314,597	6,579,046

Similarly, in both flow diagrams the saleable products to be economically exploited are: a) the excess electrical power, b) hydrogen and c) >99 v/v% H<sub>2</sub>SO<sub>4</sub>. As can be seen in Table 9.8, in both flow diagrams, similar product market costs are derived.

**Table 9.8:** Value of saleable products for both flow diagrams.

Product	Value in PFD1, €/yr	Value in PFD2, €/yr
Hydrogen (8.0 €/kg)	6,073,834	6,073,834
H <sub>2</sub> SO <sub>4</sub> (0.45 €/kg)	109,982	109,982
Electrical power (0.092 €/kWh)	7,031,382	6,971,668
Total products market value (2016)	13,215,198	13,155,484

#### 9.4.2.2. Fixed Capital Cost Calculations and Operational Expenses

Based on the detailed cost calculation of the individual process units and the total major equipment cost, the Fixed Capital Investment and the Working Capital Investment are calculated according to the developments of Table 9.9. Notice that the remaining categories of direct, indirect and other costs are calculated using relevant ratios of the total purchased equipment cost.

At the commencement of operation, startup funds and operational costs should be available to the set in motion the production process. The cost associated to this expenditure is called the production expense. This expenditure includes significant process variable, such as raw materials, utilities etc. Table 9.10 presents the total expenditures involve in running both process plants.

#### 9.4.2.3. Economic Indices and Final Assessment

Gross Profit (R): The difference between sales revenue and process expenses, excluding income tax, gives the total gross profit R:

$$R = S - CT_w \quad (9.1)$$

Where, S is the total sales revenue (resulting from product sales) (€/year) and  $CT_w$  the total operating expenses, including depreciation, (€/year)

Net Profit (P): The difference between the gross profit, income tax and the depreciable capital investment. Therefore, it is a function of the quantity of finished product sales. Increase in profit can be obtained only by the use of effective methods, which reduce the operation expenses:

$$P = R \cdot (1 - t) \quad (9.2)$$

Return on Investment (ROI): The rate of return on investment is expressed on an annual percentage basis. It is the yearly profit as a ratio of the initial investment necessary. It is calculated after income tax has been deducted from the gross or pre-tax income. The remaining net income may be used either for paying dividends or re-investment. ROI is given by (calculated for one particular year or as an average over the project life time):

$$ROI = P / (I_F + I_W) \quad (9.3)$$

**Table 9.9: Fixed and Working Capital investment for both flow diagrams (Peters et al., 1911).**

Cost type	Estimation	Cost in PFD1, €	Cost in PFD2, €
<b>Direct costs</b>			
Major Equipment Costs (MEC)	Simulated	19,937,053	20,250,158
Installation costs	47%MEC	9,370,415	9,517,574
Instrumentation and control	36%MEC	7,177,339	7,290,057
Piping	68%MEC	13,557,196	13,770,107
Insulations	8%MEC	1,594,964	1,620,013
Electrical	11%MEC	2,193,076	2,227,517
Building and services	18%MEC	3,588,670	3,645,028
Land improvements	10%MEC	1,993,705	2,025,016
Service facilities	70%MEC	13,955,937	14,175,111
Land	6%MEC	1,196,223	1,215,009
<i>Total Direct Capital Costs (DC)</i>		74,564,578	75,735,591
<b>Indirect costs</b>			
Engineering and supervision	33%MEC	6,579,227	6,682,552
Construction expenses	41%MEC	7,974,821	8,100,063
<i>Total Indirect Capital Costs (IC)</i>		14,554,049	14,782,615
<b>Other costs</b>			
Legal fees	4%MEC	797,482	810,006
Contractor's fees	22%MEC	4,386,152	4,455,035
Contingencies	44%MEC	8,772,303	8,910,070
<i>Total Other Capital Costs (OC)</i>		13,955,937	14,175,111
<b>Total costs</b>			
Fixed Capital Investment (I <sub>F</sub> )	DC+IC+OC	103,074,563	104,693,317
Working Capital (I <sub>w</sub> )	15%I <sub>F</sub>	15,461,185	15,703,998
<b>Total Fixed Capital Investment (I)</b>		118,535,748	120,397,315

Payout Time (POT): The payout time is the theoretically projected time range within which the original fixed capital investment is recovered through cash flow. The calculation method for payout time includes the recovery factor. POT is usually measured as the time from the

start of the production to recover the capital investment. However, it does not include time value of money. The payout time is given by:

$$POT = I / (P + e \cdot I_F) \tag{9.4}$$

**Table 9.10:** Production expenditures for both flow diagrams.

Cost type	Estimation	Cost in PFD1, €/yr	Cost in PFD2, €/yr
<b>A. Direct Production Costs</b>			
1. Raw Materials and Utilities	Simulated	3,314,597	6,579,046
2. Labor	Calculated	225,270	225,270
3. Supervision	15%A2	33,791	33,791
4. Maintenance	5%I <sub>F</sub>	5,153,728	5,234,666
5. Operating Supplies	15%A4	773,059	785,200
6. Laboratory	10%A2	22,527	22,527
7. Overheads	1%(A1-A6)	95,230	128,805
<i>Total Direct Production Costs (DPC)</i>		9,618,202	13,009,305
<b>B. Annual Fixed Costs</b>			
1. Total Taxes	1%I <sub>F</sub>	1,030,746	1,046,933
2. Insurances	1%I <sub>F</sub>	1,030,746	1,046,933
3. Depreciation	10%I <sub>F</sub>	10,307,456	10,469,332
4. Contingencies	60%(A2+A3+A4)	3,247,673	3,296,236
<i>Total Annual Fixed Costs (AFC)</i>		15,616,621	15,859,434
<b>C. General Costs</b>			
1. Administration	20%A2	45,054	45,054
2. Marketing	2%(A1-A6)	192,364	260,186
3. Interests	8%B3	824,597	837,547
<i>Total General Costs (TGC)</i>		1,062,015	1,142,787
<b>Total Annual Production Cost (CT<sub>w</sub>)</b>		<b>26,296,838</b>	<b>30,011,526</b>

Venture Profit (V): An approximate measure of the profitability of a process plant that takes into account the size of the project and the related risk is the venture profit. It is also vital in situations where different investment options are compared. Venture profit is the annual net earnings in excess of a minimum acceptable return on investment:

$$V = P - (i+h) \cdot I \quad (9.5)$$

The above economic criteria and indices are calculated for both cases and compared in Table 9.11.

**Table 9.11:** *Economic performance of both process plants.*

<b>Economic criterion</b>	<b>Symbol</b>	<b>Value in PFD1</b>	<b>Value in PFD2</b>
Expenses including depreciation	CT <sub>w</sub> , €/yr	26,296,838	30,011,526
Income (from sales of products)	S, €/yr	13,215,197	13,155,483
Gross profit	R, €/yr	-13,081,641	-16,856,043
Net profit	P, €/yr	-9,680,415	-12,473,472
Return on Investment	ROI (%)	-8.17	-10.36
Payout Time	POT (years)	189.04	-60.07
Venture profit	V, €/yr	-31,016,849	-34,144,988

As can be concluded from the comparison of PFD1 and PFD2 scenarios (see Table 9.11), the former is economically more promising, due to the smaller operating expenditures and larger revenue from sales. The larger production cost in the latter case is mainly attributed to the large price for I<sub>2</sub> purchase. In terms of the H<sub>2</sub> production cost (by taking into account the entire flowsheet for both cases) the calculated values, i.e., 34.64 €/kg for PFD1 and 39.53 €/kg for PFD2, are significantly larger than the H<sub>2</sub> production from conventional plants (lies in the range 6-10 €/kg). In combination with the estimated values for the Return on Investment, Payout Time and Venture profit, it can be seen that the proposed technology is far from economically affordable for any investor.

On the other hand, as it was thoroughly discussed in the present thesis, the utilization of Black Sea H<sub>2</sub>S is stimulated more from environmental and social motivations than from economic. Though, it is difficult to quantify the relevant environmental gains from a technology like this, even if a complete life-cycle analysis is performed. Taking into account the great respect is given by the European and the nearby countries on the amelioration of the Black Sea ecosystem, an additional “optimized” scenario is assessed to realistically evaluate the technical, economical and, in the same time, the environmental sustainability of the designed plants. More specifically, both flowsheets are further analyzed under the

assumption that a 60% subsidy on the operational expenditures will be granted to lessen the total investment (this is actually a common practice for small- to medium- scale energy plants that are decentralized and serve the dual scope of producing energy/fuels from renewable resources and treating environmental threats). The economic evaluation of the two flowsheets is presented in Table 9.12.

**Table 9.12:** *Economic performance of both process plants under the “optimized” scenario (i.e., 60% subsidy on the operational expenditures).*

<b>Economic criterion</b>	<b>Symbol</b>	<b>Value in PFD1</b>	<b>Value in PFD2</b>
Expenses including depreciation	CT <sub>w</sub> , €/yr	10,518,735	12,004,610
Income (from sales of products)	S, €/yr	13,215,197	13,155,483
Gross profit	R, €/yr	2,696,462	1,210,586
Net profit	P, €/yr	1,995,382	895,834
Return on Investment	ROI (%)	1.68	0.74
Payout Time	POT (years)	9.63	10.59
Venture profit	V, €/yr	-787,632	-1,930,886

As expected, the economic potential of both “optimized” cases is significantly improved, since the values for gross and net profits are positive. On the other hand, the PFD1 flowsheet, which remains the most promising one, is marginally feasible. The POT value is approximately equal with the lifetime of the plant and the ROI value is smaller than the minimum acceptable Return on Investment (10%). Coupled with the involved risk for technologies like this, the latter leads to a negative Venture profit value. This fact, in turn, suggests that even under the notion of the reduced operational expenditures, more progress needs to be made to constitute the process economically feasible and sustainable. Provided that, in the near future, the technology will be further optimized, thus decreasing the production cost and the related risk, and the H<sub>2</sub> market demand will increase, thus the designed capacity can be reconsidered, the concomitant production of H<sub>2</sub>, electrical power and H<sub>2</sub>SO<sub>4</sub> from Black Sea H<sub>2</sub>S in an integrated plant will be, without any doubt, an economically attractive technology.

## REFERENCES

- American Petroleum Institute. (2002). API 620: Design and construction of large welded low pressure storage tanks. API Standard.
- Aspen Technology Inc. (2000). Aspen Plus user guide, Available at: <https://web.ist.utl.pt/ist11038/acad/Aspen/AspUserGuide10.pdf>. Accessed: 08/02/2017.
- Baasel W.D. (1976). Preliminary chemical engineering plant design. Elsevier.
- Becherif M., Ramadan H.S., Cabaret K., Picard F., Simoncini N., Bethoux O. (2015). Hydrogen energy storage: New techno-economic emergence solution analysis. *Energy Procedia*, 74: pp. 371-380.
- Couper J.R., Penney W.R., Fair J.R., Walas S.M. (2003). Chemical process equipment selection and design. Elsevier Inc., U.S.A.
- Eudy L., Post M. (2014). BC transit fuel cell bus project: Evaluation results report. National Renewable Energy Laboratory, Technical Report.
- Ferrero D., Gamba M., Lanzini A., Santarell M. (2016). Power-to-gas hydrogen: Techno-economic assessment of processes towards a multi-purpose energy carrier. *Energy Procedia*, 101: pp. 50-57.
- Hamedani R.S., Bocci E., Villarini M., Di Carlo A., Naso V. (2016). Techno-economic analysis of hydrogen production using biomass gasification - A small scale power plant study. *Energy Procedia*, 101: pp. 806-813.
- King M.J., Davenport W.G., Moats M.S. (2013). Chapter 9 - Production of  $H_2SO_{4(l)}$  from  $SO_{3(g)}$ , *sulfuric acid manufacture* (second edition), pp. 103-121.
- Kiparissides C. (2008). Design of chemical reactors. AUTH, Thessaloniki.
- Koukos I. (2009). Introduction to chemical plant design. Tziola Edition, Athens.
- Liberatore R., Lanchi M., Caputo G., Felici C., Giaconia A., Sau S., Tarquini P. (2012a). Hydrogen production by flue gas through sulfur-iodine thermochemical process: Economic and energy evaluation, *International Journal of Hydrogen Energy*, 37: pp. 8939-8953.
- Liberatore R., Lanchi M.L., Giaconia A., Tarquini P. (2012b). Energy and economic assessment of an industrial plant for the hydrogen production by water-splitting through the sulfur-iodine thermochemical cycle powered by concentrated solar energy. *International Journal of Hydrogen Energy*, 37: pp. 9550-9565.
- Paras S. (2014). Technological and economic study of chemical installations. Aristotle University of Thessaloniki, Chemical Engineering Laboratory, Chemical Engineering Department.
- Penev M. (2013). Hybrid hydrogen energy storage. National Renewable Energy Laboratory, Available at: <http://www.h2fcsupergen.com/wp-content/uploads/2013/06/Hybrid-Hydrogen-Energy-Storage-Michael-Penev-National-Energy-Research-Laboratory.pdf>. Accessed: 08/02/2017.
- Peters M.S., Timmerhaus K.D. (1991). Plant design and economics for chemical engineers. McGraw-Hill International Editions.
- Pure Energy Center: Hydrogen electrolyzer. (2016). Available at: <http://pureenergycentre.com/hydrogen-electrolyser/>. Accessed: 10/03/2017.
- Smith R. (2005). Chemical process design and integration, England: John Wiley & Sons, Ltd.
- Stewart M., Lewis O.T. (2012). Heat exchanger equipment field manual common operating problems and practical solutions. Elsevier, U.S.A, Gulf Professional Publishing.
- Tremel A., Wasserscheid P., Baldauf M., Hammer T. (2015). Techno-economic analysis for the synthesis of liquid and gaseous fuels based on hydrogen production via electrolysis. *International Journal of Hydrogen Energy*, 40: pp. 11457-11464.

# CHAPTER

# 10

## CONCLUSIONS AND SUGGESTIONS FOR FUTURE RESEARCH

Contents	Page
10.1. Conclusions. . . . .	287
10.2. Suggestions for future research. . . . .	296



## 10.1. CONCLUSIONS

The present chapter attempts to conclude on the major findings of the present thesis, regarding the proposed concept of the work and its relevant objectives, to describe the achieved scientific progress and to outline specific suggestions for future research. As it was discussed in the Introduction (Chapter 1), this thesis was divided in two distinct parts, the first (Part I) dealing with the catalytic decomposition of  $\text{H}_2\text{S}$  in the absence and presence of  $\text{H}_2\text{O}$  (Chapters 4, 5 and 6) and the second (Part II) referring to the  $\text{H}_2\text{S}$  electrolysis in a proton ( $\text{H}^+$ ) conducting electrochemical membrane reactor (Chapters 7 and 8). This work overall aimed to the development of a proton ( $\text{H}^+$ ) conducting electrochemical membrane reactor, which will facilitate the efficient exploitation of the  $\text{H}_2\text{S}$ -rich Black Sea water for  $\text{H}_2$  production, via the development of a  $\text{H}_2\text{S}$  tolerant, electronically conductive and active anode composite. Several interesting new results were found and summarized in Sections 10.1.2 and 10.1.3. Moreover, the major conclusions of the preliminary feasibility study of the proposed integrated technology are presented in Section 10.1.4. Finally, the future work plans arising from the above studies, are discussed in Section 10.2.

### 10.1.1. Overall Concept

It is well known that the global energy demands constantly increase due to the worldwide urbanization and despite several on-going regulations and directives, the conventional fossil energy resources are depleting. Emerging energy and environmental concerns force now the global society to utilize “clean” fuels and efficient conversion technologies. In this context, hydrogen, if derived from carbon-neutral resources, is considered as an environmental friendly energy vector, which can drive and support future energy developments. Among the different sustainable approaches for  $\text{H}_2$  production, the decomposition of hydrogen sulfide ( $\text{H}_2\text{S}$ ), using the excess electricity of intermittent renewable sources, is of particular interest.

Among other industrial and natural sources,  $\text{H}_2\text{S}$ , which can be found in large quantities in Black Sea waters (where nearly 90% of the water is anoxic) with a total sulphide pool of  $4.6 \cdot 10^9$  tons, annually growing by  $4 \cdot 10^6$  tons, can be considered as an important  $\text{H}_2$  source. In particular, in the Black Sea,  $\text{H}_2\text{S}$  is produced as a result of a complex microbial sulphur cycle, involving a simultaneous carbon cycle, which is replenished by organic and inorganic carbon

sources in the basin and from the waters influx. In the anoxic region, the  $\text{H}_2\text{S}$  concentration steadily increases with depth, approaching a constant level of 9.5 mg/l at around 1,500 m. Due to the depletion of oxygen in the top layer, the depth level of the interface layer is rising steadily at an increasing rate, potentially diminishing the thickness of the upper aerobic zone and forcing sulphide-rich waters to the surface of the Marmara and Mediterranean seas. This would threaten the ecosystem and the economy in the Black Sea region; thus, sufficient countermeasures should be taken to secure and stabilize the surrounding environment. As mentioned above, apart from the well-known harmful effects of the Black Sea  $\text{H}_2\text{S}$  to human health and the surrounding ecosystem, hydrogen sulphide may serve as a future energy source for hydrogen generation. From theoretical calculations, it was estimated that it could be possible to produce 270 Mio. tons of  $\text{H}_2$  ( $3.83 \cdot 10^{19}$  J thermal or  $8.97 \cdot 10^{15}$  Wh electrical energy), equivalent to 808 Mio. tons of gasoline or 766 Mio. tons of natural gas.

The process steps of a potential  $\text{H}_2$  production technology from  $\text{H}_2\text{S}$ , contained into Black Sea waters, are as follows (the proposed process in the present thesis): a) pumping sea water, containing  $\text{H}_2\text{S}$  (0.36 mmol/l at 1,000 m depth) to the surface, b) extraction of  $\text{H}_2\text{S}$  from water, and c) electrochemical decomposition of  $\text{H}_2\text{S}$  to  $\text{H}_2$  and  $\text{SO}_x$ . To date, several alternatives have been proposed for the production of hydrogen via  $\text{H}_2\text{S}$  decomposition, which are currently at different stages of development, involving thermochemical, photochemical, plasmochemical and electrochemical methods. The majority of these approaches present certain disadvantages attributed to their particular high energy requirements and low efficiencies, rendering their commercialization still in doubt. The most commonly employed method is the catalytic decomposition of  $\text{H}_2\text{S}$ , which however takes place at high temperatures in order to achieve conversions exceeding 80%. A novel approach for  $\text{H}_2\text{S}$  electrolysis, based on a proton-conducting ceramic electrochemical membrane reactor, was proposed in the present PhD thesis, which could also act as a method to eliminate  $\text{H}_2\text{S}$  emissions from petroleum hydro-treatment operations, natural gas and coal gasification industries. Note that, proton conducting materials have become the subject of intensive research due to their potential to reduce the operating temperature of solid oxide fuel cells, thus allowing the use of inexpensive materials. In more detail, the  $\text{H}_2\text{S}$  electrolysis is conducted by feeding diluted  $\text{H}_2\text{S}$  in excess  $\text{H}_2\text{O}$  mixtures at the cell anode, while the cathode is exposed to oxidizing conditions. When an anodic overpotential is applied,  $\text{H}_2\text{S}$  and

H<sub>2</sub>O are co-electrolyzed producing H<sup>+</sup>, which are transferred through the H<sup>+</sup>-conducting solid electrolyte to the cathode, where pure hydrogen is formed. As a result, pure H<sub>2</sub> can be produced and separated in a single-step process.

For the development of such a complex process, one of the major issues was the optimal selection of cell materials, especially of the anode electrode, which is going to be exposed to the H<sub>2</sub>S-containing reacting mixture. To this direction, the anode material had to exhibit high electro-catalytic activity towards H<sub>2</sub>S decomposition, high electronic/ionic conductivity, good adherence on the solid electrolyte surface, and tolerance to H<sub>2</sub>S rich environments.

### 10.1.2. H<sub>2</sub>S Catalytic Decomposition in the Absence/Presence of H<sub>2</sub>O

As it was already highlighted, the selection of the material to be employed as the anode in the H<sup>+</sup> proton conducting membrane reactor/fuel cell was critical for the successful operation of the proposed system. In this context and prior to the electrochemical tests, a series of catalysts, namely, i) 20 wt.% Cu supported REOs (Cu/REOs), ii) 20 wt.% Cu supported Ce<sub>1-x</sub>Sm<sub>x</sub>O<sub>8</sub> (20 wt.% Cu/Ce<sub>1-x</sub>Sm<sub>x</sub>O<sub>8</sub>), iii) ceria supported transition metal (Co, Ni, Fe and Cu) and iv) bimetallic (Cu<sub>20-x</sub>Co<sub>x</sub>/CeO<sub>2</sub>) (x = 0, 5, 10, 15, 20 wt.%), were synthesized via the wet impregnation method and evaluated in terms of their activity and stability towards H<sub>2</sub>S decomposition in the absence of H<sub>2</sub>O. In all cases, the experimental results were accompanied by the corresponding thermodynamic calculations. Moreover, both “fresh” and H<sub>2</sub>S-treated (i.e., “Aged” and “Sulphated”) catalyst samples were characterized in terms of their chemical composition and microstructure (BET, XRD, SEM, XPS, TPR, sulfur elemental analysis).

Taking into account that hydrogen sulfide is one of the most difficult substances one can deal within the chemical world, the development of a system for its treatment at high temperatures was demanding and challenging. So, a suitable experimental apparatus was designed and constructed, using stainless steel type 316 for most of its parts, as it is able to withstand moderately high temperatures and corrosion and is widely commercially available, to carry out the study of the catalytic decomposition of hydrogen sulfide towards hydrogen production. For the catalytic experiments, a U-tube quartz reactor was also

employed, while the composition analysis of the gas outlet flow was performed by an online gas chromatograph.

The first objective of this work was to investigate the catalytic decomposition of  $\text{H}_2\text{S}$  to  $\text{H}_2$  in the absence of  $\text{H}_2\text{O}$ , using Cu catalysts supported on rare earth oxides ( $\text{La}_2\text{O}_3$ ,  $\text{CeO}_2$ ,  $\text{Sm}_2\text{O}_3$ ,  $\text{Pr}_6\text{O}_{11}$ ,  $\text{Nd}_2\text{O}_3$ ,  $\text{Gd}_2\text{O}_3$ ). The optimal performance was identified for the  $\text{Sm}_2\text{O}_3$ - and  $\text{CeO}_2$ -supported catalysts, as they demonstrated  $\text{H}_2\text{S}$  conversion values equal to 11.0% and 10.0%, at  $T = 700\text{ }^\circ\text{C}$ , respectively. Note that, the optimal performance of both  $\text{Sm}_2\text{O}_3$ - and  $\text{CeO}_2$ -supported catalysts was also revealed by the XPS and TPR analysis: the respective reduction peaks shifted to smaller temperatures, compared to the rest catalysts, and the atomic concentrations (at.%) for the corresponding lanthanides were larger. The superiority of the Cu/ $\text{CeO}_2$  catalyst can be attributed also to its excellent redox properties (superior reducing capacity, compared to the rest Cu/REOs catalysts, high oxidation state of Cu species). The remaining Cu-based catalysts exhibited lower  $\text{H}_2\text{S}$  conversion values, with the following order of performance:  $\text{Sm}_2\text{O}_3 > \text{CeO}_2 > \text{Gd}_2\text{O}_3 > \text{Pr}_6\text{O}_{11} > \text{La}_2\text{O}_3 > \text{Nd}_2\text{O}_3$ . In the sequence, in order to further improve the performance of the optimum 20 wt.% Cu/ $\text{Sm}_2\text{O}_3$  catalyst, its efficiency was investigated using mixed  $\text{Ce}_{1-x}\text{Sm}_x\text{O}_6$  (where  $x = 0, 0.25, 0.5, 0.75$  and 1) carriers. However, it was found that the Ce addition to the  $\text{Sm}_2\text{O}_3$  support presented a relatively minor effect, despite its pronounced impact on the textural properties. Hence, it can be concluded that the superiority of  $\text{Sm}_2\text{O}_3$ - and  $\text{CeO}_2$ -based samples can be mainly ascribed to the intrinsic characteristics of these particular carriers in conjunction to the presence of copper, rather than to their textural characteristics.

In the next step, a series of transition metal catalysts (Co, Ni, Fe and Cu) supported on  $\text{CeO}_2$  were prepared and evaluated with respect to their catalytic performance during the  $\text{H}_2\text{S}$  decomposition reaction. The beneficial effect of transition metals to ceria, as well as, the observed trend in catalytic activity, were verified by the relevant kinetic experiments, performed at  $P_{\text{H}_2\text{S}} = 1\text{ kPa}$  and differential conditions ( $\text{H}_2\text{S}$  conversion smaller than 25%). More specifically, under homogeneous reaction conditions (absence of catalyst) the  $E_{\text{act}}$  was equal to 36.4 kcal/mol, while in the presence of 20 wt.% Co-, Ni-, Fe-, and Cu- $\text{CeO}_2$  catalysts, the apparent activation energy substantially decreased to 15.6, 15.3, 18.7, and 23.8 kcal/mol, respectively, indicating once again the pronounced role of the M/ $\text{CeO}_2$  catalysts in the  $\text{H}_2\text{S}$  decomposition reaction. From the tested catalysts, the cobalt containing one

demonstrated the optimal behavior throughout the range of the studied temperatures, followed in turn by the nickel, iron and copper catalysts. Specifically, in the temperature range of 550-650 °C the Co/CeO<sub>2</sub> and Ni/CeO<sub>2</sub> catalysts exhibited almost identical activity, while at higher temperatures the cobalt catalyst clearly surpassed the rest of the transition metal catalysts. Finally, by varying the loading of the optimal Co/CeO<sub>2</sub> catalyst from 15 to 60 wt.%, it was discovered that the metal loading, in this specific range, did not significantly affect the H<sub>2</sub>S decomposition reaction. In summary, the 20 wt.% Co/CeO<sub>2</sub> sample demonstrated the optimum activity performance under the selected conditions, achieving similar conversion values to the ones predicted by the reaction equilibrium.

However, since the 20 wt.% Co/CeO<sub>2</sub> catalyst exhibited a catalytic performance almost identical to that predicted by thermodynamics at higher temperatures, in an effort to further improve the efficiency of the catalytic system at lower temperatures (i.e., 550-650 °C), the Co active phase was chosen to be enhanced by the presence of a second transition metal entity, namely, copper. To this end, bimetallic Cu<sub>20-x</sub>Co<sub>x</sub>/CeO<sub>2</sub> (x = 0, 5, 10, 15 and 20) catalysts were prepared, via the wet impregnation method, and thoroughly investigated. It should be noted that through this investigation of bimetallic Cu<sub>20-x</sub>Co<sub>x</sub>/CeO<sub>2</sub> (x = 0, 5, 10, 15, 20 wt.%) catalysts during the H<sub>2</sub>S decomposition reaction under identical operation conditions, the 20 wt.% Co/CeO<sub>2</sub> sample demonstrated again the most promising performance; the maximum achieved H<sub>2</sub>S conversion was 34% at T = 850 °C. On the other hand, a notable smaller conversion (25.9%) was measured in the case of the 20 wt.% Cu/CeO<sub>2</sub> sample. In light of the characterization studies and the activity results, the superior catalytic performance of Co/CeO<sub>2</sub> catalysts could be ascribed to their better resistance to reduction, associated with the formation of Co<sup>3+</sup> species in a Co<sub>3</sub>O<sub>4</sub>-like phase and the high O/Ce surface ratio. This may also contribute to the enhanced sulfur tolerance of Co-based catalysts. Based on stability experiments, physicochemical characterizations were performed, which revealed that the crystalline phases that occurred in the case of the "Fresh" catalyst were no longer present. Instead, new crystalline structures appeared, in which Co<sub>3</sub>O<sub>4</sub> was fully converted into Co<sub>1-x</sub>S<sub>y</sub> of hexagonal structure, while CeO<sub>2</sub> into Ce<sub>10</sub>S<sub>14</sub>O<sub>γ</sub> of square structure (XRD), respectively. This fact demonstrates that sulfur derived from H<sub>2</sub>S decomposition is not simply deposited on the catalyst as elemental S, but interacts with its constituents, thus creating new active phases that appear to be distinguished by

high performance stability. In other words, by the in-situ sulfation and reduction of the catalyst's counterparts, the system remains remarkably stable. The above findings were also confirmed by the Scanning Electron Microscopy (SEM) images, in which the above characteristic structures, that may be responsible for the stability of the catalyst, clearly appeared.

Also prior to the electrochemical tests, the evaluation of the optimum Co/CeO<sub>2</sub> catalytic system, in H<sub>2</sub>S decomposition reaction towards H<sub>2</sub> production was examined also in the presence of excess H<sub>2</sub>O, under conditions that simulated the Black Sea water. In this context, a series of CeO<sub>2</sub>-supported Co catalysts (Co/CeO<sub>2</sub>), were synthesized and evaluated, in terms of their catalytic activity and stability, during the H<sub>2</sub>S decomposition reaction towards hydrogen in the presence of H<sub>2</sub>O (90 v/v%). It was clearly revealed that the H<sub>2</sub>O conversion was essentially negligible, both in the absence or presence of the catalyst (bare CeO<sub>2</sub>) for the selected feed composition. However, it can be stated that the combined presence of H<sub>2</sub>S and H<sub>2</sub>O in the reaction feedstock mixture (i.e., 1 v/v% H<sub>2</sub>S, 90 v/v% H<sub>2</sub>O, balanced with Ar), enhanced the H<sub>2</sub>S conversion to H<sub>2</sub>, as it was already predicted by the thermodynamic calculations. Without any doubt, for the catalytic decomposition of H<sub>2</sub>S in the presence of H<sub>2</sub>O, the 30 wt.% Co/CeO<sub>2</sub> catalyst demonstrates the optimum activity and, in the same time, a remarkably stable behaviour. This stability can be safely attributed to the in-situ sulfation of the catalysts' active components, during their exposure to the feedstock mixture. Once more, the produced elemental sulfur was not simply deposited on the catalyst surface, but interacted with its counterparts to create new active and stable phases. Furthermore, by taking into account the marginal differences in the structural and textural characteristics of Co/CeO<sub>2</sub> fresh catalysts with different Co loadings, the superiority of the 30 wt.% Co/CeO<sub>2</sub> sample can be related to the nature of the metal-carrier interactions. These factors affect both the type and quantity of the produced Co- and CeO<sub>2</sub>-based sulfur compounds, as well as, the surface characteristics of the catalysts (i.e., oxidative state, oxygen mobility, surface structure, etc.). These promising findings could pave the way for the development of active and stable catalytic materials to be applied as anode electrodes, in a proton H<sup>+</sup> conducting solid electrolyte electrochemical membrane reactor, able to effectively manage the H<sub>2</sub>S-containing sources towards H<sub>2</sub> production, such as the proposed H<sub>2</sub>S quantities found in Black Sea waters.

### 10.1.3. H<sub>2</sub>S Electrolysis in the Proton (H<sup>+</sup>) Conducting Electrochemical Membrane Reactor

Several methods and thermal treatment protocols were applied and examined in order to fabricate an efficient conductive cell. The relevant experimental findings were enhanced with the physicochemical characterization of the materials, via XRD and SEM methods. As the applied feedstock (i.e., H<sub>2</sub>S/H<sub>2</sub>O) was considered to be especially troublesome, since it promotes corrosion, poses a health and environmental threat, and can be converted to even more toxic and environmentally hazardous compounds (e.g., SO<sub>2</sub> or H<sub>2</sub>SO<sub>4</sub>), the optimization of the selected materials was a fundamental step for the development of a promising fuel cell. To avoid the general challenges that H<sub>2</sub>S creates, i.e., poisoning and/or decomposition of cell electrodes, the cell materials development in this thesis includes the following compounds:

BaZr<sub>0.7</sub>Ce<sub>0.2</sub>Y<sub>0.1</sub>O<sub>3</sub> (BZCY72): A BZCY (NorECs, 2016) disk was selected as the H<sup>+</sup>-conducting solid electrolyte/membrane, where the cathode and anode materials were deposited. The anode was synthesized using Co<sub>3</sub>O<sub>4</sub>/CeO<sub>2</sub>, as it exhibits sufficient electronic conductivity and tolerance to SO<sub>2</sub>/H<sub>2</sub>S/H<sub>2</sub>O atmospheres. Furthermore, BaGd<sub>0.8</sub>La<sub>0.2</sub>Co<sub>2</sub>O<sub>6-δ</sub> (BGLC) was selected as the cathode material. The respective electrochemical characterization experiments involved polarization, AC impedance and electrocatalytic studies under H<sub>2</sub>/H<sub>2</sub>O and H<sub>2</sub>S/H<sub>2</sub>O mixtures. It was revealed that in the presence of H<sub>2</sub>S, cobalt and cerium were converted to sulphides, which presented a beneficial impact on the cell performance and durability.

The electrochemical performance of the Co<sub>3</sub>O<sub>4</sub>/CeO<sub>2</sub> mixed oxide electrode, when exposed to H<sub>2</sub>/Ar mixtures, was examined by employing a proton conducting Co<sub>3</sub>O<sub>4</sub>-CeO<sub>2</sub>/BaZr<sub>0.7</sub>Ce<sub>0.2</sub>Y<sub>0.1</sub>O<sub>3</sub>/Co<sub>3-a</sub>O<sub>4</sub>-CeO<sub>2</sub> symmetrical cell. The impact of cell temperature (600-850 °C) and hydrogen partial pressure, p<sub>H<sub>2</sub></sub> = 1-10 kPa, at both dry and wet atmospheres (p<sub>H<sub>2</sub>O</sub> = 0-2.5 kPa) on the overall cell and electrode performance was thoroughly assessed by means of AC electrochemical impedance spectroscopy (EIS). The experimental runs showed that as the temperature increased, the cell and electrode conductivities also increased, while they remained essentially unaffected by the hydrogen feed partial pressure both in dry and wet conditions. By the modeling of the AC impedance spectra, it was found that the critical step determining the electrode performance is the diffusion of H<sup>+</sup> to the electrochemical

three-phase boundary zone, a step which becomes more difficult at high hydrogen and steam feed concentrations due to the space charge effect.

The electrochemical behavior of  $\text{Co}_3\text{O}_4/\text{CeO}_2$  composite in  $\text{H}_2\text{S}$ -containing atmospheres under excess  $\text{H}_2\text{O}$  (90 v/v%) conditions was also examined in a proton conducting ceramic symmetrical cell of the type  $\text{Co}_3\text{O}_4\text{-CeO}_2/\text{BZCY72}/\text{Co}_3\text{O}_4\text{-CeO}_2$ . AC impedance spectroscopy studies, under different  $\text{H}_2\text{S}$  feed concentrations (0-1 v/v%) and temperatures (700-850 °C), in conjunction with physicochemical characterization measurements of the fresh and aged (after  $\text{H}_2\text{S}$ -treatment) electrodes-cells, were conducted to systematically assess the electrochemical performance and stability behavior of the electrode. A promising stable electrochemical behavior was achieved, being favored as the  $\text{H}_2\text{S}$  feed content and cell temperature increased. AC impedance spectra revealed contributions from charge transfer and mass transport steps, with the latter being in general more critical for the overall system; it was associated with the adsorption, diffusion and surface processes of the  $\text{H}_2\text{S} + 2\text{H}_2\text{O} \rightleftharpoons 3\text{H}_2 + \text{SO}_2$  and  $\text{H}_2\text{S}$  reaction intermediates. Although the electrolyte (BZCY72) itself was not affected by the  $\text{H}_2\text{S}$  treatment, significant modifications in the structural phases and morphology of the electrode were observed by the SEM and XRD studies of the used samples. The in-situ reduction and sulfation of the electrode along with the in situ rearrangement of conductive phases resulted in more electro-active surfaces with higher porosity and better electronic conductivity, facilitating both the charge transfer and mass transport processes. Finally, by employing AC impedance measurements, the electrochemical performance of an electrochemical cell consisting of Y-doped barium zirconate (BZCY72) as the solid electrolyte,  $\text{Co}_3\text{O}_4\text{-CeO}_2$  mixed oxide as the anode exposed to 1 v/v%  $\text{H}_2$ , balanced with Ar and 1 v/v%  $\text{H}_2\text{S}$ -30 v/v%  $\text{H}_2\text{O}/\text{Ar}$ , and  $\text{BaGd}_{0.8}\text{La}_{0.2}\text{Co}_2\text{O}_{6-\delta}$  (BGLC) perovskite as the cathode electrode exposed to air, was evaluated. It was found, that the cell showed a similar behavior under  $\text{H}_2$  and  $\text{H}_2\text{S}$ -containing mixtures, with the latter case indicating a slightly lower overall cell conductance and higher electrode resistance, which however remained stable for more than five hours of operation. This promising behavior could open new perspectives for the development of efficient, IRES powered, proton conducting ceramic  $\text{H}_2\text{S}$  and  $\text{H}_2\text{O}$  co-electrolysis cells, towards “green” hydrogen production.

#### 10.1.4. Feasibility Analysis

Finally, in order to gain insight into the practical implementation of the proposed concept, the feasibility of an integrated scalable process towards the remediation of the Black Sea ecosystem and  $H_2$  generation through the co-electrolysis of rich  $H_2S/H_2O$  mixtures, was examined in this thesis. Two different process flow diagrams were developed and assessed, depending on the downstream management options of the generated  $SO_2$  by-product. Overall, the two operating schemes consisted of 4 distinct process steps and targeted to a hydrogen production of approximately 100 kg/hr (operating goal): i) pumping Black Sea water from 1 km depth ( $H_2S$  concentration: 14 ppm) and  $H_2S$  enrichment up to a concentration of 0.5 v/v%  $H_2S/H_2O$ , ii)  $H_2$  production (100 kg/hr) through  $H_2S/H_2O$  co-electrolysis at 850 °C and 2 bar, iii) purification and separation of the proton conducting electrochemical membrane reactor exit streams ( $H_2$  and  $SO_2$  products), iv)  $H_2SO_4$  production, under two different options, and overall heat management (through a natural gas burner along with flue gas power recovery). Both process flow diagrams were assessed in terms of operating flexibility, electricity/heat requirements and economic criteria. They were designed to produce enough electrical power to sustain the overall operation. However, in terms of economic criteria and by taking into account the estimated values for the Return on Investment, Payout Time and Venture profit, it can be concluded that the proposed technology is far from economically affordable for any investor. However, as it was thoroughly discussed in the present thesis, the utilization of Black Sea  $H_2S$  is stimulated more from environmental and social motivations than from economic. Though, it is difficult to quantify the relevant environmental gains from a technology like this, even if a complete life-cycle analysis is performed. Taking into account the great interest given by the European and the nearby countries on the amelioration of the Black Sea ecosystem, an additional “optimized” scenario was assessed to realistically evaluate the technical, economical and, in the same time, the environmental sustainability of the designed plants. More specifically, both flowsheets were further analyzed under the assumption that a 60% subsidy on the operational expenditures will be granted to lessen the total investment (this is actually a common practice for small- to medium-scale energy plants that are decentralized and serve the dual scope of producing energy/fuels from renewable resources and treating environmental threats). Under the above assumptions, the economic criteria were

improved. On the other hand, the plant economic feasibility is still in doubt and further research and progress (e.g., larger efficiencies, cheaper materials, energy integration, co-utilization of other renewable energy resources, etc.) is still needed to reduce the presently high investment risk. As the demand for  $H_2$  is expected to significantly increase in the years to come and the relevant technologies will be more mature, the proposed technology could stand among them, provided that it will be designed to operate with significantly higher  $H_2$  production capacities.

## 10.2. SUGGESTIONS FOR FUTURE RESEARCH

In general, any future work concerns deeper analysis of particular mechanisms, new concepts, different methods, or simply curiosity. In the above context and by taking into account the encouraging results generated by this PhD thesis, the suggestions for future research work will focus on further improvement of the system and its implementation to other relevant applications. Therefore, some thoughts for future research efforts toward the electrochemical  $H_2S$  splitting to hydrogen are listed below:

- Elaboration of detailed mechanistic studies on the catalytic  $H_2S$  decomposition reaction in the absence and presence of excess water to explore the reaction scheme govern the superior catalytic activity of  $Co_3O_4/CeO_2$  catalysts.
- Employment of different deposition methods (3D-printing, Laser Pulse Deposition), new cell configurations (electrode supported cells) and partial modification of anode composites to decrease the overall cell and electrode resistance, thus achieving higher electrochemical performances.
- Development of cathode electrodes to operate effectively under fuel cell (exposed to air) and membrane reactor (exposed to inert atmosphere) mode of operation.
- Upon successful implementation, employment of the concept in other interesting  $H_2S$  relevant applications, such as the treatment of sour gas deposits and  $H_2S$ -containing geothermal fluids.

Certainly, since research has no limits, the aforementioned list of future research plans is not exclusive but it can be thoroughly expanded based on the interesting findings of the present thesis.

# APPENDIX

CURRICULUM VITAE

A



## PERSONAL INFORMATION

## Tzouliana Kraia

📍 Alex. Michailidi 19, 54640, Thessaloniki, Greece

☎ (+30) 2310 498378 📠 (+30) 6972 211400

✉ [jouliana.kraia.uowm@gmail.com](mailto:jouliana.kraia.uowm@gmail.com) / [tzkraia@cperi.certh.gr](mailto:tzkraia@cperi.certh.gr)

Sex Female | Date of birth 20/04/1986 | Nationality Greek

## WORK EXPERIENCE

February 2015 - November 2015

## Postgraduate Researcher

Dept. of Mechanical Engineering, University of Western Macedonia (UOWM); Bakola and Sialvera, 50132, Kozani, Greece; [www.mech.uowm.gr](http://www.mech.uowm.gr)

- Participation in the Research Project: "Development of novel catalyst composites via the synergy of structure/surface promoters for the simultaneous abatement of Nitrogen (NO<sub>x</sub>) and Nitrous (N<sub>2</sub>O) oxides". Source of funding: Ministry of Education and Life Long Learning, THALIS
  - Laboratory organization, equipment operation-maintenance, experiments performing, edit and evaluation of experimental data, communication with project partners, co-supervision of undergraduate and Master students, proposals reporting writing, events-meetings organization
- Business or sector** Higher Education and Fundamental Research

May 2012 - January 2015  
& August 2015

## Postgraduate Researcher

Chemical Process & Energy Resources Institute (CPERI), Centre for Research & Technology Hellas (CERTH); 6<sup>th</sup> km Charilaou-Thermi Rd, 57001 Thermi, Thessaloniki, Greece; [www.certh.gr](http://www.certh.gr)

- Participation in the Research Project: "H<sub>2</sub> production from H<sub>2</sub>S decomposition in micro-structured proton conducting solid oxide membrane reactors". Source of funding: European Union, Black Sea ERA.NET call
  - Laboratory organization, equipment operation-maintenance, experiments performing, edit and evaluation of experimental data, communication with project partners, co-supervision of undergraduate and Master students, proposals reporting writing, events-meetings organization
- Business or sector** Scientific and Applied Research and Technology

## EDUCATION AND TRAINING

May 2012 – June 2017

## Ph.D. Candidate

EQF level 8

Dept. of Mechanical Engineering, University of Western Macedonia (UOWM), Kozani, Greece, in collaboration with Chemical Process & Energy Resources Institute (CPERI), Centre for Research & Technology Hellas (CERTH), Thessaloniki, Greece

- Thesis: "Remediation of Black Sea ecosystem through H<sub>2</sub>S decomposition in conventional catalytic converters and proton conducting solid oxide membrane reactors for "Green" H<sub>2</sub> production"

January 2016 - September 2016

## Energy Production in Electrochemical Reactors

EQF level 8

Department of Chemistry, Faculty of Mathematics and Natural Sciences, University of Oslo (UiO), Oslo, Norway

- "Hydrogen production from H<sub>2</sub>S/H<sub>2</sub>O electrolysis in proton conducting solid oxide membrane reactors", in the frame of IKY-Scholarship

November 2014 - December 2014

## Development of Cell Reactors

EQF level 8

Institute of Micro Process Engineering, Karlsruhe Institute Technology (KIT), Karlsruhe, Germany

- "Fabrication and evaluation of a cell reactor", in the frame of H<sub>2</sub>S-Proton project, visiting researcher

October 2010 - October 2011 **Master of Science in Energy Systems, MSc** EQF level 7

School of Science and Technology, International Hellenic University (IHU), Thessaloniki, Greece

- Thesis: "Renovation vs. new construction. An integrated comparison"
- Specialization stream: Renewable Energy

October 2004 - October 2010 **Diploma in Mechanical Engineering - Bachelor of Science in BSc** EQF level 6

Dept. of Mechanical Engineering, University of Western Macedonia (UOWM), Kozani, Greece

- Thesis: "Synthesis and study of the structural characteristics of the microstructure, and hydrogenation / dehydrogenation of bimetallic materials stoichiometry  $Zr_{0.7}Ti_{0.3}Cr_{2-x}V_xNi_y$  ( $x=0.4, 0.8$   $y=0, 0.4$ )"
- Specialization stream: Energy

## PERSONAL SKILLS

Mother tongue(s) Greek

Other language(s)

	UNDERSTANDING		SPEAKING		WRITING
	Listening	Reading	Spoken interaction	Spoken production	
English	C2	C2	C2	C2	C2
Level C2 Certification of English language (excellent knowledge) from the International Hellenic University (IHU)					
French	A1	A2	A1	A1	A2

Levels: A1/A2: Basic user - B1/B2: Independent user - C1/C2 Proficient user  
[Common European Framework of Reference for Languages](#)

Digital competence

SELF-ASSESSMENT				
Information processing	Communication	Content creation	Safety	Problem solving
Proficient user	Proficient user	Proficient user	Proficient user	Proficient user
Holder of the National Computers Skills Certification (equivalence with ECDL)				

- Excellent command of Microsoft Office suite (Word, Excel, Access, PowerPoint)
- Good command of technical software for management of energy systems (RETScreen, HOMER)
- Excellent command of data design and processing software (Origin)
- Good command of 2D and 3D computer-aided design and drafting software (AutoCAD)

Communication skills

- Ability to speak in front of an audience with fluency and clarity
- Active in scientific discussions, demonstrating maturity and strong ability to defend ideas
- Ability to communicate and collaborate with groups of varying knowledge background within a multicultural environment

Organisational / managerial skills

- Organization and support of events and meetings in the frame of the BlackSea-ERA.NET H<sub>2</sub>S-Proton project: Kick-off meeting, Skype meetings
- Organization of presentations at Final Conference meeting, BS-ERA.NET (December 11-12<sup>th</sup>, 2012 Bucharest, Romania), BSEC meeting (May 21<sup>st</sup>, 2013, Istanbul, Turkey), and completion of BS-ERA.NET Pilot Call projects (May 12<sup>th</sup>, 2015, Bucharest, Romania)
- Ability to develop and use administrative tools and procedures in research projects
- Technical reporting and financial management, giving attention to detail and accuracy
- Supervision of diploma/master thesis and training of students and research staff (Annex II)

- Job skills**
- Familiar with EU funding tools (FP7, H2020, ERANET, INTERREG, ERASMUS, etc.) and building of consortia
  - Ability to assess and initiate activities in problems-solving independently and in team work
  - Design, management and updates of H<sub>2</sub>S-PROTON Project website: [www.h2sproton.cperi.certh.gr](http://www.h2sproton.cperi.certh.gr)
  - Ability to be creative when working autonomously or as part of a team in an international context
  - Stress tolerance and ability to take responsibility
  - Ability to apply knowledge in practical solutions and make reasoned decisions
  - Knowledge on day-to-day life in a research laboratory environment

- Other skills**
- Design of the H<sub>2</sub>S-PROTON Project logo
  - Experience and willingness to travel
  - Interest in new learning experiences
  - Amateur pianist

**Driving licence** B

## ADDITIONAL INFORMATION

---

- Publications**  
(Annex I)
- 1 Chapter in a Book
  - 6 publications in Scientific Peer-Reviewed Journals
  - 21 publications in Conference Proceedings

- Presentations in Conferences**  
(Annex I)
- Participation with oral and poster presentations in 21 National and International Scientific Conferences and Symposia

- Research Projects**
- European Union, Black Sea ERA.NET: "H<sub>2</sub> production from H<sub>2</sub>S decomposition in micro-structured proton conducting solid oxide membrane reactors", 2012-2015
  - Ministry of Education and Life Long Learning, THALIS: "Development of novel catalyst composites via the synergy of structure/surface promoters for the simultaneous abatement of Nitrogen (NO<sub>x</sub>) and Nitrous (N<sub>2</sub>O) oxides", 2011-2015

- Seminars / Courses**
- "Ecological Transportation in Thessaloniki", ECOCITY, International Hellenic University, May 2011, Thessaloniki, Greece
  - "Energy Strategic Management", International Hellenic University, June 2011, Thessaloniki, Greece
  - "Strategies and Best Practice in Local Government", International Hellenic University, November 2011, Thessaloniki, Greece

- Honours and awards**
- Holder of a Training and Specialization Research Scholarship awarded by the Chemical Process & Energy Resources Institute (CPERI), Centre for Research & Technology Hellas (CERTH) (2012-2015)
    - CPERI-BASF agreement "FCC catalyst evaluation for BASF using pilot plant and bench scale facilities"
    - H<sub>2</sub>S-PROTON: "Hydrogen production from H<sub>2</sub>S decomposition in high temperature proton conducting solid oxide membrane reactors", Black Sea – ERA-Net program
  - Holder of a Scholarship (IKY) "Integrated Management of Sea and Inland Waters", be financed by the Financial Mechanism of the European Economic Area (FM EEA, 2009-2014) and the Public Investments Programme, for the elaboration of a part of a doctoral thesis, in cognitive fields falling within the field of sea and inland water resources managements in University/Institution in Norway
  - Holder of Conference Attendance Aid Grant, awarded by the SSI-21 Grant Commission

- Memberships**
- Technical Chamber of Greece

## ANNEXES

- Annex I: List of publications of research
- Annex II: List of Supervisions and Trainings of students

## ANNEX I: Publications

**Chapter in a Book:**

“Bio-hydrogen: Production technologies, prospects and socio-economic aspects”, Z. Ioakeimidis, Tz. Kraia, M. Ouzounidou, G.E. Mamellos, Ch. 12 in “*Biofuels - Sustainable Energy*”, Editors: N. Karnavos, A. Lappas and G.E. Mamellos; Tziolas Editions, **2014**.

**Publications in Scientific Peer-Reviewed Journals:**

1. “An electrocatalytic membrane-assisted process for hydrogen production from H<sub>2</sub>S in Black Sea: Preliminary results”, D. Ipsakis, Tz. Kraia, G.E. Mamellos, M. Ouzounidou, S. Voutetakis, R. Dittmeyer, A. Dubbe, K. Haas-Santo, M. Konsolakis, H.E. Figen, N.O. Guldal, S.Z. Baykara, *International Journal of Hydrogen Energy* **40** (2015) 7530-7538.
2. “Hydrogen production by Ethanol Steam Reforming (ESR) over CeO<sub>2</sub> supported transition metal (Fe, Co, Ni, Cu) catalysts: Insights into the structure-activity relationships”, Michalis Konsolakis, Zisis Ioakimidis, Tzoulia Kraia, George Mamellos, *Catalysts*, **6** (2016) 39.
3. “H<sub>2</sub>S in Black Sea: Turning an environmental threat to an opportunity for clean H<sub>2</sub> production via an electrochemical membrane reactor. Research progress in H<sub>2</sub>S-PROTON Project”, Tzoulia Kraia, Michalis Konsolakis and George E. Mamellos, *MATEC Web of Conferences*, **41** (2016), 04002.
4. “Electrochemical performance of Co<sub>3</sub>O<sub>4</sub>/CeO<sub>2</sub> electrodes in H<sub>2</sub>S/H<sub>2</sub>O atmospheres in a proton-conducting ceramic symmetrical cell with BaZr<sub>0.7</sub>Ce<sub>0.2</sub>Y<sub>0.1</sub>O<sub>3</sub> solid electrolyte”, Tz. Kraia, S. Wachowski, E. Vøllestad, R. Strandbakke, M. Konsolakis, T. Norby, G.E. Mamellos, accepted for publication (<https://doi.org/10.1016/j.ssi.2017.04.010>).
5. “Catalytic decomposition of H<sub>2</sub>S to H<sub>2</sub> production over ceria supported transition metal (Co, Ni, Fe and Cu) catalysts”, Tz. Kraia, M. Ouzounidou, M. Konsolakis, G.E. Mamellos, submitted.
6. “Techno-economic & Feasibility Assessment Study of an Autonomous Energy System Exploiting H<sub>2</sub>S from Black Sea Waters Towards H<sub>2</sub> and H<sub>2</sub>SO<sub>4</sub>”, D. Ipsakis, Tz. Kraia, P. Fylaki, M. Ouzounidou, S. Papadopoulou, S. Voutetakis and \*G.E. Mamellos, In preparation.

**Publications in Conference Proceedings**

1. T. Kraia, S.S. Makridis, E. Pavlidou, A. Ioannidou, E.S. Kikkinides, A.K. Stubos, “Synthesis, structural and hydrogenation characteristics of Ni-substituted AB<sub>2</sub>-type (Zr-rich) compounds”, *5<sup>th</sup> International Conference on Surfaces, Coatings and Nanostructured Materials (NANOSMAT-5)*, Reims Congress Centre, October 19<sup>th</sup>-21<sup>st</sup>, **2010**, Reims, France.
2. T. Kraia, M. Ouzounidou, V. Stathopoulos, M. Konsolakis, S. Voutetakis, G. Mamellos, “Hydrogen production from H<sub>2</sub>S decomposition in micro-structured proton-conducting (H<sup>+</sup>) solid oxide membrane reactors”, *12<sup>th</sup> Panhellenic Symposium on Catalysis*, October 25<sup>th</sup>-27<sup>th</sup>, **2012**, Chania, Greece.
3. T. Kraia, M. Ouzounidou D. Ipsakis, M. Konsolakis S. Voutetakis, G. Mamellos, “H<sub>2</sub>S catalytic decomposition over transition metal catalysts supported on mixed oxides”, *9<sup>th</sup> National Conference on Chemical Engineering*, May 23<sup>rd</sup>-25<sup>th</sup>, **2013**, Athens, Greece.
4. R. Dittmeyer, G. Mamellos, S.S. Voutetakis, M. Ouzounidou, T. Kraia, S.Z. Baykara, A. Dubbe, “Development of a proton-conducting electrochemical membrane reactor for catalyst-aided generation of Hydrogen from H<sub>2</sub>S/H<sub>2</sub>O mixtures”, *11<sup>th</sup> International Conference on Catalysis in Membrane Reactors*, July 07<sup>th</sup>-11<sup>th</sup>, **2013**, Porto, Portugal.
5. T. Kraia, M. Ouzounidou, G. Mamellos, D. Ipsakis, S. Papadopoulou, S. Voutetakis, “Decomposition of H<sub>2</sub>S to H<sub>2</sub> in the absence and presence of H<sub>2</sub>O: Catalytic experiments and thermodynamic calculations”, *16<sup>th</sup> Conference Process Integration, Modelling and Optimisation for Energy Saving and Pollution Reduction*, September 29<sup>th</sup>-October 02<sup>nd</sup>, **2013**, Rhodes, Greece.
6. T. Kraia, M. Ouzounidou, M. Konsolakis, G. Mamellos, V. Stathopoulos, “Development of an innovative solid proton conductor electrolyte membrane reactor to produce H<sub>2</sub> from H<sub>2</sub>S”, *6<sup>th</sup> Panhellenic Conference of Ceramics*, April 03<sup>rd</sup>-04<sup>th</sup>, **2014**, Athens, Greece.
7. T. Kraia, M. Ouzounidou, M. Konsolakis, G. Mamellos, V. Stathopoulos, “Development of transition metal catalysts deposited on mixed rare earth oxides for the efficient decomposition of H<sub>2</sub>S”, *6<sup>th</sup> Panhellenic Conference of Ceramics*, April 03<sup>rd</sup>-04<sup>th</sup>, **2014**, Athens, Greece.
8. D. Ipsakis, T. Kraia, G.E. Mamellos, M. Ouzounidou, S. Voutetakis, R. Dittmeyer, A. Dubbe, K. Haas-Santo, M. Konsolakis, H.E. Figen, N.O. Guldal, S.Z. Baykara, “An electrocatalytic membrane-assisted process for hydrogen production from H<sub>2</sub>S in Black Sea: Preliminary results”, *International Conference on Clean Energy (ICCE-2014)*, June 08<sup>th</sup>-12<sup>th</sup>, **2014**, Istanbul, Turkey.
9. T. Kraia, D. Ipsakis, M. Ouzounidou, M. Konsolakis, G. Mamellos, “Catalytic decomposition of H<sub>2</sub>S to H<sub>2</sub> in the absence/presence of H<sub>2</sub>O over Cu/Co-based catalysts supported on CeO<sub>2</sub>”, *Fundamentals and Applications of Cerium Dioxide in Catalysis*, July 11<sup>th</sup>-14<sup>th</sup>, **2014**, Udine, Italy.

10. T. Kraia, M. Ouzounidou, M. Konsolakis, V. Stathopoulos, G. Marnellos, "Catalytic decomposition of H<sub>2</sub>S over mixed-oxides CeO<sub>2</sub>-Co<sub>3</sub>O<sub>4</sub>", *13<sup>th</sup> Panhellenic Symposium on Catalysis*, October 16<sup>th</sup>-18<sup>th</sup>, **2014**, Pella, Greece
11. Tz. Kraia, M. Konsolakis, M. Ouzounidou, V. Stathopoulos, G.E. Marnellos, "H<sub>2</sub> production during H<sub>2</sub>S decomposition in the presence of excess H<sub>2</sub>O on catalytic systems of Co/CeO<sub>2</sub>" *10<sup>th</sup> National Conference on for Renewable Energy Sources*, November 26<sup>th</sup>-27<sup>th</sup>, **2014**, Thessaloniki, Greece.
12. D. Ipsakis, Tz. Kraia, P. Fylaki, M. Ouzounidou, S. Papadopoulou, S. Voutetakis, G.E. Marnellos, "Design and feasibility study of an integrated H<sub>2</sub>S utilization process from the Black Sea waters to energy and H<sub>2</sub>SO<sub>4</sub> production", *10<sup>th</sup> National Conference on Chemical Engineering*, June 04<sup>th</sup>-06<sup>th</sup>, **2015**, Patra, Greece.
13. Tz. Kraia, G.E. Marnellos, "Electrochemical-aided management of H<sub>2</sub>S pollutant for H<sub>2</sub> generation and environmental protection", *NMP Istanbul Brokerage Event (HORIZON 2020 NMPB 2016-2017)*, October 22<sup>nd</sup>, **2015**, Sabanci University, Istanbul, Turkey.
14. Tz. Kraia, G.E. Marnellos, "H<sub>2</sub>S in Black Sea: Turning an environmental threat to an opportunity for clean energy production. Progress achieved and experience gained in the framework of BLACK SEA ERANET, H<sub>2</sub>S-PROTON project", *8<sup>th</sup> International Black Sea Symposium on Science, Technology & Innovation in the Black Sea: Moving Forward*, November 19<sup>th</sup>-20<sup>th</sup>, **2015**, Athens, Greece.
15. Tz. Kraia, M. Konsolakis, G.E. Marnellos, "H<sub>2</sub>S in Black Sea: Turning an environmental threat to an opportunity for clean H<sub>2</sub> production via an electrochemical membrane reactor. Research progress in H<sub>2</sub>S-PROTON Project", *1<sup>st</sup> Mini Conference on Emerging Engineering Applications (MCEEA 2015)*, November 26-27<sup>th</sup>, **2015**, Chalkida, Greece.
16. Tz. Kraia, S. Wachowski, E. Vøllestad, R. Strandbakke, M. Konsolakis, G.E. Marnellos, T. Norby, "Remediation of Black Sea ecosystem via H<sub>2</sub>S electrolysis in a proton-conducting membrane reactor for "green" H<sub>2</sub> production", *18<sup>th</sup> International Conference on Solid State Protonic Conductors*, 18<sup>th</sup>-23<sup>rd</sup> September, **2016**, Oslo, Norway.
17. Tz. Kraia, M. Konsolakis, G.E. Marnellos, "High H<sub>2</sub>S content sour gas reserves process for hydrogen production on Co/CeO<sub>2</sub> catalysts", *14<sup>th</sup> Panhellenic Symposium on Catalysis*, October 13<sup>th</sup>-15<sup>th</sup>, **2016**, Patra, Greece.
18. Dimitris Ipsakis, Tzoulia Kraia, Michalis Konsolakis and George Marnellos, "Remediation of Black Sea ecosystem via H<sub>2</sub>S-H<sub>2</sub>O co-electrolysis in a proton-conducting membrane reactor for "Green" H<sub>2</sub> Production: A feasibility study of the integrated approach", *2<sup>nd</sup> HAEE INTERNATIONAL CONFERENCE, The landscape in the new era of energy transition: Challenges, investment opportunities and technological innovations*, May 18<sup>th</sup>-20<sup>th</sup>, **2017**, Athens, Greece.
19. Tz. Kraia, R. Strandbakke, M. Konsolakis, T. Norby, G.E. Marnellos, "Development of sulphur tolerant Co<sub>3</sub>O<sub>4</sub>/CeO<sub>2</sub> electrodes for simultaneous H<sub>2</sub>S/H<sub>2</sub>O electrolysis in a proton conductor cell", *10<sup>th</sup> National Conference on Chemical Engineering*, May 25<sup>th</sup>-27<sup>th</sup>, **2017**, Thessaloniki, Greece.
20. Tzoulia Kraia, Vassilis Stathopoulos, Ragnar Strandbakke, Truls Norby, George Marnellos, "Electrochemical characterization of Co<sub>3</sub>O<sub>4</sub>/CeO<sub>2</sub> mixed oxide electrode in a proton conducting solid oxide symmetrical cell", *21<sup>st</sup> International Conference on Solid State Ionics*, June 18<sup>th</sup> -23<sup>rd</sup>, **2017**, Padua, Italy.
21. Tzoulia Kraia, Vasileios Kyriakou, Michalis Konsolakis, Ragnar Strandbakke, George Marnellos, "Electrochemical performance of a Co<sub>3</sub>O<sub>4</sub>-CeO<sub>2</sub>/BZ72/BGLC proton conducting solid oxide cell fed with H<sub>2</sub>S/H<sub>2</sub>O mixtures", *21<sup>st</sup> International Conference on Solid State Ionics*, June 18<sup>th</sup> -23<sup>rd</sup>, **2017**, Padua, Italy.

## ANNEX II: Supervisions and Trainings

### Diploma Thesis

1. "Catalytic decomposition of H<sub>2</sub>S over mixed oxides supported transition metal catalysts", Efstratios Apostolakis/ Grigoriadou-Sarantidou Anna, A thesis submitted for the diploma of Mechanical Engineering on the Department of Mechanical Engineering, University of Western Macedonia, **2013**, Kozani, Greece.
2. "Catalytic decomposition of H<sub>2</sub>S towards H<sub>2</sub> production over Co/CeO<sub>2</sub> catalysts in the excess of H<sub>2</sub>O", Anestis Aggelidis, A thesis submitted for the diploma of Mechanical Engineering on the Department of Mechanical Engineering, University of Western Macedonia, **2015**, Kozani, Greece.

### Master Thesis:

1. "Feasibility study of hydrogen production and power in fuel cell reactors, from the H<sub>2</sub>S-rich Black Sea waters", Stavros Michailos, A thesis submitted for the degree of Master of Science (MSc) in Energy Systems, School of Science and Technology, International Hellenic University, **2012**, Thessaloniki, Greece
2. "Energetic assessment and economic design of an autonomous RES system for the electrochemical production of H<sub>2</sub> from H<sub>2</sub>S Black Sea Waters", Panagiota Fylaki, A thesis submitted for the degree of Master of Science (MSc) in Energy Systems, School of Science and Technology, International Hellenic University, **2014**, Thessaloniki, Greece.

**Training:**

1. "Evaluation of high H<sub>2</sub>S content sour gas reserves process for hydrogen production on Co/CeO<sub>2</sub> catalysts via catalytic reaction  $\text{CH}_4 + 2\text{H}_2\text{S} \rightarrow \text{CS}_2 + 4\text{H}_2$ ,  $\Delta H = 232 \text{ kJ/mol}$ ", Athina Mourouzidou, A training on the Department of Mechanical Engineering, University of Western Macedonia, **2014**, Kozani, Greece.
2. "H<sub>2</sub>S electrolysis in a proton conducting membrane reactor for H<sub>2</sub> production", Kwnstantinos Panwris, A training on the Department of Mechanical Engineering, University of Western Macedonia, **2015**, Kozani, Greece.